NASA Conference Publication 2045

Part 1

(NASA-CP-2045-Pt-1) ADVANCED TECHNOLOGY AIRFOIL RESEARCH, VOLUME 1, PART 1 (NASA) 454 p HC A20/MF A01 CSCL 01A

N79-20030 THRU N79-20059 Unclas G3/02 16557

Advanced Technology Airfoil Research

Volume I

Proceedings of a conference
held at Langley Research Center
Hampton, Virginia, March 7-9, 1978

NASA

NASA Conference Publication 2045

Part 1

Advanced Technology Airfoil Research

Volume I

Proceedings of a conference
held at Langley Research Center
Hampton, Virginia, March 7-9, 1978

National Aeronautics
and Space Administration

Scientific and Technical
Information Office

1979

PREFACE

This NASA Conference Publication contains the proceedings of the NASA Conference on Advanced Technology Airfoil Research held at Langley Research Center on March 7-9, 1978, which have unlimited distribution. Conference cochairmen were Alfred Gessow, NASA Headquarters, and Robert F. Bower, Langley Research Center. Honorary cochairmen were Ira H. Abbott, NASA Headquarters (retired), and Richard T. Whitcomb, Langley Research Center.

The conference was planned to provide a comprehensive review of all NASA airfoil research, conducted both in-house and under grant and contract. In addition, a broad spectrum of airfoil research outside of NASA was reviewed. A total of 64 technical papers were presented at 12 sessions. Six workshops were also held to discuss progress, further immediate and long-range research needs, and important unresolved issues. A roundtable discussion summarized the technical sessions and workshops.

This volume contains papers presented at technical sessions covering the following subjects:

(1) Airfoil Analysis and Design of Single-Element Airfoils
(2) Airfoil Analysis and Design of Multielement Airfoils
(3) Airfoil Analysis and Design Topics
(4) Research Facilities and Test Techniques
(5) Facilities and Test Technique Topics
(6) Unsteady Aerodynamics

The major thrusts of the technical sessions were in three areas: development of computational aerodynamic codes for airfoil analysis and design, development of experimental facilities and test techniques, and all types of airfoil applications. The conference proceedings are presented in two volumes: Volume I is unclassified with unlimited distribution and Volume II is unclassified but with limited distribution.

The included papers are largely as submitted as camera-ready copy. Only minor editorial revisions have been made and a title page and abstract have been added.

Use of trade names or names of manufacturers in this report does not constitute an official endorsement of such products or manufacturers, either expressed or implied, by the National Aeronautics and Space Administration.

P. K. Pierpont, Conference Organizer

CONTENTS

PREFACE iii

PART 1

1. NASA RESEARCH OBJECTIVES AND ROLES 1
Alfred Gessow

2. LANGLEY AIRFOIL-RESEARCH PROGRAM 11
Percy J. Bobbitt

3. OVERVIEW OF TWO-DIMENSIONAL AIRFOIL RESEARCH AT AMES RESEARCH CENTER 39
Gary T. Chapman

AIRFOIL ANALYSIS AND DESIGN FOR SINGLE-ELEMENT AIRFOILS

Chairman: Jerry C. South
NASA Langley Research Center

4. TRANSONIC AIRFOIL CODES 45
P. R. Garabedian

5. APPLICATION OF DIRECT-INVERSE TECHNIQUES TO AIRFOIL ANALYSIS AND DESIGN 55
Leland A. Carlson and Bruce M. Rocholl

6. LOW SPEED AIRFOIL DESIGN AND ANALYSIS 73
Richard Eppler and Dan M. Somers

7. A CONSISTENT DESIGN PROCEDURE FOR SUPERCRITICAL AIRFOILS IN FREE AIR AND A WIND TUNNEL 101
Vijaya Shankar, Norman D. Malmuth, and Julian D. Cole

8. PROSPECTS FOR COMPUTING AIRFOIL AERODYNAMICS WITH REYNOLDS AVERAGED NAVIER-STOKES CODES 119
George S. Deiwert and H. E. Bailey

9. AN EVALUATION OF FOUR SINGLE ELEMENT AIRFOIL ANALYTIC METHODS . . . 133
R. J. Freuler and G. M. Gregorek

AIRFOIL ANALYSIS AND DESIGN FOR MULTIELEMENT AIRFOILS

Chairman: Paul R. Garabedian
New York University

10. UPGRADED VISCOUS FLOW ANALYSIS OF MULTIELEMENT AIRFOILS 163
Guenter W. Brune and Joseph W. Manke

PRECEDING PAGE BLANK NOT FILMED

11. NUMERICAL SOLUTION OF THE NAVIER-STOKES EQUATIONS FOR ARBITRARY TWO-DIMENSIONAL MULTI-ELEMENT AIRFOILS 183
Joe F. Thompson, Louie Turner, W. Serrill Long, and John H. Bearden

12. THE ANALYSIS AND DESIGN OF TRANSONIC TWO-ELEMENT AIRFOIL SYSTEMS 209
G. Volpe and B. Grossman

13. IMPROVEMENTS IN SURFACE SINGULARITY ANALYSIS AND DESIGN METHODS 221
Dean R. Bristow

14. OPTIMIZATION OF MULTIELEMENT AIRFOILS FOR MAXIMUM LIFT 237
Lawrence E. Olson

AIRFOIL ANALYSIS AND DESIGN TOPICS - SESSION I

Chairman: Paul R. Garabedian
New York University

15. WAKE CURVATURE AND TRAILING EDGE INTERACTION EFFECTS IN VISCOUS FLOW OVER AIRFOILS 255
R. E. Melnik

16. A STUDY OF THE INTERACTION OF A NORMAL SHOCK WAVE WITH A TURBULENT BOUNDARY LAYER AT TRANSONIC SPEEDS 271
A. F. Messiter and T. C. Adamson, Jr.

17. RECENT DEVELOPMENTS IN FINITE ELEMENT ANALYSIS FOR TRANSONIC AIRFOILS 281
M. M. Hafez and E. M. Murman

18. SUPERCRITICAL TESTS OF A SELF-OPTIMIZING, VARIABLE-CAMBER WIND TUNNEL MODEL 297
Ely S. Levinsky and Richard L. Palko

19. APPLICATION OF NUMERICAL OPTIMIZATION TO THE DESIGN OF ADVANCED SUPERCRITICAL AIRFOILS. 315
Raymond R. Johnson and Raymond M. Hicks

AIRFOIL ANALYSIS AND DESIGN TOPICS - SESSION II

Chairman: Jerry C. South
NASA Langley Research Center

20. IMPROVED PREDICTION OF LAMINAR LEADING EDGE SEPARATION 327
R. N. Herring and W. L. Ely

21. THE PREDICTION OF TWO-DIMENSIONAL AIRFOIL STALL PROGRESSION 335
Lloyd W. Gross

22. APPLICATION OF THE AMI $C_{l_{max}}$ PREDICTION METHOD TO A NUMBER OF AIRFOILS 347
F. A. Dvorak and B. Maskew

23. A NEW FLOW MODEL FOR HIGHLY SEPARATED AIRFOIL FLOWS AT LOW SPEEDS 367
Glen W. Zumwalt and Sharad N. Naik

24. INVERSE BOUNDARY-LAYER TECHNIQUE FOR AIRFOIL DESIGN 383
M. L. Henderson

RESEARCH FACILITIES AND TEST TECHNIQUES

Chairman: Richard W. Barnwell
NASA Langley Research Center

25. LANGLEY'S TWO-DIMENSIONAL RESEARCH FACILITIES - CAPABILITIES AND PLANS 399
Edward J. Ray

26. DEVELOPMENTS IN AIRFOIL TESTING TECHNIQUES AT UNIVERSITY OF SOUTHAMPTON 415
Michael J. Goodyer

27. A NEW AIRFOIL RESEARCH CAPABILITY 425
Charles L. Ladson

28. DESIGN AND CALIBRATION OF SLOTTED WALLS FOR TRANSONIC AIRFOIL WIND TUNNELS 433
Richard W. Barnwell, William G. Sewall, and Joel L. Everhart

29. PROGRESS REPORT: SOME STEADY AND OSCILLATING AIRFOIL TEST RESULTS, INCLUDING THE EFFECTS OF SWEEP, FROM THE TUNNEL SPANNING WING 445
Franklin O. Carta, Arthur O. St. Hilaire, James B. Rorke, and W. Donald Jepson

PART 2*

FACILITIES AND TEST TECHNIQUE TOPICS - SESSION I

Chairman: John D. Lee
The Ohio State University

30. A PARAMETRIC EXPERIMENTAL STUDY OF THE SLOTTED-WALL BOUNDARY CONDITION 459
Joel L. Everhart and Richard W. Barnwell

31. TRANSONIC ASSESSMENT OF TWO-DIMENSIONAL WIND TUNNEL WALL INTERFERENCE USING MEASURED WALL PRESSURES 473
William B. Kemp, Jr.

32. RESEARCH ON SELF-CORRECTING WIND TUNNELS 487
R. J. Vidal and J. C. Erickson, Jr.

33. ANALYTICAL DESIGN OF A CONTOURED WIND-TUNNEL LINER FOR SUPERCRITICAL TESTING 499
Perry A. Newman and E. Clay Anderson

34. EVALUATION OF INTERFERENCE IN THE OSU 6 IN. BY 22 IN. TRANSONIC AIRFOIL TUNNEL 511
John D. Lee

FACILITIES AND TEST TECHNIQUE TOPICS - SESSION II

Chairman: Richard W. Barnwell
NASA Langley Research Center

35. VISUALIZATION OF THE SEPARATION AND SUBSEQUENT TRANSITION NEAR THE LEADING EDGE OF AIRFOILS 527
Anthony V. Arena and Thomas J. Mueller

36. INSTRUMENTATION, TECHNIQUES AND DATA REDUCTION ASSOCIATED WITH AIRFOIL TESTING PROGRAMS AT WICHITA STATE UNIVERSITY 539
Edward J. Rodgers, William H. Wentz, Jr., and H. C. Seetharam

37. APPLICATION OF THE LASER VELOCIMETER TO AIRFOIL RESEARCH 559
Danny R. Hoad

38. APPLICATIONS OF DYNAMIC MEASUREMENT TECHNIQUES TO WIND-TUNNEL TESTING 571
F. K. Owen

39. HOLOGRAPHY AND LDV TECHNIQUES, THEIR STATUS AND USE IN AIRFOIL RESEARCH 589
D. A. Johnson and W. D. Bachalo

*Papers 30 to 48 are presented under separate cover.

40. SECTION DRAG COEFFICIENTS FROM PRESSURE PROBE TRAVERSES OF A WING WAKE AT LOW SPEEDS 601
Lawrence C. Montoya, Paul F. Bikle, and Richard D. Banner

41. FLIGHT TEST TECHNIQUES FOR LOW SPEED AIRFOIL EVALUATION 623
M. J. Hoffmann, G. M. Gregorek, and G. S. Weislogel

42. IN-FLIGHT THREE-DIMENSIONAL BOUNDARY LAYER AND WAKE MEASUREMENTS FROM A SWEPT SUPERCRITICAL WING 643
David P. Lux

UNSTEADY AERODYNAMICS

Chairman: Samuel R. Bland
NASA Langley Research Center

43. A PROCEDURE FOR ANALYZING TRANSONIC FLOW OVER HARMONICALLY OSCILLATING AIRFOILS 657
Warren H. Weatherill, F. Edward Ehlers, and James D. Sebastian

44. A NEW TWO-DIMENSIONAL OSCILLATING WING APPARATUS FOR UNSTEADY AERODYNAMICS RESEARCH 671
Sanford S. Davis and Gerald N. Malcolm

45. SOME CALCULATIONS OF TRANSONIC POTENTIAL FLOW FOR THE NACA 64A006 AIRFOIL WITH AN OSCILLATING FLAP 689
Robert M. Bennett and Samuel R. Bland

46. OBSERVATIONS ON THE DYNAMIC STALL CHARACTERISTICS OF ADVANCED HELICOPTER ROTOR AIRFOILS 701
L. Dadone

47. TRANSONIC FLOW OVER THE NACA 64A006 WITH AN OSCILLATING FLAP - CALCULATIONS BASED ON THE EULER EQUATIONS 717
R. J. Magnus

48. ROUNDTABLE SUMMARY AND CONFERENCE CONCLUSION 729
Cochairmen: Alfred Gessow and Robert E. Bower

D1

N79-20031

NASA RESEARCH OBJECTIVES AND ROLES

Alfred Gessow
NASA Headquarters

I think that it is very fitting that this conference on advanced technology airfoils be held here at Langley, for this Center is the origin of the well-known and widely-used NASA series airfoils. It was those airfoils, more than any other single factor, I believe, that gave NACA its well-deserved international reputation. I also want to express my pleasure in being a cochairman of a conference which has as its honorary cochairmen Ira Abbott, who spearheaded much of that early effort, and Dick Whitcomb, who is responsible for getting much of the current NASA effort started.

I've put together (fig. 1) an abbreviated chronology of airfoil development in order to put the present NASA airfoil program in perspective. As you can see, the bulk of the NACA airfoil effort occurred in the 1930's and the early 1940's. Although there was some additional effort in the 1940's and early 1950's such as the "H" series for rotorcraft, NASA didn't get back into the airfoil business in a meaningful way until the late 1960's when Whitcomb began his supercritical airfoil work. The success of that effort and the extension of the technology it represented to other applications led to the present expanded airfoil program which was started in the early 1970's.

In structuring our present program, it is instructive to consider the reasons why the NACA series airfoils had the impact they had. The first and obvious one is that they were good airfoils, better in a number of respects than the ones which they eventually replaced. The second is that they were the result of a systematic development program of families of airfoils which were derived from a particular design philosophy and carefully documented. In this way, airplane designers could choose an airfoil that seemed optimum for their use and could assess what performance penalties would occur if they had to deviate from the ideal section because of practical constraints. The key to success, then, was a systematic program which resulted in families of airfoils for different applications with documented characteristics.

This view was brought home to us by the industry representatives who attended a NASA/Industry Airfoil Workshop which we held in Washington in January 1975. The purpose of that workshop was to review and discuss our airfoil program to determine its responsiveness to industry's needs. We received a number of good suggestions from that meeting and adjusted and refocused our program accordingly. The specifics can best be brought out by considering the objectives and elements of our present program (fig. 2).

As you can see, the thrust of the objectives is twofold. One is to research and provide advanced analytical and experimental methods for the design and for the determination of the characteristics of not only single element airfoils, but of multielement airfoil combinations used in aerodynamic controls and high-lift systems (fig. 3). The increased emphasis we are now giving to such airfoil systems is a result of the needs for such information

which was expressed at the 1975 workshop. The analysis and design methods which we research are made available to industry for their use in developing airfoils for their specific use and are also used by us in the second half of our program to develop and document the behavior of generic families of airfoils for a range of aircraft types as shown in figure 4.

The analysis methods which have been and are being developed draw heavily upon and benefit from the remarkable advances made in computational aerodynamics during the past few years. The use of computational codes, coupled with mathematical optimization techniques, constitute a powerful tool for turning out new airfoil designs to satisfy specific requirements. In spite of limitations, these computational methods have proven to be singularly successful for design purposes and can be used to document airfoil characteristics as well, at least at conditions involving no or small amounts of separation. Simplistically, the state of the art can be characterized by the theory-data comparison shown in figure 5. Viscous theory is fine, whether we are talking about low speed calculations or more sophisticated transonic codes, but only until separation occurs. Thus, the problem of handling viscous-dominant flows is receiving wide attention by researchers, and one approach which is starting to show promise is shown in figure 6, which gives results of Prof. Carlson's free-streamline modeling theory applied to a low speed airfoil. Another approach - the use of Navier-Stokes codes - may work for the very low Reynolds number situation wherein laminar separation occurs (fig. 7), as we can see by comparing Mehta's code with a flow visualization experiment and even for unsteady transonic flow at small angles of attack. Unfortunately, such codes do not work as yet for situations involving large regions of turbulent flow and we are placing a great deal of emphasis at our Centers in providing better turbulence models for handling such cases with Navier-Stokes codes.

We have spent and are spending a good deal of effort in the third element of the methods part of our airfoil program in improving existing facilities and developing new ones and in developing test and instrumentation techniques to extend the range and validity of 2-D data. You will be hearing talks on this aspect of our program, and I will only mention here that our stable of facilities, which includes Langley's low-turbulence pressure tunnel, 6- by 28-inch transonic tunnel, and 0.3-meter transonic cryogenic tunnel, and Ames's 2' x 2' transonic tunnel and 11' transonic tunnel, cover the complete Mach number and Reynolds number map for all classes of aircraft combinations.

Insofar as the applications part of our program is concerned, you'll be getting some detailed information regarding our efforts from the following two speakers. I will only mention a few things that we have done to be responsive to the needs and recommendations of the industry as surfaced at the January 1975 workshop: We have expanded our experimental program to document the characteristics of our new supercritical and low speed airfoil designs covering a large range of thickness and design lift coefficients, and in particular, we have included data on high-lift systems; we have initiated and now have in operation an airfoil design and analysis service at Ohio State University; and after a slow start, we have tested a large number of rotorcraft airfoils to get baseline data for new designs which are underway. Our applications program

also includes the design and testing of very thick airfoils for large cargo aircraft, very thin airfoils for turboprop application, and special purpose airfoils for wind generators, RPV's (remotely piloted vehicles), and rotating machinery.

As to where and how the program is carried out, it is clear that the bulk of the design and testing is in-house although we have gotten some excellent university help in obtaining low speed airfoil data. We also look to universities and industry for help in advancing our analytical capability. Langley is our lead Center in this program with an across-the-board capability, with Ames making particular contributions in Navier-Stokes analysis, design optimization procedures, and in acquiring high-lift system and unsteady aerodynamic data. The contributions from the various in-house and outside sources will become apparent as the papers are presented in this conference.

Before turning over the podium to the next speaker, I'd like to say that I think that we have made some solid contributions in airfoil development and hope to make a lot more in the next few years. Much of the success of the Langley program can be attributed to Bob Bower's interest and support in marshalling the resources of the Center behind the program. The other individual who has worked hard and effectively on a day-to-day basis to make the program and this conference go, who has acted as a principal spokesman for the program to the outside community, and who feeds me information as I need it with great patience and humor, Ken Pierpont. I take this opportunity to acknowledge their efforts.

DATE	TYPE	APPLICATION
EARLY 1900's	JOUKOWSKI, GOTTINGEN, NPL, ETC.	MOST AIRCRAFT
1920's	CLARK Y	PROPELLERS
1930's	NACA 4 & 5 DIGIT SERIES	MOST AIRCRAFT
	NACA 1 & 2 SERIES	PROPELLERS
1940's	NACA 6 SERIES	1ST GENERATION JET AIRCRAFT
1950's	NPL "PEAKY"	2ND GENERATION JET AIRCRAFT
1960's	NLR SHOCKLESS, WORTMANN	ROTORCRAFT
1970's	NASA SUPERCRITICAL, GA(W)-1, AND OTHER ADVANCED TECHNOLOGY PROFILES	ALL SUBSONIC AND TRANSONIC AIRCRAFT

Figure 1.- Chronology.

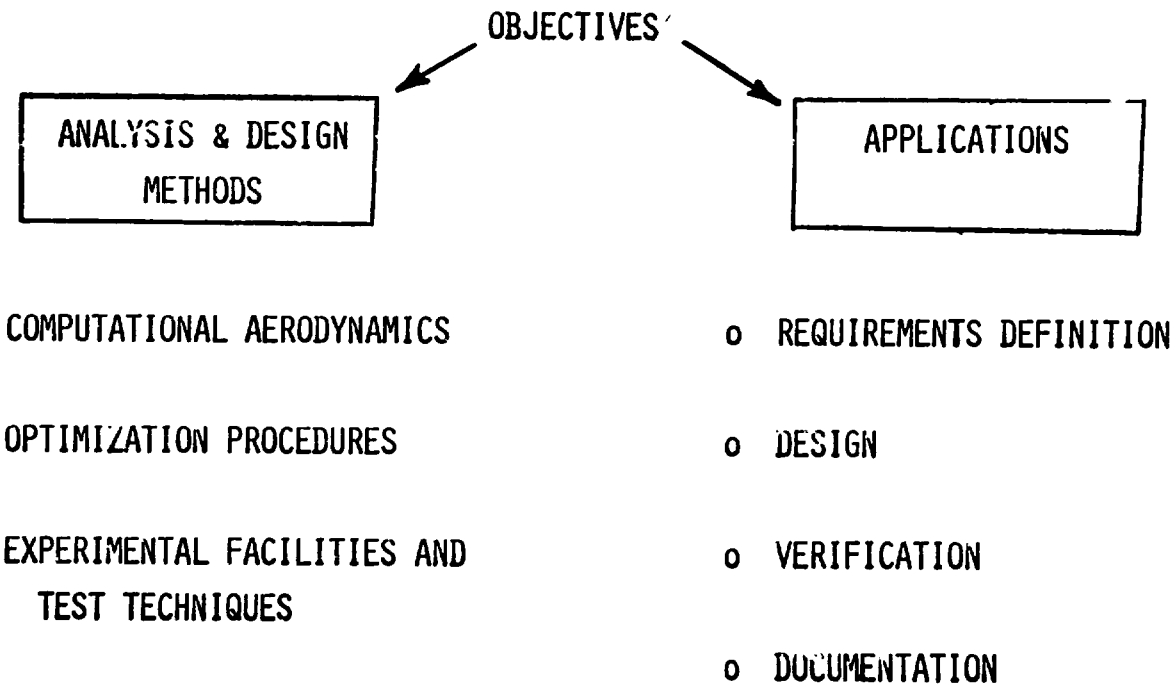

Figure 2.- NASA airfoil development program.

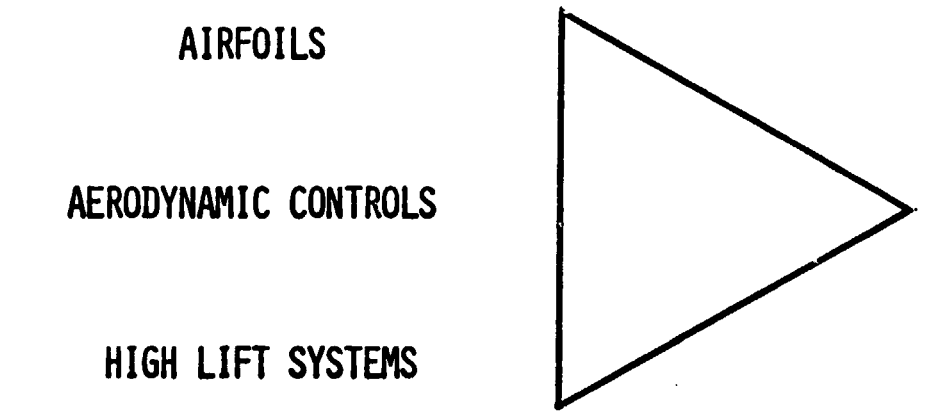

Figure 3.- Single element airfoil thrust.

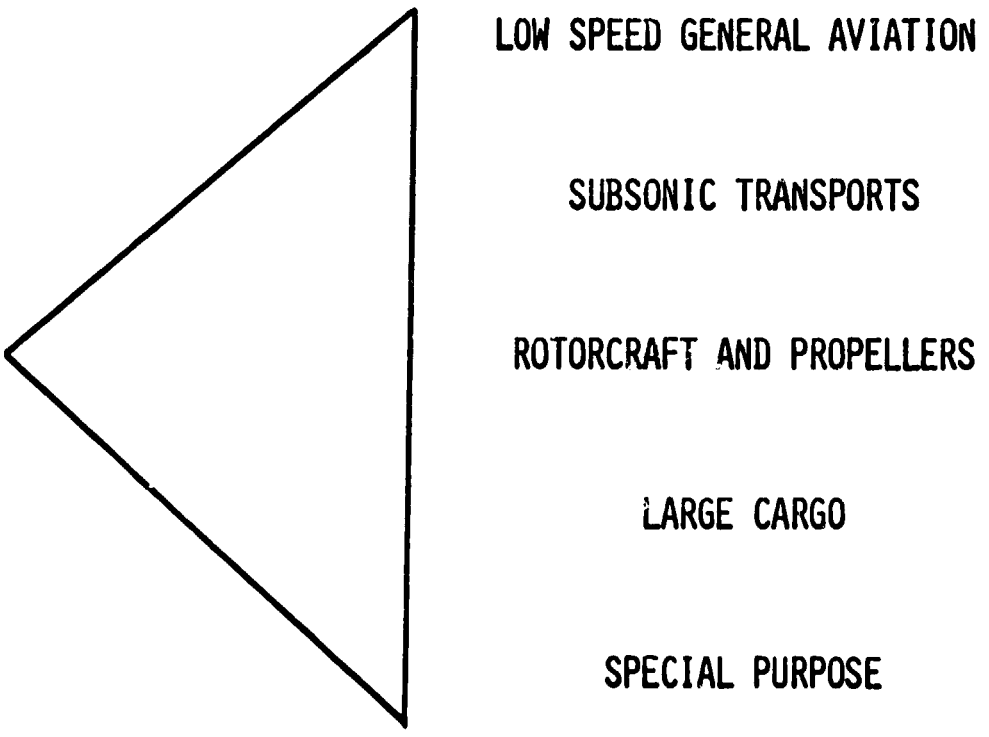

Figure 4.- Airfoil applications.

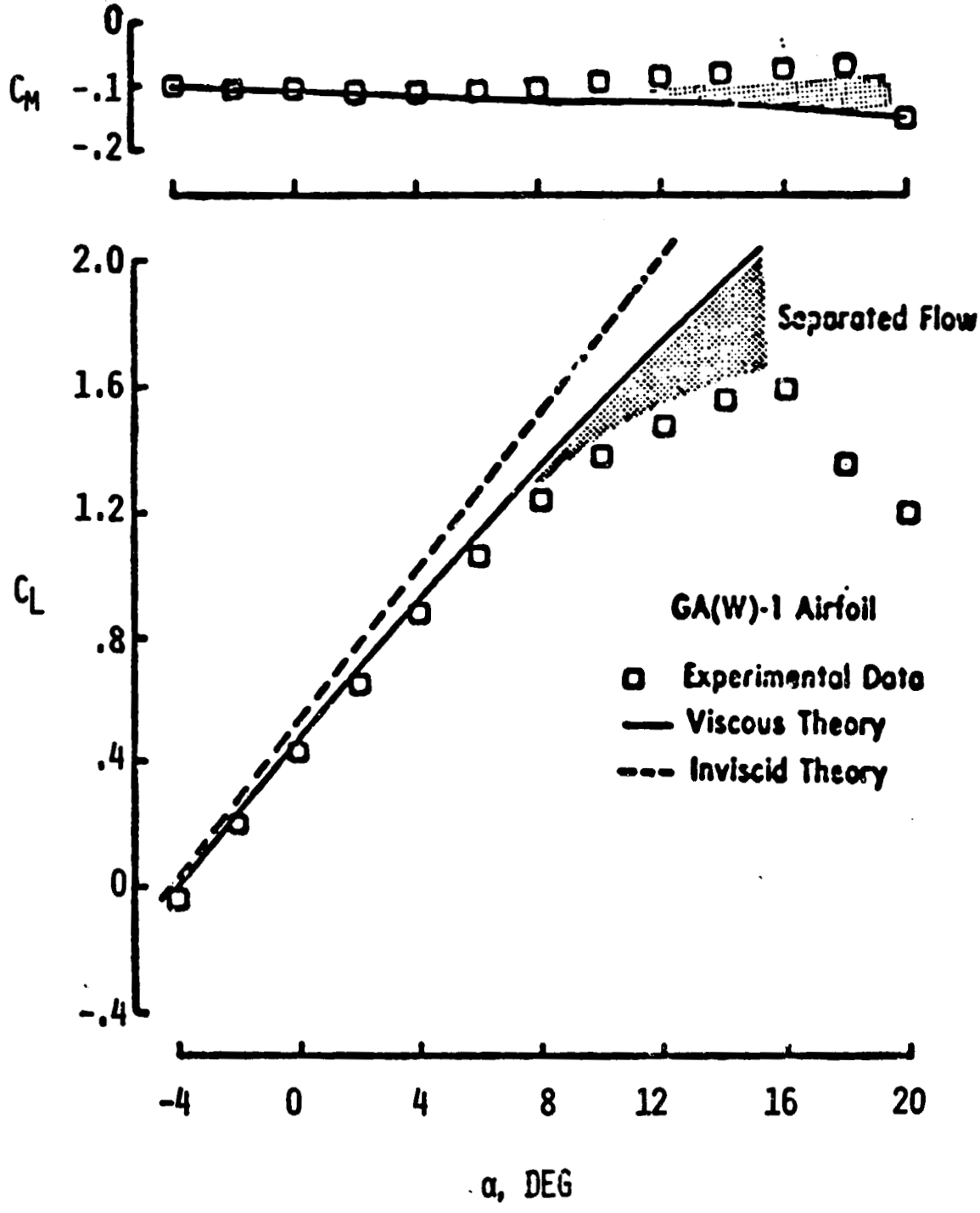

Figure 5.- Airfoil with separated flow.

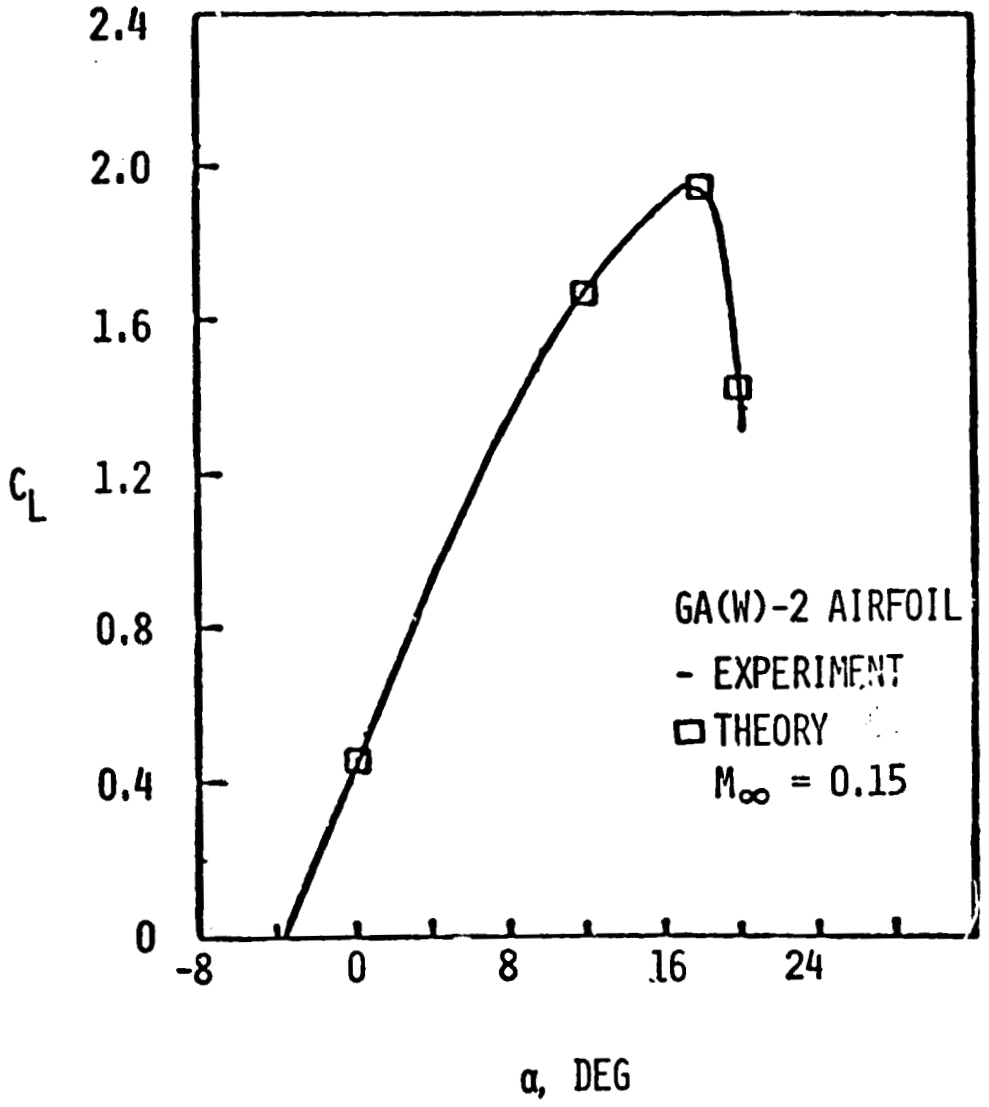

Figure 6.- Massive separation flow model.

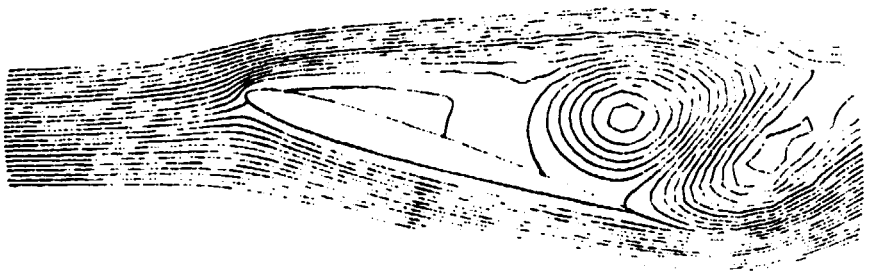

(a) Angle of attack, 15°; Reynolds number, 10^3;
9% thick symmetrical airfoil.

(b) From Prandtl, L. 1952 Essentials of Fluid Dynamics,
p. 200, figure 3.83.

Figure 7.- A qualitative comparison of leading-edge stall.

D2

2

LANGLEY AIRFOIL-RESEARCH PROGRAM

Percy J. Bobbitt
NASA Langley Research Center

INTRODUCTION

The purpose of this paper is to give an overview of past, present, and future airfoil research activities at the Langley Research Center. The immediate past and future occupy most of the discussion; however, past accomplishments and milestones going back to the early NACA years are dealt with in a broad-brush way to give a better perspective of current developments and programs. Indeed the seeds of the current surge in activity were sown a dozen years ago; the pedigree of many of Langley's present-day facilities can be traced to the mid thirties. In addition to the historical perspective, a short description of the facilities which are now being used in the airfoil program is given. This is followed by a discussion of new airfoil developments, advances in airfoil design and analysis tools (mostly those that have taken place over the past 5 or 6 years), and tunnel-wall-interference predictive methods and measurements. The last subject to be treated is future research requirements.

HISTORICAL PERSPECTIVE

Airfoil research at the Langley Memorial Aeronautical Laboratory began shortly after it was established and long before its first tunnel became operational in 1920. As assessment of the state-of-the-art of airfoil technology in the world was made and the airfoil data collected were put in a unified format and published for the benefit of the scientific community in the 1920, 1921, and 1923 NACA annuals (refs. 1 to 3). A few of these early airfoils are shown in figure 1; they indicate in a graphic way the lack of understanding of flow physics that existed in those early days. The airfoil sketched at the top is the USA 1 tested in an MIT tunnel at 13 m/sec (44 ft/sec) and is very similar to the Spad, Sopwith, Italian 2, and Eiffel 53 airfoils. The next two were tested at the Eiffel Laboratory in 1914 and were apparently designed to determine whether the performance of airfoils which are in fact two or three airfoils connected together would be superior to single-hump airfoils. Eiffel 44, the fourth from the top, has what appears to be a separation step on the top side; the philosophy behind its design is somewhat more obscure. It should be noted that the Eiffel Laboratory was probably the leading airfoil research center in the world prior to World War I and dozens of excellent airfoils were produced. The first Langley airfoil, which appeared in the 1923 NACA annual, was the Langley Memorial Aeronautical Laboratory 54. It was tested in the first NACA wind tunnel, the WT-1 5-foot tunnel, which, as noted earlier, began operating in 1920.

Reynolds number scaling was already a serious concern in 1920 and was the motivating factor in the design and construction of the variable density

tunnel (VDT). When it came on-line in 1923. it was the most advanced tunnel in the world. It could operate at pressures up to 20 atmospheres and achieve Reynolds numbers up to 3.3×10^6 for a 13-cm (5-in.) chord model. Another facility of note that was constructed in the late twenties was the 12-inch high-speed tunnel which could produce velocities up to 350 m/sec (800 mph).

The latter half of the twenties saw the development of the NACA 4-digit and modified 4-digit series of airfoils. A sketch of one of the most popular, the 4412, is given in figure 2. A calculative procedure for airfoils of arbitrary shape was also formulated and provided a more rational basis for airfoil-family design.

Several more airfoil families were generated in the thirties including the 5-digit series, the 1-series (also known as the 16-series), and the NACA laminar-flow airfoil family. A 5-digit and a laminar-flow airfoil section are depicted in figure 2 along with a GA(W)-2 for comparison. The laminar-flow series was preceded by a considerable amount of research on calculative methods for boundary layers and empirical transition criteria.

Wind-tunnel construction during the thirties was driven by a desire to test airfoils under conditions approaching the flight environment, especially those designed for extensive runs of laminar flow. The low turbulence tunnel (LTT) started running in the mid thirties and, in addition to providing useful data, served as a learning experience for the design of the Langley low-turbulence pressure tunnel (LTPT). The LTPT started operation in 1941 and is still in use.

By the mid forties, the characteristics of a large number of airfoils had been defined; design procedures were being relied on for definition of airfoil geometry and modifications to existing airfoils. A report summarizing most of these data and procedures was published in 1945 (ref. 4). This document later became the basis for a book by Ira H. Abbott and Albert E. von Doenhoff (ref. 5). The late forties saw some shift in emphasis away from airfoil-section development to high-lift systems and boundary-layer transition and control.

A change in priorities in the early fifties necessitated a reduction in airfoil research, and by the mid fifties, it had completely disappeared. Airfoil research did not commence again until 1965 when R. T. Whitcomb conceived a new type of airfoil section for high subsonic speed applications (ref. 6). By virtue of a unique top side shaping, these airfoils were able to delay the formation of shocks and hence, for a given thickness, increase the drag-rise Mach number. Since these airfoils are able to sustain large regions of supercritical flow without shock formation near their design condition, they have been termed "supercritical" or "shockless" airfoils.

The first Whitcomb supercritical airfoil was a two-element design; it was followed closely by a single-element concept. Its value was quickly grasped by the aircraft industry and demands for supercritical airfoils for a variety of flight conditions and applications soon followed. This demand and interest led to a number of actions. It was decided in 1968 to reactivate Langley's airfoil test facilities; a series of supercritical airfoils were designed; theoretical efforts to provide a design method were commenced; and flight demonstration projects using the T2-C and F8V-1 aircraft were instituted. The first

dividends from these actions came in the 1970-71 time period when flight tests clearly validated the airfoil concept and the Langley 6- by 19-inch transonic tunnel became operational. The first design and analysis codes for supercritical airfoils were published in 1972. These codes, developed at the NYU Courant Institute by a team of scientists led by P. R. Garabedian (ref. 7), are now in use all over the world.

The breakthrough in the design of airfoils for high subsonic applications precipitated a renewed effort to develop improved airfoils for low speeds. With the aid of a computer code developed at Lockheed under Langley contract by J. A. Braden, S. H. Goradia, and W. A. Stevens (ref. 8), R. T. Whitcomb designed the GA(W)-1 airfoil. It was tested in 1972 and showed a potential for better climb characteristics than airfoils in common use. Requests for the design of, and data on, similar airfoils with different thickness ratios were numerous.

By 1973, the number of Langley researchers and organizations engaged in airfoil research to explore the new concepts had increased in response to industry pressures for more data. Informal communication and individual planning no longer provided the coordination required of such a large effort. Consequently, in 1973, airfoil-research activities were programmized. Since that time, progress in the formulation of new airfoil designs and computer codes with improved capabilities has been remarkable. Some of the major milestones of the past 4 years are as follows:

Langley 6- by 28-inch transonic tunnel and 0.3-meter transonic cryogenic tunnel became operational.

Low-speed, medium-speed, and new supercritical airfoil families were defined.

Low-drag general aviation airfoils were developed.

New airfoil design and analysis methods were formulated.

Theoretical and experimental research on massive separation began.

Theoretical and experimental studies on wall interference were initiated.

General aviation airfoil design and analysis service was created.

With the exception of the airfoil design service, these items are discussed in the subsequent sections. The airfoil design service, created in 1976 at Ohio State University, gives the general aviation industry access to the latest computer codes for airfoil design and analysis. Scientists, expert in the application of all NASA-developed codes, are available to render whatever level of service is required.

TEST FACILITIES

The NACA and its successor, the NASA, have always been in the forefront of wind-tunnel technology and test techniques. Tunnel facilities developed

over the past few years for airfoil tests and those being used in the program that were constructed many years ago continue to provide a unique capability for two-dimensional testing. The four wind tunnels which are used primarily for airfoil research are:

Langley low-turbulence pressure tunnel
Langley 6- by 19-inch transonic tunnel
Langley 6- by 28-inch transonic tunnel
Langley 0.3-meter transonic cryogenic tunnel (20- by 60-cm test section)

The Langley 8-foot transonic pressure tunnel has also been used for airfoil tests but this was done prior to the 6- by 28-inch transonic tunnel and the 0.3-meter transonic cryogenic tunnel becoming available.

The low-turbulence pressure tunnel (LTPT), as noted earlier, began operation in 1941 and is still in regular use (see fig. 3). It is still superior to most tunnels in the world over its operating range, which is Mach numbers from 0.1 to 0.4 and Reynolds numbers (based on a 0.6-m (2-ft) chord) from 1.0×10^6 to 30×10^6. New general aviation airfoils are developed with the aid of this facility; low-speed characteristics of supercritical airfoils are also explored. In addition, the excellent flow quality of the LTPT makes it ideal to carry out research on airfoils designed for natural or controlled laminar flow. Planned improvements for this facility will enable it to obtain accurate data for very high-lift systems and for airfoils at higher angles of attack than is now possible.

The 6- by 19-inch transonic tunnel came on-line in 1971 and has been utilized for both routine airfoil tests and technique-development research. A cross-section drawing of this facility is given in figure 4. It is a blowdown-type tunnel with no independent control of Mach number and Reynolds number. A 15-cm (6-in.) chord model can be tested to Reynolds numbers of 4.5×10^6 up to a Mach number of 1.0. Future utilization of the 6- by 19-inch tunnel will be primarily in the area of technique development with special emphasis on wind-tunnel wall interference.

The workhorse facility of the airfoil research is the 6- by 28-inch transonic tunnel, depicted in figure 5. Its normal Mach number range is from 0.3 to 1.0 with Reynolds numbers up to 13.5×10^6 for Mach numbers above 0.5. Independent control of Mach number and Reynolds number is possible. The 6- by 28-inch tunnel is used for research on every type of airfoil, including high-speed general aviation, supercritical, propeller, and rotorcraft. In the near future, the capabilities of this facility will be enhanced by the installation of a dynamic "rig" to carry out unsteady oscillatory and dynamic motion tests. Sidewall boundary-layer-control plates will also be provided to increase the maximum angle of attack at which useful data can be obtained.

The most versatile airfoil facility is the 0.3-meter transonic cryogenic tunnel (TCT) equipped with its 20- by 60-cm test section. A photograph of this facility is given in figure 6 and shows the unusual geometry of the tunnel with the test section at the top and the return leg at the bottom. The sketches given in figure 7 illustrate this fact more clearly. The bottom sketch shown is the original three-dimensional octagonal test section, the one in the middle

is the two-dimensional insert with schlieren system in place, and the top sketch is a self-streamlining two-dimensional section soon to be constructed.

The use of nitrogen at cryogenic temperatures gives rise to Reynolds numbers up to a factor 5 larger than those of a conventional air tunnel. It also allows one to control Mach number, Reynolds number, and dynamic pressure independently, a capability more important perhaps in three-dimensional than in two-dimensional testing, since aeroelastic and Reynolds number effects can be isolated. Reynolds numbers up to 50×10^6 can be obtained for a 15-cm (6-in.) chord model. Production testing in the TCT should commence in the fall after completion of a number of minor improvements.

Further details on the capabilities and plans for Langley's two-dimensional research facilities can be found in the paper by E. J. Ray in these proceedings (ref. 9).

Research aircraft have been used as test facilities as well as wind tunnels. An F8V-1 fighter and a T2-C trainer aircraft were provided with new wings to determine the performance of supercritical sections in flight. In both applications, the supercritical wings proved superior to the original ones.

Similar proof tests of the new general aviation airfoil sections have been conducted. The GA(W)-1 was tested on the Advanced Technology Light Twin-Engine (ATLIT) aircraft, originally a Piper Seneca, and the GA(W)-2 on the Beech Sundowner. The latter is shown in flight near Columbus, Ohio, in figure 8.

NEW AIRFOIL DEVELOPMENTS

Langley's airfoil research program involves a variety of airfoil types including

Low-speed general aviation*
Low-speed natural laminar flow
Medium speed
Transport-type supercritical*
Large cargo supercritical
Laminar-flow control (LFC) supercritical
Helicopter*
Fighter
Propeller

By far, the most effort has been expended on the three airfoil types indicated by the asterisks, and most of the subsequent discussion treats the accomplishments and plans for these types. New designs for the other types of airfoils (except LFC supercritical) have in some cases just been tested and, in others, are awaiting test or fabrication. The LFC airfoil is being developed under the NASA Energy Efficient Transport, Laminar Flow Control Project and is listed above only for completeness.

Comparisons of experiment with calculated results from the best low-speed and supercritical-airfoil predictive methods have generally shown that the

theories are accurate. Theoretically determined pressure distributions and lift and moment coefficients correlate well with experiment; absolute-drag levels are sometimes in poor agreement. However, predictions of relative-drag level and drag-rise Mach number can usually be relied on. A result of these observations is that a philosophy has been adopted to test only a few representative samples of each type of airfoil to establish the validity of the theory. This philosophy has been applied in the case of the new Langley low-speed airfoil family. Figure 9 shows the range of thicknesses and lift coefficients of the new designs as well as their status. Five airfoils have already been tested, and four others have been designed for future testing. These test results coupled with available computer codes will enable other airfoils of this type to be designed with complete confidence. Additional information on NASA's low- and medium-speed airfoils can be obtained from the McGhee-Beasley paper in these proceedings (ref. 10).

The matrix of shapes which constitute the NASA supercritical airfoil family is shown in figure 10. Design lift coefficients vary from 0 to 1.0, and thickness ratios from 0.02 to 0.21. This family is based on improved design procedures developed by R. T. Whitcomb and were defined by using the transonic Bauer-Garabedian-Korn analysis code (ref. 7). Only two designs have been tested to date; four others are in the planning stages. Many other designs are available for test, as indicated by the solid dots, but it is likely that only about half will be so honored.

Rotor-airfoil research has the same objectives as those for conventional airfoils, that is, the evaluation of new airfoil-design methodology by wind-tunnel and flight tests and development of improved sections. Unfortunately, their achievement is considerably more difficult with current methods. Analysis tools which apply for two-dimensional steady flow must, in some rational way, be applied to the rapidly changing, three-dimensional environment of a rotor blade where relative velocities may change from high subsonic to low subsonic, or reverse direction in one revolution. Results contained in the proceeding papers by G. J. Bingham, K. W. Noonan, and H. E. Jones and C. E. Morris, Jr. would seem to indicate that progress is being made in this area (refs. 11 and 12).

Three new rotor airfoils designed for tests on the AH-1G helicopter as well as in Langley's two-dimensional wind tunnels are shown in figure 11. Each has been designed by a different method: the first using a transonic hodograph equation solution technique, the second using a linear-potential-equation method with compressibility corrections (parametric crestline), and the third using the transonic full-potential-equation method (supercritical technology) of F. Bauer, P. Garabedian, and D. Korn (ref. 7). All three have been tested in both the Langley 6- by 19-inch and 6- by 28-inch transonic tunnels as well as in flight.

The total rotor-airfoil-development effort can best be judged by the fact that a total of 29 airfoils have been tested, 21 in the 6- by 28-inch tunnel and 8 in the 6- by 19-inch tunnel. Some of the participating organizations involved are

6- by 19-inch transonic tunnel
NASA
U.S. Army R&T Laboratories (AVRADCOM)
Bell Helicopter Textron
National Aerospace Laboratory (NLR), Netherlands

6- by 28-inch transonic tunnel
Bell Helicopter Textron
Boeing Co.
Hughes Aircraft Co.
Sikorsky Aircraft
Wortmann

THEORETICAL DEVELOPMENTS

The ability to design airfoils and to analyze flows about them has grown by leaps and bounds over the past 10 years. Aided and abetted by a new generation of computers and improved solution techniques, designers can now quickly analyze supercritical airfoils with and without shocks and multielement airfoils, taking into account viscous effects. Significant progress has also been made in the treatment of airfoils with regions of separated flow. Many of the advancements cited have come out of the Langley airfoil-research program and many more are in store.

Specific areas where significant progress has been made and/or effort is being applied are

Design and analysis codes
Shock/boundary-layer interaction
Trailing-edge interaction
Leading-edge bubble interaction
Separated flow
Multielement airfoil analysis
Unsteady flow

A short discussion of each of these topics follows.

Perhaps the most significant development in airfoil theory in the past decade was the formulation of the hodograph design and "circle-plane" analysis codes for supercritical airfoils by the Garabedian-Korn-Bauer team at the NYU Courant Institute (ref. 7). The original and improved versions of these two programs are in use around the world and constitute one of the key technology advances being utilized by the aircraft industry in the design of the next generation of commercial transports. Figure 12 shows an airfoil which was designed using both the design and analysis codes. The top side geometry depicted was arrived at through repeated runs of the design code; the bottom side resulting from these same calculations was further modified by using the analysis code to make successive changes in the bottom contour until the desired pressure distribution was obtained. The pressure distribution depicted in figure 13 was obtained from the analysis code for a Mach number of 0.73 and a lift coefficient of 0.60.

A second set of programs capable of solving both the analysis and design problems was put together by L. Carlson of Texas A & M about 2 years ago (ref. 13). Carlson solves the full potential equations in the physical plane on a Cartesian coordinate system. His method has one advantage over the hodograph approach of Garabedian in that it can design airfoils for input pressure distributions with shocks. An example of this feature is given in figure 13. The design program was given the pressure distribution defined by the dashed line with a shock at approximately the 75-percent-chord station. The computer program produced the airfoil shown at the bottom and the slightly modified pressure distribution given by the solid line. Inserting the derived airfoil shape into the analysis program produced the circles and triangles which are in nearly perfect agreement with actual design input (the solid line).

One of the most vexing problems in airfoil analysis is the determination of drag, particularly at high subsonic speeds when imbedded shocks occur and under separated flow conditions. Most of the boundary-layer routines in use today for calculation of boundary-layer displacement thickness and skin-friction drag do not apply in regions where strong interactions occur with the inviscid flow. Three of these interaction regions are being studied in the Langley airfoil-research program; these are shock/boundary-layer, trailing-edge, and leading-edge bubble interaction.

The shock/boundary-layer interaction problem has been studied under NASA grant at the University of Michigan for the past 3 or 4 years. The investigation started with an idealized laminar-boundary-layer/oblique-shock case and proceeded through a series of steps to the normal-shock/turbulent-boundary-layer problem discussed in these proceedings in a paper by A. F. Messiter and T. C. Adamson (ref. 14). The next step will be to take this localized analysis and patch it into one of the full-potential airfoil-analysis programs such as the one developed by F. Bauer, P. Garabedian, and D. Korn described earlier (ref. 7).

The trailing-edge interaction may be even more important from a drag standpoint since the last 5 to 10 percent of the airfoil is responsible for most of the error in drag predictions. Empirical fixes currently employed in the boundary-layer routines near the trailing edge are generally reliable in terms of pressure-distribution predictions but are not consistent for drag estimates. R. E. Melnik of Grumman Aerospace Corporation has carried out a detailed analytical treatment of the trailing-edge interaction which holds promise of improved drag prediction. He has found that accounting for the effect of wake curvature is crucial, and an airfoil analysis computer code, due to A. Jameson, has been modified to include this effect. A pressure distribution made using this code is shown in figure 14. It is for the Korn 0.75 airfoil at a Mach number of 0.7 and a section lift coefficient of 0.669. Theoretical and experimental pressures are clearly in excellent agreement; the drags are not. The theoretical drag was 0.0082 as compared to an experimental value of 0.0107. There is some opinion that the experimental value is too high by about 20 counts, but this cannot be verified. (There is a general concern about most experimental drag data.) Drag correlations made using data on a GA(W)-2 airfoil at supercritical speeds obtained in an Ohio State University wind tunnel with a divided plenum are quite good. More research is required to obtain or identify "interference

free" experimental data. Further details of the trailing-edge-interaction methodology can be found in the paper by R. E. Melnik in these proceedings (ref. 15).

Theoretical treatment of the leading-edge bubble interaction has been attempted by W. R. Briley and H. McDonald (ref. 16) using an iterative technique whereby the pressure is prescribed and boundary-layer profiles and displacement thicknesses are determined. The pressure is recalculated for the effective shape, and a new pressure input is formulated based on differences between the old and new pressures. In a low-level effort, the same type of problem is being attempted at Langley using a different procedure whereby the displacement thickness is prescribed. This procedure, which has been developed by J. E. Carter and S. F. Wornom of Langley (ref. 17), is thought to have certain advantages over the pressure-prescribed method. It has been successful in calculating separated-flow bubbles in a depression and at the juncture of an afterbody-sting combination.

Airfoil flows with large amounts of separation have been calculated for a number of years using linear methods and empirical assumptions related to the point of separation and the separated region itself. More recently, these flow problems have been attacked using both numerical time-asymptotic methods for the Navier-Stokes equation and finite-difference relaxation methods for various forms of the nonlinear-potential-flow equation. The latter are used with a boundary-layer routine which is applied up to the point of separation.

R. W. Barnwell of Langley was the first to extend the ideas developed using linear potential equations to the finite difference approach (ref. 18). In Barnwell's calculation the separation point was not solved for; it was prescribed. An extension of his approach, whereby the separation point is determined in the calculation, has been undertaken by L. Carlson of Texas A & M under NASA grant (ref. 19). Some preliminary results have been obtained and an example is shown in figures 15 and 16. These figures show the pressure distribution at an angle of attack of 18° and lift vs. angle of attack for the GA(W)-2 airfoil at a free-stream Mach number of 0.15. Note in figure 15 that the flow separates at about 60 percent of the chord. Also, it should be recognized that at an angle of attack of 18°, the airfoil is beyond its maximum lift. Further exploration of this technique is underway.

So far the discussion of theoretical developments has been constrained to single-element airfoils. Progress has also been made in the analysis of multielement systems. Several analytical methods have been developed around the country over the past 6 years, and their capabilities and limitations are fairly well known. The features of the multielement program developed by Lockheed for Langley (ref. 8), and later modified by Boeing to make it more efficient (ref. 20), are listed in figure 17. This is the same program described earlier in the "Historical Perspective" section as having been used by Whitcomb to design the GA(W)-1 low-speed airfoil. As can be seen in figure 17, the program computes all the quantities of interest for as many as 7 elements. Correlations of theory with experiment show that this computer code yields results of good accuracy up to the point of flow separation. Further improvements are contemplated to improve the accuracy of the drag prediction, including an improved

slot-flow analysis and a trailing-edge-interaction patch. The former would be attempted by applying operator splitting methods to the Navier-Stokes equations.

A companion study using the time-averaged Navier-Stokes equations is being carried out under NASA grant at Mississippi State University (ref. 21). It has reached the point where a two-element, compressible, turbulent flow code is now being debugged. A mapping procedure is used to transform the airfoil elements and the external flow field onto the interior of a rectangle where the equations are solved. The coordinate system in the physical plane is shown in figure 18. Note that the coordinate grid seems to compress in regions where the most resolution is required. It is expected that this computer program when fully developed will provide an excellent bench mark by which more approximate and faster techniques can be judged, including those treating separated flows.

The ability to analyze two-dimensional unsteady transonic flows is very much inferior to what one can do with steady flows. This is natural since the unsteady nonlinear potential equation is much more difficult to solve. A number of procedures have been tried; the two developed under the Langley program which have had the most success are the nonlinear, small-disturbance solution of Weatherill, Ehlers, and Sebastian (Boeing) (ref. 22) and the full-potential-equation solution of Isogai at Langley. An example calculation from the Isogai code is given in figure 19. It is for a steady, high Mach number flow where data are available. Theoretical results from a purely inviscid calculation and one in which the boundary-layer displacement effect is included are plotted. The lack of a proper accounting of the shock/boundary-layer interaction is the probable cause for much of the disagreement.

An extension of the Isogai code to include the effect of an oscillating flap is discussed in a paper by R. M. Bennett and S. R. Bland in these proceedings (ref. 23).

TUNNEL-WALL INTERFERENCE

The discussion of wind-tunnel-wall interference research has been isolated in a separate section, apart from theoretical developments and facilities, because of its special character and importance. Langley research in this area involves both theoretical and experimental studies for the assessment and elimination of wall interference. A list of many of these activities follows:

Slotted walls
- Barnwell correction of slot parameter
- Parametric slotted wall study in 6- by 19-inch transonic tunnel
- Slot flow diagnostic surveys in 8-foot transonic pressure tunnel

Adaptive walls
- Flexible wall experiment in 6- by 19-inch transonic tunnel
- Flexible wall theoretical prediction
- Two-dimensional adaptive walls for 0.3-meter transonic cryogenic tunnel

Some of these are discussed in the following paragraphs.

R. W. Barnwell has done an exhaustive study of slotted-wall boundary conditions and has provided new insights into the deficiencies of older methods. With the aid of existing data, he has derived a semiempirical design method for slotted-wall tunnels. Some of the data utilized came out of a parametric experimental study conducted in the 6- by 19-inch transonic tunnel by Everhart and Barnwell and reported elsewhere in these proceedings (ref. 24).

Very little data are available on the details of the flow in, and adjacent to, tunnel wall slots. More is needed to enable a better assessment of viscous effects and homogeneous boundary-condition assumptions. An experimental investigation is being carried out in the 8-foot transonic pressure tunnel to provide some of the needed data.

Langley has had a cooperative effort in adaptive wall research with the University of Southampton, England, for several years (ref. 25). In-house the 6- by 19-inch transonic tunnel has been used to explore this technique. Calculations carried out by Newman (LaRC) and Anderson (DCW Industries) for comparison with the 6- by 19-inch tunnel tests are discussed in their paper included in these conference proceedings (ref. 26). All of these activities have contributed to the design of an adaptive-wall two-dimensional section for the 0.3-meter transonic cryogenic tunnel.

A third approach to the wall interference problem has been proposed in the proceedings paper by W. B. Kemp, Jr. (ref. 27). Through the use of pressures measured near the tunnel walls as boundary conditions in a tunnel flow analysis program, he is able to determine whether a flow is correctable and, if so, what the corrections should be. The method, in effect, eliminates the need for a detailed knowledge of slot flows, porous wall flows, and so forth.

FUTURE RESEARCH REQUIREMENTS

A recurring theme in much of the research discussed was the need to improve the accuracy of drag predictions. Existing codes must be modified or new codes created to include the effects of strong interactions and flow separation. Although not discussed previously, turbulence models are also a source of drag error and a strong effort is needed to improve them.

Good progress in the prediction of flows with large separation was indicated, but many of the techniques are new and require further exploration. In order to obtain accurate data to validate these theories, it is mandatory that sidewall treatments in two-dimensional facilities be implemented and refined.

There is a dearth of unsteady pressure data at supercritical speeds. In addition to classical oscillatory data, dynamic-stall and buffet-type flows must be simulated. Wall interference corrections for unsteady motions is an area that has hardly been scratched.

Improved wall correction procedures for steady flow are still a requirement; the use of measured wall pressures should be pushed. Streamline-wall test sections should be "hard wired" to computers so that the wall adjustments can be automated.

As knowledge of flow stability improves, more research will be carried out on natural laminar flow and laminar flow with suction. This will require, in many cases, improvements in tunnel flow quality and reduced tunnel noise. Continued improvement in analysis tools to account for new stability theories and data will also be necessary.

Full-scale Reynolds number data are always desired. Only a few facilities around the world can obtain the levels required for large-transport airfoil sections. Detailed comparisons of the data from these facilities are required to ferret out error sources; efforts to obtain boundary-layer diagnostic data should be increased.

Finally, it should be recognized that airfoils are used in a three-dimensional environment. Considerably more effort to include the effects of sweep and taper in the design of airfoil sections is needed. In addition, the different environments of the wing root, midspan region, and tip should be better defined so that airfoil sections can be designed taking into account these differences.

Clearly, there are many research opportunities and challenges in airfoil aerodynamics. If they are undertaken with the same enthusiasm as that applied during the past decade, then another quantum leap in airfoil-aerodynamics capabilities can be expected.

APPENDIX

SYMBOLS

In this appendix, symbols which are used on the figures are defined.

C_p	pressure coefficient, $\frac{p - p_\infty}{q_\infty}$
C_p^*	sonic pressure coefficient, $\frac{p^* - p_\infty}{q_\infty}$
c	airfoil chord
c_d	section drag coefficient, $\frac{\text{Drag force}}{q_\infty c}$
c_l	section lift coefficient, $\frac{\text{Lift}}{q_\infty c}$
c_m	section pitching-moment coefficient, $\frac{\text{Pitching moment}}{q_\infty c^2}$
M_∞	free-stream Mach number
p	local static pressure
p_∞	free-stream static pressure
p^*	static pressure at sonic velocity
q_∞	free-stream dynamic pressure
R	unit Reynolds number
R_c	Reynolds number based on airfoil chord
t	maximum airfoil thickness
V_∞	free-stream velocity
α	angle of attack
δ^*	boundary-layer displacement thickness
ρ_∞	free-stream density

REFERENCES

1. Sixth Annual Report of the National Advisory Committee for Aeronautics - 1920. U.S. Government Printing Office, 1921.

2. Seventh Annual Report of the National Advisory Committee for Aeronautics - 1921. U.S. Government Printing Office, 1923.

3. Ninth Annual Report of the National Advisory Committee for Aeronautics - 1923. U.S. Government Printing Office, 1924.

4. Abbott, Ira H.; Von Doenhoff, Albert D.; and Stivers, Louis S., Jr.: Summary of Airfoil Data. NACA Rep. 824, 1945. (Supersedes NACA WR L-560.)

5. Abbott, Ira H.; and Von Doenhoff, Albert E.: Theory of Wing Sections. Dover Publ., Inc., c.1959.

6. Whitcomb, Richard T.; and Clark, Larry R.: An Airfoil Shape for Efficient Flight at Supercritical Mach Numbers. NASA TM X-1109, 1965.

7. Bauer, F.; Garabedian, P.; and Korn, D.: A Theory of Supercritical Wing Sections, With Computer Programs and Examples. Volume 66 of Lecture Notes in Economics and Mathematical Systems, Springer-Verlag, 1972.

8. Braden, J. A.; Goradia, S. H.; and Stevens, W. A.: Mathematical Model for Two-Dimensional Multicomponent Airfoils in Viscous Flow. NASA CR-1843, 1971.

9. Ray, Edward J.: Langley's Two-Dimensional Research Facilities - Capabilities and Plans. Advanced Airfoil Technology Research, Volume I, NASA CP-2045, Pt. 1, 1979. (Paper 15 of this compilation.)

10. McGhee, Robert J.; Beasley, William D.; and Whitcomb, Richard T.: NASA Low- and Medium-Speed Airfoil Development. Advanced Airfoil Technology Research, Volume II, NASA CP-2046, 1979.

11. Bingham, Gene J.; Noonan, Kevin W.; and Jones, Henry E.: Results of an Investigation of Several New Rotorcraft Airfoils as Related to Airfoil Requirements. Advanced Airfoil Technology Research, Volume II, NASA CP-2046, 1979.

12. Morris, Charles E. K., Jr.: A Flight Investigation of Rotor Airfoils. Advanced Airfoil Technology Research, Volume II, NASA CP-2046, 1979.

13. Carlson, L. A.: Transonic Airfoil Design Using Cartesian Coordinates. NASA CR-2578, 1976.

14. Messiter, A. F.; and Adamson, T. C., Jr.: A Study of the Interaction of a Normal Shock Wave With a Turbulent Boundary Layer at Transonic Speeds. Advanced Airfoil Technology Research, Volume I, NASA CP-2045, Pt. 1, 1979. (Paper 21 of this compilation.)

15. Melnik, Robert E.: Wake Curvature and Trailing Edge Interaction Effects in Viscous Flow Over Airfoils. Advanced Airfoil Technology Research, Volume I, NASA CP-2045, Pt. 1, 1979. (Paper 20 of this compilation.)

16. Briley, W. Roger; and McDonald, Henry: Numerical Prediction of Incompressible Separation Bubbles. J. Fluid Mech., vol. 69, pt. 4, June 24, 1975, pp. 631-656.

17. Carter, James E.; and Wornom, Stephen F.: Solutions for Incompressible Separated Boundary Layers Including Viscous-Inviscid Interaction. Aerodynamic Analyses Requiring Advanced Computers, Part I, NASA SP-347, 1975, pp. 125-150.

18. Barnwell, Richard W.; Sewell, William G.; and Everhart, Joel L.: Design and Calibration of Slotted Walls for Transonic Airfoil Wind Tunnels. Advanced Airfoil Technology Research, Volume I, NASA CP-2045, Pt. 1, 1979. (Paper 18 of this compilation.)

19. Carlson, Leland A.; and Rocholl, Bruce M.: Application of Direct-Inverse Techniques to Airfoil Analysis and Design. Advanced Airfoil Technology Research, Volume I, NASA CP-2045, Pt. 1, 1979. (Paper 5 of this compilation.)

20. Brune, Guenter W.; and Manke, Joseph W.: Upgraded Viscous Flow Analysis of Multielement Airfoils. Advanced Airfoil Technology Research, Volume I, NASA CP-2045, Pt. 1, 1979. (Paper 10 of this compilation.)

21. Thompson, Joe F.; Turner, Louis; Long, W. Serril; and Bearden, John H.: Numerical Solution of the Navier-Stokes Equations for Arbitrary Two-Dimensional Multi-Element Airfoils. Advanced Airfoil Technology, Volume I, NASA CP-2045, Pt. 1, 1979. (Paper 11 of this compilation.)

22. Weatherill, Warren H.; Ehlers, F. Edward; and Sebastian, James D.: A Procedure for Analyzing Transonic Flow Over Harmonically Oscillating Airfoils. Advanced Airfoil Technology Research, Volume I, NASA CP-2045, Pt. 2, 1979. (Paper 43 of this compilation.)

23. Bennett, Robert M.; and Bland, Samuel R.: Some Transonic Potential Flow Calculations for the NACA 64A006 Airfoil With an Oscillating Flap. Advanced Airfoil Technology Research, Volume I, NASA CP-2045, Pt. 2, 1979. (Paper 45 of this compilation.)

24. Everhart, Joel L.; and Barnwell, Richard W.: A Parametric Experimental Study of the Slotted-Wall Boundary Condition. Advanced Airfoil Technology Research, Volume I, NASA CP-2045, Pt. 2, 1979. (Paper 30 of this compilation.)

25. Goodyer, Michael J.: Developments in Airfoil Testing Techniques at University of Southampton. Advanced Airfoil Technology Research, Volume I, NASA CP-2045, Pt. 1, 1979. (Paper 16 of this compilation.)

26. Newman, Perry A.; and Anderson, E. C.: Analytical Design of a Contoured Wind-Tunnel Liner for Supercritical Testing. Advanced Airfoil Technology Research, Volume I, NASA CP-2045, Pt. 2, 1979. (Paper 33 of this compilation.)

27. Kemp, William B., Jr.: Transonic Assessment of Two-Dimensional Wind Tunnel Wall Interference Using Measured Wall Pressures. Advanced Airfoil Technology Research, Volume I, NASA CP-2045, Pt. 2, 1979. (Paper 31 of this compilation.)

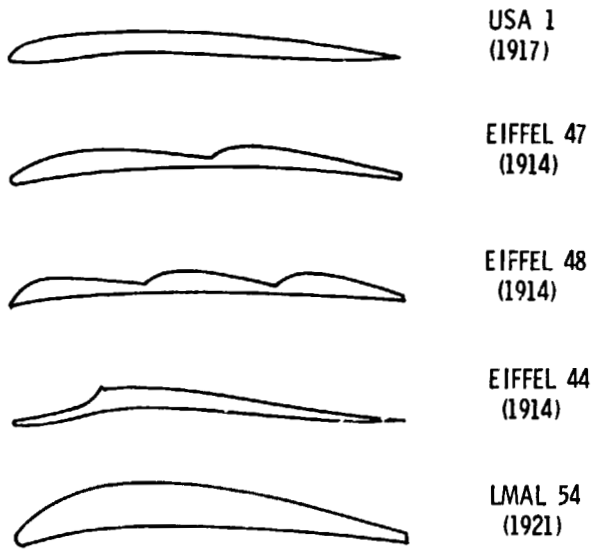

Figure 1.- Early airfoil shapes.

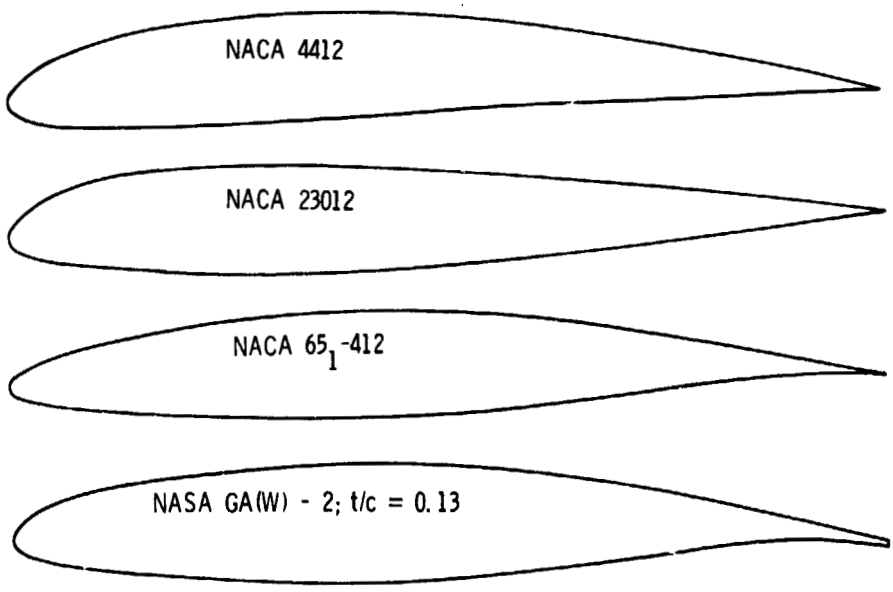

Figure 2.- Comparison of older NACA airfoils with the NASA GA(W)-2 airfoil.

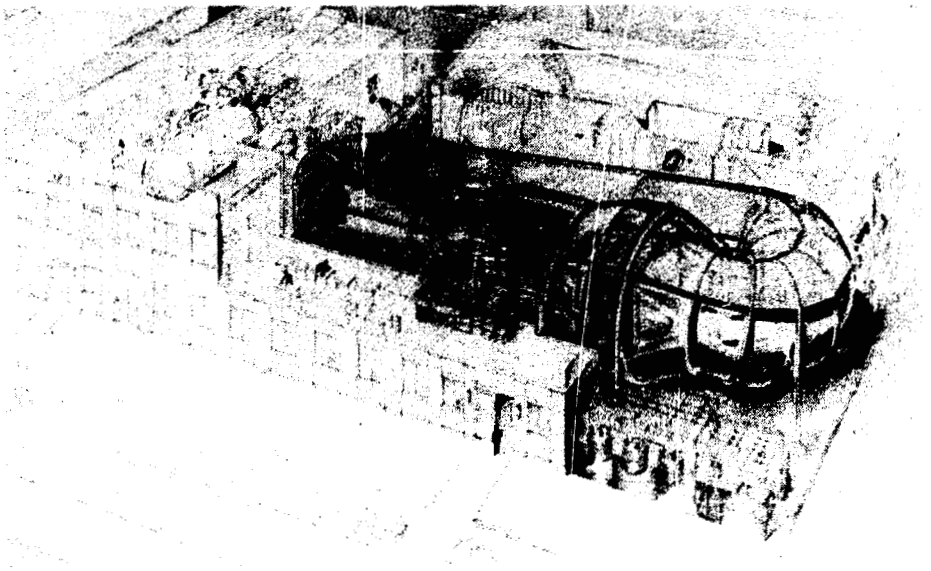

Figure 3.- The Langley low-turbulence pressure tunnel.

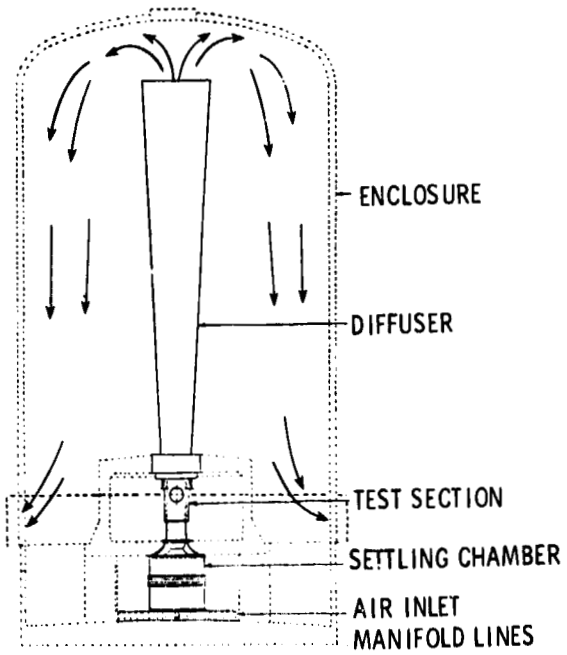

Figure 4.- Cross-section drawing of Langley 6- by 19-inch transonic tunnel.

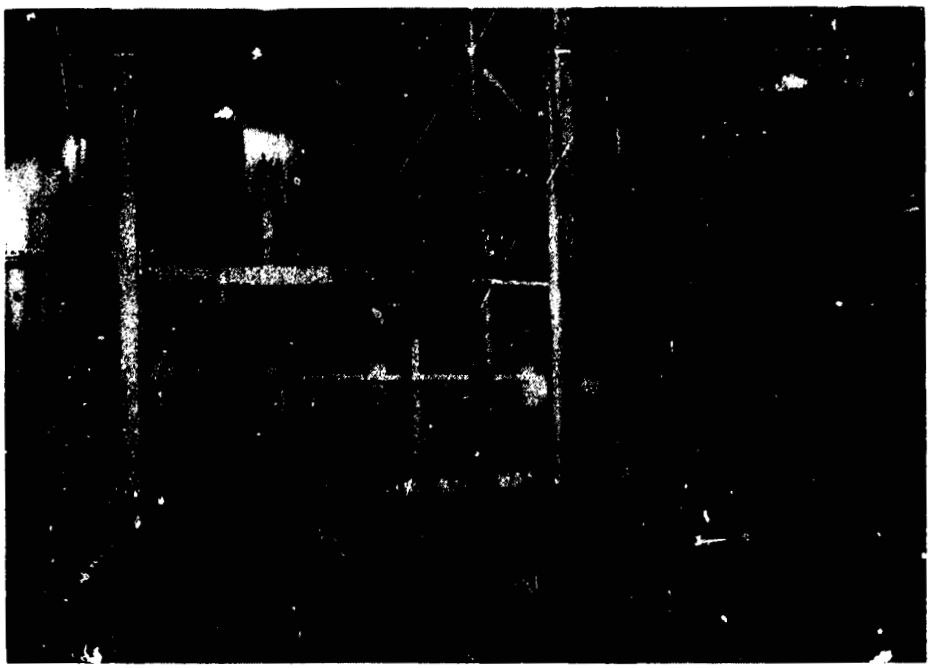

Figure 5.- Photograph of the Langley 6- by 28-inch transonic tunnel.

Figure 6.- Photograph of the Langley 0.3-meter transonic cryogenic tunnel with 20- by 60-cm two-dimensional test section.

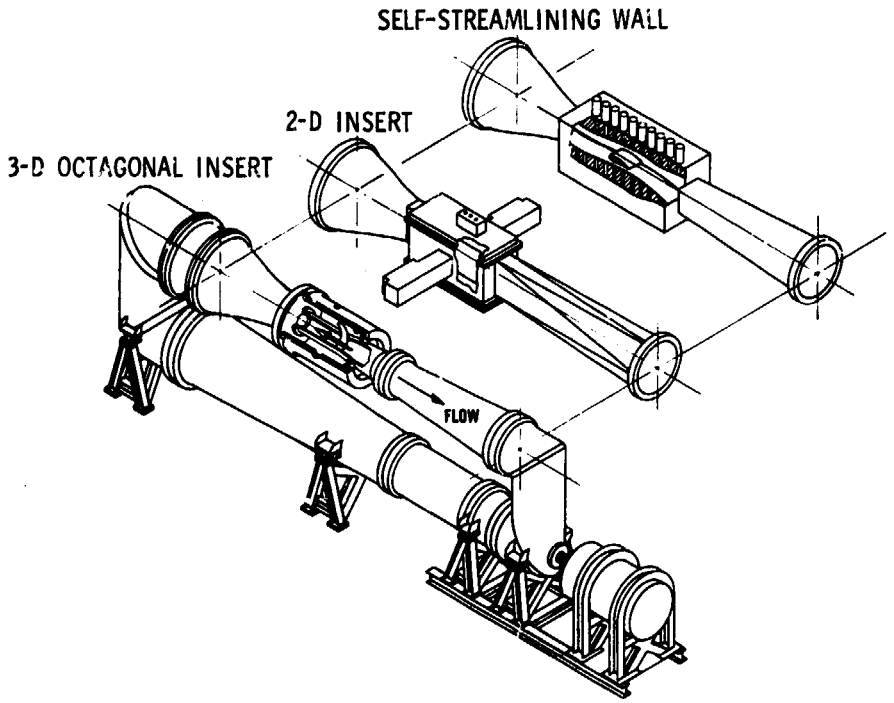

Figure 7.- Interchangeable test section capability of 0.3-meter transonic cryogenic tunnel.

Figure 8.- GA(W)-2 airfoil on Beech Sundowner.

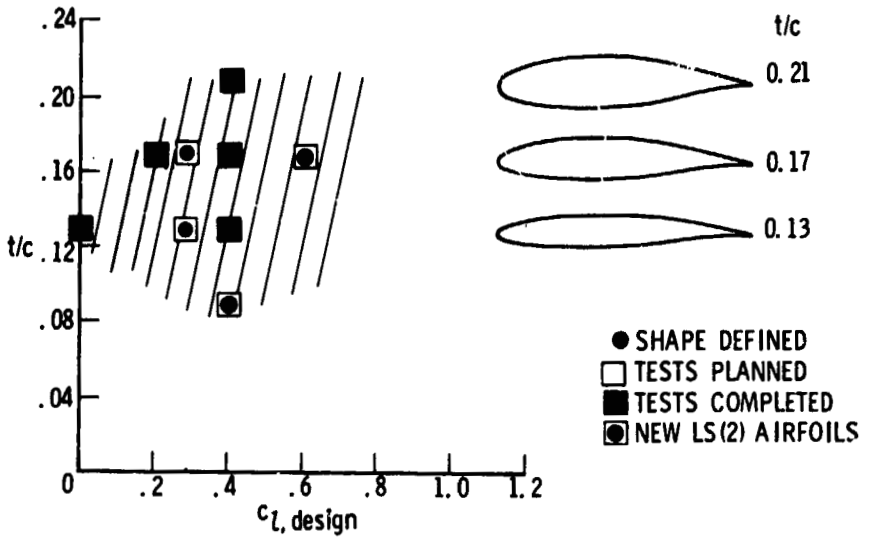

Figure 9.- Langley low-speed airfoil family.

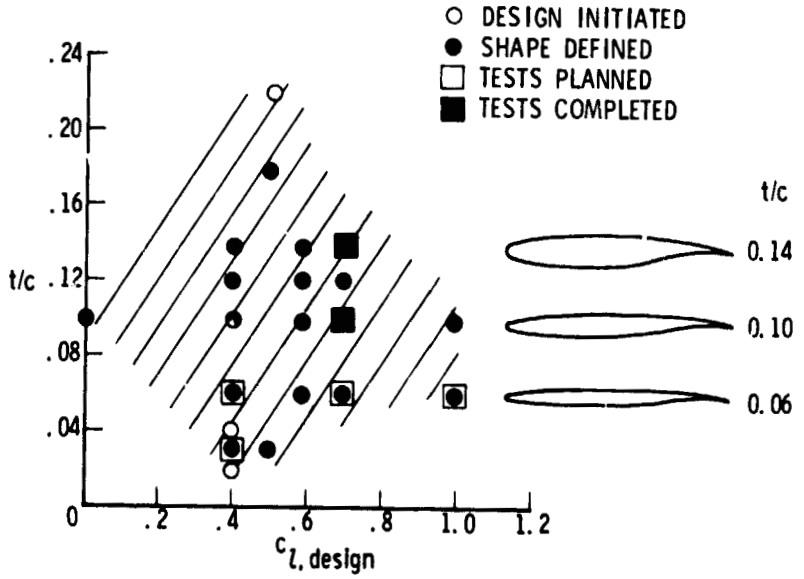

Figure 10.- NASA supercritical airfoil family.

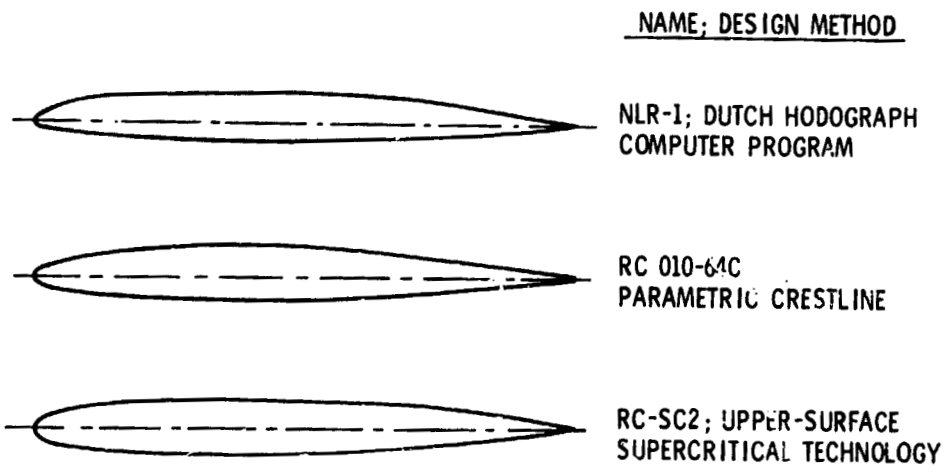

Figure 11.- Airfoils for AH-1G flight test.

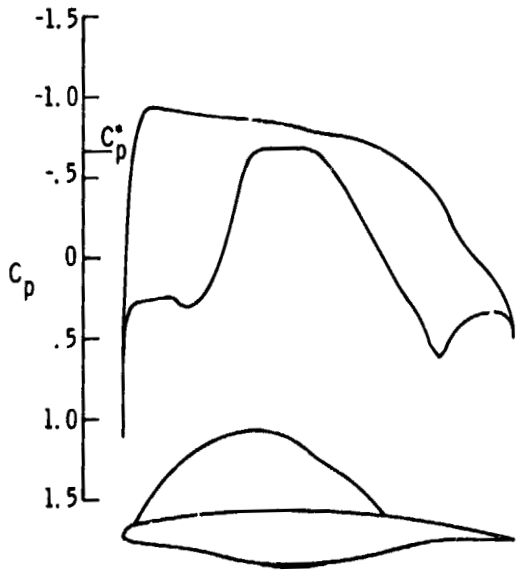

Figure 12.- Pressure distribution over an LFC airfoil calculated by the Korn-Garabedian analysis program.
$M_\infty = 0.73$; $c_l = 0.60$.

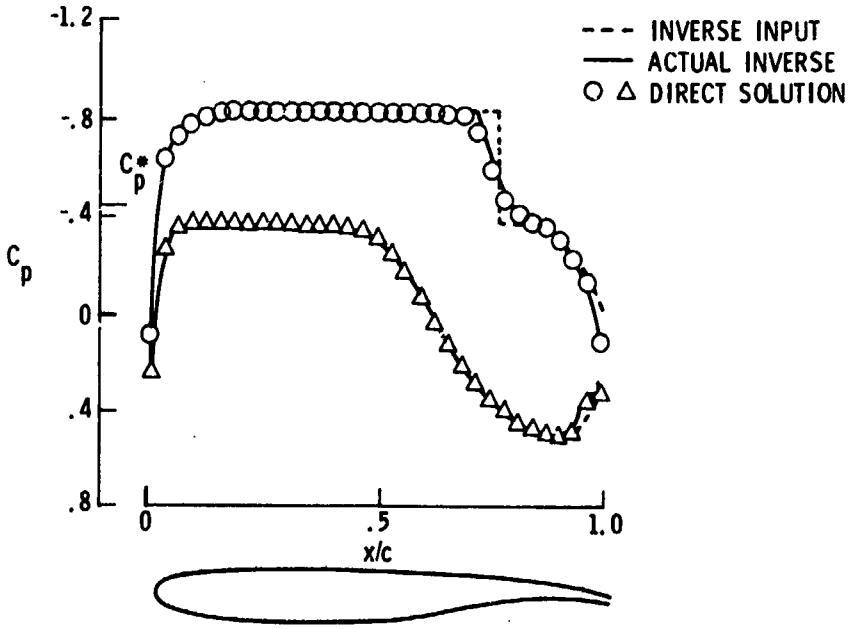

Figure 13.- Comparison of direct and inverse C_p distributions calculated by Carlson computer codes. $M_\infty = 0.80$; $\alpha = -0.5^\circ$.

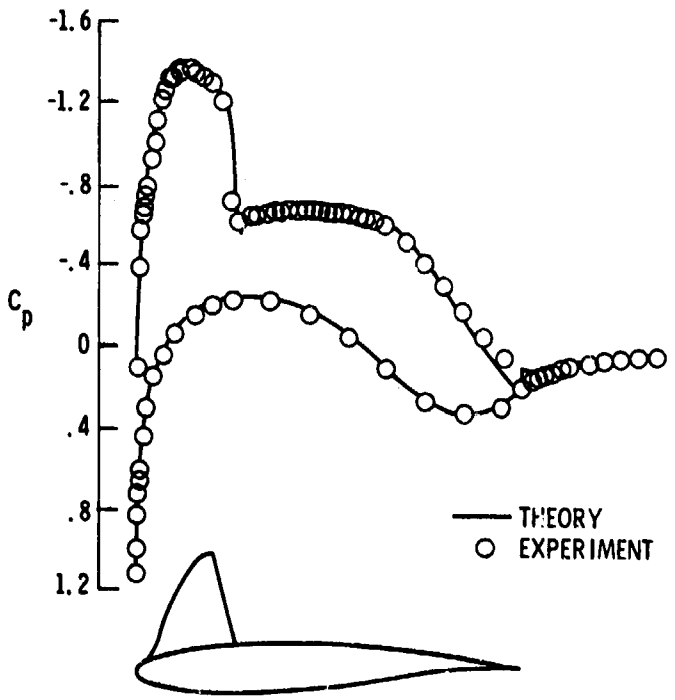

Figure 14.- Theoretical pressure distribution on Korn 0.75 airfoil including trailing-edge interaction. $M_\infty = 0.7$; $c_l = 0.669$.

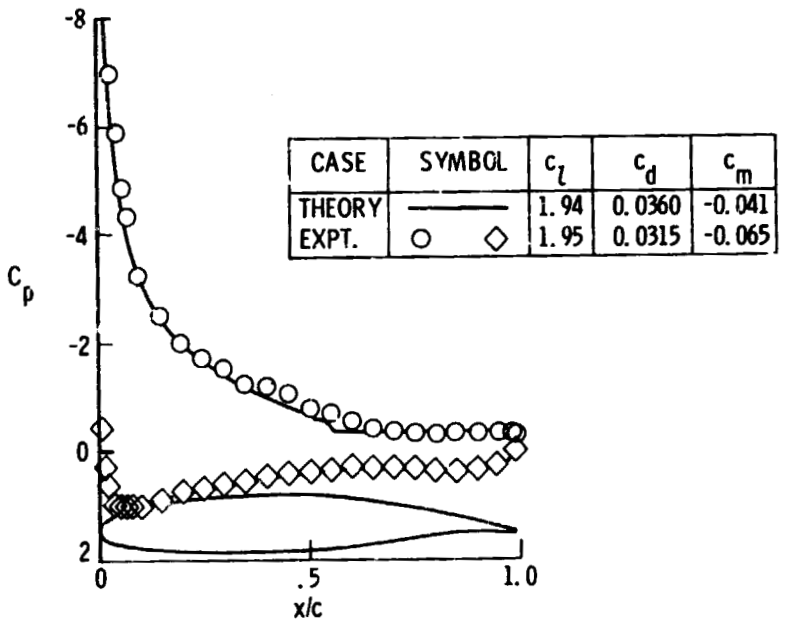

Figure 15.- Theoretical and experimental pressure distribution comparisons for GA(W)-2 airfoil with large separated flow region. $M_\infty = 0.15$; $\alpha = 18^o$.

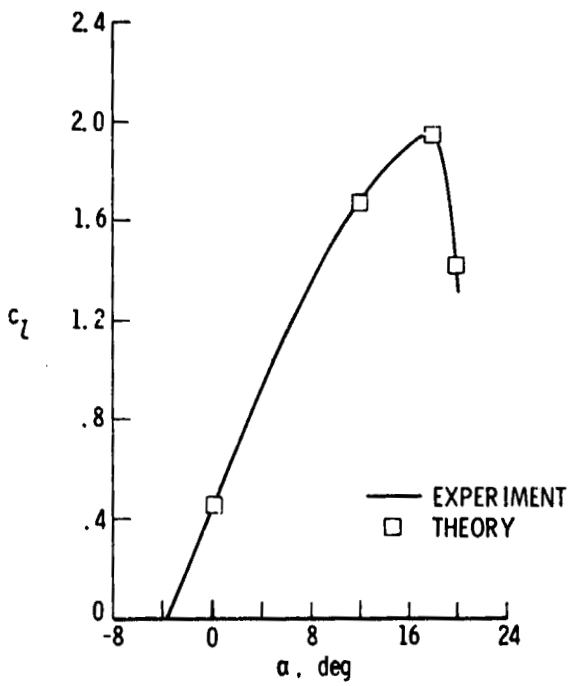

Figure 16.- Experimental and theoretical variations of c_l with α for GA(W)-2 airfoil.

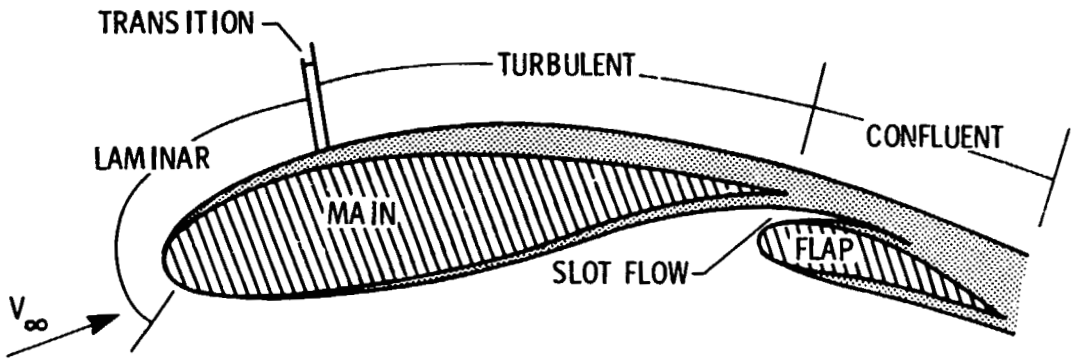

CAPABILITIES

- 1 TO 7 COMPONENTS
- VARIABLE α, M_∞ AND R
- FIXED AND/OR FREE TRANSITION
- COMPUTES c_l, c_d, c_m, AND BOUNDARY LAYERS, C_p

PROGRAM FEATURES

- POTENTIAL-FLOW SOLUTION
- BASIC BOUNDARY LAYER
- SLOT-FLOW ANALYSIS
- CONFLUENT BOUNDARY LAYERS
- COMBINED SOLUTION

Figure 17.- Two-dimensional viscous-flow multielement airfoil program features.

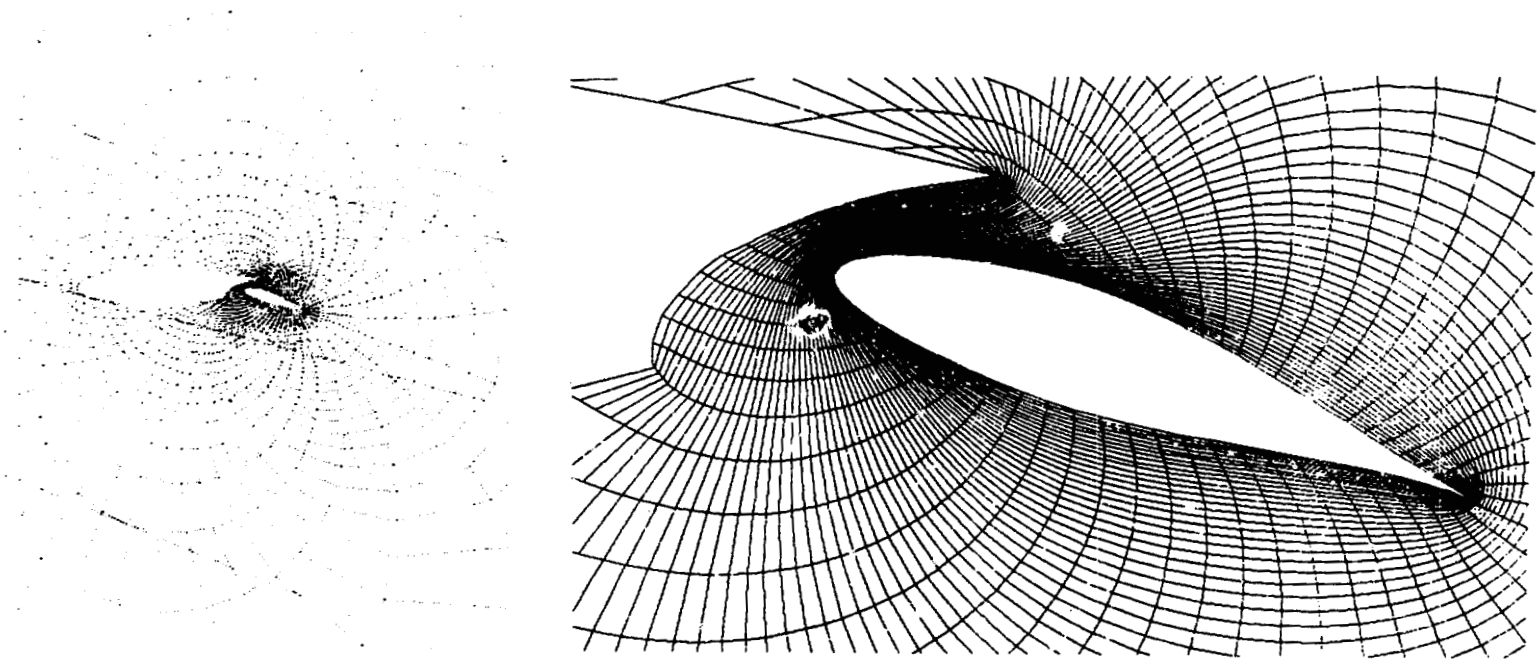

Figure 18.- Grid in physical plane for Navier-Stokes solution of multielement airfoils.

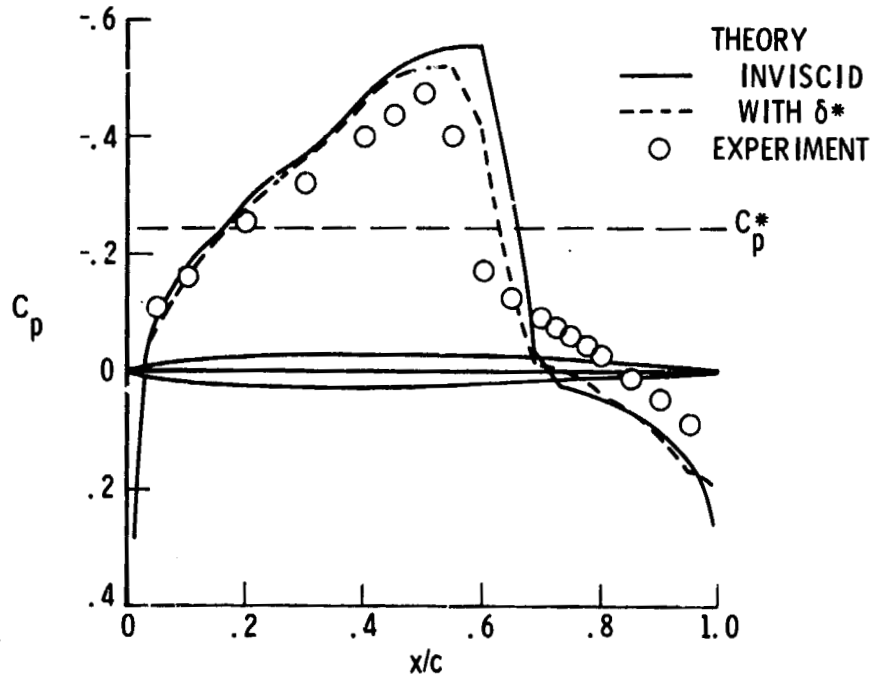

Figure 19.- Steady flow calculation for the NACA 64A006 airfoil using Isogai unsteady potential flow code. $M_\infty = 0.875$; $\alpha = 0$.

D3

N79-20033

3

OVERVIEW OF TWO-DIMENSIONAL AIRFOIL RESEARCH AT AMES RESEARCH CENTER

Gary T. Chapman
NASA Ames Research Center

INTRODUCTION

The five basic elements of the two-dimensional airfoil research program at Ames Research Center are illustrated in figure 1. These elements are experimental, theoretical (including computational), validation, design optimization, and industry interaction. The figure also shows the direction of flow of the information, starting with experimental and theoretical and moving to validation, design optimization, and industry interaction. As in any good program, the information also flows in the reverse direction to provide the needs and guides for the research. The following material treats each area briefly and notes other Ames papers presented at this conference that cover the topics more completely. In other topic areas, recent publications are cited to provide more complete details.

THEORETICAL RESEARCH

The theoretical work can be divided into two major areas: computational aerodynamics computer codes and turbulence modeling.

Computational Codes- The primary work falls into three areas: Navier-Stokes codes, Euler codes, and multielement airfoil codes. Deiwert and Bailey's paper, presented at this conference, reviews the work on time-averaged Navier-Stokes prediction of two-dimensional airfoil aerodynamics at Ames. As analyses tools, these codes are becoming very useful, but they are still too time-consuming (15-30 min on a CDC 7600) to be useful for design work. Some very good results have been obtained with these codes when used for transonic buffet, an area that cannot be predicted by less sophisticated codes.

The paper by Olson provides a good example of work in progress on prediction of complex multielement airfoils at low speeds. Although the technology is sufficiently well advanced to allow determination of optimum slat and flap settings, the codes do not give good absolute values of the aerodynamic characteristics, particularly the drag coefficient.

Finally, J. Steger has developed a time-dependent Euler code that has been modified for easy use with an assortment of airfoil problems by W. Chyu. This code treats pitching and/or plunging airfoils with a time-varying free-stream velocity. In addition, the code can treat a spatially varying upstream boundary condition to allow consideration of a two-dimensional airfoil in a shear flow. This can be considered as an approximation of a rotor blade encountering a wake from a previous blade.

PAGE INTENTIONALLY BLANK

Turbulence Modeling- Turbulence modeling is a crucial area of research for the success of any computational method that attempts to predict viscous drag and/or strongly interacting viscous flows such as separation or shock boundary-layer interaction. A major effort is under way at Ames, primarily under the direction of M. Rubesin. This is a highly complex subject, and I will not deal with it in detail. The simple algebraic turbulence models of the eddy viscosity type do an adequate job for fully attached flows, with more sophisticated one- and two-equation models being required as the viscous interaction becomes more important. However, computational time also increases significantly. The simple eddy viscosity models, however, do not predict drag better than about 5%. This may be sufficient for two-dimensional airfoils since we normally wish only to select good candidate airfoils to use in three-dimensional wing design.

A primary requirement for good turbulence modeling is good experimental data. This is the area where much work needs to be done.

EXPERIMENTAL RESEARCH

For discussion purposes, experimental research is divided into two areas: methodology and data base.

Experimental Methodology- This area deals basically with the development of new experimental methods, particularly those that have application in two-dimensional airfoil research. Four new experimental methods are of interest: laser velocimetry, holography, skin friction gages, and an airfoil oscillatory apparatus.

Laser velocimetry is covered in two papers - one from Ames and one sponsored by Ames. These are the papers by Johnson (Ames) and Owens, respectively. Johnson (Ames) shows the high degree of accuracy that has been obtained in both potential and viscous flows with the laser velocimeter. These included very accurate Reynolds shear stress measurements in a shock-induced separation on an airfoil at Mach number 0.8. The Owens paper shows the application of conditional sampling techniques to provide temporal as well as spatial resolution of time periodic flows. The laser velocimeter has reached the stage of a highly accurate research tool. However, at this point it is not a production test device in the sense that a highly trained individual is still required for operation and data interpretation.

The use of holography in two-dimensional testing is also discussed in the paper by Johnson (Ames). Although this technique is much newer than the laser velocimeter, it already shows excellent promise. The potential for completely mapping the density field in a single picture makes for much more rapid data-gathering than the laser velocimeter. Holography has been shown to be very accurate, both by comparison with laser velocimetry data and with surface static pressures. This latter comparison suggests the possibility of testing nonpressure-instrumented models and hence cutting manufacturing costs considerably.

A new experimental apparatus that provides new data for unsteady aerodynamics has been developed. This new two-dimensional airfoil oscillating apparatus for the Ames 11-Ft Transonic Tunnel is reported in a paper by Davis and Malcolm at this conference. The test apparatus allows for a wide range of test conditions: reduced frequencies to 0.35; Mach numbers from 0.4 to 1.2; Reynolds numbers to 12 million; center of rotation from plus infinity to minus infinity (pure plunge to oscillation about any point on or off the airfoil); static angles of attack to 16°; and pitching amplitude of ±2°. The apparatus has automated real-time data acquisition, first harmonic analysis, and display capability provided by a dedicated minicomputer. The apparatus is operational and has already greatly expanded the data base in this area.

A significant amount of work is going on at Ames to develop simple and accurate skin friction gages. Two types are under development: the "buried" wire gage and a very small floating element mounted on a crystal gage. The "buried" wire gage development is nearly complete and has been reported by Murthy and Rose (ref. 1). This gage is similar in principle to most heated wire or film skin friction gages but differs in construction. The heated wire, after being soldered to the leads, is pulled snuggly to the surface of a plastic button (leads pass through holes in the button). A drop of solvent is placed on the surface around the wire, bringing the substrate (button) material into suspension. When the solvent evaporates, a smooth, very thin coat is deposited over the wire. Gages constructed in this manner are inexpensive, simple to use, repeatable, and fairly accurate.

The floating element gage is nearing the point of first test. The basic idea is similar to all floating element gages. The major difference is that the crystal mount (the deflecting beam) is very rigid, allowing movement of only a few millionths of an inch. This requires a special sensing method. The technique used here is a surface acoustic wave detection method — the surface acoustic wave speed being linearly proportional to the stress in the beam surfaces caused by deflection of the beam. This device is much more expensive that a "buried" wire gage but has the potential for much higher accuracy and does not require in-place calibration.

Data Base- The data base work covers three primary areas: steady, unsteady, and turbulence. Data base information is seldom isolated from some other activity because it is normally acquired to validate a theory or develop a better understanding on which a more complete theory can be developed. This is particularly true of the two-dimensional airfoil research at Ames. Examples of steady data base can be found in the papers by Lores, Burdges, Shrewsbury, and Hicks, and by Johnson (Vought) and Hicks. Examples of unsteady data can be found in the paper by Davis and Malcolm and for turbulence in the paper by Johnson (Ames).

VALIDATION

Validation is the step whereby theory and experiment are brought together for comparison. It can be used both to validate the theory or point out errors in the experiment. This is a continual area of activity that is never

really finished. I would like to describe briefly one example in the area of wind-tunnel wall interference. Much has been said about the need for a good set of interference-free wind-tunnel data on an airfoil at transonic speed. In an attempt to assess wall interference in the 2 by 2 ft transonic wind tunnel at Ames (this is a slotted test section facility), some interesting points have been discovered. This discovery results from a more complete comparison of experiment and theory. The experiment was with an NACA 64A010 airfoil. Both pressure distribution and flow fields were measured (the latter with the laser velocimeter). Computations were made with a small disturbance transonic code under conditions for which the theory would be expected to be valid.

First, calculations were made at the set angle of attack. At this condition, the lift and pressure distribution were missed badly, but the flow angle measurement (one chord height above the model) was predicted very well upstream and over the leading edge but deviated downstream of the leading edge. A second calculation was performed at an angle of attack that resulted in the correct lift coefficient. At this condition, the pressure distribution, while not exact, was realistic; however, the stream angle was not correct anywhere although the agreement improved in the downstream portion of the flow. This suggests that the classical angle-of-attack correction method used for transonic wall effect is not valid in general.

DESIGN OPTIMIZATION

The application of numerical optimization procedures — with existing airfoil computational methods — to the problem of airfoil design has been actively researched at Ames. Work has been under way in three different areas: transonic airfoils, low-speed improved $C_{L_{max}}$ airfoils, and rotor airfoils. There are two papers on transonic airfoil designs that are the result of cooperative programs with industry. These are the papers by Lores (Lockheed-Georgia) et al., and Johnson (Vought) and Hicks. These two papers illustrate the power, as well as the limitations, of this method of design.

In the area of low-speed airfoils designed to improve $C_{L_{max}}$, there has been considerable success. A recent leading edge modification (30% of upper surface) of an NACA 63_2215 resulted in a 20% improvement in $C_{L_{max}}$ at landing conditions. Other cases have also been designed and tested. A design methodology has evolved and been verified, and a handbook of leading edge modifications (theoretically defined) for the most widely used NACA airfoils is underway.

The rotor airfoil section work is unique in that these sections require multipoint designs. The retreating blade (shock-induced stall at $M = 0.4$ and 0.5) and advancing blade transonic effects must be considered. A recent three-point design has been tested and found satisfactory although not the best possible. This area of multipoint design will continue to receive greater attention.

INDUSTRY INTERACTION

Industry interaction is not an area of research but rather a mode of operation that is essential to good applied research. The two papers described in the foregoing section regarding transonic airfoil design optimization (Lores et al., and Johnson (Vought) and Hicks) are examples of this industry interaction. The importance of the two-way nature of this interaction is crucial to the foregoing work. NASA gets direct input of industry's needs as well as active evaluation of the validity of the research it is conducting. Industry gets the fastest possible transfer of new technology, often long before complete publication or documentation is available. This is a continuing area of activity with a shift towards interacting for complete three-dimensional wing design problems.

CONCLUDING REMARKS

In conclusion, the two-dimensional airfoil aerodynamics research at Ames Research Center has been briefly described. Although in many respects it is a small program, the contributions are substantial.

REFERENCE

1. Murthy, V. S.; and Rose, W. C.: Buried Wire Gages for Wall Shear Stress Measurements, AIAA Paper 78-798. San Diego, Calif., April 19-21, 1978.

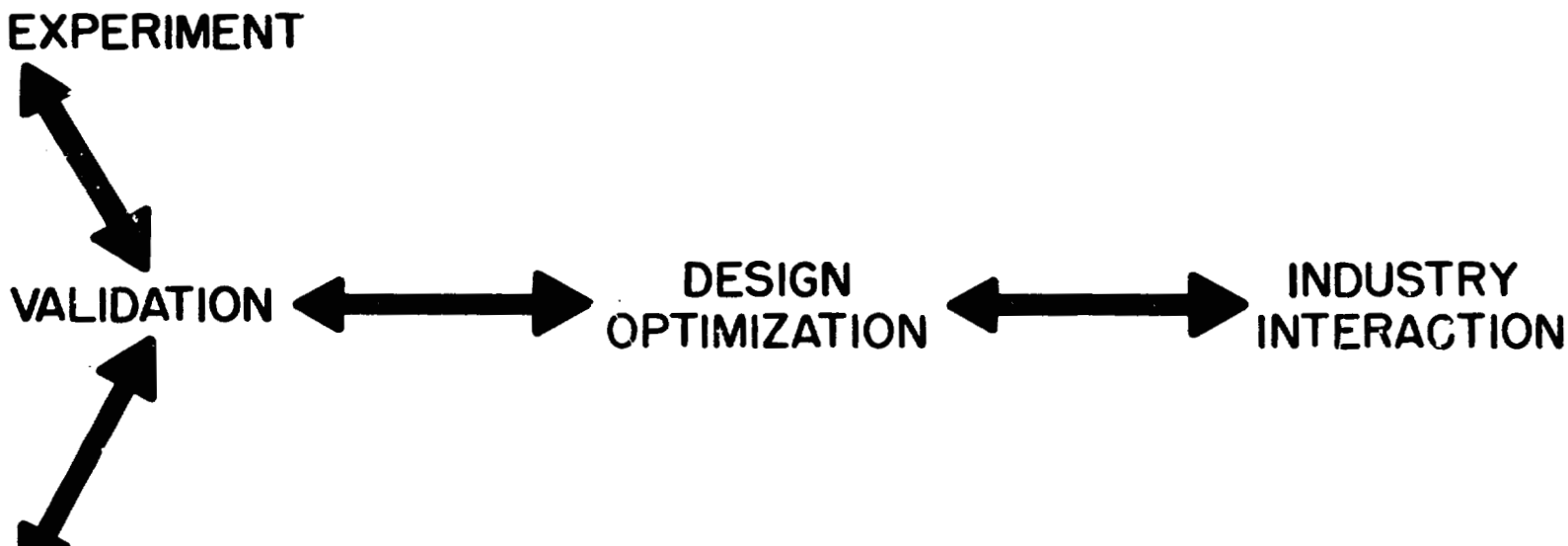

Figure 1.- Two-dimensional airfoil research at Ames Research Center.

D4

N79-20034

4

TRANSONIC AIRFOIL CODES*

P.R. Garabedian
New York University

SUMMARY

Three books on supercritical wing sections have been published recently that document and list codes for the design and analysis of transonic airfoils. The codes have had a significant impact on the development of supercritical wing technology. This paper is devoted to several new contributions to the theory on which the codes are based. It has become possible to prescribe the pressure distribution within a reasonable tolerance even over the supersonic portion of a shockless airfoil. The purely subsonic problem of modeling the flow near the trailing edge has been handled in a way that eliminates any appreciable loss of lift in practice. Boundary layer effects are taken into account in an empirically satisfactory fashion. The work has been extended to the case of cascades of airfoils appropriate for the design of compressor and turbine blades. These methods of computational fluid dynamics have produced a family of airfoils that deliver outstanding performance over a wide range of conditions.

INTRODUCTION

In the last few years three books have appeared that list computer codes for the design and analysis of transonic airfoils (refs. 1,2,3). The design code relies on the method of complex characteristics in the hodograph plane to construct shockless airfoils. The analysis code uses artifical viscosity to calculate flows with weak shock waves at off-design conditions. Comparisons with experiments show that an excellent simulation of two-dimensional wind tunnel tests is obtained. The codes have been widely adopted by the aircraft industry as a tool for the development of supercritical wing technology.

SYMBOLS

f complex analytic function

h real function

*Work supported by NASA under Grants NGR-33-016-167 and NGR-33-016-201 and by the U.S. Dept. of Energy under Contract EY-76-C-02-3077 with N.Y.U.

i	square root of -1
k	real constant
M	Mach number
q	speed
u	function of x and y
u_1	even function of y
u_2	even function of y
x	canonical coordinate
y	canonical coordinate
ξ	characteristic coordinate
η	characteristic coordinate
θ	flow angle
ρ	density
ϕ	velocity potential
ψ	stream function

ANALYSIS AND DESIGN

For analysis, differencing of the partial differential equations of gas dynamics that do not adhere to strict conservation form turns out to give the best representation of boundary layer-shock wave interaction over a broad range of conditions (ref. 2). An improved formula for the wave drag compensates for errors in the conservation of mass across shocks that are of the third order in the shock strength. Modern techniques of conformal mapping and fast Fourier transform have led to an upgraded analysis code that has unusual speed and accuracy (ref. 3).

Corrections for the displacement thickness of the turbulent boundary layer have been made in both the design and the analysis codes. Even more important is an adequate model of the flow near

the trailing edge of the airfoil. It suffices to represent the wake by a pair of parallel streamlines across which the pressure balances. Large favorable pressure gradients can be tolerated on the lower surface to provide for heavy aft loading. However, a Stratford distribution should be used at the rear of the upper surface to limit the adverse pressure gradient there so as to avoid separation. Airfoils designed with this in mind perform well over a wide range of conditions.

Shockless airfoils serve as an acceptable mathematical model for the design of supercritical wing sections. Drag creep can be reduced by restricting the size of the supersonic zone in the shockless flow. The design method has been extended to include cascades of airfoils such as occur in compressors and turbines. Present codes can handle gap-to-chord ratios down to unity (see figures 1 and 2). The concept of a supercritical compressor blade has been tested successfully by Harry Stephens of Pratt and Whitney Aircraft in a cascade wind tunnel of the DFVLR in Germany (see figure 3).

The latest version of the design code enables one to assign the pressure distribution with a certain tolerance and still obtain shockless flow when it exists (ref. 3). This is achieved by formulating a new boundary value problem in the unit circle of the complex plane of one of the characteristic coordinates for the gas dynamics equations. It is worthwhile to review briefly the theory underlying the new code, which seems to be quite successful in practice.

In terms of characteristic coordinates ξ and η , the partial differential equations for the velocity potential ϕ and stream function ψ of plane compressible flow can be expressed in the form

$$\phi_\xi = i \frac{\sqrt{1-M^2}}{\rho} \psi_\xi \quad , \quad \phi_\eta = -i \frac{\sqrt{1-M^2}}{\rho} \psi_\eta$$

where M is the local Mach number and ρ is the density. Through analytic continuation the equations remain valid in the complex domain. The speed q and angle θ of the flow are related to ξ and η by the formulas

$$\log f(\xi) = \int \sqrt{1-M^2} \frac{dq}{q} - i\theta \quad ,$$

$$\log \overline{f(\bar{\eta})} = \int \sqrt{1-M^2} \frac{dq}{q} + i\theta \quad ,$$

where f is an analytic function mapping the flow onto a region that can be taken as the unit circle $|\xi| < 1$. Analytic continuation around the sonic line can be performed along paths on

which $1-M^2$ does not vanish.

The problem of finding an airfoil on which the pressure is a prescribed function of the arc length is equivalent to the problem of finding a profile on which the speed is assigned as a function $q = q(\phi)$ of the velocity potential. In the unit circle $|\xi| < 1$ this reduces to the question of determining the map function f and the stream function ψ from boundary conditions of the form

$$\mathrm{Re}\{\log f(\xi)\} = h(q) \quad ,$$

$$\mathrm{Re}\{\psi(\xi,\bar{\xi}) - ik\,\phi(\xi,\bar{\xi})\} = 0 \quad ,$$

where h is known in terms of q and k is a given real constant. This nonlinear boundary value problem can be solved iteratively by first guessing ϕ so that f can be calculated and then computing ψ and ϕ so that the process can be repeated. For an appropriate choice of h and k the iterations converge even in the transonic case to a shockless solution that yields the prescribed pressure distribution, except for minor deviations that must be expected in the supersonic zone. (See figures 4 and 5.)

Numerical computations suggest that the boundary value problem that has been formulated in the complex domain is well posed. This has been proved in a very special case by Sanz (ref. 4). He considers the Euler-Poisson-Darboux equation

$$u_{xx} + u_{yy} + \frac{1}{3y}\,u_y = 0$$

obtained by bringing the Tricomi equation into canonical form. The problem becomes to find a solution u in the unit circle with prescribed values of $\mathrm{Re}\{u\}$ on the boundary. Sanz introduces a decomposition

$$u(x,y) = y^{2/3}u_1(x,y^2) + u_2(x,y^2)$$

of u into two solutions that are easily reflected across the x-axis. He is led to boundary value problems for u_1 and u_2 in the upper unit semicircle that can be solved in closed form.

Numerous examples of shockless airfoils have been calculated by the method of complex characteristics using the code with prescribed $q(\phi)$. These include symmetric airfoils with two supersonic zones (figs. 4 and 5), compressor airfoils suitable for stators (fig. 1), and turbine airfoils with large turning angles (fig. 4). The procedure is largely automatic, and it is rela-

tively easy to implement new ideas about design that depend on the pressure distribution. However, further conformal transformation of the characteristic coordinates will be required if gap-to-chord ratios significantly lower than unity are desired.

It would be of interest to generalize the method of designing shockless airfoils based on giving a pressure distribution to the case of three-dimensional transonic flow past a swept wing. This might be achieved by modifying the analysis code appropriately and introducing an artifical viscosity that smears shocks. To start with it would be helpful to have a fast STAR version of the swept wing code published recently by Jameson and Caughey (refs. 2 and 5). Work on these proposals is in progress at the Courant Mathematics and Computing Laboratory.

REFERENCES

1. Bauer, F.; Garabedian, P.; and Korn, D.: Supercritical Wing Sections, Lecture Notes in Economics and Mathematical Systems, vol. 66, Springer-Verlag, New York, 1972.

2. Bauer, F.; Garabedian, P.; Korn, D.; and Jameson, A.: Supercritical Wing Sections II, Lecture Notes in Economics and Mathematical Systems, vol. 108, Springer-Verlag, New York, 1975.

3. Bauer, F.; Garabedian, P.; and Korn, D.: Supercritical Wing Sections III, Lecture Notes in Economics and Mathematical Systems, vol. 150, Springer-Verlag, New York, 1977.

4. Sanz, J.: A Well Posed Boundary Value Problem in Transonic Gas Dynamics, OER Research and Development Report C00-3077-149, Courant Math. and Computing Lab., New York Univ., February 1978.

5. Jameson, A.; and Caughey, D.: Numerical Calculation of the Transonic Flow Past a Swept Wing, ERDA Research and Development Report C00-3077-140, Courant Inst. Math. Sci., New York Univ., June 1977.

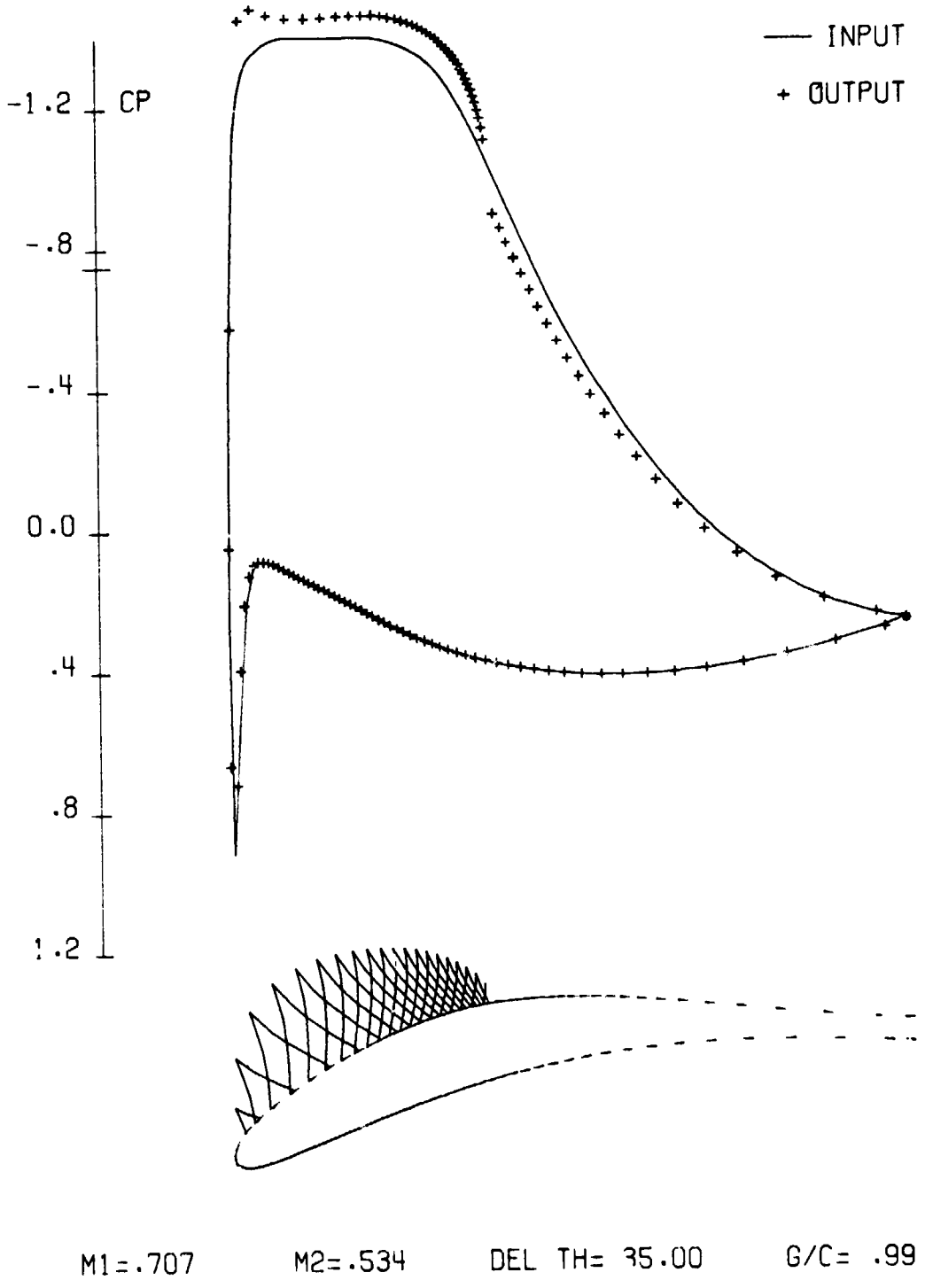

Figure 1.- Stephens stator blade.

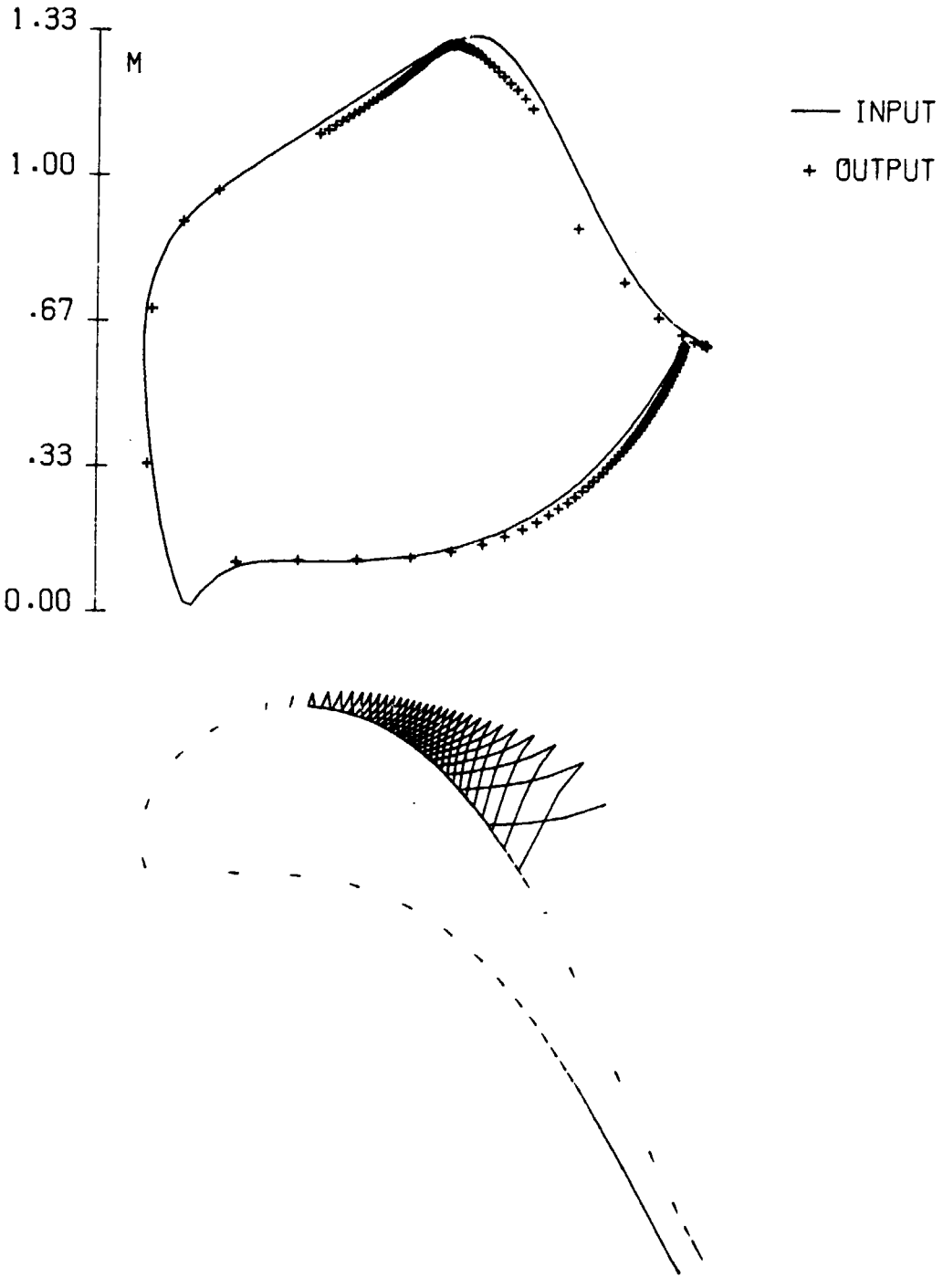

Figure 2.- Sanz turbine blade.

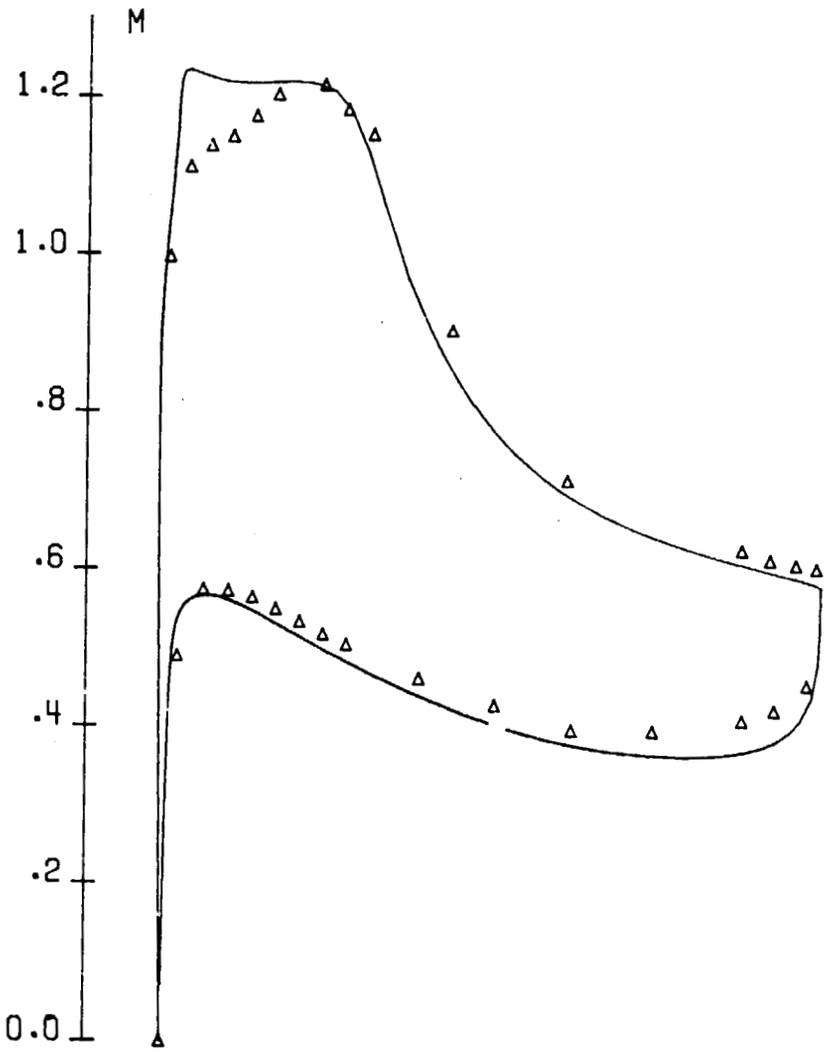

PRATT AND WHITNEY COMPRESSOR AIRFOIL R=1.1 MILLION

— THEORY M1=.780 M2=.480 DEL TH=25.0

△ EXPERIMENT M1=.775 M2=.544 DEL TH=25.5 LOSS=.0196

Figure 3.- Supercritical compressor test data.

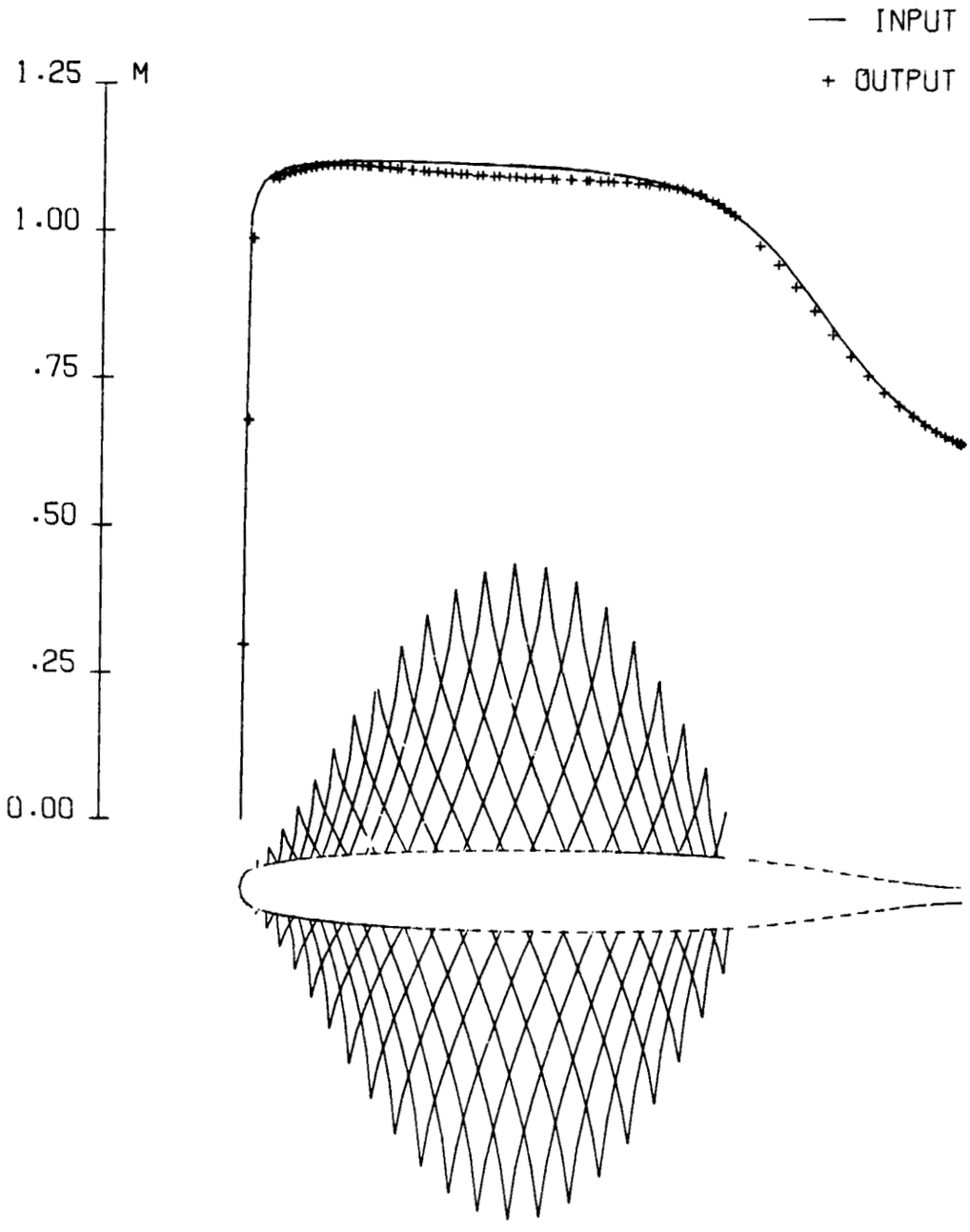

Figure 4.- Symmetric shockless airfoil.

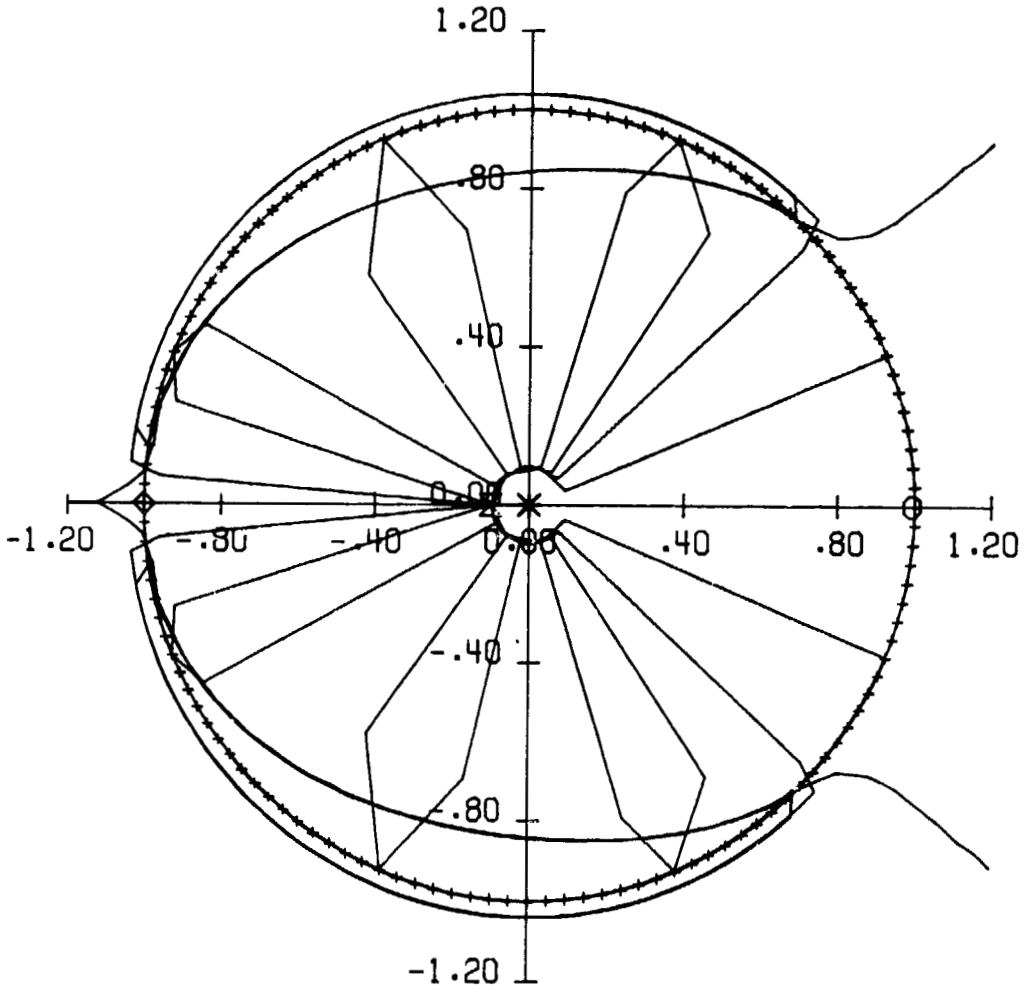

M=.831 CL= .000 DX=-.000 DY= .021 T/C=.110

Figure 5.- Complex hodograph plane.

D5

N79-20035

5

APPLICATION OF DIRECT-INVERSE TECHNIQUES TO AIRFOIL ANALYSIS AND DESIGN*

Leland A. Carlson
Bruce M. Rocholl**
Texas A&M University

SUMMARY

During the past few years, the direct-inverse technique has been developed into a numerical method, called TRANDES, that is suitable for the analysis and design of subsonic and transonic airfoils and for the evaluation of design concepts. This paper provides a general description of the method, demonstrates its application to a design-analysis type of problem, and finally, discusses a new usage of the method for the low speed high lift case.

INTRODUCTION

The basic concept of the present method (refs. 1-4) is to have a technique which can be used in either the direct (analysis) mode in which the airfoil shape is prescribed and the flowfield and surface pressures are determined, or in the direct-inverse (design) mode in which an initial nose shape is given along with the pressure distribution on the remainder of the airfoil. In the latter case, the flowfield and actual airfoil shape are computed.

The resultant computer program, called TRANDES, (ref. 5), has several unique features. In order to achieve accuracy, the method utilizes the full inviscid potential flow equation; and in order to remain simple, it solves the problem in a stretched Cartesian grid system that maps the infinite physical plane to a rectangular computational box. Further, to avoid at supersonic points difficulties associated with nonalignment of the coordinates and the flowfield, a rotated finite difference scheme is used in the solution; and the resulting transformed finite difference equations are solved iteratively by column relaxation sweeping from upstream to downstream. Finally, the method does include the effects of weak viscous interaction. The basic idea in the design case is to treat the airfoil determined by the inverse method as the displacement surface and to subtract from it a displacement thickness determined by a Nash-Macdonald (ref. 6) turbulent boundary layer computation in order to obtain the actual airfoil coordinates. It should be noted that the present program determines the airfoil shape simultaneously

*Supported by NASA Grant NSG 1174
**Presently with the Boeing Co., Seattle, WA

with the flowfield relaxation solution. For the analysis case, the approach is to calculate a boundary layer displacement thickness and to use it to correct the location of the displacement surface (i.e. airfoil ordinate plus δ^*). The flowfield is then solved iteratively with the displacement surface being updated every ten relaxation cycles.

Now, in the design mode, the shape of the nose region (typically 6-10% chord) is specified and a pressure distribution is prescribed over the remainder of the airfoil. Thus, the appropriate airfoil boundary condition in the direct region near the leading edge is the surface tangency requirement and in the inverse region, where the pressure is specified, it is essentially the specification of the derivative of the perturbation potential in the x-direction. In order to satisfy these at the airfoil boundary, which in general will not coincide with the Cartesian grid points, the derivatives in the boundary conditions are expanded as two term Taylor series about a dummy point inside the airfoil. The derivatives in these series are then written in finite difference form using second order formulas for all first derivatives and at least first order ones for higher derivatives. In the direct region, central differences are used for x-derivatives and forward (on the upper surface) for the y-derivatives. However, to prevent numerical instability, the inverse region uses a second order backward difference formula for the first term of the Taylor series representing the x-derivative. For details concerning the finite difference formulation, boundary conditions, etc., see references 2-5, and 7.

Currently, the program can be easily used to design or analyze an airfoil at a specific flight condition. Figure 1 shows such a result for the design of a low lift airfoil having a sonic rooftop followed by a linear recovery. Supercritical shockless airfoils have also been designed and examples are presented in reference 7.

Now any numerical method needs to have its accuracy verified. As a result, comparisons with other methods (refs. 8,9) have been conducted for airfoils ranging from 4 to 16% thick and Mach numbers up to 0.85. Some of these results are presented in references 2, 4, and 10; and, in general, the agreement is excellent. In addition, comparisons have been made with transonic experimental data obtained at the NAE (Ottawa) (ref. 7) and at the Ohio State University. A typical comparison with the OSU data is shown for the GA(W)-2 airfoil in figure 2. In general, the agreement for C_P, C_L, C_D, and C_M is quite acceptable.

Symbol definitions are given in an appendix.

APPLICATION TO DESIGN

To demonstrate the usefulness of the present combined design-analysis method, consider the problem of designing an airfoil having a rooftop plateau followed by a Stratford recovery (ref. 11). (It should be noted that a Stratford recovery is used here only for example purposes. While such a pressure distribution has the advantage that it maintains the boundary layer at a constant margin from separation, it also has several disadvantages which will

be mentioned later). In addition, two design concepts will be compared. In the first case, the airfoil will be designed at a low C_L with a sonic upper surface rooftop pressure plateau; while in the second case, the airfoil will be designed with a supercritical plateau at a moderate C_L. The airfoils will then be analyzed and compared at conditions other than the design point to see which one has the better characteristics.

The results for the critical rooftop design, which had a target C_L of 0.35, are shown in figure 3. The solid line is the design C_p distribution, and the final airfoil shape after accounting for the boundary layer is the one shown. Notice the reverse curvature on the upper surface and the resultant airfoil thinning. This behavior is typical of airfoils employing Stratford distributions, and frequently it leads to shapes that are structurally too thin in the vicinity of the trailing edge.

How was this shape obtained? Since the method requires the specification of the leading edge region, the nose shape can be used to control the trailing edge thickness. This approach is demonstrated in figure 4 and works easiest if an analytical nose shape controlled by a single parameter is utilized. Here the nose shapes are those associated with NACA 00XX airfoils. Notice that as the shape parameter increases, the trailing edge thickens. In addition, it should be noted that all the results in figure 4 were obtained using the same C_p boundary conditions and that each case is completely independent. Thus, obvious physical unrealities such as trailing edge crossing do not affect the final design shape. Also, asymmetric nose shapes may be used.

As indicated by figure 4 and shown specifically in figure 5, there is a unique relationship between the values of the nose shape parameters and the trailing edge ordinates. Usually the variation is essentially linear; and thus, after obtaining the results for two cases, the desired trailing edge ordinates can be obtained on the third try.

Sometimes in an aft-camber design case if the computed upper and lower surfaces are not almost parallel near the trailing edge, the flow in that vicinity will deviate from the desired pressure distribution and try to stagnate, with resultant separation. Usually by slightly adjusting back and forth the starting point of the upper surface recovery, a location can be found which will yield acceptable trailing edge slopes and pressures. This procedure may require a few extra iterations and some adjustment in nose shape, but it is normally not difficult.

Figure 6 shows the design pressure distribution and resultant airfoil shape obtained when the airfoil was designed for a higher C_L and with a Mach 1.1 supercritical rooftop. Since this airfoil was designed at higher lift (C_L = .55), the lower surface pressure distribution had a larger aft bucket. This case demonstrates the disadvantage of using a Stratford recovery on a highly aft-cambered airfoil in that the airfoil thickness is less than 2% aft of 80% chord.

Now an essential requirement of a design method, from an engineering

standpoint, is that when the designed airfoil is analyzed at the design condition, the computed C_p distribution should agree with the C_p distribution used for the design. Such analysis results are shown in figures 1, 3, and 6 and were obtained using the present method with viscous interaction included. As can be seen, the agreement is excellent. It is believed that these comparisons verify the engineering consistency of the method and, since the analysis results usually agree with experimental data, that the airfoils designed by this method should perform as predicted.

APPLICATION TO ANALYSIS

One of the difficulties associated with using a Cartesian grid for an analysis computation is that such a grid does not place a large number of points near the leading edge. Thus, the wave drag coefficient, which is determined by integration of the pressure coefficient, has an inherent error. Previous studies have determined this error is consistent and primarily a function of airfoil shape and grid spacing; and thus, correction factors can be determined from calculations at subcritical speeds where the wave drag should be zero. Unfortunately, the correction procedure suggested in reference 5 may be partially in error; and while research is continuing, the results presented in this section have been obtained using the following technique.

At a Mach number, $M_{\infty_{sub}}$, for which the flow is entirely subcritical, determine for each angle of attack, α, the normal, $C_{N_{sub,\alpha}}$, and axial, $C_{A_{sub,\alpha}}$, force coefficients. Then find the drag correction from

$$\Delta C_{DW_{sub,\alpha}} = C_{A_{sub,\alpha}} + C_{N_{sub,\alpha}} \tan\alpha$$

Next find the correction at the desired supercritical Mach number, M_∞, by

$$\Delta C_{DW_{M_\infty,\alpha}} = \Delta C_{DW_{sub,\alpha}} \sqrt{\frac{1-M_{\infty_{sub}}^2}{1-M_\infty^2}}$$

Then correct C_A at M_∞ by

$$C_{A_{corr}} = C_{A_{orig}} - \Delta C_{DW_{M_\infty,\alpha}}$$

and find

$$C_{DW_{M_\infty,\alpha}} = C_{N_{M_\infty,\alpha}} \sin\alpha + C_{A_{corr}} \cos\alpha$$

The total drag is then given by

$$C_D = C_{DW} + C_{DF}$$

where C_{DF} is the skin friction drag determined by the Squire-Young method. While not perfect, this approach seems to yield good estimates. Also, the investigation is continuing and the method does not as yet include a correction for non-conservative differencing. Finally, $M_{\infty_{sub}}$ used to determine the correction factors should be as high as possible.

Some typical analysis results are shown in figures 7-9. Figure 7 shows the effect of varying angle of attack at the design Mach number for Airfoil 109B (critical rooftop design), while figure 8 portrays variations due to changes in M_∞. As α increases, the flow on the upper surface goes supercritical and a shock forms. However, there is a desirable pressure plateau aft of the shock wave (ref. 12) which will permit boundary layer recovery. While the analysis results indicate no separation for the conditions shown, there probably would be shock induced separation at higher α's. Because of the Stratford recovery, such separation would probably lead to a large separated region and a very sharp break in the C_L (α) curve.

As can be seen in figure 8, as M_∞ increases a supersonic bubble forms and grows and eventually terminates in a shock wave for $M_\infty \geq 0.79$. Aft of the supersonic zone, the pressures closely follow the original design distribution with no separation. These, and other studies, showed that at a C_L of 0.35, drag divergence occurs at M_∞ of 0.78.

Similar studies were performed for Airfoil 209 (supercritical rooftop design), and the angle of attack variation is shown in figure 9. Note that the pressure distribution variation at positive angles of attack is considerably different from that of Airfoil 109B (fig. 7) in that a shock wave forms immediately and C_D increases rapidly. Interestingly, the upper surface pressure continues to follow the original Stratford recovery aft of the shock wave. Also, other studies indicate possible shock induced separation for $M_\infty \geq 0.77$ even at zero angle of attack.

Analysis results such as these can also be used to compare airfoils obtained using different design philosophies. An example for the two designs being considered here is shown in figure 10. Notice that for Airfoil 109B, C_D is relatively constant up to C_L's of 0.55, while Airfoil 209 exhibits a steady increase in C_D. In addition, other calculations indicate that 109B has little or no drag creep for $0.5 \leq M_\infty \leq 0.74$ and $C_L \leq 0.5$. However, Airfoil 209 has 6-18 counts of drag creep in the same range.

Now it should be pointed out that these results <u>are not</u> critical of supercritical airfoils. In fact, Airfoil 109B, whose shape was determined by the inverse method using a "critical" rooftop could be used at C_L's up to 0.55 with low drags. Thus, it is in essence a supercritical airfoil and could be used at design lift coefficients up to 0.55. The point is that with the design philosophy and assumptions used in these examples, the inverse technique appears to yield the best results by designing the shape with a critical rooftop at a low C_L. The airfoil then can, at least in this case,

be used at higher lift coefficients.

APPLICATION TO THE HIGH LIFT CASE

A few years ago Barnwell (ref. 13) demonstrated that the direct-inverse technique could be successfully applied to the low speed high lift case. By specifying the separation point, he was able to obtain excellent agreement with experiment by solving the small perturbation equation with direct boundary conditions upstream of separation and inverse boundary conditions (pressure specified) downstream of separation. Thus, the question arose -- could similar results be obtained using the full potential flow equation with viscous interaction and letting the separation point be determined as part of the solution?

With these ideas, the low speed high lift case has been modeled as shown in figure 11; and TRANDES has been appropriately modified. On the lower surface, the flowfield is determined using direct boundary conditions (airfoil specified) including the effects of weak viscous interaction. On the upper surface, the flowfield is also computed directly, with viscous interaction up to the separation point, which is determined as part of the solution. Downstream of separation, inverse boundary conditions are utilized; and the pressure is assumed to be constant in the separated zone. The present studies have shown that the separated zone pressure, which is computed as part of the solution, must be determined by conditions at both the separation point and at the trailing edge and not just on conditions in the vicinity of separation. This result is in agreement with the conclusion of Gross (ref. 14) that conditions at the downstream end of the separation bubble determine bubble pressure. For the present studies, it has been found adequate to approximate the separated pressure by

$$C_{P_{sep}} = \frac{-2(\phi_{ITE} - \phi_{sep})}{\Delta x}$$

where ϕ_{ITE} and ϕ_{sep} are the perturbation potentials at the trailing edge and the separation point, respectively.

Now in principle, the separated wake region should probably be accurately modeled with respect to physical phenomena and details; and this approach has been taken by other investigators (refs. 14-17). In the present model, however, the wake is treated very simply in that it is assumed to be inviscid with a constant pressure across the pseudo trailing edge formed by the upper and lower displacement surfaces.

Finally, initial calculations with this model have indicated that the separation point location, and thus the lift, is strongly dependent upon the boundary layer transition point. Thus, the viscous interaction scheme in TRANDES has been modified to include an initial laminar boundary layer (computed by a compressible Thwaites method), natural transition, and then a

turbulent boundary layer computed by the Nash-Macdonald method. For those cases where laminar separation occurs prior to separation, a long or short bubble, depending upon local flow conditions, is empirically modeled, and then transition is assumed.

The calculation procedure uses the same iterative successive column relaxation scheme used in the basic program except that the separation point and separated pressure level are permitted to vary. A convergence history for a typical case is shown in figure 12. Initially some oscillation occurs on each grid; but, as can be seen, the values quickly converge. Normally, four hundred iterative cycles are performed on both the medium and fine grids. The former normally yields 66 points on the airfoil, while the latter yields 130.

Results for a GA(W)-2 airfoil are shown in figures 13 and 14. In both cases, the lower surface remained entirely laminar, although results with an all turbulent lower surface boundary layer showed no significant differences. On the upper surface transition with a short separation bubble occurred near the leading edge. In general, comparison with experimental data (ref. 18) is good with respect to C_p, separation point, separated pressure level, and C_L; and thus the method is quite promising.

Figure 15 shows a comparison with experiment of C_L versus angle of attack for the same airfoil. Similar results have also been obtained at other Reynolds numbers. At the present time, research on this approach to the high lift problem is continuing in order to ensure that $C_{L_{max}}$ can be determined accurately.

As a final note, this procedure has also been applied to Airfoil 109B discussed previously. Surprisingly, the design Stratford recovery used at Mach 0.74 seems to also affect the low speed flow since a sharp break occurred in C_L (α) at 19 degrees and a C_L of 2.08, indicating another disadvantage of using a Stratford recovery.

CONCLUDING REMARKS

Based upon the results presented here, the following remarks can be stated: (1) The present viscous analysis method (TRANDES) is suitable for engineering estimates of transonic airfoil data; (2) The present inverse design method accounts for the effects of weak viscous interaction in the airfoil design process and is numerically consistent with analysis results; (3) The complete potential flow equation coupled with a boundary layer method can be used in a direct-inverse fashion to accurately compute the flow about airfoils at low speeds having massive separation.

APPENDIX

SYMBOLS

C_A	axial force coefficient
C_D	two-dimensional drag coefficient
C_{DF}	profile drag coefficient
C_{DW}	wave drag coefficient
C_L	two-dimensional lift coefficient
C_M	two-dimensional quarter chord moment coefficient
C_N	normal force coefficient
C_P	pressure coefficient
c	chord
M_∞	freestream Mach number
RN	freestream Reynolds number
α	angle of attack
ΔC_{DW}	wave drag coefficient correction
δ^*	boundary layer displacement thickness
δ_{te}	trailing edge thickness
Δx	length of separated region
ϕ	perturbation potential

Subscripts

corr	corrected value
ITE	trailing edge
sep	separation point or region
sub,α	case where flow is entirely subcritical and at angle of attack α
orig	uncorrected original value
M_∞,α	at angle of attack α and Mach number M_∞

REFERENCES

1. Carlson, L.A.: Inverse Transonic Flow Calculations using Experimental Pressure Distributions. AIAA Journal, Vol. 12, No. 4, April 1974, pp. 571-572.

2. Carlson, L.A.: Transonic Airfoil Flowfield Analysis Using Cartesian Coordinates. NASA CR-2577, August 1975.

3. Carlson, L.A.: Transonic Airfoil Design Using Cartesian Coordinates. NASA CR-2578, April 1976.

4. Carlson, L.A.: Transonic Airfoil Analysis and Design Using Cartesian Coordinates. Journal of Aircraft, Vol. 13, No. 5, May 1976, pp. 349-356.

5. Carlson, L.A.: TRANDES: A Fortran Program for Transonic Airfoil Analysis or Design. NASA CR-2821, June 1977.

6. Nash, J.F.; and Macdonald, A.G.J.: The Calculation of Momentum Thickness in a Turbulent Boundary Layer at Mach Numbers up to Unity. Aero. Res. Council, C.P. No. 963, 1967.

7. Carlson, L.A.: Inverse Transonic Airfoil Design Including Viscous Interaction. NASA CP-2001, November 1976, pp. 1387-1395.

8. Jameson, A.: Transonic Flow Calculations for Airfoils and Bodies of Revolution. Grumman Aero. Report 390-71-1, December 1971.

9. Bauer, F.; Garabedian, P.; Korn, D.; and Jameson, A.: Supercritical Wing Sections II. Springer-Verlag, New York, 1975.

10. Freuler, R.J.; and Gregorek, G.M.: An Evaluation of Four Single Element Airfoil Analytic Methods. Advanced Technology Airfoil Research, Volume I, NASA CP-2045, Pt. 1, 1979. (Paper 9 of this compilation.)

11. Stratford, B.S.: The Prediction of Separation of the Turbulent Boundary Layer. Journal of Fluid Mechanics, Vol. 5, Part 1, January 1959, pp. 1-16.

12. Whitcomb, R.T.: Review of NASA Supercritical Airfoils. Proc. of the IXth ICAS Congress, Haifa, Israel, Paper 74-10, August 1974.

13. Barnwell, R.W.: Two Inviscid Computational Simulations of Separated Flow about Airfoils. AIAA Paper 76-379, July 1976.

14. Gross, L.W.: The Prediction of Two-Dimensional Airfoil Stall Progression. AIAA Paper 78-155, January 1978.

15. Henderson, M.L.: A Solution to the 2-D Separated Wake Modeling Problem and its Use to Predict $C_{L_{max}}$ of Arbitrary Airfoil Sections. AIAA Paper 78-156, January 1978.

16. Maskew, B.; and Dvorak, F.A.: Investigation of Separation Models for the Prediction of $C_{L_{max}}$. American Helicopter Society Paper 77-33-01, May 1977.

17. Zumwalt, G.W.; and Nark, S.N.: An Analytical Model for Highly Separated Flow on Airfoils at Low Speeds. Wichita State Univ. Report AR-77-2, May 1977.

18. McGhee, R.J.; Beasley, W.D.; and Somers, D.M.: Low-Speed Aerodynamic Characteristics of a 13-Percent Thick Airfoil Section Designed for General Aviation Applications. NASA TMX-72697, May 1977.

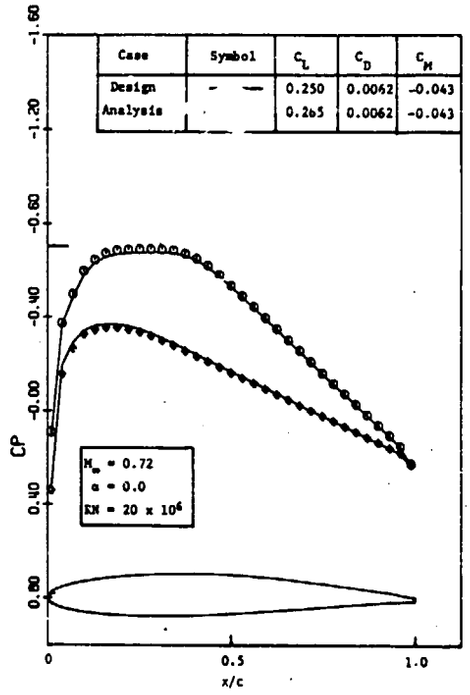

Figure 1.- Airfoil shape and comparison of design and analysis results for a low lift airfoil.

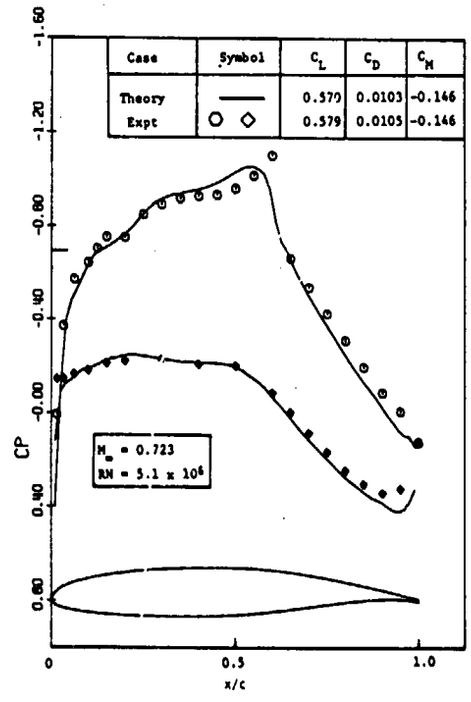

Figure 2.- Comparison of TRANDES analysis results with experimental data for a GA(W)-2 airfoil.

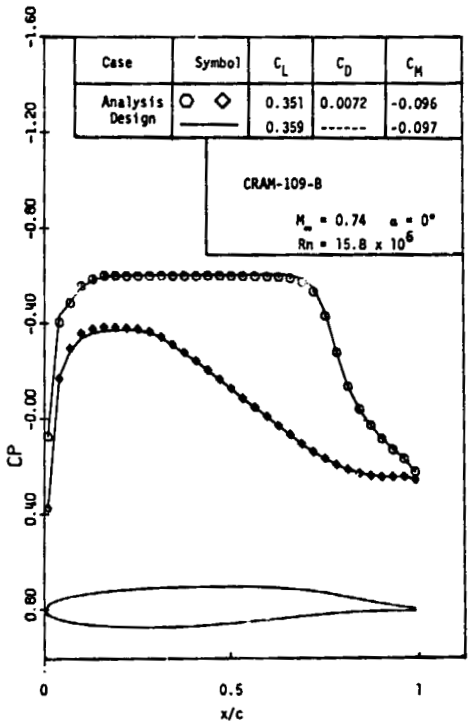

Figure 3.- Profile shape and comparison of design and analysis pressure distributions for CRAM-109-B.

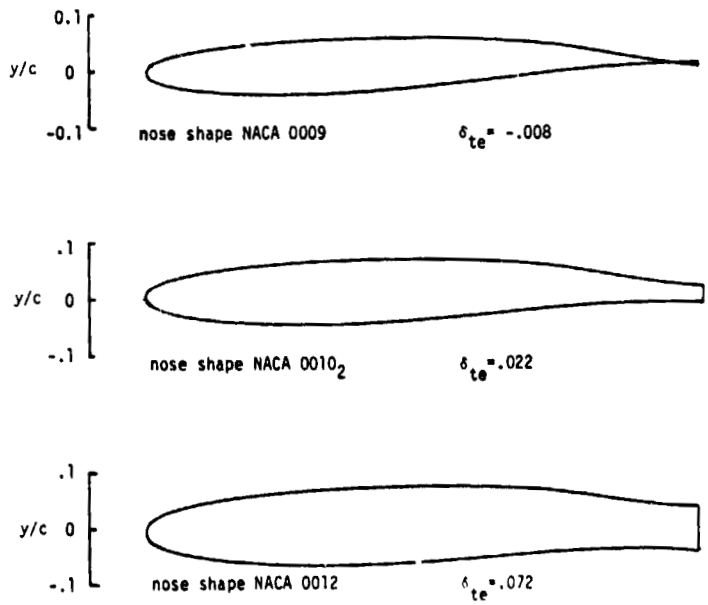

Figure 4.- Variation of trailing-edge thickness with nose-shape thickness for three nose shapes.

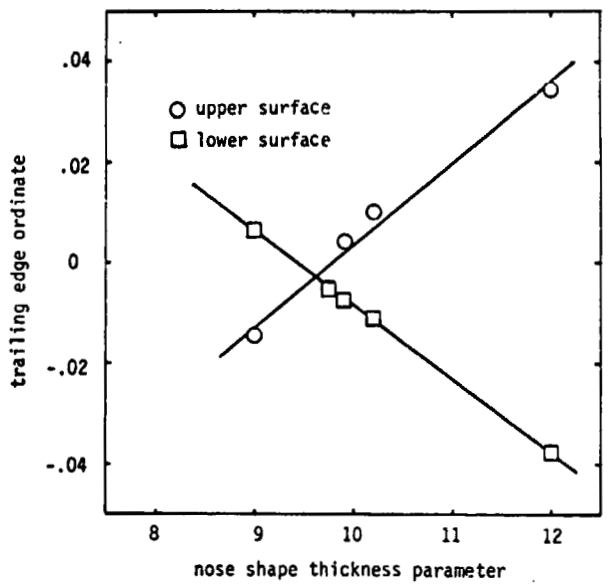

Figure 5.- Variation of trailing-edge ordinates with nose-shape thickness for upper and lower surfaces.

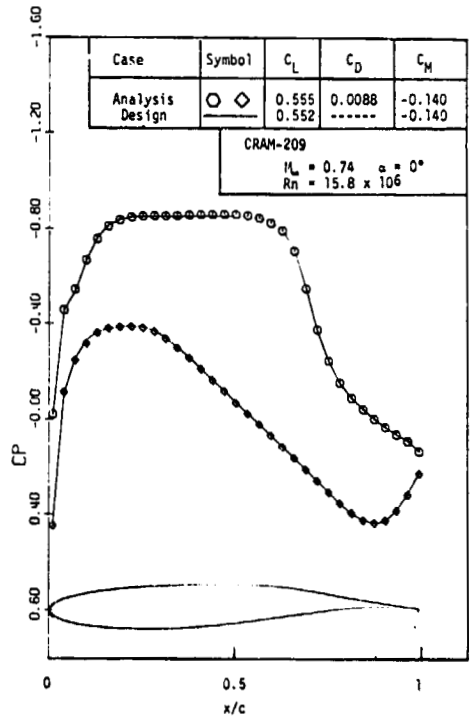

Figure 6.- Profile shape and comparison of design and analysis pressure distributions for CRAM-209.

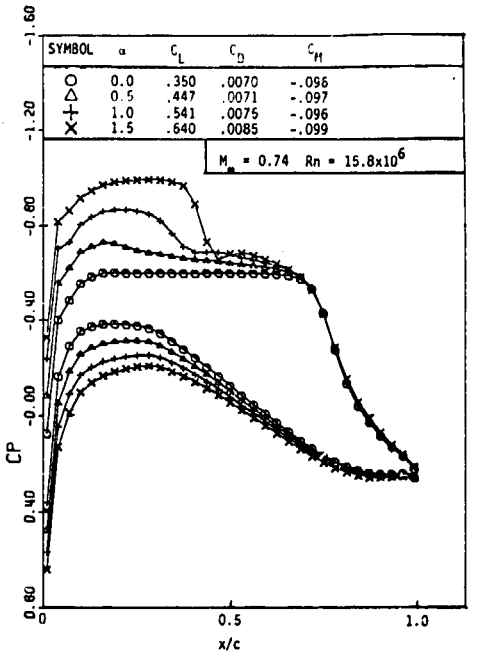

Figure 7.- Comparison of pressure distributions at four angles of attack for CRAM-109-B.

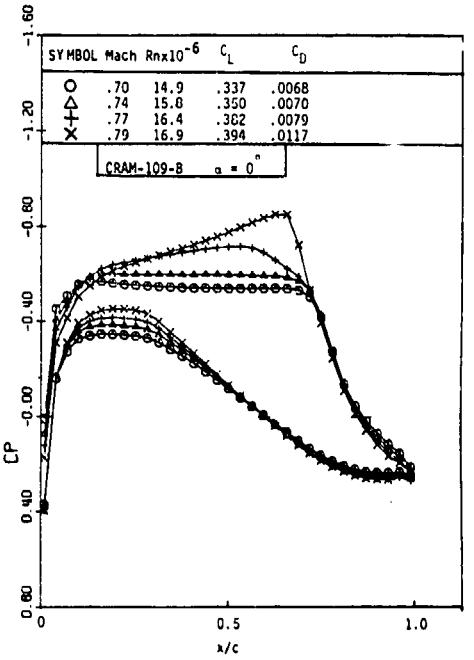

Figure 8.- Comparison of pressure distributions at four Mach numbers for CRAM-109-B.

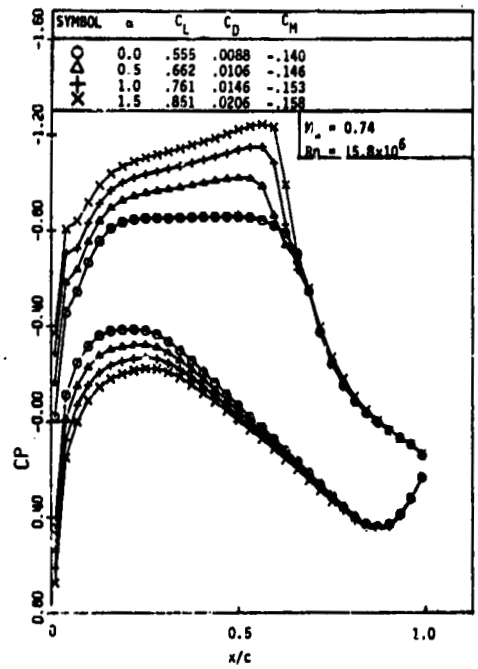

Figure 9.- Comparison of pressure distributions at four angles of attack for CRAM-209.

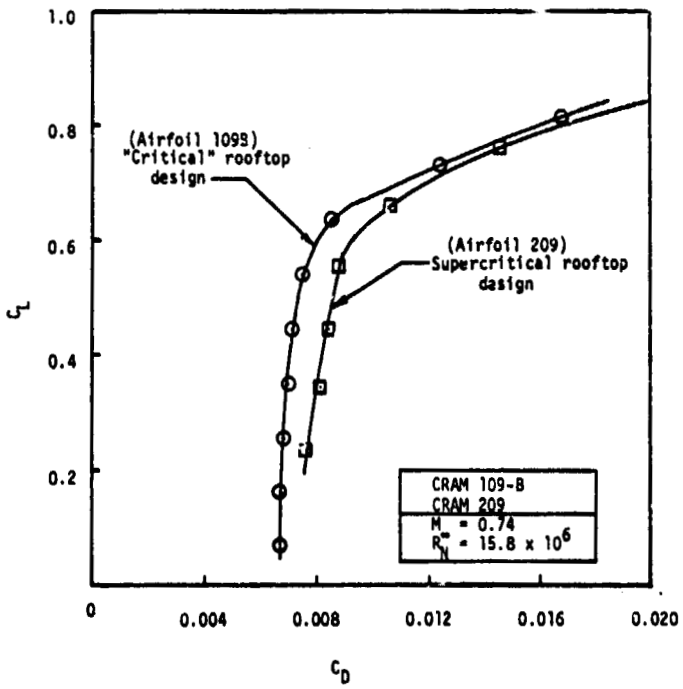

Figure 10.- Comparison of drag polars.

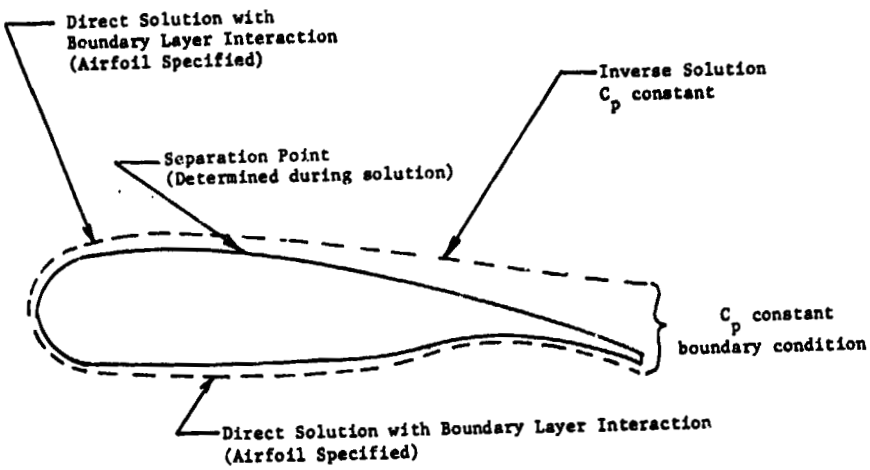

Figure 11.- Problem formulation.

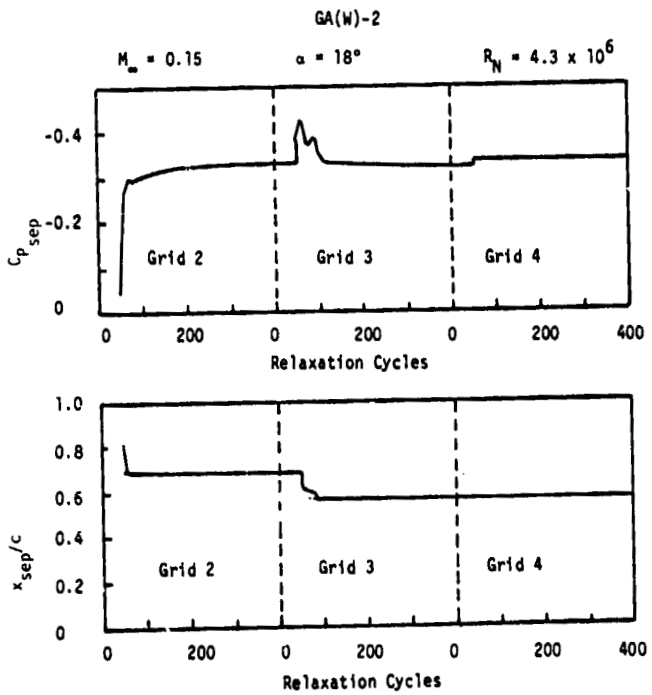

Figure 12.- Separation point and pressure behavior during relaxation process.

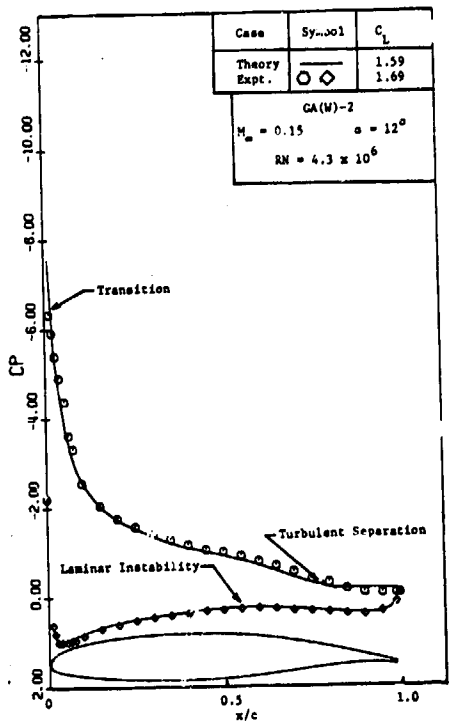

Figure 13.- Theoretical and experimental pressure-distribution comparisons. Laminar turbulent case; $\alpha = 12^{o}$.

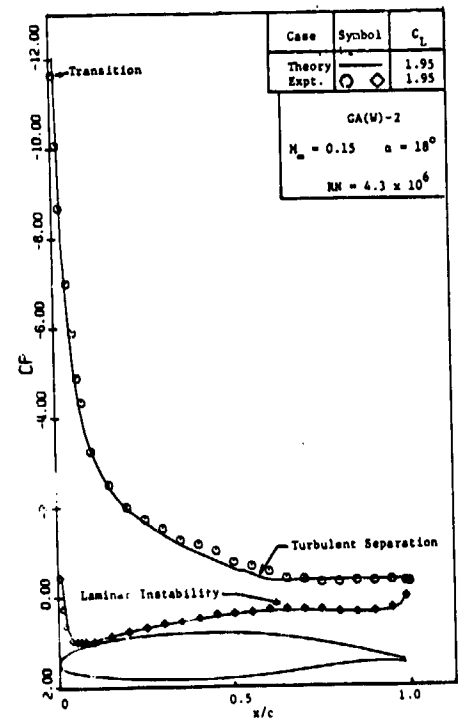

Figure 14.- Theoretical and experimental pressure-distribution comparisons. Laminar turbulent case; $\alpha = 18^{o}$.

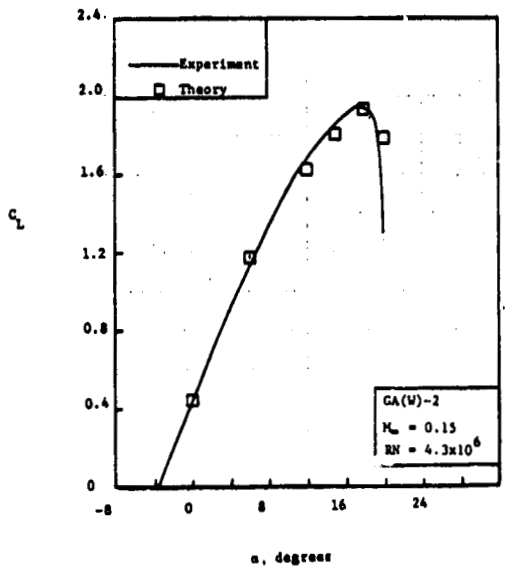

Figure 15.- Comparison of theory and experiment for C_L plotted against α for a GA(W)-2 airfoil.

D6

LOW SPEED AIRFOIL DESIGN AND ANALYSIS

6

Richard Eppler
Universität Stuttgart, West Germany

Dan M. Somers
NASA Langley Research Center

SUMMARY

A low speed airfoil design and analysis program has been developed which contains several unique features. In the design mode, the velocity distribution is not specified for one but many different angles of attack. Several iteration options are included which allow the trailing edge angle to be specified while other parameters are iterated. For airfoil analysis, a panel method is available which uses third-order panels having parabolic vorticity distributions. The flow condition is satisfied at the end points of the panels. Both sharp and blunt trailing edges can be analyzed. The integral boundary layer method with its laminar separation bubble analog, empirical transition criterion, and precise turbulent boundary layer equations compares very favorably with other methods, both integral and finite-difference. Comparisons with experiment for several airfoils over a very wide Reynolds number range were very favorable. Applications to high lift airfoil design were also demonstrated.

INTRODUCTION

The application of potential flow theory together with boundary layer theory to airfoil design and analysis was accomplished many years ago. Since that time, high speed computers have allowed results to be obtained more cheaply and quickly than through the use of wind tunnels. Accordingly, the tendency today is toward more and more commonly applicable computer programs. The programs reduce the amount of required wind tunnel testing to that of fundamental phenomena and allow airfoils to be tailored to each specific application.

The program described in this paper has been developed over the past 20 years. We hope to demonstrate that it has reached a stage where some progress can be made in low speed airfoil design and analysis.

This paper does not repeat all of the details included in other papers. Special emphasis is given, however, to those features which are new or different from those in other mathematical models.

SYMBOLS

C_f	skin-friction coefficient
c	airfoil chord
c_d	section profile-drag coefficient
c_l	section lift coefficient
c_m	section pitching-moment coefficient about quarter-chord point
H_{12}	shape factor, $\frac{\delta_1}{\delta_2}$
H_{32}	shape factor, $\frac{\delta_3}{\delta_2}$
l	length
P	point
R	Reynolds number based on free-stream conditions and airfoil chord
R_{δ_2}	Reynolds number based on local conditions and boundary layer momentum thickness
t	thickness of airfoil
U	free-stream velocity
u	local velocity on airfoil
V	velocity; main pressure recovery design variable
x	airfoil abscissa; length
α	angle of attack relative to zero-lift line, deg
α^*	angle of attack relative to zero-lift line for velocity specification in design method, deg
δ_1	boundary layer displacement thickness
δ_2	boundary layer momentum thickness
δ_3	boundary layer energy thickness
ν	kinematic viscosity
ω	total amount of pressure recovery

ω' initial slope of pressure recovery

Subscripts:

l lower surface; local point on airfoil

lm lower surface main pressure recovery

N last point on airfoil

n variable number

u upper surface

um upper surface main pressure recovery

∞ free-stream conditions

DISCUSSION

Inviscid Method

The potential flow part of the mathematical model is incompressible at this time. Two different modes of operation are available.

Design mode.- The first mode is the inverse or design method described in references 1 and 2. This method differs from other inverse methods in that the velocity distribution is not specified for only one angle of attack. Instead, angles of attack which will result in constant velocity over specified segments of the airfoil are input. In other words, pairs of parameters are specified: the first being the segment of the airfoil; the second, the angle of attack relative to the zero-lift line, α^*, which will result in constant velocity over that segment. (See fig. 1.) Of course, some matching conditions must be met to guarantee a smooth velocity distribution for all angles of attack. Toward the trailing edge, on both surfaces, a main pressure recovery can be specified. Finally, a short closure contribution must be introduced to insure that the trailing edge will be closed. The example airfoil shown in figure 1 is specified by the following:

(1) For the upper surface segment from the trailing edge forward to about $x/c = 0.15$, $\alpha^* = 8^0$. Within this segment, the main pressure recovery is specified starting at $x/c = 0.50$.

(2) For the upper surface segment from $x/c = 0.15$ to 0.05, $\alpha^* = 10^0$.

(3) For the upper surface segment from $x/c = 0.05$ to the leading edge, $\alpha^* = 12^0$.

(4) For the entire lower surface, $\alpha^* = 2^0$. The main pressure recovery on the lower surface is specified starting at about $x/c = 0.45$.

In reality, the segments corresponding to the various α^* values are not specified in x/c but rather in the conformal mapping plane in which the airfoil is represented by a circle. So far, no difficulties have arisen in correlating the arcs of the circle with the segments of the airfoil.

It should be remembered that for any given velocity distribution there does not necessarily exist a "normal" airfoil. For example, the closure contributions could be quite large which would result in a very large trailing edge angle. The closure contributions could also give rise to a region of negative thickness near the trailing edge. Accordingly, several iteration options have been included which allow the trailing edge angle to be specified while certain α^* values or the total amount of pressure recovery is iterated. The choice of iteration option allows questions such as the following to be answered: What laminar bucket width is possible given a certain amount of pressure recovery? What amount of pressure recovery is required to produce the desired laminar bucket width? The iteration option selected for the example airfoil iterates the amount of upper and lower surface pressure recovery while holding the α^* values fixed.

Analysis mode.- The second mode of operation is an airfoil analysis method. The method employs panels with distributed surface singularities (fig. 2). The panels are defined by a third-order spline fit of the airfoil coordinates with the end points of the panels being the input airfoil coordinates themselves. The surface singularities consist of a parabolic vorticity distribution. The flow condition, which requires the inner tangential velocity to be zero, is satisfied at each airfoil coordinate (i.e., at the end points of the panels, not the mid-points). Thus, no restrictions are placed on the point distribution, no smoothing or rearranging of the coordinates is performed, only the original airfoil coordinates are used. An option is included, however, by which additional points can be splined in between the original coordinates. This option is helpful if a portion of the airfoil has a sparse number of points or if part of the airfoil is to be geometrically rotated about a flap hinge point. In the latter case, the connection between the forward portion of the airfoil and the flap is defined by an arc consisting of additional points which are generated automatically according to an input length.

As in other panel methods, a singularity arises from the circulation around the airfoil which is unconstrained unless required to satisfy a Kutta condition. Two different cases are involved.

The first case is a sharp trailing edge having either a zero or non-zero angle. The inner tangential flow condition fails in this case at the trailing edge. Therefore, it is replaced by the condition that the normal velocity, relative to the bisector of the trailing edge angle, be zero. This condition can only be satisfied if the vorticities on the upper and lower surfaces approach the same value but with opposite signs as the trailing edge is approached. This means that the velocities have to be the same on both sides of the trailing edge. Thus the normal flow condition along with equal velocities on both sides of the trailing edge can be considered as a Kutta condition.

Unfortunately, a second singularity is caused by a finite change in the circulation around the airfoil which results in an infinite change in the velocity at the sharp trailing edge. No wonder the equation system is singular for every Kutta condition. Thus, an additional equation is required while one equation already in the equation system can be omitted. This additional equation consists of an extrapolation of the vorticity to the trailing edge and an averaging at the trailing edge. The omission of one of the equations in the system can sometimes cause errors at the point whose flow condition is governed by the omitted equation. In other words, the equation system is not exactly singular, due to small numerical approximations. So, none of the equations is omitted and the entire equation system is multiplied by the transposed matrix. This implies that all the equations are solved as accurately as possible in a least-squares sense. The results of this procedure are very precise.

The second case is a blunt trailing edge (fig. 3) - one in which the upper and lower surface trailing edge points are not the same. For this case, two different procedures have been examined.

The first procedure extends the airfoil along straight "wake limits" having constant opposite vorticity (fig. 3, top). At both the upper and lower surface trailing edge points, a normal velocity condition must be satisfied. No flow condition is satisfied in the wake.

The second procedure introduces at the base of the airfoil not only a vorticity but also a source distribution (fig. 3, bottom). Both are linear distributions over the base length and determined such that no flow singularitites occur at either of the two trailing edge points.

Both blunt trailing edge models have one more flow condition than unknown vorticities. The $n + 1$ equations for n unknowns are treated in the same manner as the sharp trailing edge case even though they are much less critical with respect to circulation changes.

For all cases the computing times are moderate; the results, very precise. A comparison of the design and the panel methods for the example airfoil is shown in figure 4.

Viscous Method

The laminar and turbulent boundary layer development is computed by a simple method (ref. 3) using, like many others, integral momentum and energy equations. It has been shown that laminar boundary layer development is predicted quite well by this method. The turbulent boundary layer routines are based upon the best available empirical skin friction, dissipation, and shape factor laws. No further errors are introduced by mathematical simplifications like integrating the ordinary differential equations from the momentum and energy laws by averaging the right sides of the equations.

Of special interest are the predictions of transition from laminar to turbulent boundary layer and the separation of the turbulent boundary layer. The tendency toward separation is determined solely by the shape factor

$$H_{32} = \frac{\delta_3}{\delta_2}$$

where δ_3 is energy thickness and δ_2 is momentum thickness. (Note that H_{32} has the opposite tendency from H_{12} which contains the displacement thickness δ_1 instead of the energy thickness.) For laminar boundary layers there exists a constant and reliable lower limit of H_{32}, which equals 1.515 and corresponds to laminar separation. For turbulent boundary layers no such unique and reliable limit has been determined. It can be stated, however, that the turbulent boundary layer will separate if H_{32} goes below 1.46 and will not separate if H_{32} remains above 1.58. It has been noticed that thicker boundary layers tend to separate at lower H_{32} values. In the present method, turbulent separation is predicted if H_{32} drops to 1.46. This is a fairly good assumption because the method usually predicts relatively low values of H_{32}. The uncertainty is not as bad as it first appears in that H_{32} changes rapidly near separation. Nevertheless, results must be checked carefully with respect to turbulent separation.

The second feature of special interest is the prediction of transition. Two different procedures are in vogue today - the amplification method and the shape-factor — Reynolds-number method. The first procedure requires much more computing time because many frequencies must be traced to find the one wave which is suddenly amplified to the ratio set as the transition limit. The better procedure cannot be selected until we know more about transition. The differences between the two procedures are small for normal airfoil applications as the local Reynolds number changes quickly near transition. So, we still use the simple criterion shown in figure 5. Thus, the transition Reynolds number depends only on the shape factor H_{32}. Adverse pressure gradients and, hence, low values of H_{32} result in lower transition Reynolds numbers and vice versa. As will be seen later, it is very informative to plot the boundary layer development in this form.

It must be pointed out that the boundary layer development immediately after transition has a significant influence on the entire flow. In our program the prediction of transition results in a switch from the laminar skin friction, dissipation, and shape factor laws to the turbulent ones, without changing H_{32} and δ_2. This is also done if laminar separation is predicted before the transition criterion is reached. The H_{32} development

for the linearly decreasing velocity distribution defined by

$$V = V_\infty(1 - x/l)$$

is shown in figure 6 for Reynolds numbers ranging from 0.125×10^6 to 32×10^6 where Reynolds number $R = V_\infty l/\nu$. This plot illustrates the well-known fact that the laminar boundary layer shape factor H_{32} and laminar separation are independent of Reynolds number. It also shows that for high Reynolds numbers, transition occurs before laminar separation. For turbulent boundary layers, H_{32} and separation do depend on Reynolds number. The most important information to be gained from figure 6 is the behavior of H_{32} at the beginning of the turbulent boundary layer. For higher Reynolds numbers, H_{32} increases immediately to values greater than about 1.7. For lower Reynolds numbers this increase is less rapid and the maximum values of H_{32} are lower. For a Reynolds number of 0.125×10^6, H_{32} remains below 1.58 which means that the method cannot determine whether or not an attached turbulent boundary layer exists. Such results must be studied in more detail. In figure 7 the laminar and turbulent skin-friction laws, $C_f(R_{\delta_2}, H_{32})$ are presented. The laminar law has an exponent of -1. The turbulent law is a slightly modified Ludwieg-Tillman law with an exponent of -0.232. This law is experimentally derived and tested for R_{δ_2} between 10^3 and 10^5 as shown by the phantom lines in figure 7. Below R_{δ_2} equal to 10^3, these lines continue in some manner. The flat plate case has been investigated in more detail and the results indicate that the flat plate line continues more or less steadily and finally bends down to the laminar law line rather steeply, depending on roughness and free-stream turbulence.

In our method, the Ludwieg-Tillman law is extrapolated along straight lines. This probably represents an upper limit for C_f for R_{δ_2} less than 10^3. But it is obvious that for R_{δ_2} equal to 10^2 the laminar and turbulent laws differ little and for lower R_{δ_2} the turbulent C_f values are below the laminar ones.

For results such as those shown in figure 6, it is interesting to look at the C_f values computed by our method. For every point x/l, R_{δ_2} and H_{32} are known and, hence, C_f is known. The variation of C_f with R_{δ_2} is shown in figure 7. The result is remarkable. The curves for $R = 0.125 \times 10^6$ and $R = 0.25 \times 10^6$ do not even come close to an area where one can confidently speak of a turbulent skin-friction law. Such "underdeveloped" turbulent boundary layers exist in nature only in the form of laminar separation bubbles. After examining many different cases, it was determined that there is a certain

analogy between the predicted "underdeveloped" turbulent boundary layers with low H_{32} values and laminar separation bubbles. The boundary layer results computed by our method show a stronger bubble analogy as Reynolds number decreases and as the adverse pressure gradient after transition becomes steeper. If the analogy occurs in the results, the only way to alleviate it is to reduce the adverse pressure gradient after transition. The experimental results for laminar separation bubbles show the same tendencies. Accordingly, it is very helpful to have this bubble analog in the computed results.

In summary, the boundary layer method has generated good results for many, very different cases. It should be noted, however, that no fundamental problem exists in replacing the boundary layer subroutines in our program with other subroutines. Some applications will be discussed in the next section. But before that a few comparisons with other boundary layer methods will be made.

Two shape factor developments computed by a program written by Konhauser, which uses the Cebeci-Smith method (ref. 4), are shown by dashed curves in figure 6. The two curves, which are for the Reynolds numbers of 8×10^6 and 16×10^6, agree quite well with the present method for x/l up to about 0.2. Then as x/l increases, the results computed by the Cebeci-Smith method show considerably less tendency toward separation. This demonstrates that the separation limit of H_{32} equal to 1.46 that we use is conservative with respect to turbulent separation. Comparisons for lower Reynolds numbers are not possible at this time because Mr. Konhauser has been unable to obtain results from the Cebeci-Smith method at lower Reynolds numbers.

The development of displacement thickness along the upper surface of an RAE 101 airfoil for an angle of attack of 8.2^0 and a Reynolds number of 1.6×10^6 is shown in figure 8. This case was computed by J. L. Hess using a Cebeci-Smith program with different numbers of elements and different smoothing procedures (ref. 5). The results from the program as indicated by the symbols agree very well with those computed by Hess with the greatest number of elements. This agreement is remarkable indeed knowing that this is the first comparison of this type which we have made and is not the result of a careful choice of data.

The curves in figure 9 demonstrate that, in using integral momentum and energy laws, the introduction of mathematical simplifications can cause much larger errors than those which result from the use of a one parameter method. In figure 9, our method and a method developed by L. Truckenbrodt (ref. 6) are compared with experimental results obtained by Wortmann (ref. 7). Truckenbrodt's method is based upon the same skin-friction and dissipation laws as the present method, but includes further mathematical simplifications which produce an error of about 50 percent for the adverse pressure gradient shown.

In the present method, the momentum thickness at the trailing edge is used for the calculation of the drag by a Squire-Young type formula. We have found that our method predicts slightly higher drag values than those measured

experimentally. We hesitate to change the skin-friction laws or other parts of the program, however, as the differences between our predictions and experimental measurements depend upon the wind tunnel in which the experiments were performed. (See figs. 10 and 11.)

It should be mentioned that the program includes a lift coefficient correction due to boundary layer separation but, as yet, does not include one due to boundary layer displacement thickness.

As a final remark, the development of the laminar boundary layer should be discussed. It is very informative to plot this development as shown in figure 5. This plot reveals several important points. For a constant velocity segment ($\alpha = \alpha^*$), the boundary layer approaches the Blasius solution having a shape factor H_{32} of 1.573 and increasing momentum thickness δ_2. This corresponds to the vertical lines in figure 5. As the angle of attack is increased, the velocity distributions become concave over the forward portion of the airfoil or, in other words, the airfoil "pulls a peak" at the leading edge. These concave distributions are similar to those which produce Hartree boundary layers. But, whereas the Hartree boundary layers result in lower but still constant shape factors, the curves in figure 5 show increasing H_{32} with increasing R_{δ_2} for α greater than α^*. This means that these velocity distributions are more concave than the Hartree (power law) distributions. Thus, as the angle of attack is increased even more, these distributions will result in laminar separation at the leading edge. This problem is eliminated by the introduction of segments having higher α^* values near the leading edge. Obviously, it is much easier to control the development of the shape factor by manipulating α^* values than by changing a given velocity distribution at only one angle of attack.

Applications

In this section, we shall apply the mathematical model to a variety of airfoil problems. The final result is always a plot which includes c_l versus c_d, c_l versus α, c_m versus α, and transition and separation versus c_l as is normally plotted for wind tunnel results. It is, of course, very easy to obtain more details such as pressure distributions, boundary layer development, and laminar separation bubble analogs.

The first application is a sailplane airfoil designed for low drag at a Reynolds number of about 3×10^6 and a soft stall at a Reynolds number of about 1×10^6. The soft stall can easily be achieved by introducing a moderate concave pressure recovery on the upper surface and by preventing laminar separation and the rapid forward movement of transition with increasing angle of attack. The latter feature requires only increasing α^* values toward the leading edge.

The theoretical results agree well with the experimental measurements obtained by D. Althaus as shown in figure 10. In the wind tunnel experiment, transition location was determined by the stethoscope method which seems to detect only fully developed turbulence and, thus, the experimental transition locations lie somewhat downstream of the theoretical ones although the trends with angle of attack agree well. The stall observed in free flight was very soft.

The next application shows that the program produces reasonable results for higher Reynolds numbers as well. The coordinates of an NACA 64_3-618 airfoil were input and the theoretical results are compared with the experimental measurements (ref. 8) in figure 11.

The program can also be applied at very low Reynolds numbers. Airfoil 387 was designed for model airplanes. At these low Reynolds numbers, the bubble analog indicated that only very slight adverse pressure gradients were possible and, accordingly, a relatively thin airfoil (t/c = 0.09) resulted. This airfoil was recently tested by Volkers (ref. 9). The theoretical results compare favorably with experiment for a Reynolds number of 2×10^5 (fig. 12), even though the measurements do show the typical effect of laminar separation bubbles. For a Reynolds number of 1×10^5, the experiment shows even more the effect of laminar separation bubbles, but still with attached turbulent flow at the trailing edge. For a Reynolds number of 6×10^4, both experiment and theory indicate a large amount of separation. It seems remarkable that the experimentally determined critical Reynolds number agrees so well with that predicted by the theory.

High lift airfoils can also be designed and analyzed with the program. One such airfoil designed by Chen (ref. 10) is shown in figure 13. Notice that the panel method has predicted some oscillations in the velocity distributions. (The occurrence of these oscillations is common for the newer airfoil designs as opposed to the older NACA airfoils for which the panel method predicts smooth velocity distributions.) The objective of this airfoil design was to achieve on the upper surface a certain length of constant velocity followed by a Stratford pressure recovery (ref. 11). The boundary layer development for this airfoil showed early transition due to the oscillations in the velocity distributions. These results, of course, were unrealistic and, accordingly, a new airfoil, 1220, was designed with the same objective (fig. 14). To demonstrate that the oscillations in the velocity distributions for the Chen airfoil were not produced by the panel method, the velocity distributions from the panel method are included for the new airfoil.

The boundary layer results for this airfoil are quite interesting. If the transition point is just ahead of the pressure recovery, the predicted boundary layer remains attached until the closure contribution is reached. This occurs at a Reynolds number of 6×10^6 (fig. 15). This demonstrates that the method predicts the boundary layer development for an extreme pressure recovery quite well. (This had already been tested by M. Schulz.) At a Reynolds number of 3×10^6, an intense laminar separation bubble was predicted at the beginning of the pressure recovery. At a Reynolds number of 9×10^6,

transition is predicted further ahead of the pressure recovery and a thicker (turbulent) boundary layer arrives at the beginning of the pressure recovery than if the flow had remained laminar up to that point. And so, again the precise initial conditions for the Stratford pressure recovery are not satisfied and early turbulent boundary layer separation is again the result. This must be true for every airfoil having a Stratford pressure recovery derived from one initial condition.

Accordingly, a new airfoil was designed which would not exhibit the undesirable characteristics of the previous airfoil. Because maximum lift normally occurs, in flight, at lower Reynolds numbers, the objective of the new design was to develop a high lift coefficient at a Reynolds number of 1×10^6 while still maintaining a soft stall for practical reasons. The airfoil which resulted is shown in figure 16. The α^* distribution for the forward portion of the upper surface was chosen such that no sudden movement of laminar separation or transition is possible. This feature is demonstrated in figure 17 in which all the curves show decreasing H_{32} with increasing R_{δ_2}. The pressure recovery is concave but not nearly as extreme as the Stratford distribution. It should be mentioned that the total amount of pressure recovery for this distribution is only slightly less than that of the Stratford distribution. Thus, the moderate pressure recovery results in more lift.

Another feature of this design is that the upper and lower surface velocities ahead of the closure contribution were not required to be equal as in the case of the Chen airfoil. It has already been demonstrated by the NACA 6-series airfoils that this condition is not necessary.

The theoretical results for this new airfoil are shown in figure 18. The maximum lift coefficients to be achieved by such airfoils are surely above 2.

CONCLUSIONS

The present program system of combined potential flow and boundary layer theories has been discussed. Applications and comparisons with experiments over a very wide range of Reynolds numbers have been shown. The results are most satisfactory and open the door to the tailoring of airfoils for specific objectives.

REFERENCES

1. Eppler, R.: Direct Calculation of Airfoils From Pressure Distribution. NASA TT F-15417, 1974.

2. Eppler, R.: Results of the Combined Application of Boundary Layer and Profile Theory. NASA TT F-15416, 1974.

3. Eppler, R.: Praktische Berechnung Laminarer und Turbulenter Absauge-Grenzschichten (Practical Calculation of Laminar and Turbulent Suction Boundary Layers). Ingenieur-Archiv, Bd. 32, 1963, pp. 221-245.

4. Cebeci, T.; and Smith, A. M. O.: Analysis of Turbulent Boundary Layers. Academic Press, 1974.

5. Hess, J. L.: A Fully Automatic Combined Potential-Flow Boundary-Layer Procedure for Calculating Viscous Effects on the Lifts and Pressure Distributions of Arbitrary Three-Dimensional Configurations. MDC J7491, Douglas Aircraft, 1977.

6. Truckenbrodt, E.: Ein Quadratur-Verfahren zur Berechnung der Laminaren und Turbulenten Reibungsschicht fuer Zweidimensionale und Axialsymmetrische Stroemung. Ingenieur-Archiv, Bd. 20, 1952, pp. 211-228.

7. Wortmann, F. X.: A Contribution to the Design of Laminar Profiles for Gliders and Helicopters. TIL/T.4903, British Ministr. Aviat., Feb. 1960.

8. Abbott, I. H.; Von Doenhoff, A. E.; and Stivers, L. S., Jr.: Summary of Airfoil Data. NACA Rep. 824, 1945.

9. Volkers, D. F.: Preliminary Results of Windtunnel Measurements on Some Airfoil Sections at Reynolds Numbers Between 0.6 x 10^5 and 5.0 x 10^5. Memorandum M-276, Delft University of Technology, Department of Aerospace Engineering, The Netherlands, 1977.

10. Bingham, G. J.; and Chen, A. W.: Low-Speed Aerodynamic Characteristics of an Airfoil Optimized for Maximum Lift Coefficient. NASA TN D-7071, 1972.

11. Stratford, B. S.: The Prediction of Separation of the Turbulent Boundary Layer. J. Fluid Mech., vol. 5, pt. 1, Jan. 1959, pp. 1-16.

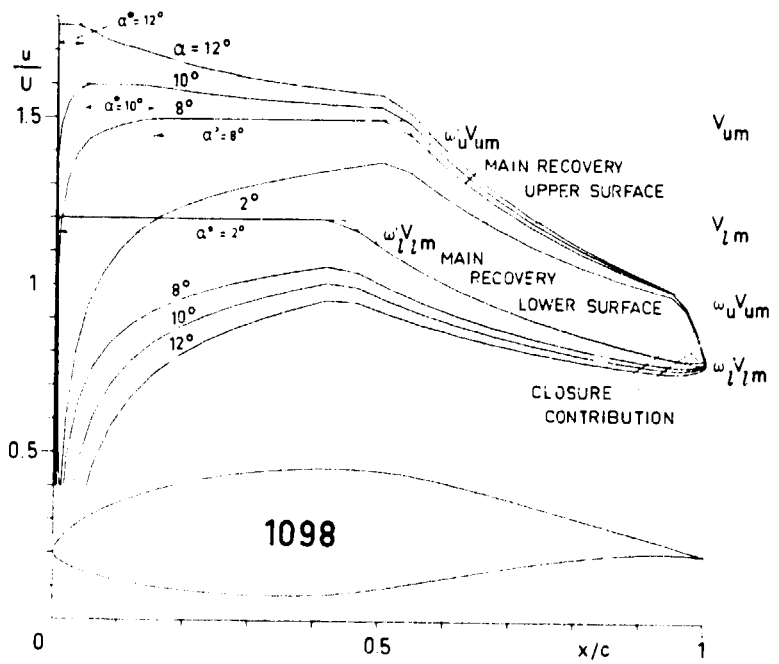

Figure 1.- Design method. (α relative to zero-lift line.)

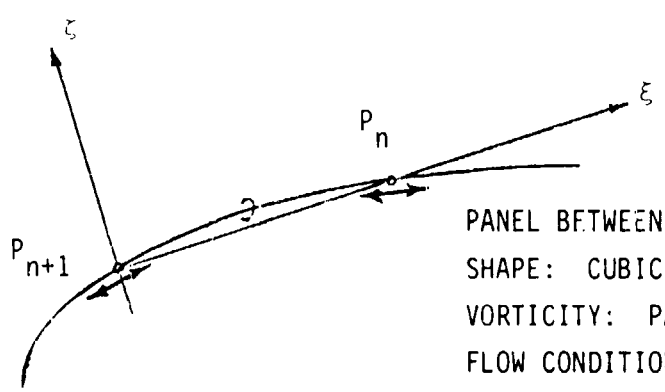

PANEL BETWEEN P_n AND P_{n+1}:
SHAPE: CUBIC
VORTICITY: PARABOLIC
FLOW CONDITION: INNER TANGENTIAL FLOW
COMPONENT EQUALS ZERO AT P_n AND P_{n+1}

Figure 2.- Panel method.

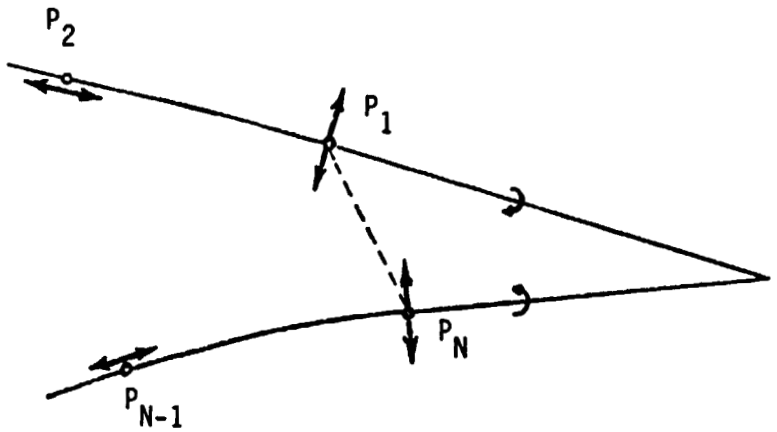

WAKE 1: $P_N = -P_1$ (KUTTA-CONDITION)
TRIANGULAR WAKE WITH CONSTANT OPPOSITE VORTICITY
NORMAL FLOW CONDITION AT P_1 AND P_N
NO FLOW CONDITION AT THE WAKE

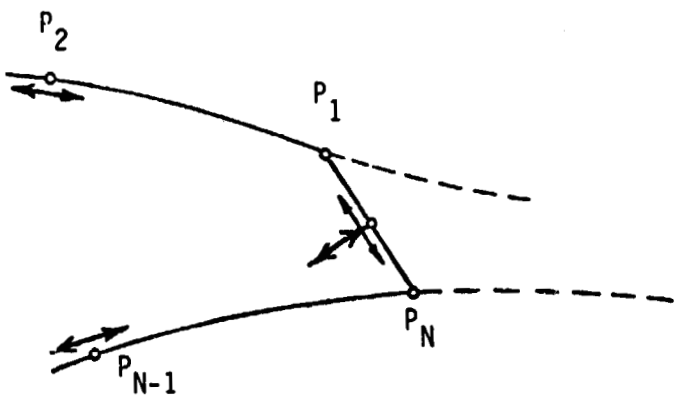

WAKE 2: $P_N = -P_1$ (KUTTA)
LINEAR VORTICITY AND SOURCE DISTRIBUTION AT THE BASE SUCH THAT NO FLOW SINGULARITY EXISTS AT P_1 AND P_N. FLOW CONDITIONS: INNER TANGENTIAL AND INNER NORMAL VELOCITY EQUALS ZERO AT THE MIDDLE OF THE BASE

Figure 3.- Blunt trailing edge.

C-2

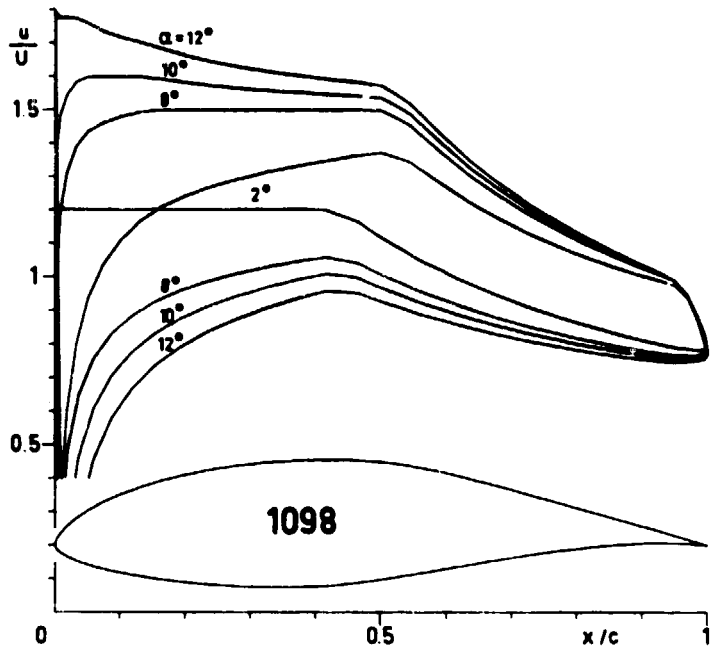

Figure 4.- Comparison of design and panel methods.
(α relative to zero-lift line.)

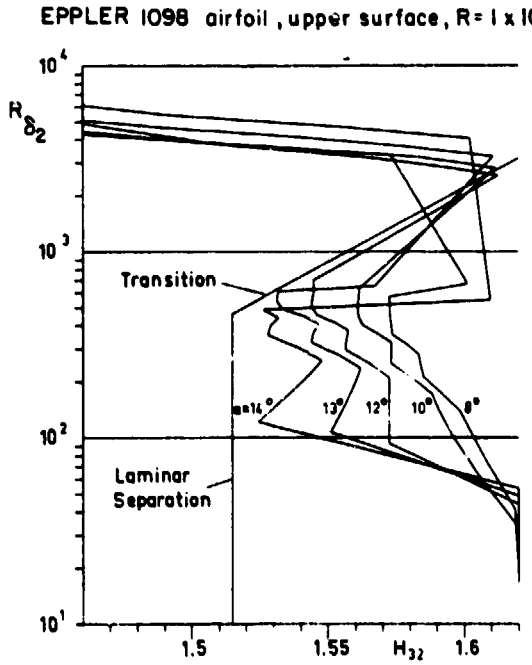

Figure 5.- Boundary layer development.

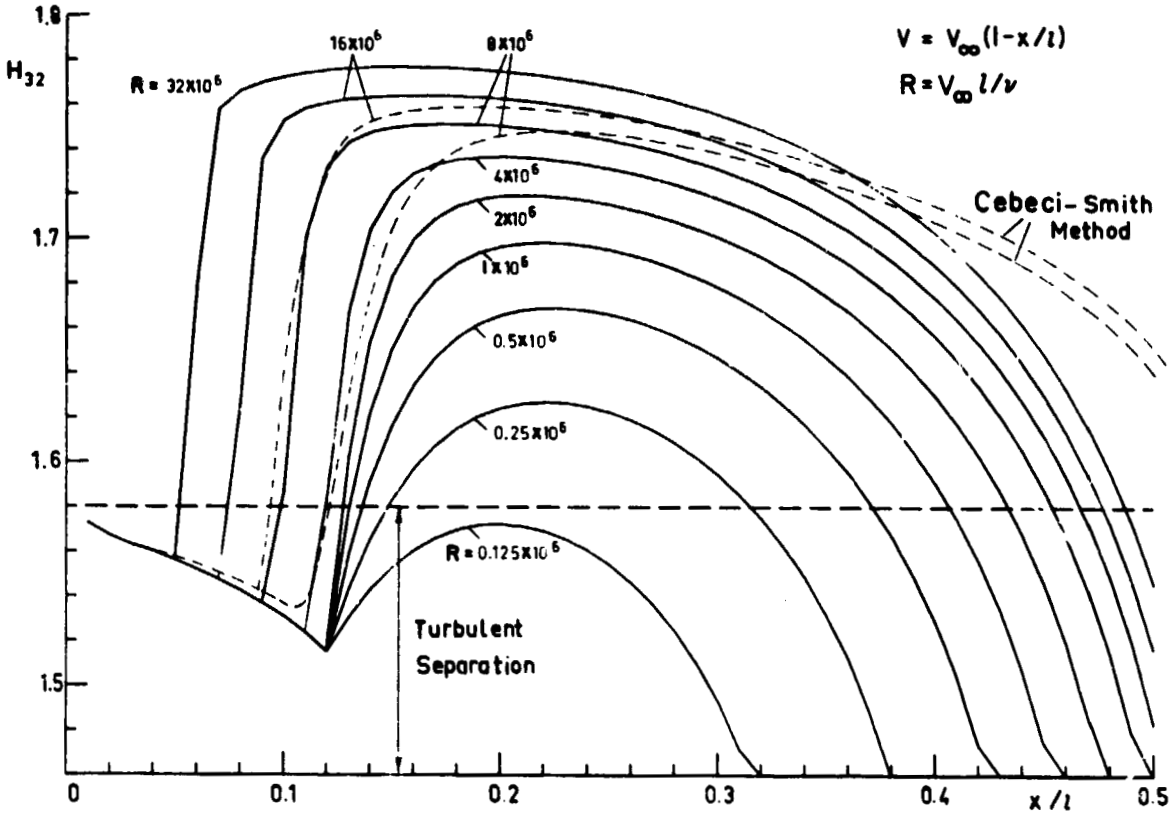

Figure 6.- Comparison of short-cut and finite-difference methods.

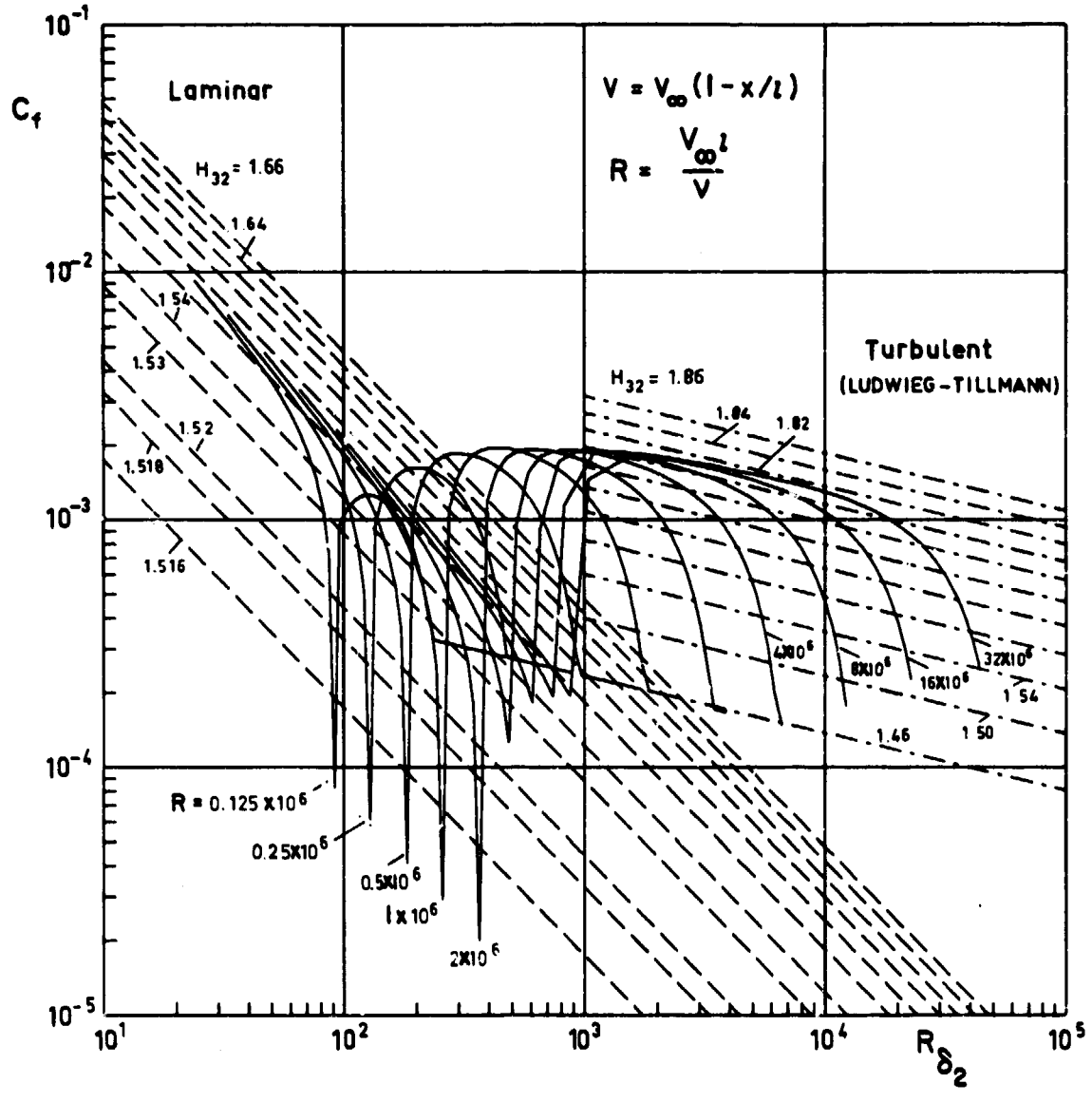

Figure 7.- Skin-friction coefficients.

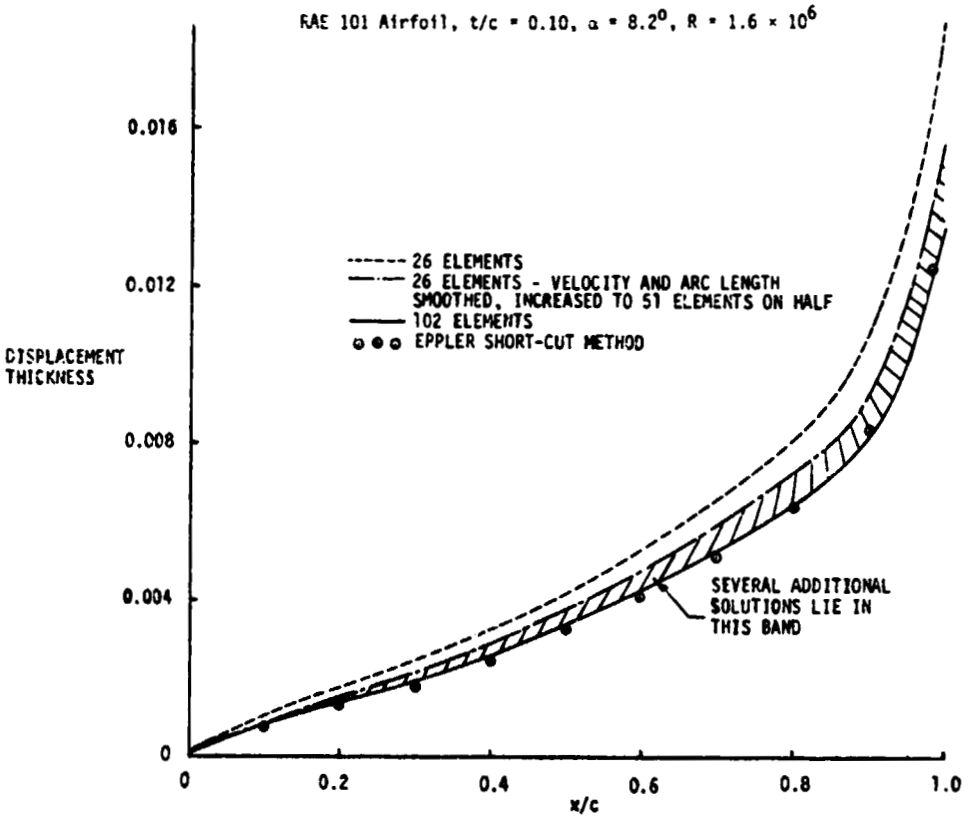

Figure 8.- Comparison of displacement thicknesses.

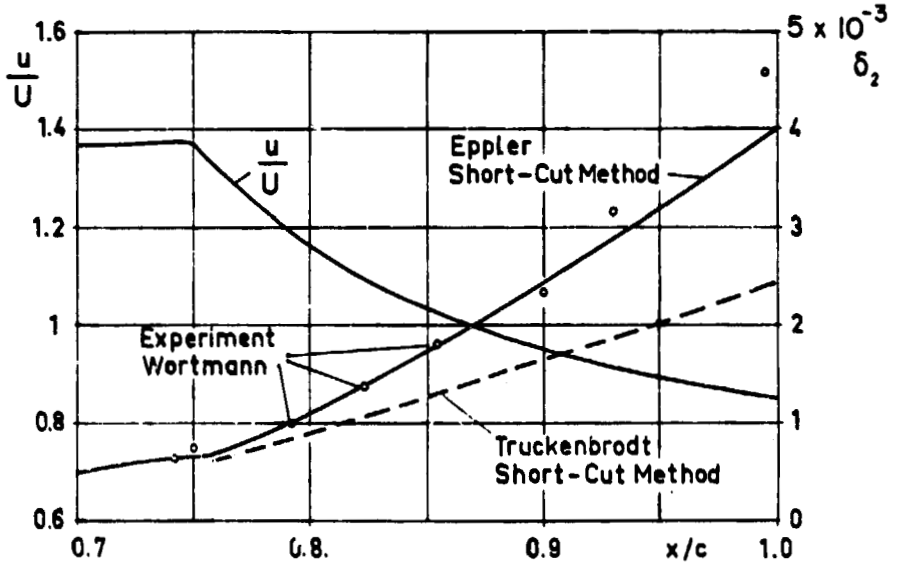

Figure 9.- Comparison of momentum thicknesses.

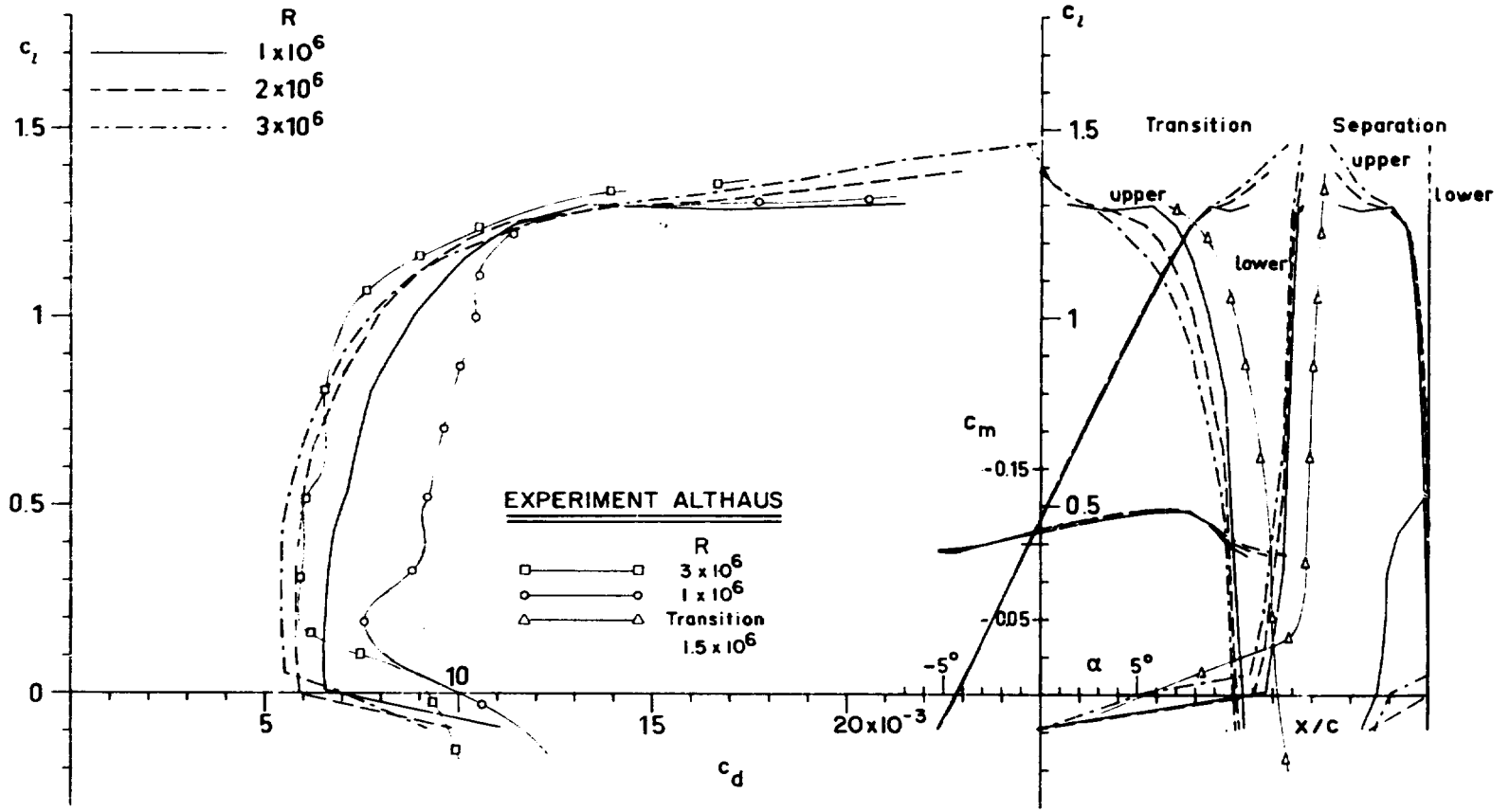

Figure 10.- Comparison of experiment and theory for EPPLER 603 airfoil.

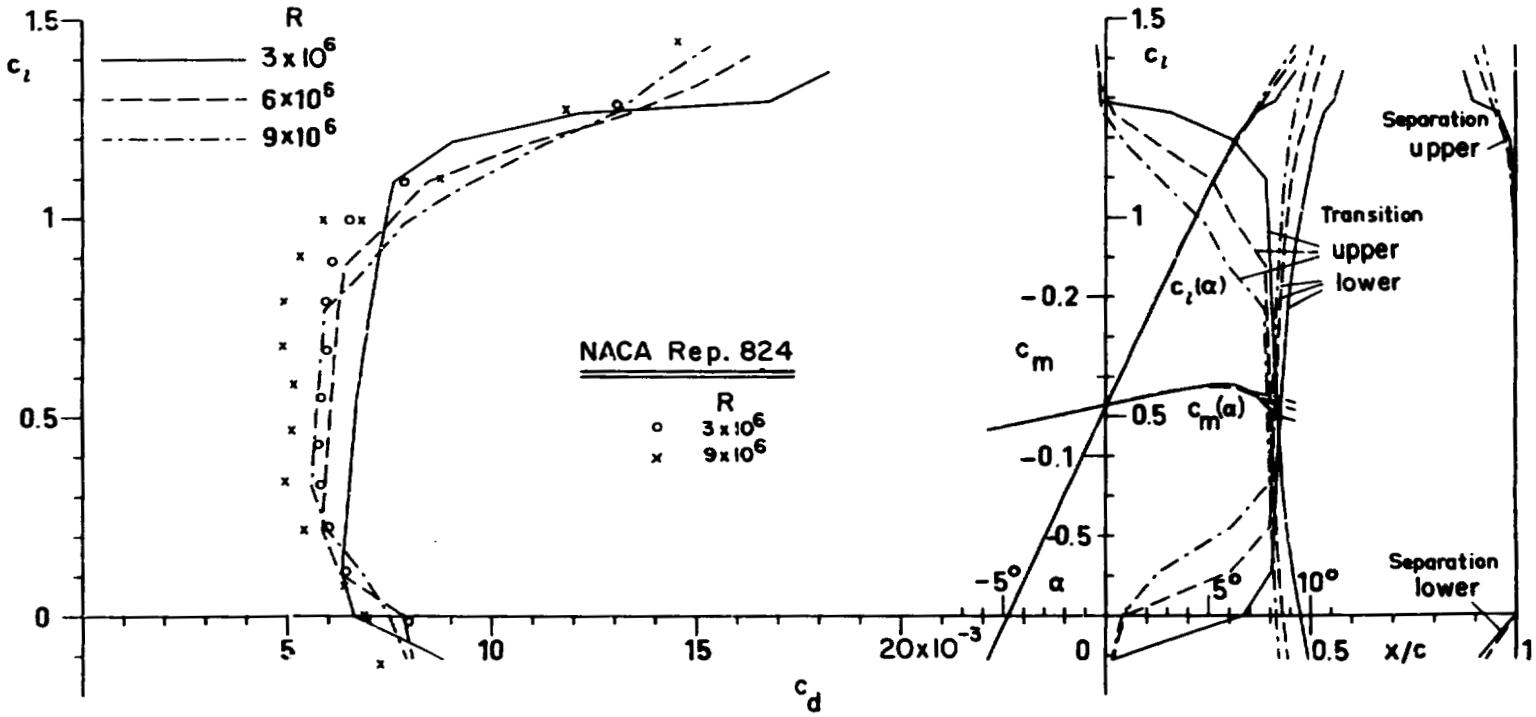

Figure 11.- Comparison of experiment and theory for NACA 64_3-618 airfoil.

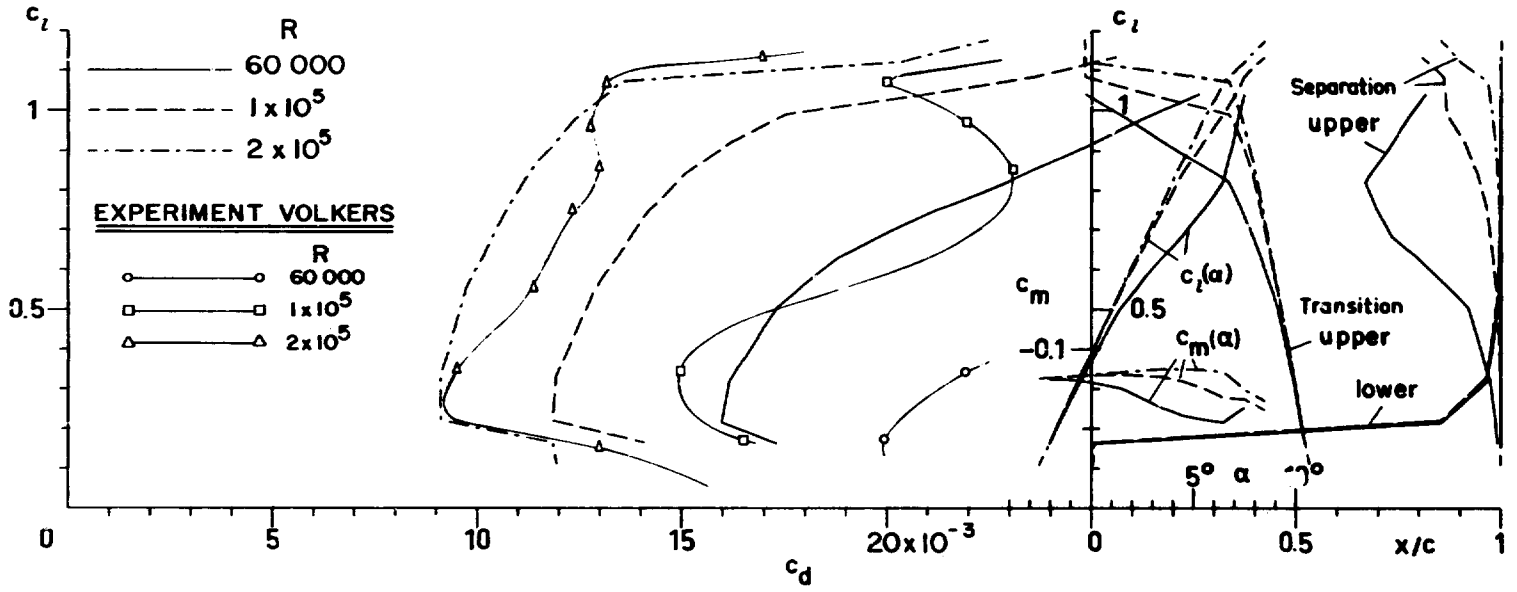

Figure 12.- Comparison of experiment and theory for EPPLER 387 airfoil.

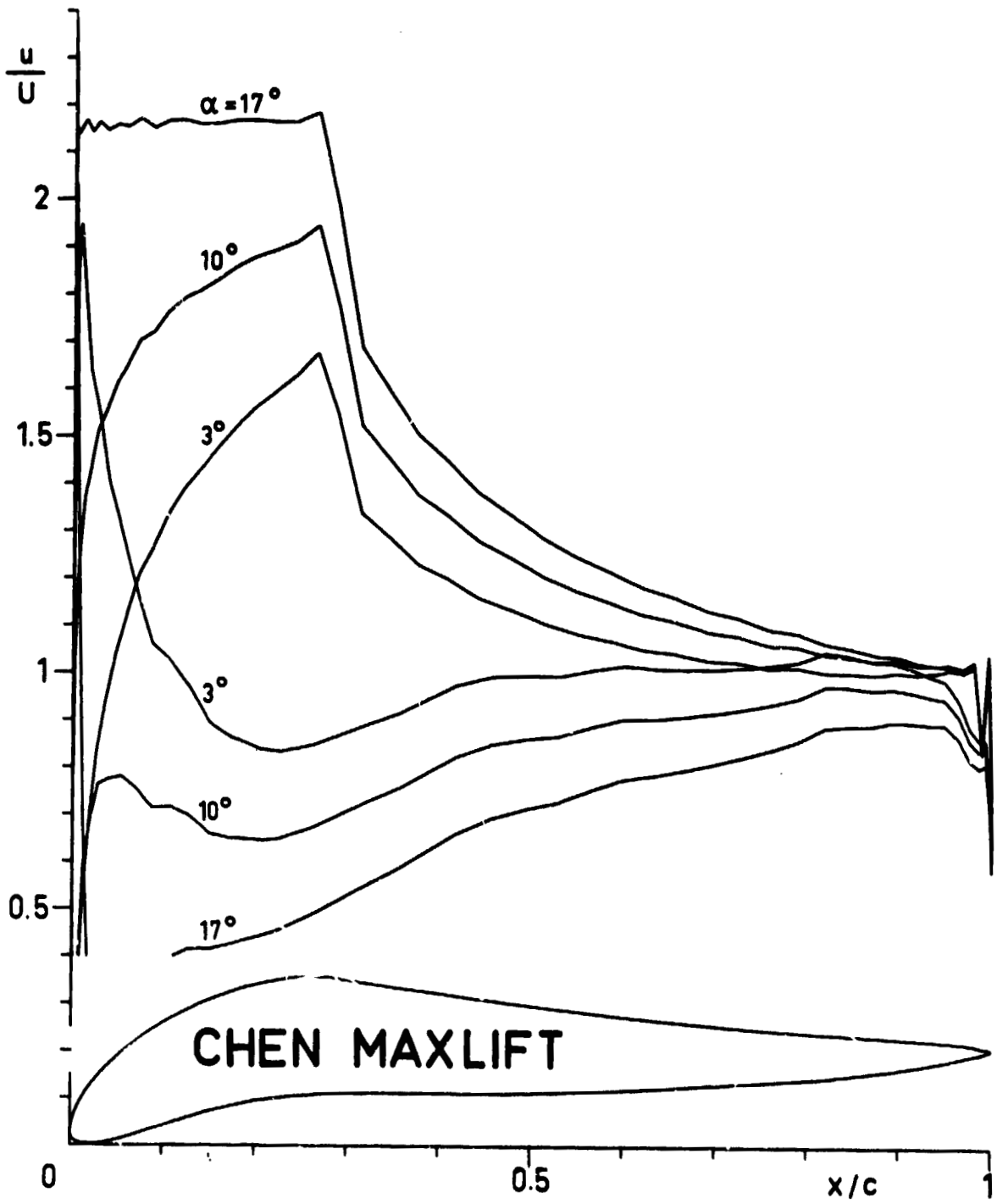

Figure 13.- Chen maximum lift airfoil. (α relative to zero-lift line.)

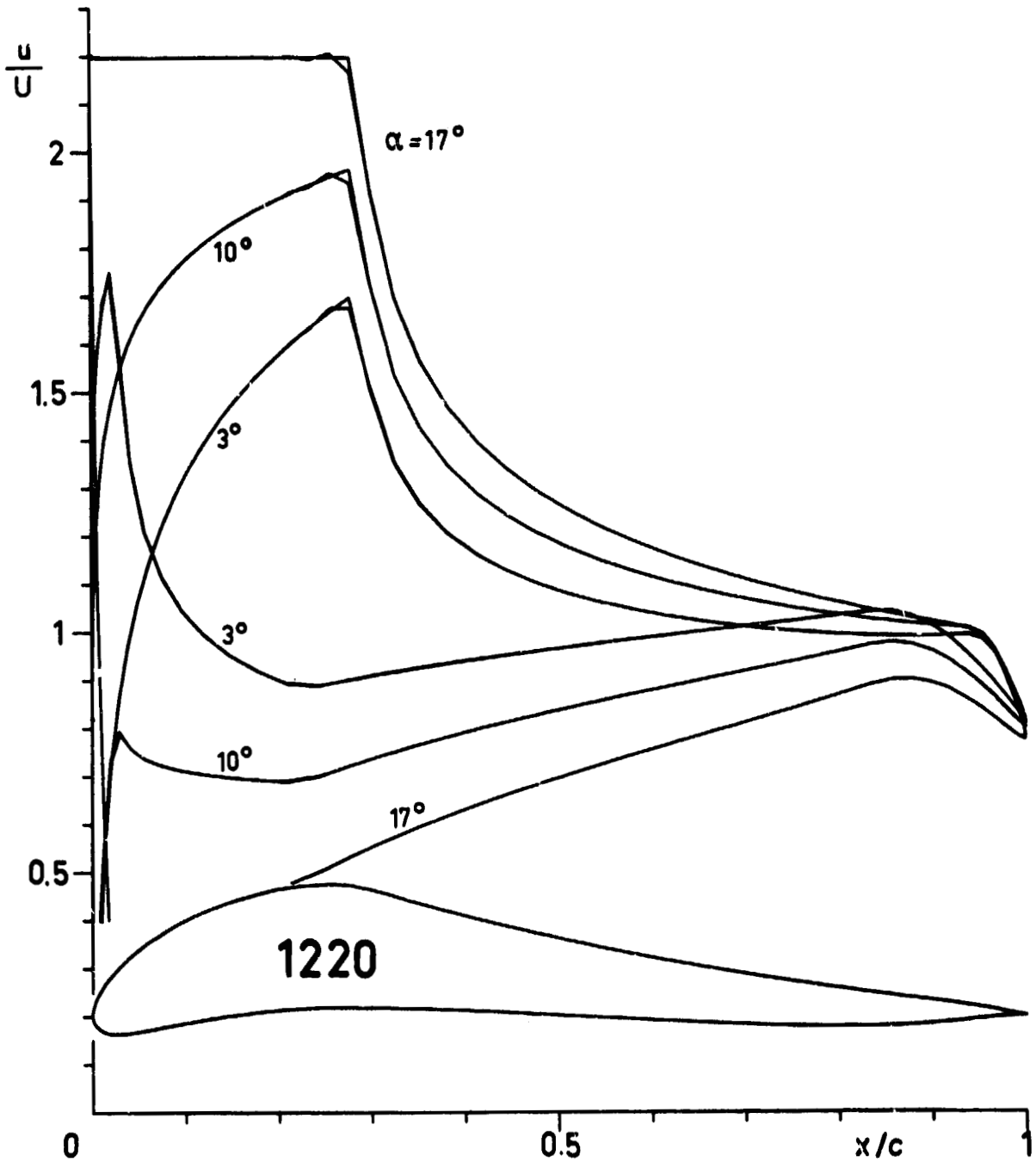

Figure 14.- EPPLER 1220 airfoil. (α relative to zero-lift line.)

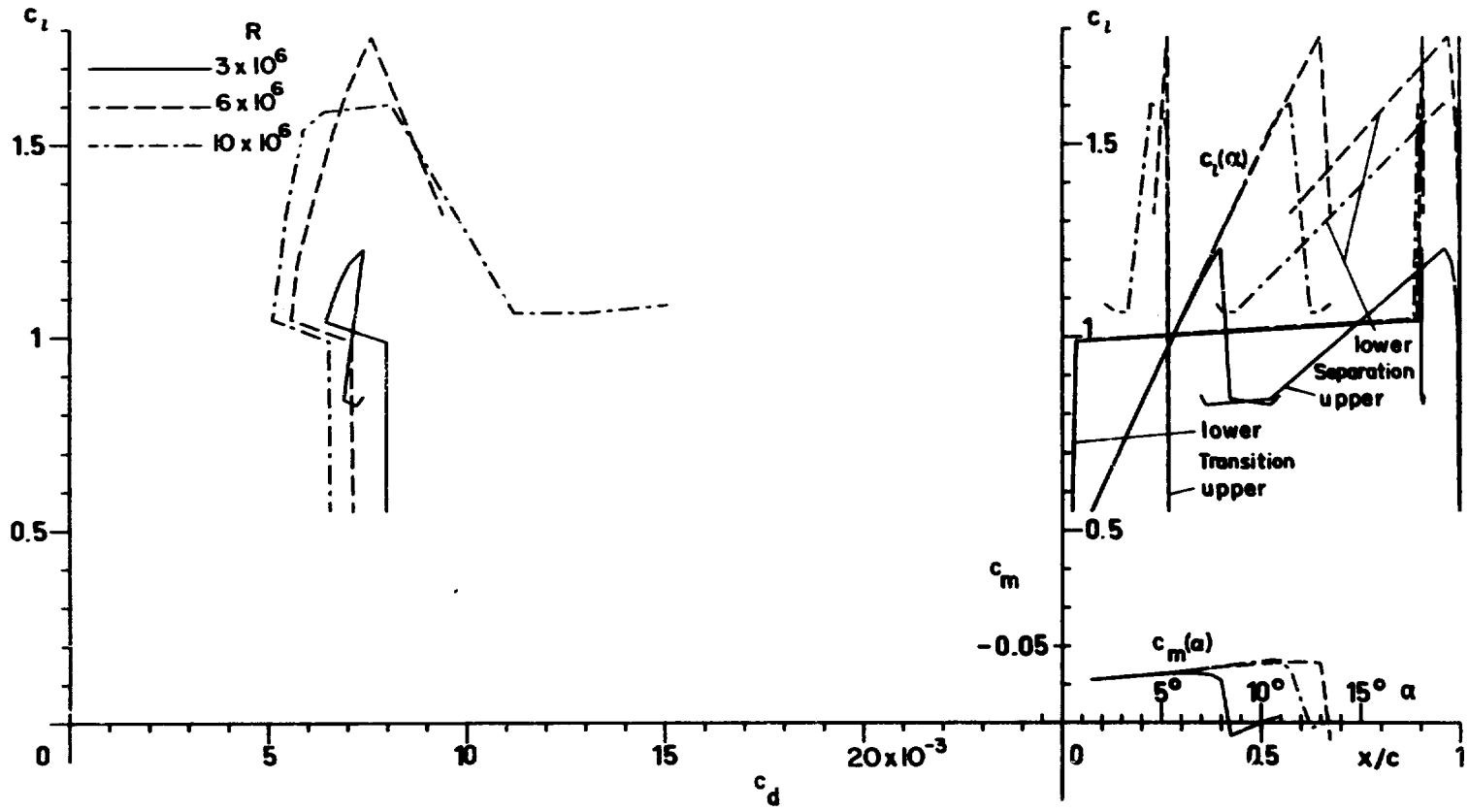

Figure 15.- Theoretical results for EPPLER 1220 airfoil.

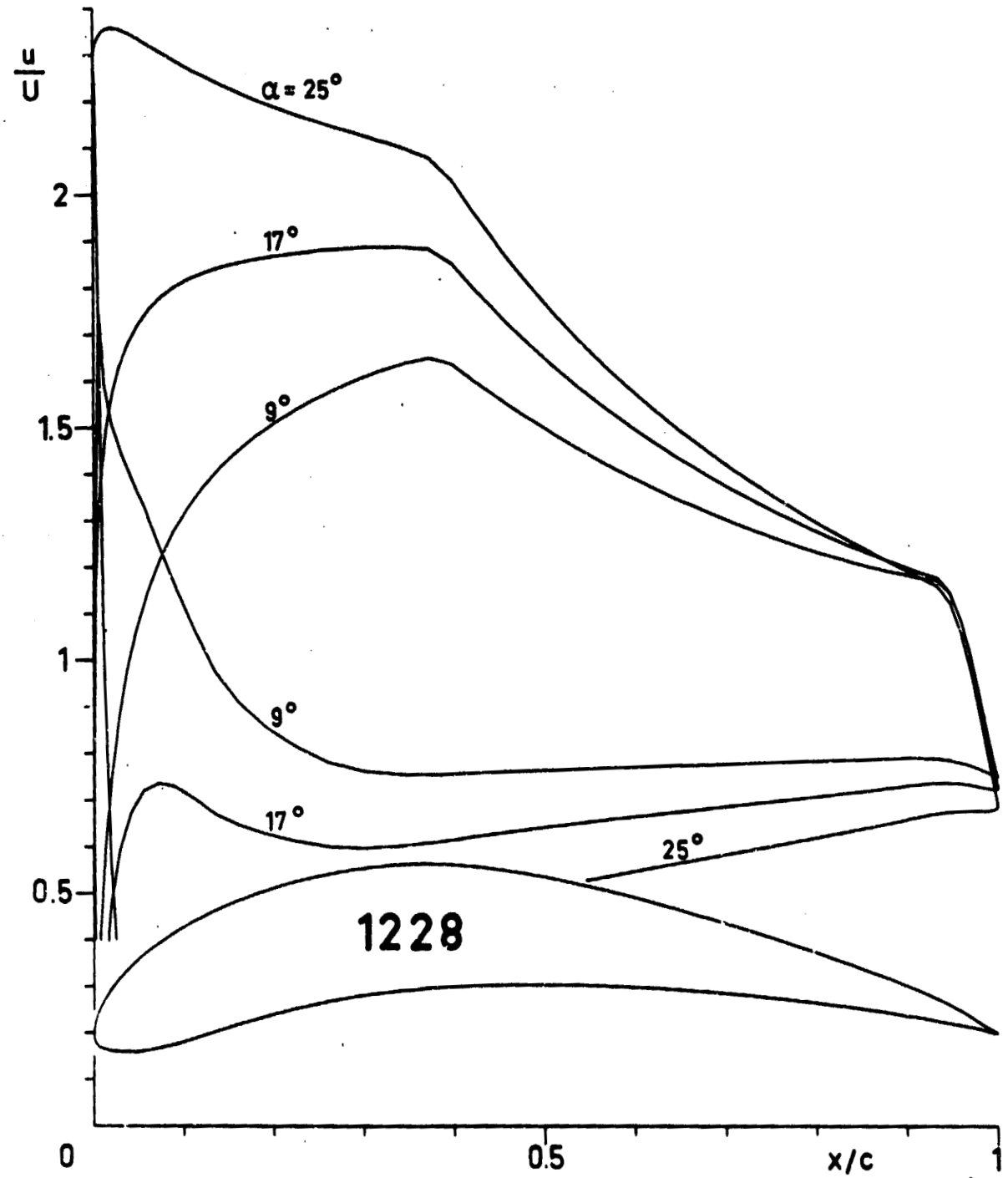

Figure 16.- EPPLER 1228 airfoil. (α relative to zero-lift line.)

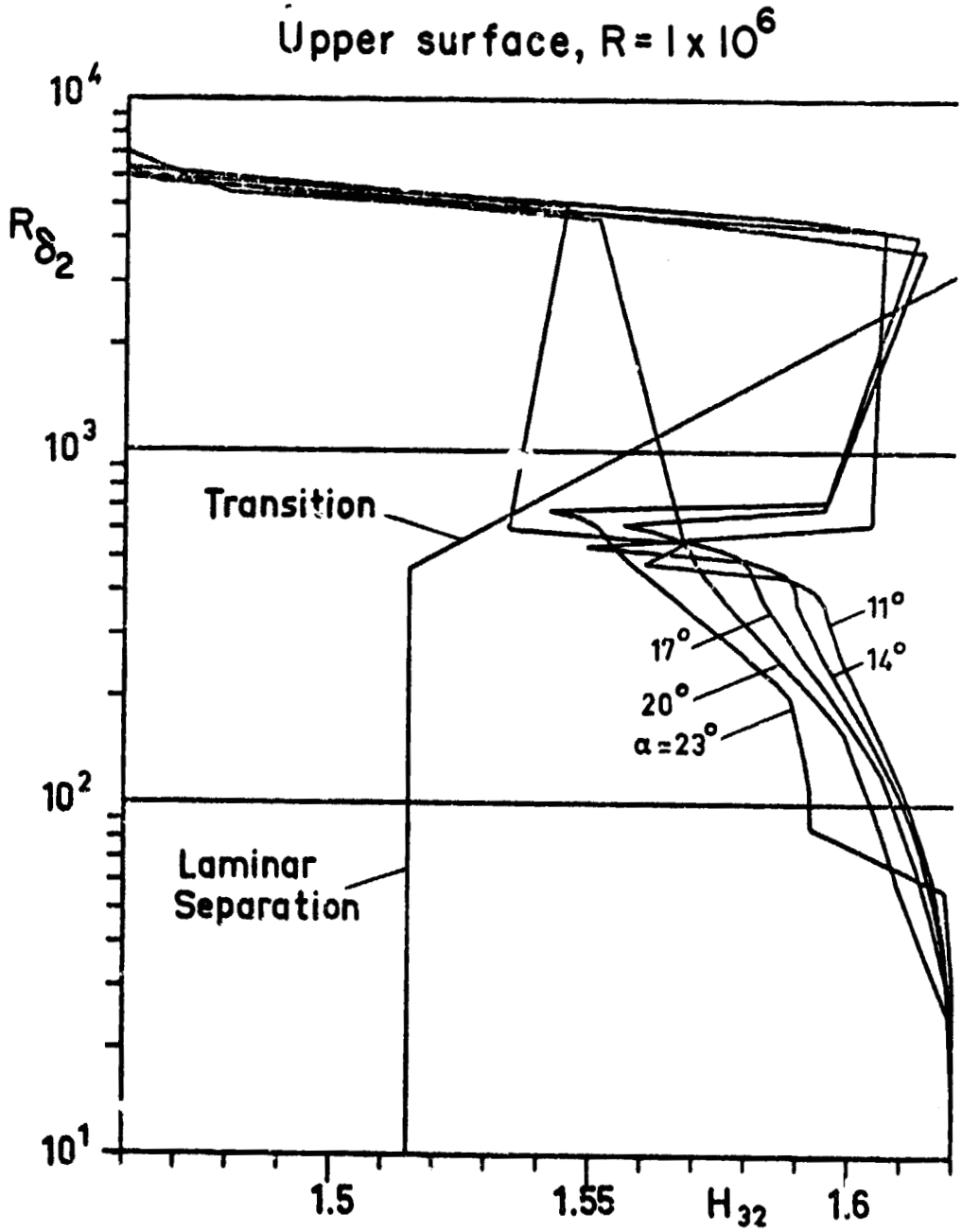

Figure 17.- Boundary layer development for EPPLER 1228 airfoil.

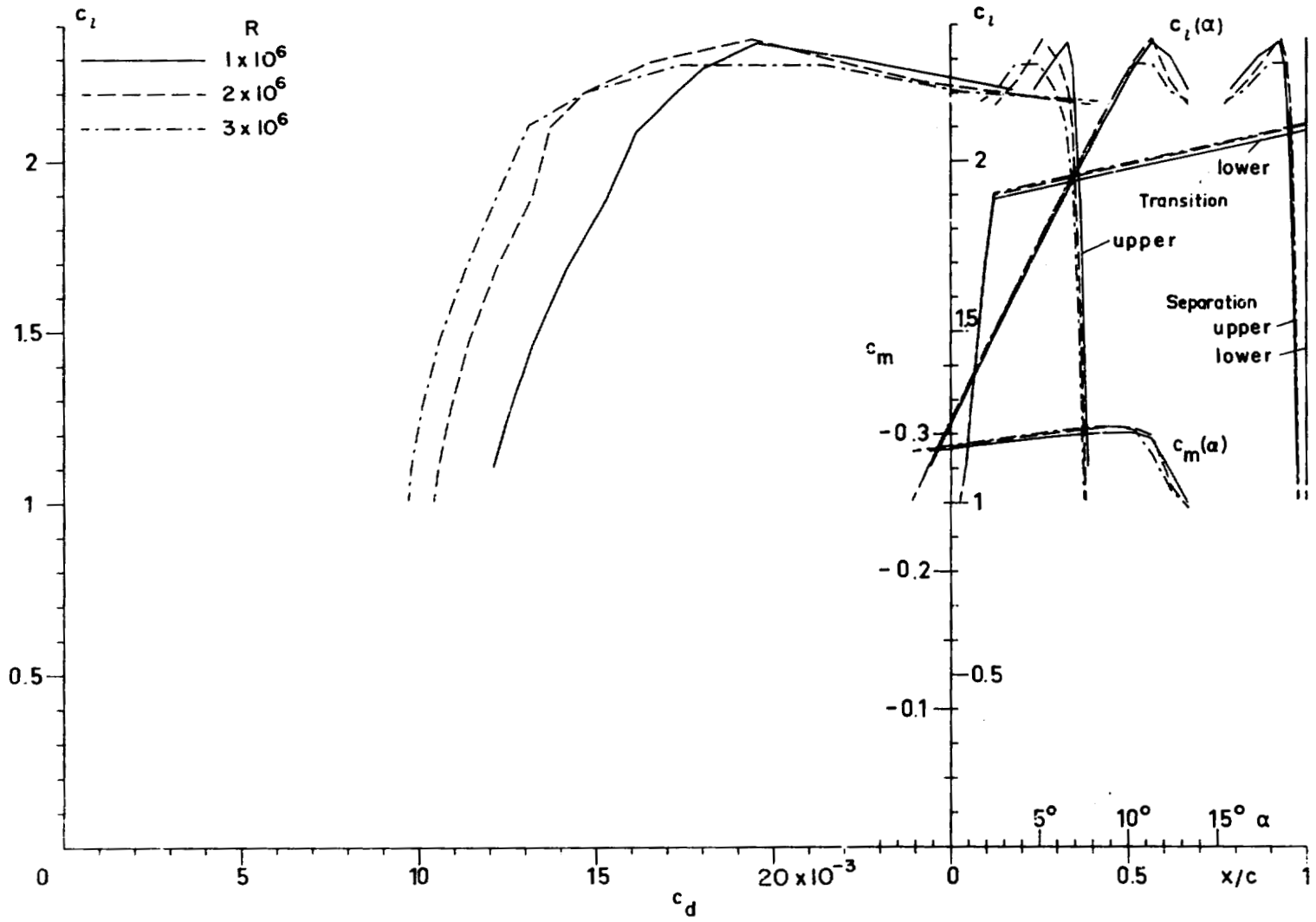

Figure 18.- Theoretical results for EPPLER 1228 airfoil.

D7

7

A CONSISTENT DESIGN PROCEDURE FOR SUPERCRITICAL AIRFOILS IN FREE AIR AND A WIND TUNNEL*

Vijaya Shankar and Norman D. Malmuth
Rockwell International Science Center

Julian D. Cole
University of California, Los Angeles

SUMMARY

A computational inverse procedure for transonic airfoils in which shapes are determined supporting prescribed pressure distributions is presented. The method uses the small disturbance equation and a consistent analysis-design differencing procedure at the airfoil surface. This avoids the intermediate analysis-design-analysis iterations. The effect of any openness at the trailing edge is taken into account by adding an effective source term in the far field. The final results from a systematic expansion procedure which models the far field for solid, ideal slotted and free jet tunnel walls are presented along with some design results for the associated boundary conditions and those for a free flight.

INTRODUCTION

Computational design or inverse procedures for transonic airfoils in which shapes are determined supporting prescribed pressure distributions have been in use since the early work of Nieuwland[1]** which employed hodograph methods to calculate shock-free supercritical flow about a family of quasi-elliptical airfoils. Later Garabedian and Korn[2] developed a more general hodograph procedure to design highly cambered shock-free airfoils. In spite of their usefulness, hodograph procedures for design purposes have several disadvantages. They require too many input parameters, are restricted to shock-free solutions, and are not easily extendable to design of three-dimensional wings. Steger and Klineberg[3] treated the problem within a small-disturbance framework solving the continuity and vorticity equation at interior points. To insure consistency between the analysis and the design formulation, they applied appropriate discretization procedures to the vorticity equation at the airfoil grid points. However, the first-order system with velocity components as dependent variables produces a difficulty in the treatment of singularities at the airfoil nose and trailing edge. The effect of nose and trailing edge singularities could be greatly reduced by

*Part of the work was presented at the AIAA 16th Aerospace Sciences Meeting, Paper No. 78-103. A portion of this effort was sponsored by the Air Force Office of Scientific Research under U.S. Air Force Contract No. F44620-76-C-0044.

**Reference citation is given by numerical superscript.

using a scalar formulation involving the velocity potential. Tranen[4] employed the full potential equation to remedy the deficiency inherent in the small disturbance formulation at the leading and trailing edges. To overcome the inaccuracies and inconsistencies in his formulation associated with the discretization procedures at the boundary, iterations must be employed between direct and inverse solvers. Also, in the full potential formulation, boundary conditions are to be applied at the exact airfoil surface. Since the airfoil surface is unknown in the design problem, errors propagate due to application of boundary conditions at some assumed airfoil surface. Carlson[5] used ghost point and higher order accurate methods to handle airfoil boundary points. Rather than employing the circle plane as in Tranen's procedure, Carlson used a Cartesian framework. However, even his procedure is not consistent in the sense that the discretizations used for C_p in the analysis and those in the design phase are not of the same form. The former uses a central differenced ϕ_x for C_p calculations while the latter employs a special backward differenced ϕ_x involving ghost points. As a result, perfect agreement between his analysis and design calculations is not to be expected, especially near the shock. Also, the problems associated with open trailing edges are not addressed in his work. The trailing edge is made to close by altering the nose shape. However, in his intermediate calculations, large open trailing edges occur. The final results are questionable since the effect of openness is not included in the far field for the intermediate solutions.

In this paper, a small-disturbance model employing the velocity potential as the dependent variable is used for the implementation of the design algorithm. This procedure simplifies the treatment of boundary conditions and alleviates the need for mappings that arise in a full potential equation formulation. A mixed boundary value problem is solved in which Neumann data are specified in the first few percent of the chord length where the assumed shape is retained, and Dirichlet conditions are prescribed on the rest of the airfoil where the pressure is to be modified. One important thrust of the present work is in developing a consistent discretization procedure for the airfoil grid points. If the converged C_p output from the analysis is not altered, then the design mode recovers the same airfoil shape without any discontinuity in the airfoil slope at the shock wave, overcoming a deficiency in Carlson's work. Another significant feature of the numerical implementation not considered by the previous investigators is the effect of an open trailing edge in the far field. In the present work, this is accounted for with the addition of the necessary source terms in the far field. Design of thick trailing edge airfoils is of interest in inviscid flow to achieve a reasonable trailing edge thickness after accounting for the viscous displacement thickness. Some amount of trailing edge thickness is required from a structural stability point of view. Figure 1 schematically explains the design philosophy followed in this paper. The top of Figure 1 shows a conventional airfoil at transonic speed producing a shock on the upper surface. Specifying a shockless pressure distribution on the upper surface would flatten the upper surface of the conventional airfoil, thereby producing an openness at the trailing edge. This is shown in the middle of Figure 1. The amount of trailing edge openness can be reduced by specifying a lower surface pressure distribution with a large aft end loading. This kind of loading undercuts the lower surface producing a Whitcomb[6] type supercritical airfoil.

A typical supercritical airfoil design is presented in the Results section. The effects of wind tunnel walls in the computation of transonic airfoil design and analysis have also been studied. The downstream and upstream infinity conditions for the solid, ideal slotted, and free jet tunnel walls have been derived from a systematic asymptotic solution of the small-disturbance integrodifferential equation.

SYMBOLS

$\vec{B}$	scaled mass flux vector
C	chord
C_L	lift coefficient
c_n	section normal-force coefficient
$C_p\Big\|_{i-1/2,j}$	pressure coefficient at half node points
$F'_{u,\ell}$	upper and lower airfoil slopes
H	scaled half tunnel wall height
K	transonic similarity parameter
M	Mach number
M_∞	free stream Mach number
Q	effective source strength due to airfoil trailing edge openness
$x,\tilde{y}$	coordinate system
$y_{u,\ell}$	upper and lower airfoil ordinates
ϕ	velocity potential
ϕ_{FF}	far field velocity potential
α	angle of attack
δ	maximum airfoil thickness
γ	specific heat ratio

EQUATION AND BOUNDARY CONDITIONS

The transonic small disturbance equations are formally derived by an asymptotic expansion procedure[7] applied to the Euler equations. For an airfoil whose upper and lower surfaces are defined by $y_{u,\ell} = \delta F_{u,\ell}(x) - \alpha x$ the perturbation potential satisfies the equation

$$[K - (\gamma+1)\phi_x]\phi_{xx} + \phi_{\bar{y}\bar{y}} = 0 \qquad (1)$$

The large lateral propagation of transonic disturbances is taken into account by the use of the scaled coordinate $\bar{y} = y\delta^{1/3}M_\infty^{2/3}$. The limit process is $\delta \to 0$, $M_\infty \to 1$, while x,y, and $K = (1-M_\infty^2)/(M_\infty\delta^{2/3})$ remain fixed. The quantity α is the angle of attack.

Consistent with the small disturbance formulation, the airfoil boundary conditions are applied on a slit of $\bar{y} = 0$. In the case of pure analysis the airfoil boundary condition (flow tangency) is of Neumann type.

$$\phi_{\bar{y}}(x,0\pm) = F'_{u,\ell}(x) - \frac{\alpha}{\delta}, \qquad -1 \leqslant x \leqslant 1 \qquad (2)$$

The airfoil leading and trailing edges are at $x = -1$ and $x = 1$ respectively. In the design problem, the airfoil shape corresponding to a given pressure distribution is sought. However, the small disturbance theory cannot resolve the nose region accurately. Therefore, the nose shape of an existing airfoil is specified for up to 5-10% of the chord length and a desired pressure distribution over the rest of the chord is prescribed. The boundary conditions then become a mixed Neumann-Dirichlet type. On the portion of the airfoil where the nose shape is specified, the boundary condition applied is given by Eq. (2). Over the rest of the airfoil a scaled pressure coefficient

$$C_p = -2\left(\delta^{2/3}/M_\infty^{3/4}\right)\phi_x(x,0\pm) \qquad (3)$$

is prescribed. With $\phi_x(x,0\pm)$ known from Eq. (3), the perturbation potential $\phi(x,0\pm)$ is calculated by integration. This value of $\phi(x,0\pm)$ is then imposed at the airfoil slit as a Dirichlet type boundary condition. Figure 2 schematically illustrates the mixed Neumann-Dirichlet type boundary condition.

FAR FIELD

To avoid mapping procedures which bring infinity to a finite distance from the airfoil, but compromise the difference method, an approximate asymptotic solution for ϕ valid at large distances from the airfoil is used as far field

boundary condition. The type of far field depends on whether the airfoil is kept in free air or a solid, slotted or porous wall wind tunnel. The far field expressions to be used in this paper will now be discussed.

Free Air

Figure 2 shows the far field arrangement. Along the outer boundary ABCDE, the perturbation potential ϕ is computed from

$$\phi_{FF} = -\frac{\Gamma\theta}{2\pi} + \frac{Q\log\tilde{r}}{2\pi} + \ldots \tag{4}$$

where Γ is the circulation around the airfoil, $\theta = \tan^{-1}(\sqrt{K}\tilde{y}/x)$, Q is an effective source strength due to any openness at the trailing edge, and $\tilde{r} = \sqrt{x^2 + k\tilde{y}^2}$. Only dominant terms are kept in Eq. (4).

An expression for the source strength Q is obtained by considering the integral form of Eq. (1). The divergence theorem is used to obtain this integral relation in the cut region R shown in Figure 3

$$\iint_R \nabla\cdot\vec{B}\,dA = \oint_{C_1+C_2} \vec{B}\cdot\vec{n}\,ds \tag{5}$$

where $\vec{B} = (K\phi_x - \frac{(\gamma+1)}{2}\phi_x^2)\vec{i} + \phi_{\tilde{y}}\vec{j}$ is a scaled mass flux vector. Since $\vec{B}$ is is conserved across shock waves, no special boundary terms appear if shocks are present in the flow. Expanding Eq. (5) results in

$$\int_{-1}^{1} [\phi_{\tilde{y}}]dx = \int_{C_1} \left(K\phi_x - \frac{(\gamma+1)}{2}\phi_x^2\right)d\tilde{y} - \phi_{\tilde{y}}dx \tag{6}$$

Substituting Eq. (4) into Eq. (6) and simplifying gives

$$Q = \frac{1}{\sqrt{K}}\int_{-1}^{1} [\phi_{\tilde{y}}]dx, \text{ where } [\ ] \text{ denotes jump} \tag{7}$$

If the airfoil trailing edge is closed, then $\int_{-1}^{1} [\phi_{\tilde{y}}]\, dx$ is zero and no source term is present. While designing an airfoil to support a given pressure distribution the magnitude of the trailing edge openness is not known a priori. In the calculation, Q is therefore evaluated by nonlinear iteration procedure analogous to that employed in obtaining the circulation term Γ for an analysis problem. If there is trailing edge openness, and if the source term is not included in the far field, then the solution obtained may be questionable.

Wind Tunnel

To establish the appropriate boundary conditions on a finite computational domain for a tunnel simulation, the far field corresponding to $x \to \pm\infty$ has been derived using a Green's function method. Only the final results to the dominant order for the solid, ideal slotted and free jet tunnel wall cases are reported here. The airfoil is positioned midway between the walls. Thus, the airfoil slit is at $\tilde{y} = 0$ and the tunnel boundaries are at $\tilde{y} = \pm H$. The appropriate boundary conditions on the tunnel walls are

$$\phi_{\tilde{y}}(x,\pm H) = 0 \qquad \text{for solid wall}$$

$$\phi_{\tilde{y}}(x,\pm H) \pm \frac{1}{FH}\phi(x,\pm H) = 0 \qquad \text{for slotted and free jet} \tag{8}$$

where F is the slot parameter:

$$F = \frac{s}{\pi H} \ln \operatorname{cosec}\left(\frac{-a}{2s}\right) \tag{9}$$

where s is the distance between slot centers and a is the slot width. For free jet case $F = 0$.

To dominant order in the Karman-Guderley $(x,\tilde{y})$ plane, the far fields corresponding to these tunnel cases at $x \to \pm\infty$ are:

Solid wall:

$$4h\phi = \pm K^{-1/2}\left\{t(1)(x-1) + \int_{-1}^{1} t(\xi)\,d\xi\right\}$$

$$+ \frac{\gamma+1}{2K}\int_{-h}^{h} d\eta \int_{-\infty}^{\infty}\left[u^2(\xi,\eta) - \frac{[t(1)]^2}{16h^2}\right]d\xi + 2h\Gamma(\operatorname{sgn}\tilde{y})H(x) + O\left(e^{-\lambda_1|x|}\right) \tag{10}$$

where $t(1) = F_u(1) - F_\ell(1)$, ξ,η are dummy variables for x and y, $h = \sqrt{K}\,H$, $H(x) = 1$ for $x > 0$ and $H(x) = 0$ for $x < 0$, and $u = \phi_x$.

Slotted and free-jet wall:

$$\phi \to 0 \qquad \text{as } x \to -\infty$$

$$\phi \to \frac{\Gamma}{2}\ \operatorname{sgn} \tilde{y} - \frac{1}{1+\bar{\tau}}\,\frac{\tilde{y}}{H} + \cdots \quad \text{as } x \to +\infty \tag{11}$$

Eqs. (11) assume no downwash at upstream infinity. Other expressions can be derived for different upstream assumptions. In this connection, the drag, lift, and pressure distribution can be shown to be unaffected by addition of upstream down flow.

CONSISTENCY

When the pressure distribution from the analysis calculation is used as an input for design, a consistent discretization procedure would recover the airfoil shape exactly, even across the shock. To achieve this agreement, dummy points below the airfoil surface are used. Figure 4 shows the grid points near the airfoil surface. The points (i, j-1) are the dummy points.

Analysis

From the known airfoil shape $(\phi_{\tilde{y}})_{i,j}$, at the beginning of each relaxation cycle the dummy point values $\phi_{i,j-1}$ are obtained from the central difference formula

$$\phi_{i,j-1} = \phi_{i,j+1} - 2\Delta\tilde{y}(\phi_{\tilde{y}})_{i,j} \tag{12}$$

This expression is then used in the finite differenced form of $\phi_{\tilde{y}\tilde{y}}$ in Eq. (1) at the airfoil points (i,j)

$$\left[\left(K - (\gamma+1)\phi_x\right)\phi_{xx}\right]_{i,j} + \frac{2\phi_{i,j+1} - 2\phi_{i,j}}{(\Delta\tilde{y})^2} = \frac{2(\phi_{\tilde{y}})_{i,j}}{\Delta\tilde{y}} \tag{13}$$

The nonlinear term in Eq. (13) is central differenced at elliptic points and one-sided backward differenced at hyperbolic points. To improve stability near the sonic region Jameson's[8] pseudo-time operator is used in the relaxation procedure. Once the analysis procedure converges, the pressure distribution on the airfoil is computed at half node points

$$C_p\big|_{i-1/2,j} = -\frac{2\delta^{2/3}}{M_\infty^{3/4}}\,\phi_x\big|_{i-1/2,j} \tag{14}$$

where

$$\phi_x\big|_{i-1/2,j} = (\phi_{i,j} - \phi_{i-1,j})/(x_{i,j} - x_{i-1,j}) \tag{15}$$

Design

As mentioned earlier in this paper, a portion of the airfoil shape ($\phi_{\tilde{y}}$) near the nose is specified (from x = -1 to x = XD in Figure 2). On the portion of the airfoil under design, the pressure coefficient $C_{p_{i-1/2,j}}$ is specified at half node points. From $C_{p_{i-1/2,j}}$, the perturbation potential $\phi_{i,j}$ on the airfoil surface is obtained from Eqs. (14) and (15)

$$\phi_{i,j} = \phi_{i-1,j} - \frac{M_\infty^{3/4}}{2\delta^{2/3}}\,C_{p_{i-1/2,j}}\,(x_{i,j} - x_{i-1,j}) \tag{16}$$

At the airfoil grid points where the shape $\phi_{\tilde{y}}$ is specified, Eq. (13) is used to evaluate the potential $\phi_{i,j}$ (usual SLOR scheme). Since this potential keeps changing during the relaxation cycle, the potential $\phi_{i,j}$ over the designed portion is updated accordingly at the beginning of each relaxation cycle using Eq. (16). After the mixed analysis-design solution converges, the slope $(\phi_{\tilde{y}})_{i,j}$ of the resulting airfoil is computed from Eq. (13) as

$$\phi_{\tilde{y}}\big|_{i,j} = \frac{\Delta\tilde{y}}{2}\left[\left(K - (\gamma+1)\phi_x\right)\phi_{xx}\right]_{i,j} + \frac{1}{\Delta\tilde{y}}\,(\phi_{i,j+1} - \phi_{i,j}) \tag{17}$$

From the slope $\phi_{\tilde{y}}$, the airfoil ordinates are calculated from the quadrature formula

$$y_{u,\ell}(x) = y_{u,\ell}(x_D) + \delta \int_{x_D}^{x} \left\{ \phi_{\tilde{y}} \Big|_{u,\ell} + \frac{\alpha}{\delta} \right\} dx \qquad (18)$$

$$x_D \leq x \leq 1$$

where $y_{u,\ell}(XD)$ are the upper and lower y values of the airfoil at X = XD, where the boundary condition changes from analysis to design. Since Eqs. (13), (14), and (15) are used in the same manner in the analysis and design, the discretization procedure is consistent.

RESULTS

To check the consistency logic developed in the previous section, a test case was run. An analysis calculation for the NACA 0012 airfoil at $M_\infty = 0.75$, $\alpha = 2°$ was first performed. The pressure distribution from the analysis calculation was then used as an input for the design problem to check if the NACA 0012 airfoil shape would be recovered even across the shock. The results are shown in Table 1. The upper (y_u) and lower (y_ℓ) surface ordinates from the design calculation agreed with the original NACA 0012 airfoil up to four significant figures, thus establishing consistency of the method.

Figure 5 shows a design calculation performed on the previous NACA 0012 analysis solution to get rid of the upper surface shock. The dotted line shows the analysis solution, and the solid line shows the prescribed shockless pressure distribution. The resulting airfoil is shown by the solid line. It is seen that a slight flattening of the upper surface determined in the design phase eliminates the shock. This reshaping produces an openness at the trailing edge which was properly accounted for by the effective source term in the far field.

Analysis calculations were performed over the shock-free airfoil designed in free air, (shown in Figure 5), using solid wall tunnel boundary conditions. The airfoil that produces a shockless pressure distribution in free air may produce a shock when tested in the wind tunnel. This is illustrated by the results shown in Figure 6. From the figure, it is evident that when the tunnel wall is sufficiently far away from the airfoil, the pressure distribution remains shockless. As the tunnel wall is brought closer to the airfoil, the shock appears and moves downstream.

Figure 7 shows a supercritical airfoil design with NACA 0012 nose shape. First, an analysis solution was generated over the NACA 0012 airfoil at $M_\infty = 0.8$ and $\alpha = 2°$. This is shown by the dotted line in Figure 7. Then a supercritical pressure distribution was specified with a large loading on the aft end of the airfoil. The resulting airfoil resembles a Whitcomb type supercritical airfoil which is characterized by a substantially reduced curvature on the mid chord region of the upper surface together with increased camber near the trailing edge.

An off design calculation on this supercritical airfoil at $M_\infty = 0.78$ is shown in Figure 8. For qualitative comparison, off design and design calculations on the NASA 11% thick supercritical airfoil are also shown. At off design Mach numbers the shock reappears.

The effect of wind tunnel walls on the performance of the free air shock free supercritical airfoil is shown in Figure 9. Only the upper surface pressure is shown for solid, ideal slotted ($F = 0.279$) and free jet ($F = 0$) tunnel cases. The solid line in Figure 9 refers to the shock free, free air pressure distribution. For tunnel wall height to a chord ratio of 6, the shock reappears in all the tunnel wall cases. As expected, the solid wall produces a stronger shock while the free jet case produces a weaker one.

CONCLUDING REMARKS

An efficient and inexpensive design-analysis code has been developed for two-dimensional airfoils. The consistent differencing procedure employed at the airfoil boundary allows use of the same code in either analysis or design-analysis mode without requiring any modification. In the algorithm, the effect of an open trailing edge is properly accounted for, a factor ignored by other workers. The fact that no mapping is involved in the two-dimensional work makes the extension of the algorithm to three dimensional wing design feasible and attractive.

REFERENCES

1. Nieuwland, G. Y., "Transonic Potential Flow Around a Family of Quasi-Elliptical Aerofoil Sections," NLR-TR-T.172, National Lucht-en Ruimtevaart Laboratorium, Amsterdam, 1967.
2. Garabedian, P. R., and Korn, D. G., "Numerical Design of Transonic Airfoils," Numerical Solution of Partial Differential Equations--II, Academic Press, 1971.
3. Steger, J. L., and Klineberg, J. M., "A Finite Difference Method for Transonic Airfoil Design," AIAA J., Vol. 11, No. 5, May 1973, pp. 628-635.
4. Tranen, T. L., "A Rapid Computer Aided Transonic Airfoil Design Method," AIAA Paper No. 74-501, June 1974.
5. Carlson, L. A., "Transonic Airfoil Analysis and Design Using Cartesian Coordinates," Proc. AIAA 2nd Computational Fluid Dynamics Conference, June 19-20, 1975, pp. 175-183.
6. Whitcomb, R. T., "Review of NASA Supercritical Airfoils," ICAS Paper 74-10, August 1974.
7. Cole, J. D., "Twenty Years of Transonic Flow," Document G1-82-0878, July 1969, Boeing Scientific Research Laboratories, Seattle, Wash.
8. Jameson, A., "Iterative Solutions of Transonic Flows over Airfoils and Wings, Including Flows at Mach 1," Communications of Pure and Applied Mathematics, Vol. 27, 1974, pp. 283-309.

TABLE 1.- CONSISTENCY CHECK

$[M_\infty = 0.75;\ \alpha = 2^0]$

x/C	y Analysis		C_p		y Design	
	Upper	Lower	Upper	Lower	Upper	Lower
.045	3.47139	-3.4713	-.73743	.24451	3.47139	-3.47139
.075	4.27675	-4.2767	-.88529	-.00489	4.27675	-4.27675
.265625	6.05798	-6.0579	-1.1407	-.3006	6.05801	-6.05799
.39	5.92235	-5.9223	-1.1547	-.26837	5.92242	-5.92238
.453125	5.65088	-5.6508	-.46496	-.23615	5.65097	-5.65091
.546875	5.06204	-5.0620	-.37826	-.18103	5.06215	-5.06207
.765625	3.08328	-3.0832	-.14389	-.03554	3.08347	-3.08335
.96	.76099	-.7609	.18687	.22115	.76102	-0.76101

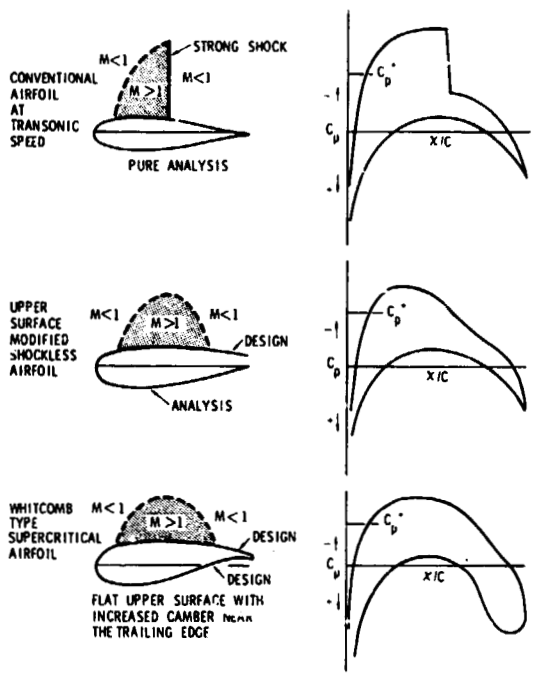

Figure 1.- Supercritical airfoil design.

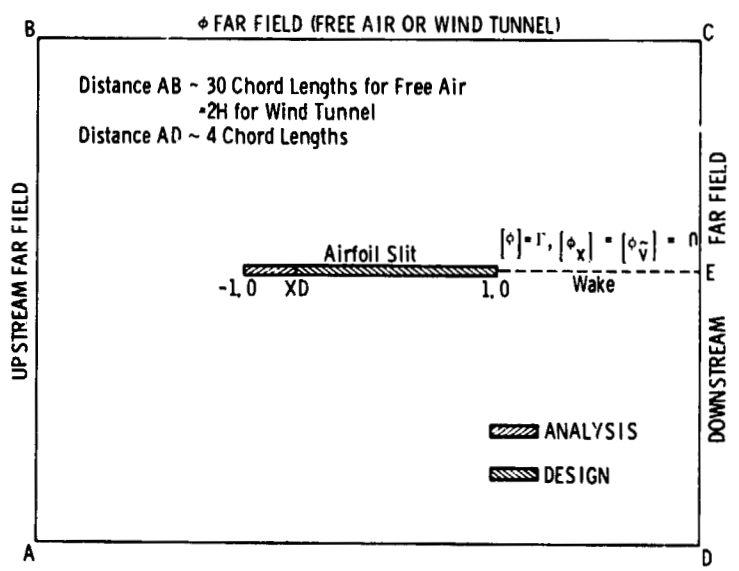

Figure 2.- Boundary conditions and far-field arrangement.

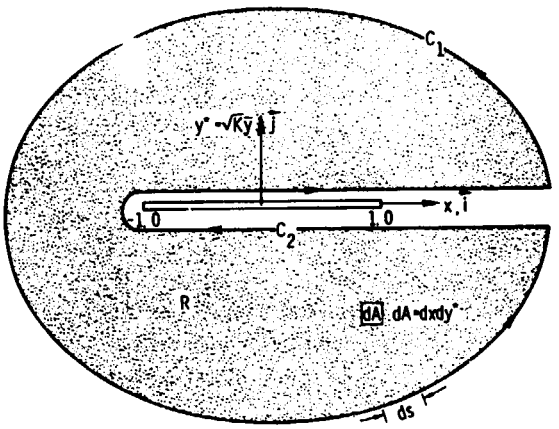

$$\int_{-1}^{1} |\phi_{\tilde{y}}| dx = \oint_{C_1} \left(K\phi_x - \frac{\gamma+1}{2}\phi_x^2\right) d\tilde{y} - \phi_{\tilde{y}} dx$$

$$Q = \frac{1}{\sqrt{K}} \int_{-1}^{1} |\phi_{\tilde{y}}| dx$$

Figure 3.- Cut region for far field.

$$\phi_{\tilde{y}}\Big|_{i,j} = \frac{\phi_{i,j+1} - \phi_{i,j-1}}{2\Delta\tilde{y}}$$

$$\phi_x\Big|_{i-1/2,j} = \frac{\phi_{i,j} - \phi_{i-1,j}}{\Delta x}$$

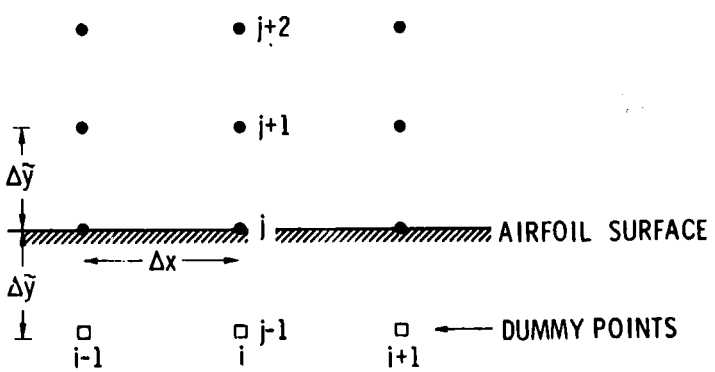

Figure 4.- Dummy-point arrangement.

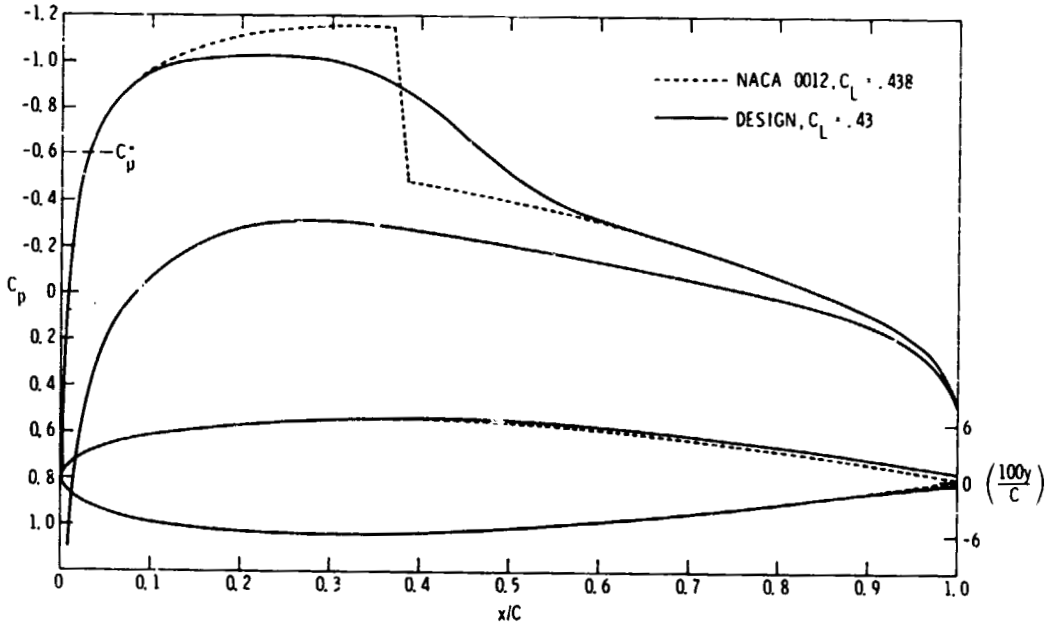

Figure 5.- Transonic design. Shock elimination. $\alpha = 2°$; $M_\infty = 0.75$.

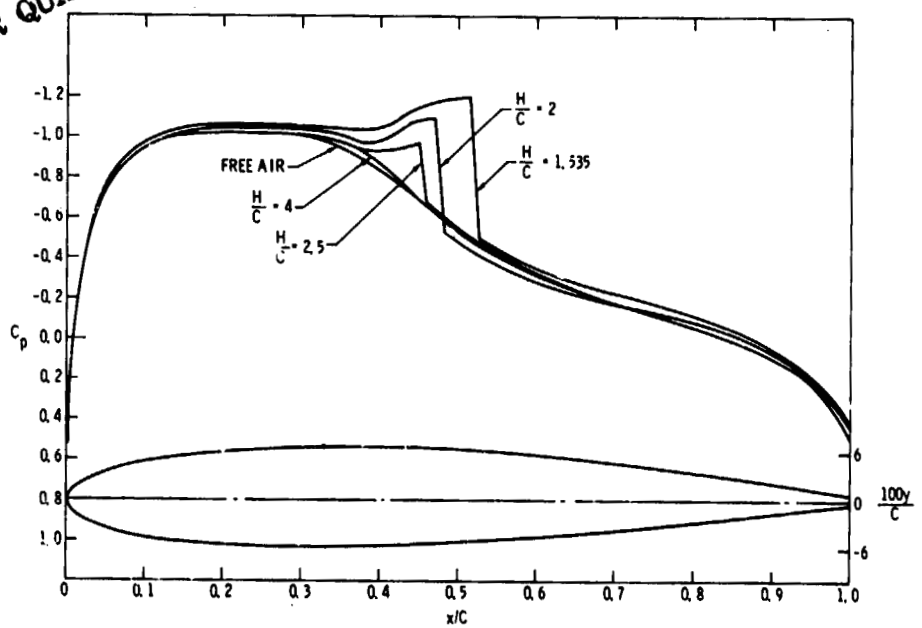

Figure 6.- Effect of solid tunnel walls on the performance of a free-flight shock-free airfoil. $M_\infty = 0.75$; $\alpha = 2°$.

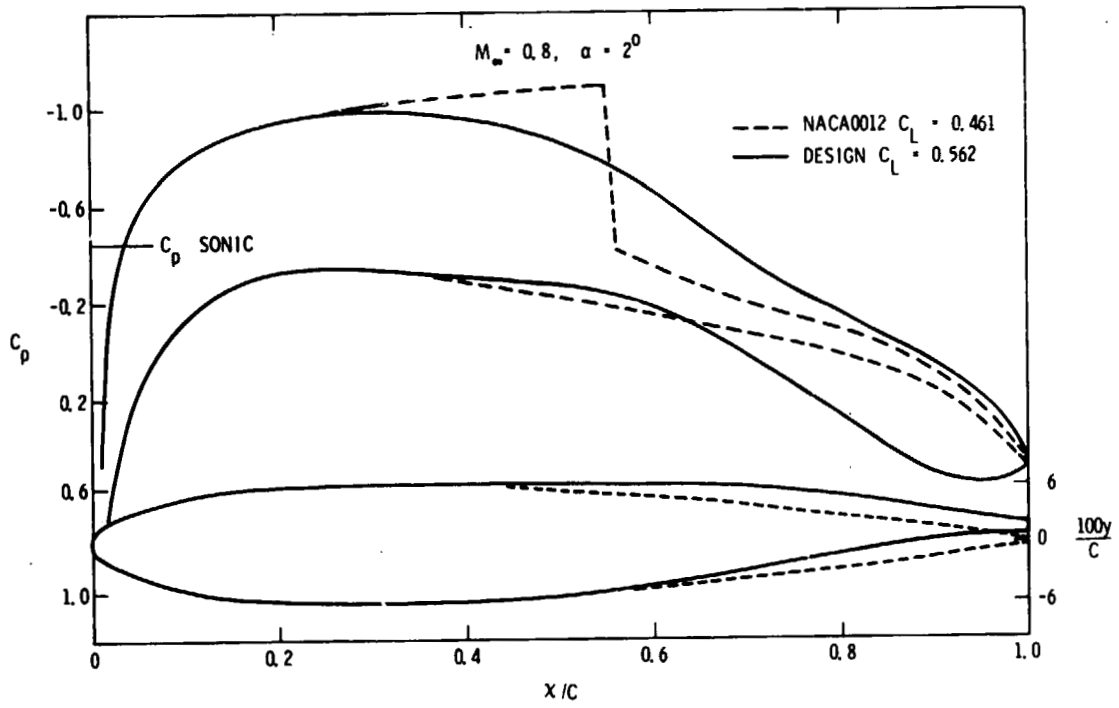

Figure 7.- Supercritical-airfoil design with NACA 0012 nose shape. $M_\infty = 0.8$; $\alpha = 2°$.

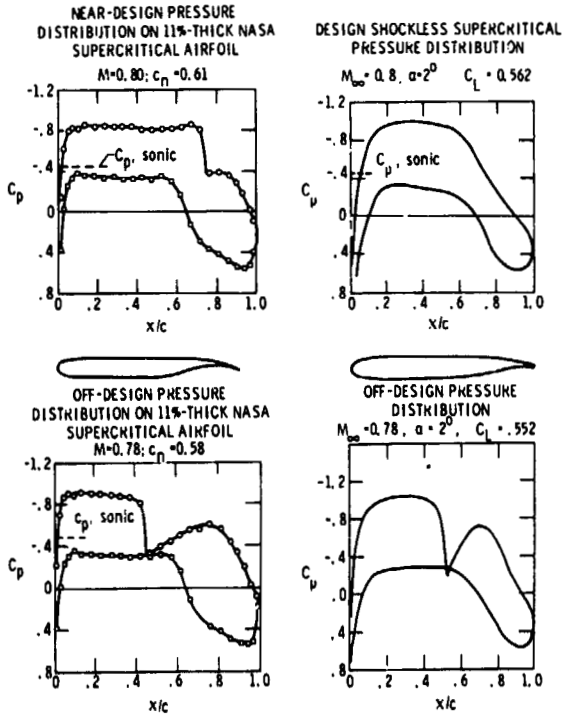

Figure 8.- Off-design pressure distribution.

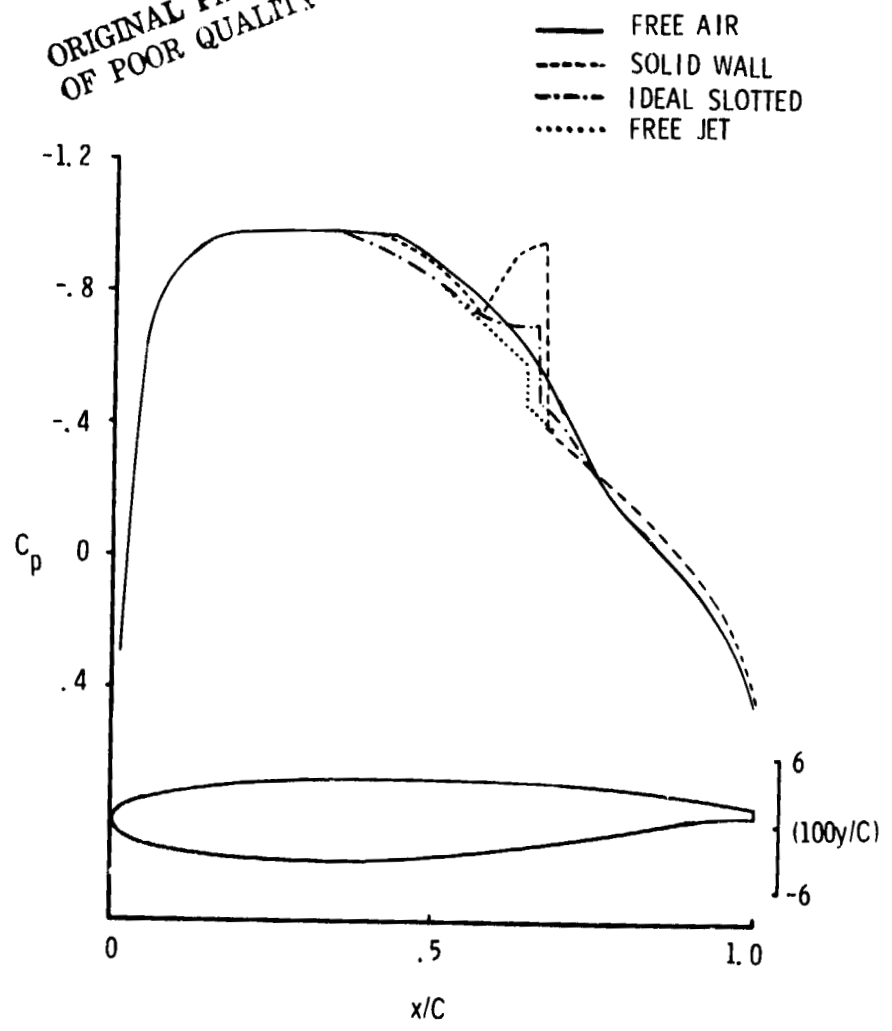

Figure 9.- Performance of a free-flight shock-free airfoil in a wind tunnel. $M_\infty = 0.8$; $\alpha = 2°$; $H/C = 6$.

8

PROSPECTS FOR COMPUTING AIRFOIL AERODYNAMICS WITH REYNOLDS AVERAGED NAVIER-STOKES CODES

George S. Deiwert and H. E. Bailey
NASA Ames Research Center

SUMMARY

The Reynolds averaged Navier-Stokes equations are solved numerically for a variety of transonic airfoil configurations where viscous phenomena are important. Illustrative examples include flows past sensitive geometries, Reynolds number effects, and buffet phenomena.

INTRODUCTION

The prediction of viscous phenomena in airfoil aerodynamics involves descriptions of both boundary-layer and inviscid flow regions and their interaction with one another. For flows where the boundary layer remains attached, the two flow regions may be analyzed separately and their interaction determined iteratively. This generally requires solving the compressible Euler equations (or a suitable subset) for the inviscid field and the boundary-layer equations for the viscous region near solid surfaces. The flow regions posing computational difficulty in these cases are the near wake, with its trailing edge singularity, and possible shock/boundary-layer interaction regions. When the viscous-inviscid interactions are strong, and there is flow separation or even buffeting, it is more reasonable to solve the Navier-Stokes equations for compressible flows. These equations describe the coupling between the viscous and inviscid regions, describe the elliptic behavior in regions of flow separation, and do not contain the singularity at the trailing edge.

In this paper several illustrative examples are presented in which viscous effects are important to transonic airfoil flows. All viscous numerical solutions are obtained from the Reynolds averaged Navier-Stokes equations and all are compared with appropriate experimental data. Two computer codes are used at present to generate flow field solutions: a fully implicit code, described in reference 1, and a mixed explicit/implicit code, described in reference 2. Both produce comparable results and are competitive in their computational efficiency. Symbol definitions are given in an appendix.

SHOCKLESS LIFTING AIRFOIL

Consider first the shock-free supercritical profile designed analytically by Garabedian and Korn (ref. 3). A series of experiments for design and

off-design conditions were performed at the NAE by Kacprzynski et al. (ref. 4) and by Kacprzynski (ref. 5). Comparisons at the design conditions with the inviscid theory of Garabedian and Korn suggest that the wind-tunnel test conditions for Mach number and angle of attack be corrected by subtracting 0.015 and 0.89°, respectively. This was in fact done and a series of comparisons between experiment and inviscid theory were made at a variety of off-design conditions (ref. 4). Figure 1 shows one such comparison for a test Mach number of 0.755 and an angle of attack of 0.12°, just slightly off the design conditions of 0.750 and 0.0°, respectively. Included are inviscid solutions for both the corrected ($M = 0.740$, $\alpha = -0.77°$) and uncorrected conditions. Clearly, the "corrected" solution shows better agreement with experiment, though it fails to predict drag coefficient C_D accurately. Also included in this figure is a viscous solution from a Navier-Stokes code at the uncorrected test conditions. The inclusion of viscous effects results in the same overall improvement as correcting the wind tunnel test conditions. Furthermore, both drag and lift are predicted accurately.

A second example, shown in figure 2, is for a high-lift configuration, where the test Mach number is 0.747 and angle of incidence is 2.96°. As in figure 1, the corrected inviscid solution for $M = 0.732$ and $\alpha = 2.07°$ agrees much better with experiment than do the uncorrected inviscid results. Again, drag is not well predicted and, in this case, neither is lift. Inclusion of viscous effects, by means of the Navier-Stokes equations, results in similar overall improvement without corrections to wind tunnel test conditions. However, both drag and lift are better predicted.

Kacprzynski et al. (ref. 4) state that the only justification for their correction is that it leads to the best agreement in pressure distribution between theory and experiment for the design case. In addition, the large discrepancies, particularly in Mach number, were not explainable. Previous experience indicated that Mach number corrections should be practically zero and angle of attack corrections less than 0.89°. It is suggested here, based on the results shown in figures 1 and 2, that viscous effects are of primary consideration for this particular airfoil configuration, and that tunnel corrections, while probably necessary, are not as great as indicated by inviscid theory.

Two possible explanations for this sensitivity of an inviscid design to viscous effects are: 1) the critical rapid expansion region at the nose of the airfoil is altered by viscous effects, and 2) the high aft camber results in fairly large viscous displacement thicknesses. Hence, we find an inviscid design producing a configuration that is highly sensitive to viscous phenomena.

To further support the validity of viscous solutions, a series of computations were made for nominal test Mach numbers of 0.75 and angles of attack ranging from -1.54° to 4.34°. The results of these computations are compared with experiment in figure 3 in the form of a drag polar (fig. 3(a)) and lift curve (fig. 3(b)). The agreement in both cases is very good.

Included in the drag polar are linearized inviscid results (which, of course, predict zero drag) and nonlinear inviscid results from the Garabedian and Korn code. The viscous solutions for angles of incidence greater than 3°

indicate buffet and are illustrated by two C_L vs C_D branches for angles 3.25° and 4.34°. The lift and drag vary periodically along the branch corresponding to the particular angle of incidence. Other angles of incidence greater than 3° (not shown) would exhibit different paths of periodic variation.

The buffet domain is more clearly illustrated in figure 3(b) for lift as a function of angle of attack. Here, for a given incidence, the minimum and maximum lift values define a buffet envelope. Note that the buffet onset and buffet boundaries are not necessarily confirmed nor repudiated by experiment. The experiments were static and not designed to define buffet conditions. The correspondence of maximum C_L, however, suggests similar buffet onset in the experiment.

To realize agreement between computation and experiment, the results shown in the lift curve suggest, for no Mach number corrections, suitable angle of attack corrections of roughly -0.3° for the 6% wall porosity experiment of reference 4 and -1.3° for the 20.5% wall porosity experiment of reference 5.

NACA 0012 AIRFOIL

Recent experiments in the AEDC 1-ft transonic tunnel on an NACA 0012 airfoil by Kraft and Parker were compared with similar experiments by Vidal et al. (ref. 6) in the Calspan 8-ft transonic tunnel. Results for a test Mach number of 0 80 and a 1° angle of attack indicate differences in shock position and trailing edge pressure between the two experiments. Two possible explanations for these discrepancies included 1) differences in wind-tunnel effect and 2) a Reynolds number effect. The Calspan experiments were performed at a chord Reynolds number of 1.0×10^6 and the AEDC experiments at 2.25×10^6. Computed Navier-Stokes solutions for each of these Reynolds numbers were compared with experiment by Potter and Adams (ref. 7) for upper surface pressure distribution and are reproduced in figure 4. The computed results agree with experiment at corresponding Reynolds numbers, suggesting that the difference in shock position is due to a Reynolds number effect. The low Reynolds number solution ($Re = 1\times10^6$) indicates the presence of separated flow downstream of the mid-chord position while the high Reynolds number solution ($Re = 2.25\times10^6$) is attached. This difference in flow pattern is reasonable in view of the fact that the low Reynolds number flow is transitional near the mid-chord of the airfoil and thus more susceptible to separation than the fully developed, higher Reynolds number flow. There are insufficient experimental data to confirm the existence or absence of separated flow.

Included for comparison in figure 4 is an inviscid solution obtained from transonic small perturbation theory (ref. 7). It is seen by comparison that for these relatively low Reynolds numbers the consideration of viscous effects is important since the lift coefficient may be strongly affected by shock wave location, which in turn is strongly affected by viscosity.

CIRCULAR ARC (18%)

A series of experiments and computations for the transonic flow over an 18% biconvex circular arc airfoil has been performed at the Ames Research Center (refs. 8-15). Results from these studies indicate the existence of three separate flow domains that are defined by Mach number and Reynolds number. Figure 5, taken from reference 12, shows the experimentally determined boundaries of these flow domains. For Mach numbers less than 0.73, the flow is always steady, with flow separation occurring near the trailing edge of the airfoil. For Mach numbers greater than 0.78, the flow is always steady, with separation occurring at the foot of the shock and closing in the near wake. In between exists an unsteady periodic regime in which the flow alternates between shock-induced separation and fully attached flow.

Surface pressure comparisons between viscous computations and experiment in each of the three flow regimes is shown in figure 6 (taken from ref. 14). For the low Mach number ($M = 0.72$) steady flow with trailing edge separation, the agreement is excellent. For the high Mach number ($M = 0.783$) steady flow with shock-induced separation, the comparisons are only qualitatively correct. In this case the computed solution indicates the presence of a strong oblique shock, while the experiment indicates a weak oblique shock. While both strong and weak shock solutions will satisfy the governing equations, the computer code at present does not yield the weak solution shown in the experiment. Both computation and experiment exhibit shock-induced separation with closure realized in the near wake. Size of the reverse flow region is reasonably well predicted (see refs. 13 and 15). For the unsteady flow regime, the pressure distribution over the airfoil surface is unsteady. Comparisons for this case will be discussed subsequently.

Shown in figure 7 are selected frames from a high-speed shadowgraph movie of the upper aft portion of the airfoil during experimental tests. Figure 7(a) shows a normal shock at about 65% chord with flow separation occurring just ahead of the trailing edge. This corresponds to the low Mach number regime. Figure 7(b) shows a time-dependent sequence of the same region for the unsteady regime and illustrates the periodic nature of the alternating shock-induced separation/fully attached flow. Figure 7(c) shows a steady oblique shock at nearly 60% chord with separation initiated at the foot of the shock.

Figure 8 shows computed Mach contours for the three flow regimes; figures 8(a), 8(b), and 8(c) correspond to steady flow with trailing edge separation, unsteady periodic flow, and steady flow with shock-induced separation, respectively. The comparison of results between figures 7 and 8 illustrates that the computer simulation reflects the appropriate physical behavior of this configuration and describes all three flow regimes observed experimentally. The only real point of discrepancy remains in the weak vs strong oblique shock in the steady flow high Mach number case.

Finally, in figure 9, the surface pressure time histories for the computed and experimental unsteady flows are compared. Flow conditions were for $M = 0.754$, $\alpha = 0°$, and $Re = 11 \times 10^6$ in both the computation and experiment. The computed results simulated the wind-tunnel walls as boundary conditions.

Comparisons are made at a mid-chord location and near a 3/4-chord location on both upper and lower surfaces simultaneously. Remarkable agreement is found both in form and amplitude of the variations. The reduced frequency of the oscillations agreed to within 20%.

Clearly, viscous effects are important in all three flow regimes observed for the 18% circular arc airfoil. The success of the computer code in simulating such flows, particularly in the unsteady regime, gives confidence in its utility.

COMPUTATIONAL EFFICIENCY

At present, two computer codes are used at Ames to solve the Reynolds averaged Navier-Stokes equations for compressible flows. One is based on the mixed explicit/implicit algorithm developed by MacCormack (ref. 16) and the other on the fully implicit algorithm developed by Beam and Warming (refs. 17 and 18) and Briley and McDonald (ref. 19). Both codes are competitive in terms of cost and reliability of results. In addition, both codes are in a continued state of development and are constantly being improved in terms of efficiency. For example, flow over the Korn airfoil was simulated using the fully explicit code of 1974 and required 13 hr of CDC 7600 time to obtain a converged solution. An improved version (1976) employing a mixed explicit/implicit operator reduced the computer requirements to 90 to 120 min. The present version (mixed explicit/implicit, 1978) requires only 20 to 30 min for the same configuration. Modifications are presently underway to reduce this time by one-half.

Both of the present codes use algebraic eddy viscosity models to describe the Reynolds stresses in terms of mean field gradients. Discussions of these models for the mixed code are presented in references 8, 9, and 13 and for the fully implicit code by Baldwin and Lomax (ref. 20). It is possible that these models can have a significant influence on the reliability of the results. A continued effort exists at Ames to further improve the reliability of the turbulence transport models.

CONCLUDING REMARKS

Three illustrative examples have shown that consideration of viscous effects is important for computing airfoil aerodynamics in a variety of situations. Included are sensitive shapes (such as the Korn supercritical airfoils), the definition of buffet boundaries, Reynolds number effects, separated flows, and unsteady flows. In addition it has been shown, by comparison with experiment, that computer codes based on the Reynolds averaged Navier-Stokes equations can provide adequate simulations of these flows for the evaluation of a given design. The computational efficiency of these codes is steadily being improved such that they are expected to be an effective analytical tool in the near future.

APPENDIX

SYMBOLS

c	airfoil chord
C_D	drag coefficient
C_L	lift coefficient
C_p	pressure coefficient
C_p^*	critical pressure coefficient
M	free-stream Mach number
P_t	total pressure
Re	free-stream Reynolds number based on chord
t	time
x	chordwise coordinate
α	free-stream angle of attack
ΔP	incremental pressure from the mean surface pressure

REFERENCES

1. Steger, J. L.: Implicit Finite Difference Simulation of Flow About Arbitrary Geometries with Application to Airfoils. AIAA Paper 77-665, June 1977.

2. Deiwert, G. S.: Recent Computation of Viscous Effects in Transonic Flow. A. I. van de Vooren and P. J. Zandberge, eds., Lecture Notes in Physics 59, Springer-Verlag, New York, 1976, pp. 159-164.

3. Garabedian, P. R., and Korn, D. G.: Numerical Design of Transonic Airfoils. Numerical Solution of Partial Differential Equations - II. Academic Press, New York, 1971, pp. 253-271.

4. Kacprzynski, J. J.; Ohman, L. H.; Garabedian, P. R.; and Korn, D. G.: Analysis of the Flow Past a Shockless Lifting Airfoil in Design and Off-design Conditions. NRC, Aeronautical Report LR-554, Nov. 1971.

5. Kacprzynski, J. J.: A Second Series of Wind Tunnel Tests of the Shockless Lifting Airfoil No. 1. NRC/NAE Wind Tunnel Project Report 5x5/0062, June 1972.

6. Vidal, R. J.; Catlin, P. A.; and Chudyk, D. W.: Two-Dimensional Subsonic Experiments with an NACA 0012 Airfoil. Calspan Report No. RK-5070-A-3, Dec. 1973.

7. Potter, J. L.; and Adams, J. C.: Computational Aerodynamics Requirements in Conjunction with Experimental Facilities. Future Computer Requirements for Computational Aerodynamics, NASA CP-2032, Feb. 1978.

8. Deiwert, G. S.: Numerical Simulation of High Reynolds Number Transonic Flows. AIAA Journal, vol. 13, Oct. 1975, pp. 1354-1359.

9. Deiwert, G. W.: High Reynolds Number Transonic Flow Simulation. R. D. Richtmyer, ed., Lecture Notes in Physics 35, Springer-Verlag, New York, 1975, pp. 132-137.

10. Deiwert, G. W.; McDevitt, J. B.; and Levy, L. L., Jr.: Simulation of Turbulent Transonic Separated Flow Over an Airfoil. Aerodynamic Analyses Requiring Advanced Computers, Part I, NASA SP-347, 1975.

11. Baldwin, B. S.; MacCormack, R. W.; and Deiwert, G. S.: Numerical Techniques for the Solution of the Compressible Navier-Stokes Equations and Implementation of Turbulence Models. Computational Methods for Inviscid and Viscous Two- and Three-Dimensional Flow Fields, AGARD-LS-73, Feb. 1975.

12. McDevitt, J. B.; Levy, L. L. Jr.; and Deiwert, G. S.: Transonic Flow about a Thick Circular-Arc Airfoil. AIAA Jornal, vol. 14, May 1976, pp. 606-613.

13. Deiwert, G. S.: Computation of Separated Transonic Turbulent Flows. AIAA Journal, vol. 14, June 1976, pp. 735-740.

14. Levy, L. L. Jr.: An Experimental and Computational Investigation of the Steady and Unsteady Transonic Flow Field About an Airfoil in a Solid-Wall Test Channel. AIAA Paper 77-678, June 1977.

15. Seegmiller, H. L.; Marvin, J. G.; and Levy, L. L. Jr.: Steady and Unsteady Transonic Flow. AIAA Paper 78-160, Jan. 1978.

16. MacCormack, R. W.: An Efficient Explicit-Implicit-Characteristic Method for Solving the Compressible Navier-Stokes Equations. SIAM-AMS Proceedings of the Symposium on Computational Fluid Dynamics, New York, April 16-17, 1977.

17. Beam, R.; and Warming, R. F.: An Implicit Finite-Difference Algorithm for Hyperbolic Systems in Conservation-Law-Form. J. Comp. Physics, vol. 22, Sept. 1976, pp. 87-110.

18. Beam, R.; and Warming, R. F.: An Implicit Factored Scheme for the Compressible Navier-Stokes Equations. AIAA Paper 77-645, June 1977.

19. Briley, W. R.; and McDonald, H.: An Implicit Numerical Method for the Multi-Dimensional Compressible Navier-Stokes Equations. Report M911363-6, United Aircraft Research Laboratories, 1973.

20. Baldwin, B. S.; and Lomax, H.: Thin Layer Approximation and Algebraic Model for Separated Turbulent Flows. AIAA Paper 78-257, Jan. 1978.

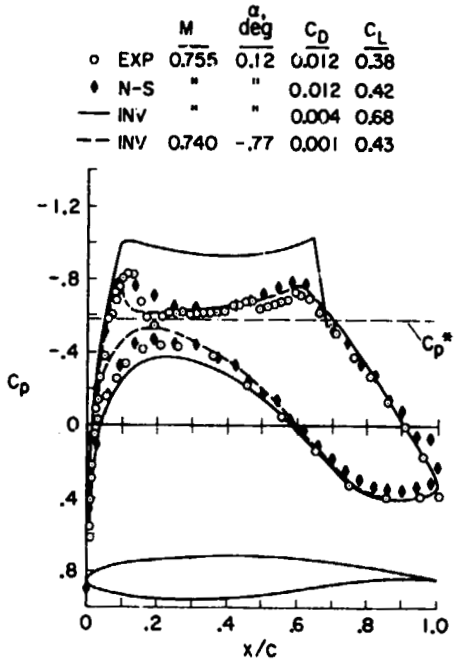

Figure 1.- Surface pressure distribution over Korn 1 airfoil at near-design conditions. Re = 21 × 10^6.

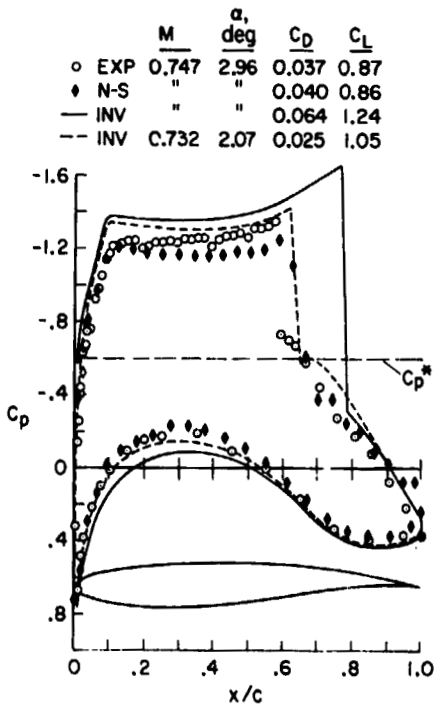

Figure 2.- Surface pressure distribution over Korn 1 airfoil at high lift conditions. Re = 21 × 10^6.

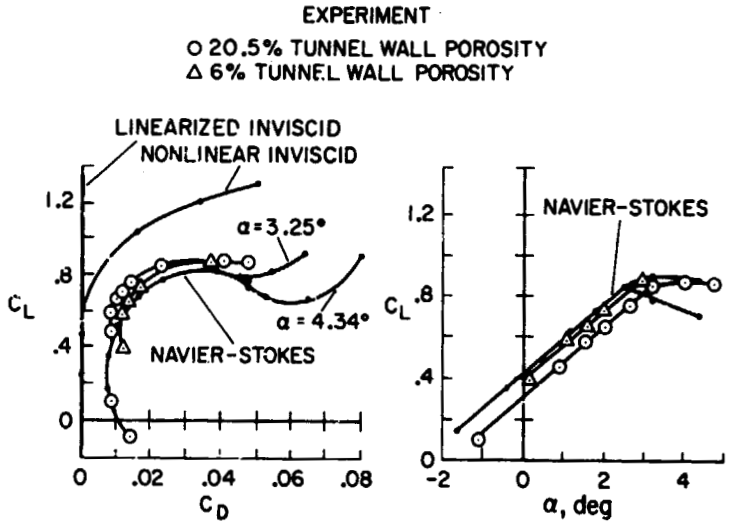

(a) Drag polar. (b) Lift curve.

Figure 3.- Drag polar and lift curve for Korn 1 airfoil at nominal Mach number of 0.75. Re = 21 × 10^6.

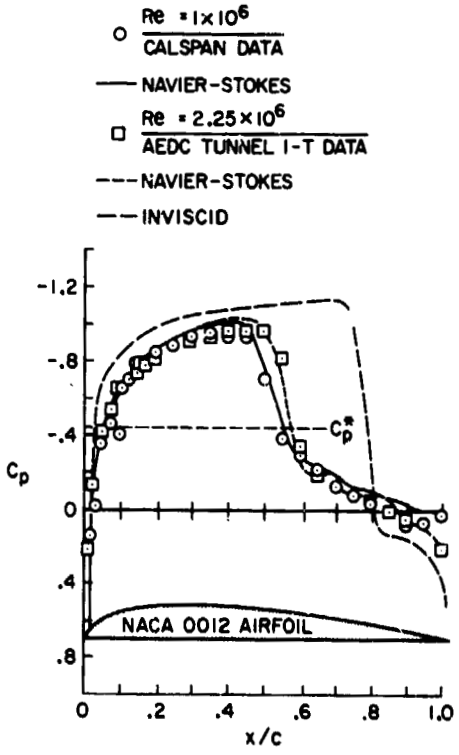

Figure 4.- Upper surface pressure distribution over NACA 0012 airfoil. M = 0.80; α = 1°.

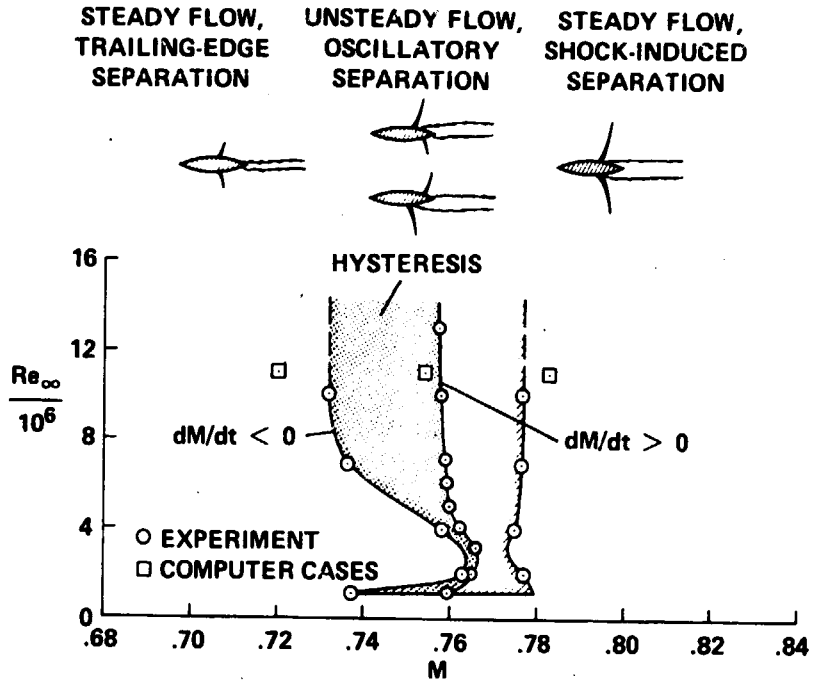

Figure 5.- Experimental flow domains for the 18-percent-thick circular-arc airfoil.

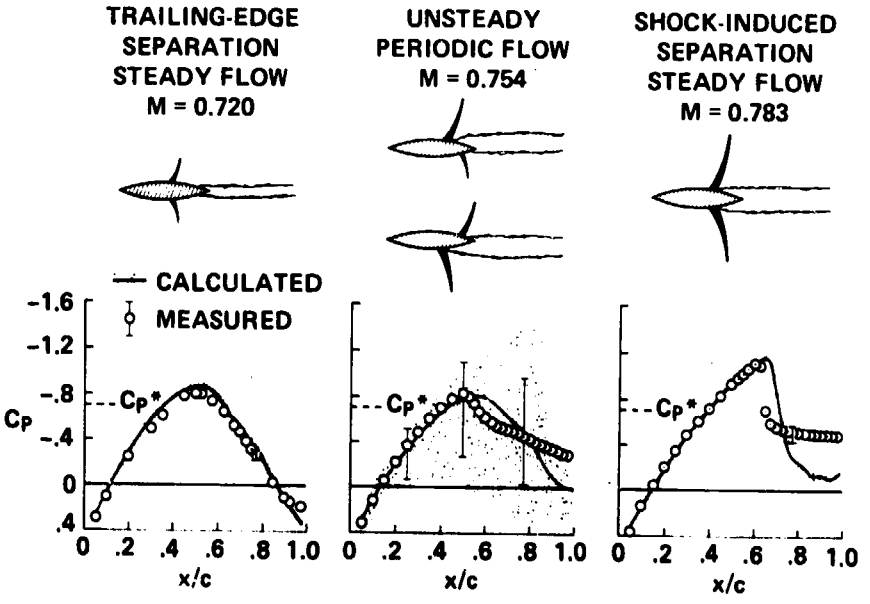

Figure 6.- Computed and experimental pressure distributions on the 18-percent-thick circular-arc airfoil. Re = 11 × 10^6; $\alpha = 0°$.

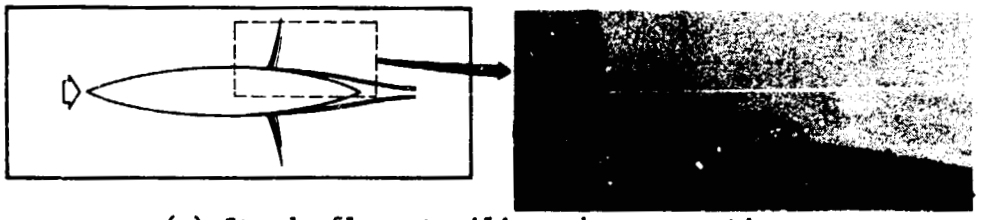

(a) Steady-flow, trailing-edge separation.

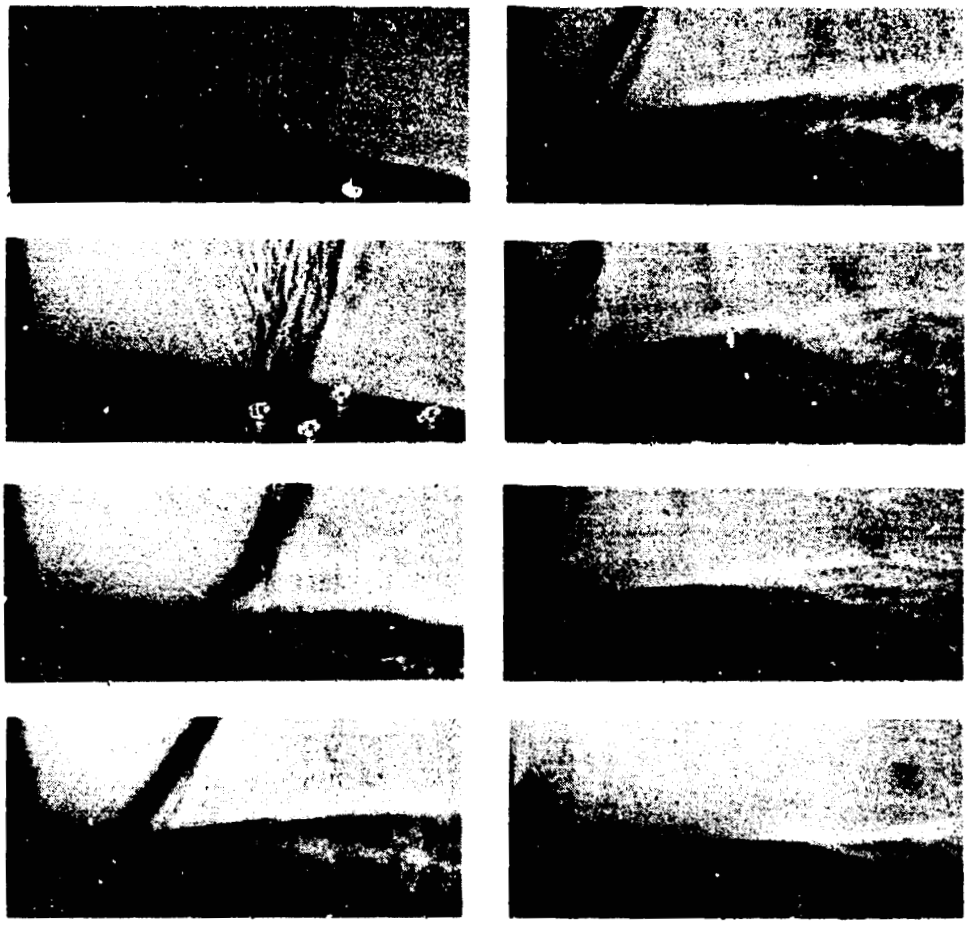

(b) Unsteady flow, oscillatory separation.

(c) Steady flow, shock-induced separation.

Figure 7.- Boundary-layer separation on the 18-percent-thick circular-arc airfoil from a shadowgraph movie. Re = 11 × 10^6; $\alpha = 0^\circ$.

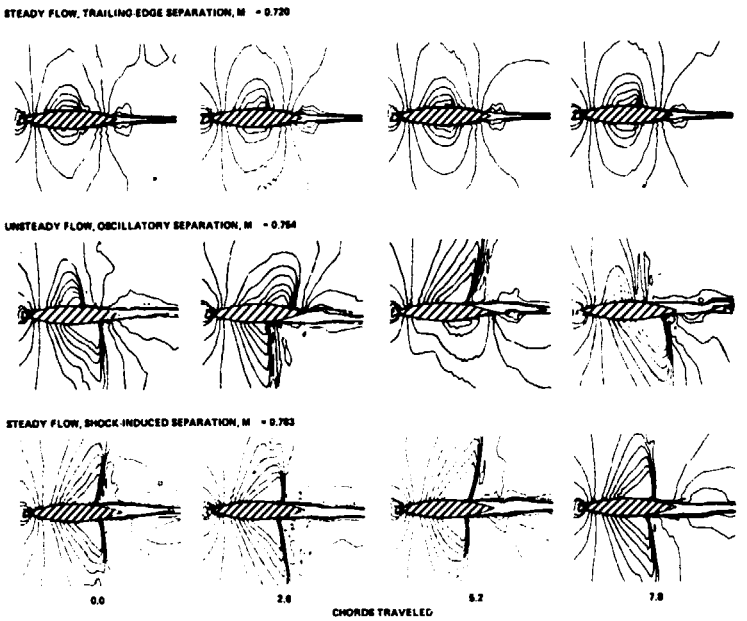

Figure 8.- Computed Mach contours in the flow field about the 18-percent-thick circular-arc airfoil. Re = 11 × 10^6; α = 0°.

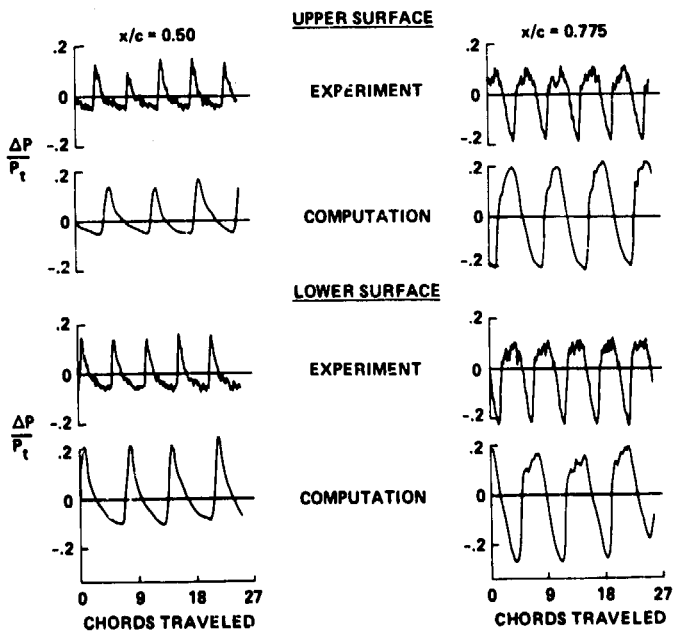

Figure 9.- Surface pressure time histories on the 18-percent-thick circular-arc airfoil with unsteady flow. M = 0.76; Re = 11 × 10^6; α = 0°.

D9

9

AN EVALUATION OF FOUR SINGLE ELEMENT AIRFOIL ANALYTIC METHODS*

R. J. Freuler and G. M. Gregorek
General Aviation Airfoil Design and Analysis Center
The Ohio State University

SUMMARY

A comparison of four computer codes for the analysis of two-dimensional single element airfoil sections is presented for three classes of section geometries. Two of the computer codes utilize vortex singularities methods to obtain the potential flow solution. The other two codes solve the full inviscid potential flow equation using finite differencing techniques, allowing results to be obtained for transonic flow about an airfoil including weak shocks. Each program incorporates boundary layer routines for computing the boundary layer displacement thickness and boundary layer effects on aerodynamic coefficients.

Computational results are given for a symmetrical section represented by an NACA 0012 profile, a conventional section illustrated by an NACA 65A413 profile, and a supercritical type section for General Aviation applications typified by a NASA LS(1)-0413 section. Experimental results from The Ohio State University 15 cm (6 in.) by 56 cm (22 in.) Transonic Airfoil Tunnel are also given. The cases presented include operating conditions at subsonic, subcritical, and near critical or supercritical Mach numbers. The four codes are compared and contrasted in the areas of method of approach, range of applicability, agreement among each other and with experiment, individual advantages and disadvantages, computer run times and memory requirements, and operational idiosyncrasies.

INTRODUCTION

The General Aviation Airfoil Design and Analysis Center (GA/ADAC) was established at The Aeronautical and Astronautical Research Laboratory (AARL), The Ohio State University, under contract to NASA Langley Research Center in June 1976. GA/ADAC offers a comprehensive service to the general aviation community in the form of airfoil selection and design and analysis work as well as consultation in the areas of wind tunnel testing and flight testing work. An important feature of GA/ADAC is the large library of computer codes which has been established and is maintained at AARL. This computer program library re-

*This work has been supported in part by NASA Langley Research Center Contract NAS1-14406.

132

presents a wide variety of airfoil related computer codes collected in one location onto one computer system, with more than thirty computer codes in the areas of single element airfoil analysis and design, multi-element airfoil analysis and design, wing analysis, and propeller aerodynamic and acoustic performance analysis available for use.

A comparative evaluation of the four computer codes most frequently used at GA/ADAC for the analysis of two-dimensional single element airfoil sections is presented in this paper for three classes of airfoil section geometries: symmetric, conventionally cambered, and aft-cambered. Theoretical predictions of pressure distributions and aerodynamic coefficients for the three airfoils are compared with measurements taken in the 15 cm x 56 cm Transonic Airfoil Tunnel at AARL.

The symbols used herein are defined in an appendix.

COMPUTER CODES

The computer codes used for the comparisons are designated as follows: (1) Garabedian, by F. Bauer, P. Garabedian, D. Korn, and A. Jameson and detailed in references 1 and 2; (2) Carlson, by L. A. Carlson and explained in references 3 and 4; (3) Smetana, by F. Smetana, D. Summey, N. Smith, and R. Carden and documented in references 5 and 6; and (4) Eppler, by R. Eppler and D. Somers and soon to be documented in a NASA Technical Note. It should be mentioned that the versions of these computer codes in use at GA/ADAC are maintained as up-to-date as possible; yet, in some instances, these versions are not the most current since each of the codes, with the exception of the Smetana code, is constantly being refined and improved by the respective program authors. For example, the Carlson code is currently being modified to include the effects of a laminar boundary layer and the Eppler code may soon be modified to iterate on the boundary layer displacement thickness.

A brief description of the method of approach for the four codes will be given here; the literature cited (refs. 1-6) contains the detailed explanations. The Garabedian code is a transonic code that employs a finite difference solution to the full inviscid potential flow equation for a conformally mapped airfoil. The boundary layer displacement is added iteratively to the airfoil ordinates in order to evaluate airfoil section performance including viscous effects. The Carlson code is also a transonic code and is similar to Garabedian, but it uses a finite difference solution to the full inviscid potential flow equation for an airfoil in a stretched Cartesian coordinate system, instead of for a conformally mapped airfoil. The Smetana program is a strictly subcritical code employing a method of vorticity distributed over an airfoil approximated by a closed polygon. An iterative approach to boundary layer effects is included. The approach used in the Eppler code is similar to the Smetana code, but it differs in that the vorticity is distributed over an airfoil shape approximated by curved panels and that there is no iteration on the boundary layer displacement thickness.

A summary of the methods of approach for the inviscid flow and the technique of handling the boundary layer for each computer code is given in table 1. The iterative procedure referred to in table 1 is that of: (1) obtaining an inviscid flow solution for the original airfoil; (2) obtaining a boundary layer solution based on the inviscid flow solution; (3) modifying the airfoil shape by adding the boundary layer displacement thickness to the airfoil; (4) obtaining an inviscid flow solution for the modified airfoil; and, (5) repeating steps 2 through 4 until convergence criteria are satisfied.

AIRFOIL SECTIONS

Three classes of airfoil section geometries are included in these comparative results. A symmetrical airfoil section is represented by the well documented NACA 0012 profile (ref. 7 and 8) shown in figure 1. To provide a sufficient number of airfoil ordinates for computational purposes, computer generated coordinates for the NACA 0012 (ref. 9) were used with the airfoil section being defined by 47 ordinates for both upper and lower surfaces. Although no attempt has been made in this work to evaluate the performance of the individual computer codes with respect to sensitivity of computational results to airfoil ordinate density, a sufficient number of coordinates (i.e. at least 35 to 40) has been used to provide consistent, reliable results. Ordinate density has been distributed such that there is a higher density of points concentrated in regions of greater airfoil curvature. This is a particular requirement for the two subcritical codes because of the nature of the distributed vorticity methods of flow solution.

Results for a conventional section are illustrated by a NACA 65A413 airfoil (fig. 2). The ordinates for this section, 63 in number, were obtained by the method of reference 10. Some drag prediction comparisons for another NACA 6A-series section, a 64A010, are also included.

The third class of airfoil geometries investigated is the aft-cambered Whitcomb supercritical type section. In this paper, the results for a derivative of such a section designed specifically for general aviation applications, the NASA LS(1)-0413 airfoil (fig. 3), are presented. The ordinates used for the LS(1)-0413, known also as the GA(W)-2 airfoil, are those listed in reference 11.

AIRFOIL DATA SUMMARY COMPARISONS

For the two subcritical codes, Smetana and Eppler, a comparison of the three airfoils in terms of airfoil data summary plots is of interest. As shown in figure 4 for the NACA 0012, the comparison with experiments reported in reference 7 is quite good. Note that the wind tunnel test is shown as the solid line while the theory is given by the symbols, a reversal of usual conventions. The Eppler code shows a break-over in the C_L (lift coefficient)

versus alpha (angle of attack) plot produced by using the predicted separation point to define an "effective" angle of attack. The Smetana code merely identifies a predicted separation point, but makes no attempt to compensate for the effects of separation. The free transition option was specified in the Smetana code for this comparison and the following two airfoil data summaries. The Eppler code always uses natural transition, although it does allow a variable roughness option.

In figure 5, computational results are shown for a NACA 65A413 airfoil compared to the wind tunnel results for a NACA 65_1-412 of reference 7. Both codes may be observed to predict the laminar drag bucket for this NACA 6-series section.

The airfoil data summary comparisons for the NASA LS(1)-0413, shown in figure 6, point out the difficulty Eppler has with some airfoils with regard to the angle of zero lift. This appears to be related to the lack of an iterative boundary layer solution and is more noticeable with supercritical type, blunt trailing edged airfoil shapes. The wind tunnel results are those of McGhee, et al. (ref. 12).

PRESSURE DISTRIBUTION COMPARISONS

The detailed pressure distribution comparison cases which follow include operating conditions at subcritical and near critical or supercritical Mach numbers. The computational results are compared with experimental results from The Ohio State University 15 cm (6 in.) by 56 cm (22 in.) Transonic Airfoil Tunnel. The OSU 6 x 22 wind tunnel is a low-interference transonic facility for airfoil testing over the Mach number range of 0.30 to 1.07 and a Reynolds number range of 2 to 15 million based on 15.24 cm (6 in.) model chord (refs. 13 and 14). The angle of attack used in the computational results is the effective angle of attack, α_{eff}, obtained from the set angle of attack in the wind tunnel corrected for wall effects according to the empirically derived relation:

$$\alpha_{eff} = \alpha_{set} - 0.17\ C_L$$

It should be noted that for all the supercritical pressure distribution comparisons, the drag coefficient listed for Carlson has been omitted. Total drag as predicted by Carlson requires a wave drag correction to be applied that was not available to the authors at this writing.

Figure 7 shows the comparisons for all the codes for the NACA 0012 airfoil at a Mach number of about 0.35 over a range of angles of attack. The pressure distributions are in good agreement, though the Eppler code predicts a somewhat higher suction peak than the other codes at the higher angles of attack. Drag comparisons for the subcritical codes using the free transition option are quite good. The less accurate drag predictions by the two transonic codes is a result of attempting to simulate free transition by fixing turbulent boundary

layer transition a few percent chord in front of the Smetana predicted naturally occurring transition location.

Comparisons for the NACA 0012 at an angle of attack of zero over a range of Mach numbers is given in figure 8. Both the Smetana and Eppler codes show a tendency to predict lower pressures in the nose region at the near critical Mach number condition, and of course can not correctly predict the distribution at supercritical conditions. Both transonic codes identify the strength and location of the shock quite well.

Comparisons of the transonic codes and wind tunnel results for the NACA 0012 at supercritical conditions are given in figure 9. The Mach number is nominally 0.80 and results are given for three angles of attack. Note that the Carlson code appears to predict somewhat higher values of lift and a corresponding prediction of a shock located further aft on the airfoil. This appears to be caused by an uncertainty in angle of attack in the Carlson code, with a trend toward results being obtained at a slightly higher angle of attack than the input angle of attack for many airfoils. Thus, in general. Carlson results should be examined as pressure versus lift coefficient, moment versus lift coefficient, etc., instead of angle of attack. Since direct comparisons with wind tunnel angle of attack were desired for this study, matching angle of attack was more convenient, so this approach has been used. Both codes indicate a tendency to recover more pressure on the aft upper surface than is observed in the wind tunnel tests for this airfoil (and most other airfoils as well). In figure 9c the large discrepancy in shock location may be explained by the fact that the predicted local Mach number in front of the shock is in excess of 1.47, a shock Mach number that poses difficulty for both the theory and the wind tunnel.

For the transonic codes, careful selection of input parameters relating to convergence and relaxation factors are required to encourage the codes to produce any meaningful results for an airfoil when the free stream Mach number and lift coefficient exceed certain values. The empirical relationship below, suggested by Dr. R. Whitcomb, appears to describe these limiting values:

$$M + t/c + 0.1\ C_L \geq 0.92$$

Here M is the free stream Mach number, t/c is the airfoil thickness ratio and C_L is the lift coefficient.

In figures 10 and 11, results are presented for the NACA 65A413 airfoil section for a subcritical and slightly supercritical Mach number. This comparison shows both the Garabedian and Carlson codes over-predicting the lift. Carlson's over-prediction could be related to the angle of attack uncertainty previously discussed but no consistent reason can be presented for Garabedian's results, particularly for the generally higher pressures predicted on the lower surface (fig. 10). This characteristic in Garabedian occurs infrequently and may be circumvented by using the matching-lift-coefficient option (which essentially compensates for any uncertainty in angle of attack in either the wind tunnel or computer code). Also, the theoretical predictions of drag, though consistent with each other, are lower than the wind tunnel results.

(The wave drag contribution in figure 11 is less than 0.0002, and thus the Carlson skin friction drag as shown approximates the total drag).

Comparisons for the NASA LS(1)-0413 airfoil section are given in figures 12 and 13. Figure 12 shows the computational and experimental results obtained for a nearly zero angle of attack through a range of Mach numbers from 0.45 to 0.80. For this airfoil, agreement with the wind tunnel results at subcritical conditions is excellent for both the pressure distributions and the aerodynamic coefficients. It is interesting to note in figure 12c that the pressure distributions and shock locations predicted by Garabedian and Carlson differ noticeably, presumably for reasons mentioned earlier; yet in figure 12d the pressure distributions predicted by the codes are nearly identical. (The wind tunnel results in 12d may be influenced by the strong shock present at the condition illustrated). This comparison points out the uncertainties in angle of attack are dependent not only on the input airfoil but also on the specific input conditions as well.

The results for the NASA LS(1)-0413 at a nominal Mach number of 0.72 over a range of angles of attack are presented in figure 13. In figure 13a, both transonic codes exhibit some interesting characteristics. Carlson, although the lift nearly matches the wind tunnel results, has difficulty properly defining the nose region on the lower surface. This may be due to the fact the Cartesian grid used does not place a large number of computational points near the leading (and trailing) edge. Although the Garabedian result accurately describes the lower surface nose region including the shock location, the lift prediction is too low as a result of over-predicting the pressure recovery on the upper surface. In figure 13b these same trends may be observed to a lesser degree. In 13c the results are more characteristic of the codes: Garabedian showing a reasonable lift and drag prediction with a slightly higher than wind tunnel observed pressure recovery over the trailing edge region; and Carlson exhibiting results at an apparently higher effective angle of attack for the input angle of attack which matches the wind tunnel and the Garabedian results.

In figure 14, comparisons are shown for Carlson with wind tunnel results (fig. 13c) by both matching angle of attack and selecting angle of attack which is matching the wind tunnel lift coefficient. Note that the expected excellent agreement of the pressure distribution and the aerodynamic coefficients with the wind tunnel test is obtained when lift coefficients are matched.

DRAG PREDICTIONS

Drag coefficient predictions by the Garabedian code are generally consistent and accurate enough to enable use of the code to predict the drag rise characteristics and the drag divergence Mach number for most airfoils. The version of the Garabedian code in use at GA/ADAC for the past 18 months employs the latest wave drag calculation techniques and the fast Poisson solver for the subsonic region of flow which improves the rate of convergence (ref. 2).

Figure 15 shows good agreement between the Garabedian code predicted and the OSU 6 by 22 wind tunnel observed total drag for Mach numbers well into the drag rise. It should be noted that the Reynolds number was not to be held constant in these results, but varied from 3.8 to 5.9 million. The angle of attack was nominally zero. Transition was specified as fixed at 0.075c for the Garabedian code which seems consistent for the LS(1)-0413, a turbulent flow airfoil by design, at these conditions. The sudden decrease in skin friction drag shown for this airfoil in the drag rise region is a result of shock-induced separation due to the strong shock present. The relatively larger region of computer predicted separated flow behind the shock on the upper surface of the airfoil results in a lower skin friction drag coefficient.

Drag rise characteristics for the symmetric, NACA 64A010 airfoil section are given in figure 16. Excellent agreement between theory and wind tunnel is again observed. The boundary layer transition was fixed at 0.05c in both the wind tunnel and computer code. The Reynolds number varied from 3.5 million at Mach 0.5 to about 5 million at Mach 0.85. The angle of attack was held at zero.

COMPUTER REQUIREMENTS

All four airfoil analysis codes are run on the GA/ADAC computer facility located at AARL. The computer system is a dual processor system using Harris SLASH 6 and SLASH 5 processors. The SLASH 6, which is used for all of GA/ADAC's airfoil work, is a medium-sized, 24 bit word computer system with 64K words (192K bytes) of main memory. For purposes of comparison, the SLASH 6 is about an average factor of 8 times slower in heavy floating point FORTRAN programs than an IBM System 370 Model 168. Of special interest is the fact the calculations on the SLASH 6 are performed with over 11 decimal digits of accuracy while single precision on IBM mainframes affords approximately 7 decimal digits accuracy. The 11+ digit accuracy of the computer used at GA/ADAC is well suited for most scientific calculations including airfoil analysis, thus avoiding the necessity to maintain 15-16 digit accuracy like that of a CDC mainframe or double precision on an IBM machine.

Table 2 lists several computer related characteristics of the four codes. Of most interest are the memory requirements and the run times for the programs. All the codes have been folded into the SLASH 6 such that the largest program requires 48K words. All programs are overlaid to varying degrees to reduce memory requirements. Per case run times, where a "case" is a calculation at one Mach number, one Reynolds number, and one angle of attack, are expressed in a normalized form. The single case run time used for normalization is that of the Smetana code. For the SLASH 6, time T is on the order of 90-100 seconds. A range of times is shown for the two transonic codes since convergence to a solution varies depending on whether the case is subcritical or supercritical and on a user-supplied convergence tolerance. The Carlson code has the longest running time per case when results are carried to the fine grid, which was used in all cases for the previous comparisons. The medium grid result of

Carlson can be used if desired with an accompanying reduction in computation time. The Smetana code has no convergence criteria, relying instead on a program-fixed number of inviscid flow/boundary layer iterations to achieve a converged solution and resulting in a very consistent run time per case. The Eppler code is the most rapid of the four codes and typically requires a small percentage of time T per case. All of the codes have some form of hard copy plot capability.

OBSERVATIONS AND CONCLUSIONS

Based on the results presented here and the extensive exercise of these four single-element airfoil analysis codes, the following observations and remarks can be made.

THE SMETANA CODE: is a subcritical code; uses vorticity distributed around a closed polygonal airfoil; is reasonably well documented; has flexible boundary layer routines, allowing free or fixed transition; has had drag prediction "tuned" for flight Reynolds numbers, giving good drag coefficients over the Reynolds number range of 1 to 15 million; obtains the pressure distribution from iteration with boundary layer; exhibits good angle of zero lift identification; and identifies laminar bubbles. But it: has no design mode; incorporates no evaluation of the effects of boundary layer separation; has a convergence criteria no more sophisticated than a fixed number of iterations; and may provide misleading drag results at low Reynolds numbers due to the tuning factor applied to the drag calculations.

THE EPPLER CODE: is a subcritical code; uses vorticity distributed around a curved panel airfoil; has good boundary layer routines, applicable over a wide range of Reynolds numbers; exhibits good performance at low Reynolds numbers; has a design mode, although the mode is difficult to use at first; provides a separation effects estimate, giving rise to a predicted break in lift coefficient versus angle of attack; executes very quickly, resulting in inexpensive per case computing costs; and contains more empiricism than the other codes. But it: has no iteration with the boundary layer; exhibits difficulty in identifying angle of zero lift, especially for airfoils of the supercritical type cusped trailing edge (which is related to no boundary layer iteration); and has limited documentation.

THE GARABEDIAN CODE: is a transonic code; employs a finite difference solution to the full inviscid potential flow equation for a conformally mapped airfoil; iterates on boundary layer displacement thickness; gives good pressure distributions and shock location as long as the local Mach number does not exceed 1.4; provides reasonable wave drag estimates and can be used for drag rise predictions; and has flexible input options, allowing to specify either angle of attack or coefficient of lift. But it: has no laminar boundary layer or transition criteria; employs a boundary layer smoothing process which can tend to artifically thicken the boundary layer and slow down convergence; and is not well suited for Mach numbers less than 0.3.

THE CARLSON CODE: is a transonic code; employs a finite difference solution to the full inviscid potential flow equation for an airfoil in a stretched Cartesian coordinate system; iterates on boundary layer thickness; gives good pressure distributions; has easy to use design mode; and incorporates a massive separation prediction technique. But it: has no laminar boundary or transition criteria (but one is currently being added); does not have an input option for matching lift coefficient; exhibits an uncertainty in angle of attack; and needs improvement in prediction of the wave drag coefficient.

APPENDIX

SYMBOLS

Measurements and calculations were made in the U.S. Customary Units. They are presented herein in the International System of Units (SI) with the equivalent values given parenthetically in the U.S. Customary Units.

α	angle of attack, deg
c	chord
C_D	drag coefficient
C_L	lift coefficient
C_M	pitching-moment coefficient
C_P	pressure coefficient
K	= 1024
M	Mach number
RE	Reynolds number
T	computer solution time per case
t/c	airfoil thickness-to-chord ratio

REFERENCES

1. Bauer, F., Garabedian, P., Korn, D., and Jameson, A., Supercritical Wing Sections II, A Handbook, Lecture Notes in Economics and Mathematical Systems, Vol. 108, Springer-Verlag, New York, 1975.

2. Bauer, F., Garabedian, P., and Korn, D., Supercritical Wing Sections III, Lecture Notes in Economics and Mathematical Systems, Vol. 150, Springer-Verlag, New York, 1977.

3. Carlson, L. A., "Transonic Airfoil Analysis and Design Using Cartesian Coordinates", Journal of Aircraft, Vol. 13, No. 5, May 1976, pp. 349-356.

4. Carlson, L. A., "TRANDES: A FORTRAN Program for Transonic Airfoil Analysis or Design", NASA CR-2821, June 1977.

5. Smetana, F. O., Summey, D. C., Smith, N. S., and Carden, R. K., "Light Aircraft Lift, Drag, and Moment Prediction - A Review and Analysis", NASA CR-2523, May 1975.

6. Stevens, W. A., Goradia, S. H., and Braden, J. A., "Mathematical Model For Two-Dimensional Multi-Component Airfoils in Viscous Flows", NASA CR-1843, July 1971.

7. Abbott, Ira H., von Doenhoff, Albert E., Theory of Wing Sections, Including A Summary of Airfoil Data, Dover Publications, Inc., New York, 1959.

8. Abbott, Ira H., von Doenhoff, Albert E., and Stivers, Louis S., "Summary of Airfoil Data", NACA TR 824, 1945.

9. Ladson, C. L., and Brooks, C. W., "Development of a Computer Program to Obtain Ordinates for NACA 4-Digit, 4-Digit Modified, 5-Digit, and 16 Series Airfoils", NASA TM X-3284, November 1975.

10. Ladson, C. L., and Brooks, C. W., "Development of a Computer Program to Obtain Ordinates for NACA 6- and 6A-Series Airfoils", NASA TM X-3069, September 1974.

11. McGhee, Robert J., and Beasley, William D., "Effects of Thickness of an Initial Low-Speed Family of Airfoils for General Aviation Applications", NASA TM X-72843, June 1976.

12. McGhee, Robert J., Beasley, William D., and Somers, Dan W., "Low-Speed Aerodynamic Characteristics of a 13-Percent-Thick Airfoil Section Designed for General Aviation Applications", NASA TM X-72697, 1975.

13. Lee, John D., "Evaluation of Interference in the OSU 6 in. by 22 in. Transonic Airfoil Tunnel", Advanced Technology Airfoil Research, Volume I, NASA CP-2045, Pt. 2, 1979. (Paper 34 of this compilation.)

14. Lee, John D., Gregorek, G. M., and Korkan, K. D., "Testing Techniques and Interference Evaluation in the OSU Transonic Airfoil Facility", AIAA Paper No. 78-1118, presented at the 11th AIAA Fluid and Plasma Dynamics Conference, Seattle, Washington, July 10-12, 1978.

TABLE 1. COMPARISON OF FOUR SINGLE ELEMENT AIRFOIL ANALYSIS CODES

COMPUTER CODE	SOLUTION APPROACH	BOUNDARY LAYER CHARACTERISTICS			
		ITERATIVE	LAMINAR	TRANSITION	TURBULENT
Garabedian, et al.	Transonic, finite difference solution of full inviscid potential flow equation for conformally mapped airfoil	Yes	No	Fixed only	Nash-Macdonald
Carlson	Transonic, finite difference solution of full inviscid potential flow equation for airfoil in stretched Cartesian coordinates	Yes	No	Fixed only	Nash-Macdonald
Smetana, et al.	Subcritical, distributed vorticity over an airfoil shape approximated by a closed polygon	Yes	Yes	Natural or fixed	Goradia, and Truckenbrodt
Eppler	Subcritical, distributed vorticity over an airfoil shape approximated by curved panels	No	Yes	Natural only, variable "roughness"	Empirical

TABLE 2. COMPUTER RELATED CHARACTERISTICS OF FOUR SINGLE ELEMENT AIRFOIL ANALYSIS CODES.

COMPUTER CODE	DESIGN MODE	MEMORY* REQUIREMENTS	HARD COPY PLOT CAPABILITY	SOURCE STATEMENTS	PER CASE RUN TIMES
Garabedian, et al.	No**	48,000	Yes	3080	10T-20T
Carlson	Yes	43,000	Printer Plot	2586	10T-36T
Smetana, et al.	No	28,000	Yes	2458	T***
Eppler	Yes	43,000	Yes	2050	0.15T

*All programs are overlaid on GA/ADAC Computer System, requirements listed in words.

**A separate design code by Garabedian, et al., is available (ref. 2).

***Time T is approximately 90-100 seconds on GA/ADAC computer system.

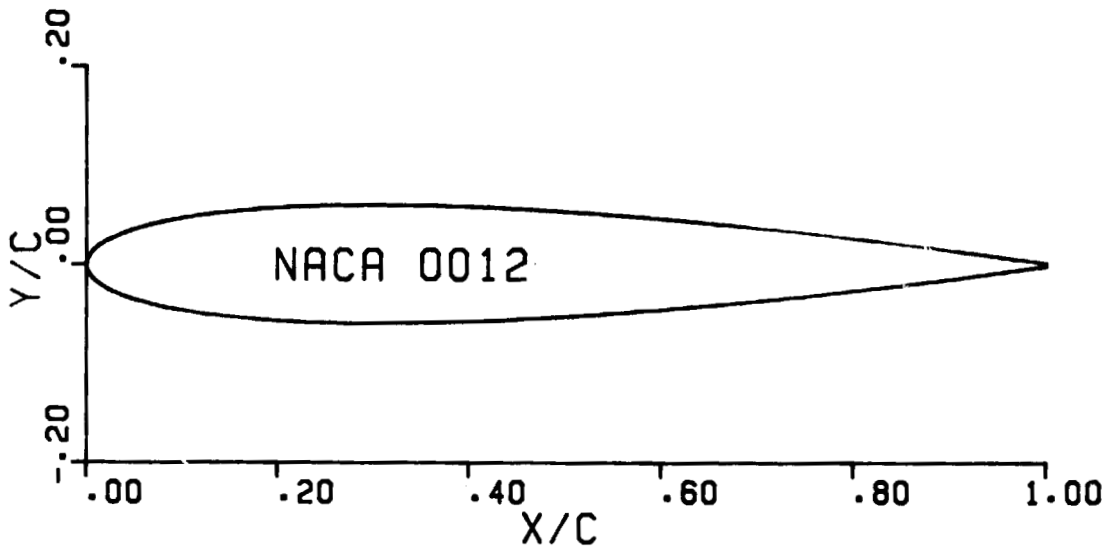

Figure 1.- The NACA 0012 airfoil section.

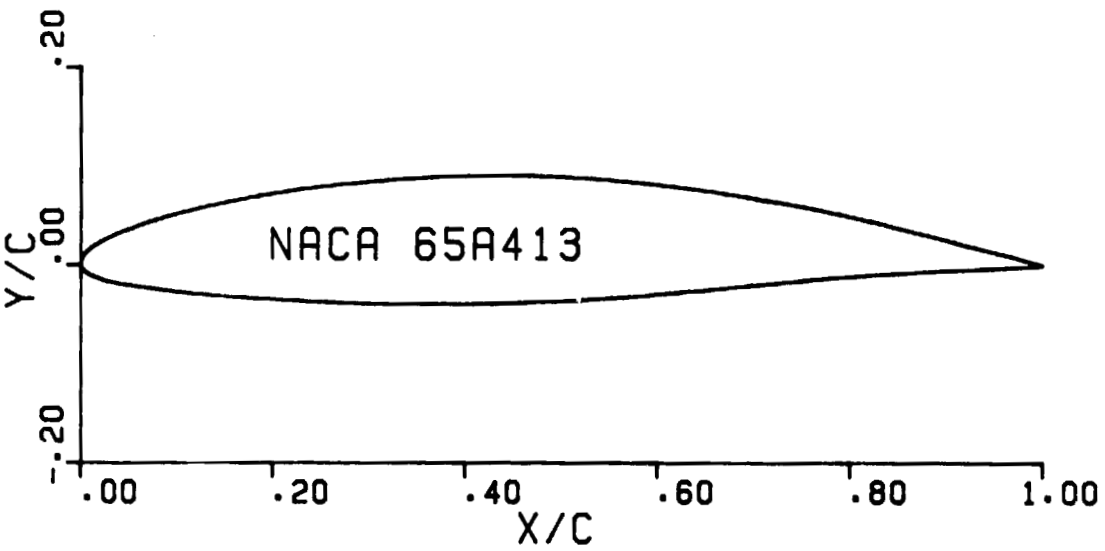

Figure 2.- The NACA 65A413 airfoil section.

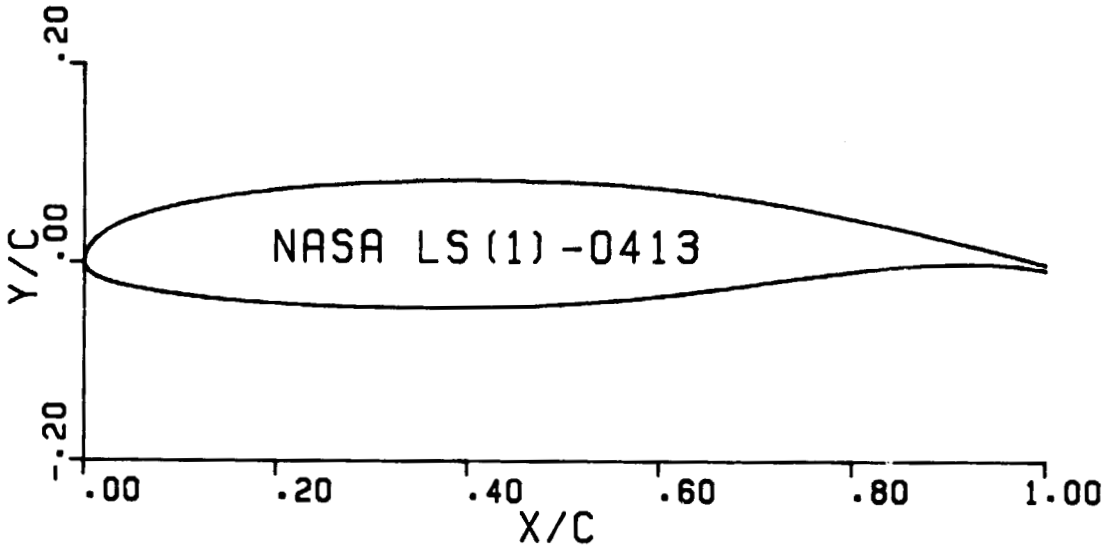

Figure 3.- The NASA LS(1)-0413 airfoil section.

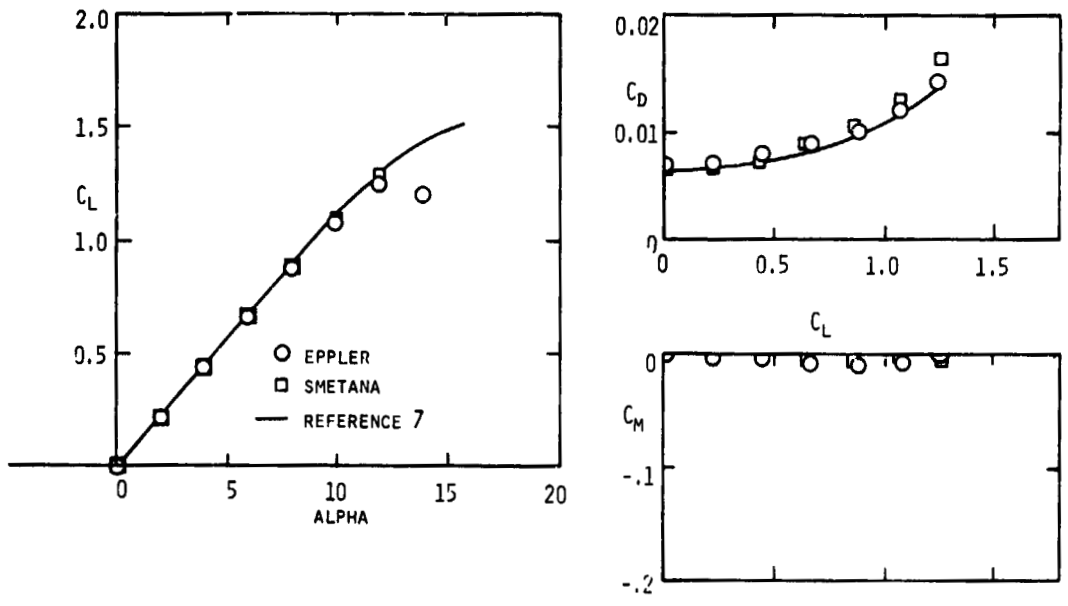

Figure 4.- NACA 0012 airfoil-section characteristics. Computational results are for a Reynolds number of 6 million at a Mach number of 0.20.

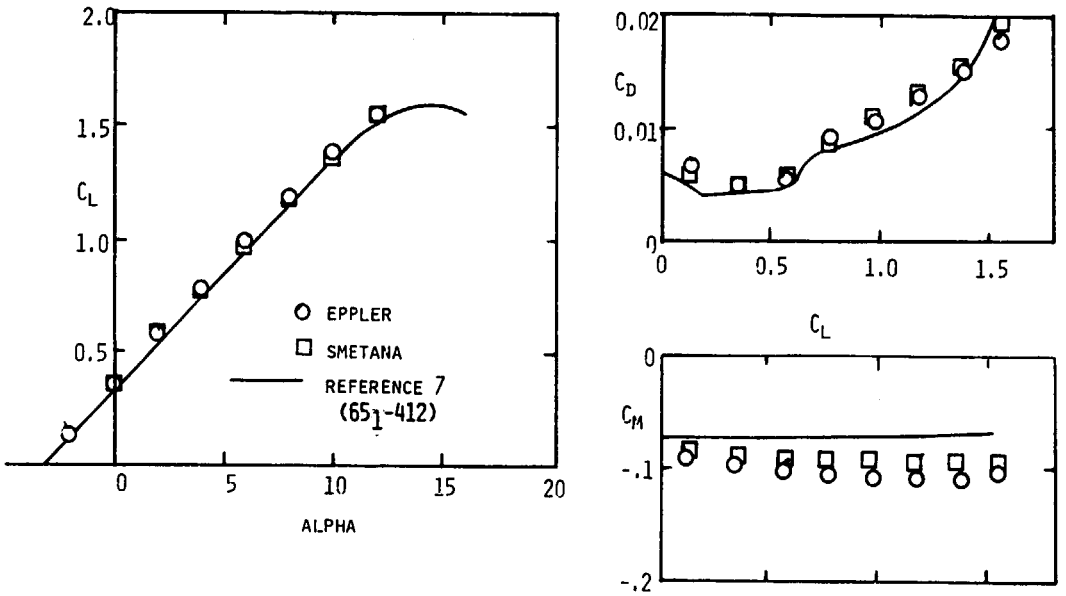

Figure 5.- NACA 65A413 airfoil-section characteristics. Computational results are for a Reynolds number of 6 million at a Mach number of 0.20. Comparison is made to a 65_1-412 airfoil of reference 7.

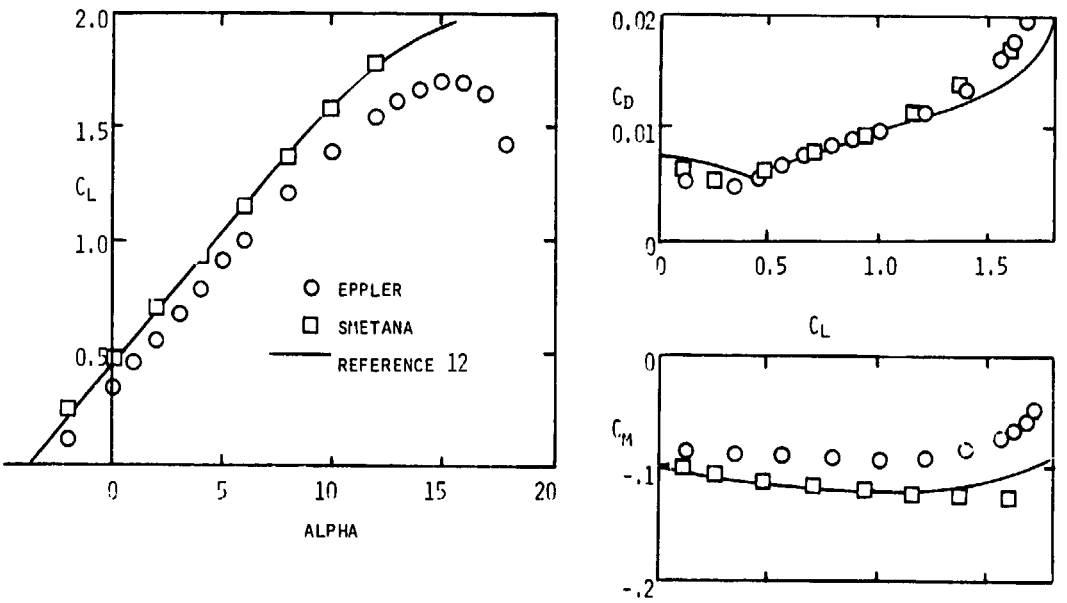

Figure 6.- NASA LS(1)-0413 airfoil-section characteristics. Computational results are for a Reynolds number of 6 million at a Mach number of 0.20.

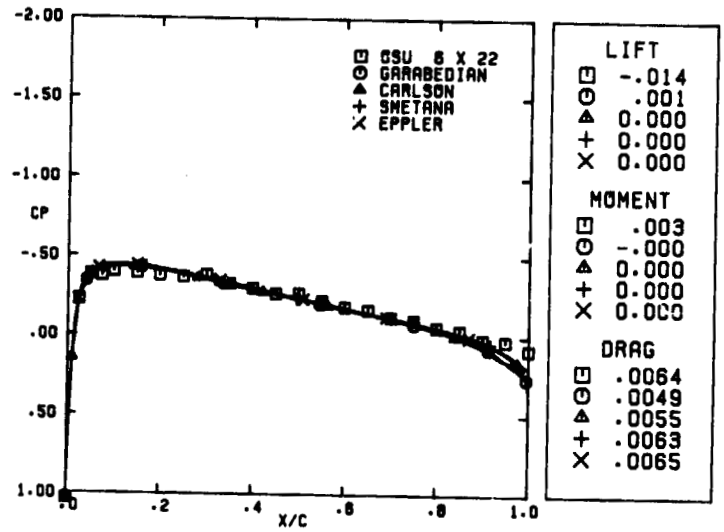

(a) M = 0.351; RE = 3.65 million; $\alpha = 0^{o}$.

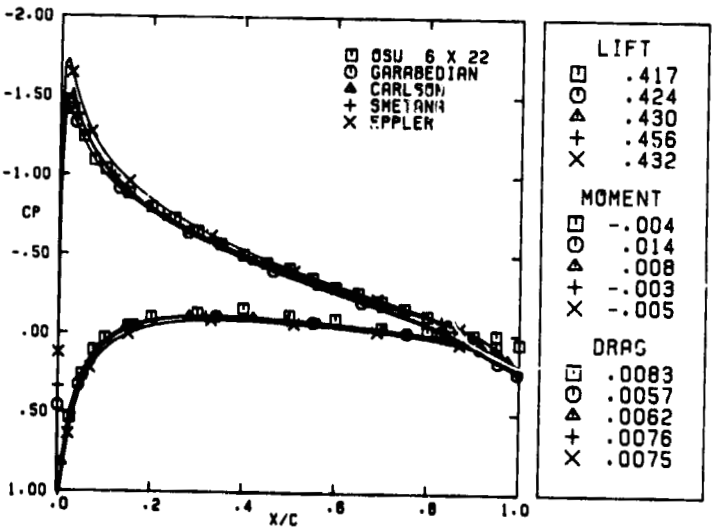

(b) M = 0.345; RE = 3.24 million; $\alpha = 3.93^{o}$.

Figure 7.- Comparison of computer-code predictions with wind-tunnel results for an NACA 0012 airfoil section at a subcritical Mach number over a range of angles of attack.

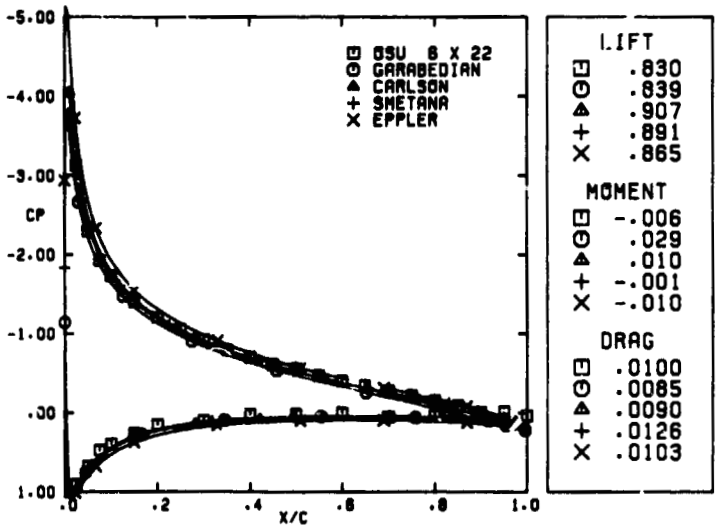

(c) M = 0.342; RE = 3.39 million; $\alpha = 7.88^{o}$.

Figure 7.- Concluded.

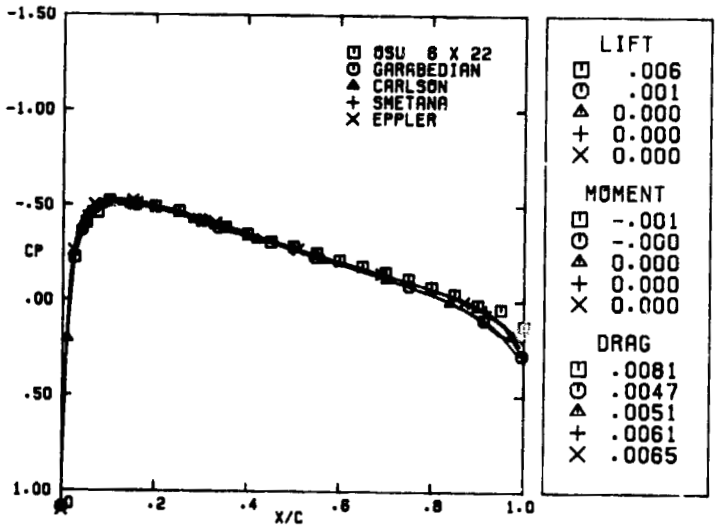

(a) M = 0.575; RE = 4.68 million.

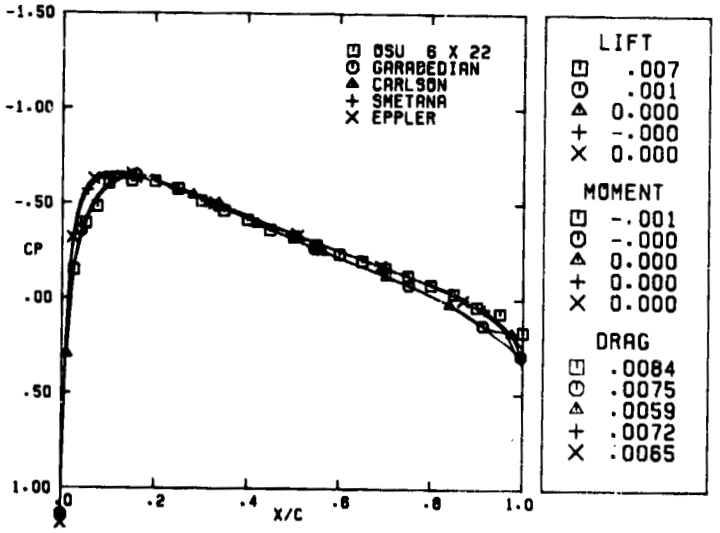

(b) M = 0.725; RE = 5.34 million.

Figure 8.- Comparison of computer-code predictions with wind-tunnel results for an NACA 0012 airfoil section at an angle of attack of zero over a range of Mach numbers.

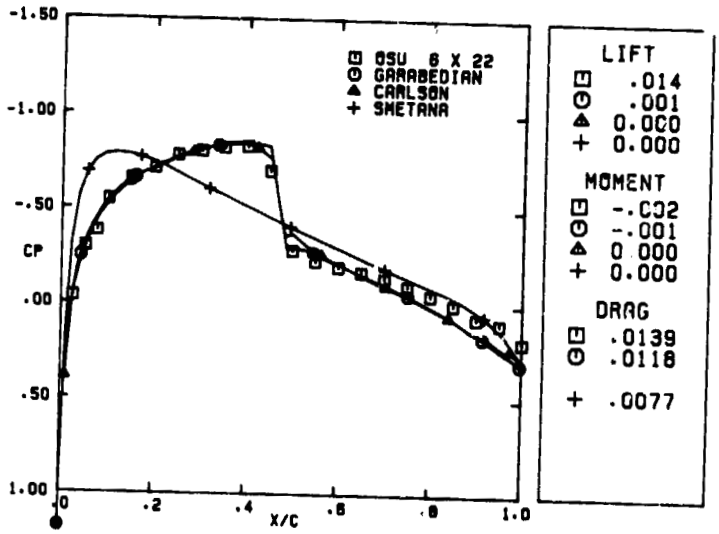

(c) M = 0.808; RE = 6.12 million.

Figure 8.- Concluded.

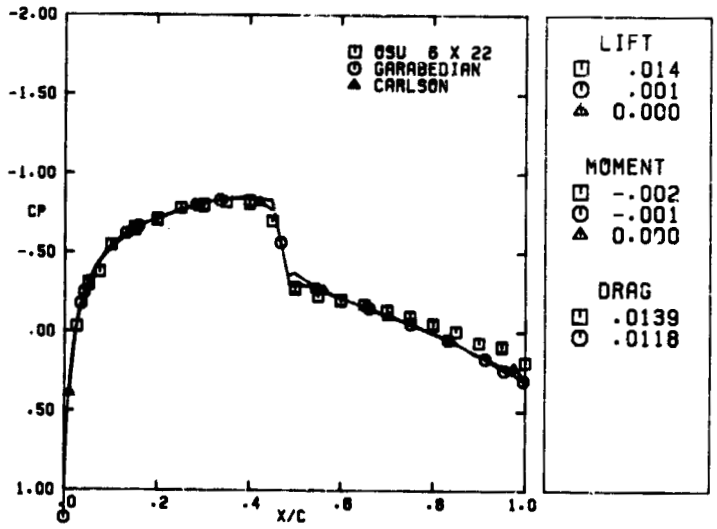

(a) M = 0.808; RE = 6.12 million; $\alpha = 0^{\circ}$.

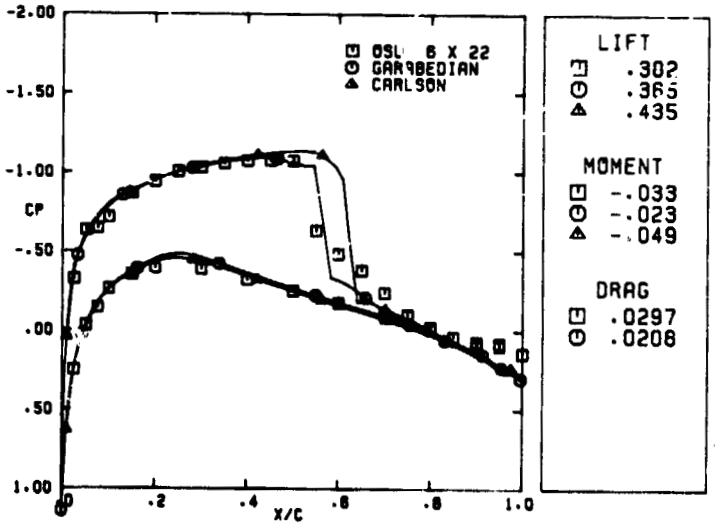

(b) M = 0.804; RE = 5.57 million; $\alpha = 1.94^{\circ}$.

Figure 9.- Comparison of computer-code predictions with wind-tunnel results for an NACA 0012 airfoil section at a supercritical Mach number over a range of angles of attack.

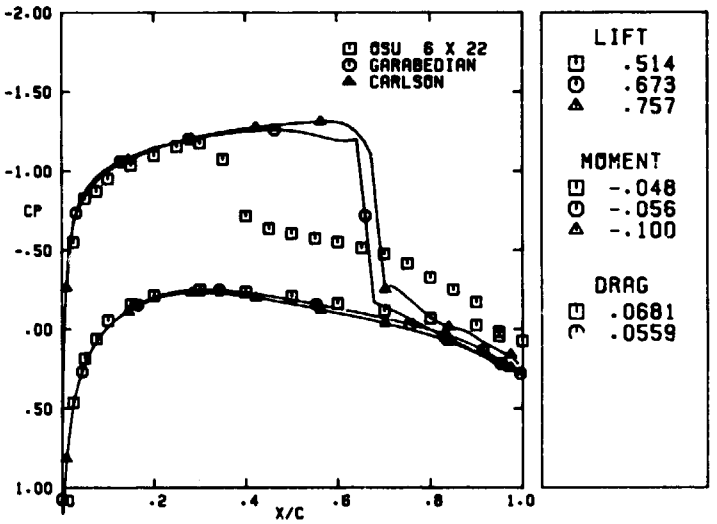

(c) M = 0.803; RE = 6.31 million; $\alpha = 3.92^{\circ}$.

Figure 9.- Concluded.

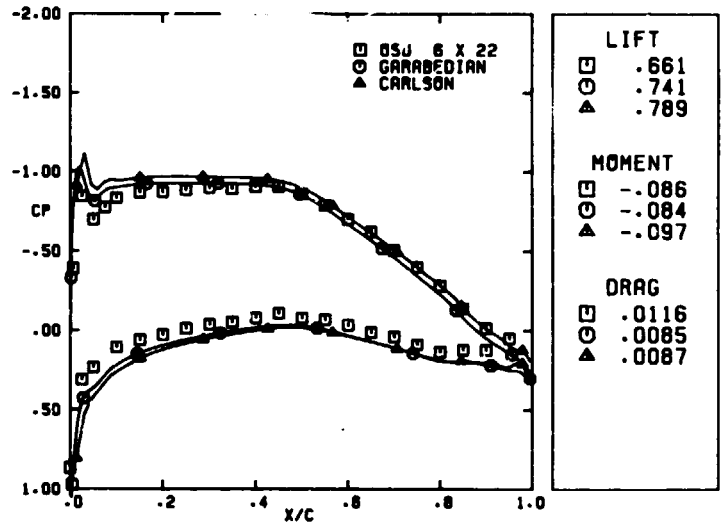

Figure 10.- Comparison of computer-code predictions with wind-tunnel results for an NACA 65A413 airfoil section at M = 0.517, RE = 7.08 million, and $\alpha = 2.90^{\circ}$.

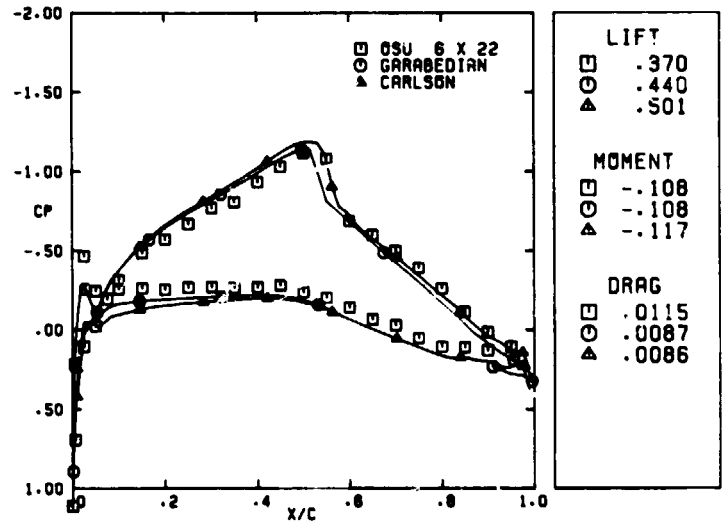

Figure 11.- Comparison of computer-code predictions with wind-tunnel results for an NACA 65A413 airfoil section at M = 0.700, RE = 8.20 million, and $\alpha = -0.06^{\circ}$.

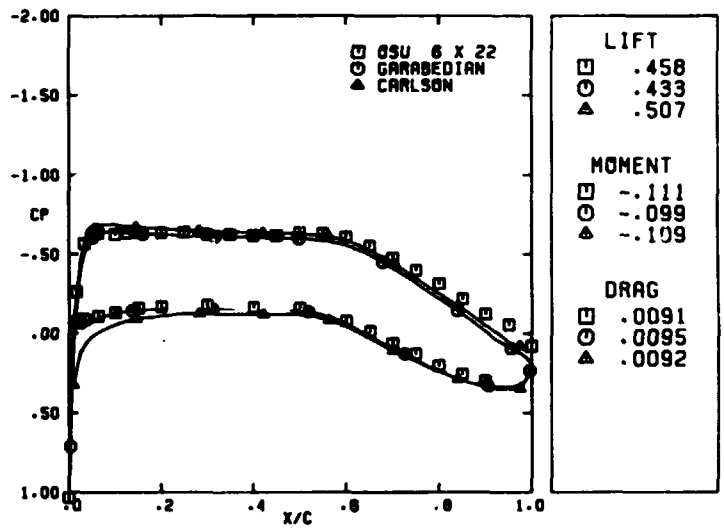

(a) M = 0.454; RE = 3.75 million; $\alpha = -0.07^{\circ}$.

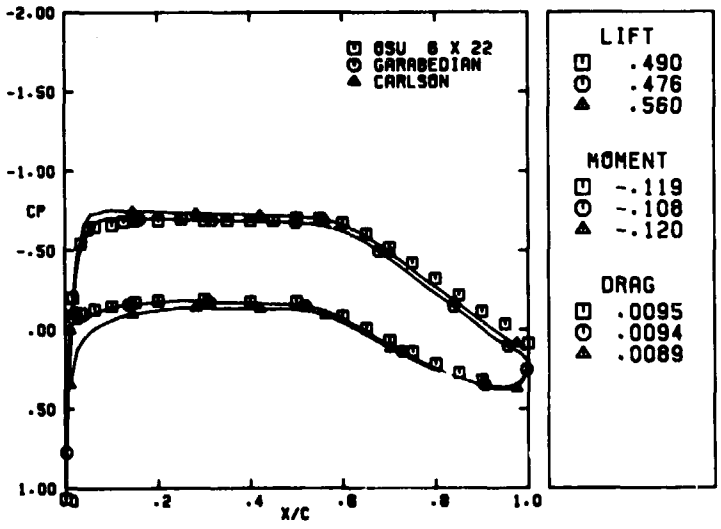

(b) M = 0.578; RE = 4.98 million; $\alpha = -0.07^{\circ}$.

Figure 12.- Comparison of computer-code predictions with wind-tunnel results for an NASA LS(1)-0413 airfoil section at an angle of attack of zero over a range of Mach numbers.

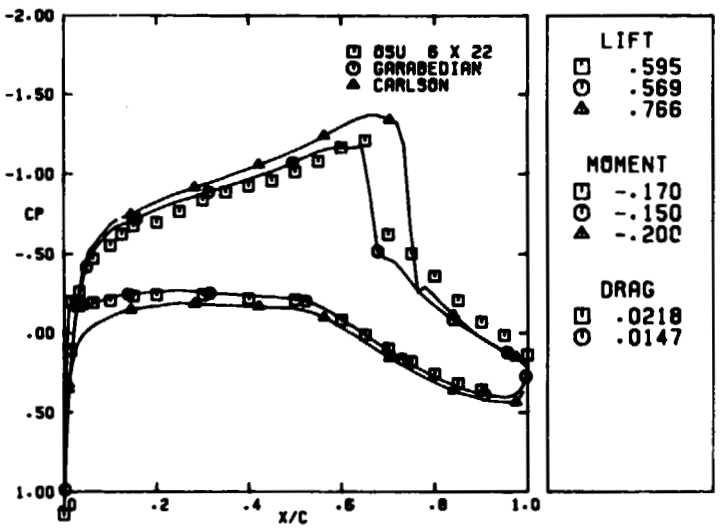

(c) M = 0.755; RE = 5.11 million; $\alpha = -0.06^{\circ}$.

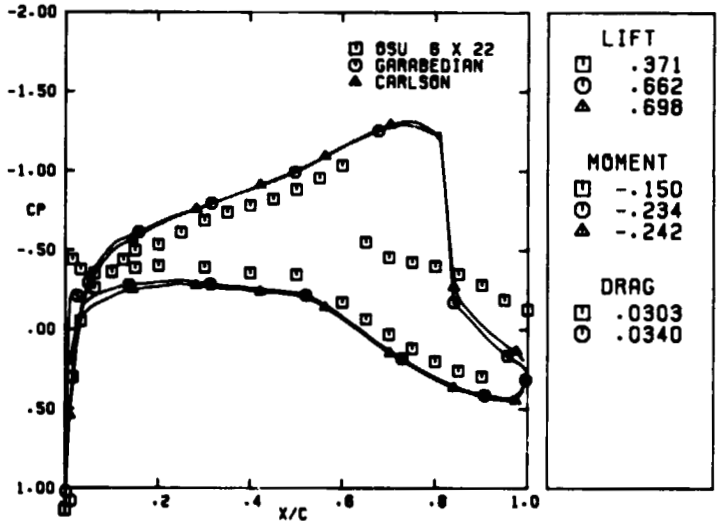

(d) M = 0.802; RE = 5.90 million; $\alpha = -0.06^{\circ}$.

Figure 12.- Concluded.

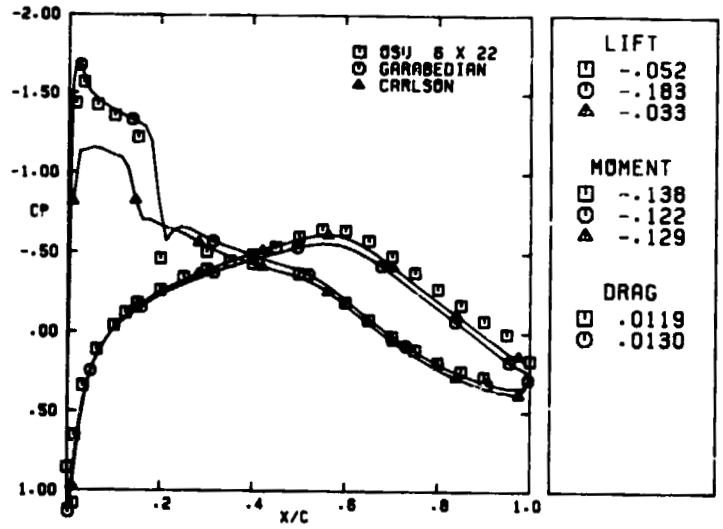

(a) M = 0.722; RE = 4.68 million; $\alpha = -3.99^{\circ}$.

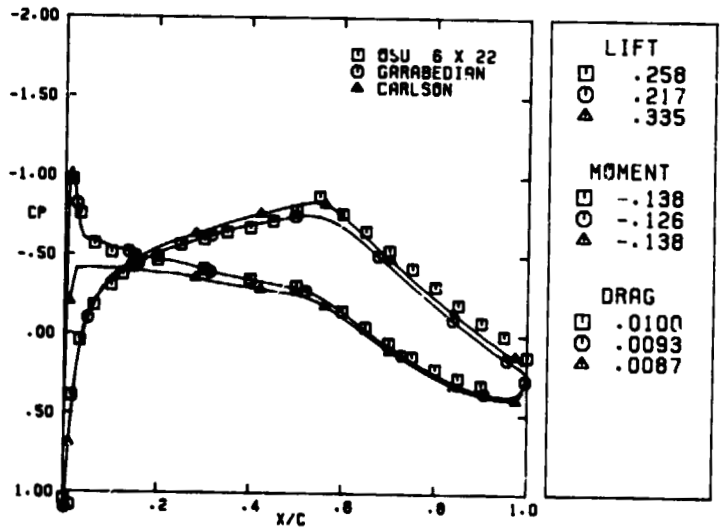

(b) M = 0.721; RE = 6.03 million; $\alpha = -2.04^{\circ}$.

Figure 13.- Comparison of computer-code predictions with wind-tunnel results for an NASA LS(1)-0413 airfoil section at a Mach number of 0.722 over a range of angles of attack.

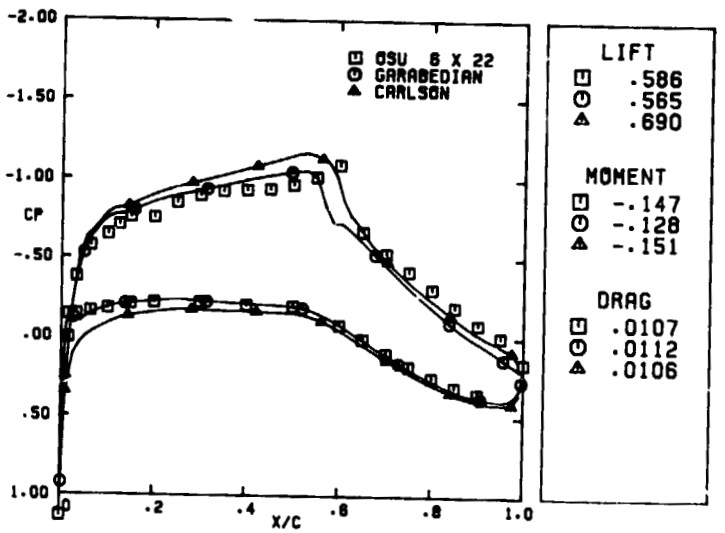

(c) M = 0.722; RE = 4.69 million; $\alpha = -0.09^{c}$

Figure 13.- Concluded.

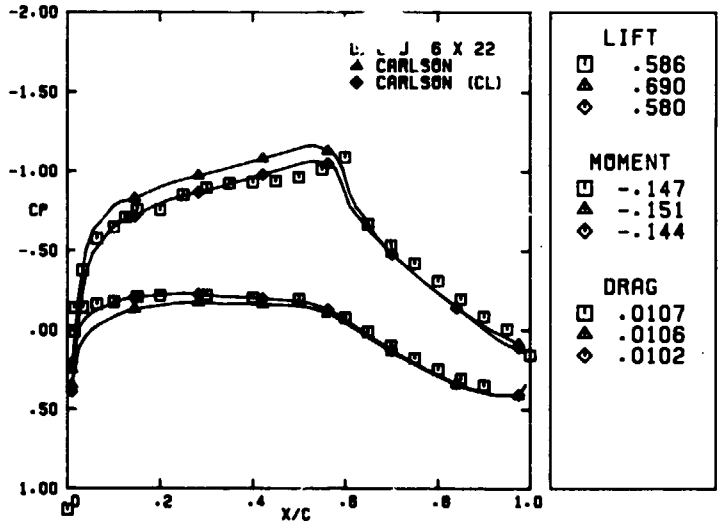

Figure 14.- Comparison of results from the Carlson code obtained by attempting to match lift coefficient to wind-tunnel result. NASA LS(1)-0413 airfoil; M = 0.722; RE = 4.69 million; $\alpha = -0.09^{o}$.

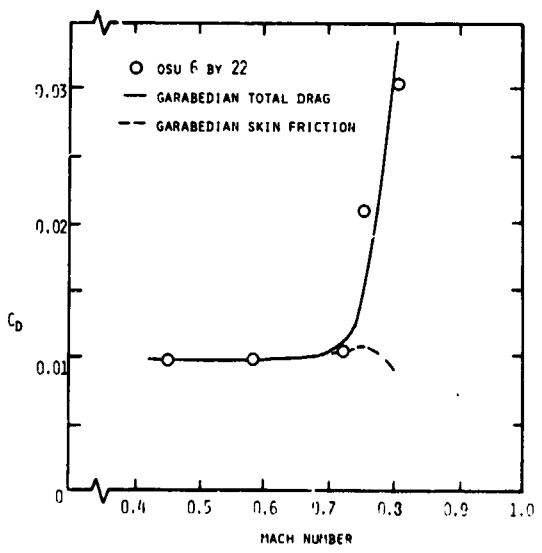

Figure 15.- Comparison of the Garabedian code prediction and wind-tunnel result for the drag-divergence characteristics of the NASA LS(1)-0413 airfoil section at zero angle of attack.

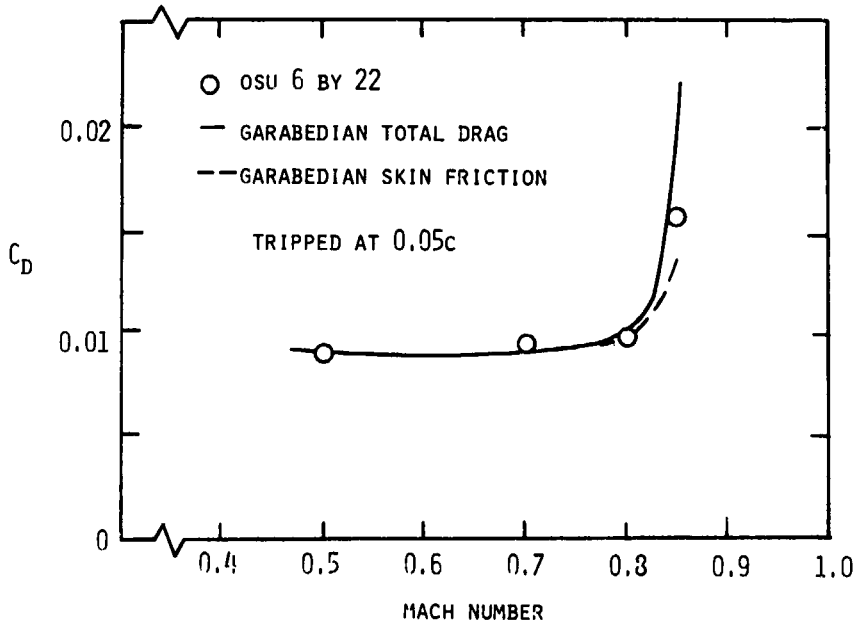

Figure 16.- Comparison of the Garabedian code prediction and wind-tunnel result for the drag-divergence characteristics of the NACA 64A010 airfoil section at zero angle of attack.

10

UPGRADED VISCOUS FLOW ANALYSIS OF MULTIELEMENT AIRFOILS*

Guenter W. Brune and Joseph W. Manke

The Boeing Company

SUMMARY

A description of an improved version of the NASA/Lockheed multielement airfoil analysis computer program is presented. The improvements include several major modifications of the aerodynamic model as well as substantial changes of the computer code. The modifications of the aerodynamic model comprise the representation of the boundary layer and wake displacement effects with an equivalent source distribution, the prediction of wake parameters with Green's lag-entrainment method, the calculation of turbulent boundary layer separation with the method of Nash and Hicks, the estimation of the onset of confluent boundary layer separation with a modified form of Goradia's method, and the prediction of profile drag with the formula of Squire and Young. The paper further describes the modifications of the computer program for which the structured approach to computer software development was employed. Important aspects of the structured program development such as the functional decomposition of the aerodynamic theory and its numerical implementation, the analysis of the data flow within the code, and the application of a pseudo code are discussed.

Computed results of the new program version are compared with recent experimental airfoil data. The comparisons include global airfoil parameters such as lift, pitching moment and drag coefficients, and distributions of surface pressures and boundary layer velocity profiles.

INTRODUCTION

In the past, high lift design and technology rested in the hands of a few experienced aerodynamicists. Design methodology and criteria were heavily influenced by the analytical inviscid flow methods and the experimental data available. With the advent of high-speed computers and the appearance of improved models for turbulent flows, many complex problems, including high-lift design and analysis, were attacked theoretically.

---

* The work reported in this paper was supported partly by NASA-Langley contract NAS1-14522 and partly by the Independent Research and Development Program of The Boeing Company.

One such approach to high-lift, multielement airfoil analysis was developed at Lockheed-Georgia under the sponsorship of the NASA-Langley Research Center (ref. 1). This program was among the first attempts at analyzing the complex viscous flow about slotted airfoils and has received worldwide distribution and usage. A unique feature of this multielement airfoil program is the model of the confluent boundary layer flow (ref. 2).

Over the years, the original version of the program was modified extensively to improve its predictions for different types of high-lift airfoils. Many improvements, mainly in the area of the potential flow calculation, were made by researchers at the Langley Research Center (ref. 3). For this reason, the code is generally referred to as the NASA/Lockheed multielement airfoil program. A version for single element airfoils was recently extracted from the multielement airfoil code by researchers at North Carolina State University (ref. 4).

Widespread and steady usage of the computer program clarified its strengths and weaknesses. Both favorable and unfavorable aspects have been brought to the surface by continued attempts at using the program as an engineering tool. The more serious shortcomings were the lack of agreement between the documentation and the available version of the code and the high failure rate in applying the method for various configurations. However, the program was found to contain sufficient positive features to justify its choice as a starting point for additional theoretical work in the high-lift area.

This paper briefly describes the aerodynamic theory and the corresponding computer program of a new version of the multielement airfoil program; a detailed description can be found in references 5 and 6. Symbols are defined in an appendix.

MULTIELEMENT AIRFOILS

The flow around high-lift airfoils is characterized by many different inviscid and viscous flow regions. Their complex physics is illustrated by figure 1. In particular, the existence of confluent boundary layers and the regions of separated flow distinguish the high-lift airfoil problem from the aerodynamic problem of airfoils at cruise conditions. The various flow regions, including the outer potential flow, the ordinary laminar and turbulent boundary layers, viscous wakes, and the confluent boundary layer, are analyzed by the code. Furthermore, the prediction of transition from laminar to turbulent boundary layer flow and the prediction of the onset of boundary layer separation are a necessary part of the code. Cove separation and large scale separation phenomena, however, are not modeled.

PROGRAM MODIFICATIONS

The new program version differs from the baseline version (ref. 3) in the following areas:

1) The method used to represent the effect of the viscous flow on the outer potential flow, termed equivalent airfoil representation in the baseline version of the program, has been modified. It has been replaced by the surface transpiration method which uses a distribution of sources along airfoil surfaces and wake centerlines to model boundary layer and wake displacement effects.

2) The flow model of the potential core region has been changed. The new method performs independent boundary layer and wake calculations. These calculations utilize the ordinary laminar and turbulent boundary layer routines of the baseline version of the code, and in addition, the lag-entrainment method of reference 7 for wake flows. The revised flow model of the core region calculates the location of the wake centerlines.

3) An attempt is made to predict the onset of separation of the confluent boundary layer by a modified version of Goradia's confluent boundary layer method. In this method, the power law velocity profile of the wall layer is replaced by Coles' two-parameter velocity profile (ref. 8).

4) The drag prediction method of Squire and Young (ref. 9) has been incorporated into the program, replacing the previous pressure and skin friction integration scheme.

5) The original method used for the prediction of separation for ordinary turbulent boundary layer flow has been replaced by the Boeing version of the method of Nash and Hicks (ref. 10).

6) The modifications of the aerodynamic theory required a major overhaul of the computer code. Most parts of the code have been rewritten using a systematic approach to computer software design. This work was guided by a functional decomposition of the many aspects of the aerodynamic model and its numerical implementation. In addition, a detailed study was made of the data flow within the program, and the logic of the code was outlined prior to the actual program development using a pseudo code. The most important aspects of this work are briefly reviewed in this paper.

AERODYNAMIC FLOW MODELS

The aerodynamic theory of the new version of the computer program is outlined below with emphasis on modifications. The aerodynamic analysis and its numerical implementation assume two-dimensional, subsonic flow in which all boundary layers are attached to the airfoil surface.

Potential Flow

Inviscid, irrotational flow is calculated using the stream function approach of Oeller (ref. 11). Laplace's equation is solved subject to the boundary condition of a constant value of the stream function on airfoil surfaces. The meth-

od is of the panel type, see figure 2, with a constant strength vortex distribution on each panel of the airfoil surface. A formulation of the Kutta condition is imposed which requires the tangential velocities at the upper and lower surface trailing edge points to be equal. Compressibility effects are taken into account by employing the Karman-Tsien rule.

Viscous Flow Representation

Oeller's stream function method has been modified in order to account for displacement effects of boundary layers and wakes within the potential flow solution. An equivalent distribution of sources simulating the viscous flow displacement thickness is placed on the surface and wake centerline of an airfoil component. This is the surface transpiration method which, within the framework of thin boundary layer theory, is completely equivalent to the method of geometrically adding the displacement thickness to the basic airfoil geometry. Application of this technique is computationally efficient, since most of the aerodynamic influence coefficients do not change during the solution procedure.

The strength σ of the equivalent source distribution is obtained from

$$\sigma = \frac{d}{ds} (\delta^* U)$$

where δ^* denotes the displacement thickness of either boundary layer or wake, and the symbol U stands for the inviscid flow velocity on airfoil surface and wake centerline. The variable s represents arc length. The computed source distribution is discretized using panels with constant source strength on the surface and wake centerline of each airfoil component.

It should be emphasized that the employed flow model does not account for wake curvature effects. Consequently, constant strength vortex panels are only used on the surface of an airfoil and not on its wake centerline, see figure 2.

Wake Centerline

The capability of computing the position of wake centerlines has been added to the program as part of the revision of the flow model in the core region, see figure 1. A wake centerline is part of the stagnation streamline.

Since the potential flow problem is solved on the basis of a stream function approach, which in addition to the surface velocity provides the value of the stream function for each stagnation streamline, it is convenient to also use the stream function formulation to trace wake centerlines. This is done in an iterative procedure beginning with an assumed initial position of a wake centerline. During each step of this iteration the locations of all panels of the wake centerline are updated simultaneously by solving a linearized form of the following stream function equation:

$$\psi_m = \psi\ (\vec{x})$$

Here, ψ_m denotes the known value of the stream function at a stagnation streamline. The variable $\vec{x}$ represents the array of unknown panel corner point coordinates of the wake centerline.

Laminar Boundary Layer

Laminar boundary layer characteristics are calculated with the compressible method of Cohen and Reshotko (ref. 12) who reduced the problem to simple quadrature. Application of a compressible method seems to be necessary for slotted high-lift airfoils, since laminar boundary layers often exist in the slot between neighboring airfoil components, where even at low free stream Mach numbers the flow is highly compressible with velocities approaching and frequently exceeding sonic conditions.

Laminar separation is predicted with the criterion of Goradia and Lyman (ref. 13) which is an empirical correlation of the local values of the Mach number gradient with the momentum thickness Reynolds number. Either laminar stall or the occurrence of laminar short bubble separation is predicted. In the case of laminar short bubbles, subsequent turbulent reattachment of the separated laminar boundary layer is assumed, but neither the length of the separation bubble nor the details of the flow within the bubble are modeled.

The computer program provides two options for transition from laminar to turbulent boundary layer flow. The user can either specify fixed transition points, such as the location of trip strips, or can compute free transition. In the latter case, a standard two-step approach is employed.

Turbulent Boundary Layer

Two different integral methods determine the characteristics of ordinary turbulent boundary layers. The method of Truckenbrodt (ref. 14) is used during the iterative solution procedure. It is an incompressible approach based on the momentum and energy integral equations. Goradia (ref. 1) introduced the idea of constraining the shape factor H, defined as the ratio of energy dissipation thickness to momentum thickness, in order to avoid premature separation of the turbulent boundary layer during the first cycles of the iteration. This approach avoids failures of the boundary layer integration at separation and can be viewed as an artificial way of modeling separated flows. The integral method of Nash and Hicks (ref. 10), which accounts for the history of turbulent shear stresses, is applied at the end of the iterative solution procedure for the purpose of computing boundary layer separation. Displacement thickness and skin friction obtained from the method of Nash and Hicks are not utilized.

Wake Flow

The properties of turbulent wakes are analyzed with the lag-entrainment method of reference 7. The method is formulated in terms of the momentum integral equation, the entrainment equation, and an empirical equation for the streamwise rate of change of the entrainment coefficient. The entrainment equation is derived from the definition of the entrainment coefficient, which represents the change of mass flow within the wake layer. An incompressible version of Green's treatment of wake flow is used, neglecting the effects of curvature on the mean flow and the turbulence structure of the wake.

Confluent Boundary Layer

The program computes confluent boundary layers with the model of Goradia (ref. 2). In this model, the confluent boundary layer downstream of the core region is divided into two regions. In the first region, turbulent mixing of wake and boundary layer is incomplete. The mean velocity profile clearly shows the remainder of the wake profile, see figure 3. In the second region, the effect of the wake is not visible in the mean velocity profile which is similar to that of a wall jet. Downstream of the second region, the confluent boundary layer degenerates into an ordinary turbulent boundary layer.

Goradia formulated an integral method by subdividing the confluent boundary layer into several layers and assuming the validity of boundary layer equations and self-similarity of the mean velocity profile in each of these layers. The method is incompressible, neglects curvature effects, and relies to a large extent on empirical information about shear stress, the rate of growth of various layers, and velocity profiles. Furthermore, the model ignores multiple wakes and multiple potential cores that might exist near the trailing edge of a high-lift airfoil consisting of more than two components. The shape factor H of the layer adjacent to the airfoil surface, termed the wall layer, is constrained in order to avoid program failures in regions of separated flow. For this reason, Goradia's confluent boundary layer method is applied during the iteration procedure, when unrealistic potential flow pressure distributions can cause premature boundary layer separation.

The described flow model has been modified to predict separation of confluent boundary layers. The power law velocity profile of the wall layer has been replaced by Coles' two-parameter profile (ref. 8), which is known to provide a realistic representation of ordinary turbulent boundary layers near separation. The shape factor of the wall layer is not constrained in this modification, but most other features of Goradia's confluent boundary layer model including its empirical content are retained.

Iterative Solution Procedure

The solution is iterative, since most of the individual flow problems and their

coupling are nonlinear. The computer program uses a conventional cyclic iteration procedure in which each cycle consists of the following steps:

Step 1: A potential flow solution for the multielement airfoil is calculated. During the first cycle of the iteration, the calculation is performed without any representation of viscous flow displacement effects.

Step 2: The positions of the wake centerlines are computed.

Step 3: Solutions of all viscous flow problems including laminar and turbulent boundary layers, confluent boundary layers, and viscous wakes are calculated with the potential flow velocities and wake centerline locations obtained in the previous steps as input data. At the end of this computational step, the displacement thicknesses of all boundary layers and wakes are available.

Step 4: A source distribution representing the displacement effect of all viscous layers is computed.

The computer program does not rely on a convergence criterion. Instead, five iteration cycles are always executed and the user of the program must judge the quality of the solution.

In order to assist the iteration scheme in arriving at a converged solution, the source strength σ computed in Step 4 of each cycle is modified by adding 2/3 of σ computed in this iteration cycle to 1/3 of σ computed in the previous iteration cycle.

Forces and Moments

At the end of each iteration cycle, airfoil lift and pitching moment coefficients are computed by an integration of surface pressure and skin friction. Profile drag is obtained by applying the formula of Squire and Young (ref. 9). The total profile drag of a multielement airfoil is assumed to be the sum of the contributions of its components. The drag of each airfoil component in turn is calculated from the values of boundary layer momentum thickness and surface velocity at the component trailing edge.

COMPUTER CODE

The new version of the code is written in the CDC FORTRAN extended 4 (FTN4) language and will run under the CDC Network Operating System (NOS). The CDC overlay system is used to assure that the code will execute in a field length less than 100 K octal.

The programming methodologies used to design and develop the new version of the computer code include a functional decomposition of the aerodynamic theory, a

data flow analysis, and a control flow analysis.

Each of these related design tasks was performed several times in an iterative manner to produce a final design for the new version of the computer code before changes or improvements to the baseline code were made. The final design resulted in major changes of the baseline version of the program in the following sections: upper level control routines, geometry preprocessing routines, and the potential flow solution routines. The final design was also used to integrate the new aerodynamic models into the baseline code. Table 1 lists all subroutines in the baseline version of the code and indicates the type of changes made to incorporate them in the new version.

The functional decomposition of the code was based on the engineering specification of the aerodynamic models and the numerical techniques necessary for their solution. Figure 4 shows the upper level decomposition chart where the major functions are defined in engineering terms. The complex physics of the flow about multielement airfoils is reflected in these charts.

The data flow analysis of the code was done for each module identified in the functional decomposition by specifying the input and output data for the module as well as its own decomposition. Control of the data flow within a module is maintained by requiring that the input to any of its submodules must be either an input to the module or the output of another of its submodules.

The control flow analysis of the new code was done with the aid of a pseudo code, which is a small set of simple logic and loop statements which suffice to describe the control within a module of the functional decomposition. Although the submodules of a module can be used in any sequence and any number of times to complete the function of the module, it is an aim of the design process to keep the control within a module as simple as possible. All new subroutines in the code include as comment cards the pseudo code for the module which they implement.

TEST-THEORY COMPARISONS

In the following comparison of theoretical and experimental airfoil data, three versions of the NASA/Lockheed multielement airfoil program are referred to:

Version A: This is the baseline version of the computer program with minor modifications. The baseline version was available from the NASA in June 1976.

Version B: This version, described in reference 15, differs from version A in two areas. Profile drag is predicted by the Squire and Young formula. Separation of ordinary turbulent boundary layers is calculated using the method of Nash and Hicks.

Version C: This is the version of the program described in this paper.

A large number of airfoil configurations were analyzed using the program versions listed above. Only a few results of this program evaluation, concerning the GA(W)-1 airfoil and a Boeing multielement high-lift airfoil (figure 5), are discussed in this paper. A detailed report of this evaluation is contained in reference 6.

GA(W)-1 Airfoil

This airfoil was chosen to test the program capability of predicting performance characteristics of single airfoils. Figure 6 contains the theoretical lift, pitching moment, and drag curves and their comparison with experimental data of McGhee and Beasley (ref. 16). Both Version A and the new program Version C predict identical lift and moment curves that in turn agree well with measured GA(W)-1 data up to the onset of trailing edge stall at about 8 degrees angle of attack. Trailing edge stall is not modeled by any of the program versions.

Considerable differences between all drag polars are shown in figure 6. Version A, utilizing an integration of surface pressure and skin friction in the prediction of profile drag, gives the highest drag coefficients. Version C, applying the Squire and Young formula, offers drag values that are lower than the corresponding experimental drag coefficients. The lack of agreement of the three drag polars emphasizes the fact that even for single airfoils at low speed the problem of obtaining accurate drag computations is not yet solved.

Surface pressures of the GA(W)-1 at 8 degrees angle of attack, computed by program Version C and plotted in figure 7, agree well with their experimental counterparts. In this figure, the symbols S and LS refer to theoretical points of turbulent separation and laminar short bubbles, respectively. The symbol FT indicates the experimental trip strip location which is specified as a fixed transition point in the computer simulation. A laminar short bubble with subsequent turbulent reattachment of the boundary layer is indicated near the upper surface leading edge, and turbulent boundary layer separation is predicted theoretically near the upper surface trailing edge. The latter prediction is confirmed by the experimental pressure distribution which shows a constant pressure downstream of the theoretical point of separation.

Boeing High-Lift Airfoil

The Boeing four-element high-lift airfoil was used as the main test case for multiple airfoils. It consists of a wing section with a leading edge flap and a double-slotted trailing edge flap. Global airfoil parameters and detailed distributions of surface pressures and boundary layer data are available for comparisons. The data were obtained in the Boeing Research Wind Tunnel (BRWT) on a model with a 2 foot unextended wing chord and a 5 foot span. Careful blowing of the wall boundary layers was applied in order to closely approximate a two-dimensional flow pattern across the whole span of the airfoil.

The lift curve, pitching moment, and drag polar of this airfoil at a Reynolds number of two million, based on the wing reference chord, are given in figure 8. The experimental lift coefficients are balance data that are within 1.5% of the lift obtained by pressure integration. The profile drag of the airfoil is the result of wake rake measurements taken at a fixed spanwise position relatively free from interference effects of flap supporting brackets and pressures taps. The maximum spanwise variation of the measured airfoil drag is indicated in figure 8.

All attempts failed when using program Version A to obtain a converged solution for this airfoil. Program Version B arrived at converged solutions between 8 and 20 degrees angle of attack, but underpredicted the lift by a considerable amount. The theoretical predictions of program Version C match the experimental lift coefficients well at angles of attack below the onset of trailing edge stall, which is theoretically predicted by the program to take place at about 16 degrees.

The theoretical values of the profile drag of Version C are relatively close to the measured profile drag. In judging the quality of this drag comparison, the reader should recall the problems of two-dimensional high-lift testing and the uncertainties in applying the Squire and Young formula to multielement airfoils.

Figure 9 contains comparisons of theoretical and experimental surface pressures of wing and main flap at 8.4 degrees angle of attack. This figure confirms the earlier finding that Version C indeed provides the best theoretical results. Differences between the theory of Version C and experiment are noted in cove regions and on the upper surface of the wing near the leading edge. The latter problem is due to the failure of the program to accurately simulate the flow on the lower surface of the leading edge device.

Figure 10 shows boundary layer velocity profiles at several chordwise stations on the upper wing surface. The experimental velocity profiles reveal that very little confluence of the wake behind the leading edge device and the wing boundary layer has taken place and that an initially existing weak confluent boundary layer above the wing has degenerated early into an ordinary turbulent boundary layer. This feature of the flow field is very well simulated by Version C, but not by Versions A and B.

CONCLUSIONS

The following conclusions about the reliability and quality of the predictions of the new program are drawn:

1) The reliability of the program executions has been greatly improved. All test cases have produced converged solutions within a few iteration cycles. This improvement is a consequence of the application of the structured approach to computer programming where much attention was paid to the functional decomposition of the aerodynamic model, its numerical implementation, and the data flow within the code.

2) The accuracy of the program predictions has been improved. This is due to several major modifications of the aerodynamic model - above all, due to the different representation of the viscous flow displacement effects and the improved model of the potential core region.

3) The computed results are consistent with the basic assumptions of the aerodynamic model. Best results are obtained in cases where most of the flow is attached to the airfoil's surface, but the quality of the predictions gradually deteriorates with increasing trailing edge stall and cove separation.

4) The usefulness of the confluent boundary layer method of Goradia and its modification developed for the purpose of predicting confluent boundary layer separation have not yet been tested. Configurations were chosen for most of the program evaluation with little confluence of wakes and boundary layers.

5) The performance of the program needs to be tested for configurations at off optimum shape design.

6) The evaluation of the computer program was hampered by the shortage of reliable experimental high-lift data. Additional wind tunnel testing of some of the more important high-lift airfoil configurations will increase confidence in their predicted performance.

APPENDIX

SYMBOLS

C	airfoil reference chord
C_d	drag coefficient
C_ℓ	lift coefficient
C_m	pitching moment coefficient about the quarter chord point
C_p	surface pressure coefficient
$\tilde{H}$	ratio of energy dissipation thickness and momentum thickness
M_∞	free stream Mach number
R_N	Reynolds number formed by free stream velocity and airfoil reference chord
s	arc length
U	inviscid surface velocity or wake centerline velocity
U_∞	free stream velocity
u	boundary layer velocity parallel to airfoil surface
X	x - coordinate of global axis system
$\vec{x}$	array of panel corner points
Y	coordinate normal to airfoil surface
α	angle of attack
δ^*	displacement thickness
σ	source strength
ψ	stream function
ψ_m	stream function value at a stagnation streamline

Abbreviations

FT	fixed transition
LS	laminar short bubble
S	separation

REFERENCES

1. Stevens, W. A.; Goradia, S. H.; and Braden, J. A.: Mathematical Model for Two-Dimensional Multi-Component Airfoils in Viscous Flow. NASA CR-1843, July 1971.

2. Goradia, S. H.: Confluent Boundary Layer Flow Development with Arbitrary Pressure Distribution, Ph.D Thesis, Georgia Institute of Technology, August 1971.

3. Morgan, H. L., Jr.: A Computer Program for the Analysis of Multi-Element Airfoils in Two-Dimensional Subsonic, Viscous Flow, Aerodynamic Analyses Requiring Advanced Computers, Conference, Langley Research Center in Hampton, Virginia, March 1975.

4. Smetana, F. O.; Summey, D. C.; Smith, N. S.; and Carden, R. K.: Light Aircraft Lift, Drag, and Moment Prediction - A Review and Analysis. NASA CR-2523, May 1975.

5. Brune, G. W. and Manke, J. W.: An Improved Version of the NASA/Lockheed Multi-Element Airfoil Analysis Computer Program. NASA CR-145323, March 1978.

6. Brune, G. W.; and Manke, J. W.: A Critical Evaluation of the Predictions of the NASA/Lockheed Multi-Element Airfoil Computer Program. NASA CR-145322, March 1978.

7. Green, J. E.; Weeks, D. J.; and Brooman, J. W. F.: Predictions of Turbulent Boundary Layers and Wakes in Compressible Flow by a Lag-Entrainment Method. RAE TR 72231, January 1973.

8. Coles, D. E.: The Law of the Wake in the Turbulent Boundary Layer, J. of Fluid Mech., Vol. 1, pp. 191-226, 1956.

9. Squire, H. B.; and Young, B. A.: The Calculation of the Profile Drag of Airfoils. RAE-Report R. & M. No. 1838, November 1937.

10. Nash, J. F.; and Hicks, S. G.: An Integral Method Including the Effects of Upstream History on the Turbulent Shear Stress, Computation of Turbulent Boundary Layers - 1968, AFOSR-IFP-Stanford Conference, August 1968.

11. Oeller, H. J.: Die inkompressible Potentialströmung in der ebenen Gitterstufe (Incompressible Potential Flow in Two-Dimensional Cascades), Wissenschaftliche Gesellschaft für Luft-und Raumfahrt E. V., pp. 349-353, Jahrbuch 1962, (In German, not translated).

12. Cohen, C. B.; and Reshotko, E.: The Compressible Laminar Boundary Layer with Heat Transfer and Arbitrary Pressure Gradient, NACA Rep. 1294, 1956.

13. Goradia, S. H.; and Lyman, V.: Laminar Stall Prediction and Estimation of $c_{\ell_{max}}$, Journal of Aircraft, Vol. 11, No. 9, September 1974.

14. Truckenbrodt, E.: Ein Quadraturverfahren zur Berechnung der laminaren and turbulenten Reibungsschicht bei ebener und rotationssymmetrischer Strömung, Ing. Arch., Vol. 20, pp. 221-228, 1952 (NASA TM-1379, 1955).

15. Brune, G. W.; Hahn, M.; Mark, J. L.; and Manke, J. W.: Modification and Clarification of the NASA/Lockheed Multielement Airfoil Computer Program, Boeing-Document D6-45072, February 1977.

16. McGhee, R. J.; and Beasley, W. D.: Low Speed Aerodynamic Characteristics of a 17-Percent Thick Airfoil Section Designed for General Aviation Applications, NASA TN D-7428, 1973.

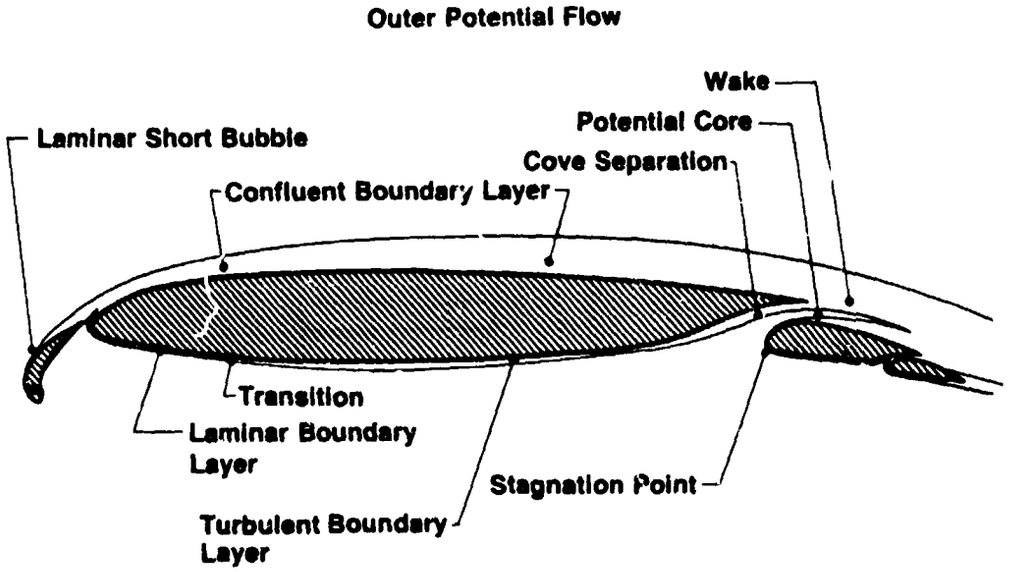

Figure 1.- Flow regions of multielement airfoils.

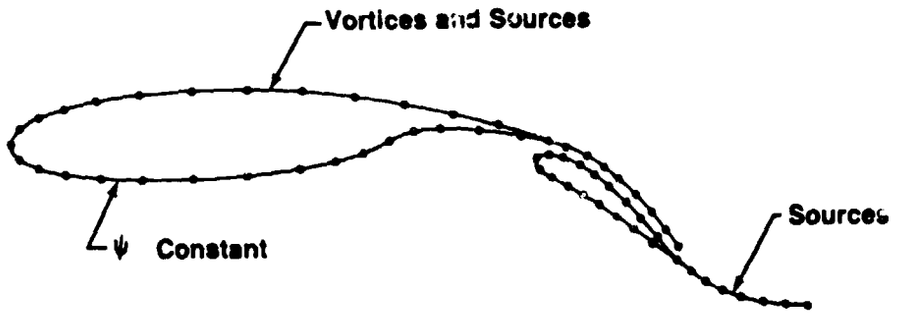

Figure 2.- Potential-flow singularities.

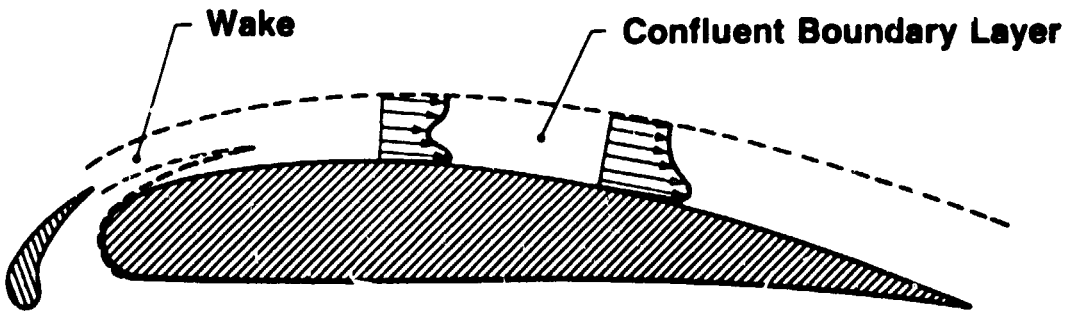

Figure 3.- Mean velocity profiles of confluent boundary layer.

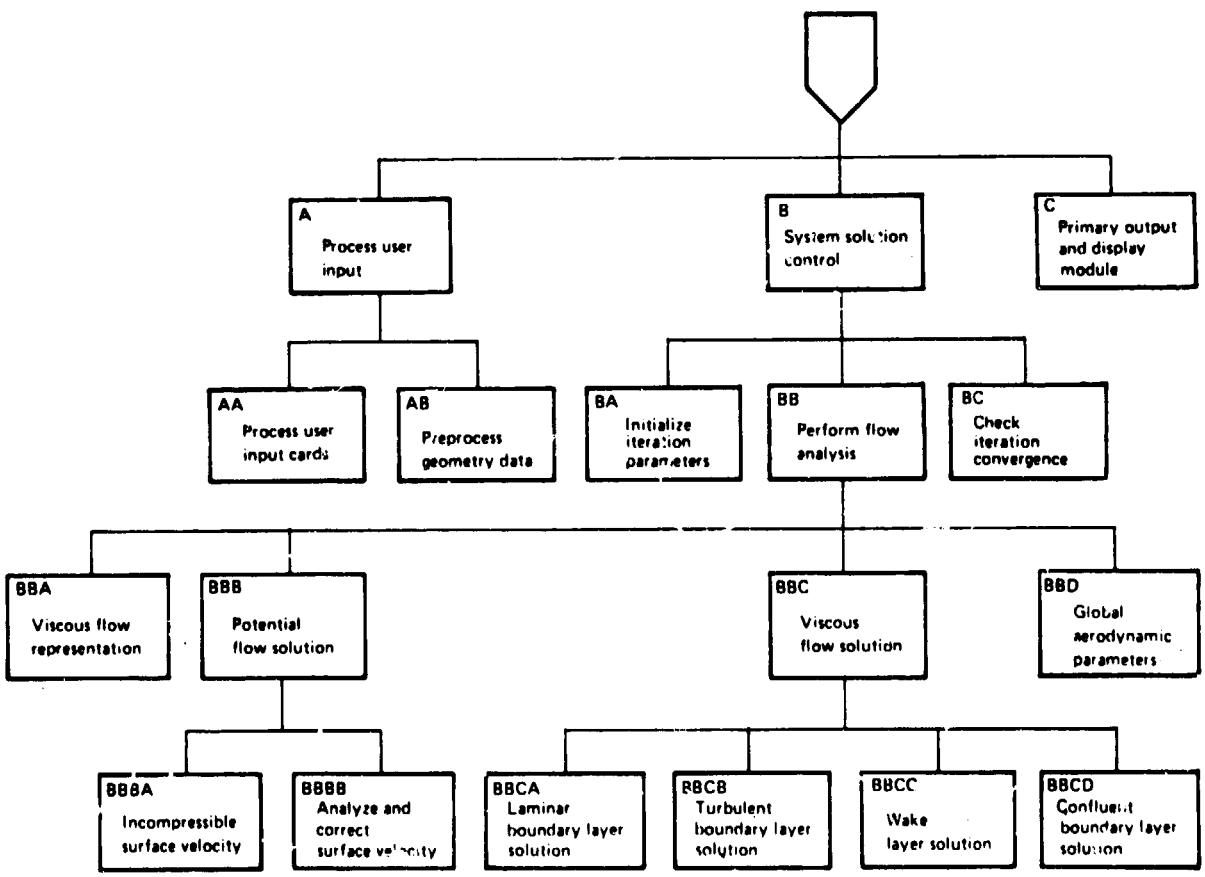

Figure 4.- Functional decomposition of NASA-Lockheed program.

Figure 5.- Airfoil geometries.

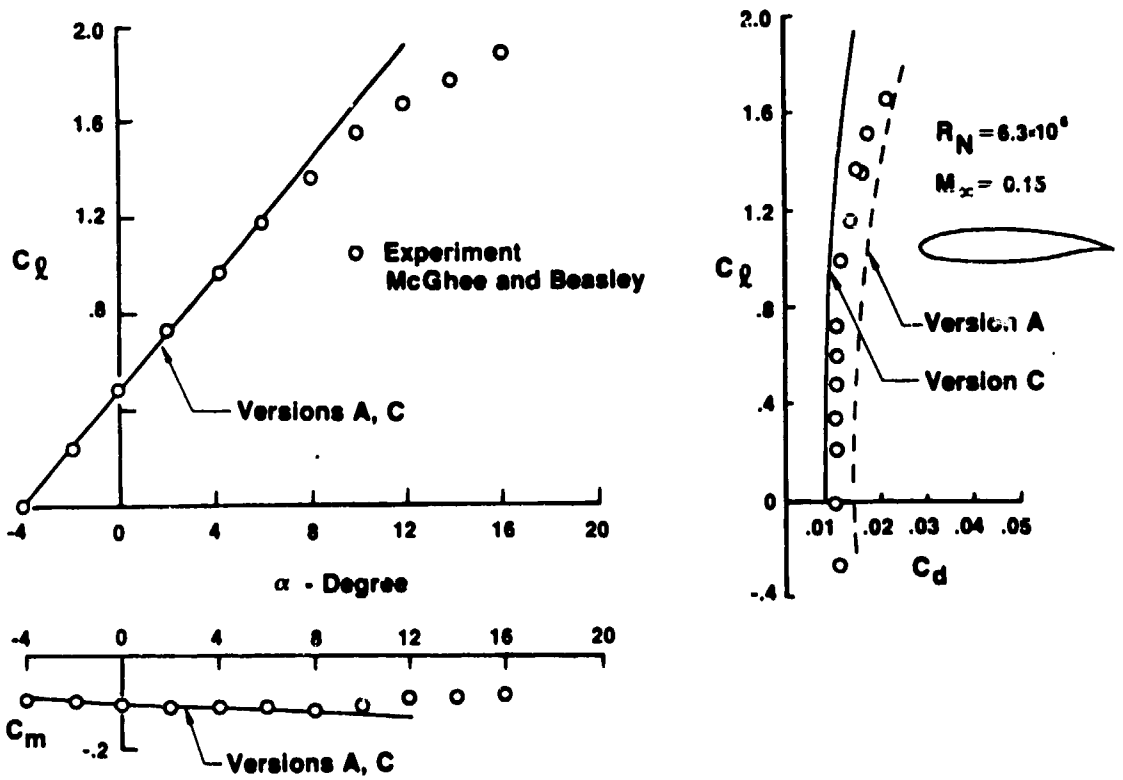

Figure 6.- Lift, drag, and pitching moment of GA(W)-1 airfoil.

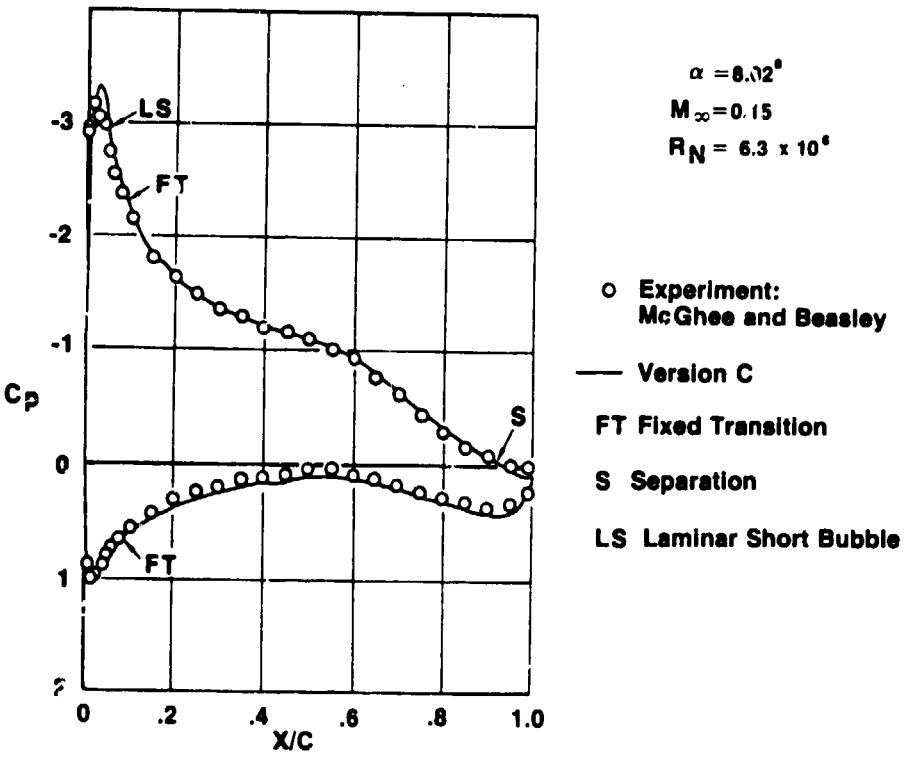

Figure 7.- Surface pressure of GA(W)-1 airfoil.

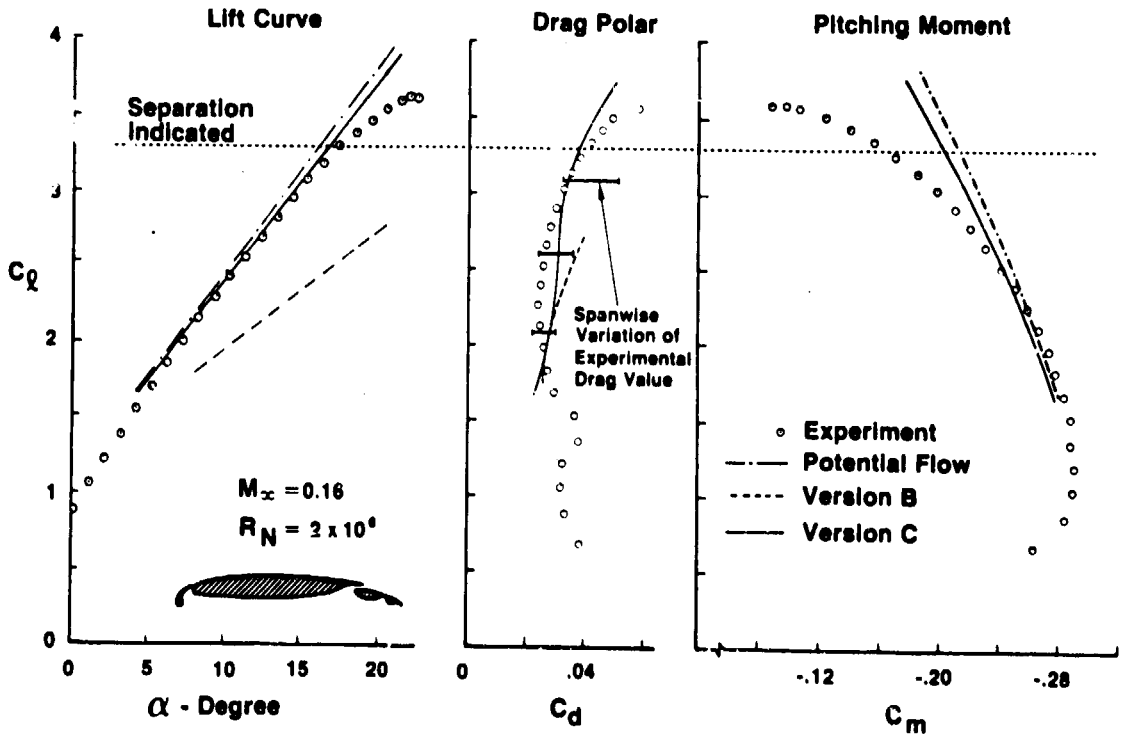

Figure 8.- Characteristics of Boeing four-element airfoil.

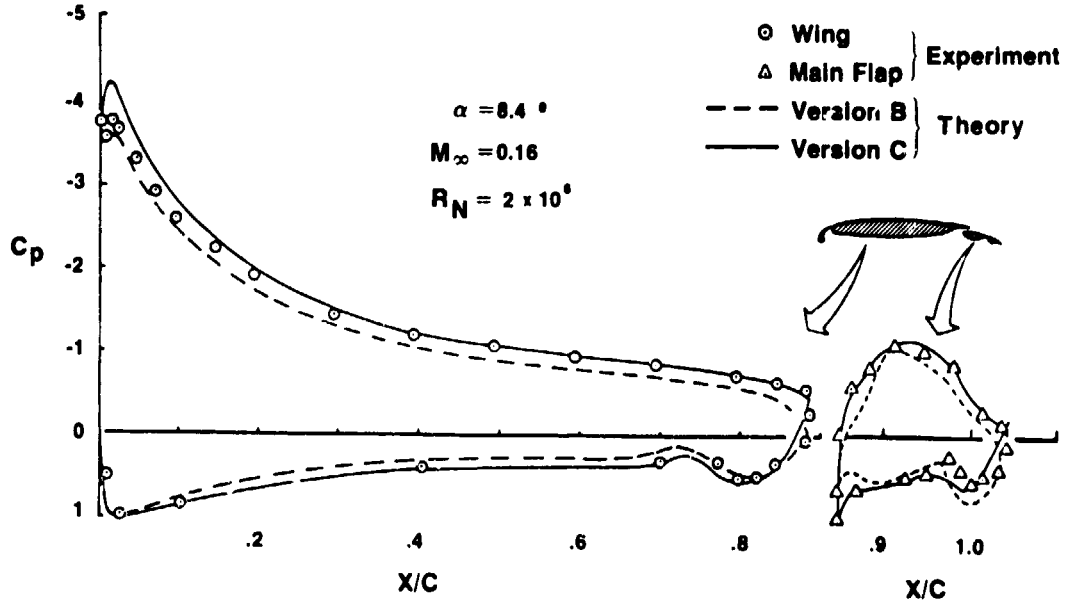

Figure 9.- Surface pressure of Boeing four-element airfoil.

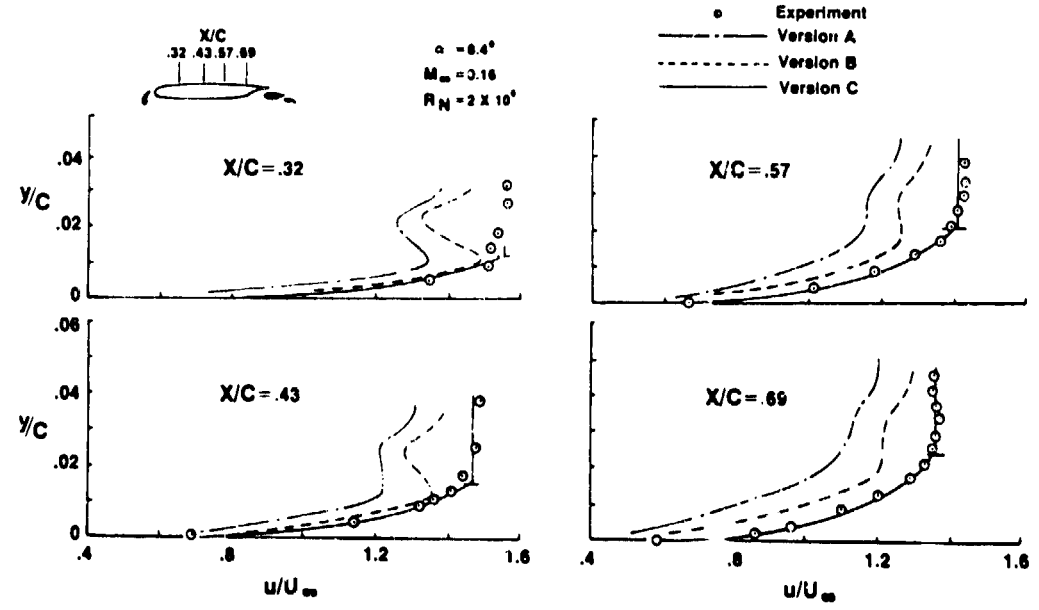

Figure 10.- Boundary-layer profiles on upper surface of Boeing four-element airfoil.

D11

N79-20041

11

NUMERICAL SOLUTION OF THE NAVIER-STOKES EQUATIONS FOR ARBITRARY TWO-DIMENSIONAL MULTI-ELEMENT AIRFOILS*

Joe F. Thompson, Louie Turner, W. Serrill Long, and John H. Bearden
Mississippi State University

SUMMARY

The development of a numerical simulation of time-dependent, turbulent, compressible flow about two-dimensional multi-element airfoils of arbitrary shape is described. The basis of this simulation is a technique of automatic numerical generation of coordinate systems fitted to the multiple bodies regardless of their number or shape.

Incompressible solutions have been run for NACA airfoils at Reynolds numbers as high as 10^6, but present drag predictions are about twice the experimental values. Procedures have been developed whereby the coordinate lines are automatically concentrated in the boundary layer at any Reynolds number. The compressible turbulent solution involves an algebraic eddy viscosity turbulence model. The laminar version has been run for transonic flow at free-stream Mach numbers up to 0.9.

INTRODUCTION

The overall purpose of the present research project is to develop a numerical simulation of time-dependent, turbulent, compressible flow about two-dimensional multi-element airfoils of arbitrary shape. The basis of this simulation is a technique of automatic numerical generation of coordinate systems fitted to the multiple bodies regardless of their number or shape. This procedure eliminates the shape of the bodies as a complicating factor and allows the flow about arbitrary bodies to be treated essentially as easily as that about simple bodies. All computation can be done on a rectangular transformed field with a square mesh regardless of the shape or number of bodies in the physical field.

In the effort thus far, numerical solutions have been developed for the time-dependent incompressible Navier-Stokes equations for laminar flow about arbitrary multiple airfoils, and the compressible Navier-Stokes equations for laminar and turbulent flow about single airfoils. Continuous refinement of the techniques is being made as higher Reynolds numbers are considered. A number of papers have reported the work so far in references 1-8, and the coordinate system code has been made available for general use as described in reference 8.

*Research sponsored by NASA Langley Research Center under Grant NGR 25-001-055.

C-3

The development of the compressible turbulent solution is now being extended to multiple airfoils using a new coordinate system configuration having the infinity boundary collapsed to a point. Refinement of this solution and the incompressible solution for multiple airfoils is also continuing. Finally, the search for improvements in the iterative solutions involved continues in order to improve the computational efficiency of all the solutions.

Symbols are defined in an appendix.

BOUNDARY-FITTED COORDINATE SYSTEM

General Formulation

The basic idea of the boundary-fitted coordinate systems is to numerically generate a curvilinear coordinate system having some coordinate line coincident with each boundary of the physical region of interest, regardless of the shape of these boundaries. This is done by taking the curvilinear coordinates to be solutions of an elliptic partial differential system, with constant values of one of the curvilinear coordinates specified as Dirichlet boundary conditions on each boundary. Values of the other coordinate are either specified in a monotonic variation over a boundary as Dirichlet boundary conditions, or are determined by Neumann boundary conditions thereon. In the latter case, the curvilinear coordinate lines can be made to intersect the boundary according to some specified condition, such as normalcy or parallel to some given direction. It is also possible to exercise control over the spacing of the curvilinear coordinate lines in the field in order to concentrate lines in regions of expected high gradients.

In any case, the numerical generation of the coordinate system is done automatically for any shape boundaries, requiring only the input of points on the boundary. The technique has been described in detail in earlier reports (ref. 1 and 7) and the computer code, together with instructions for and examples of its use in the numerical solution of partial differential equations, is given in reference 8.

As mentioned previously, the curvilinear coordinates are generated by solving an elliptic system of suitable form. One such system is

$$\xi_{xx} + \xi_{yy} = P(\xi,\eta) \tag{1a}$$

$$\eta_{xx} + \eta_{yy} = Q(\xi,\eta) \tag{1b}$$

with Dirichlet boundary conditions, one coordinate being specified to be equal to a constant on the body and equal to another constant on the outer boundary, with the other coordinate varying monotonically over the same range around both the body and the outer boundary.

Since it is desired to perform all numerical computations in the uniform rectangular transformed plane, the dependent and independent variables must be interchanged in Eq. (1). This results in the coupled system

$$\alpha x_{\xi\xi} - 2\beta x_{\xi\eta} + \gamma x_{\eta\eta}$$

$$= - J^2[x_\xi P(\xi,\eta) + x_\eta Q(\xi,\eta)] \qquad (2a)$$

$$\alpha y_{\xi\xi} - 2\beta y_{\xi\eta} + \gamma y_{\eta\eta}$$

$$= - J^2[y_\xi P(\xi,\eta) + y_\eta Q(\xi,\eta)] \qquad (2b)$$

where

$$\alpha = x_\eta^2 + y_\eta^2 \qquad \gamma = x_\xi^2 + y_\xi^2$$

$$\beta = x_\xi x_\eta + y_\xi y_\eta \qquad J = x_\xi y_\eta - x_\eta y_\xi$$

(Transformation relations are given in ref. 8).

The system described by eq. (2) is a quasilinear elliptic system for the coordinate functions $x(\xi,\eta)$ and $y(\xi,\eta)$ in the transformed plane. This set is considerably more complex than the linear system specified by eq. (1), but the boundary conditions are specified on straight boundaries, and the coordinate spacing in the transformed plane is uniform.

The coordinate lines may be spaced as desired around the boundaries, since the assignment of the coordinate values to the [x,y] boundary points is arbitrary. Control of the radial spacing of the coordinate lines is accomplished by varying the functions $P(\xi,\eta)$ and $Q(\xi,\eta)$ in equations (2).

Automatic Concentration of Coordinate Lines into a Boundary Layer

Consider the coordinate system generation equations (2) applied to the one-dimensional case of straight boundaries parallel to the x-axis. With η = constant on these boundaries, and the ξ-lines being normal to the boundaries, we have $y_\xi = y_{\xi\xi} = y_{\xi\eta} = 0$, and the x-equation is identically zero so

that the coordinate equations reduce to

$$\gamma y_{\eta\eta} + J^2 Q y_{\eta} = 0 \tag{3}$$

This can be made a perfect differential by choosing the form of the control function Q to be

$$Q(\eta) \equiv - \frac{\gamma}{J^2} \frac{f''(\eta)}{f'(\eta)} \tag{4}$$

where the minus sign has been introduced merely for convenience. Then eq. (3) can be integrated to yield

$$y(\eta) = c_1 f(\eta) + c_2 \tag{5}$$

The constants of integration may be evaluated from the boundary conditions: $y(1) = y_1$, $y(J) = y_J$ so that

$$y(\eta) = y_1 + (y_J - y_1) \left(\frac{f(\eta) - f(1)}{f(J) - f(1)} \right) \tag{6}$$

This equation can then be solved for $f(\eta)$ to yield

$$\frac{f(\eta) - f(1)}{f(J) - f(1)} = \frac{y(\eta) - y_1}{y_J - y_1} \tag{7}$$

which, with arbitrary definition of f(1) and f(J), will yield the required $f(\eta)$, and hence the required $Q(\eta)$ via substitution in eq. (4), to produce a desired distribution $y(\eta)$. The evaluation of $Q(\eta)$ may be done without actual evaluation of $f(\eta)$, however, by solving eq. (3) for Q to produce

$$Q(\eta) = - \frac{\gamma}{J^2} \frac{y''}{y'} \tag{8}$$

Now a number of smooth functions for $y(\eta)$, such as exponentials, logarithmic functions, hyperbolic functions, etc., may be found which will concentrate lines near y_1 with a spread out to y_2. However, since the boundary

layer thickness at high Reynolds number is only a very small fraction of the distance to outer boundary of the computational field, such smooth functions cannot allow the lines to spread rapidly enough outside of the boundary layer. The result is that nearly all of the lines in the field will be within a few boundary layer thicknesses of the body, with a great gap near the outer boundary.

Therefore, a composite function was used for $y(\eta)$, formed by joining a logarithmic function to a quartic polynomial near the edge of the boundary layer. This function is constructed as follows: assume that it is desired to space the lines in the boundary layer such that the change in velocity from each to the next is the same. Let the velocity profile in the boundary layer be approximated by the exponential

$$u(y) = 1 - e^{-cy} \tag{9}$$

Let the edge of the boundary layer be defined by

$$u = 0.99 \text{ at } y = \delta$$

Then the decay factor c will be given by

$$c = -\frac{1}{\delta} \ln (0.01)$$

Now solve eq.(9) for y(u):

$$y(u) = -\frac{1}{c} \ln (1-u) \tag{10}$$

In order to achieve the same velocity change from each line to the next, take $u = 0.99 \left(\frac{\eta-1}{\eta_\delta-1}\right)$ where η_δ is the line at the edge of the boundary layer. Substitution in eq. (10) then yields

$$y(\eta) = -\frac{1}{c} \ln \left[1 - 0.99 \left(\frac{\eta-1}{\eta_\delta-1}\right)\right], 1 \leq \eta \leq \eta_\delta \tag{11}$$

Let this logarithmic function be joined to a quartic polynomial at some line inside or at the outer edge of the boundary layer. Thus with the function at $\eta=N$, the polynomial is of the form

$$y(\eta) = y'(N)\ [\eta-N] + \frac{1}{2}\, y''(N)\ [\eta-N]^2$$

$$+ \frac{1}{6}\, y''(N)\ [\eta-N]^3 + a(\eta-N)^4 + y(N)$$

$$N \leq \eta \leq J \tag{12}$$

Here y'(N) is functional notation, etc. The derivatives are determined by differentiation of eq. (11), with evaluation at η=N. The remaining coefficient "a" is used to satisfy the boundary condition at the outer boundary, $y(J) = y_J$. Thus

$$a = \frac{y_J - y(N) - y'(N)\ [J-N] - \frac{1}{2}\, y''(N)\ [J-N]^2 - \frac{1}{6}\, y''(N)[J-N]^3}{(J-N)^4}$$

Note that the junction to the polynomial need not occur at the edge of the boundar layer, but anywhere inside it. It has been found advantageous to place the junction two or three lines inside the boundary layer.

Thus if the boundary layer thickness, δ, and the number of lines therein, η_δ, are specified, along with the distance to the outer boundary, y_J, and the total number of lines J, and the junction line N, the control function $Q(\eta)$ can be evaluated from

$$Q(\eta) = -\frac{\gamma}{J^2}\, \frac{\frac{0.99}{\eta_\delta - 1}}{1 - 0.99\ (\frac{\eta-1}{\eta_\delta-1})}, \eta = 1,2,\text{--}, N \leq \eta_\delta \tag{13a}$$

$$Q(\eta) = -\frac{\gamma}{J^2}\, \frac{y'(N) + y''(N)\ [\eta-N] + 12a[\eta-N]^2}{y'(N) + y''(N)\ [\eta-N] + \frac{1}{2}\, y''(N)\ [\eta-N]^2 + 4a[\eta-N]^3}$$

$$\eta = N,\ N+1,\ \text{---},\ J \tag{13b}$$

with the required derivatives given by

$$y^{(k)}(N) = \frac{\frac{(k-1)!}{c}\ (\frac{0.99}{N-1})^k}{[1 - 0.99\ (\frac{\eta-1}{N-1})]^k},\ k = 1,2,3 \tag{14}$$

and y(N) by

$$y(N) = -\frac{1}{c} \ln\left[1 - 0.99 \left(\frac{N-1}{\eta_\delta - 1}\right)\right] \tag{15}$$

Although this analysis is developed for the one-dimensional case of a flat boundary, the same general results will be achieved by its use with curved boundaries since curvature tends to affect both the boundary layer thickness and the line control in the same way. Thus convex curvature thins the boundary layer but also causes the lines to concentrate to a greater degree near the boundary.

An example of coordinate systems generated with this concentration of lines in boundary layers is shown in figure 1.

The exponential velocity distribution in eq. (9) may be replaced by the Blasius distribution, and this has been done in practice since a more even spacing is obtained in the lower part of the boundary layer in that case.

Truncation Error Induced by the Coordinate System

Some attention must be paid to the rapidity of the change of coordinate line spacing with strong attraction, else truncation error in the form of artificial diffusion may be introduced as follows: Consider the finite difference approximation of a first derivative with variation only in the x-direction to which the ξ-lines are normal. Then

$$f_x = \frac{y_\eta f_\xi}{x_\xi y_\eta} = \frac{f_\xi}{x_\xi} \tag{16}$$

The difference approximation then would be

$$f_x = \frac{f_{i+1} - f_{i-1}}{x_{i+1} - x_{i-1}} + T_i \tag{17}$$

where T_i is the local truncation error. Taylor series expansions of f_{i+1} and f_{i-1} about f_i then yield, after some algebraic rearrangement,

$$T_i = -\frac{1}{2} (f_{xx})_i \, (x_{i+1} + x_{i-1} - 2x_i) \tag{18}$$

But the last factor is simply the difference approximation of $x_{\xi\xi}$ so that

$$T = \frac{1}{2} x_{\xi\xi} f_{xx}$$

This truncation error thus introduces a numerical diffusive effect in the difference approximation of first derivatives. Care must therefore be taken that the second derivatives of the physical coordinates (i.e., the rate of change of the physical spacing between curvilinear coordinate lines) are not too large in regions where the dependent variables have significant second derivatives in the direction normal to the closely spaced coordinate lines.

Just what is a permissible upper limit to the rate of change of the line spacing is problem dependent. Consider, for instance, viscous flow past an infinite flat plate parallel to the x-direction. Here the velocity parallel to the wall changes rapidly from zero at the wall to its free stream value over a small distance that is of the order of $\frac{1}{\sqrt{R}}$, where R is the Reynolds number, $R = \frac{U_\infty x}{\nu}$, based on freestream velocity, U_∞, the distance from the leading edge of the plate, x, and the kinematic viscosity, ν. The equation for the time rate of change of the velocity parallel to the wall is

$$u_t = -uu_x - vu_y + \frac{1}{R}(u_{xx} + u_{yy}) \tag{19}$$

Recalling that the large spacial variation in velocity occurs in the y-direction, coordinate lines would be contracted near the plate. The truncation error introduced by this contraction would be

$$T(v) = (-\frac{v}{2} y_{\eta\eta}) u_{yy} \tag{20}$$

This introduces a negative numerical viscosity $(-\frac{v}{2} y_{\eta\eta})$, since v and $y_{\eta\eta}$ are both positive.

The effective viscosity is thus reduced (effective Reynolds number increased), so that the velocity gradient near the wall is steepened. Therefore care should be taken that $y_{\eta\eta}$ is limited so that the numerical viscosity $(-\frac{v}{2} y_{\eta\eta})$ is not significant in comparison with the physical term $(\frac{1}{R})$. The situation is mitigated somewhat of the fact that the numerical viscosity is proportional to the small velocity normal to the wall, this velocity being of order $\frac{1}{\sqrt{R}}$. Actually this limit is conservative, since the normal velocity drops to zero at the wall and only attains the order $\frac{1}{\sqrt{R}}$ on the outer portion

of the region of large gradient of velocity parallel to the wall, where u_{yy} is very small.

Transformation of Infinity to an Interior Circuit

With multiple-bodies involving two closely-spaced bodies, the coordinate line spacing in the area between the bodies will not be too good with the type of coordinate system generated by the original TOMCAT code (ref. 8) as illustrated in figure 2. This results from the smoothness of solutions of Poisson equations, the contours of which tend to avoid concave regions. Coordinate system control can improve the situation somewhat as shown in reference 3.

However, with two bodies, an even better system can be obtained by first transforming the remote outer boundary circle to a small interior circle, or even a point, by the analytical complex transformation $Z' = \frac{1}{Z}$. Here $Z = x + iy$ is a point in the physical plane, while $Z' = x' + iy'$ is a corresponding point in the transformed plane. These original and transformed boundary circuits are illustrated in figs. 3&4 for an airfoil-flap combination.

The coordinates (x',y') of the transformed boundary circuits are then input to the TOMCAT code in the usual manner, with the body circuits comprising the entire top and bottom sides of the rectangular transformed plane and one half of the small outer boundary circle appearing on a portion of the left and right sides. The result of the TOMCAT code, in the form of ξ and η lines drawn in the $x' - y'$ plane, is shown in fig. 5 for a wing-slat.

The inverse analytic transformation, $Z = \frac{1}{Z'}$, back to the $x - y$ plane then produces coordinate lines of constant ξ and η in the $x - y$ plane as shown in figs. 6-8, the second figure being an expanded view of the slot region. A similar coordinate system for a leading edge slat configuration is shown in figs. 9&10.

INCOMPRESSIBLE SOLUTION

The incompressible solution is written in the primitive variable formulation, and some description has been given in reference 3. The solution is completely implicit, so that all equations are solved simultaneously at each time step. The construction essentially parallels that described for the compressible solution in the next section, with the exception that the Poisson equation for the pressure has no time derivative, of course. On the airfoil surface, the pressure is determined by iteratively adjusting the pressure at each point on the surface in proportion to the divergence of the velocity at the same point, so that upon convergence the continuity equation is satisfied on the airfoil surface (ref. 3).

This code has been written with great generality, so that it can serve as a research tool with which different numerical representations can be evaluated. The following features can be selected simply by input options without changing the code:

(a) 2-point central convective derivatives
(b) 6-point central convective derivatives
(c) 2-point upwind convective derivatives
(d) 3-point upwind convective derivatives
(e) 4-point cross derivatives
(f) 7-point cross derivatives
(g) product-of-average nonlinear terms
(h) average-of-product nonlinear terms
(i) fully nonlinear
(j) second-order linearization
(k) conservative form
(l) nonconservative form
(m) time-dependent form
(n) steady-state form

Input options can also select several starting procedures as follows:

(a) Impulsive start from rest
(b) Impulsive start from potential flow
(c) Accelerating start from rest
(d) Decreasing penetration start
(e) Increasing Reynolds number start

The pressure boundary condition can be selected as from the continuity equation as discussed above or from the normal momentum equation applied on the body. These boundary conditions can be either first or second order. The time derivative can be either first or second order, and first or second-order projection can be used for the initial guess for the iteration at each time step if desired. Diffusion based on the change between time steps can be activated if desired, as can be flux-corrected transport or a two cell wave length filter.

The code also contains the following choices of iteration scheme, with selection by input option:

(a) point SOR with computed acceleration parameters
(b) line SOR, either rows or columns
(c) ADI
(d) Stone strongly implicit

The point SOR iteration uses a variable acceleration parameter field, the parameter at each point being continually adjusted to be equal to the locally linearized optimum. This feature is important at high Reynolds number since the optimum acceleration parameter depends on both the local velocity and the mesh spacing. Finally, a multi-grid iteration form of this same code has been written, and three variations of the multi-grid algorithm are now under study.

These codes treat the full incompressible Navier-Stokes equations for any number of multiple bodies and thus can handle all configurations produced by the TOMCAT coordinate code. Experimentation is now in progress with all these options at high Reynolds number.

The incompressible Navier-Stokes solution has also been written in the vorticity-stream function formulation (ref. 6) and in the integro-differential (vorticity-velocity) formulation (ref. 9), as well as the primitive variable formulation discussed above. Results for flow about NACA single symmetric and 6-series airfoils at high Reynolds number (10^6) have been obtained. These high Reynolds number results, however, predict drag that is about twice the experimental value, indicating the need for further development.

Some typical results as described in ref. 9 are shown in figures 11-13 for a Reynolds number of 10^6. Some lower Reynolds number results for a multiple airfoil are shown in figs. 14-16.

COMPRESSIBLE SOLUTION

Numerical Formulation

The compressible solution is based on the full Navier-Stokes equations in fully conservative form in the transformed coordinates. At the interior field points, a second-order backward time, central space scheme is used to represent the differential equations. Along the body surface, the continuity equation is represented using second-order, one-sided space differences.

Turbulence Model

The compressible code also includes an algebraic two-layer turbulent eddy viscosity model as used in reference 10 (termed Model 3 therein).

Results

The compressible code is still under development, but preliminary results are shown in figs. 17-21 for a NACA 0018 airfoil at 5° angle of attack, Mach number of 0.9, Reynolds number of 20,000, and surface temperature of 0.8.

The Mach contours in figure 18 show a rather diffuse shock and the thick boundary layer resulting from the somewhat low Reynolds number. The velocity vectors of figure 19 indicate separation on the upper surface. The peak in the density profiles ahead of and behind the airfoil (fig. 21) are compression and expansion waves resulting from the impulsive start from incompressible potential flow.

CONCLUDING REMARKS

Both the incompressible and compressible solutions are still under development. The search also continues for the most appropriate multi-element coordinate configurations. As noted, a wide variety of numerical procedures is under evaluation in order to develop an efficient treatment of high Reynolds number flow.

APPENDIX

SYMBOLS

ξ	Curvilinear Coordinate
η	Curvilinear Coordinate
x	Cartesian Coordinate
y	Cartesian Coordinate
p	Coordinate Control Function for ξ
Q	Coordinate Control Function for η
α	Metric Function Defined with Equations (2)
β	Metric Function Defined with Equations (2)
γ	Metric Function Defined with Equations (2)
J	Jacobian, Also Total Number of Coordinate Lines Around Body
f	General Function
c_1, c_2	Constants of Integration
c	Exponential Decay Factor
u	Velocity Component
δ	Boundary Layer Thickness
M	Free-stream Mach Number
N	Junction Line
a	Coefficient in Quartic Polynomial
T	Truncation Error
t	Time
R	Reynolds Number
v	Velocity Component
z	Complex Variable

Subscripts

ξ	Denotes Differentiation with Respect to ξ
η	Denotes Differentiation with Respect to η
x	Denotes Differentiation with Respect to x
y	Denotes Differentiation with Respect to y
t	Denotes Differentiation with Respect to t
δ	Denotes Value at Edge of Boundary Layer
J	Denotes Value at Outer Boundary
N	Denotes Value at Junction Line

REFERENCES

1. Thompson, J. F., Thames, F. C., and Mastin, C. W., "Automatic Numerical Generation of Body-Fitted Curvilinear Coordinate System for Fields Containing Any Number of Arbitrary Two-Dimensional Bodies," Journal of Computational Physics, 15, 299, (1974).

2. Thames, F. C., Thompson, J. F., and Mastin, C. W., "Numerical Solution of the Navier-Stokes Equations for Arbitrary Two-Dimensional Airfoils," Proceedings of NASA Conference on Aerodynamic Analyses Requiring Advanced Computers, Langley Research Center, NASA SP-347, (1975).

3. Thompson, J. F., Thames, F. C., Mastin, C. W., and Shanks, S. P., "Use of Numerically Generated Body-Fitted Coordinate Systems for Solution of the Navier-Stokes Equations," Proceedings of the AIAA 2nd Computational Fluid Dynamics Conference, Hartford, Connecticut, (1975).

4. Thompson, J. F., Thames, F. C., Shanks, S. P., Reddy, R. N., and Mastin, C. W., "Solutions of the Navier-Stokes Equations in Various Flow Regimes on Fields Containing Any Number of Arbitrary Bodies Using Boundary-Fitted Coordinate Systems," Proceedings of V International Conference on Numerical Methods in Fluid Dynamics, Enschede, the Netherlands, Lecture Notes in Physics, Springer-Verlag, (1976), Vol. 59, p. 421.

5. Thompson, J. F., Warsi, Z. U. A., and Amlicke, B. B., "Numerical Solutions for Laminar and Turbulent Viscous Flow Over Single and Multi-Element Airfoils Using Body-Fitted Coordinate Systems," Advances in Engineering Science, Proceedings of 13th Annual Meeting Society of Engineering Science Hampton, Virginia, (1976), NASA CP-2001.

6. Thames, F. C., Thompson, J. F., Mastin, C. W., and Walker, R. L., "Numerical Solutions for Viscous and Potential Flow About Arbitrary Two-Dimensional Bodies Using Body-Fitted Coordinate Systems," Journal of Computational Physics, 24, 245 (1977).

7. Thompson, J. F., Thames, F. C., Mastin, C. W., "TOMCAT - A Code for Numerical Generation of Boundary-Fitted Curvilinear Coordinate Systems on Fields Containing Any Number of Arbitrary Two-Dimensional Bodies," Journal of Computational Physics, 24, 274 (1977).

8. Thompson, J. F., Thames, F. C., and Mastin, C. W., "Boundary-Fitted Curvilinear Coordinate System for Solution of Partial Differential Equations on Fields Containing Any Number of Arbitrary Two-Dimensional Bodies," NASA CR-2729 (1977).

9. Reddy, R. N. and Thompson, J. F., "Numerical Solution of Incompressible Navier-Stokes Equations in the Integro-Differential Formulation Using Boundary-Fitted Coordinate Systems," Proceedings of the AIAA 3rd Computational Dynamics Conference, Albuquerque, 1977.

10. Deiwert, G. S., "Computational of Separated Transonic Turbulent Flows," AIAA Journal, 14, 735 (1976).

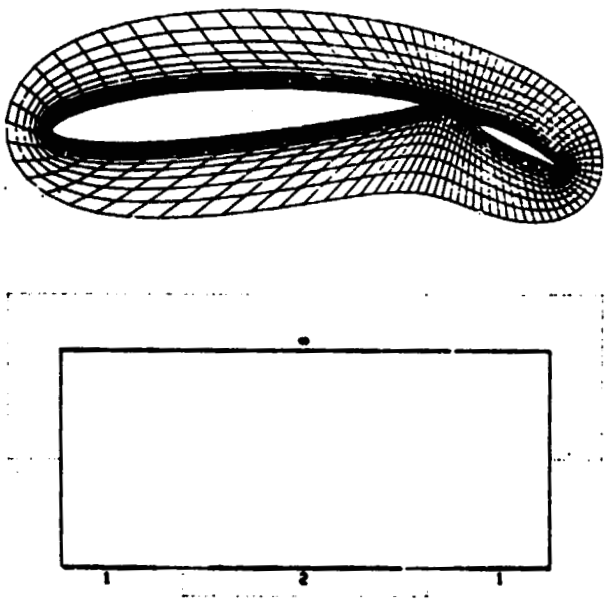

Figure 1.- Wing-flap coordinate system. Original NOMCAT form.

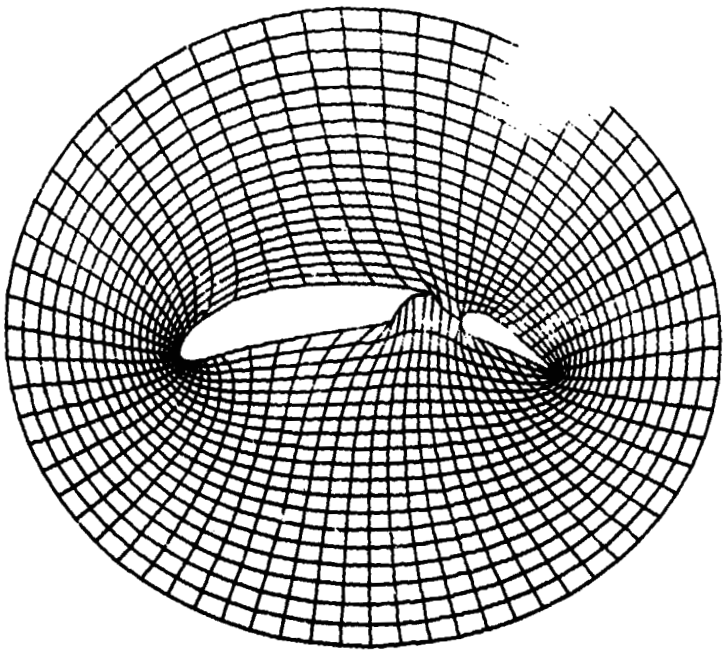

Figure 2.- Wing-flap coordinate system. Poor spacing in concave region.

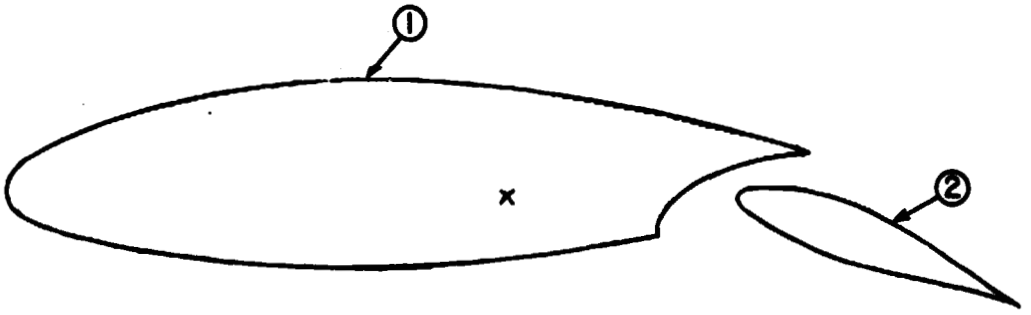

Figure 3.- Modified NACA 64_3-418 wing flap.

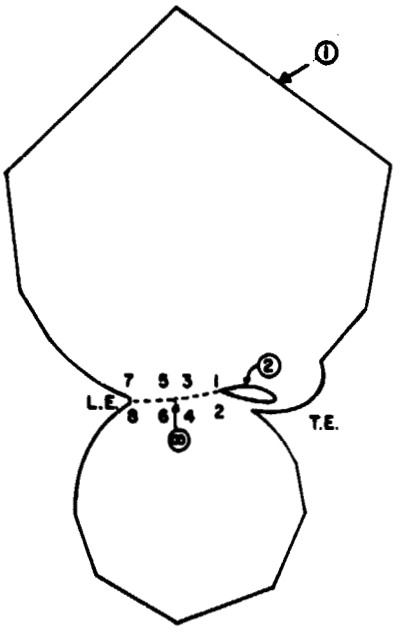

Figure 4.- Transformed modified wing-flap configuration.

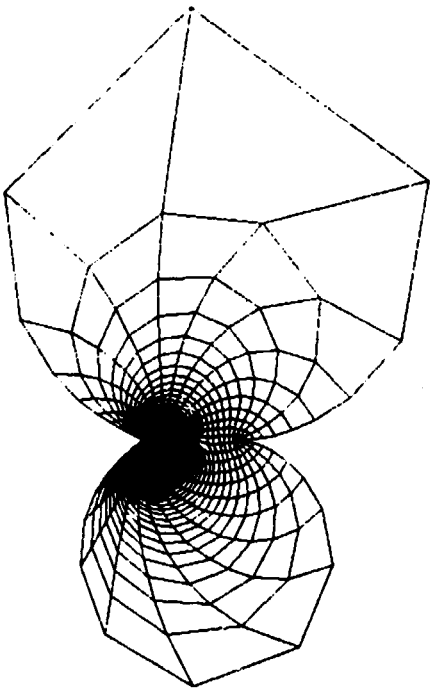

Figure 5.- Coordinate lines in transformed plane for wing slat.

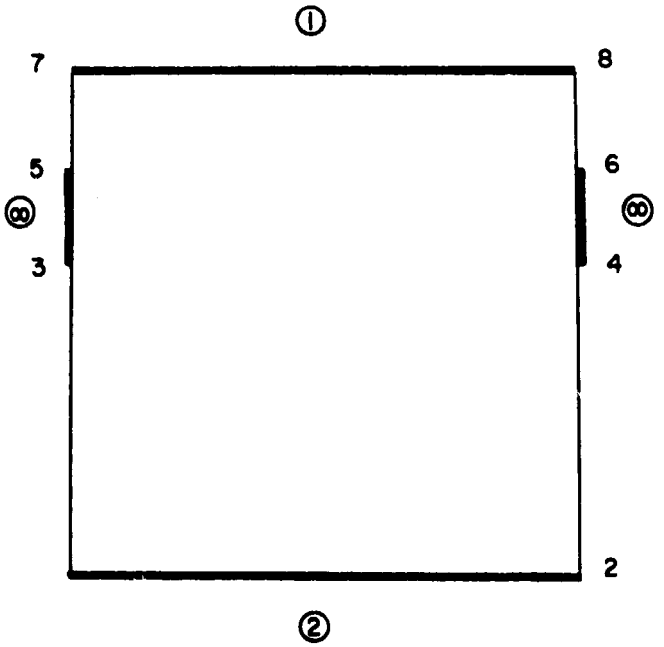

Figure 6.- Rectangular computational plane for wing flap.

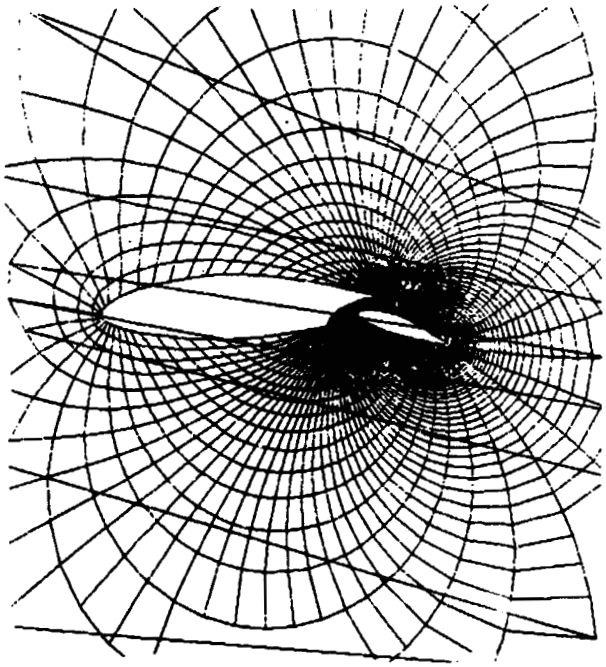

Figure 7.- Wing-flap coordinate system.

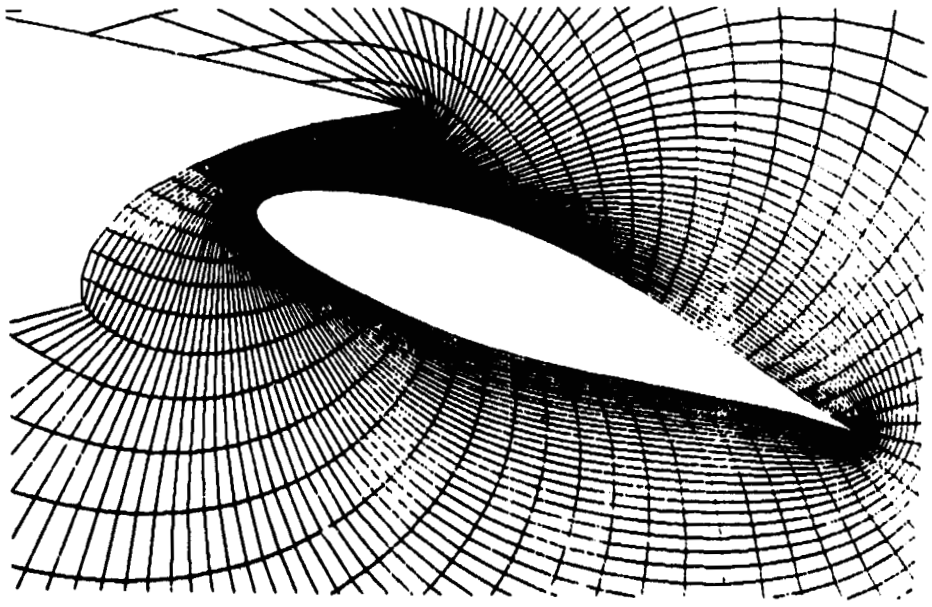

Figure 8.- Expanded view of wing-flap coordinate system.

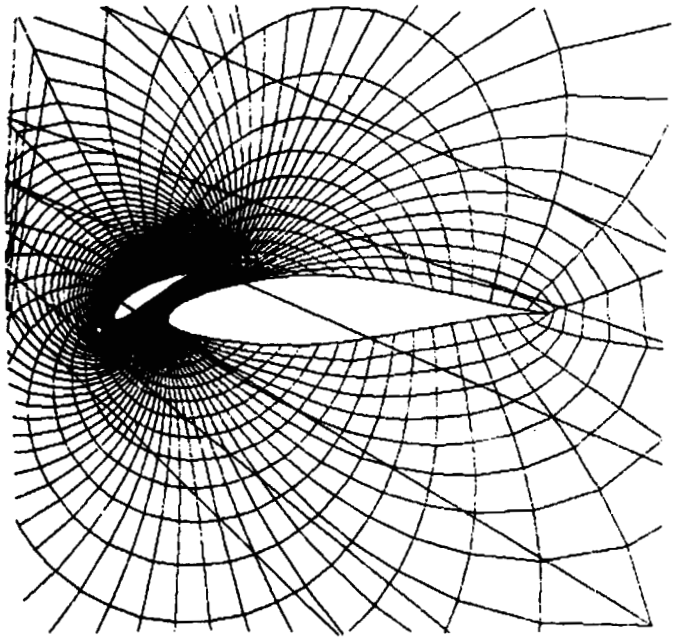

Figure 9.- Wing-slat coordinate system.

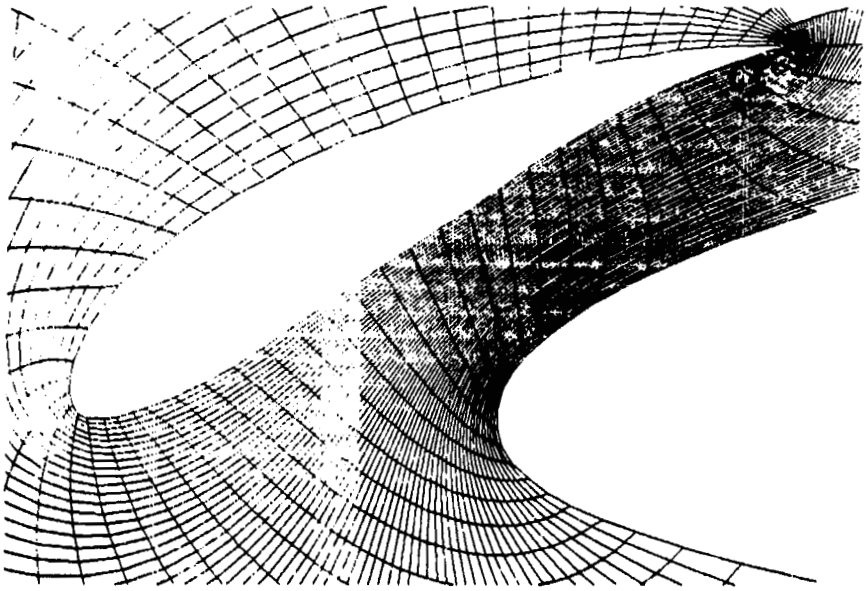

Figure 10.- Expanded view of wing-slat coordinate system.

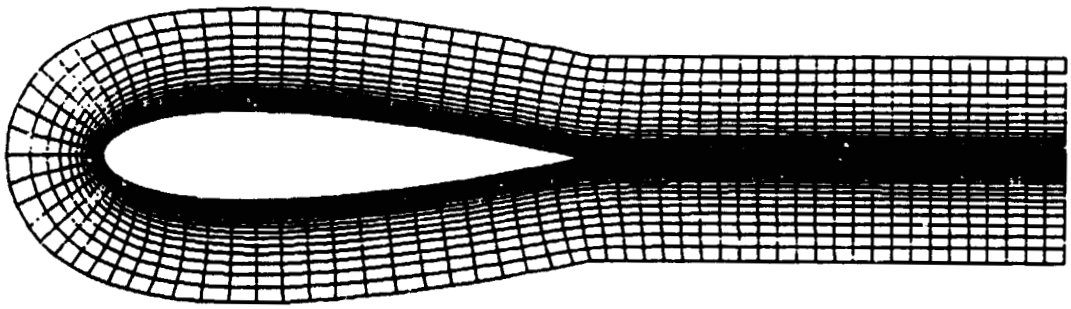

Figure 11.- Coordinate system of NACA 0018 airfoil. R = 1,000,000.

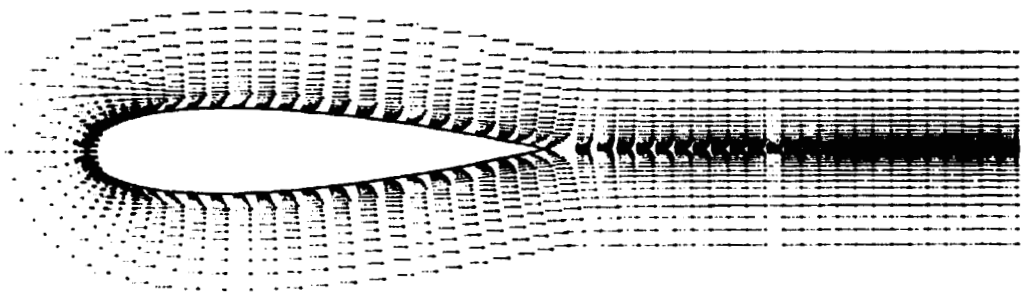

Figure 12.- Velocity vector field of NACA 0018 airfoil. R = 1,000,000; $\theta = 0^{o}$; T = 2.25.

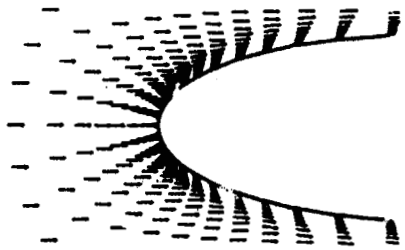

LEADING EDGE DETAILS

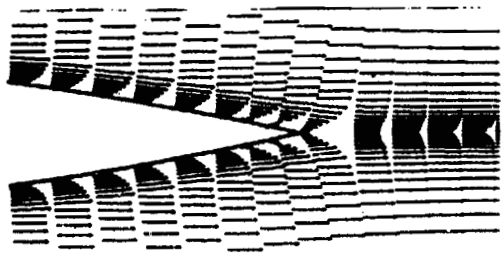

TRAILING EDGE DETAILS

Figure 13.- Velocity vector field of NACA 0018 airfoil. Leading- and trailing-edge details; R = 1,000,000; $\theta = 0^{o}$; T = 2.25.

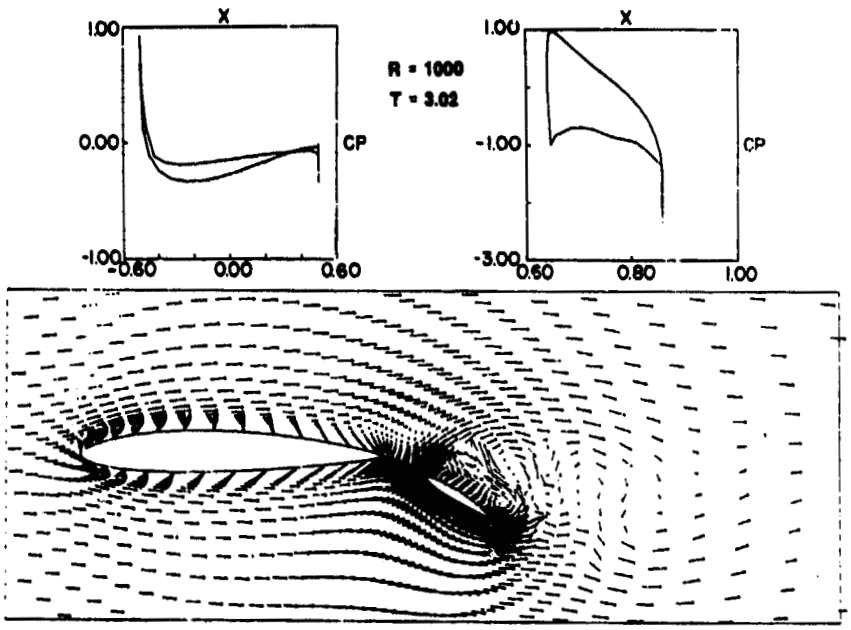

Figure 14.- Multiple airfoil.

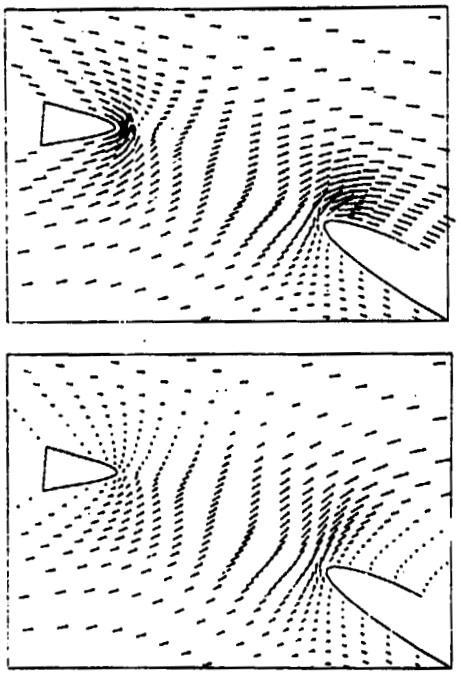

Figure 15.- Slot detail of multiple airfoil.

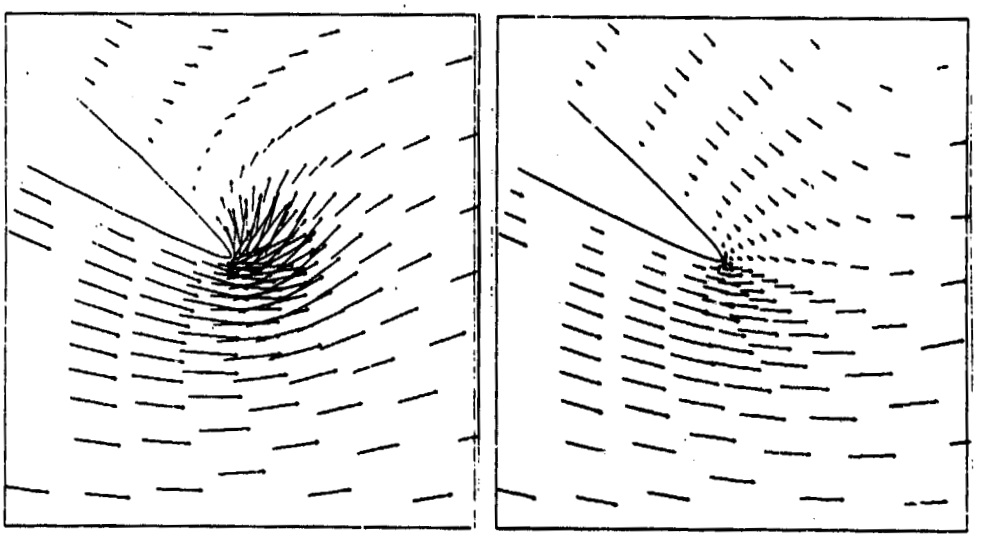

Figure 16.- Aft trailing-edge detail of multiple airfoil.

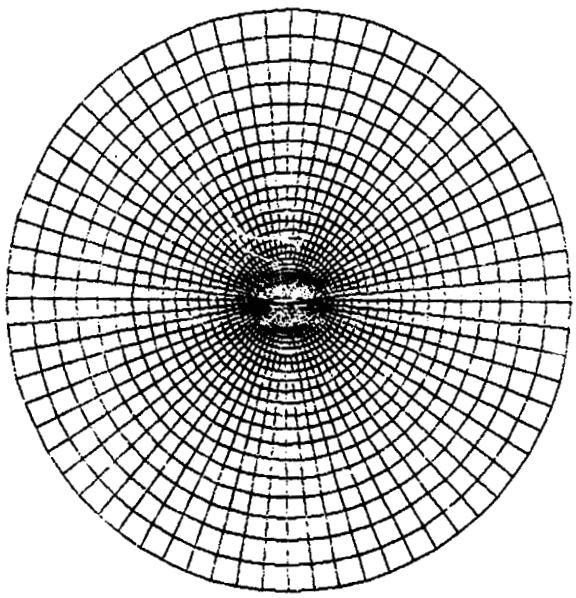

Figure 17.- Coordinate system of NACA 0018 airfoil. R = 20,000.

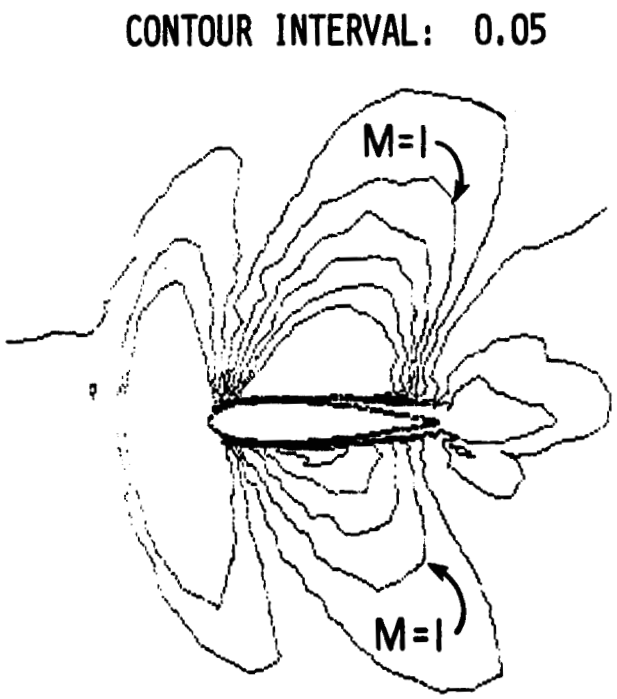

Figure 18.- Mach contours. M_∞ = 0.9: R = 20,000; $\theta = 5^\circ$; T = 1.277.

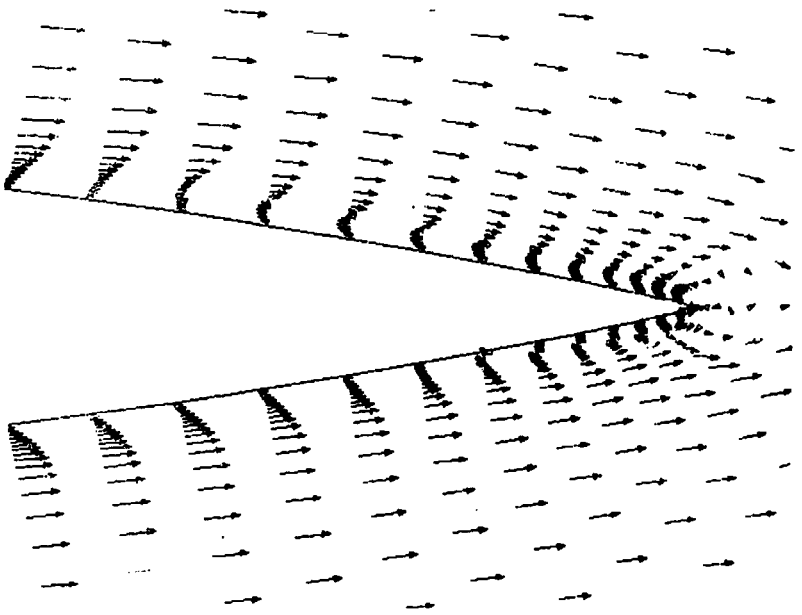

(a) Trailing edge.

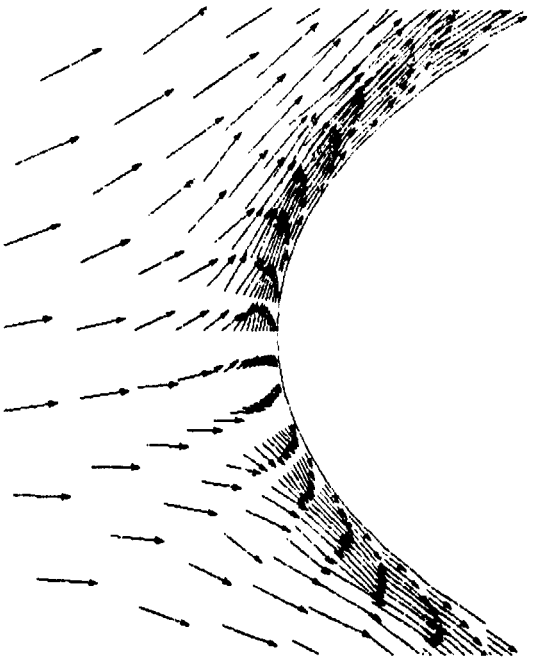

(b) Leading edge.

Figure 19.- Velocity vectors. $M_\infty = 0.9$; $R = 20{,}000$; $\theta = 5^\circ$; $T = 1.277$.

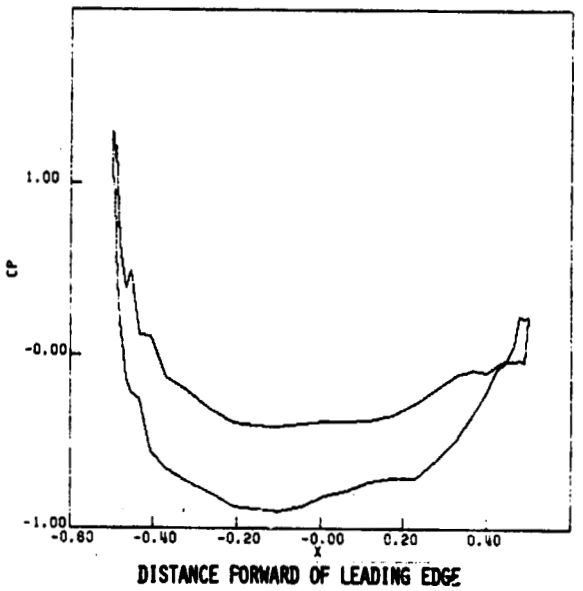

Figure 20.- Surface pressure.

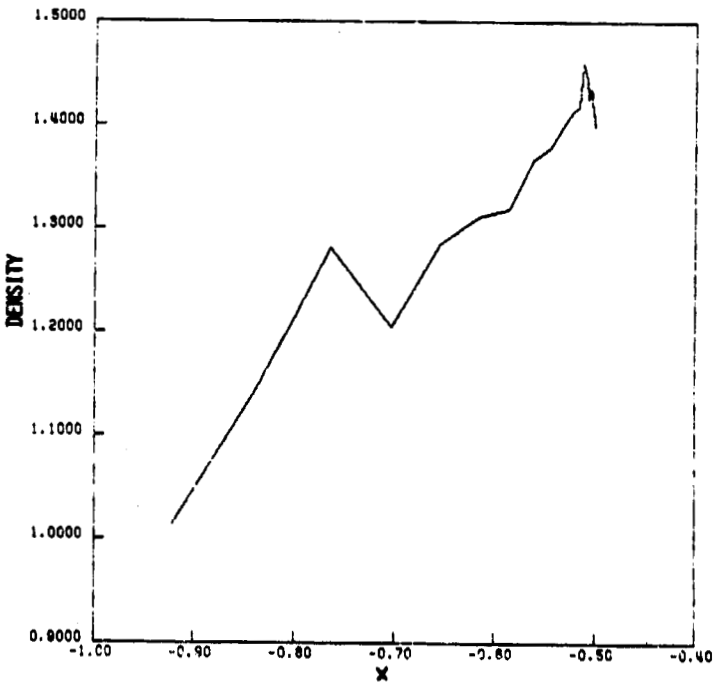

Figure 21.- Density forward of leading edge.

D12

12

THE ANALYSIS AND DESIGN OF TRANSONIC TWO-ELEMENT AIRFOIL SYSTEMS*

G. Volpe and B. Grossman
Grumman Aerospace Corporation

INTRODUCTION

This paper describes the multiphase effort in the development of tools for the analysis and design of two-element airfoil systems -- that is, airfoils with a slat or a flap at transonic speeds. The first phase involved the development of a method to compute the inviscid flow over such configurations. In the second phase the inviscid code was coupled to a boundary layer calculation program in order to compute the loss in performance due to viscous effects. In the third phase, which is currently in progress, an inverse code that constructs the airfoil system corresponding to a desired pressure distribution is to be developed. The symbols are defined in an appendix.

TWO-ELEMENT AIRFOIL ANALYSIS

The methodology used to compute the inviscid flow over two-element airfoil systems has been described in previous reports (ref. 1-3). It will be summarized here only briefly. The flow field over such configurations is obtained by mapping the doubly connected physical domain into an annulus. The transformation itself follows from the work of Ives (ref. 4), and it is the result of five sequential mappings. The first, a Karman-Trefftz transformation, opens up the main airfoil into a near circle; the second turns the near circle into a perfect one. Then the second airfoil is opened up and transferred to the interior of the main circle. Finally, the second foil is mapped into a circle while managing to retain the shape of the first circle. With this transformation the entire physical space is mapped into the annular region between the two circles with infinity becoming a single point between them.

The governing equations for the inviscid, irrotational compressible flow are written in this computational domain using the metric of the mapping. A potential function is then introduced to reduce the number of equations to one. The mapping introduces several singularities in the potential equation, but since the mapping is analytic and the transformation is known everywhere, the singularities can be removed analytically. The metric of the transformation is thus normalized with its value at the infinity point, and terms corresponding

* This work was supported by the Office of Naval Research through Contract No. N00014-75-C-0722

to the free stream and the circulatory flows around each element are subtracted from the potential function. The result is a second-order partial differential equation for a reduced potential function, which is continuous and single-valued everywhere. As usual in transonic flow problems the equation is of mixed type and is solved numerically. The boundary conditions imposed are, of course, that the normal component of velocity be zero at each surface. The equation contains two circulation constants that are evaluated by applying the Kutta condition at each trailing edge.

In the computational domain a simple polar coordinate system emanating from the center of the annulus automatically generates an orthogonal grid in which both airfoils lie along grid lines. An accurate application of the boundary conditions is then made in a relatively straightforward manner. As described in reference 2, an additional stretching is used to concentrate points near the leading and trailing edges of both elements and to place both trailing edge points and the point of infinity exactly at grid points. The numerical procedure employs standard relaxation techniques along with a non-conservative, type-dependent, rotated difference scheme. To make sure that the field is never swept at more than 90° from the streamline direction, the computational domain is divided into four regions along the ring going through the infinity point, as shown in figure 1, and then the region over each of the airfoil surfaces is swept from the leading edge to the trailing edge. Figure 2 shows a typical computational grid as it appears in the physical plane. The appropriate high level of concentration of mesh points is obtained near the leading and trailing edges and in the gap.

The configuration shown in figure 2 is a classic one, and the results of a computation for a Mach number of 0.6 and an angle of attack of 6° are given in Figure 3. Very large supersonic regions can be seen to be present on both elements. These are evident in figure 4, which gives the sonic line along with some computed streamlines.

Transonic data for two-element airfoil systems are scarce, and there are little data at any speed where viscous effects are negligible. However, data recently made available by the David Taylor Research and Development Center have made possible the verification of the results of the method. The airfoil-slat combination shown in figure 5 was designed for low-speed application on a circulation control wing. The unconventional back end of the main airfoil was designed to operate as a Coanda jet. A jet of high velocity air is ejected tangentially along the upper surface near the trailing edge of the main airfoil. The jet wraps around the rounded trailing edge entraining the outer flow. The result is an airfoil system with a very high circulation. The slat is deployed to prevent flow separation near the leading edge of the main component. The case shown in figure 5 is for a low Mach number, an angle of attack of 12°, and zero blowing. Because of the small amount of aft loading, viscous effects on the main airfoil are small and because of the high angle of attack there is very little separation on the slat. As a result there is very good agreement between the computations and the experimental data. Leading edge expansions are predicted correctly on both elements. The only discrepancy is on the lower surface of the slat where a small separation bubble is likely to exist. The lift coefficient on this configuration is 1.83.

Blowing can be simulated in the computational method by shifting the rear stagnation point on the main airfoil away from its geometrical location toward the lower surface, as seen in figure 6. The location itself is chosen to match the circulation around the main airfoil. The streamline pattern in figure 6 has been computed for an angle of attack of 4.6° and a moderate amount of blowing. In this case the slat is practically aligned with the oncoming flow. The computed pressure coefficient distribution and the experimental data are compared in figure 7. Agreement in this case is even better. Now there is no flow separation on the lower surface of the slat, and there is good agreement in this region also. Leading edge peaks are correctly predicted and the large expansion near the trailing edge of the main component corresponding to the Coanda jet is also in agreement. The lift coefficient in this case is 4.70.

Unfortunately, not all airfoil systems are as free of viscous effects as this one. Therefore, the inviscid code has been coupled to a boundary layer program to account for viscous effects as described in reference 3. Consideration is presently limited to airfoil systems whose boundary layers do not merge but develop independently on each of the two airfoils. Boundary layer growth is computed using standard laminar and turbulent boundary layer methods. Transition points are either input or determined from empirical criteria, and checks are made for short and long bubble laminar separation. The presence of the boundary layer is accounted for in the outer inviscid flow by employing a surface source flow formulation for the boundary conditions as described by Lighthill (reference 5). The viscous flow over the airfoil system is then computed by solving iteratively for the outer inviscid flow and the boundary layer in a self-consistent fashion. At shock waves the computed pressure is smeared over a few mesh points and at the trailing edges the displacement thickness is extrapolated from upstream. Since separation is a frequent problem in multielement airfoil systems, a crude separated flow model has been incorporated into the program to enable it to run to completion. However, results in cases where the model is implemented are not necessarily accurate.

Results of computations with the viscous program are compared in figure 8 with experimental data obtained on another slat configuration tested at a Mach number of 0.649, and angle of attack of 4.6°, and a Reynolds number of 20 million. The agreement on the slat is not very good, but turbulent separation was predicted on the lower surface. The trend in the pressure is, however, correct, and the measured trailing edge pressure value is quite close to the predicted value. Because of the slenderness of the slat, separation on this element has little effect on the main airfoil. Agreement here is much better both on the upper and on the lower surface. In particular, the theory correctly predicts the multiple peaks in the pressures that have been measured near the leading edge. The flow accelerates to supersonic velocities, goes through a shock, and then quickly reaccelerates to supersonic speeds. This pattern is seen more clearly in figure 9 where some computed Mach line contours for this case are shown. To be noted are the supersonic region spanning the entire gap with the exit of the slot essentially sonic and the sonic bubble just behind it.

DESIGN OF TWO-ELEMENT AIRFOIL SYSTEMS

An analysis program can be of great help in the design of new airfoil configurations, but even so the analytical design could be a long process. The program would have to be run repeatedly with many contour modifications to achieve the desired flow characteristics. A computer program which could solve the inverse problem would indeed be valuable. An inverse program is one that generates the airfoil system that corresponds to a given pressure or velocity distribution. The development of such a program is currently underway. The approach to the inverse problem is that described by Tranen in reference 6 for the single airfoil design. The method consists of prescribing a desired velocity distribution on a starting airfoil system. The input velocities are integrated on each of the two airfoil surfaces to get the potential on the boundaries of the computational domain. The Dirichlet problem in the annulus is then solved and the normal component of velocity on the boundaries is computed. The boundaries are not necessarily streamlines now, but the computed normal velocities at the boundaries can be used to find nearby streamlines which are taken to be sought-after contours. This procedure is repeated until the normal velocity at the boundaries is driven to zero. But convergence is very fast. In the single airfoil design three or four iterations are usually sufficient. Of course, one could elect to design only one airfoil element or pieces of one or of both elements. In such cases a mixed boundary value problem needs to be solved, but this does not entail any additional numerical difficulties.

A difficulty with airfoil design is that no full solution of the inverse problem has ever been given, even for the case of incompressible flow over a single airfoil. The problem arises because there is no assurance that a physically acceptable airfoil shape will follow from an arbitrarily prescribed pressure distribution. For a given surface pressure distribution an airfoil will generally not close at the trailing edge and the upper and lower surfaces may intersect. Provisions have to be made to allow the achievable pressure distribution to vary somewhat from the initially prescribed values to obtain closure. Also it is probably true that if we wish to design both airfoil elements completely one will not be able to specify the pressure distribution on one element without taking into account the effect on this element due to the flow characteristics required on the second element. But this situation should not arise often in practice though. More likely will be the problem of redesigning only one of the airfoils or, even more commonly, only pieces of one element. This brings about the third type of design problem to be considered. In the case of a mixed design there are some regularity conditions that must be satisfied at the point where one switches from a geometry to a velocity boundary condition. This problem, as the trailing edge closure problem, is not unique to the two-element design, but is also present in the single airfoil design. It has not been dealt with satisfactorily even in this case.

CONCLUDING REMARKS

Beyond completion of the inverse code there are additional tasks that need to be undertaken to make the tools more useful to the designer. Melnik et al. have recently developed a more rational model for the viscous trailing edge. Its implementation in the analysis would certainly be an improvement. Also the viscous analysis code would have to be generalized to take into account the possibility of the boundary layers and/or wakes from the two elements merging as might be the case where the two elements are very closely spaced. In the design problem the desirable characteristics of a pressure distribution need to be determined. Clearly one wants shocks to be weak and to eliminate, or at least reduce, boundary layer separation. A bit harder to determine is what to design for, or try to achieve, on the surfaces along the slot between the two airfoils. Experimental data would serve as a useful guideline in this task. Shortcomings of previous designs and discrepancies between data and theory can give useful indications on which are the desirable pressure characteristics and which are the undesirable ones.

APPENDIX

SYMBOLS

A	radius of point of infinity in annular domain
C_ℓ	lift coefficient
CP	pressure coefficient
C_μ	blowing coefficient
M_∞	free-stream Mach number
r	radial direction in annular domain
R	radius of inner ring corresponding to secondary airfoil in annular domain
Re	Reynolds number
α	angle of attack
θ	azimuthal direction in annular domain

REFERENCES

1. Grossman, B. and Melnik, R.E., "The Numerical Computation of the Transonic Flow Over Two-Element Airfoil Systems," Proceedings of the Fifth International Conference on Numerical Methods in Fluid Mechanics, Springer-Verlag, pp. 220-237, June 1976.

2. Grossman, B. and Volpe, G., "An Analysis of the Inviscid Transonic Flow Over Two-Element Airfoil Systems," Office of Naval Research Report ONR-CR215-241-1, June 1977.

3. Grossman, B. and Volpe, G., "The Viscous Transonic Flow Over Two-Element Airfoil Systems," AIAA paper 77-688, June 1977.

4. Ives, D.C., "A Modern Look at Conformal Mapping, Including Doubly Connected Regions," AIAA Paper 75-842, June 1975.

5. Lighthill, M.J., "On Displacement Thickness," J. Fluid Mech. vol. 4, pp. 383-392, 1958.

6. Tranen, T.L., "A Rapid Computer Aided Transonic Airfoil Design Method," AIAA paper no. 74-501, June 1974.

7. Melnik, R.E., Chow, R., and Mead, H.R., "Theory of Viscous Transonic Flow Over Airfoils at High Reynolds Number," AIAA Paper 77-680, June 1977.

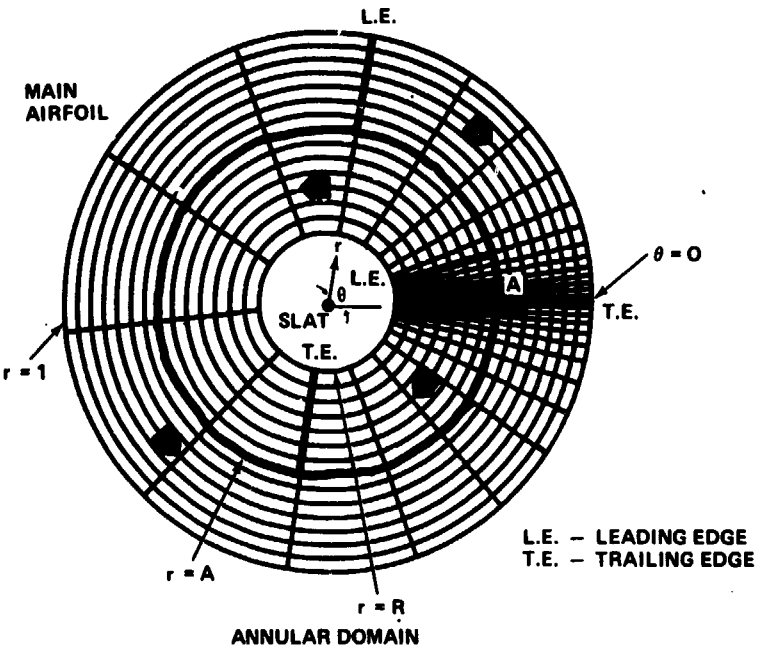

Figure 1.- Coordinate grid.

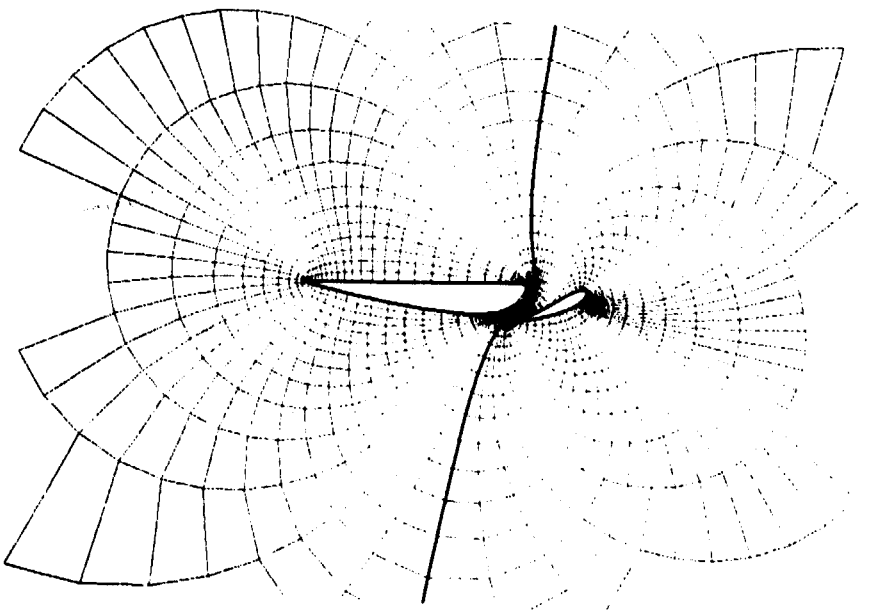

Figure 2.- Coordinate grid. Clark Y airfoil; 30 percent Maxwell slat; 10 percent gap.

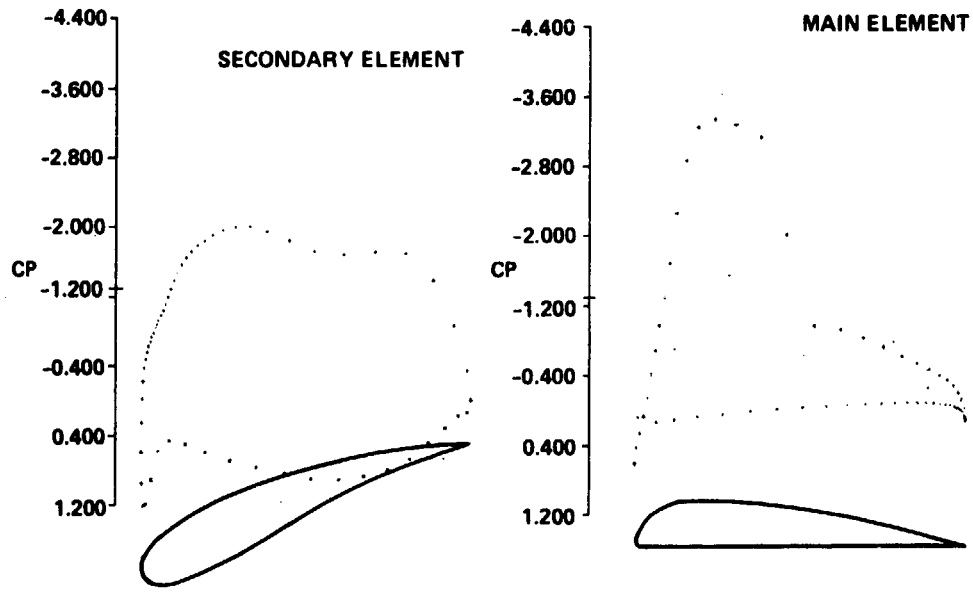

Figure 3.- Clark Y airfoil with 30 percent Maxwell slat. $M_\infty = 0.6$; $\alpha = 6°$.

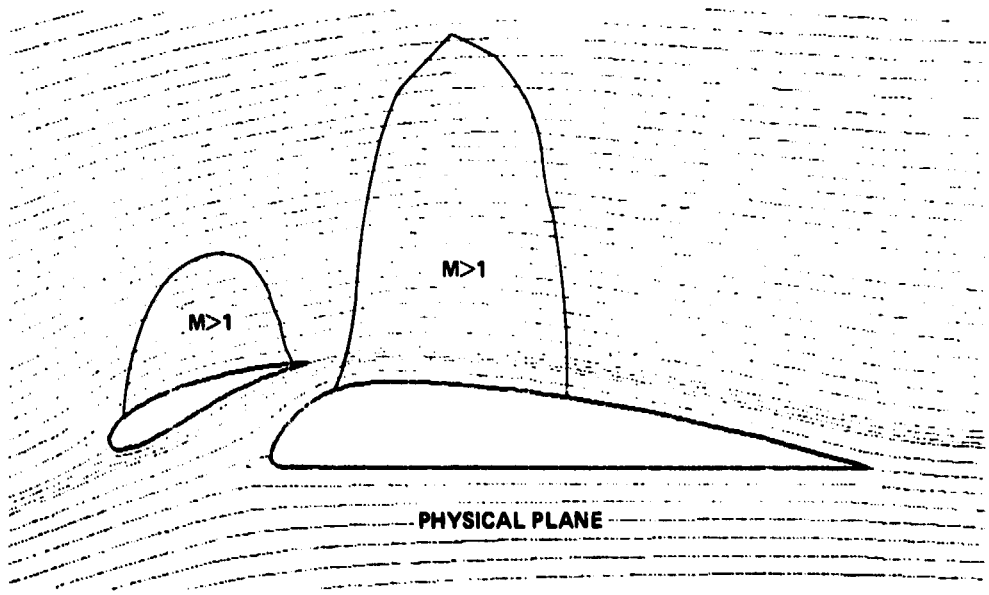

Figure 4.- Computed streamlines for Clark Y airfoil with 30 percent Maxwell slat. $M_\infty = 0.6$; $\alpha = 6°$.

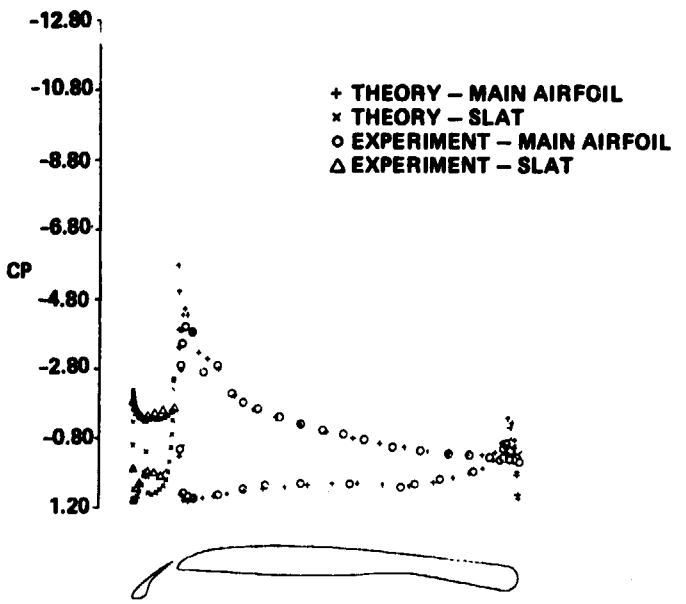

Figure 5.- Computed and experimental surface pressures on a CCW airfoil with 25° slat. $M_\infty = 0.1$; $\alpha = 12°$; $C_\mu = 0$.

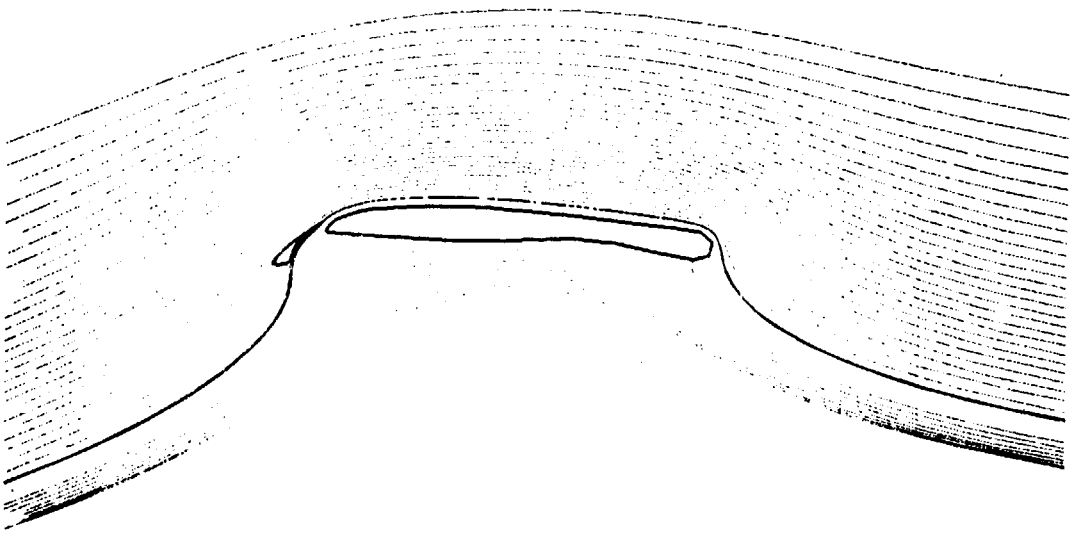

Figure 6.- Computed streamlines. CCW aifoil with 25° slat; $M_\infty = 0.1$; $\alpha = 4.6°$; $C_\mu = 0.1285$.

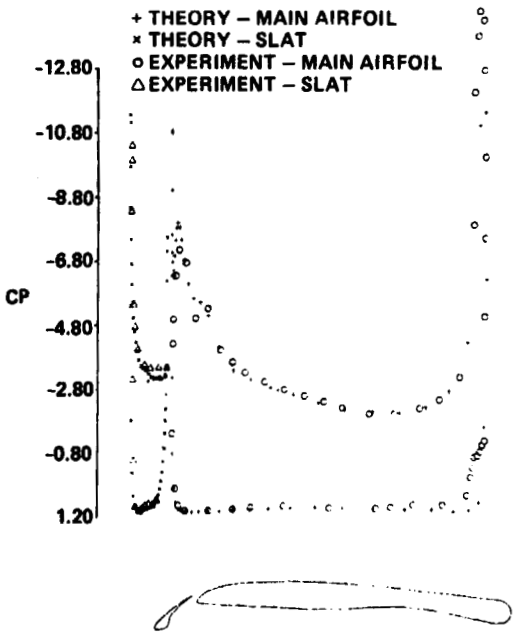

Figure 7.- Computed and experimental surface pressures on a CCW airfoil with 25° slat. $M_\infty = 0.1$; $\alpha = 4.6°$; $C_\mu = 0.1285$.

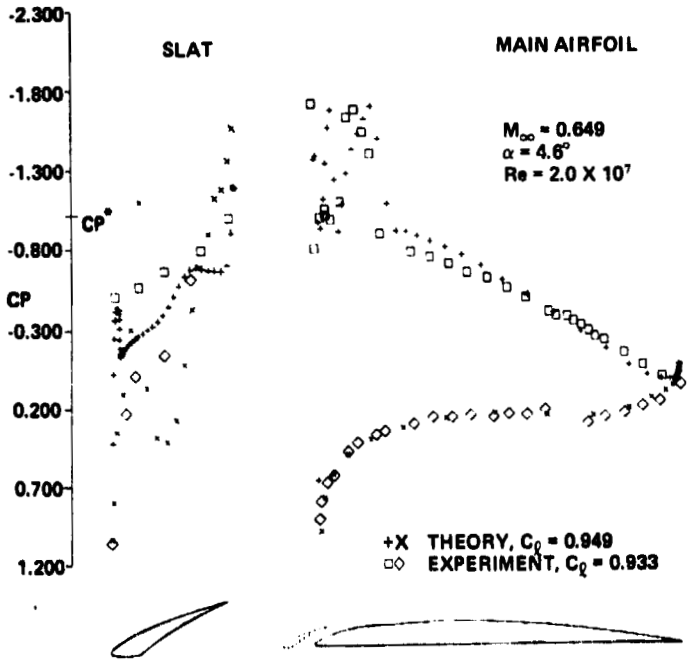

Figure 8.- Computed and experimental surface pressures on an NACA 64A406 airfoil with 7.8A slat.

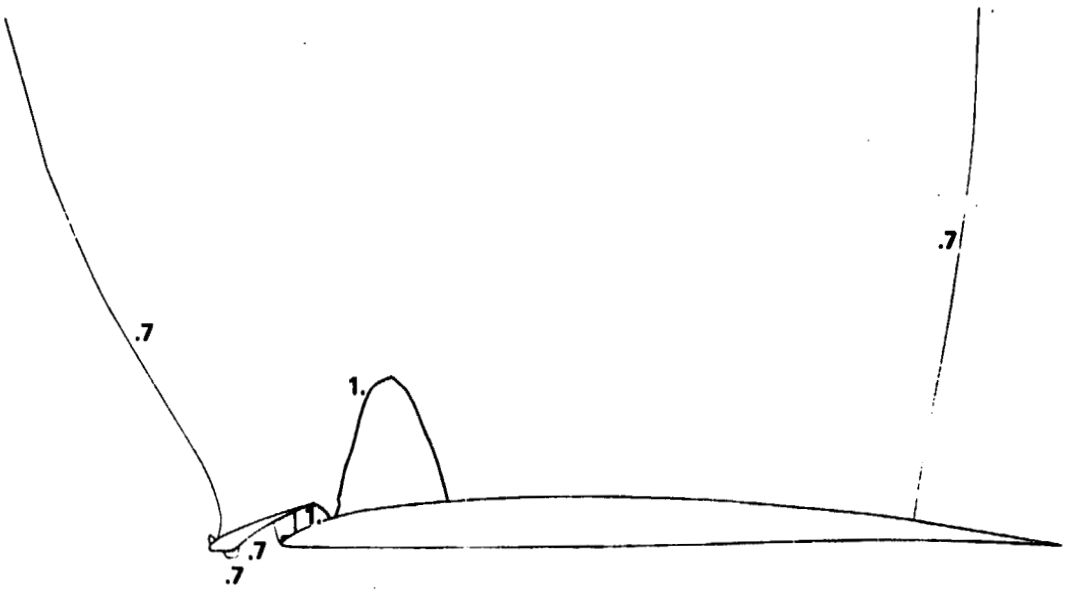

Figure 9.- Computed Mach number contours. NACA 64A406 airfoil with 7.8A slat; $M_\infty = 0.649$; $\alpha = 4.6°$.

D/3

N79-20043

13

IMPROVEMENTS IN SURFACE SINGULARITY ANALYSIS AND DESIGN METHODS

Dean R. Bristow
McDonnell Aircraft Company
McDonnell Douglas Corporation

SUMMARY

The coupling of the combined source-vortex distribution of Green's potential flow function with contemporary numerical techniques is shown to provide accurate, efficient, and stable solutions to subsonic inviscid analysis and design problems for multi-element airfoils. The analysis problem is solved by direct calculation of the surface singularity distribution required to satisfy the flow tangency boundary condition. The design or inverse problem is solved by an iteration process. In this process, the geometry and the associated pressure distribution are iterated until the pressure distribution most nearly corresponding to the prescribed design distribution is obtained. Typically, five iteration cycles are required for convergence. A description of the analysis and design method is presented, along with supporting examples.

INTRODUCTION

The surface panel method philosophy for solving arbitrary incompressible potential flow problems involves the mating of classical potential theory with contemporary numerical techniques. Classical theory is used to reduce an arbitrary flow problem to a surface integral equation relating boundary conditions to an unknown singularity distribution (Reference 1).The contemporary numerical techniques are then used to calculate an approximate solution to the integral equation (References 2-14).

All properly formulated surface panel methods are exact in the sense that the difference between the approximate numerical solution and the exact solution to the integral equation can be made arbitrarily small at the expense of increasing the number of computations. This does not imply that all panel methods are equally successful. Indeed, vast differences exist with respect to prediction accuracy versus computational effort, reliability, simplicity, and applicability to an inverse solution mode for design problems.

The major distinguishing characteristics of panel methods are depicted in Figure 1. For the special case of two-dimensional flow, nearly all the possible combinations of Figure 1 have been formulated and tested at McDonnell Aircraft Company (MCAIR). The most successful of the tested formulations was selected as the foundation for the MCAIR Multi-Element Airfoil Analysis and Design Computer Program, herein after designated the MCAIR Airfoil Program. The analysis (direct) mode calculates the velocity distribution of an arbitrary airfoil geometry, whereas the design (inverse) mode iterates to generate the geometry most nearly corresponding to a prescribed surface velocity distribution. Unusually rapid and consistent convergence is obtained because the inverse algorithm includes all the first order terms in the relationship between arbitrary geometry and velocity perturbations.

This paper presents background theory, the formulation, and representative numerical solutions for the MCAIR Airfoil Program.

NOMENCLATURE

c_ℓ	Airfoil lift coefficient
c_p	Pressure coefficient $[1 - (\frac{V}{V_\infty})^2]$
$\vec{n}$	Unit normal vector to a boundary
$\vec{V}$	Flow velocity
γ	Vortex density
μ	Doublet density
σ	Source Density

SUBSCRIPTS

E	External (fluid) side of a boundary
I	Internal side of a boundary
N	Normal component
T	Tangential component
∞	Free stream conditions

SURFACE SINGULARITY THEORY

Any three-dimensional, incompressible, potential flow field can be considered to be induced by a suitable distribution of source and doublet singularity densities on flow boundary surfaces (Reference 1). It is usually convenient to treat the flow field as the sum of a uniform free stream $\vec{V}_\infty$ plus a disturbance potential field associated with the presence of the body (Figure 2). Then the total velocity $\vec{V}$ at any field point can be expressed as

$$\vec{V} = \vec{V}_\infty + \vec{\nabla}\phi \tag{1}$$

where ϕ is the potential of the disturbance field.

The value of ϕ at an arbitrary field point P can be expressed in the following form:

$$\phi = \frac{1}{4\pi} \iint \left\{ -\frac{\sigma}{r} + \mu \frac{\partial}{\partial n} \left(\frac{1}{r}\right) \right\} ds \qquad (2)$$

where ds is a differential area element at arbitrary surface point Q of the body; r is the distance to point P; n is the distance measured along an axis normal to the body surface at Q, positive outward; and σ and μ are functions of location on the body surface, i.e., functions of Q. σ and μ are respectively the source and doublet densities.

For two-dimensional flow, it is generally more convenient to use vortex singularities in place of doublets. As is proved in Reference 4, a surface doublet distribution of density μ can be replaced by an equivalent vortex distribution where the vortex density vector $\vec{\gamma}$ satisfies the following equation at each surface point:

$$\vec{\gamma} = \vec{n} \times \vec{\nabla}\mu \qquad (3)$$

$\vec{n}$ is the local unit normal vector pointing into the flow field.

It is noteworthy that there is no limit to the number of different solution source - vortex distributions corresponding to any given flow field. The theoretical distinction between the different distributions is best illustrated by examining the imaginary flow field internal to the boundaries (Figure 3). Consider two-dimensional flow. The discontinuity across any surface sheet of sources and vortices can be expressed as follows:

$$V_{N_E} - V_{N_I} = \sigma \qquad (4)$$

$$V_{T_E} - V_{T_I} = \gamma \qquad (5)$$

where σ and γ are the local source and vortex densities. For solid body boundary conditions ($V_{N_E} = 0$), Equation (4) indicates that a vortex-only solution will correspond to $V_{N_I} = 0$ at every internal boundary point. The unique internal flow field generated by zero normal velocity boundary conditions is, of course, stagnation. Then Equation (5) indicates that $V_{T_E} = \gamma$ everywhere on the external surface.

A particularly useful combined source-vortex distribution corresponds to the uniform internal flow field $\vec{V}_I = \vec{V}_\infty$. For this case, Equations (4) and (5) imply that the source and vortex densities are equal to the external perturbation velocity components, i.e.,

$$V_N = V_{N_\infty} + \sigma \qquad (6)$$

$$V_T = V_{T_\infty} + \gamma \qquad (7)$$

Subscript E has been omitted for brevity. The above combined source-vortex distribution is equivalent to the application of Green's third identity (Reference 15) to the perturbation potential ϕ. A schematic of Equations (6) and (7) is presented in Figure 4.

An illustration of the nature of three different singularity distributions corresponding to the same potential field is presented in Figure 5. The theoretical singularity distributions for a source solution, vortex solution, and the combined Green's identity source-vortex solution are shown for the flow around an infinite circular cylinder with flow tangency boundary conditions. It is interesting that the combined source-vortex distribution is a fifty percent blend of the source only and vortex only solutions. Green's identity typically provides a source distribution more mild than the source only solution and a vortex distribution more mild than the vortex only solution.

The combined source-vortex distribution of Green's identity is especially suitable for application to a numerical panel method. The equality between singularity densities and disturbance flow velocity means that regardless of either boundary conditions or geometry, the singularity magnitudes cannot become disproportionately large. This contrasts sharply with source only solutions, for which the source density can increase without bounds as body thickness approaches zero even though the velocity remains finite everywhere. The practical significance is that the mild source-vortex distributions associated with Green's identity eliminate excessive velocity gradients between boundary condition control points, thereby reducing the possibility of leakage. The relationships between disturbance flow velocity and singularity density holds regardless of boundary conditions, be they Neumann, Dirichlet, or mixed. These relationships can always be used to eliminate half the unknown singularity densities a priori, leaving no more effective unknowns that a source only or vortex only approach.

TWO-DIMENSIONAL SOLUTION FORMULATION

The present formulation is based on the combined source-vortex distribution of Green's identity (Equations 6 and 7). Low order panel modeling is employed to the effect that source gradient and surface curvature corrections on each panel are ignored. However, the use of internal potential boundary conditions and the application of the velocity - singularity strength equality results in close to higher order prediction accuracy for most practical geometric shapes. The advantage of the low order modeling is the simplicity inherent in establishing inverse capability.

The geometry of each airfoil element is simulated by a closed polygon, where the polygon segment end points are assumed to lie on the actual airfoil. The midpoint of each segment (panel) is selected as the boundary condition control point.

For Neumann prescribed normal velocity boundary conditions, the source density distribution is established a priori from Equation (6). It is assumed that the source density is uniform on each panel.

The gist of the solution to analysis problems is to determine the appropriate vortex distribution. The vortex density is assumed to vary linearly on each panel and to be continuous at panel end points, with one exception. If the geometry has any slope discontinuities such as a sharp trailing edge, the vortex density is allowed to be discontinuous at the corresponding panel end point. This is consistent with exact theoretical solutions, for which

corners are reflected as discontinuities in the vortex distribution. The magnitude of the discontinuity is an additional unknown which is determined through the introduction of an internal boundary condition control point near the corner. The distance from the corner is nominally selected as 1% of the local panel length.

Instead of directly imposing prescribed normal velocity boundary conditions at the control points, a theoretically equivalent approach first applied by Morino, et al (Reference 13) is used. Consistent with the internal velocity field $\vec{V}_I = \vec{V}_\infty$, uniform internal perturbation potential is prescribed at each control point of an airfoil element. In the present two-dimensional formulation, this is easily accomplished by specifying that the analytical line integral of perturbation velocity component along an internal path connecting adjacent control points be zero.

The circulation of each airfoil element is controlled by either of two methods at the discretion of the user. First, the net vortex strength can be prescribed directly. Alternately, a Kutta condition can be applied in which the velocity normal to the trailing edge bisector is set equal to zero at a location approximately 2% local segment length downstream. The nominal 2% value has been selected because it consistently provides lift coefficient prediction accuracy that agrees within 1% of the virtually exact conformal solution of Catherall et al. (Reference 16) for typical panel models.

Imposition of the potential boundary conditions and one circulation control equation per airfoil element establishes a system of linear equations with the same number of unknown vortex densities as equations. This number is equal to the sum of the total number of panels and total number of sharp corners. Solution to the system renders the complete set of singularities known.

At each control point, the surface velocity is calculated from Equation (7) and, for steady state flow, the pressure distribution is calculated by Bernoulli's equation

$$c_p = 1 - \left(\frac{V_T}{V_\infty}\right)^2 - \left(\frac{V_N}{V_\infty}\right)^2 \qquad (8)$$

Force and moment integration is performed under the assumption that the control point pressure applies uniformly to each panel.

Inverse solutions are generated in accordance with the iterative-linearization philosophy developed in Reference 17. For the elements to be designed in a multi-element airfoil system, the following steps are involved:

(1) The user prescribes a design pressure or velocity distribution around the surfaces of the various elements.

(2) The user prescribes a starting geometry to initialize the calculations and the location of one point per element to be fixed in space, such as the trailing edge.

(3) The program solves the direct problem for the geometry, in order to determine the change in velocity distribution required to achieve the prescribed values.

(4) The program calculates the rate of change of surface velocity with respect to an arbitrary change in surface angle distribution. Each element perimeter remains fixed. If the tangential component of velocity at the control point of the ith panel is designated V_{T_i} and if the surface angle of the jth panel is designated θ_j, then the array A_{ij} is calculated where

$$A_{ij} = \frac{\partial V_{T_i}}{\partial \theta j}$$

(5) The change in surface angle distribution is calculated in accordance with the prescribed velocities and the following first order expression:

$$\Delta V_{T_i} \tilde{=} \sum_j (A_{ij} \Delta\Theta_j)$$

(6) The geometry is corrected by the program and steps (3)- (5) are repeated as a series of iteration cycles.

The most difficult and important step in formulating the inverse capability is to generate the matrix A_{ij}. It is noted that all terms were incorporated in deriving the partial derivative, including singularity strength changes and the displacement of panels j+1, j+2, etc. corresponding to the surface angle change $d\Theta_j$. The corresponding singularity strength changes are obtained by a first order expansion to the boundary condition equation. In order to obtain numerical stability in the inverse process, the velocities are prescribed not only at the panel midpoints but at endpoints as well. Then the solution involves minimizing the mean square error between the prescribed and calculated distributions.

EXAMPLE SOLUTIONS

The following examples demonstrate the numerical behavior of the present MCAIR Airfoil Program as compared to alternate approaches.

The benefits of using a combined source-vortex distribution versus source-only is improved accuracy for (1) thin highly loaded airfoils and for (2) sharp concave corners. Examples of the former are presented in Reference 14 and are not repeated here. The latter is typical of wing-fuselage intersections and is represented by the wedge-cylinder example of Figure 6. Both

the present method and the Douglas Neumann source method (Reference 2) were applied to the geometry using identical panel modeling (244 panels). The results are virtually identical except near the sharp concave corner, in which region the source solution diverges while the present solution properly approaches stagnation.

The advantage of the internal potential boundary conditions is reflected in the calculated pressure distribution for the Karman-Trefftz airfoil of Figure 7. In each of the three calculated panel method distributions, the combined source-vortex distribution of Green's identity was applied and the exact lift coefficient from the Catherall-Sells solution was prescribed. Converting from the direct imposition of zero normal velocity boundary conditions to prescribed internal perturbation potential generates the same type of accuracy improvement as obtained by applying higher order corrections for source gradient and panel curvature effects. For each of the three panel method solutions, the conversion from calculated singularity density to surface velocity was conducted by the most accurate approach, namely, Equation (7) for potential boundary conditions and the summation of influence coefficients for flow tangency.

The third example demonstrates prediction accuracy of the MCAIR method for one of the few two-element airfoils for which an exact conformal mapping solution is available for comparison (Reference 18). Using a total of 66 panels, the geometry and calculated pressure distributions at zero incidence are presented in Figure 8. The agreement with the exact solution is good, including the calculated lift corresponding to the trailing edge bisector Kutta condition.

The objective of the first inverse example is to design a circular cylinder by the MCAIR method using a nearly flat plate for the starting geometry (Figure 9). The exact analytical surface velocity distribution was prescribed, and the converged solution geometry of Figure 9 was obtained after four iteration cycles. The panel endpoints are within a maximum distance of 0.002 radius of lying on a circle. The complete partial derivatives of velocity with respect to surface angle change were necessary but not sufficient for obtaining convergence about the periphery of this example. The use of mild combined source-vortex singularites is also a factor. To illustrate, the example was repeated, but this time vortex-only singularities were used to induce the flow field in accordance with the analysis method of Dvorak and Woodward (Reference 7). The geometry never converged (Figure 10) but oscillated $\pm 30^{\circ}$ in the leading edge region from one iteration cycle to the next.

The final example demonstrates inverse solution capability for the two-element Williams airfoil presented earlier in Figure 8. The starting geometry of Figure 11 was used to initialize the calculations, and the calculated surface velocity distribution of Figure 8 was prescribed on both elements. The geometry converged and agreed with the target geometry to within a tolerance of one-tenth of one degree in five iterations (Figure 11).

The above examples are typical of the accuracy and numerical stability of the MCAIR Airfoil Program. On the CDC CYBER 173, a two-element airfoil

analysis solution using 70 panels total requires approximately 4 seconds computing time. For the corresponding inverse solution, approximately 20 seconds is required per iteration cycle.

CONCLUDING REMARKS

The use of the source-vortex distribution of Green's identity coupled with internal perturbation potential boundary conditions provides a simple, accurate, reliable, and efficient procedure for solving airfoil incompressible potential flow problems. For a wide range of geometric shapes, low order paneling modeling generates prediction accuracy usually associated with higher order solutions. The procedure is especially suitable for application to inverse design problems.

REFERENCES

1. Lamb, Sir Horace, Hydrodynamics, 6th Edition, Cambridge University Press, 1932.

2. Hess, J.L. and Smith, A.M.O., "Calculation of Potential Flow About Arbitrary Bodies," Progress in Aeronautical Sciences, Vol. 8, Pergamon Press, New York, 1966.

3. Hess, J.L., "Higher-Order Numerical Solution of the Integral Equation for the Two-Dimensional Neumann Problem," Computer Methods in Applied Mechanics and Engineering, Vol. 2, No. 1, February 1973.

4. Hess, J.L., "Calculation of Potential Flow about Arbitrary Three-Dimensional Lifting Bodies," MDC Report J5679-01, October 1972.

5. Martensen, E., "Berechnung der Druckverteilung an Gitterprofilen in Ebener Potentialstromung mit einer Fredholmschen Integralgleichung," Archive for Rational Mechanics and Analysis, Vol. 3, No. 3, 1959.

6. Oellers, H.J., "Die Inkompressible Potentialstromung in der Ebener Gitterstuffe," Jahrbuch 1962 der Wissenschaftlichen Gesellschaft fur Luft-und Raumfahrt, pp. 349-353.

7. Dvorak, F.A., and Woodward, F.A., "A Viscous/Potential Flow Interaction Analysis Method for Multi-Element Infinite Swept Wings," NASA CR-2476, November 1974.

8. Stevens, W.A., Goradia, S.H., and Braden, J.A., "Mathematical Model for Two-Dimensional Multi-Component Airfoils in Viscous Flow," NASA CR-1843, July 1971.

9. Halsey, N.D., "Methods for the Design and Analysis of Jet-Flapped Airfoils," AIAA Paper No. 74-188, February 1974.

10. Maskew, B., "A Subvortex Technique for the Close Approach to a Discretized Vortex Sheet," Vortex-Lattice Utilization Workshop, NASA Langley Research Center, May 1976.

11. Tulinius, J.R., "Theoretical Prediction of Thick Wing and Pylon-Fuselage-Fanpod-Nacelle Aerodynamic Characteristics at Subcritical Speeds," NASA CR137578, July 1974.

12. Johnson, F.T., and Rubbert, P.E., "Advanced Panel-Type Influence Coefficient Methods Applied to Subsonic Flows," AIAA Paper 75-50, January 1975.

13. Chen, L.T., Suciu, E.O., and Morino, L., "A Finite Element Method for Potential Aerodynamics Around Complex Configurations," AIAA Paper 74-107, January 1974.

14. Bristow, D.R., "Recent Improvements in Surface Singularity Methods for the Flow Field Analysis About Two-Dimensional Airfoils," AIAA Paper 77-641, June 1977.

15. Kellogg, O.D., Foundations of Potential Theory, Dover Publications, Inc., New York, 1953, p. 219.

16. Catherall, D., Foster, D.N., and Sells, C.C.L., "Two Dimensional Incompressible Flow Past a Lifting Aerofoil," R.A.E. TR-69118, 1969.

17. Bristow, D.R., "A New Surface Singularity Method for Multi-Element Airfoil Analysis and Design," AIAA Paper 76-20, January 1976.

18. Williams, B.R., "An Exact Test Case for the Plane Potential Flow About Two Adjacent Lifting Aerofoils," Aeronautical Research Council R&M No. 3717, September 1971.

TABLE 1.- MODIFICATIONS OF THE SUBROUTINES IN THE BASELINE VERSION

Subroutine	No change	Minor change	Major change	Delete
MAIN			X	
POINT	X			
SLOPE	X			
TRANS			X	
DISTP	X			
FTLUD				X
DIR	X			
LSQ				X
PROOT	X			
MAIN1			X	
READIT		X		
GEOM			X	
ROTRAN			X	
ASLOT			X	
NORMAL			X	
MAIN 2			X	
CHEN			X	
MATRIX			X	
POTLF			X	
CAMBER				X
SMOOTH	X			
VOVBT				X
THICK				X
COMPR			X	
STAG			X	
MAIN 3			X	
LOAD			X	
LAMNA		X		
BLTRAN		X		
TURBL		X		
TURB		X		
DERIV		X		
START		X		
CONFBL				X
CONF 5				X
CONF 7		X		
CONF 8		X		
DLIM	X			

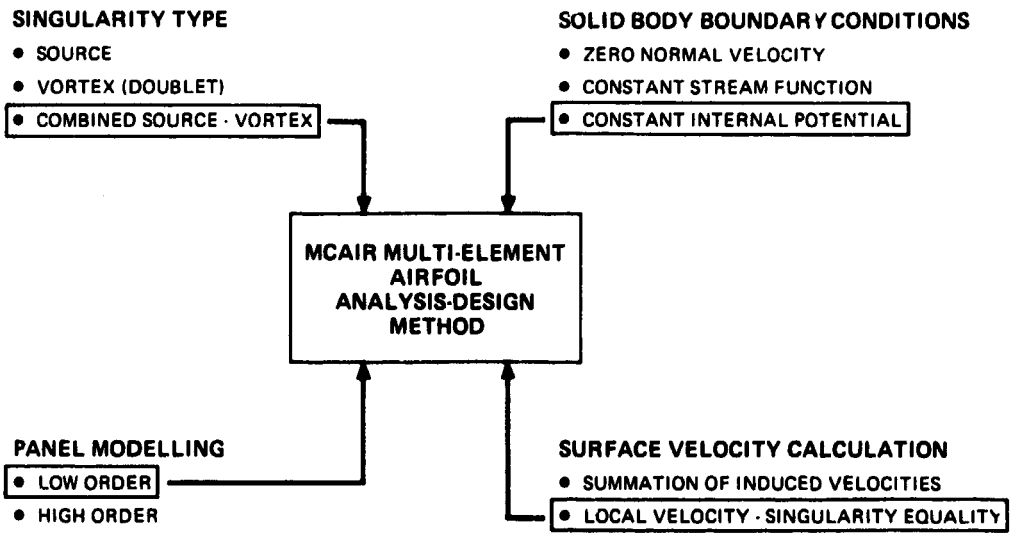

Figure 1.- Diagram of surface singularity panel methods for incompressible, potential flow.

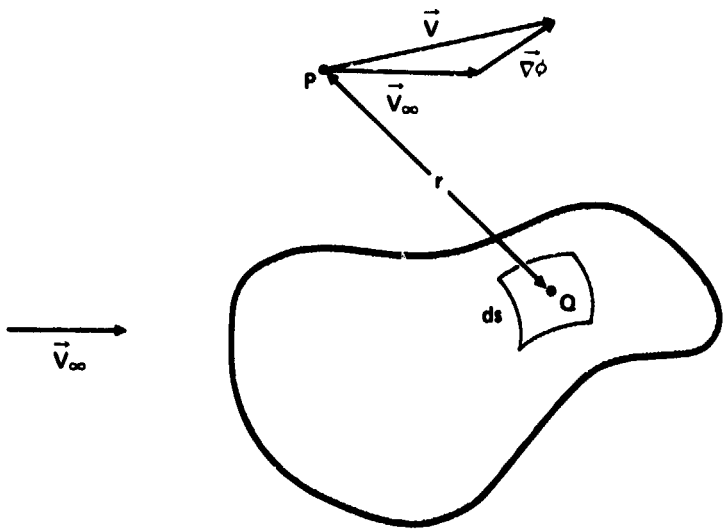

Figure 2.- Body immersed in an unbounded flow field.

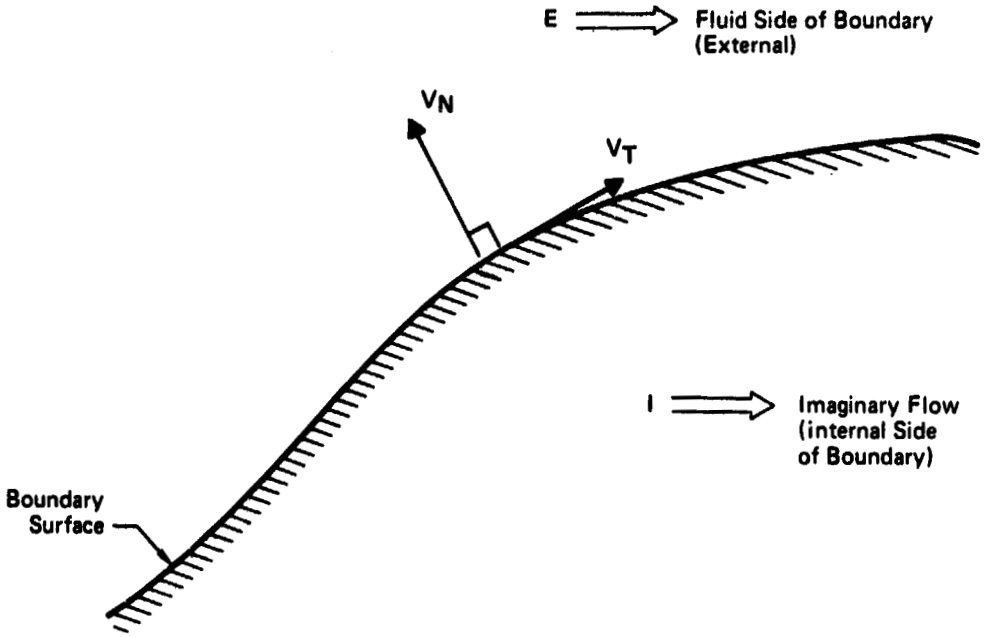

Figure 3.- Two sides of a flow boundary surface.

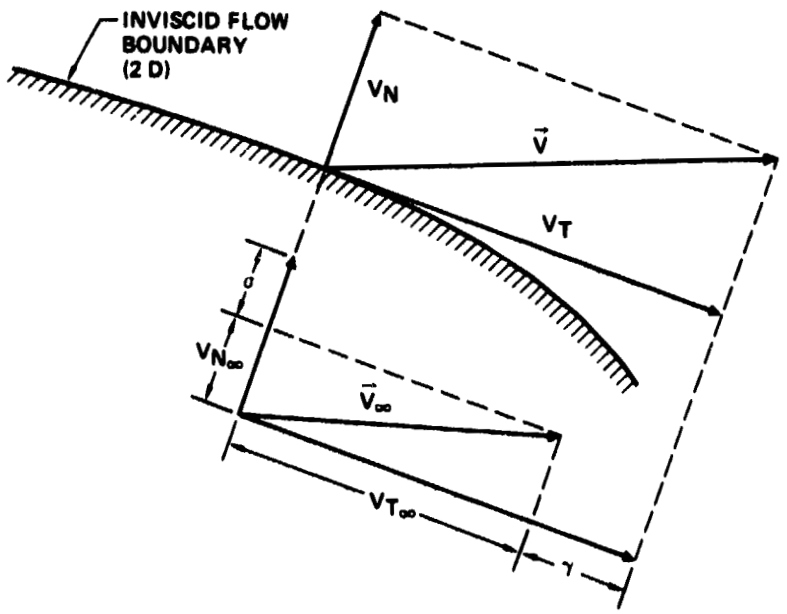

Figure 4.- Green's identity velocity-singularity relationship.

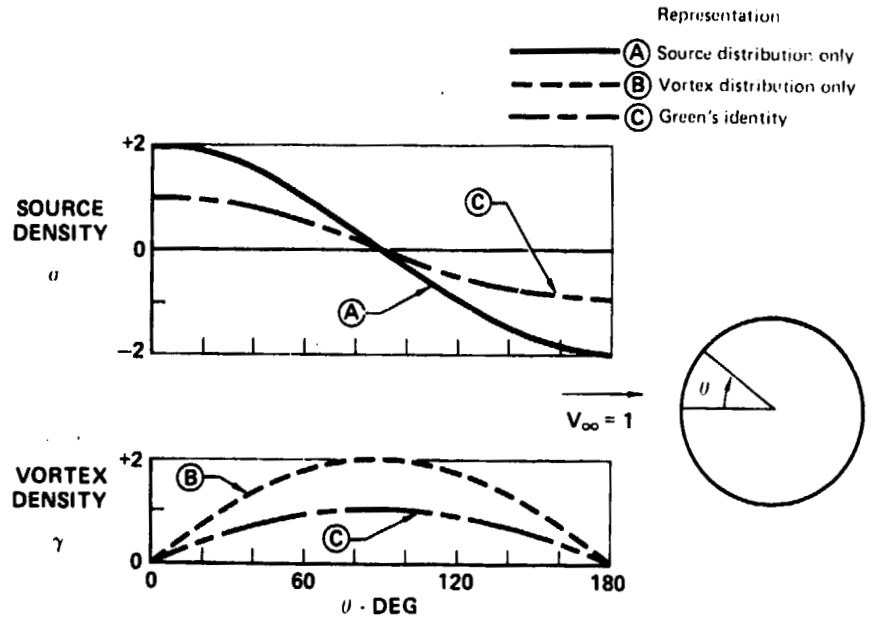

Figure 5.- Equivalent singularity representations for a circular cylinder.

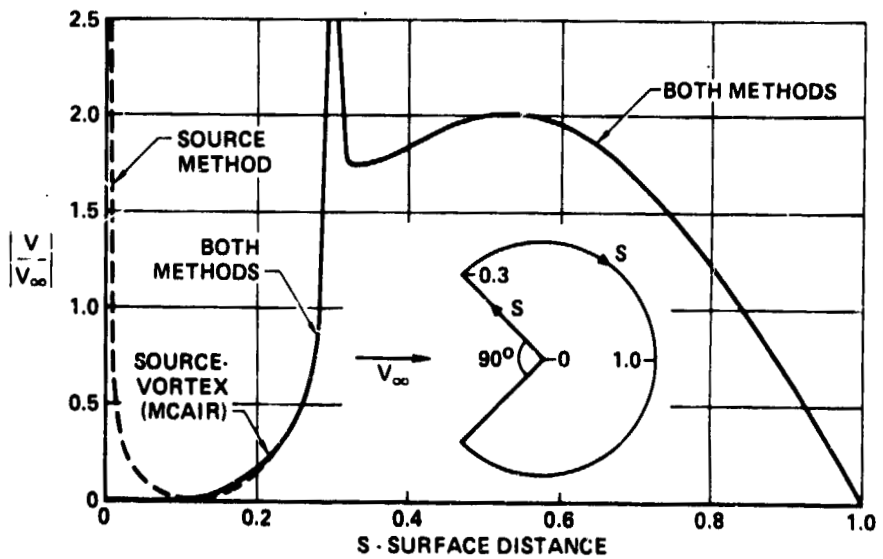

Figure 6.- Comparisons of source and source-vortex solutions. Concave corner flow.

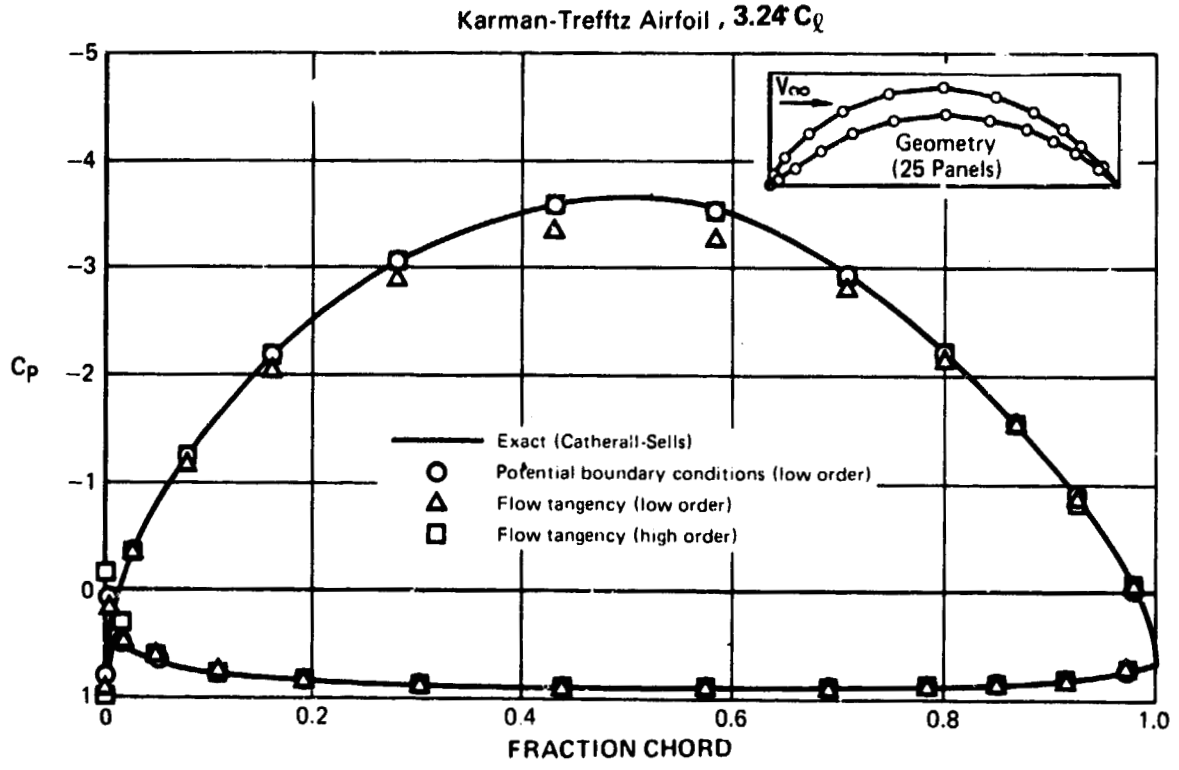

Figure 7.- Effect of panel modeling and boundary conditions.

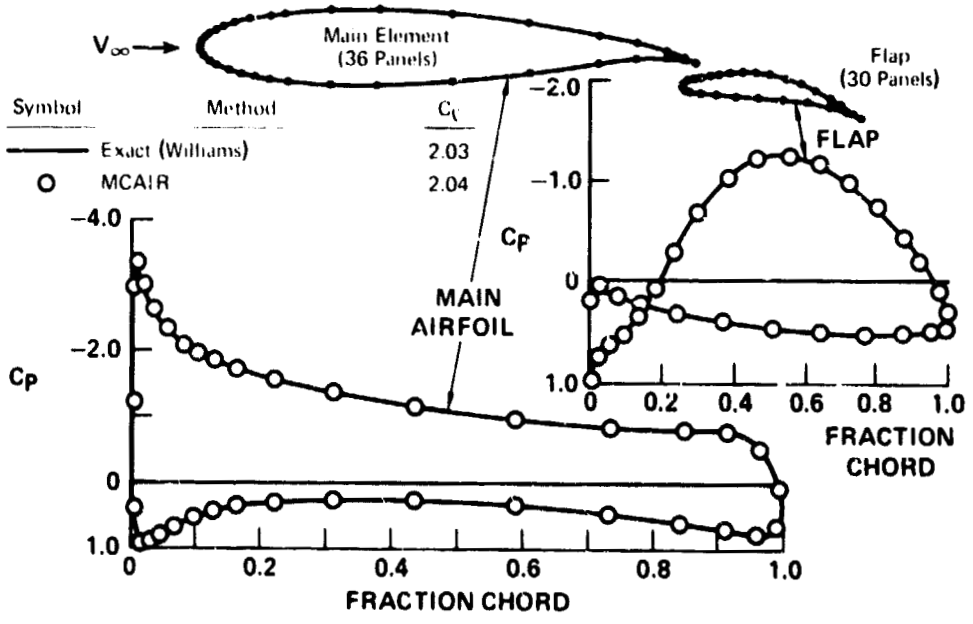

Figure 8.- Two-element airfoil solution. MCAIR method.

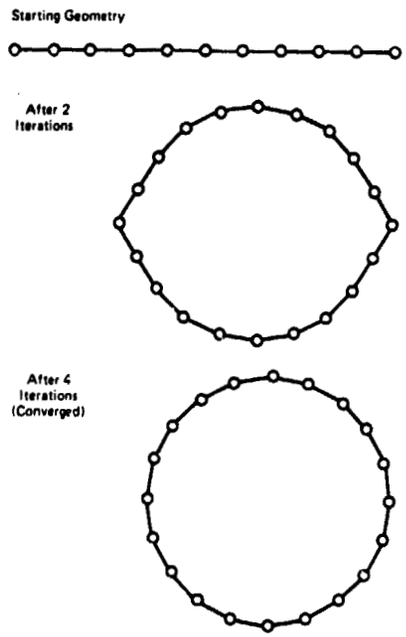

Figure 9.- Circular-cylinder inverse solution. MCAIR method.

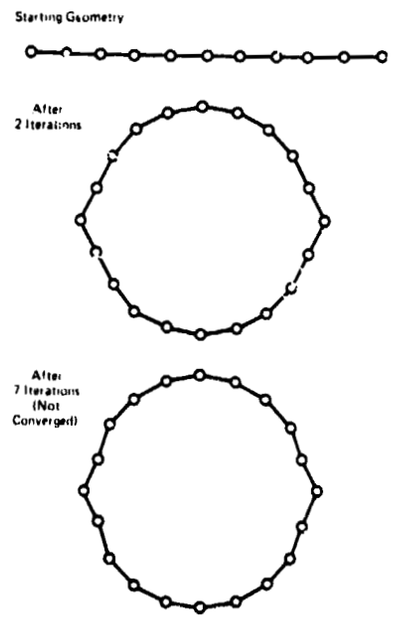

Figure 10.- Circular-cylinder inverse solution.
Vortex-only method.

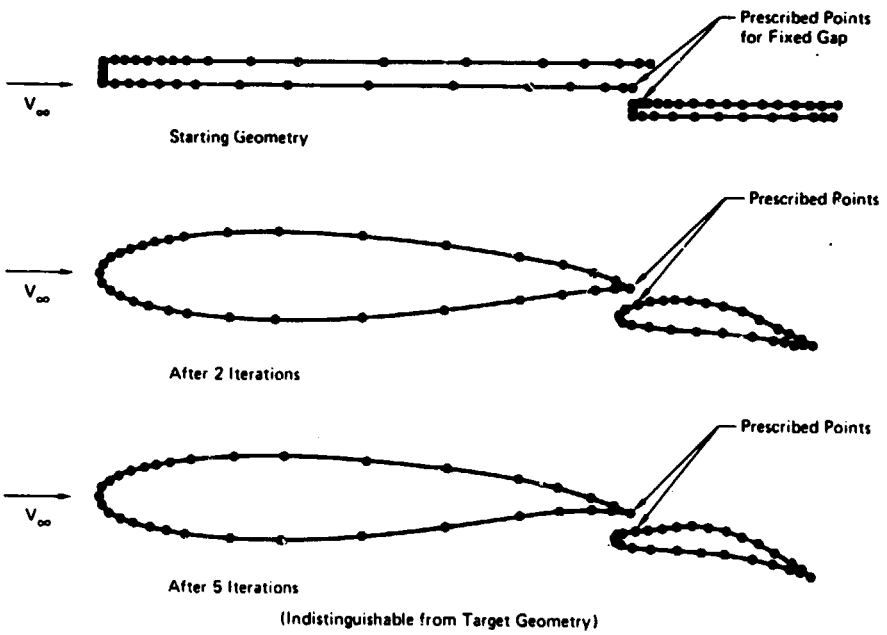

Figure 11.- Two-element airfoil inverse solution.
MCAIR method.

OPTIMIZATION OF MULTIELEMENT AIRFOILS FOR MAXIMUM LIFT

14

Lawrence E. Olson
NASA Ames Research Center
and
Aeromechanics Laboratory
U. S. Army Aviation R & D Command

SUMMARY

Two theoretical methods are presented for optimizing multielement airfoils to obtain maximum lift. The analyses assume that the shapes of the various high-lift elements are fixed. The objective of the design procedures is then to determine the optimum location and/or deflection of the leading- and trailing-edge devices. The first analysis determines the optimum horizontal and vertical location and the deflection of a leading-edge slat. The structure of the flow field is calculated by iteratively coupling potential-flow and boundary-layer analysis. This design procedure does not require that flow separation effects be modeled. The second analysis determines the slat and flap deflection required to maximize the lift of a three-element airfoil. This approach requires that the effects of flow separation from one or more of the airfoil elements be taken into account. The theoretical results are in good agreement with results of a wind-tunnel test used to corroborate the predicted optimum slat and flap positions.

INTRODUCTION

To achieve acceptable takeoff and landing performance, modern fixed-wing aircraft typically use mechanical high-lift devices such as leading-edge slats and slotted flaps. An essential step in the development of high-lift wings is the determination of the position (horizontal location, vertical location, and deflection) of the slat and/or flaps required to maximize aerodynamic performance. Theoretical methods which predict the optimum position of slats and flaps for multicomponent airfoils are being developed to: (1) reduce the number of high-lift configurations which must be evaluated experimentally; (2) reduce substantially the amount of wind-tunnel testing required to optimize a multicomponent airfoil; and (3) insure that experimentally determined optimums are true optimums. Two criteria generally used to evaluate the performance of a high-lift airfoil are maximum lift coefficient ($C_{\ell_{max}}$) and maximum lift to drag ratio $(C_\ell/C_d)_{max}$ at a given lift coefficient. This paper addresses the problem of optimization for maximum lift. At present, drag is not considered a criterion in the theoretical optimization method because the drag of multielement airfoils cannot be predicted accurately.

Configuration optimization of multielement airfoils for maximum lift is separable into two general classes of problems. This classification depends on the level of sophistication required of the aerodynamic analysis to determine the structure of the flow field and to evaluate the airfoil performance. Configurations which can be optimized without modeling the effects of flow separation are called Class 1 design problems. Configuration optimization which requires that the effects of flow separation be modeled are called Class 2 problems. For Class 1 optimization, viscous effects are determined by an analysis based on laminar and turbulent boundary-layer flows on the various airfoil surfaces. This type of analysis is simpler, requires less computation effort, and is generally more reliable than the separated flow modeling techniques required for Class 2 problems.

Section I outlines the aerodynamic analysis including a brief description of the separated flow model. The Class 1 design procedure is then used in Section II to determine the optimum position of a leading-edge slat. Optimization of the deflection angles of a slat and of a slotted flap for a three-element configuration is presented as a Class 2 design problem in Section III. Section IV briefly describes the experimental study conducted to obtain data for verification of the analysis techniques presented in this paper, and Section V compares theory with experiment for both optimization methods.

SYMBOLS

A wing area = cb

AR wing aspect ratio = b^2/A

b wing span

c airfoil reference chord = 1.7 m

C_d section drag coefficient = $\dfrac{\text{airfoil drag}}{(1/2)\ \rho_\infty U_\infty^2 c}$

C_f skin-friction coefficient at the upper surface trailing edge of airfoil component

C_ℓ airfoil lift coefficient = $\dfrac{\text{airfoil lift}}{(1/2)\ \rho_\infty U_\infty^2 c}$

C_L wing lift coefficient = $\dfrac{\text{wing lift}}{(1/2)\ \rho_\infty U_\infty^2 A}$

C_p airfoil surface pressure coefficient = $\dfrac{p-p_\infty}{(1/2)\ \rho U_\infty^2}$

p static pressure

Re reference chord Reynolds number = $\dfrac{U_\infty c}{\nu}$

s	chordwise distance along airfoil surface (measured from stagnation point)
s^*	dimensionless distance from separation point (eq. (6))
u	s-direction velocity component at outer edge of boundary layer
U_∞	free-stream velocity
v	velocity component normal to airfoil surface
x,y	horizontal and vertical coordinates in coordinate system of main airfoil
α	angle of attack, deg
δ	component deflection, deg
ν	kinematic viscosity
ρ	fluid density
τ_w	wall shear stress

Subscripts:

f	flap
m	main element
s	slat
∞	free stream

I. AERODYNAMIC ANALYSIS

General Comments

The objective of the theoretical analysis is to determine the position of a high-lift element (or elements) required to achieve maximum lift. Up to three design variables are required to specify position of each element. These position variables plus the angle of attack of the overall configuration result in a multidimension design space which is searched to determine the optimum position. As a result, not only must the aerodynamic analysis accurately predict the flow-field structure for a wide variety of configurations, but it must also be computationally efficient if the optimization technique is to be a useful design tool. It should be noted that the primary objective of the theoretical analysis is to determine the position of a high-lift element (or elements) required to achieve maximum lift.

Although the present analysis should give a reasonable estimate of the maximum lift coefficient of an optimized configuration, a more accurate computation of $C_{\ell_{max}}$ will be the subject of future study.

Potential-Flow Calculation

The potential-flow calculation is a singularity method where each of the airfoil contours (fig. 1) is represented by a large number (from 40 to 80) of straight line segments. A linear distribution of vorticity is placed on each of these segments. The present potential-flow analysis (ref. 1) not only provides the accurate surface pressure distributions required for subsequent boundary-layer analyses, but it is also computationally efficient. This efficiency is essential because a typical optimization calculation requires from 200 to 500 potential-flow solutions to complete the design procedure.

Boundary-Layer Analysis

The structure of the laminar, transitional, and turbulent boundary layers is calculated using the pressure field determined from the potential-flow analysis. For the three-element configuration considered in this study, a complete optimization calculation requires between 500 and 2000 solutions for conventional boundary layers such as those on the upper and lower surface of the leading-edge slat shown in figure 1. The need for computational efficiency resulted in the selection of the finite-difference method of Blottner (ref. 2) for solving the boundary-layer equations. The correlations of Smith (ref. 3) are used to determine the point of laminar instability. The transitional and turbulent boundary-layer eddy viscosity model of Cebeci (ref. 4) and Cebeci, Kaups, Mosinakis and Rehn (ref. 5) is then used to calculate Reynolds stresses. If laminar boundary-layer separation occurs, the empirical criteria of Gaster (ref. 6) is used to determine whether turbulent reattachment occurs. If reattachment is indicated, the calculation is continued as a turbulent boundary layer. If the criterion of Gaster indicates catastrophic flow separation, the boundary-layer calculation is terminated. A boundary-layer calculation of this type takes only 0.1 to 0.2 sec on the CDC 7600 computer.

The structure of the confluent boundary layer on the flap upper surface (fig. 1) is determined using the finite difference method of reference 7, a method which takes from 20 to 30 sec on the CDC 7600 computer for each confluent-boundary-layer calculation.

Potential-Flow/Boundary-Layer Coupling

The effect of boundary-layer displacement and entrainment on the inviscid flow is simulated by linear source distributions (fig. 1) placed on the straight line segments used to define the airfoil contours. The strength of the source distribution is equal to $d(u_e\delta^*)/ds$ where u_e is the velocity

at the edge of the boundary layer, δ^* is the local boundary-layer displacement thickness, and s is the arc length measured along the airfoil surface. This type of potential-flow/boundary-layer coupling is particularly useful when optimizing the position of high-lift devices because the displacement effect of any particular boundary layer can conveniently be "frozen." For example, the boundary layer on the lower surface of the flap (fig. 1) is not appreciably affected by changes in the leading-edge slat position. Therefore, the flap lower-surface boundary layer need only be computed for the initial slat position. The displacement effect for subsequent slat positions is then based on the flap lower-surface source strength distribution as calculated with the slate in the initial position.

Separated Flow Analysis

The separated flow model developed for the present study is similar to the source distribution method of Jacob and Steinbach (ref. 8). The separated flow model requires that the static pressure distributions in the separated zone (fig. 2) be nearly constant. This constant pressure condition in the separated region is approximated by requiring that the static pressure at s_2 (the central panel in the separated zone) and the the static pressure at s_3 (the trailing edge of the airfoil) both be equal to the static pressure at s_1 (the boundary-layer separation location). Thus

$$C_p(s_2) = C_p(s_1) \tag{1}$$

and

$$C_p(s_3) = C_p(s_1) \tag{2}$$

A two-parameter source distribution located on the surface of the airfoil in the separated zone (fig. 3) is introduced to enforce the above conditions. The functional form of the source distribution is given by

$$v = 2.5\, v_{max} s^* \qquad 0 \leq s^* \leq 0.4 \tag{3}$$

$$v = v_{max} \qquad 0.4 \leq s^* \leq 0.6 \tag{4}$$

$$v = v_{max} - (v_{max} - v_3)(5s^*-3)^2/4 \qquad 0.6 \leq s^* \leq 1.0 \tag{5}$$

where

$$s^* = (s - s_1)/(s_3 - s_1). \tag{6}$$

The separation location calculated from a previous iteration is used to determine the maximum source strength in the separated zone (v_{max}) and the

source strength at the airfoil trailing edge (v_3) so that equations (1) and (2) are satisfied. The airfoil static pressure distribution obtained from this solution is then used to recompute the airfoil upper-surface boundary layer and a new separation point is determined. This process is repeated until convergence is achieved.

Figure 4 compares the theoretically predicted lift for a range of angle of attack with experiment (ref. 9) for a GA(W)-1 airfoil. Figure 5 presents a similar comparison for a three-element configuration tested by Foster, Irwin, and Williams (ref. 10). The agreement between theory and experiment is good for both cases at angles of attack below stall. At angles of attack near stall the lift is underpredicted by approximately 8% for the GA(W)-1 airfoil and by 3% for the three-element configuration.

II. SLAT OPTIMIZATION: A CLASS 1 PROBLEM

The objective of this optimization procedure is to theoretically determine the position (horizontal location, vertical location, and deflection) of a leading-edge slat for maximum lift based on aerodynamic calculations which do not model the effect of flow separation. The analysis is based on the premise that, at the maximum lift coefficient at which attached flow can be maintained on the main airfoil, the optimum slat position for maximum lift minimizes the suction peak on the upper surface of the main element. For configurations which stall abruptly this is a reasonable assumption. However, for configurations which stall gradually, the validity of such an assumption remains to be proven.

The constrained function minimization method described by Vanderplaats in reference 11 and Vanderplaats and Moses (ref. 12) is used to numerically optimize the slat position so that the suction peak in the leading-edge region on the main component is minimized. This minimization is performed with the main element at a fixed angle of attack. The design variables (fig. 6) are slat horizontal and vertical location, and slat deflection. All three parameters are referenced to the slat trailing edge and can be varied independently.

Slat translation and deflection are subject to two constraints. The first constraint – that there be no flow separation on the slat upper surface – is applied to prevent the slat from moving into a separated flow regime. Numerically, this condition is satisfied by requiring that the skin-friction coefficient at the trailing edge of the upper surface of the slate, C_{f_s}, be slightly positive (i.e., $C_{f_s} \geq 0.0001$). The second constraint requires that the slat trailing edge be no closer than 0.02 c to the surface of main element (a reasonable slat gap for this configuration (ref. 10)). This constraint prevents the slat wake from merging with the boundary layer on the wing upper surface so that the computationally time consuming confluent boundary-layer calculation for the viscous flow above the main element can be replaced by a computationally efficient conventional boundary-layer calculation.

Figure 7 shows a sequence of positions through which the slat is moved during the numerical design procedure. For this particular example, the angle of attack of the main airfoil is 15°. With the slat in the initial position (slat position no. 1) it is lightly loaded, whereas the leading-edge region of the main airfoil is highly loaded, resulting in a large suction peak and a strong adverse pressure gradient. After nine iterations, each requiring the calculation of the gradient of the suction peak with respect to the three slat position variables, the analysis has converged and the slat position which minimizes the suction peak at an angle of attack of 15° has been determined. In this final position, the suction peak (and therefore the adverse pressure gradients on the main airfoil) has been substantially reduced in exchange for an increased loading on the slat. The numerical design thus yields a slat loading which is limited by the constraint that flow separation not occur on the slat upper surface. Figure 8 shows the surface pressure distributions for angles of attack of 13°, 19°, and 24° of the main airfoil. The slat position for all angles of attack is such that the suction peak is minimized and the slat upper-surface boundary layer is on the verge of separation.

Figure 9 shows the results of the analysis for a sequence of angles of attack from 13° to 24°. The figure shows the variation in slat horizontal position, slat vertical position and slat deflection as a function of angle of attack. Also shown is the skin-friction coefficient at the trailing edge of the upper surface of the main element, C_{f_m}. In figure 9, as the angle of attack is increased, the boundary layer on the main airfoil approaches separation (i.e., $C_{f_m} \to 0$). This separation is caused by an increase in the adverse pressure gradient on the main airfoil with angle of attack (see fig. 8) even though the slat is maintained in a position which minimizes the suction peak in the leading-edge region of the main component. Extrapolation of the numerical results predicts incipient flow separation ($C_{f_m} = 0$) on the main airfoil at an angle of attack of 24°. The slat position for this angle of attack is specified as the theoretically predicted optimum location required to give maximum lift, an assertion which will be verified by comparison with experiment.

III. SLAT/FLAP DEFLECTION OPTIMIZATION: A CLASS 2 PROBLEM

The objective of this optimization analysis is to determine the slat and flap deflections to obtain maximum lift for a three-element airfoil such as that shown in figure 10. The slat deflection is defined relative to a pivot point at the slat trailing edge. Thus the slat gap and slat overlap are independent of slat deflection. The pivot point for the flap is located on the flap upper surface directly below the wing trailing edge. Thus the flap gap and overlap are only weakly dependent on flap deflection. The optimum slat deflection and optimum flap deflection for maximum lift are determined by direct search relative to the two design variables, δ_s and δ_f. The effect of slat deflection and of flap deflection on computed $C_{\ell_{max}}$ is shown in figures 11 and 12, respectively. The slat gap for these calculations was 0.02 c and the flap gap was 0.03 c. These gaps are sufficiently large to insure that there is no strong interaction

between the wakes and the upper-surface boundary layers. It was also assumed, therefore, that the viscous flows on the upper surface of the main wing and flap could be analyzed as conventional boundary layers.

IV. EXPERIMENTAL OPTIMIZATION

As part of this study tests were conducted in the NASA Ames 40-by-80-Foot Wind Tunnel to experimentally determine optimum slat and flap positions for comparison with the theoretical predictions. The rectangular planform wing used in these tests (fig. 13) is equipped with a full-span leading-edge slat and a full-span single-slotted flap. The slat chord is 0.17 c and the flap chord is 0.40 c. The basic airfoil section is on RAE 2815. A detailed description of the slat, main airfoil, and flap shapes can be found in reference 10. The wing span is 16 m and the extended chord is 2.15 m. The relatively high aspect ratio of 7.5 and the rectangular planform result in a configuration with nearly two-dimensional flow over much of the wing span. Also, the use of a high aspect-ratio finite wing eliminates adverse wind-tunnel wall interference effects associated with two-dimensional high-lift airfoils which span the entire test section.

The slat and flap brackets permit continuous adjustment of the horizontal and vertical locations and the deflection of both elements. Data taken included lift using the wind-tunnel balance and surface static pressures along the model centerline. All data were obtained at a Reynolds number of 3.8×10^6 and a Mach number of 0.10.

V. COMPARISON OF THEORY AND EXPERIMENT

The experimentally and theoretically optimized slat positions are compared in figure 14 for a fixed flap deflection of 10°. The theoretical prediction is based on the Class 1 design procedure presented in Section II. It is to be noted that the largest differences between theory and experiment is 4° of slat deflection. The measured wing maximum lift coefficient with the slat in the theoretically optimized position differs only 4% from the experimentally measured maximum lift coefficient with the slat in the experimentally optimized position.

The comparison between theory and experiment for the slat/flap deflection optimization is summarized in figures 11 and 12. The experimentally measured maximum lift coefficient of the wing, $C_{L_{max}}$, is presented together with the wing centerline section maximum lift coefficient, $C_{\ell_{max}}$. The experimental value of $C_{\ell_{max}}$ was determined by correcting the measured $C_{L_{max}}$ for aspect ratio effects using the lifting line theory described by Glauert (ref. 13). The experimentally determined slat and flap deflections required to maximize the total wing lift are in good agreement with the optimum slat and flap deflections determined from the Class 2 analysis presented in Section III.

VI. CONCLUDING REMARKS

Optimization of multielement airfoils for maximum lift is separable into two general classes of problems. Class 1 problems are defined as those configurations which can be optimized using attached-flow, boundary-layer analysis. Class 2 design problems are defined as those which require the modeling of separated flows. A computationally efficient theoretical method for each class of problems is presented so that the position of leading- and trailing-edge high-lift devices can be optimized to obtain maximum lift. A Class 1 design procedure is described and applied to the optimization of the position of a leading-edge slat. A Class 2 analysis method is then described and applied to the optimization of the deflection of a leading-edge slat and a trailing-edge single-slotted flap to obtain maximum lift. In this investigation the effects of flow separation are modeled using surface source distributions located in the separated zones.

The theoretically optimized positions obtained from the Class 1 and Class 2 design procedures were then used as preliminary slat and/or flap positions for a wind-tunnel test of a three-element configuration. The refined optimum configurations derived from the wind-tunnel experiment are in good agreement with the theoretical results, indicating that both analysis methods are useful and reliable design tools.

REFERENCES

1. Olson, L. E.; and Dvorak, F. A.: Viscous/Potential Flow About Multi-Element Two-Dimensional and Infinite-Span Swept Wings: Theory and Experiment. AIAA Paper 76-18, AIAA 14th Aerospace Sciences Meeting, Washington, D. C., Jan. 26-28, 1976.

2. Blottner, F. G.: Variable Gird Scheme Applied to Turbulent Boundary Layers. Computer Methods in Appl. Mech. and Eng., vol. 4, Sept. 1974, pp. 179-194.

3. Smith, A. M. O.: Transition, Pressure Gradient and Stability Theory. Proc. 9th International Congress of Applied Mechanics, Brussels, vol. 7, 1957, pp. 234-244.

4. Cebeci, Tuncer: Calculation of the Three-Dimensional Boundary Layer I. Swept Infinite Cylinders and Small Cross Flow. AIAA J., vol. 12, no. 6, June 1974, pp. 779-786.

5. Cebeci, Tuncer; Kaups, Kalle; Mosinakis, G. J.; and Rehn, J. A.: Some Problems of Calculations of Three-Dimensional Boundary Layer Flows on General Configurations. McDonnell Douglas Report No. MDC J5884, April 1973.

6. Gaster, M.: The Structure and Behavior of Laminar Separation Bubbles. ARC 28-226, 1967.

7. Dvorak, F. A.; and Woodward, F. A.: A Viscous/Potential Flow Interaction Analysis Method for Multi-Element Infinite Swept Wings. vol. 1, NASA CR-2476, Nov. 1974.

8. Jacob, K., and Steinbach, D.: A Method for Prediction of Lift for Multi-Element Airfoils with Separation, AGARD-CP-143, V/STOL Aerodynamics, April 1974.

9. McGhee, Robert J.; and Beasley, William D.: Low-Speed Aerodynamic Characteristics of a 17-Percent-Thick Airfoil Section Designed For General Aviation Applications. NASA TN D-7428, 1973.

10. Foster, D. N., Irwin, H. P., and Williams, B. R.: The Two Dimensional Flow Around a Slotted Flap. RAE Tech. Report 70164, Sept. 1970.

11. Vanderplaats, Garret N.: CONMIN-A Fortran Program for Constrained Function Minimization. NASA TM X-62,282, 1973.

12. Vanderplaats, Garret N.; and Moses, Fred: Structural Optimization by Methods of Feasible Directions. Computers & Structures vol. 3, 1973, pp. 739-755.

13. Glauert, H.: The Elements of Aerofoil and Airscrew Theory. Cambridge at the University Press, 1948.

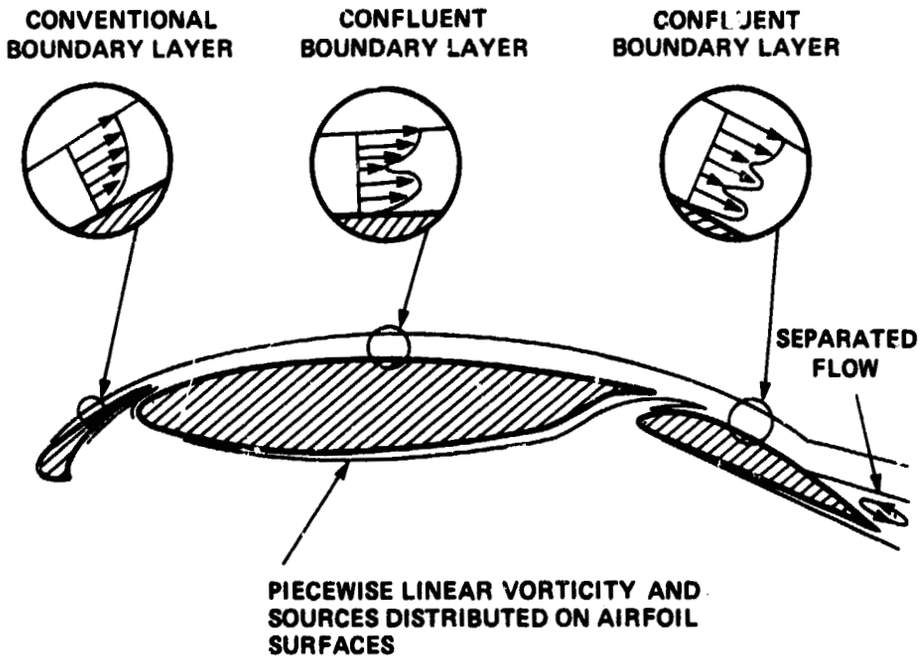

Figure 1.- Flow about multielement airfoil.

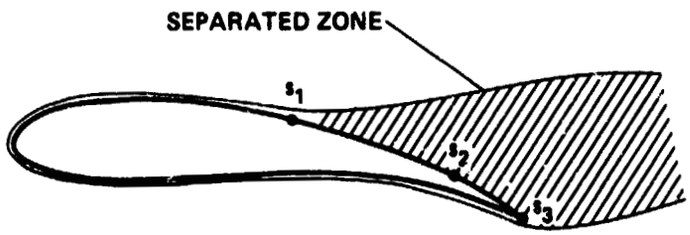

s_1 = BOUNDARY-LAYER SEPARATION POINT
s_2 = CENTER PANEL IN SEPARATED ZONE
s_3 = TRAILING EDGE OF AIRFOIL

REQUIRE: $C_p(\text{at } s_1) = C_p(\text{at } s_2) = C_p(\text{at } s_3)$

Figure 2.- Separated flow model.

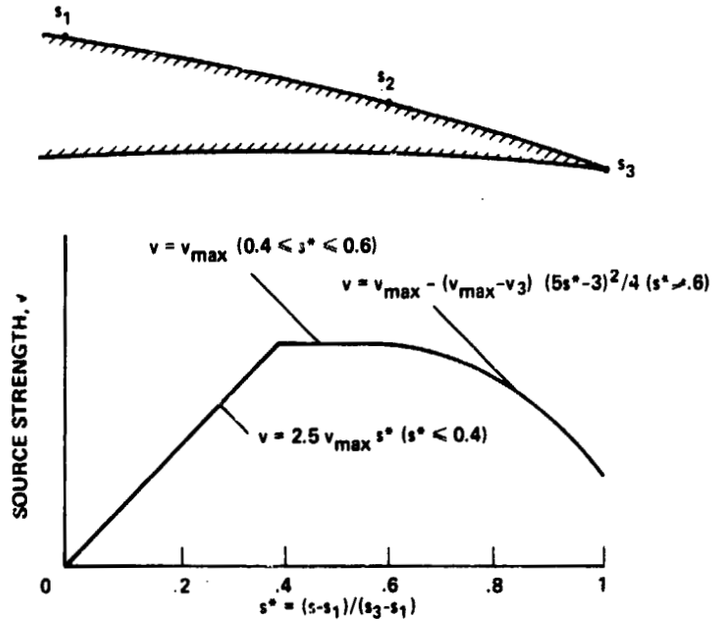

Figure 3.- Two-parameter source distribution in separated zone.

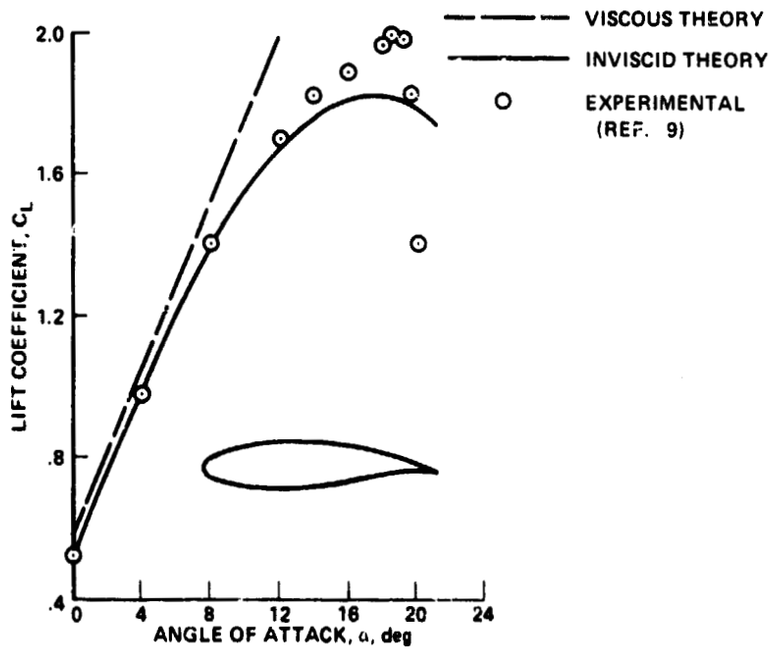

Figure 4.- Comparison of experimental and calculated lift on a GA(W)-1 airfoil. Re = 5.7×10^6; M = 0.15.

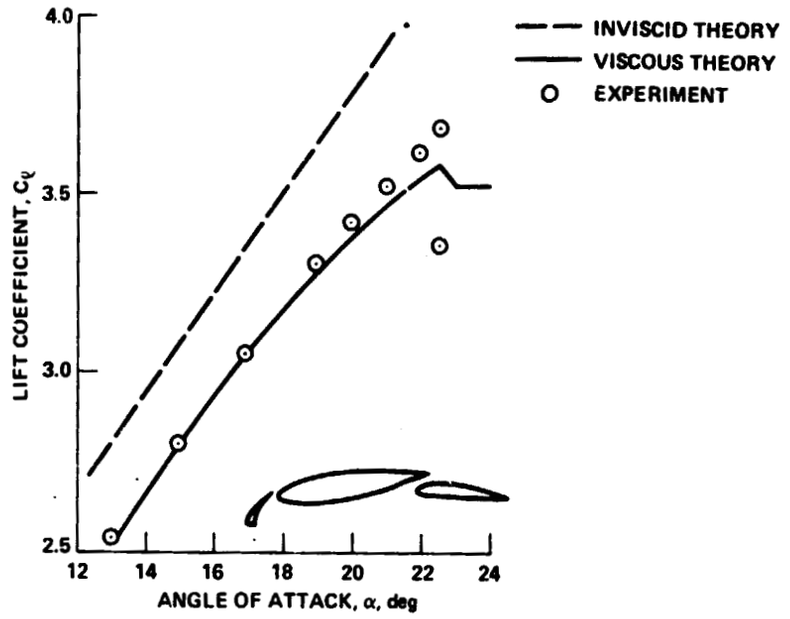

Figure 5.- Comparison of experimental and calculated lift on a three-element airfoil. Re = 3.8×10^6; M = 0.20.

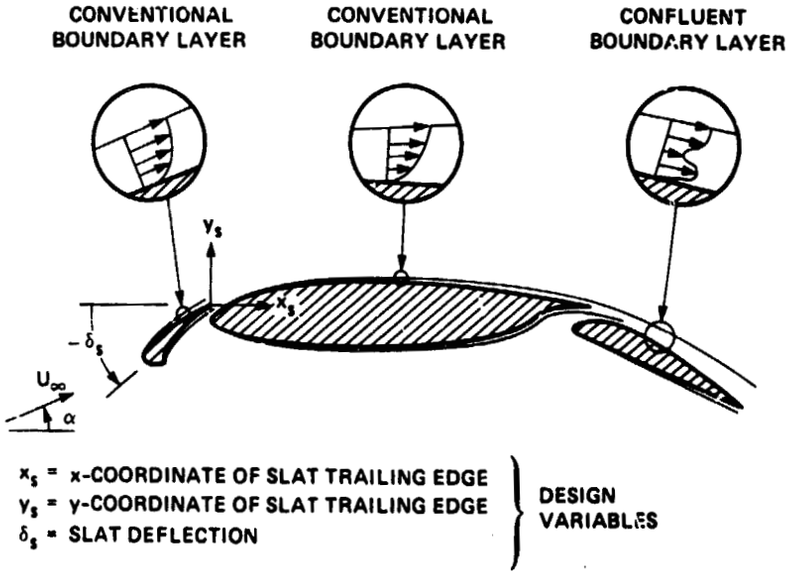

Figure 6.- Aerodynamic analysis for leading-edge slat-position optimization for maximum lift.

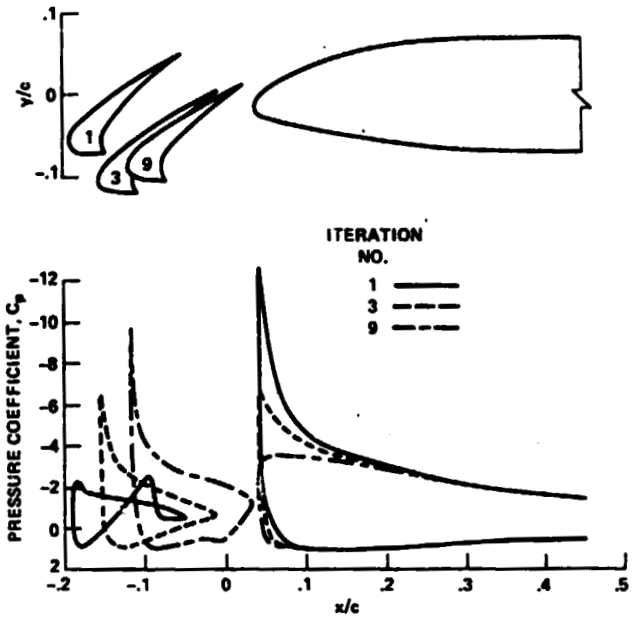

Figure 7.- Minimization of main airfoil suction peak at an angle of attack of 15°. δ_f = 10°; Re = 3.8 × 10^6; M = 0.10.

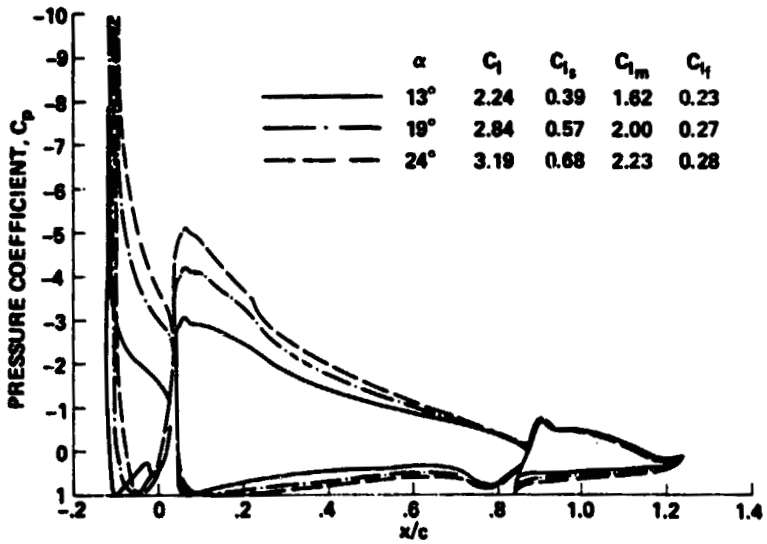

Figure 8.- Pressure distribution on a three-element airfoil with slat positioned to minimize the suction peak on the main airfoil. δ_f = 10°; Re = 3.8 × 10^6; M = 0.10.

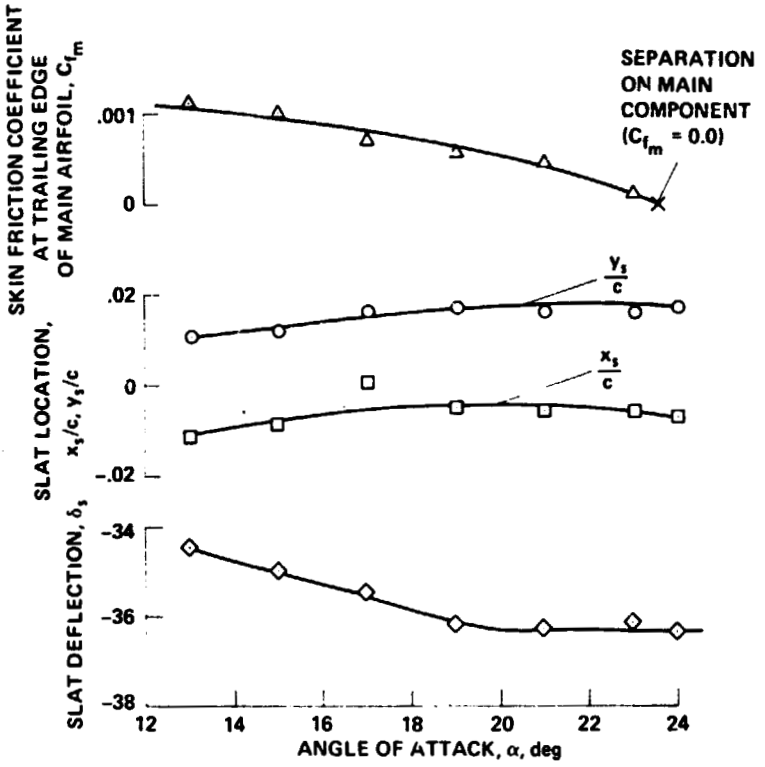

Figure 9.- Effect of configuration angle of attack on the skin-friction coefficient at the trailing edge of the main component and on the slat position required to minimize the suction peak on the main component. $\delta_f = 10^o$; Re = 3.8×10^6; M = 0.10.

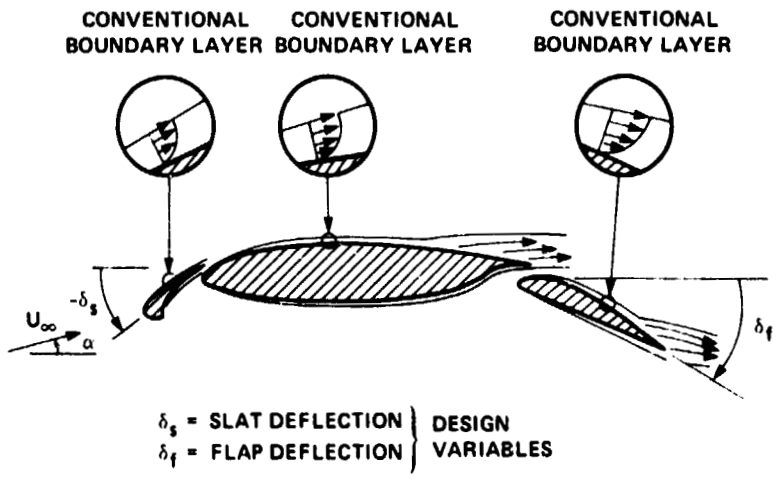

Figure 10.- Aerodynamic analysis for leading-edge slat and trailing-edge flap-deflection optimization for maximum lift.

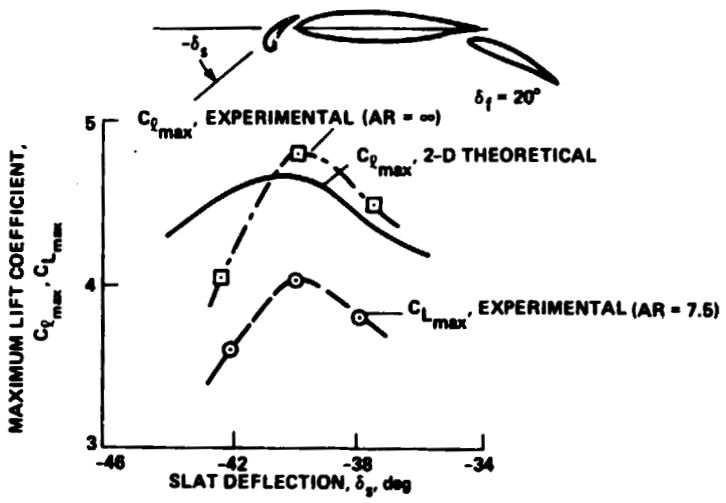

Figure 11.- Comparison of the effect of slat deflection on the computed maximum airfoil lift $C_{\ell_{max}}$ with the effect of slat deflection on the measured wing maximum lift $C_{L_{max}}$ for three-element configuration. Re = 3.8 × 10^6; M = 0.10.

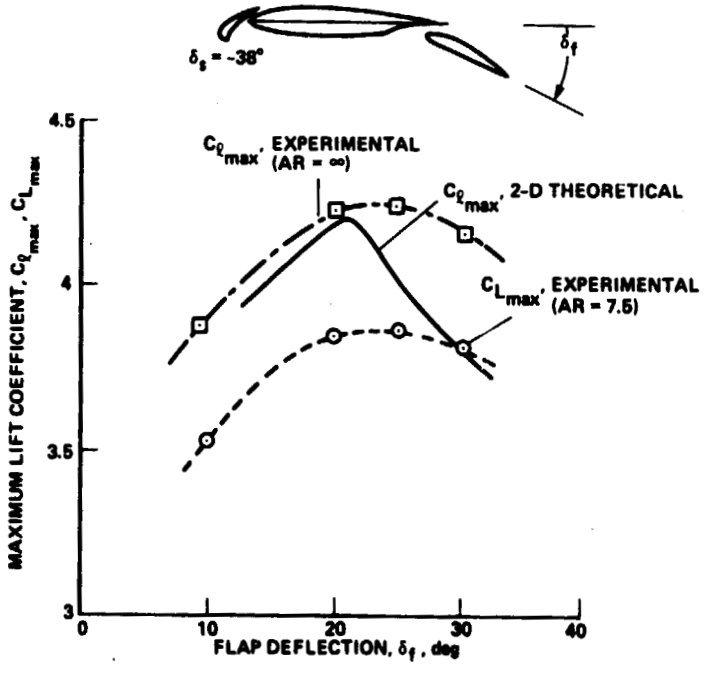

Figure 12.- Comparison of the effect of flap deflection on the computed maximum lift $C_{\ell_{max}}$ with the effect of flap deflection on the measured wing maximum lift $C_{L_{max}}$ for a three-element configuration. Re = 3.8 × 10^6; M = 0.10.

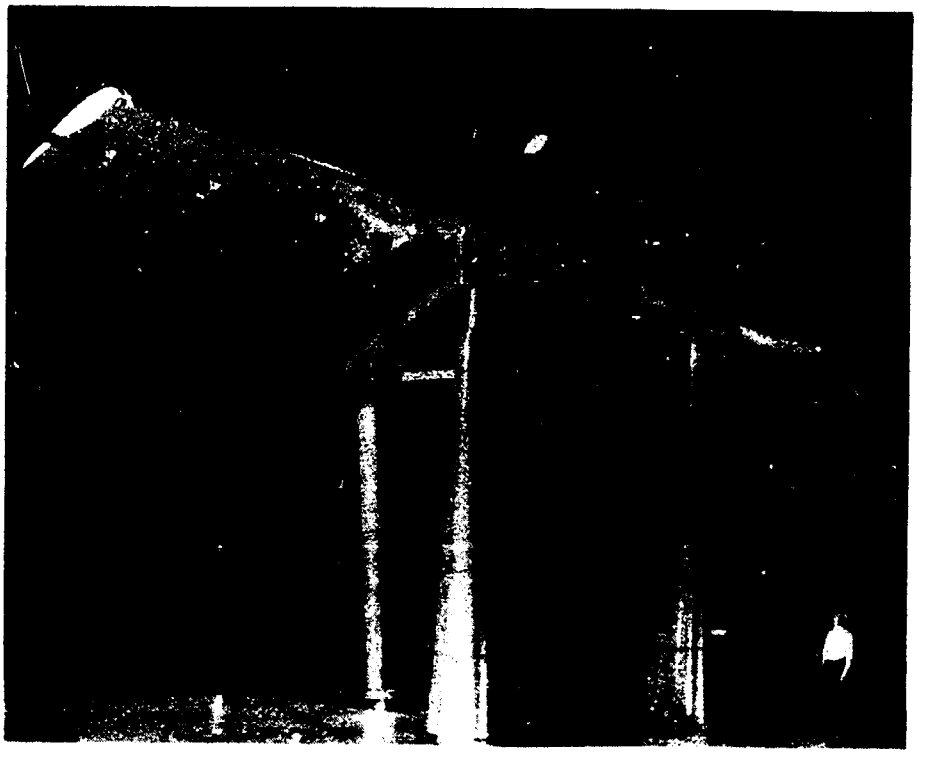

Figure 13.- Wind-tunnel model used to determine experimentally optimum slat and flap positions for maximum lift.

SLAT LOCATION	x_s/c	y_s/c	δ_s	$C_{L_{max}}$ (EXPERIMENTAL)
A	-0.007	0.017	-36	3.16
B	-0.009	0.010	-40	3.28

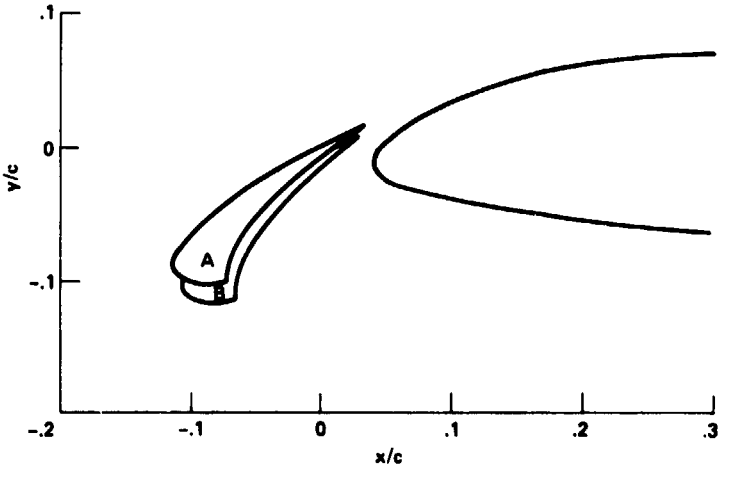

Figure 14.- Comparison of theoretically and experimentally optimized leading-edge slat position. Position A is theoretical; position B is experimental; $\delta_f = 10^o$; Re = 3.8×10^6.

D15

WAKE CURVATURE AND TRAILING EDGE INTERACTION EFFECTS IN VISCOUS FLOW OVER AIRFOILS*

R.E. Melnik
Grumman Aerospace Corporation

SUMMARY

This paper describes a new theory developed by the author and his colleagues for analyzing viscous flows over airfoils at high Reynolds numbers. The theory includes a complete treatment of viscous interaction effects induced by the curved wake behind the airfoil and accounts for normal pressure gradients across the boundary layer in the trailing edge region. A brief description of a computer code that was developed to solve the extended viscous interaction equations is given. Comparisons of the theoretical results with wind tunnel data for two rear loaded airfoils at supercritical conditions are presented.

INTRODUCTION

Two classes of theoretical methods are currently employed in the analysis of viscous flows over airfoils; one based on a direct numerical solution of the Reynolds-averaged equations of turbulent flow (e.g., refs. 1 and 2) and the other on an approximate boundary layer type formulation. Because of the magnitude of the computational task direct solutions of the Reynolds equations have been restricted to relatively crude grids. Because of the long computing times and poor resolution, these methods are not yet suitable for practical applications. Most existing methods of analyzing the problem are based on the displacement surface concepts of conventional boundary layer theory (e.g., see ref. 3). Unfortunately these approaches themselves are not entirely satisfactory because they neglect certain strong interaction effects that occur near trailing edges and shock impingement zones. In addition, most of the boundary layer formulations employed in the past were incomplete in that they ignored certain effects due to the wake. These effects are formally the same order of magnitude (as a function of the Reynolds number, R_e for $R_e \to \infty$) as the usual displacement effects on the airfoil surface and should be included in a completely consistent theory.

There are two wake effects, one due to its thickness and the other to its curvature. The wake thickness effect leads to a semi-infinite equivalent displacement body that enters into the determinaton of the outer inviscid solution. Although there are no conceptual difficulties in doing this, the wake thickness terms have usually been dropped or drastically approximated (e.g., ref. 3) in most previous studies in the interest of simplifying the computations. The wake curvature effect arises from the turning of the low momentum flow in the wake along the curved streamlines behind the airfoil.

*This work was partially supported by NASA under Contract NAS 1-12426.

254

A consistent application of the method of matched asymptotic expansions (for $R_e \to \infty$) leads to a matching condition requiring a discontinuity of the pressure across the trailing streamline of the outer inviscid flow. This leads to an effect similar to a jet flap with a negative jet momentum coefficient and hence, to a reduction of the lift coefficient. Although the need to include the wake curvature terms has been recognized in the past (refs. 4-6) it was only recently (ref. 7) that a completely consistent computation including the wake has been carried out.

It is well known that the boundary layer approximations break down in shock wave boundary-layer interaction zones (see ref. 8). The present author and R. Chow has shown (ref. 9) that the boundary layer approximations also fail in interaction regions near trailing edges. Analysis of the higher-order terms indicates that normal pressure gradients are important across the boundary layer and must be included in a correct lowest-order description of the flow in these regions.

The present author and R. Chow have developed a complete theory for the inner region near cusped trailing edges. We also developed a simple procedure for using the local trailing edge solution to correct the conventional boundary layer formulation (ref. 7). The resulting theory correctly treats the wake and the strong interaction region near trailing edges. Both effects are potentially important because they directly influence the Kutta condition and can therefore have a large global effect on the lift, drag, and moment of the airfoil section.

In the present paper we briefly describe the new viscous theory including a description of the numerical methods employed to solve the resulting interaction equations. Typical theoretical results are compared with wind tunnel data on rear loaded airfoils and some conclusions are drawn regarding the practical importance of wake curvature effects.

In the present work we do not provide for a rational analysis of the shock wave boundary interaction problem arising in supercritical cases. Instead a local numerical smoothing of the boundary layer and inviscid solutions near shock impingement points is employed that enables the viscous theory to function in these cases. Experience has indicated that the smoothing only affects the local pressure distribution near the shock wave and does not greatly influence the predicted section characteristics of the airfoil. Although the new theory is strictly applicable only to cusped airfoils, a computer code was written that is applicable to more general airfoils with nonzero trailing edge angles. Results obtained to date indicate that the theory provides useful results for these more general airfoil sections.

BOUNDARY LAYER FORMULATION

In this section we review the matching conditions that couple the viscid and inviscid flow solutions in the conventional boundary layer formulation. The structure of the flow field at high Reynolds number is sketched in figure 1. There are several regions consisting of the outer inviscid flow,

thin shear layers on the airfoil, and in the wake and strong interaction regions near the trailing edge and shock impingement points. The conventional boundary layer formulation leads to matching conditions coupling the inviscid flow to the thin shear layers outside the strong interaction regions. There are several equivalent statements of the matching conditions (see ref. 10) that follow directly from the fact that the flow in the shear layers is governed by the boundary layer equations. The matching conditions are independent of the particular closure assumptions used to model the Reynolds stresses, and the various forms are all equivalent in the limit $R_e \to \infty$. In the present study we have used the surface source formulation because it was best suited for matching to the strong interaction solutions and because it eliminates the need to modify the airfoil geometry in the solution procedure.

In this formulation the inviscid flow equations are solved subject to viscous boundary conditions on the airfoil and in wake given by:

$$V = \frac{1}{\rho_e} \frac{d\rho_e U_e \delta^*}{d S} \qquad \text{on the airfoil surface } (N = 0) \tag{1}$$

$$\Delta V = \frac{1}{\rho_e} \frac{d\rho_e V_e \delta^*}{d S} \qquad \text{on the wake streamline } (N = 0) \tag{2}$$

$$\Delta U = - U_e (\delta^* + \theta) \kappa \qquad \text{on the wake streamline } (N = 0) \tag{3}$$

where V is velocity component normal to the airfoil surface, ΔV and ΔU are the jumps in the normal and tangential components of velocity across the wake streamline, ρ_e and U_e are the density and tangential velocity along the airfoil and wake, δ^* and θ are the displacement and momentum thicknesses of the shear layers, S and N are curvilinear coordinates along the normal to the streamline defining the airfoil and wake centerline, and κ is the curvature of the wake streamline. The three matching conditions can be formally derived from a standard asymptotic analysis in the limit $R_e \to \infty$.

Since the wake curvature condition is not as familiar as the other conditions we summarize the steps in its derivation. The condition arises from the pressure variation induced across the wake by the nonuniform velocity profile in the wake. A typical velocity profile and pressure variation in the wake are sketched in figure 2. In an inviscid flow the pressure gradient $\partial p/\partial N$ would be roughly constant across the wake and equal to

$$\left(\frac{\partial p}{\partial N}\right)_{\text{Inviscid}} = - \rho_e U_e^2 \kappa \tag{4}$$

In the viscous flow the pressure gradient is related to the actual velocity and density profiles in the wake $U(N,S)$, $\rho(N,S)$ by the normal momentum equation, as follows

$$\frac{\partial p}{\partial N} = - \rho(N,S)\, U^2(N,S) \kappa(S) \tag{5}$$

where it has been assumed that the streamlines in the wake are parallel, a justifiable assumption only in the part of the wake outside the trailing edge region. Subtraction of equations (4) and (5) followed by integration with respect to N and the imposition of the condition that the pressure in the viscous flow approach the linear variation implied by equation (4) as $N \to \pm \infty$ leads to the relation

$$\Delta P \equiv P^{+} - P^{-} = - C_J(S)\kappa(S) \tag{6}$$

where

$$C_J = - \rho_e U_e^2 (\delta^* + \theta) \qquad < 0 \tag{7}$$

and P^{+}, P^{-} are the limiting values of the pressure in the outer inviscid flow on the upper and lower sides of the wake streamline, as indicated in figure 2. Equation (6) is similar to the boundary condition that arises in jet flap analysis, except that there C_J is the jet momentum coefficient which is a positive constant that is given as part of the data.

For small discontinuities, the pressure and velocity discontinuities are related by $\Delta P = - \rho_e U_e \Delta U$. Combining this expression with Equation (6) leads to the wake condition given in equation (3). In the present work we employ an irrotational approximation to the outer inviscid flow and the wake curvature condition is implemented by prescribing a jump in velocity potential, Γ, across the wake streamline, where

$$\Gamma \equiv \phi^{+} - \phi^{-} \tag{8}$$

Since $\Delta U = d\Gamma/dS$ we arrive at the final condition used in the computation, namely

$$\frac{d\Gamma}{dS} = - U_e(\delta^* + \theta) \frac{d\beta}{dS} \tag{9}$$

where β is the angle the wake streamline makes with the chord of the airfoil. At a given stage of the numerical solution, the right side of equation (9) is known and Γ can be evaluated by simple quadrature.

TRAILING EDGE CORRECTIONS

The source velocity, V, streamline curvature, κ, and the velocity jump, ΔU, appearing in the matching conditions all develop square root singularities and become unbounded at the trailing edges of lifting airfoils (see ref. 7). As a result, the Kutta condition cannot be satisfied, the lift cannot be determined and the conventional boundary layer theory cannot strictly be used to determine the viscous flow over lifting airfoils. Existing methods employing boundary layer theory apparently circumvent these shortcomings by numerically smoothing the inviscid and boundary layer solutions near trailing edges and by iterating the coupled inviscid and boundary layer equations to obtain a self-consistent solution. The iteration seems to eliminate the singularities but is not consistent with an order of magnitude analysis of the normal momentum equation.

A completely consistent treatment of the flow near trailing edges was carried out by the author and his associates for airfoils with cusped trailing edges (see ref. 7). In that analysis we showed that normal pressure gradients across the boundary layer and wake are important and must be included in the lowest-order description of the local solution. We also showed that the flow near the trailing edge could be treated as an inviscid rotational flow, and we obtained complete analytic solutions of the relevant equations governing the leading terms of the local solution. Readers interested in this aspect of the problem should consult ref. 7 for further details.

In this section we indicate how the local trailing edge solution can be used to correct conventional boundary layer theory to obtain composite solutions that are uniformly valid near trailing edges. In our approach we represent the solution by standard composite expressions that are valid in the inviscid, boundary layer, wake and trailing edge regions. For example, the representations for the pressure coefficient C_p and normal velocity v are written in the form

$$C_p = \overbrace{C_{p,\text{outer}}(S,N;R_e)}^{\text{from the inviscid solution}} + \overbrace{[C_{p,\text{inner}}(S,N;R_e) - C_{p,\text{com}}(S,N;R_e)]}^{\Delta C_p} \tag{10}$$

$$v = \overbrace{v_{\text{outer}}(S,N;R_e)}^{\text{from the inviscid solution}} + [v_{\text{inner}}(S,N;R_e) - v_{\text{com}}(S,N;R_e)] \tag{11}$$

where v is velocity component along a curvilinear coordinate that is normal to the airfoil at the surface. The first terms on the right side of equations (10) and (11) are solutions of the outer inviscid flow equations that satisfy a set of corrected matching conditions. The second terms in equations (10) and (11) are from solutions to the inner shear layer equations valid near the airfoil and wake, including the strong interaction zone near the trailing edge. The last term with subscript "com" is the common part of the outer and inner solution and is determined as part of the inner solution. We should stress that the individual terms in the representation are not expanded in formal sum type asymptotic series in terms of the Reynolds number as in the usual method of matched asymptotic expansions. Instead, the inner and outer terms are determined from iterative solution of the coupled inviscid and shear layer equations.

If the standard boundary layer matching conditions were employed with the above representations, the above procedure would be equivalent to the conventional boundary layer type solution and would also break down near trailing edges. The key to our approach is to develop modified or "composite" matching conditions such that the above representation reduces to the usual boundary layer and inviscid solutions outside the trailing edge region and to the appropriate strong interaction solution near the trailing edge. The fact that this representation can be made to work is due to the close relationship between the downwash generated by the vorticity in the shear layers and the surface source velocities generated by the displacement thickness.

The appropriate correction to the matching conditions are generated as follows: First, the source velocities, V, on the upper and lower sides of the airfoil are linearly combined into symmetric and antisymmetric components defined by

$$V_A \equiv \frac{1}{2}(V^+ - V^-) \qquad V_S \equiv \frac{1}{2}(V^+ + V^-) \tag{12}$$

where V^+ and V^- are computed from equation (1) evaluated on the upper and lower sides of the airfoil, respectively. Then V_A and V_S are multiplied by corrections G_A and G_S

$$V_{A\ \text{corrected}} = V_A\, G_A \quad ; \quad V_{S\ \text{corrected}} = V_S\, G_S \tag{13}$$

where G_A and G_S are the ratios of the inner solution to its common part for the antisymmetric and symmetric components of the downwash velocity as determined from the inner solution. Next, equations (13) are recombined to form corrected expressions for the source velocities on the airfoil and wake as follows:

On the Airfoil:

$$V^+_{\text{corrected}} = V_{A,\ \text{corrected}} + V_{S,\ \text{corrected}} \tag{14a}$$

$$V^-_{\text{corrected}} = V_{A,\ \text{corrected}} - V_{S,\ \text{corrected}} \tag{14b}$$

In the Wake:

$$V_{\text{corrected}} = 2\, V_{S,\ \text{corrected}} \tag{14c}$$

A similar procedure is followed to correct the wake curvature term, leading to the expression

$$\frac{d\Gamma}{dS} = -\left[U_e(\rho^*+\theta)\frac{d\beta}{dS}\right] G_W \tag{14d}$$

where G_W is the ratio of the inner solution to its common part for the pressure jump across the wake streamline as determined from the trailing edge solution. Closed form expressions for the correction factors G_A, G_S, and G_W as determined from the local trailing edge solution are given in reference 7. All three functions approach one and the matching conditions reduce to conventional boundary layer forms outside the trailing edge interaction zone. Inside the interaction zone equations (14) reduce to forms that will recover the local trailing edge solution when combined with solutions of the outer inviscid equations.

The correction functions completely eliminate the singularities arising in the conventional matching conditions and lead to solutions that are uniformly valid in the trailing edge region. We also note that the matching conditions lead to discontinuities in the pressure across the wake in the outer inviscid

solution given by the first term in equation (10). A typical solution of the outer inviscid equations which shows the jump in pressure at the trailing edge is given in figure 3. Compensating discontinuities also arise in the second and third terms of equation (10), which exactly cancel the jump in the first term leading to a composite solution that is continuous across the wake, as it should be. Similar considerations also apply to the solution for the normal component of velocity. The airfoil is not a streamline of the outer inviscid flow since v_{outer} is not equal to zero on the airfoil surface, but is in fact, equal to a function determined by the corrected viscous matching conditions. However, the sum of the various terms on the right side of equations (11) all cancel at the airfoil surface with the result that v is equal to zero at the surface and the airfoil is a stream surface in the composite solution.

SOLUTION PROCEDURE

With the modified matching conditions discussed above the determinaton of the viscous flow over airfoils is reduced to the familar problem of solving the coupled inviscid and boundary layer equations. Solution to the inviscid equations are obtained with the relaxation techniques of BGKJ (ref. 3) for the full potential flow equation. We employed the particular version developed by Jameson (ref. 11) to provide a fully conservative, "rotated" scheme. An option is also provided to allow for a standard nonconservative formulation. The calculations are carried out in a computational plane obtained by conformally mapping the airfoil to a circle. The solution employs a sequence of meshes and uses Jameson's accelerated iterative method (ref. 11) to speed convergence.

The integral parameters appearing in the matching conditions are determined from solution of the boundary layer equations. The equations were solved with simple integral methods consisting of a compressible version of Thwaite's method for the laminar boundary layer near the leading edge and Green's lag-entrainment method (ref. 12) for the turbulent flow downstream of transition. The transition point locations can either be assigned or predicted by one of three standard semiempirical methods programmed into the code. Jump conditions are imposed across the transition point to define initial data for the turbulent calculation downstream of transition. Green's lag-entrainment equations are a set ordinary differential equations, which are solved by a standard Runge-Kutta method. The lag-entrainment equations include "history effects" through an approximate treatment of the turbulent energy equation. The wake is modeled in Green's method as independent symmetric half-wakes and seems to provide a reasonable engineering description of the integral parameters in the wake. The method is known to be about as accurate as Bradshaw's "TKE" finite difference method for airfoil type flows. We modified the original method to permit a reasonable treatment of flows with slender separation bubbles. As a result, the present computer code will function when separation occurs, but the accuracy of the method in this case is uncertain.

Solutions to Green's equations are discontinuous across shock waves. In order to obtain reasonable inputs for the subsequent inviscid solution the pressure distribution input to the boundary layer equations is smoothed over

a limited region near shock waves. Experience with the code indicates that the overall solution is insensitive to the degree of local smoothing applied in this way. Although the theory is strictly rational only for airfoils with cusped trailing edges the program can be applied to airfoils with finite trailing angles. Good results have been obtained for airfoils with included angles as large as 10°.

The iteration between the inviscid and viscid solutions is controlled by monitoring the maximum residual, which is a parameter that measures the degree of convergence of the inviscid solution. The boundary layer equations are solved and the matching conditions are updated whenever the maximum residual is reduced by a specified factor, typically equal to five.

All calculations were carried out on an IBM 370/168 computer. Typical runs for a full viscous solution required about five minutes to reduce the maximum residual to 10^{-5} on a 32 x 128 point grid.

RESULTS

In this section we report on results obtained with the new program. Comparisons of the theoretical results with wind tunnel data are presented for two airfoils, one a moderately rear loaded supercritical airfoil, the KORN I, which was tested at the National Aeronautical Establishment in Ottawa, and the other a newly designed NASA supercritical airfoil with large rear loading that was tested in the NASA Langley 8-foot transonic tunnel. Theoretical results are also presented which show the effect of neglecting the wake curvature term and of using a nonconservative formulation in the inviscid solution.

The test of the KORN I airfoil at Ottawa was carried out at a Reynolds number of 21.7×10^6 with the tunnel walls set at 20.5 percent porosity. Under these conditions blockage effects were small, but downwash effects due to the walls were large. Therefore, angle of attack corrections developed for the facility were applied to the data. (See reference 7 for further details.) The airfoil was aerodynamically smooth and was tested with natural transition. The calculations were carried out with transition fixed at 10% chord. This is a reasonable estimate considering the high Reynolds number of the test. The theoretical solutions were found to be relatively insensitive to the assumed position of the transition point.

The theoretical surface pressures are compared with experimental data in figure 4 for a free stream Mach number, $M = 0.699$ and an angle of attack $\alpha = 1.69°$ (corrected). The fully conservative solution and the experimental data are seen to be in good agreement. The agreement of the nonconservative solution with the data is much poorer. Since the drag coefficient of the nonconservative solution given in the figure does not include the mass flow correction that Garabedian (ref. 13) has shown to be necessary, the favorable agreement of the uncorrected drag result with data is fortuitous.

Comparisons of theory and experiment for the lift curve at M = 0.699 are given in figure 5. The results show that the viscous and wall interference effects are about the same magnitude. The results of the theory show very good agreement with corrected wind tunnel data. The choice of conservative or nonconservative differencing seems to have only a small effect on the solution for the lift coefficient. The present code was also used to obtain a conventional boundary layer solution by dropping the terms arising from the wake and the trailing edge correction terms. The computed result is labeled SCBL theory (self-consistent boundary layer theory) in the figure. This result indicates that conventional boundary layer predicts only about half the viscous loss of lift. This is more clearly brought out in the results plotted in figure 6.

In figure 6 we present results that illustrate the separate effects of wake curvature and trailing edge interaction on the lift coefficient. Four solutions, all obtained with the present code, are presented for the variation of lift coefficient with Mach number at a fixed incidence, $\alpha = 1.69°$, including the inviscid solution, the full viscous solution, the same solution with the wake curvature terms omitted, and the conventional self-consistent boundary layer solution (SCBL) mentioned above. The results in figure 6 clearly show that the conventional boundary layer approach underpredicts the boundary layer effect by about 50 percent. The difference between the self-consistent boundary layer solution and the viscous solution without wake curvature represents the effect of normal pressure gradients in the trailing edge region. The results in figure 6 indicate that this effect and the wake curvature effect combine to make up the other 50 percent of the lift reduction induced by the boundary layer. Thus the simple displacement surface type boundary layer formulation significantly underpredicts the boundary layer effect.

The drag polar for M = 0.699 is given in figure 7. Theoretical results for the full viscous theory using both the conservative and nonconservative formulation are compared with experimental data. A similar comparison presented in reference 7 was in error due to a mistake in the nonconservative solution. The conservative and nonconservative solutions are seen to differ significantly at the higher lift coefficients where shock waves are present in the solutions. Garabedian (ref. 13) has shown that the error in the nonconservative formulation is due to a spurious sink drag at the shock wave. The conservative solution leads to a reasonable prediction of the overall shape of the drag polar, but underestimates the drag levels by about 15 percent. There is some evidence (ref. 14) that experimental uncertainty in the drag measurements might be responsible for the poor agreement shown in this case.

Much better agreement is obtained with drag measurements from the 8-foot transonic wind tunnel at the NASA Langley Research Center. In figure 8 we present the results for the drag polar of the second airfoil considered in this paper. The airfoil is a 10 percent thick, heavily rear-loaded supercritical airfoil recently designed and tested at NASA Langley. Theoretical solutions with and without wake curvature are given in the figure together with a solution obtained with the nonconservative formulation. A blockage

correction of $\Delta M = -0.01$ was employed in the theoretical computations. Although, accurate wall corrections are not available for this facility recent studies, carried out at NASA Langley Research Center, have indicated that corrections of this magnitude are appropriate. Transition was fixed in the tests by placing transition strips at 28 percent chord and was fixed at the same location in the computations. The tests were carried out at a Reynolds number of $R_e = 7.7 \times 10^6$. The results in figure 8 show that the new viscous theory with wake curvature not only predicts the shape of the drag polar but also the absolute levels of drag over a wide range of lift coefficients. The results also show that the neglect of wake curvature leads to a noticeable underprediction of the drag and that the nonconservative formulation leads to a significant overestimate of the drag.

In figure 9 we compare the theoretical and experimental pressure distributions for a point about half way up the drag rise on the polar. The results show good agreement for both the pressure distribution and shock position. The slight underpredictions of the pressure over the rear upper surface were found to be due to numerical problems with code that have since been eliminated.

The solution for the lift curve is given in figure 10. The solutions clearly show the large effect of wake curvature on the predicted lift coefficient. The type of differencing is seen to have only a slight influence on the predicted lift coefficient. Uncorrected data from the test are also plotted in the figure for reference. The results are suggestive of relatively large wall induced downwash on the airfoil. However since accurate angle of attack corrections were not available comparisons with corrected data could not be provided.

CONCLUSIONS

The main conclusions to be drawn from the results obtained to date with the new viscous theory are:

- Wake curvature and trailing edge interaction effects are required in a completely consistent theory of viscous flow over airfoils. Together they account for about a half of the reduction of lift caused by the boundary layer. They are most important for rear loaded airfoils

- The new theory leads to accurate predictions of lift and drag provided a fully conservative differencing scheme is used to solve the equations. Both the shape of the drag polar and the absolute levels of the drag are well predicted by the theory.

The above are only tentative conclusions. The uncertainties in the drag measurements of the Ottawa facility and the unknown level of the angle of attack and blockage corrections required in the Langley tunnel prevent us from drawing more definite conclusions regarding the adequacy of the new theory. A more clear-cut validation of the theory would require improved wind tunnel tests with either small wall effects or accurate and documented corrections.

REFERENCES

1. Deiwert, G.S., "Computation of Separated Transonic Turbulent Flow," AIAA J., vol. 14, 1976.

2. Baldwin, B.S. and Lomax, H., "Thin Layer Approximation and Algebraic Model for Separated Turbulent Flow," AIAA Paper 78-257, 1978.

3. Bauer, F., Garabedian, P., Korn, D. and Jameson, A., Supercritical Wing Sections II," Springer-Verlag, New York, 1975.

4. Thwaites, B., Incompressible Aerodynamics, Oxford University Press, pp. 191-194, 1960.

5. Spence, D.A. and Beasley, J.A., "The Calculation of Lift Curve Slopes, Allowing for Boundary Layer, with Application to the RAE 101 and 104 Aerofoils," Rep. Memor. Aero. Res. Counc., London, 3137, 1960.

6. Lock, R.C., "Research in UK On Finite Difference Methods for Computing Steady Transonic Flows," Symposium Transsonicum II, Springer-Verlag, New York, 1975.

7. Melnik, R.E., Chow, R. and Mead, H.R., "Theory of Viscous Transonic Flow Over Airfoils at High Reynolds Numbers," AIAA Paper No. 77-680, 1977.

8. Melnik, R.E. and Grossman, B., "Further Developments in an Analysis of the Interaction of a Weak Normal Shock Wave with a Turbulent Boundary Layer," Symposium Transsonicum II, Springer-Verlag, 1975.

9. Melnik, R.W. and Chow, R., "Asymptotic Theory of Two Dimensional Trailing Edge Flows," NASA Conference on Aerodynamic Analysis Requiring Advanced Computors NASA SP 347, 1975 (also Grumman Research Department Report RE-510J).

10. Lighthill, M.J., "On Displacement Thickness," J. Fluid Mech., Vol. 4, 1958.

11. Jameson, A., "Numerical Computation of Transonic Flow with Shock Waves," Symposium Transsonicum II, Springer-Verlag, New York, 1975.

12. Green, J.E., Weeks, D.J., and Broomen, J.W.F., "Prediction of Turbulent Boundary Layers and Wakes in Compressible Flow by a Lag Entrainment Method," RAE Tech. Report, 72231, 1973.

13. Garabedian, P.R., "Transonic Flow Theory of Airfoils and Wings," Advances in Engineering Sciences, NASA CP-2001, 1976.

14. Ohman, L.H., Kacprzynski, J.H., and Brown, D., "Some Results from Tests in the NAE High Reynolds Number Two-Dimensional Test Facility on Shockless and other Airfoils," Canadian Aero. and Space Journ., Vol. 19, 1973.

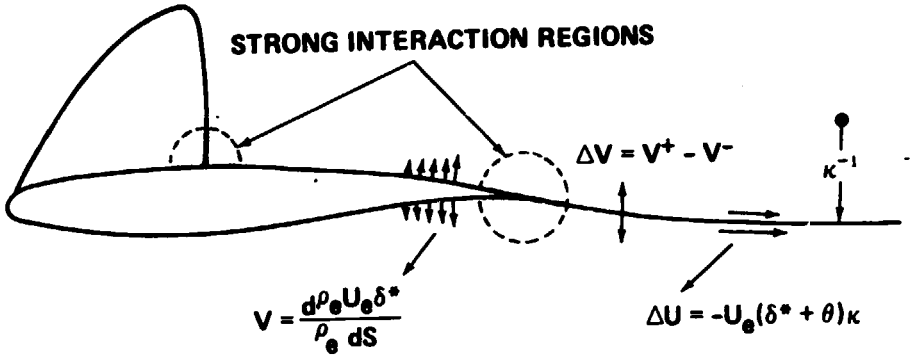

Figure 1.- Flow structure and viscous matching conditions.

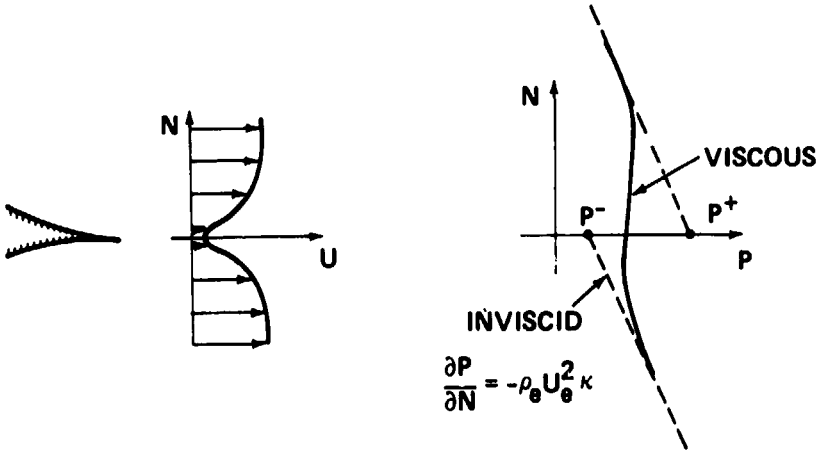

Figure 2.- Wake-curvature condition.

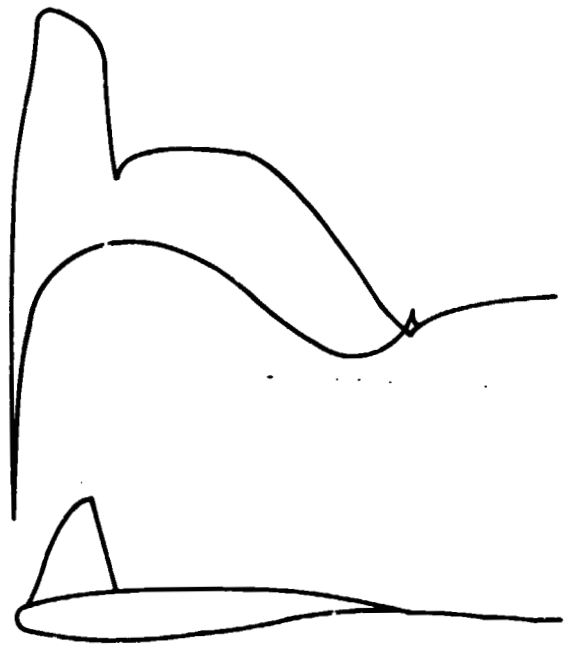

CL = .668 CD = .0082 CM = -.0989

Figure 3.- Outer inviscid solution for the pressure distribution where CL denotes lift coefficient, CD denotes drag coefficient, and CM denotes pitching-moment coefficient.

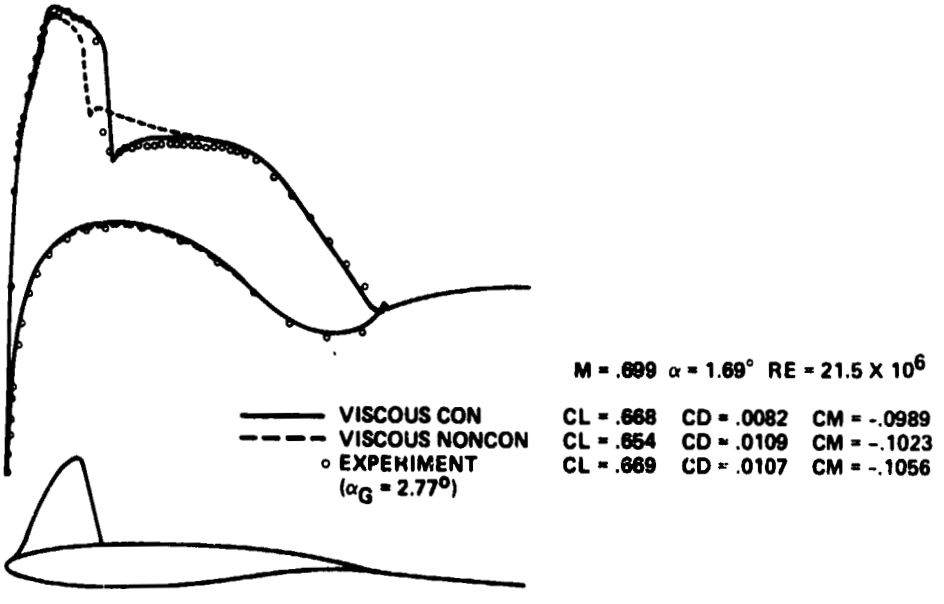

Figure 4.- Pressure distribution on a KORN I airfoil where RE denotes the Reynolds number.

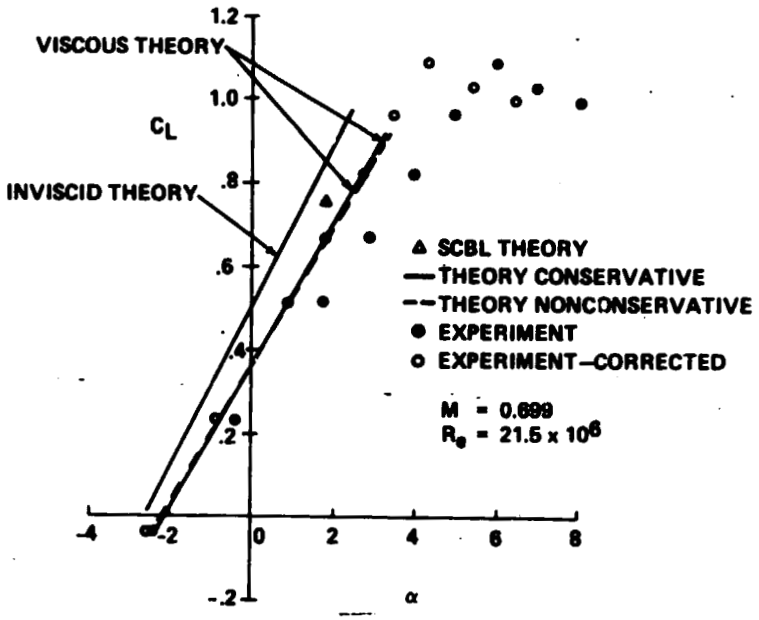

Figure 5.- Variation of lift coefficient with incidence for the KORN I airfoil.

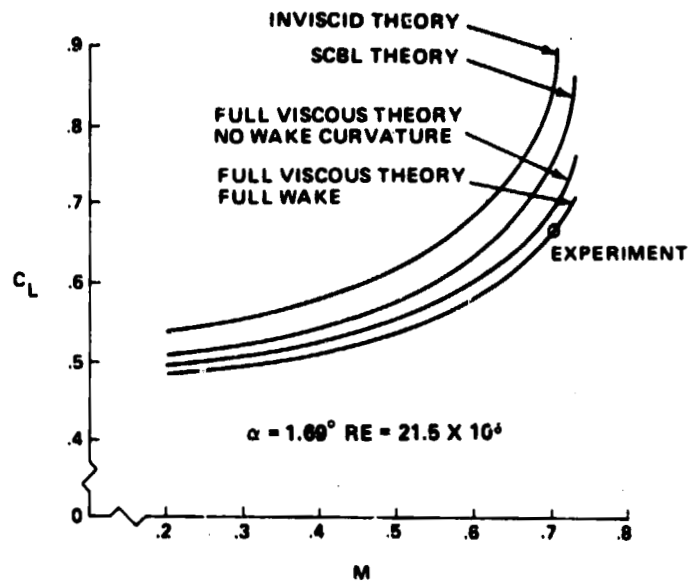

Figure 6.- Effect of wake curvature and strong interaction on lift.

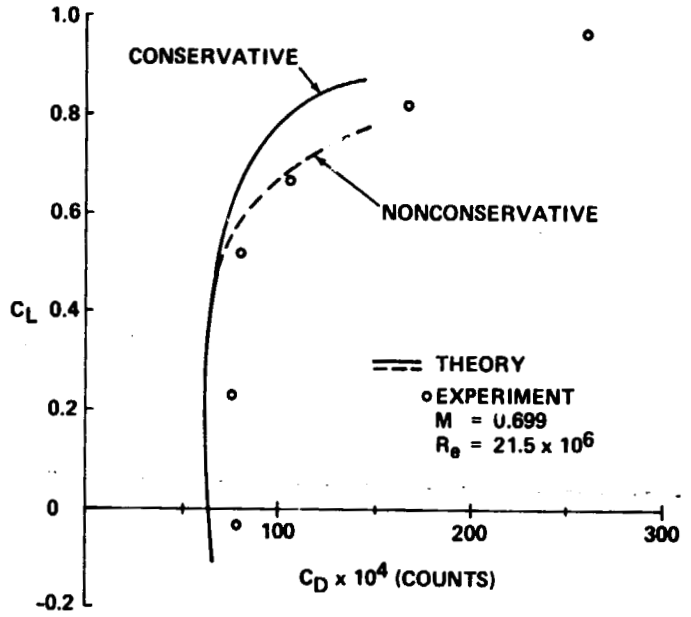

Figur- 7.- Drag polar for the KORN I airfoil.

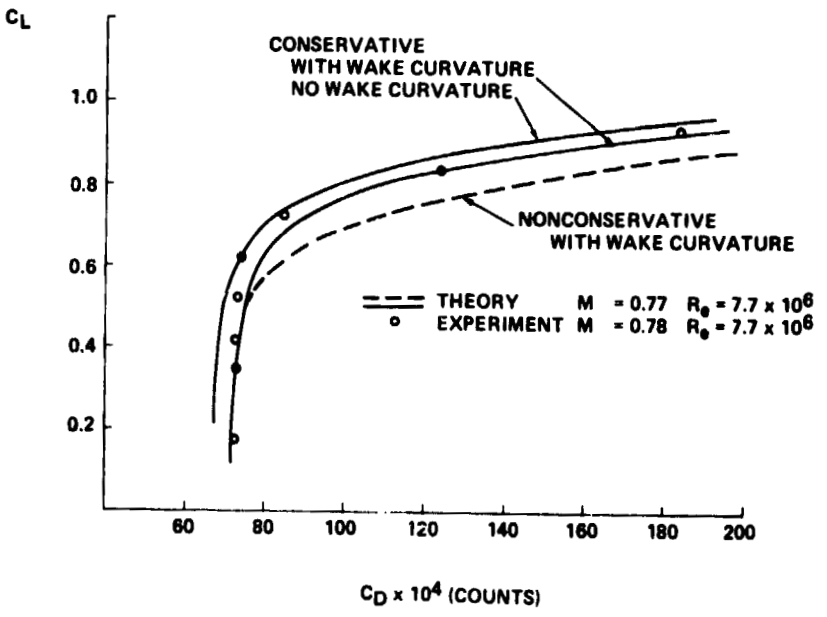

Figure 8.- Drag polar for the NASA supercritical airfoil.

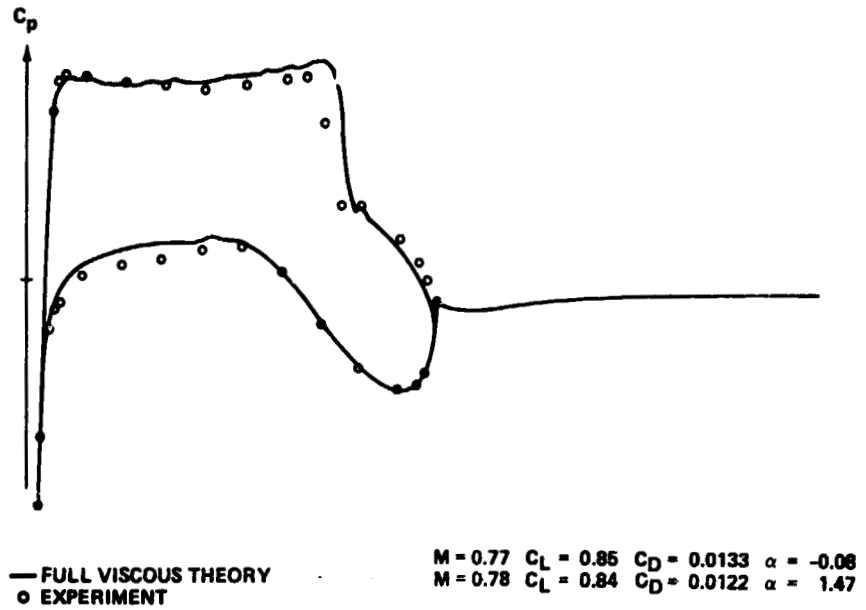

Figure 9.- Pressure distribution on the NASA airfoil.

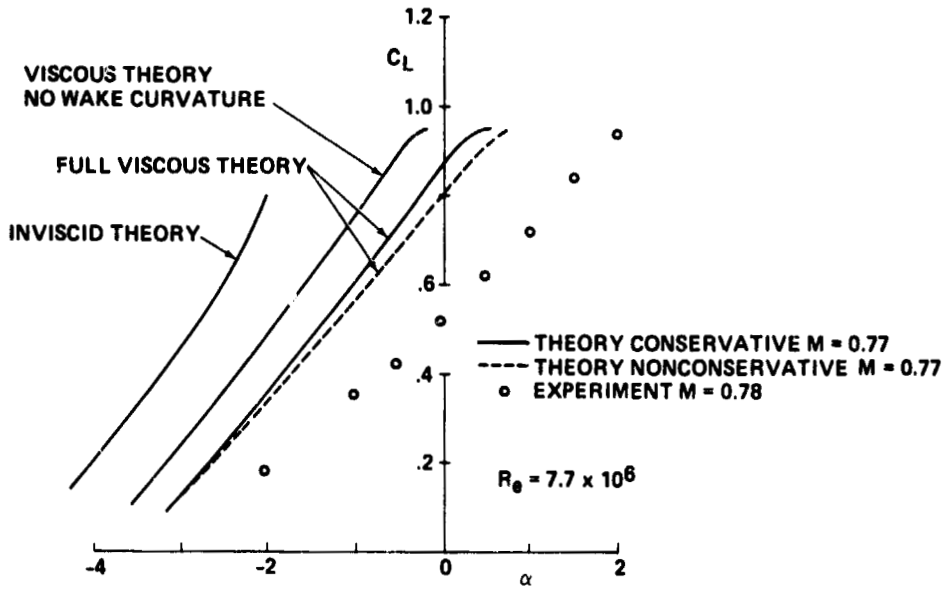

Figure 10.- Variation of lift coefficient with incidence for the NASA airfoil.

D16

N79-20046

16

A STUDY OF THE INTERACTION OF A NORMAL SHOCK WAVE WITH A TURBULENT BOUNDARY LAYER AT TRANSONIC SPEEDS*

A.F. Messiter and T.C. Adamson, Jr.
The University of Michigan

SUMMARY

An asymptotic description is derived for the interaction of a weak normal shock wave and a turbulent boundary layer along a plane wall. In the case studied the nondimensional friction velocity is small in comparison with the nondimensional shock strength, and the shock wave extends well into the boundary layer. Analytical results are described for the local pressure distribution and wall shear, and a criterion for incipient separation is proposed. A comparison of predicted pressures with available experimental data includes the effect of longitudinal wall curvature.

INTRODUCTION

In transonic flows a transition from supersonic to subsonic speeds typically occurs through a shock wave which is normal to a solid boundary. Across the boundary layer along this surface, the upstream fluid velocity decreases from its value in the external flow to zero at the wall, and the strength of an incident shock wave must decrease to zero in the supersonic part of the boundary layer; at the wall there is no discontinuity in pressure.

In the undisturbed turbulent boundary layer, viscous forces are important only in a very thin wall layer having thickness of the order of the local viscous length and velocity of the order of the friction velocity. In most of the boundary layer the mean velocity profile is nearly uniform, with a decrease from the external-flow value of the same order as the friction velocity. The flow changes caused by a weak incident normal shock wave will depend on the relative sizes of this velocity variation and the difference between the external-flow Mach number and one, i.e., on the ratio of the nondimensional friction velocity to the nondimensional shock-wave strength. Asymptotic flow descriptions have been derived for large (ref. 1), moderate (refs. 2,3,4) and small (ref. 5) values of this ratio, and the oblique-shock problem has also been studied (ref. 6). In each case the local mean pressure gradient and fluid deceleration are large enough that the flow near the shock wave may be described as an inviscid rotational flow in most of the boundary layer. In a thinner sublayer, changes in the turbulent stresses do influence the changes in velocity, and here some model must be chosen (e.g., a mixing-length model) for describing these stresses. The displacement effect of the flow changes in this sublayer is small enough that the dominant terms in the pressure are not affected. Thus the pressure is cal-

*This work was supported by NASA Langley Research Center, under Research Grant NSG 1326.

culated from the inviscid-flow equations and then is substituted into the sublayer equations for the calculation of changes in wall shear.

The present work is a continuation of the work of reference 5. Asymptotic solutions are obtained in the limit as the nondimensional friction velocity and shock-wave strength approach zero, such that the ratio of friction velocity to shock strength also approaches zero, as does the distance from the wall to the undisturbed sonic line divided by the boundary-layer thickness. The pressures found in reference 5 are shown to be modified by higher-order and curvature effects, and the calculation of wall shear is carried out, leading to a proposed criterion for incipient separation.

SYMBOLS

c_f	skin-friction coefficient
K	local wall curvature, nondimensional with L^{-1}
L	length of boundary layer, up to shock wave
M_e	Mach number in external flow ahead of shock
P, P_e, P_o	local static pressure, and external-flow static and stagnation pressures ahead of shock, nondimensional with sonic pressure ahead of shock
Re, Re^*	Reynolds number based on L and on external-flow quantities or sonic values
U, U_e	local velocity and external-flow velocity, nondimensional with critical sound speed
u_τ	nondimensional friction velocity; $u_\tau^2 = \frac{1}{2} U_e^2 c_f$
X, x	$\bar{X}/L$, $(M_e^2 - 1)^{-1/2} X/\delta$; $\bar{X}$ = coordinate along wall
$Y, y, \hat{y}$	$\bar{Y}/L$, $Y/\delta . (M_e^2 - 1)^{-1/2} y/u_\tau$; $\bar{Y}$ = coordinate normal to wall
γ	ratio of specific heats
δ	boundary-layer thickness ahead of shock, nondimensional with L
ε	$U_e - 1$
κ	von Kármán constant, taken equal to 0.41
Π	pressure-gradient parameter in velocity profile
τ_w	wall shear stress, nondimensional with undisturbed value

PRESSURE DISTRIBUTION

In the velocity defect layer, $y = Y/\delta = O(1)$, where $\delta = O(u_\tau)$, and ahead of the shock wave $U \sim 1 + \varepsilon + u_\tau u_{01}(y)$, as in figure 1. We take $u_{01} = \kappa^{-1} \ln y - \kappa^{-1} \Pi (1 + \cos \pi y)$ for $0 < y < 1$ and $u_{01} = 0$ for $y > 1$ (e.g., ref. 7), where $\kappa = 0.41$ and for zero pressure gradient Π is about 0.5. The sonic line is located at $y = \exp(2\Pi - \kappa\varepsilon/u_\tau)$, and for $u_\tau \ll \varepsilon$ this value is small. In the very thin wall layer $Y = O(u_\tau^{-1} Re^{-1})$, and the velocity $U = O(u_\tau)$ has the same form as for an incompressible flow having density and viscosity coefficient equal to the wall values in the actual flow. For $u_\tau^{-1} Re^{-1} \ll Y \ll \delta$ a mixing-length model is used for the shear stress, and the velocity profile obtained is required to match asymptotically with both the defect-layer and the wall-layer profiles. These matching conditions provide a relationship among the quantities δ, u_τ, and Re. A second such relationship is found from the momentum integral equation, in the manner described for incompressible flow, e.g., in reference 7, with quadratic terms in u_τ retained. For simplicity the total enthalpy is assumed uniform.

For $Y = O(\delta)$ immediately downstream of the shock wave, the differential equations and shock jump conditions (expanded for $u_\tau \to 0$, $\varepsilon \to 0$, and $u_\tau/\varepsilon \to 0$) show that pressure changes $O(u_\tau)$ occur over a distance $x = (M_e^2 - 1)^{-1/2} X/\delta = O(1)$. The mean velocity profile has a term $(1 + \varepsilon)^{-1}$ plus terms $O(u_\tau)$ containing a known rotational part and an unknown irrotational part (fig. 2). The shock wave is located at $x = O(u_\tau/\varepsilon)$, and so the shock jump conditions are expanded in Taylor series about $x = 0$. For a first approximation Laplace's equation in the variables x,y is solved in a quarter plane by distributing fluid sources along $x = 0$. For $(x^2 + y^2)^{1/2}$ greater than about 2, it is found that the solution is nearly that due to a point source which represents the change in boundary-layer displacement thickness (as also noted in refs. 3,4). Two correction terms, while formally of higher order, are important numerically at realistic values of u_τ and ε. One represents changes in vorticity along a streamline of the mean flow; the other accounts for the difference between streamlines and lines $y =$ constant in the calculation of the rotational part of U, and also enters in the irrotational part through the boundary condition at $x = 0$. The wall pressure with these effects included is

$$P_w/P_e = 1 + 2\gamma\varepsilon + \gamma(2\gamma - 1)\varepsilon^2 + \cdots$$

$$+ \{1 + (2\gamma - 1)\varepsilon\} \frac{4\gamma}{\pi} u_\tau \left\{1 + \frac{3\gamma}{2} \frac{u_\tau}{\kappa} \frac{2 + 3.18\,\Pi + 1.5\,\Pi^2}{1 + \Pi}\right\} x \int_0^\infty \frac{u_{01}(\eta)\, d\eta}{x^2 + \eta^2} \qquad (1)$$

The solution (1) is logarithmically infinite as $x \to 0$, as must be expected since the overall pressure change is $O(\varepsilon)$ rather than $O(u_\tau)$. Numerical solution of the nonlinear transonic small-disturbance equations would be required to obtain the correct form in a region near $x = 0$ which is small if $u_\tau/\varepsilon \ll 1$. For a wall with longitudinal curvature, the pressure gradient in the inviscid flow behind a normal shock wave has a logarithmic singularity described by

$$\Delta P = \frac{4\gamma K}{\pi} \left\{x\delta \ln \delta \sqrt{x^2 + y^2} - y\delta \left(\tan^{-1} \frac{y}{x} - \frac{\pi}{4}\right)\right\} \qquad (2)$$

The boundary-layer interaction effect for $x = O(1)$ is not large enough to change this expression, and so a curvature term can simply be added as a correction to equation (1).

The pressure distributions found by adding equations (1) and (2) are compared in figure 3 with experimental results from reference 8. For $M_e = 1.322$ and $Re = 9.4 \times 10^5$, other parameters are calculated as $\varepsilon = .247$, $u_\tau = .050$, $\delta = .0182$, and $c_f = .0032$. The shock-wave position found from the data is the origin for the pressure at 15 mm., where $y \approx 4.1$. The origin for the wall pressure is shifted upstream through $\Delta x = 2.87$, equal to the displacement of the shock wave calculated using the fact that the shock-wave slope is proportional to the y-component of velocity at $x = 0$. In the experiments the wall was a plate having longitudinal curvature which can be inferred from the measured pressures immediately behind the shock wave. The change $\Delta P/P_o$ in a y-distance of 15 mm. was taken as .015, giving $K = .21$. The theoretical curves also include a constant streamwise pressure gradient caused by cross-section area change, estimated from the data as $\Delta P/P_o = .03$ in a distance of 50 mm. The parameter Π was taken equal to the constant-pressure value $\Pi = 0.5$, which leads to a predicted location of the undisturbed sonic line at $y = .36$. If instead $\Pi = 0.4$, the prediction is $y = .30$, whereas the measured value is $y = .29$; this change in Π would influence the pressures only slightly. The wall pressures are in excellent agreement for x greater than about 3; the region $x < 3$ requiring solution of nonlinear equations is relatively large in this case, because the Reynolds number is not high enough for the upstream sonic line to be really close to the wall. The very beginning of the rise in wall pressure can be expressed by an exponential function with known rate of decay but unknown multiplicative constant, as shown in figure 3 with origin chosen tentatively for good agreement with the data. By comparison with numerical results of ref. 2, it should be possible to estimate this constant. The pressures at 15 mm. from the wall are in good agreement except for small x, where the error probably arises from approximating the shock-wave location by $x = 0$; adding the appropriate second-order term is expected to improve the agreement.

WALL SHEAR

The above description of mean-flow perturbations in terms of disturbances in an inviscid rotational flow does not remain valid as $y \to 0$. For $y = Y/\delta = O(u_\tau \varepsilon^{1/2})$, it is easily found that turbulent stresses as well as pressure and inertia terms must be retained in the boundary-layer momentum equation. This thinner layer (still much thicker than the viscous wall layer) has been called a Reynolds stress sublayer in reference 1 and a blending layer in reference 2. Double expansions as $u_\tau \to 0$ and $\varepsilon \to 0$ are assumed for the velocity components, pressure, and Reynolds stress, with the latter represented by a simple mixing-length model, chosen for analytical convenience in the belief that the results may not depend strongly on the model used. The wall shear stress has the form

$$\tau_w(x) = 1 + a\varepsilon + \frac{1}{2}a(a-1)\varepsilon^2 + \cdots + u_\tau \tau_1(x) + \varepsilon u_\tau \{(\ln \varepsilon^{1/2} u_\tau)\, \tau_{1\ell}(x) + \tau_{11}(x)\} + \cdots \quad (3)$$

where a = constant. This expansion, like that for the pressure, requires modification when x is small. The y-component of velocity and the related displacement

effect of this sublayer are small enough that the previous calculation of pressure is unaffected, and the boundary condition $v = 0$ at $y = 0$ used for $y = 0(1)$ is thereby verified. With use of the solution for pressure evaluated as $y \to 0$, it is found that $\tau_1(x)$ is proportional to the pressure perturbation, and therefore decreases monotonically with increasing x; also $\tau_{1\ell}$ is constant. The term $\tau_{11}(x)$ is obtained as a lengthy expression including terms proportional to the pressure perturbation and a positive term proportional to ln x (ref. 9). Since the pressure perturbation decreases to zero as x increases (i.e., is small for $\epsilon^{1/2\delta} \ll X \ll 1$), it follows that τ_w has a minimum. Thus for typical values of M_e and Re figure 4 shows that τ_w first decreases sharply and then rises again slowly. At a given x, τ_w decreases as ϵ increases and increases as Re increases. This behavior is in general agreement with existing experimental results.

If it is assumed that equation (3) remains a good approximation even when changes in τ_w are not small as originally assumed, a criterion for incipient separation can be proposed. For example, curve III in figure 4 is drawn for $Re^* = 10^6$ and $M_e = 1.149$, corresponding to $\epsilon = 0.12$; if ϵ is increased to 0.2, the minimum value of τ_w decreases to zero, and this is taken as an indication of incipient separation. Values of M_e corresponding to this condition, namely that $\tau_w = 0$ and $d\tau_w/dx = 0$ simultaneously, are plotted against Re^* in figure 5, and show a slow increase in the shock strength required for separation as Re increases. As a first step toward studying flows with separation, a numerical solution was also carried out for a momentum equation appropriate for describing a slender low-speed separation bubble having length $\Delta x = 0(1)$. Terms were retained to represent the laminar and turbulent stresses and the pressure gradient, which was considered known from the previous solutions because the displacement effect of the bubble was sufficiently small. Velocity profiles obtained are plotted against $\hat{y}$ in figure 6.

CONCLUDING REMARKS

The favorable comparison with experiment shown in the figures for the latter part of the pressure rise seems to imply that the asymptotic representation given here, with the addition of second-order terms as noted, does correctly include the most important features of the local flow field. A study of other second-order terms is continuing, and an analytical solution has been derived for the correction necessary in the flow behind a shock wave in a circular pipe; a comparison with existing experimental results is being carried out. It is anticipated that a comparison with numerical results of Melnick and Grossman will suggest a simple curve fit, in terms of a coordinate nondimensional with the distance to the sonic line, to fill in the wall pressure in the region near the origin. It should now be possible to incorporate these analytical representations for the local pressure and velocity into potential-flow calculations of the transonic flow past an airfoil. The predictions for wall shear, and for the Mach number at which separation first occurs, show the expected trends, and should be checked for quantitative accuracy against existing experimental data. It would seem especially important to continue the attempt at developing a rational theory of separation for turbulent boundary layers.

REFERENCES

1. Adamson, T.C., Jr.; and Feo, A.: Interaction between a Shock Wave and a Turbulent Boundary Layer in Transonic Flow. SIAM J. Appl. Math., vol. 29, 1975, pp. 121-145.

2. Melnik, P.E.; and Grossman, B.: Analysis of the Interaction of a Weak Normal Shock Wave with a Turbulent Boundary Layer. AIAA Paper No. 74-598, 1974.

3. Melnik, R.E.; and Grossman, B.: Further Developments in an Analysis of the Interaction of a Weak Normal Shock Wave with a Turbulent Boundary Layer. Symposium Transsonicum II, K. Oswatitsch and D. Rues, eds. Springer-Verlag, 1976, pp. 262-272.

4. Melnik, R.E.; and Grossman, B.: Interactions of Normal Shock Waves with Turbulent Boundary Layers at Transonic Speeds. Transonic Flow Problems in Turbomachinery, T.C. Adamson, Jr., and M.J. Platzer, eds. Plenum Press, 1977, pp. 415-433.

5. Adamson, T.C., Jr.; and Messiter, A.F.: Normal Shock Wave - Turbulent Boundary Layer Interactions in Transonic Flow near Separation. Transonic Flow Problems in Turbomachinery, T.C. Adamson, Jr., and M.F. Platzer, eds. Plenum Press, 1977, pp. 392-414.

6. Adamson, T.C., Jr.,: The Structure of Shock Wave - Turbulent Boundary Layer Interactions in Transonic Flow. Symposium Transsonicum II, K. Oswatitsch and D. Rues, eds. Springer-Verlag, 1976, pp. 244-251.

7. Cebeci, T.; and Smith, A.M.O.: Analysis of Turbulent Boundary Layers. Academic Press, 1974.

8. Ackeret, J.; Feldmann, F.; and Rott, N.: Untersuchungen an Verdichtungsstössen und Grenzschichten in schnell bewegten Gasen. Mitteilungen aus dem Institut für Aerodynamik, ETH Zürich, Nr. 10, 1946. Translated as NACA TM 1113, 1947.

9. Liou, M.S.: Asymptotic Analysis of Interaction between a Normal Shock Wave and a Turbulent Boundary Layer in Transonic Flow. Ph.D. Thesis, Department of Aerospace Engineering, The University of Michigan, 1977.

C-4

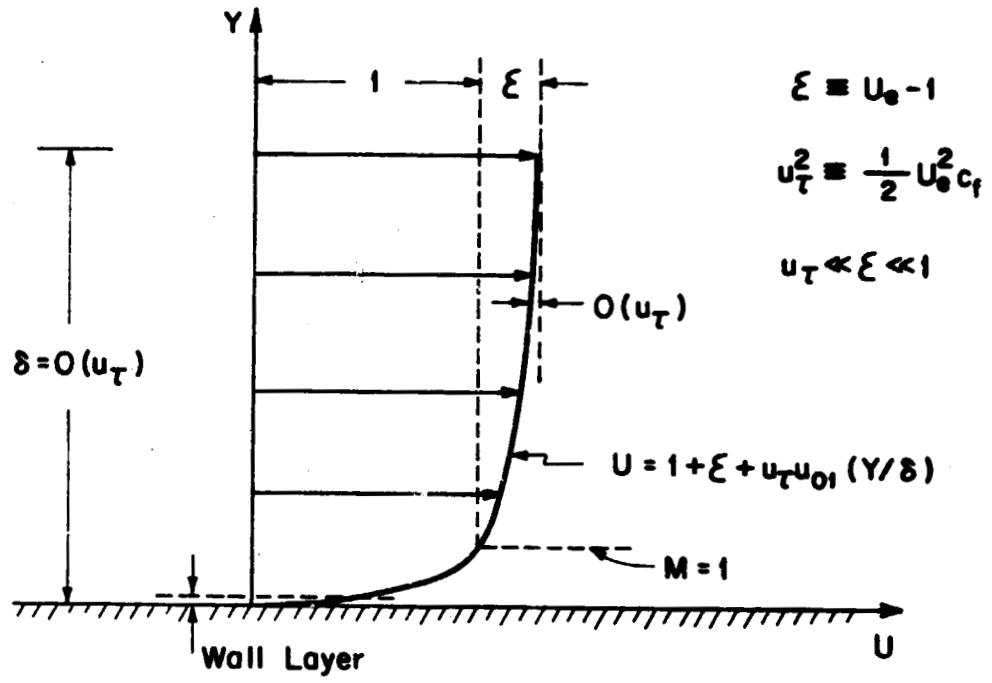

Figure 1.- Velocity profile in undisturbed boundary layer.

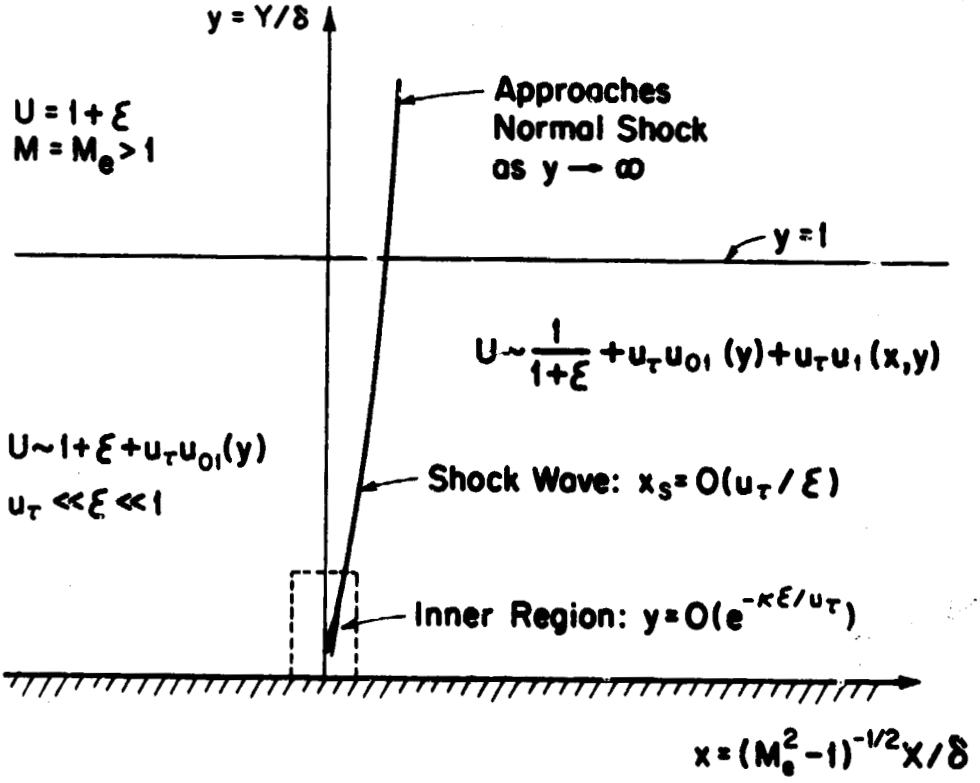

Figure 2.- Representation of outer flow field.

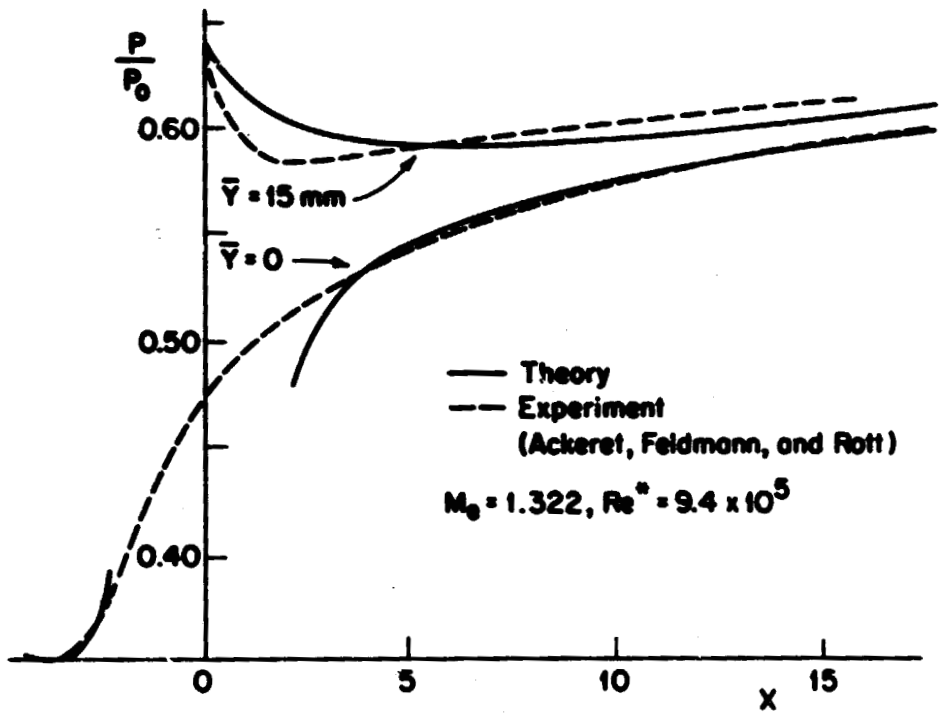

Figure 3.- Pressure distributions.

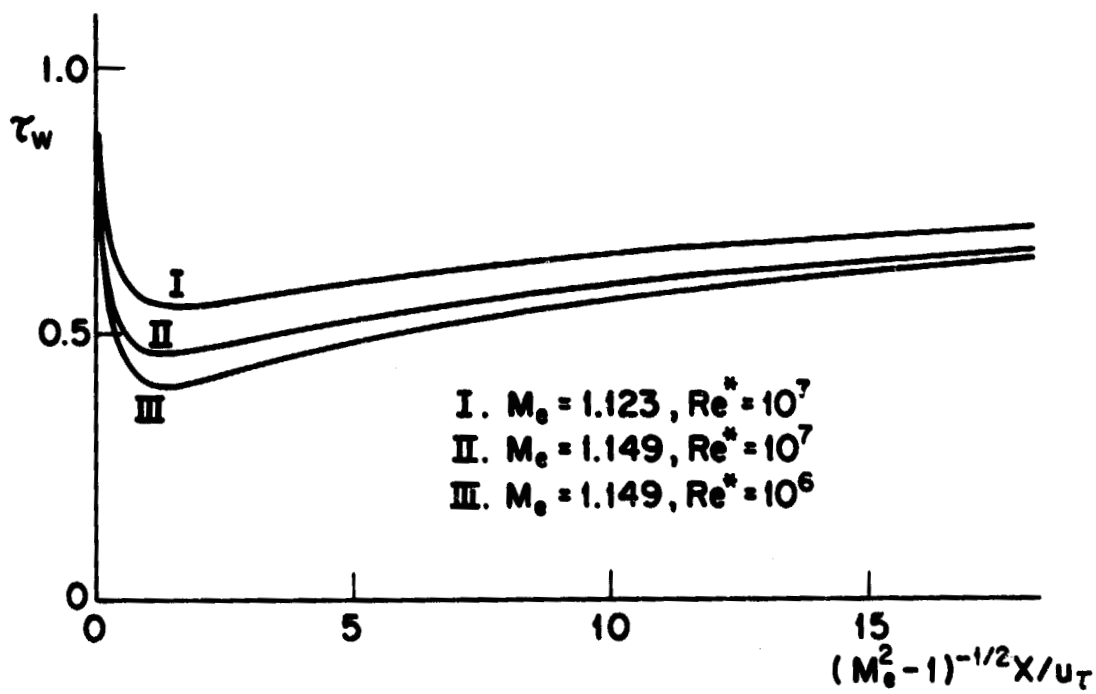

Figure 4.- Predicted wall shear stress.

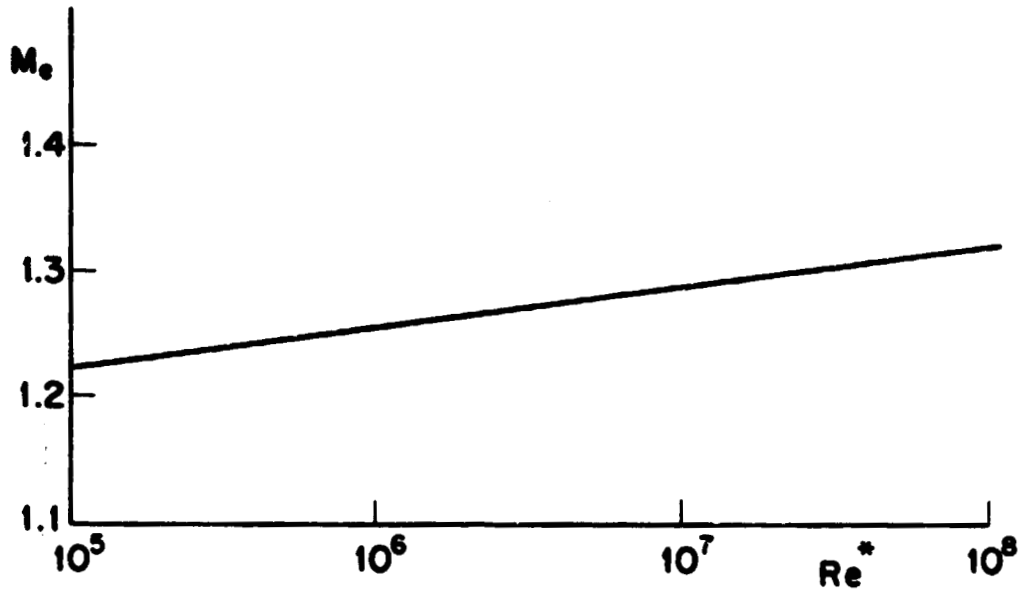

Figure 5.- Predicted variation of Mach number with Reynolds number at incipient separation.

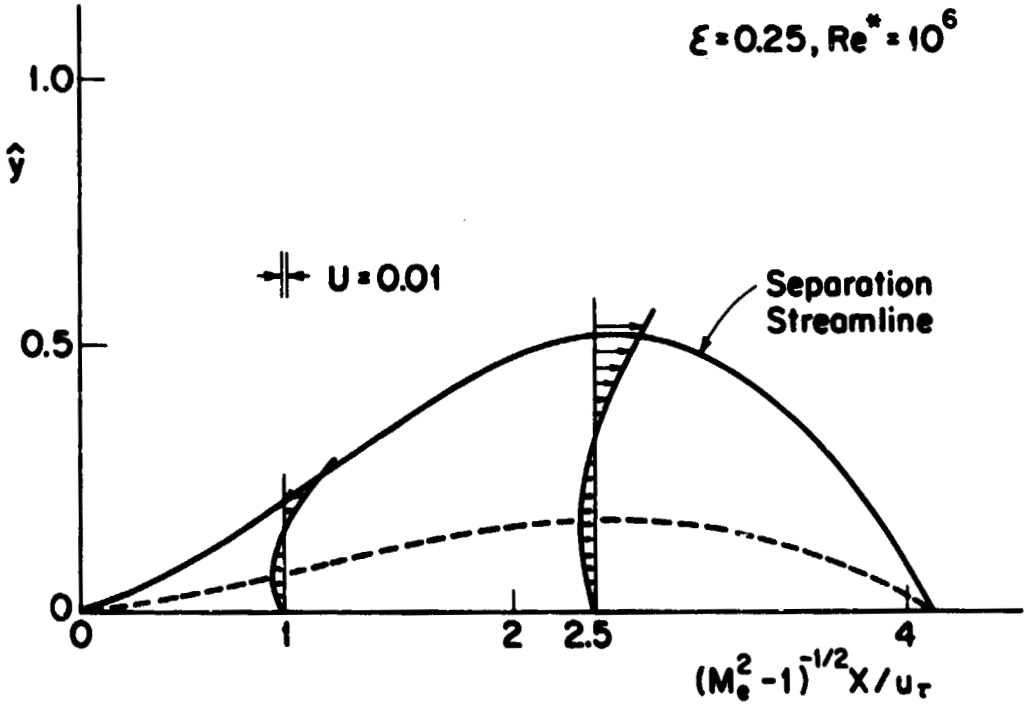

Figure 6.- Calculated velocity profiles in a slender separated-flow region.

RECENT DEVELOPMENTS IN FINITE ELEMENT ANALYSIS FOR TRANSONIC AIRFOILS*

M. M. Hafez and E. M. Murman
Flow Research Co., Kent, Washington

INTRODUCTION

The prediction of aerodynamic forces in the transonic regime generally requires a flow field calculation to solve the governing non-linear mixed elliptic-hyperbolic partial differential equations. Finite difference techniques have been developed to the point that design and analysis application are routine, and continual improvements are being made by various research groups. The principal limitation in extending finite difference methods to complex three-dimensional geometries is the construction of a suitable mesh system. Finite element techniques are attractive since their application to other problems have permitted irregular mesh elements to be employed. The purpose of this paper is to review the recent developments in the application of finite element methods to transonic flow problems and to report some recent results of our own study. In most cases, the reader is referred to the original paper for the details.

Finite element methods have been quite sucessful when applied to elliptic problems, particularly in elasticity and structures. A straightforward application of these techniques to the transonic problem involving mixed elliptic-hyperbolic equations with embedded shock waves has not proven successful. In general, either the finite element method must be modified to treat the transonic flow equations or the transonic flow equations must be modified to fit the finite element method. For the latter approach, additional terms (with hopefully small coefficients) are added to the equations representing artificial viscosity, artificial density or artificial time. The general mesh shapes used for elliptic problems result in matrices which are not well ordered. Thus either a direct matrix inversion or an explicit iterative method is required. Both of these approaches are computationally inefficient for realistic problems compared to the implicit methods which have been developed. Some work reported later in this paper may relax this conclusion. Finally, the higher order shape functions used in elliptic problems do not appear as attractive for mixed problems with shocks. In this paper, we review the subject by generally grouping together methods following the same general formulation.

SYMBOLS

All symbols are dimensionals.

A	matrix operator in equation Aw = f
C_p	pressure coefficient
c	coefficient in Tricomi equation
f	right hand side in equation Aw = f

* This work was supported under NASA Contract NAS 1-14246.

F	function in equation (5)
G	matrix in equations (6), (7)
I	functional
L	Laplace operator
M_∞	freestream Mach number
P	pressure
Q	matrix operator
R	residual operator
s	streamwise coordinate
t	time-like variable
u,v	velocity component in x,y directions
w	dummy dependent variable
x,y	independent variables
α,β	coefficients in equation (1)
γ	ratio of specific heats
δ	incremental difference operator ($\delta a = a^{n+1} - a^n$)
Δ	finite difference operator ($\Delta x = x_2 - x_1$)
ε	coefficient in equation (1)
λ	parameter in equation (4)
μ	switching factor, equation (34)
ν	coefficient in equation (1)
ρ	density
$\tilde{\rho}$	artificial density
ϕ	potential function
*	transpose operator

TIME-DEPENDENT METHODS

The Euler equations as well as the unsteady full potential equation are hyperbolic in time, whether or not the flow is locally subsonic or supersonic in space. With this in mind, Wellford and Hafez (ref. 1) solved the following augmented system for the transonic small-disturbance equation:

$$\alpha u_t = ((1 - M_\infty^2)u - \frac{\gamma+1}{2} M_\infty^2 u^2)_x + v_y + \nu_1 u_{xx} - \varepsilon_1 u \qquad (1)$$

$$\beta v_t = u_y - v_x + \nu_2 v_{yy} - \varepsilon_2 v$$

where regularization terms βv_t, $\nu_1 u_{xx}$, $\nu_2 v_{yy}$, $\varepsilon_1 u$, $\varepsilon_2 v$ are added explicitly. The coefficients ε, ν, β are assumed to be small. An implicit Crank-Nicholson finite difference scheme was used for the time derivatives and a standard Galerkin finite element approach was used for the space derivatives. Stability and convergence were rigorously analyzed. It was shown that a minimum amount of viscosity ν_1, related to the magnitude of the drag, is needed. Results shown in fig. 1 are generally in agreement with finite difference results, but the accuracy is not acceptable for the element density used. The method converged slowly, but it may be useful for unsteady problems.

Hafez, Wellford and Murman (ref. 2) considered an extention of this method to the full potential equation in the conservative form

$$\rho_t = -(\rho u)_x - (\rho v)_y \quad , \quad u_t = w_x \quad , \quad v_t = w_y \tag{2}$$

where $$w = \rho^{\gamma-1} - \left(1 - \frac{\gamma-1}{2} M_\infty^2 (u^2 + v^2 - 1)\right) = \phi_t \tag{3}$$

Again, artificial viscosity terms as well as damping terms (αw) are added to the system. If we are interested only in the steady state solution, the transient behavior is not important and a faster iterative procedure may be possible. The work is still in progress.

Phares and Kneile (ref. 3) have reported finite element solutions of the unsteady Euler equations using a time dependent method. The equations are in non-conservative form with the dependent variables being u,v,t. Isoparametric elements are used along with a Galerkin method for the spatial derivatives. A result from their study is shown in figure 2. The results look quite good, but the rate of convergence is about a hundred times slower than relaxation solutions of the full potential equation.

VARIATIONAL METHODS

For subsonic flows, the full potential equation is elliptic and there are many impressive finite element solutions. Most of this work is based on the Bateman variational principle. For transonic flows, however, the second variation ceases to be positive definite. Hafez, Wellford and Murman (ref. 2) introduced mixed variational formulations using two different functionals. The first given in terms of ϕ, u and v is:

$$I(\phi,u,v) = \iint \left\{ \frac{\lambda}{2} \left[(\phi_x - u)^2 + (\phi_y - v)^2 \right] + \rho \left[(u^2 - u\phi_x) + (v^2 - v\phi_y) \right] + p \right\} dA \tag{4}$$

where $p = \rho^\gamma / \gamma M^2$, λ is a free parameter and $\rho = \rho(u,v)$. Numerical results shown in figure 3 for the case of small-disturbance approximation indicate approximately the right solution but some apparent inaccuracies. The second functional given in terms of ϕ and ρ is:

$$I(\phi,\rho) = \iint \left[F(\rho) + \frac{1}{2} \rho(\phi_x^2 + \phi_y^2) \right] dA \tag{5}$$

where $F(\rho) = -C_1 \frac{\rho^\gamma}{\gamma-1} + C_2\rho$. The two associated Euler equations are the continuity and the energy equations in ρ and ϕ . Notice that the natural boundary condition associated with equation (5) admits the right jump conditions across the shock (i.e., mass is conserved). This is a consequence of the definition of weak solutions. The two Euler equations must be solved simultaneously. The method appears attractive, but no solutions are yet available. As an extension to the above ideas, we note that it is possible to construct a general gradient method

$$\begin{pmatrix} \delta\phi \\ \delta\rho \end{pmatrix} = -G \begin{pmatrix} \frac{\partial I}{\partial \phi} \\ \frac{\partial I}{\partial \rho} \end{pmatrix} \tag{6}$$

(7)

where G is 2 x 2 matrix. Notice if we choose $G = \begin{pmatrix} o & w_1 \\ w_2 & o \end{pmatrix}$ where $w_1 = \frac{\Delta t}{(\gamma-1)M_\infty^2}$ and $w_2 = \Delta t$, the system (equations (6) and (7)) is hyperbolic in time for subsonic as well as supersonic regions. Different choices of G may lead to faster convergence. Dissipation terms will be needed for stability and to handle flows with shocks.

Eberle (ref. 4) has recently introduced a variational finite element method for the full potential equation. Artificial viscosity terms are added which may be interpreted as an artificial compressibility. The density is retarded upstream by a small (Δx) amount. The equations are solved in a transformed plane using a relaxation method. A calculated result is shown in figure 4. Other results in Eberle's report indicate a noticeable dependence of the solution on element density, element shape and the magnitude of the artificial viscosity. We note that the work of Eberle motivated the artificial compressibility work discussed later.

LEAST SQUARES AND OPTIMAL CONTROL METHODS

Given the differential equation $Aw = f$, an associated functional whose second variation is positive definite can always be formulated using least squares, namely minimizing the residual

$$||Aw - f||^2 = (Aw,Aw) - 2(f,Aw) + (f,f)$$

$$= (A^*Aw,w) - 2(A^*f,w) + (f,f) \tag{8}$$

where the usual notation of inner products, norms, and adjoints are used. Notice that $I = (A^*Aw,w) - 2(A^*f,w)$ is the Ritz variational functional for the problem $A^*Au = A^*f$ which is automatically self-adjoint. However, the order of the equation has doubled, and therefore, a gradient method such as

$$\delta w = -I_w = -A^*(Aw - f) \tag{9}$$

will converge very slowly. In order to accelerate the convergence of the iterative process modified gradient methods can be used. We will discuss here three examples.

In the first gradient method, a modification is made such that a Poisson's equation is solved at each iteration; namely

$$L\delta w = I_w \quad \text{or} \quad \delta w = L^{-1}A^*(Aw - f) \; . \tag{10}$$

Notice that higher order inter-element continuity of the shape functions is required for the least squares method compared to a Galerkin method. This problem may be avoided by writing the differential equation as a system of

lower order equations (see Lynn and Arya(refs. 5 and 6)). As an example, consider the Tricomi equation:

$$A\phi = c(x,y)\phi_{xx} + \phi_{yy} = 0$$

Minimizing

$$\iint (c\phi_{xx} + \phi_{yy})^2 \, dA \tag{11}$$

leads to:

$$A^*A\phi = \left(\frac{\partial^2 c}{\partial x^2} + \frac{\partial^2}{\partial y^2}\right)(c\phi_{xx} + \phi_{yy})$$

$$= (c^2\phi_{xx})_{xx} + \phi_{yyyy} + (c\phi_{yy})_{xx} + (c\phi_{xx})_{yy} = 0 \quad . \tag{12}$$

Alternatively,

$$\text{let} \quad u = \phi_x \ , \quad v = \phi_y \ ; \quad \text{hence} \quad cu_x + v_y = 0 \tag{13}$$

and minimize

$$\iint \left[(u - \phi_x)^2 + (v - \phi_y)^2 + \lambda^2 (cu_x + v_y)^2 \right] dA \tag{14}$$

For simplicity, λ is taken to be unity. In general, the choice of λ may improve the rate of convergence with respect to the mesh size as well as with respect to iteration. The Euler equations then may be written as

$$\phi_{xx} + \phi_{yy} = u_x + v_y \tag{15}$$

$$(c^2 u_x)_x + (cv_y)_x - u = -\phi_x \tag{16}$$

$$(cu_x)_y + (v_y)_y - v = -\phi_y \tag{17}$$

A straightforward iterative procedure to solve equations (15) to (17) is as follows: Given ϕ , find u and v from equations (16) and (17), then using the most recent values of u and v in equation (15), a new value of ϕ is obtained. This procedure can be described by

$$(\delta u)_x + (\delta v)_y = (c^2 u_x)_{xx} + (cv_y)_{xx} + (v_y)_{yy} + (cu_x)_{xx} \tag{18}$$

In terms of ϕ , equation (18) is essentially (except for compatibility terms)

$$L\delta\phi = A^*A\phi + \cdots \tag{19}$$

It should be mentioned that the advantage of using equation (14) instead of equation (11) is that the elements used in the approximation of the latter must have continuous first derivatives, a fact which eliminates virtually all of the important practical elements. It is also worth mentioning here that a linear

element approximation leads to undesirable convergence characteristics with respect to mesh size as discussed by Lynn and Arya (refs. 5 and 6). It is obvious that if linear element trial functions are used for u and v , a bilinear approximation is needed for ϕ .

Different least square formulations of the full potential equation are given in Table I. Chan and Brashears (ref. 7) solved the transonic small-disturbance equation by least squares similar to equation (11). Fix and Gunzburger (ref. 8) as well as Glowinski et al. (refs. 9 and 10) used a formulation similar to equation (14).

For the second method, we note that A is a second order operator. The "closest" positive operator to A*A is the Biharmonic L*L ; hence an iterative procedure based on

$$L^*L\delta w = -I_w = -A^*(Aw - f) \tag{20}$$

is expected to be fast provided the inverse of $(L^*L)^{-1}$ is easily obtained. Equation (20) is also equivalent to

$$R = Aw - f \quad , \quad L^*Z = A^*R \quad , \quad L\delta w = Z \quad . \tag{21}$$

The third method results from a more elegant decomposition of equation (20) obtained by modifying the inner product, namely

$$\tilde{I} = ((Aw - f) \ , \ Q(Aw - f))$$

$$= (A^*QAw,w) - 2(A^*Qf,w) + (f,Qf) \tag{22}$$

hence,

$$\tilde{I}_w = A^*QAw - A^*Qf \tag{23}$$

where $Q^* = Q$ the choice of $Q = L^{-1}$ makes $A^*L^{-1}A$ effectively second order. The gradient method gives

$$\delta w = A^*L^{-1}(Aw - f) \tag{24}$$

and the modified gradient method gives

$$L\delta w = -A^*L^{-1}(Aw - f) \tag{25}$$

which may be decomposed into

$$LZ = Aw - f \quad , \quad L\delta w = -A^*Z \tag{26}$$

Effectively, each step has an operator of zero order. Notice that

$$\tilde{I} = -((Lz) \ , \ L^{-1}(LZ)) \ , = -(LZ,Z) \quad . \tag{27}$$

Upon integration by parts, $\tilde{I}$ becomes

$$\tilde{I} = (\nabla Z, \nabla Z) = ||\nabla Z||^2 = \iint |\nabla Z|^2 \ . \tag{28}$$

Recently Glowinski et al. (refs. 9 and 10) solved the full potential transonic flow equation using an equivalent procedure, namely

$$\text{minimize} \quad \iint |\nabla Z|^2 \, dA \quad \text{w.r.t. w} \tag{29}$$

under the constraint

$$LZ = Aw - f \quad \text{where} \quad Z = \phi - w \ . \tag{30}$$

The discussion with Professor Antony Jameson of Courant Institute helped the author in the preparation of this section of this paper.

TREATMENT OF SHOCKS

In the above formulations, expansion as well as compression shocks are admitted since the potential flow is reversible. In order to exclude expansion shocks, Glowinski et al. (refs. 9 and 10) introduced an entropy constraint* to the least squares formulation, namely

$$\nabla^2 \phi = M^2 \phi_{ss} < + \infty \tag{31}$$

A result shown in figure 5 indicates quite good agreement between the results and an exact solution for a shock-free airfoil. An alternative procedure has been introduced by Bristeau (ref. 12) in which artificial viscosity terms are explicitly added to the continuity equation in addition to the above constraint. A result is shown in figure 6. We notice here that the special assembly procedure used by Chan and Brashears (ref. 7) may effectively produce some sort of artificial viscosity in an obscure way without which the solution cannot be obtained.

FINITE VOLUMES

Finite volume methods use general nonorthogonal coordinates and consider the governing integral equations as balances of mass, momentum, and energy fluxes for each finite volume defined by the intersection of the coordinate surfaces. Rizzi (ref. 13) applied the finite volume method to the Euler equation for transonic flows and calculated the time-accurate solution until it converged to a steady state. Factored explicit and implicit difference operators were used to accelerate the calculations. Several computed examples are given in the reference.

---

*A different procedure was used by Chattot (ref. 11) in his least squares formulation of Euler Equations to exclude the expansion shock by imposing $US_x + VS_y \geq 0$.

Jameson and Caughey (ref. 14) have recently applied the finite volume method to the steady full-potential equation in conservation form by using mixed-type flux operators. Centered difference operators are used with artificial viscosity added in supersonic cells. Isoparametric mesh system is used and the equations are solved by relaxation. The method combines the advantage of finite elements for handling complicated geometries and the advantage of using simple finite difference schemes in the transformed coordinates. A typical calculation is shown in figure 7.

The same concept has been recently used by Lucchi (ref. 15) with different higher order elements and with the velocities and the density as variables. He used direct inversion to solve the matrix equation.

ARTIFICIAL COMPRESSIBILITY METHODS

Following the work of Eberle (ref. 4), we have explored the application of an artificial compressibility approach for both finite element and finite difference methods for mixed equations. The idea behind these new methods is to modify the density (and/or the speed of sound) in the supersonic region slightly (within the same order of the truncation error) and solve the resulting problem iteratively with standard methods used for the solution of elliptic problems. The density modification can be interpreted as an artificial viscosity effect. The modified equation reads

$$(\tilde{\rho}\phi_x)_x = (\tilde{\rho}\phi_y)_y = 0 \ . \tag{32}$$

For example, Jameson's fully conservative schemes can be approximated by this form where

$$\tilde{\rho} = \rho + \mu \frac{\rho}{a^2} (uu_x \Delta x + vv_y \Delta y) \tag{33}$$

and

$$\mu = \max (0, 1 - 1/M^2) \ . \tag{34}$$

We have tested an alternative form

$$\tilde{\rho} = \rho - \mu \rho_s \, \Delta s \tag{35}$$

where

$$\Delta s \rho_s = \frac{u}{q} \rho_x \Delta x + \frac{v}{q} \rho_y \Delta y \tag{36}$$

Other possible forms are under study including modification of the speed of sound.

Standard central difference formulas are used for equation (32) and $\tilde{\rho}$ evaluated at the previous iteration. In the formula for $\tilde{\rho}$, upwind differencing is used in the supersonic region. Various interative methods have been tested successfully including SOR (vertical-horizontal-SSOR), ADI, a second order explicit method, fast solver and multigrid method. A numerical result is shown in figure 8 using a three level explicit scheme. The rate of convergence of this calculation is comparable to the relaxation method. The method is still under development and details will be reported in a separate paper.

CONCLUDING REMARKS

A considerable amount of work has been reported during the last few years exploring the application of finite element methods to transonic flow problems. In general, it is found that classical finite element methods are not directly applicable. Modifications must be made either in the finite element method or the governing equation. For the latter approach, artificial viscosity terms must be added. Elliptic type solvers are required for the spatial derivatives with a suitable iterative scheme required in the time-like direction. Some of the methods appear attractive and are being applied to realistic airfoil geometries.

REFERENCES

1. Wellford, L. C.; and Hafez, M. M.: An Implicit Velocity Formulation for the Small Disturbance Transonic Flow Problem Using Finite Elements. Presented at the Symposium on Applications of Computer Methods in Engineering, University of Southern California, August 1977.

2. Hafez, M. M.; Wellford, L. C.; and Murman, E. M.: Finite Elements and Finite Differences for Transonic Flow Calculations. Finite Elements in Fluids : Chapter 12, Vol. 3 Editor, Gallagher et al., John Wiley 1978.

3. Phares, W. J., and Kneile, K. R.: Solution to the Eulerian Equations by the Finite Element Method With an Application to Transonic Flow. Arnold Eng. Development Center; ARO Inc., AEDC-TR-76-86, 1976.

4. Eberle, A.: Eine Methode Finiter Elements Zur Brechnung der Transsonischen Potential-Stromung um Profile. MBB Bericht Nr. UEE 132(0), 1977.

5. Lynn, P. P.; and Arya, S. K.: Use of the Least Squares Criterion in the Finite Element Formulation. Int. J. Num. Methods in Eng. Vol. 6, 1973, pp. 65-88.

6. Lynn, P. P.; and Arya, S. K.: Finite Elements Formulated by the Weighted Discrete Least Squares Method. Int. J. Num. Methods in Eng. Vol. 8, 1974, pp. 71-90.

7. Chan, S. T. K.; Brashears, M. R.: Finite Element Analysis of Transonic Flow. AFFDL-TR-74-11, March 1974.

8. Fix, G.; and Gunzburger, M. D.: On Least Squares Approximations to Indefinite Problems of the Mixed Type. ICASE Report No. 76-26, 1976.

9. Glowinski, R.; Periaux, J.; and Pironneau, O.: Transonic Flow Simulation by the Finite Element Method Via Optimal Control. International Symposium on Finite Element Methods in Flow Problems, Santa Margherita Ligure, Italy, June 1976.

10. Glowinski, R.; and Pironneau, O.: On the Computation of Transonic Flows. France-Japanese Conference on Functional Analysis and Numerical Analysis, Tokyo, Kyoto, September 1976.

11. Chattot, J. J.: Relaxation Approach to the Steady Euler Equations in Transonic Flow. Proceedings of AIAA 3rd Computational Fluid Dynamics Conference, Albuquerque, New Mexico, June 1977.

12. Bristeau, M. O.: Paper presented at RIA Conference, France, December 1977.

13. Rizzi, A.: Transonic Solutions of the Euler Equations by the Finite Volume Method. Symposium Transsonicum II, Springer-Veilag, 1976, pp. 567-574.

14. Jameson, A., Caughey, D. A.: Finite Volume Method for Transonic Potential Flow Calculations. AIAA Third Computational Fluid Dynamics Conference, New Mexico, June 1977.

15. Lucchi, C. W.: Developments of the Flux Finite Element Method in Two-Dimensional Potential Flow Problems. AIAA Paper 78-55, January 1978.

TABLE I.- LEAST-SQUARE FORMULATIONS FOR FULL POTENTIAL EQUATION

$$S = (\rho u)_x + (\rho v)_y$$

$$\Omega = u_y - v_x$$

$$h = \frac{1}{(\gamma-1)} (\rho^{\gamma-1} - a^2 M_\infty^2)$$

Functional

$$I(u,v) = \iint_S^2 \Omega^2$$

where $\rho = 1 - \frac{\gamma-1}{1} M_\infty^2 (u^2 + v^2 - 1)^{\frac{1}{\gamma-1}}$

$$I(u,v,\rho) = \iint_S^2 + \Omega^2 + h^2$$

where $a^2 = \frac{1}{M_\infty^2} - \frac{\gamma-1}{2} (u^2 + v^2 - 1)$

$$I(\phi,u,v) = \iint_S^2 + (u - \phi_x)^2 + (v - \phi_y)^2$$

where $\rho = 1 - \frac{\gamma-1}{2} M_\infty^2 (u^2 + v^2 - 1)^{\frac{1}{\gamma-1}}$

$$I(\phi,u,v,\rho) = \iint_S^2 + h^2 + (u - \phi_x)^2 + (v - \phi_u)^2$$

where $a^2 = \frac{1}{M_\infty^2} - \frac{\gamma-1}{2} (u^2 + v^2 - 1)$

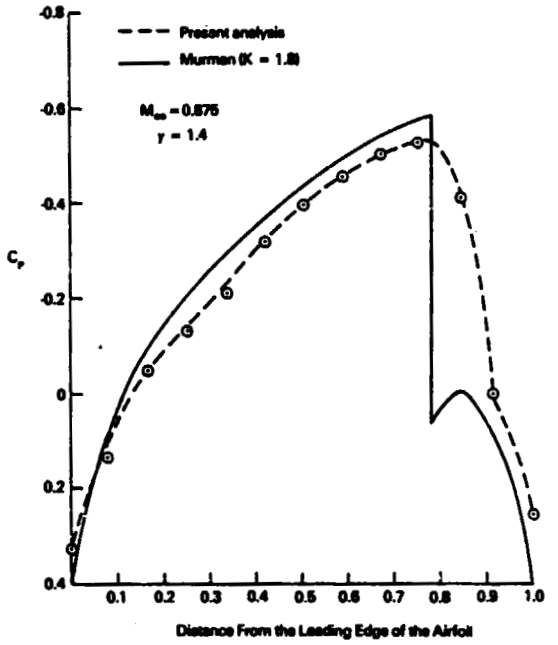

Figure 1.- Solution of transonic small-disturbance equations for parabolic-arc airfoil using implicit time-dependent finite-element method of Hafez, Wellford, and Murman (fig. from ref. 2).

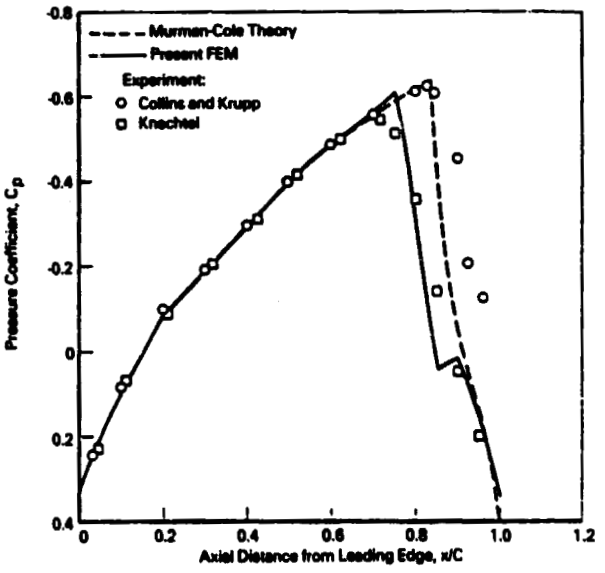

Figure 2.- Solution of Phares and Kneile using time-dependent finite-element method to solve Euler equations for flow past parabolic arc (fig. from ref. 3).

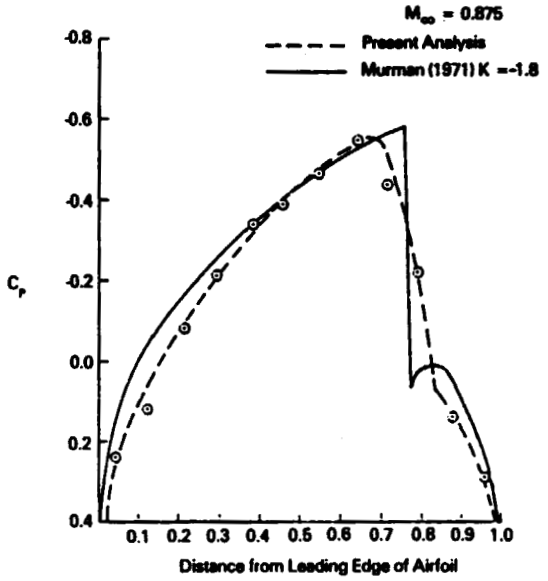

Figure 3.- Solution of transonic small-disturbance equation for flow past parabolic arc using mixed variational finite-element formulation of Hafez, Wellford, and Murman (fig. from ref. 2).

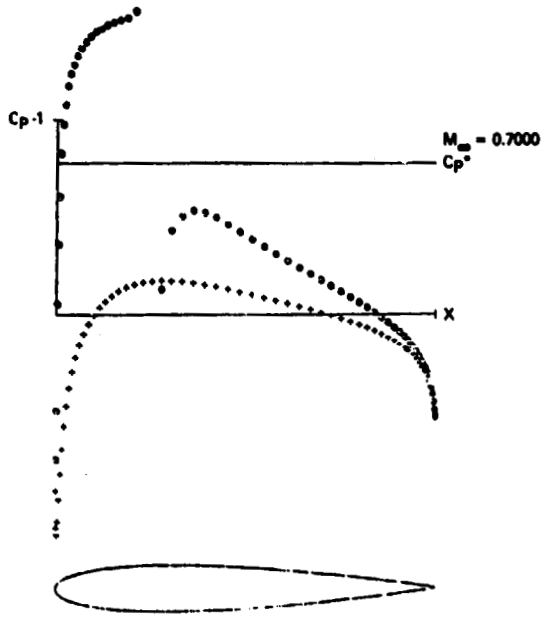

Figure 4.- Finite-element solution by Eberle for flow past NACA 0012 airfoil.

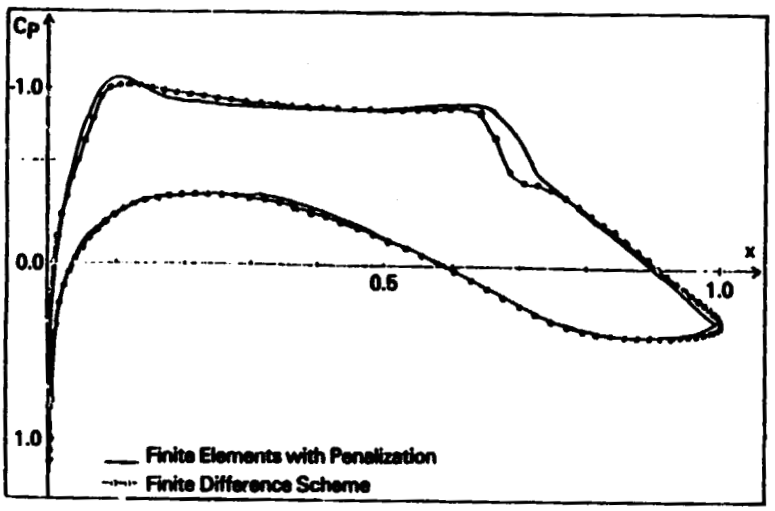

Figure 5.- Finite-element solution by Glowinski et al. for flow past Korn airfoil.

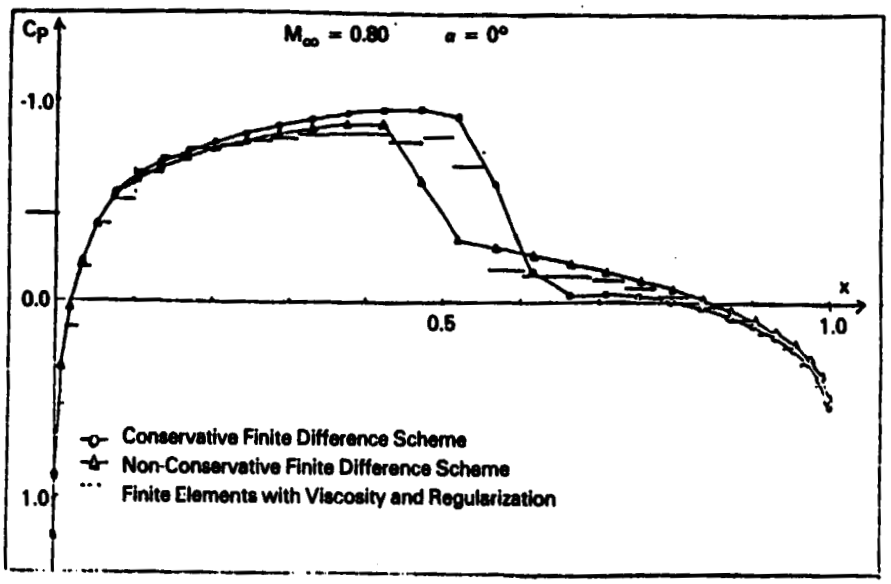

Figure 6.- Finite-element solution by Bristeau for flow past NACA 0012 airfoil.

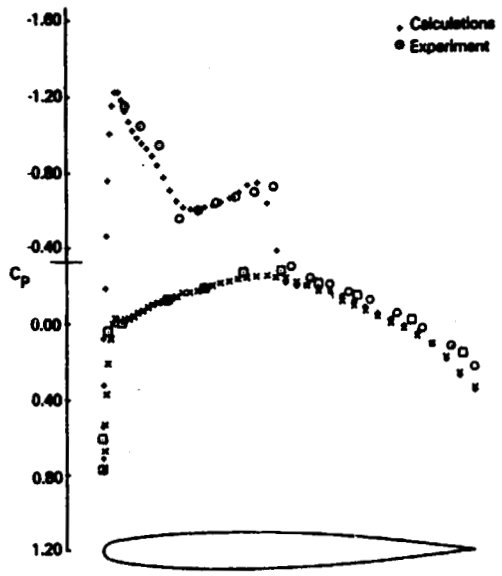

Figure 7.- Finite-volume solution of full-potential equation by Jameson and Caughey.

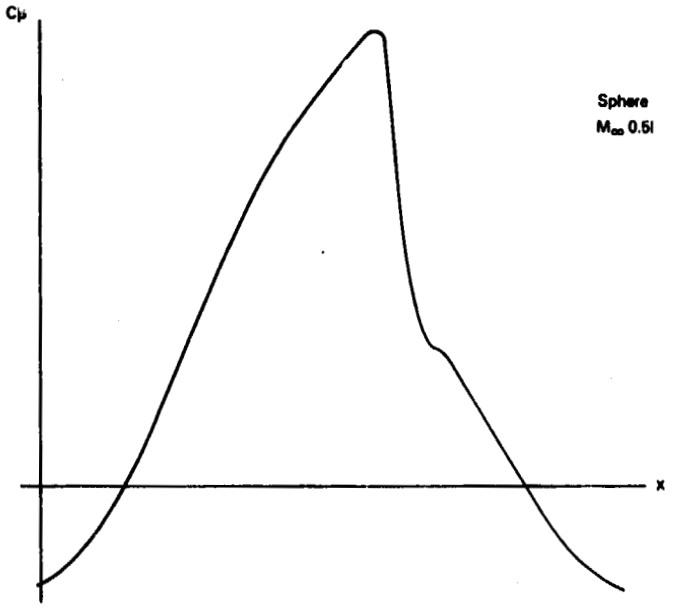

Figure 8.- Solution of full-potential equation using artificial compressibility method.

D18

N79-20048

18

SUPERCRITICAL TESTS OF A SELF-OPTIMIZING, VARIABLE-CAMBER WIND TUNNEL MODEL*

Ely S. Levinsky
General Dynamics Convair Division

Richard L. Palko
Sverdrup/ARO, Inc.

SUMMARY

A testing procedure has been used in the 16-foot Transonic Propulsion Wind Tunnel (PWT-16T) at the Arnold Engineering Development Center (AEDC) which leads to optimum wing airfoil sections without stopping the tunnel for model changes. Being experimental, the optimum shapes obtained incorporate various three-dimensional and nonlinear viscous and transonic effects presently not included in analytical optimization methods. The present method is a closed-loop, computer-controlled, interactive procedure and employs a Self-Optimizing Flexible Technology (SOFT) wing semispan model that conformally adapts the airfoil section at two spanwise control stations to maximize or minimize various prescribed merit functions (e.g., minimum drag) subject to both equality and inequality constraints (e.g., fixed lift, maximum spanwise differential deflection). The model, which employed twelve independent hydraulic actuator systems (nine functioned) and flexible skins, was also used for conventional testing (Ref. 1). Although six of seven optimizations attempted were at least partially convergent (several of which are shown herein), further improvements in model skin smoothness and hydraulic reliability are required to make the technique fully operational.

INTRODUCTION

Although considerable interest has been generated at this Advanced Technology Airfoil Research conference and in the past in the analytical design of optimum airfoils (e.g., Ref. 2-4), such methods are somewhat approximate, because of the inability of current-generation computers to evaluate the flow field with sufficient accuracy and rapidity. This is especially true under conditions of high lift or supercritical transonic flow, where boundary layer transition, separation and possible reattachment, and shock wave interaction are among the highly nonlinear flow phenomena still beyond analytical solution. In addition, the large number of flow field solutions required for each optimization may preclude analytical optimization of three-dimensional wings, even with the most advanced digital computers.

The present SOFT wing optimization procedure differs from the analytical methods in that the wind tunnel is used as an analog computer, in conjunction with a flexible and controllable

* *This work was supported by the U.S. Navy, Office of Naval Research, under Contract N00014-76-C-0742; by the U.S. Air Force Flight Dynamics Laboratory and Arnold Engineering Development Center; and by ARO, Inc.*

model, to rapidly generate aerodynamic data, instead of using a digital computer for this purpose. In both cases, the data are then supplied to a computer, which controls and optimizes wing shape by application of nonlinear programming techniques. The SOFT wing procedure will, however, be limited by the extent of wing articulation and degree of shape control that may be obtained with a wind tunnel model.

Under a previous contract for the U.S. Navy (ONR), General Dynamics Convair Division fabricated and tested a two-dimensional flexible airfoil model that could be optimized in the tunnel in a manner similar to that used for the present SOFT wing model. The 2-D model was tested under both low-speed and transonic conditions (Ref. 5), and employed five pairs of hydraulic actuators to vary leading edge radius and camber. Airfoil shape and angle of attack were controlled "on line" to minimize drag, subject to constraints, using the gradient projection optimization algorithm. Satisfactory convergence was found, even with flow separation; however, because of the intermittent blow-down type operation of the transonic test facility, a sequence of individual runs was required to complete a single optimization problem.

The present 3-D SOFT wing model was tested in PWT-16T at AEDC during the summer of 1977. Test Mach numbers ranged from 0.6 to 0.925. The SOFT wing model employed twelve independent hydraulic actuator systems similar in design to those in the 2-D model. The computer-controlled testing and optimization techniques were also similar, but the number of control channels was increased to handle the larger number of independent control variables. Because of the continuous operation of Tunnel 16T, continuous computer control of the wing could be maintained during an optimization, and under ideal circumstances, a single run in the wind tunnel was sufficient to arrive at an optimum wing shape for a prescribed test condition.

The present paper briefly describes the SOFT wing model, closed-loop testing technique and optimization procedure, summarizes several of the optimization problems attempted, and reviews the causes of various difficulties.

SYMBOLS

A_{ij}	Actuator positions in counts ($0 \leq A_{ij} \leq 1000$)
C_D	Drag coefficient
C_L	Lift coefficient
F	Objective function being minimized
g	Vector of constraints
K_i	Stepsize of i^{th} simultaneous mode point
M	Mach number
N	Iteration number
R	Restoration function
S, S_R	Vector search directions
α	Angle of attack
Λ	Lagrange multiplier vector
ϕ	Merit function to be minimized
θ	Independent variables (transformed)
∇	Gradient vector

Superscript

T	Transposed matrix
*	Best K; also uncorrected for weight tares

WIND TUNNEL MODEL

The 1/6-scale semispan model consisted of an existing fuselage with a flow-through nacelle, an existing horizontal tail surface, and the three-dimensional SOFT wing panel tested at leading edge sweep angle 26°. The wing actuators, shown schematically in Figure 1, are designed to perform the following variations:

A_{11}	Nose radius, inboard station
A_{12}	Nose deflection about 15% chord line, inboard station
A_{13}	Nose deflection about 25% chord line, inboard station
A_{14}	Upper surface humping, inboard station
A_{15}	Trailing edge deflection about 65% chord line, inboard station
A_{16}	Trailing edge deflection about 80% chord line, inboard station
A_{21}-A_{26}	Same as A_{11}-A_{16}, except at outboard stations

All systems except for the A_{14}, A_{21}, and A_{24} actuators remained functional throughout the test, giving a total of ten degrees of freedom, including α. The wing was fabricated with flexible leading edge and trailing edge skins with sliding joints to permit deflections up to 15° (nose) and 30° (trailing edge). The spars, skin sections, and linkages were designed to conform to a specific target shape designated T-1 with the actuators set at the nominal positions (Figure 2). Other target (T), envelope (E), parametric (P) and optimum (O) wing shapes tested are listed in Table 1.

The model was mounted horizontally and inverted off a sharp edge reflection plane supported from the wind tunnel sidewall. The model is shown fully assembled and installed as tested in Figure 3.

CLOSED-LOOP TEST PROCEDURE

A closed-loop testing technique was employed to set wing shape from the time that the skins were installed to avoid damaging the model. The block diagram of Figure 4 shows the basic elements of the control system and computer linkup. All actuator position changes were made through the PWT DEC System 10 computer, both for conventional and optimization runs. Conventional runs were made either by stepping the actuators through a prescribed sequence of positions at fixed α and M, or by holding the actuators fixed and stepping α through a prescribed schedule.

In general, the tunnel was run continuously while making airfoil shape changes between runs and while changing from conventional to optimization runs. Thus, even for conventional tests, the SOFT wing showed promise of being highly efficient and productive in that no tunnel down time was required to make model changes.

For optimization testing, the optimization program played a central role in that it generated the commands for changing the A_{ij} and α settings, as described below.

OPTIMIZATION PROGRAM

A flow chart of the optimization procedure, which was based on the gradient projection optimization algorithm, is presented in Figure 5. The optimization program operates in two distinct modes: "incremental" and "simultaneous." Only the incremental mode is used during the initial iteration (and restarts), during which each active actuator and angle of attack is perturbed individually to generate gradient vectors $\nabla\phi$ and ∇g of the merit function and active constraints, respectively. The number of incremental mode points per iteration depends on the number of active actuators and on the number of times the perturbations are repeated to improve accuracy (termed "cycling"). With 9 active actuators, there were 11 incremental mode points per cycle.

After the incremental mode, the vector directions S_R or S, for either restoring the constraints $g = 0$ or minimizing the objective function F during the next iteration, depending upon whether any constraints were violated at the nominal incremental mode point, are calculated by the gradient projection algorithm, which gives in matrix form:

$$F = -\phi + g\,\Lambda$$

$$S = -\nabla F$$

$$S_R = \nabla g\,(\nabla g^T \nabla g)^{-1} g$$

and

$$\Lambda = -(\nabla g^T \nabla g)^{-1}\,\nabla g^T \nabla \phi$$

The next iteration begins with the simultaneous mode, during which all active actuators and α are advanced together in the direction S or S_R, as obtained from the previous iteration, through a sequence of up to 11 test points of step size K_i. The sequence is aborted if any of the constraints are violated by more than the prescribed tolerance. Upon completion of the stepping, the computer selects the "best" of the simultaneous mode points K^* (either minimum $R = gg^T$ or minimum F), and then resets the wing shape to that configuration. The incremental mode is then repeated in preparation for the next iteration.

CONVENTIONAL RUNS

Only the conventional run data comparing the SOFT wing T-1 shape with a comparable solid-wing model equivalent to the W_{52} theoretical shape shown in Figure 2 will be presented. Figure 6 shows that wing shape T-1 experienced significantly higher drags, particularly at the higher Mach numbers, even though T-1 was set to match the W_{52} theoretical shape as closely as possible. The higher drag was most likely caused by the leading edge sliding skin joint (lap) of approximately 0.13 cm thickness that protruded out of contour on the upper surface, by a bulge that protruded out of contour in the outboard region of the aft lower surface, and by deviations in nose shape. The deviations in Figure 2 between the pre- and post-test T-1 shapes may account for the scatter band in Figure 6, since the flow at transonic conditions is highly sensitive to small changes in airfoil shape (Ref. 2). It is planned to improve the SOFT wing model for subsequent tests to approach solid model drag levels.

OPTIMIZATION RUNS

The optimization problems are summarized in Table 2, which lists Mach number, merit function, active constraints, convergence assessment, iteration number N considered optimum, and the percentage reduction in merit function. Each optimization problem was initiated with the

wing set at the T-1 target shape; the percentage of C_D^* decrease is with respect to the T-1 shape tested during the same (or closest) run sequence.

Weight tare corrections were inadvertently omitted during the on-line data reduction used to steer the direction of wing optimization. Consequently, evaluations of convergence were based upon uncorrected coefficients C_L^* and C_D^*, rather than on C_L and C_D. This error biased the optimization procedure in favor of increasing α at the expense of aft camber.

Only optimization Problem 4-2 (completed as Problem 30) will be discussed in detail. It deals with minimizing C_D^* for $C_L^* = 0.50$, subject to various inequality constraints on the actuators at Mach 0.85. As shown in Figure 7, Problem 4-2 was continued for six iterations, after which a premature shutdown was experienced, due to lubrication difficulties with a main compressor bearing. The optimization was then continued as Problem 30, without reinitialization. Figure 7 shows a graphical representation of the convergence process. All constraints are satisfied for the iterations represented by solid symbols, while the open symbols signify that at least one constraint has been violated. Iteration 17 is readily seen to have the lowest value of C_D^* with all constraints satisfied; it was, therefore, selected as optimum. The gap between Iterations 6 and 7 in Figure 7 was caused by the low q while the tunnel was shutting down during Iteration 6. The double values for C_D^* during Iterations 12 and 14 and the poor convergence displayed during this period were the result of excessive shifts in the A_{15} actuator position.

Variations of each functional actuator, α, and various dependent data functions during iteration N = 11 from Problem 30 are shown in Figure 8. The iteration, during which C_D^* is minimized, contains 11 simultaneous and 22 incremental mode points cycled twice. The precise control of actuator positions and the good repeatability of the aerodynamic data during the two incremental mode cycles are apparent.

Convergence in the C_L^*, C_D^* plane is shown in Figure 9. Also shown are the drag polars for the T-1 wing shapes run just before and after the optimization run, and that made with the optimum wing O-30 (Iteration 17). The advantage of the O-30 wing shape over T-1 at the design C_L^* is clearly apparent. Unfortunately, this same reduction was not found in C_D because of the tare effects referred to previously. A correction for tare effects (made after the test for iteration N = 4) showed that increased trailing edge deflections, decreased angles of attack, and decreased values of C_D would have been obtained with the tare correction included (Figure 10).

Similar optimization results are shown in Figures 11 through 18 for problems 3-2, 41-2, and 4-3 of Table 2. Problem 3-2 is similar to 4-2 and 30, except for reduced articulation (only the A_{12}, A_{15}, A_{22}, and A_{25} actuators were varied, subject to $A_{12} = A_{22}$ and $A_{15} = A_{25}$). Figure 11 demonstrated excellent convergence, although the C_D^* improvement (N = 20) was now much less. The reduced articulation is apparent in Figure 12 (iteration N = 18), which also shows that the simultaneous mode was aborted after the ninth point of this iteration because the constraint on A_{15}-A_{25} was violated. Figure 13 shows that the C_D^* reduction for the optimum wing shape designated O-3.2 persisted over a wide range of C_L.

Problem 41-2 dealt with minimizing C_D^* at $C_L^* = 0.25$ with full model articulation. Excellent convergence was obtained, and iteration N = 29 was selected as optimum (Figure 14). Iteration N = 21 (Figure 15) is an example of a restoration. Note that all active constraints C_L^* and $|A_{ij} - A_{2j}|$ are restored within tolerance during the simultaneous mode. The convergence of Problem 41-2 in the C_L^*, C_D^* plane is shown in Figure 16.

Optimization Problem 4-3 was similar to 4-2 and 30, except that M = 0.90 instead of 0.85. Convergence in this case was rapid, as shown in Figure 17, with N = 10 selected as optimum. The corresponding wing shape O-4.3 shows a considerable improvement over the T-1 wing, as seen in Figure 18.

The resultant optimum wings are compared with T-1 in Figure 19. Although the weight tare biased the optimum shapes toward decreased aft camber, the increased leading edge droop of the optimum shapes, especially outboard, may well signify a shape modification that leads to lower drag at moderate to high C_L. On the other hand, Problems 42 and 10 (Table 2) showed marginal and no convergence, respectively. Both problems were attempted at high C_L and showed evidence of reduced control precision, possibly due to the high airloads on the actuators and/or buffeting. Further testing with an improved SOFT wing model is planned to overcome some of these difficulties and make experimental wing optimization an operational tool for the aircraft designer.

CONCLUSIONS

A first attempt has been made at developing an experimental 3-D wing optimization procedure involving a computer-controlled SOFT wing wind tunnel model. Although six of seven optimization problems attempted were at least partially convergent, difficulties were uncovered with deviations in airfoil contour, inadequate control precision at high C_L, and hydraulic system reliability, which increased drag levels and slowed or prevented convergence. Nevertheless, the SOFT wing technique appears to promise a means of generating optimum airfoil and wing shapes, which include all aerodynamic nonlinearities and viscous effects, with a saving in test time and which might not be found by conventional testing or by numerical optimization. Of course, any optimum wings will be limited by model articulation, and will reflect effects of tunnel wall interference, test Reynolds number and model deformation under airload. Plans call for improving the model and performing further tests to make the technique more operational.

REFERENCES

1. Levinsky, E. S. and Palko, R. L.: "Semispan Wind Tunnel Test of a Computer-Controlled Self-Optimizing Flexible Technology Wing," AIAA Paper 78-786, presented at AIAA Tenth Aerodynamic Testing Conference, April 19-21, 1978.
2. Johnson, R. R. and Hicks, R. M.: "Application of Numerical Optimization to the Design of Advanced Supercritical Airfoils," Advanced Technology Airfoil Research, Volume I, NASA CP-2045, Pt. 1, 1979.
3. Lores, M. E.; Burdges, K. P.; Shrewsbury, G. D.; and Hicks, R. M.: "An Evaluation of Numerical Optimization in Supercritical Airfoil Modification and Design," Advanced Technology Airfoil Research, Volume II, NASA CP-2046, 1979.
4. Hicks, R. M.; Murman, E. M.; and Vanderplaats, G. N.: "An Assessment of Airfoil Design by Numerical Optimization," NASA TMX-3092, July 1974.
5. Levinsky, E. S.; Schappelle, R. H.; and Pountney, S.: "Transonic Testing of a Self-Optimizing Flexible Airfoil," Proceedings of the AIAA Ninth Aerodynamic Testing Conference, June 7-9, 1976.

TABLE 1.- SOFT WING SHAPES TESTED

Designation	Wing Type	A_{11}	A_{12}	A_{13}	A_{14}	A_{15}	A_{16}	A_{21}	A_{22}	A_{23}	A_{24}	A_{25}	A_{26}	σ
T-1	Target No. 1	250	250	250	X	250	250	X	250	250	X	250	250	VAR
T-2	Target No. 2	250	125	143	X	350	60	X	176	94	X	400	56	VAR
T-3	Target No. 3	250	250	250	X	332	456	X	250	250	X	256	547	VAR
E-1	Min Deflection Envelope	100	100	97	X	98	99	X	100	102	X	99	100	VAR
E-2	Max Deflection Envelope	398	401	402	X	799	801	X	401	402	X	798	796	VAR
E-3	Max Diff. Twist Envelope	250	250	250	X	250	250	X	450	250	X	450	250	VAR
P-1	T-1 + δ_{TE} = 2.6°	250	250	250	X	380	250	X	250	250	X	380	250	VAR
P-2	T-1 + δ_{TE} = 5.6°	250	250	250	X	530	250	X	250	250	X	530	250	VAR
P-3	T-1 + δ_{LE} = 4°	250	450	250	X	250	250	X	450	250	X	250	250	VAR
P-4	T-1 + δ_{LE} = 7°	250	600	250	X	250	250	X	600	250	X	250	250	VAR
O-30	Optimum, Problem 30	332	249	536	X	169	73	X	372	530	X	314	127	6.77
O-3.2	Optimum, Problem 3-2	250	417	250	X	131	250	X	490	250	X	131	250	5.71
O-6.2	Optimum, Problem 6-2	437	307	567	X	30	40	X	408	509	X	182	143	6.68
O-41.2	Optimum, Problem 41-2	733	569	272	X	112	60	X	566	291	X	111	68	4.70
O-41.2A	Optimum, Problem 41-2	783	560	374	X	46	112	X	575	230	X	144	69	4.96
O-42	Optimum, Problem 42	293	546	277	X	266	530	X	579	253	X	155	478	6.96
O-4.4	Optimum, Problem 4-3	417	381	561	X	147	225	X	539	404	X	235	240	7.07

T = Target wing; E = Envelope wing; P = Parametric wing; O = Optimum wing

TABLE 2.- SUMMARY OF OPTIMIZATION PROBLEMS: AEDC 457

Problem No.	Mach No.	Merit Function	Active Constraints	Convergence Properties	Best N	% C_D Decrease from Standard Wing
30	0.85	Min C_D*	C_L = 0.5, Δ Twist ≤ 4°	Good	17	16%
3-2	0.85	Min C_D*	C_L = 0.5, "Reduced" Articulation, Δ Twist = 0°	Excellent	20	6%
41-2	0.85	Min C_D*	C_L = 0.25, Δ Twist = 0 ± 2°	Excellent	29	17%
4-3	0.90	Min C_D*	C_L = 0.50, Δ Twist ≤ 3°	Excellent	10	14%
42	0.85	Min C_D*	C_L = 0.70 Δ Twist = 0 ± 2°	Very marginal except for last 4 iterations	33	9%
6-2	0.85	Min C_D*	$C_L + C_M/2.3$ = 0.50 Δ Twist ≤ 3°	Excellent up to N = 8 Poor for N > 9	8	18%
10	0.90	Max C_L*	C_D* = 0.11, Δ Twist ≤ 3°	Poor	None	X

C_D* = C_D - 0.0494 α (deg)

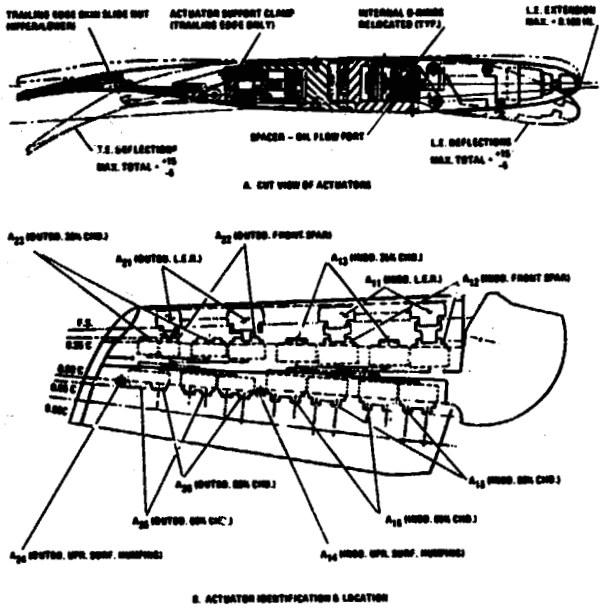

Figure 1.- Three-dimensional wing model hydraulic actuator system.

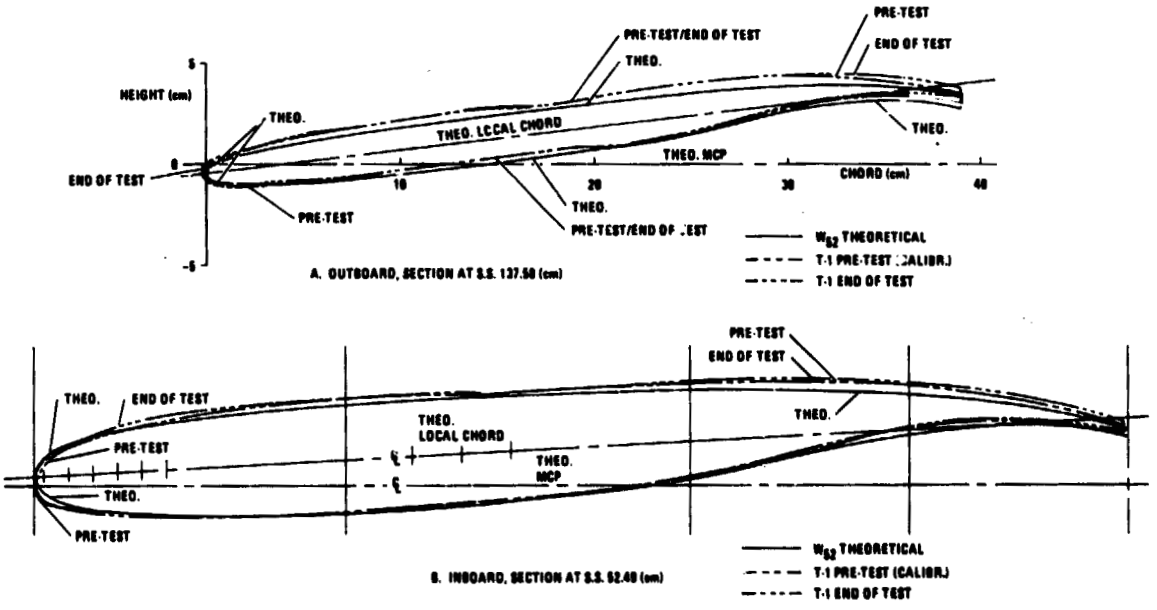

Figure 2.- T-1 actual and theoretical wing shape.

Figure 3.- Three-dimensional wing model installed in tunnel.

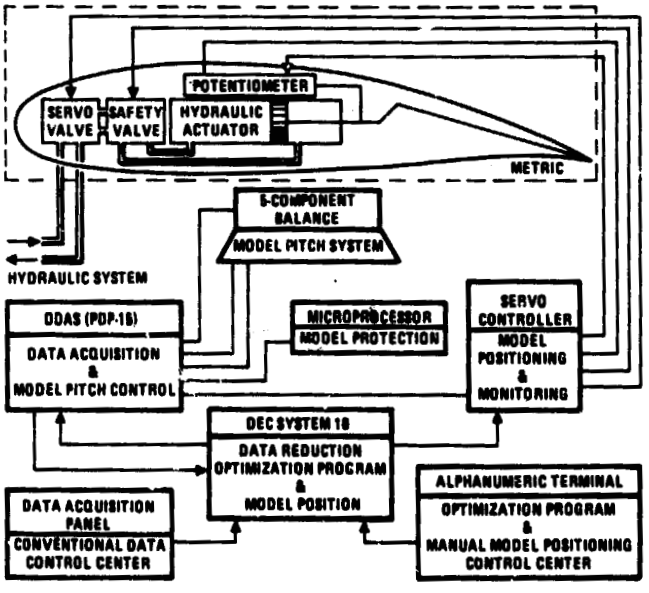

Figure 4.- SOFT wing closed-loop testing procedure.

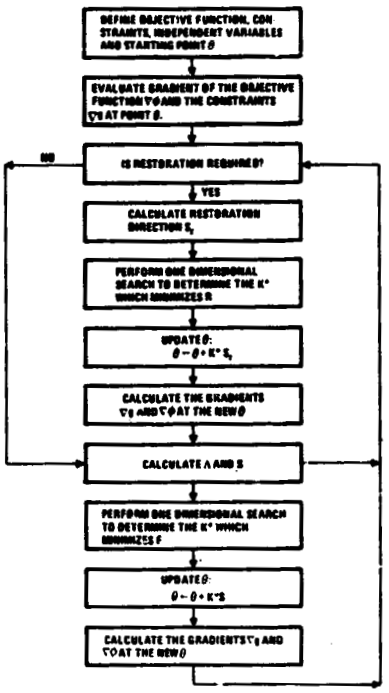

Figure 5.- Flow chart of mathematical optimization procedure.

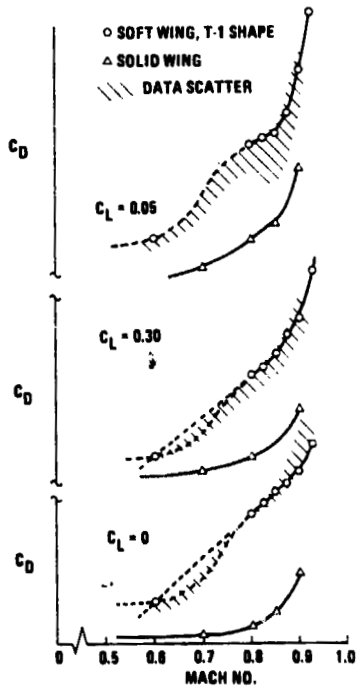

Figure 6.- SOFT wing and solid wing drag variations.

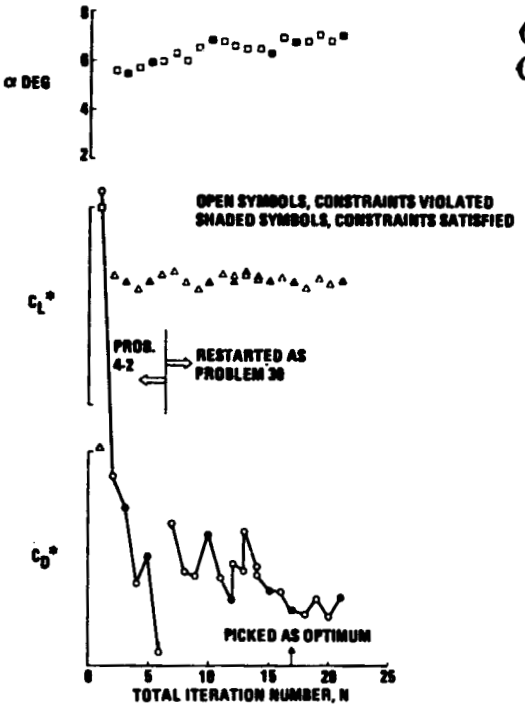

Figure 7.- Optimization summary. Problems 4-2 and 30. Minimum C_D at C_L = 0.5; Mach 0.85.

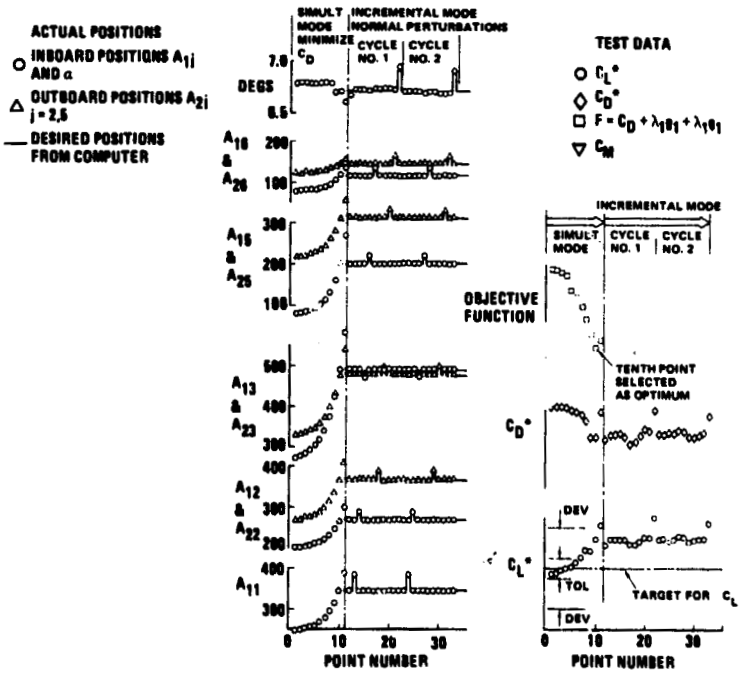

Figure 8.- Minimization of C_D. Iteration N = 11 of problem 30.

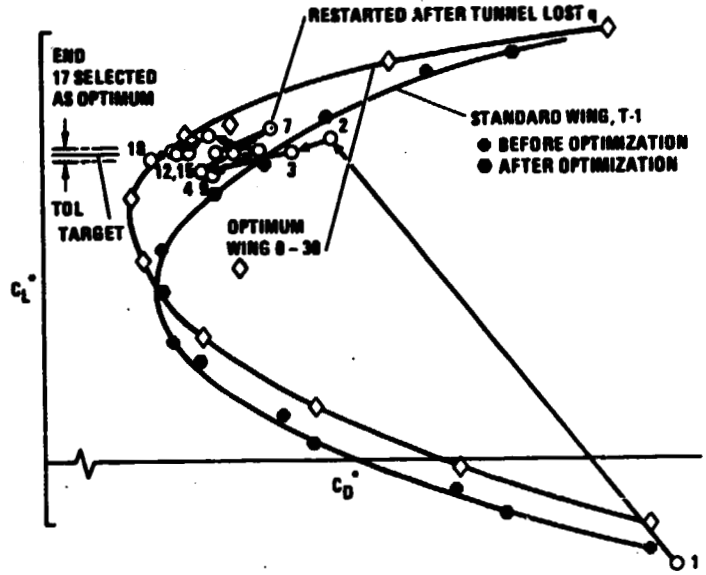

Figure 9.- Problems 4-2 and 30 in C_D^*, C_L^* plane.

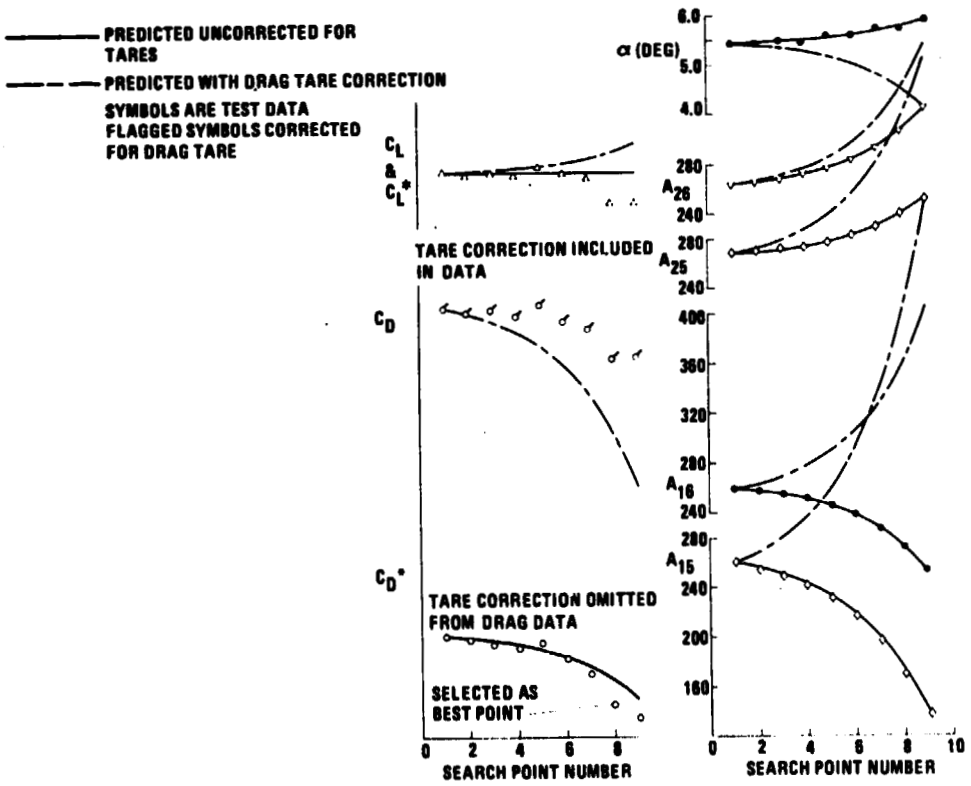

Figure 10.- Tare corrections for iteration 4 of problem 4-2.

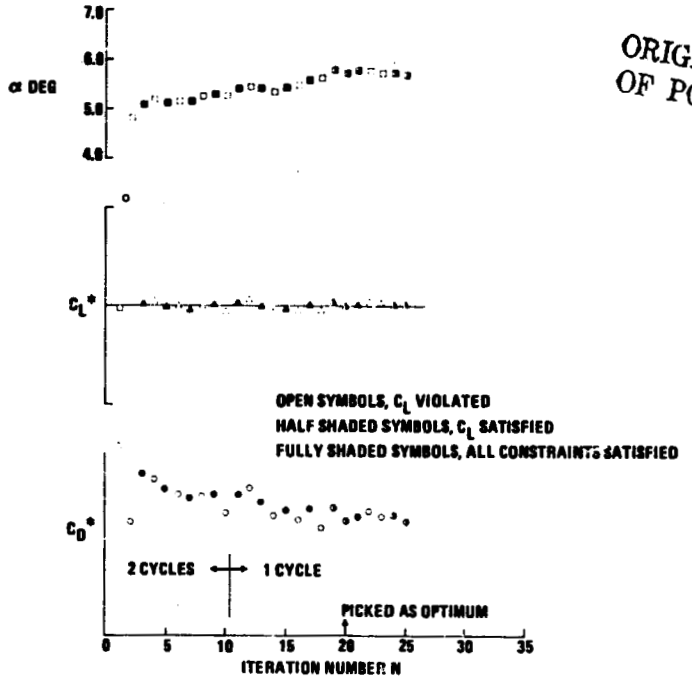

Figure 11.- Optimization summary. Problem 3-2. Minimum C_D at C_L = 0.5; limited articulation; Mach 0.85.

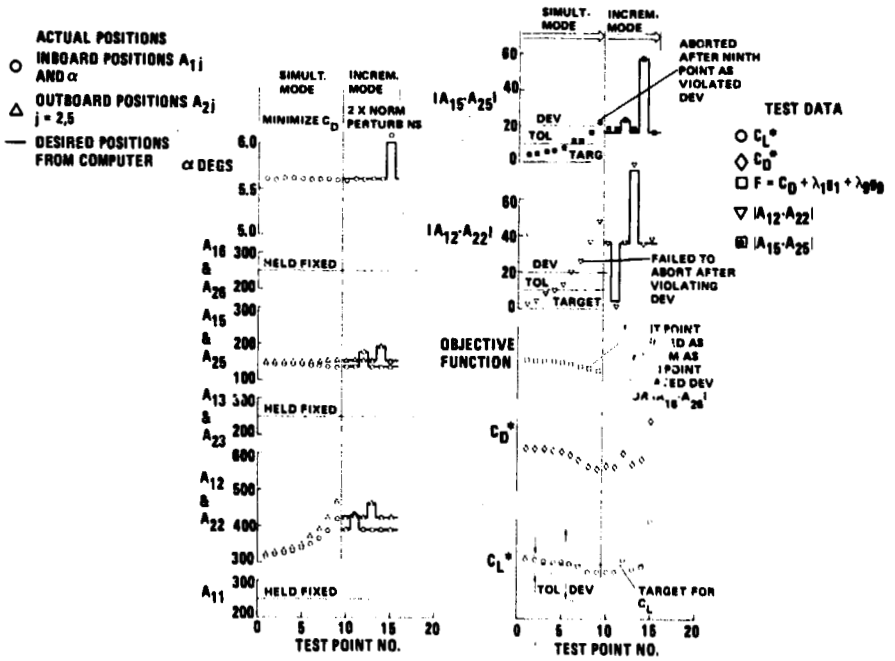

Figure 12.- Minimization of C_D. Iteration N = 18 of problem 3-2.

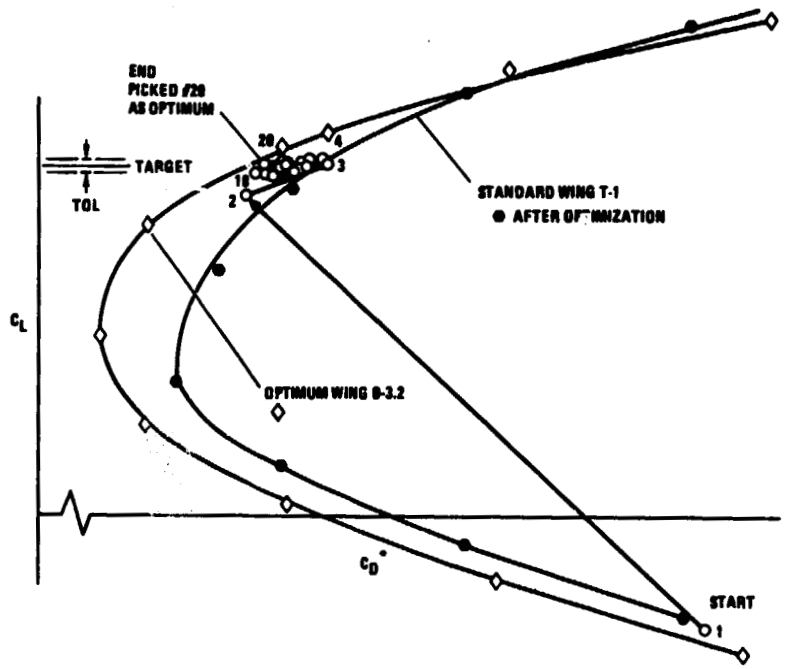

Figure 13.- Problem 3-2 in C_D^*, C_L^* plane.

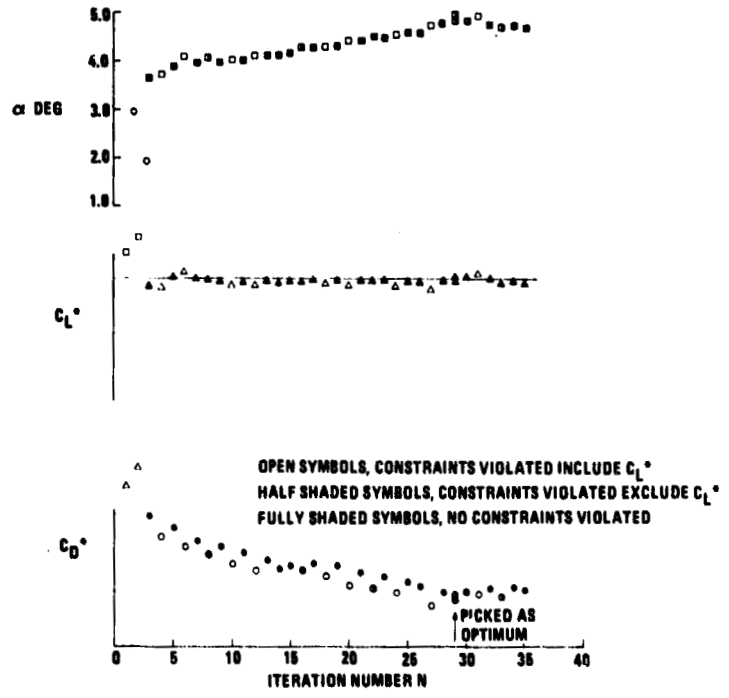

Figure 14.- Optimization summary. Problem 41-2. Minimum C_D at C_L = 0.25; Mach 0.85.

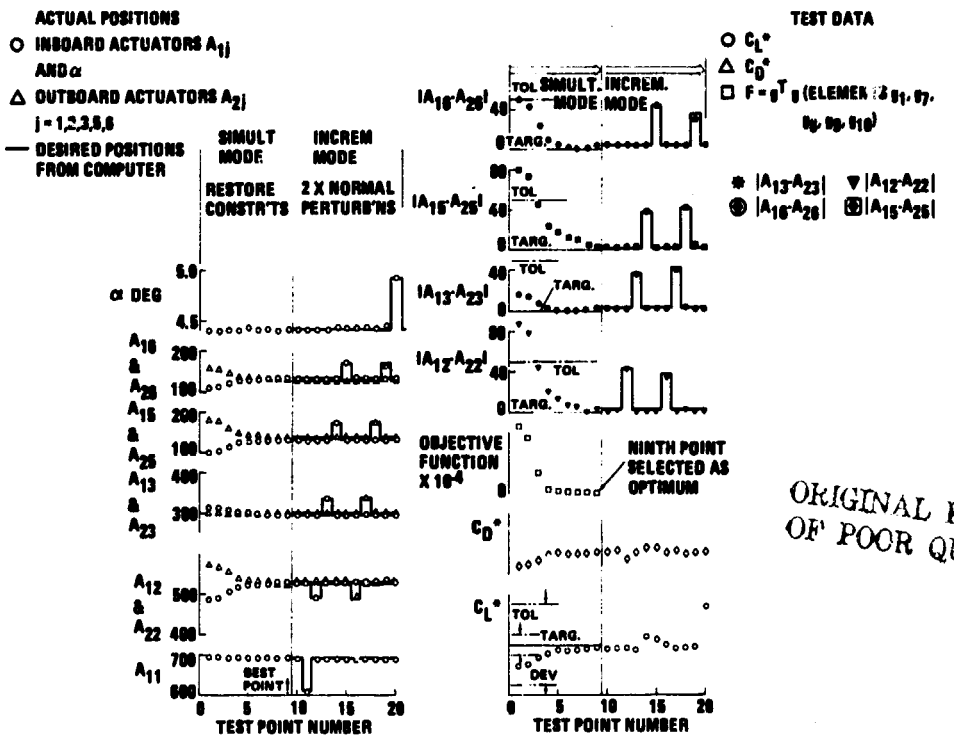

Figure 15.- Restoration of equality constraints on C_L. Iteration N = 21 of problem 41-2.

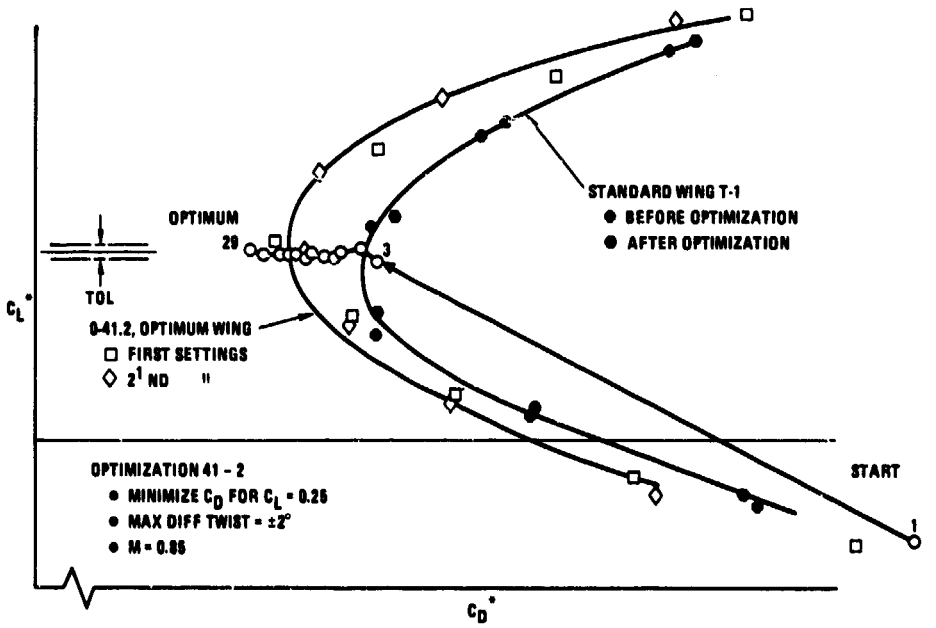

Figure 16.- Problem 41-2 in C_D^*, C_L^* plane.

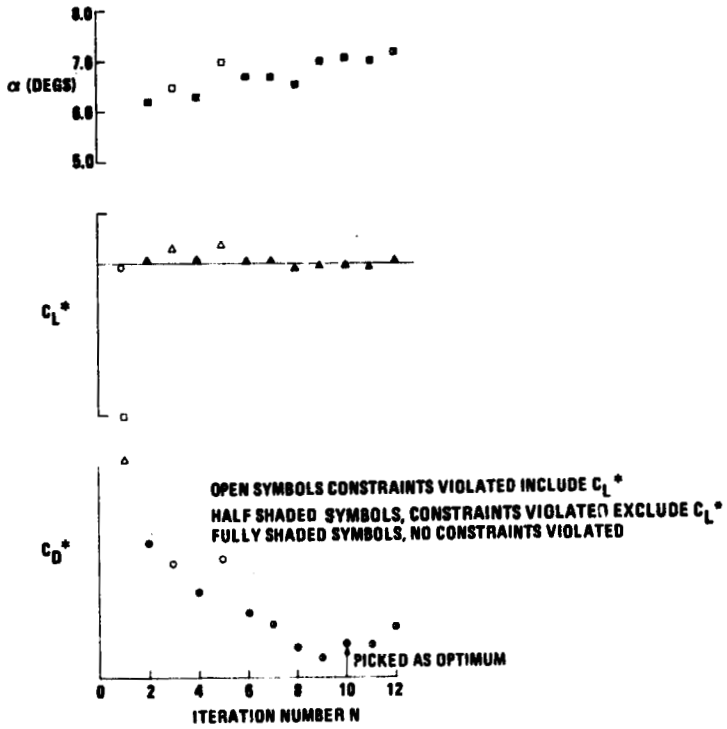

Figure 17.- Optimization summary. Problem 4-3. Minimum C_D at C_L = 0.5; Mach 0.9.

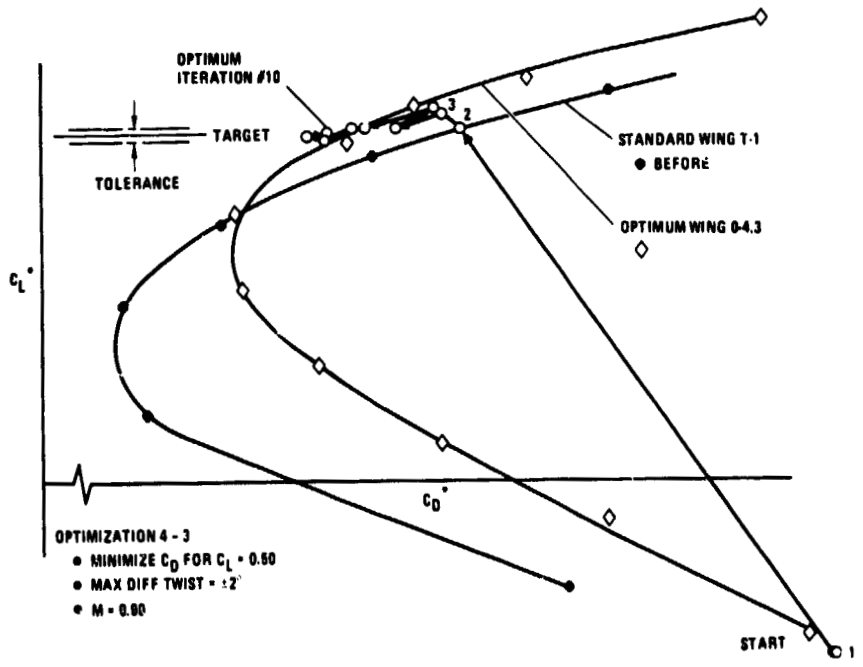

Figure 18.- Problem 4-3 in C_D^*, C_L^* plane.

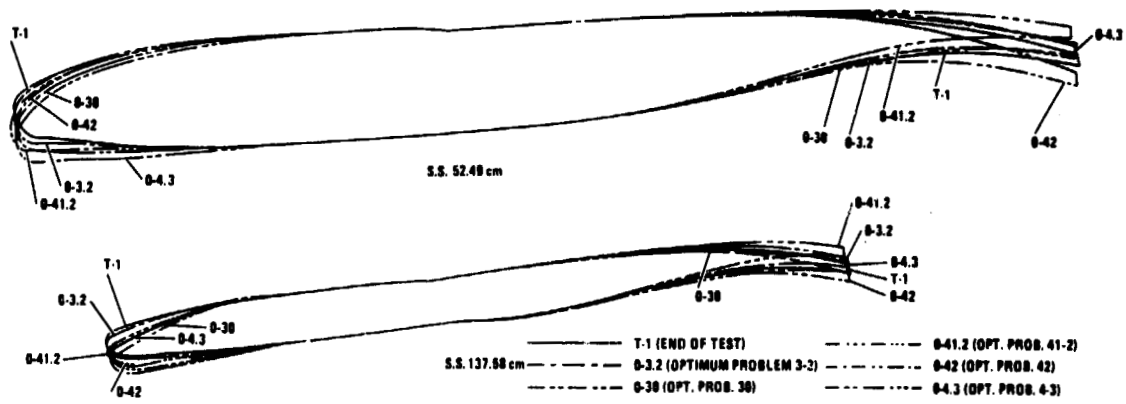

Figure 19.- Optimum wing shapes.

D19

19

APPLICATION OF NUMERICAL OPTIMIZATION TO THE DESIGN OF ADVANCED SUPERCRITICAL AIRFOILS

Raymond R. Johnson
Vought Corporation

Raymond M. Hicks
NASA Ames Research Center

SUMMARY

A recent application of numerical optimization to the design of advanced airfoils for transonic aircraft has shown that low-drag sections can be developed for a given design Mach number without an accompanying drag increase at lower Mach numbers. This is achieved by imposing a constraint on the drag coefficient at an off-design Mach number while minimizing the drag coefficient at the design Mach number. This multiple design-point numerical optimization has been implemented with the use of airfoil shape functions which permit a wide range of attainable profiles during the optimization process. Analytical data for the starting airfoil shape, a single design-point optimized shape, and a double design-point optimized shape are presented. Experimental data obtained in the NASA Ames Two-by Two-Foot Wind Tunnel are also presented and discussed.

INTRODUCTION

The design of supercritical airfoils for advanced high speed aircraft has been facilitated by the computerized analytical methods which have been developed in recent years. Although these methods provide good performance predictions for each individual design point which is considered, they do not allow the designer to automatically consider off-design characteristics during the design process. A method which does provide multiple design-point capability is described in reference 1. It is based on design by numerical optimization. An application of that method to a single design-point and a double design-point airfoil optimization is addressed in the present study. The double design-point optimization produced a low drag supercritical airfoil for a given Mach number subject to a drag constraint at a lower Mach number.

The treatment of the supercritical airfoil design problem by this method has been facilitated by the development of a set of airfoil shape functions (reference 1) which provide a wide range of attainable profiles during the design process. The coefficients of these shape functions are used as design variables in the numerical optimization technique which consists of two existing computer codes: (a) an optimization program based on the method of

feasible directions (reference 2) and (b) an aerodynamic analysis program based on an iterative solution of the full potential equation for transonic flow (reference 3).

SYMBOLS

a_i	shape function coefficients
c	chord
C_D	section drag coefficient
C_l	section lift coefficient
C_m	section pitching moment coefficient
C_p	pressure coefficient
f_i	airfoil shape functions
M	Mach number
X	airfoil abscissa
Y	airfoil ordinate

DESIGN METHOD

Only a brief description of numerical optimization will be given here. A complete discussion of the technique can be found in reference 4.

A schematic flow chart of the numerical optimization design program used during this study is shown in figure 1. A baseline airfoil is required to start each design problem. The airfoil shape is represented in the program by the following equation:

$$Y = Y_{basic} + \sum_i a_i f_i$$

where Y_{basic} is the set of ordinates of the baseline airfoil and f_i are the shape functions. The shape functions are added linearly to the baseline profile by the optimization program to achieve the desired design improvement. The contribution of each function is determined by the value of the coefficient, a_i, associated with that function. These a_i coefficients are therefore the design variables. Other inputs to the program include Mach number, angle of attack, and any constraints to be imposed on the design.

The hypothetical design problem represented by the flow chart is drag minimization at one Mach number, M_1, with drag constrained to some specified value at another Mach number, M_2. The optimization program begins by changing the design variables, one by one, from the initial value of zero to 0.001. It returns to the aerodynamics program for evaluation of the drag coefficient at both Mach numbers M_1 and M_2 after each change. The value of 0.001 is somewhat arbitrary but has been found to be an effective step change in the design variables to calculate the required partial derivatives. The partial derivatives of drag with respect to each design variable form the gradient of drag, ∇C_d. The direction in which the design variables are changed to reduce the drag coefficient at M_1 is $-\nabla C_d$ (the steepest descent direction) if the drag constraint at M_2 is not active. The optimization program then increments the design variables in this direction until the drag starts to increase because of nonlinearity in the design space or the drag constraint at Mach number M_2 is encountered. If either of these possibilities occurs, new gradients are calculated and a new direction is found that will decrease drag without violating the constraint. When a minimum value of drag for Mach number M_1 is attained with a satisfied drag constraint at M_2, the required optimized airfoil has been achieved.

AIRFOIL SHAPE FUNCTIONS

Supercritical airfoil design by numerical optimization is facilitated by using a set of geometric shape functions, each of which affects a different limited region of the profile. General classes of such functions which have been used successfully to optimize supercritical airfoils are described in reference 1. The shape functions that were used in the present study were selected from those general functions and were applied to the airfoil upper surface only. The exponential decay function and the sine functions are presented in figure 2. The exponential decay function, f_1, provided variations in curvature near the airfoil leading edge. In the sine functions, the exponents on the chordwise coordinate, x, were assigned so that the maximum perturbations of f_2, f_3, f_4 and f_5 were at 20, 40, 60, and 80 percent of the chord respectively. The width of the region affected by each sine function was controlled by the localization power, 3. Previous studies (reference 1) have found that these shape functions provide a broad range of smooth airfoil contour modifications during the optimization process.

ANALYTICAL DESIGN RESULTS AND DISCUSSION

The importance of considering off-design performance of an airfoil during the design process will be illustrated by comparing the results of a single design-point optimization with a double design-point optimization. The first involves recontouring the upper surface of an existing supercritical airfoil to reduce the wave drag at a single design Mach number. The second consists of recontouring the upper surface of the same airfoil to reduce the wave drag at the design Mach number subject to a drag constraint at a lower Mach number.

The calculated wave drag (reference 3) for Mach numbers near drag divergence for the starting airfoil and the two optimized airfoils are presented in figure 3. All these data are for 0.40 C_l, the design lift coefficient of the starting airfoil. Mach number 0.78 was arbitrarily selected as the primary design point, i.e., the Mach number at which the drag would be minimized. Results of the single design point optimization are indicated as 412M1. The drag at Mach number 0.78 is significantly less than that of the starting airfoil and as a result the drag rise occurs at a higher Mach number. However, the drag at lower Mach numbers, 0.76 and 0.77, is greater than that of the starting airfoil. This local region of drag-creep could limit the usefulness of the improved drag rise characteristics of the optimized airfoil.

In order to avoid the drag-creep problem, the airfoil was optimized a second time with an upper bound of .0005 imposed on the drag coefficient at Mach number 0.77. Results of this double design-point optimization are indicated in figure 3 as 412M2. The drag rise for this airfoil occurs at a slightly lower Mach number than it does for 412M1, but there is no drag-creep over the range of Mach numbers for which the airfoils were analyzed. Therefore, airfoil 412M2 is the more desirable design.

Chordwise pressure distributions for the starting airfoil and for airfoil 412M2 at Mach number 0.77 are presented in figure 4. The reason for the lower wave drag of the optimized airfoil is obvious. The starting airfoil has a well developed shock at approximately 40 percent of the chord, but airfoil 412M2 does not. Instead, it exhibits a gradual recompression from approximately 10 percent to 50 percent of the chord. The geometric modification which has produced the pressure distribution change is shown in figure 5. This modification is primarily a reduction in surface curvature from 5 percent to 40 percent of the chord.

The aerodynamics code that was used in the optimization program is an inviscid, potential flow analysis method. In order to account for first order viscous effects in the flow field solution, a boundary layer displacement thickness was added to the starting profile before the optimization process. The displacement thickness was calculated for the pressure distribution of the starting airfoil at a Mach number near its design condition, 0.78. It remained unchanged throughout the optimization process, and each of the optimized airfoils included this same passive displacement thickness. Therefore, the analytical characteristics of the airfoils did not reflect potential changes in boundary layer behavior due to changes in the chordwise pressure distributions.

Another aerodynamic analysis code (reference 5) was used to evaluate the active boundary layer characteristics of the starting airfoil and optimized airfoil 412M2. That computer program is also based on an iterative solution of the full potential equation for transonic flow, and it includes a momentum-integral calculation of the turbulent boundary layer parameters. During the solution, the airfoil geometry is regularly updated with the boundary layer displacement thickness. The results of the viscous analyses with that code for Mach numbers between 0.76 and 0.81 indicated that the differences in boundary layer characteristics would be small. The calculated

wave drag for the starting airfoil and airfoil 412M2 is presented in figure 6. The relative increase in the drag rise Mach number is in good agreement with the results of the inviscid code (figure 3).

EXPERIMENTAL RESULTS

Models of the starting airfoil and airfoil 412M2 were tested in the NASA Ames Two-by Two-Foot Wind Tunnel. Data were obtained at angles of attack from -4^{0} to stall at Mach numbers from 0.20 to 0.81. The test Reynolds number varied with Mach number as presented in Table I. Preliminary data from the test are presented in figures 7 and 8. The incremental values of drag coefficient, C_D, have been referenced to the minimum drag measured for either of the airfoils at each lift coefficient. Thereby, extraneous components in the absolute drag level have been excluded from the comparison.

Drag characteristics for the starting airfoil and airfoil 412M2 at lift coefficient 0.40 (figure 7) indicate a difference in drag rise Mach number of 0.02 to 0.03. This improvement is greater than had been predicted by the analytical codes (figures 3 and 6). Drag characteristics for the two airfoils at lift coefficient 0.60 (figure 8) also indicate significantly less drag for the optimized airfoil 412M2 at all Mach numbers. Therefore the airfoil performance at this off-design condition has not been adversely affected by the design improvement at 0.40 lift coefficient.

The low speed drag-creep which occurs between Mach numbers 0.60 and 0.70 for both airfoils is caused by the initial development of supercritical velocities over the upper surface and the formation of a mild shock near the leading edge. Only Mach numbers greater than 0.76 were considered during the present analytical design study, but the numerical optimization technique could also be applied to the minimization of drag-creep at the lower speeds.

CONCLUDING REMARKS

A technique for designing low-drag supercritical airfoils has been demonstrated. The technique was used to modify the upper surface of an existing 12 percent thick supercritical section to achieve a substantial drag reduction at Mach number 0.78 without an accompanying drag increase at lower Mach numbers. The ability to treat this and other multiple design-point problems has been achieved by the use of a set of airfoil shape functions which provide the necessary flexibility in the profiles that are attainable by the numerical optimization design technique. Such capability is important because each design point might require the modification of a different region of the profile.

The two design-point problem considered in the present study illustrates the advantage of design by numerical optimization. Aerodynamic requirements at any number of off-design conditions are handled automatically without manual intervention by the designer. Therefore, it provides a powerful tool for the

design of airfoils to meet specified performance goals throughout a flight envelope.

REFERENCES

1. Hicks, R. M.; Vanderplaats, G. N.: Application of Numerical Optimization to the Design of Supercritical Airfoils without Drag-Creep. SAE Paper 770440, 1977.

2. Vanderplaats, G. N.: CONMIN-A Fortran Program for Constrained Function Minimization. NASA TM X-62,282, 1973.

3. Jameson, A.: Iterative Solution of Transonic Flows over Airfoils and Wings Including Flows at Mach 1. Comm. Pure Appl. Math., Vol. 27, pp 283-309, 1974.

4. Vanderplaats, G. N.; Hicks, R. M.; Murman, E. M.: Application of Numerical Optimization Techniques to Airfoil Design. NASA SP-347, Part II, 1975.

5. Bauer, F.; Garabedian, P.; Korn, D.; Jameson, A.: Supercritical Wing Sections II. Lecture Notes in Economics and Mathematical Systems, Vol. 108, Springer-Verlag, 1975.

TABLE I. - WIND TUNNEL TEST PARAMETERS

Mach Number	Angle of Attack Range	Reynolds Number
0.20	-4^{o} to stall	1.9×10^{6}
0.40	↓	3.0×10^{6}
0.60	↓	4.0×10^{6}
0.70	↓	↓
0.75	↓	↓
0.76	↓	↓
0.77	↓	↓
0.78	↓	↓
0.79	↓	↓
0.80	↓	↓
0.81	↓	↓

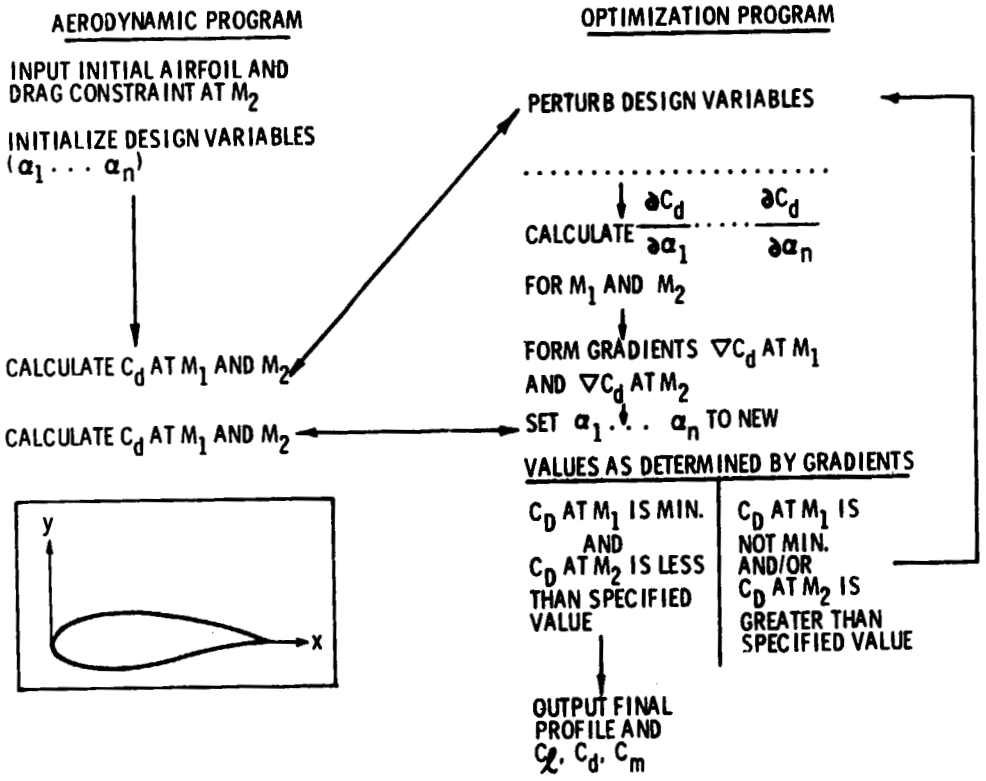

Figure 1.- Flow chart of numerical optimization design program.

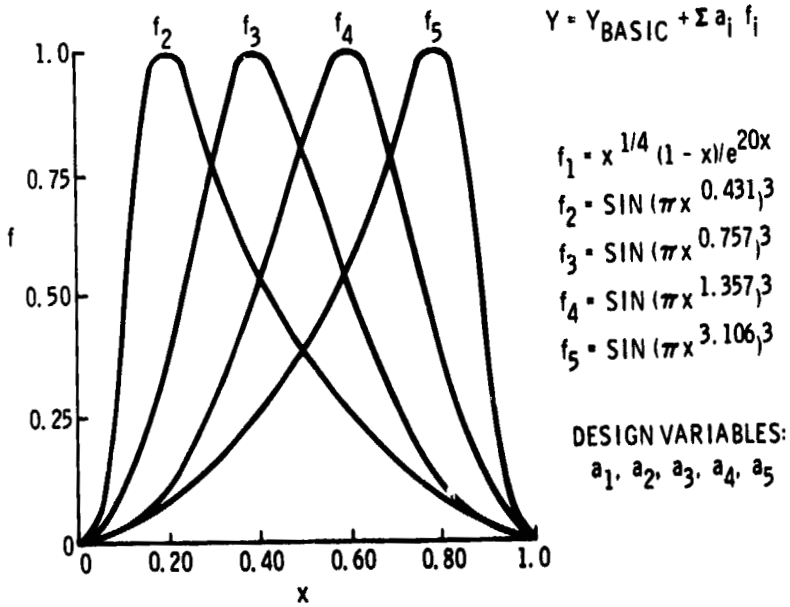

Figure 2.- Airfoil shape functions.

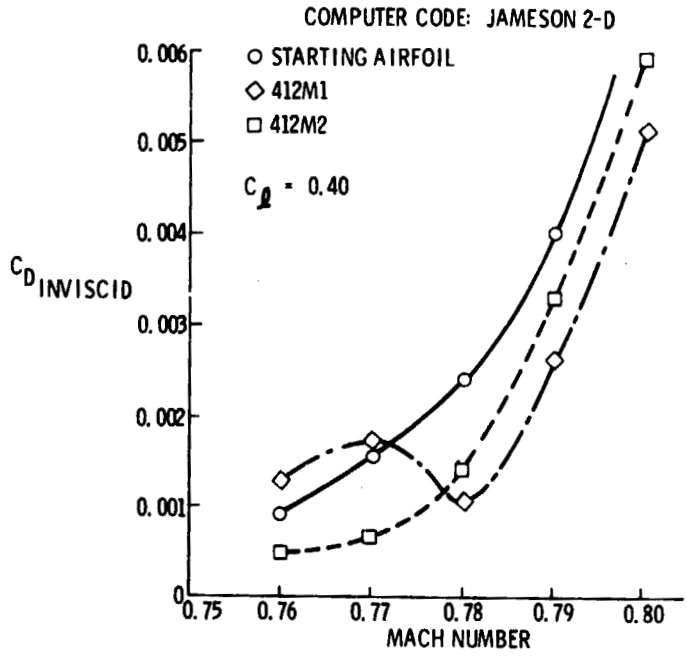

Figure 3.- Airfoil section optimization.

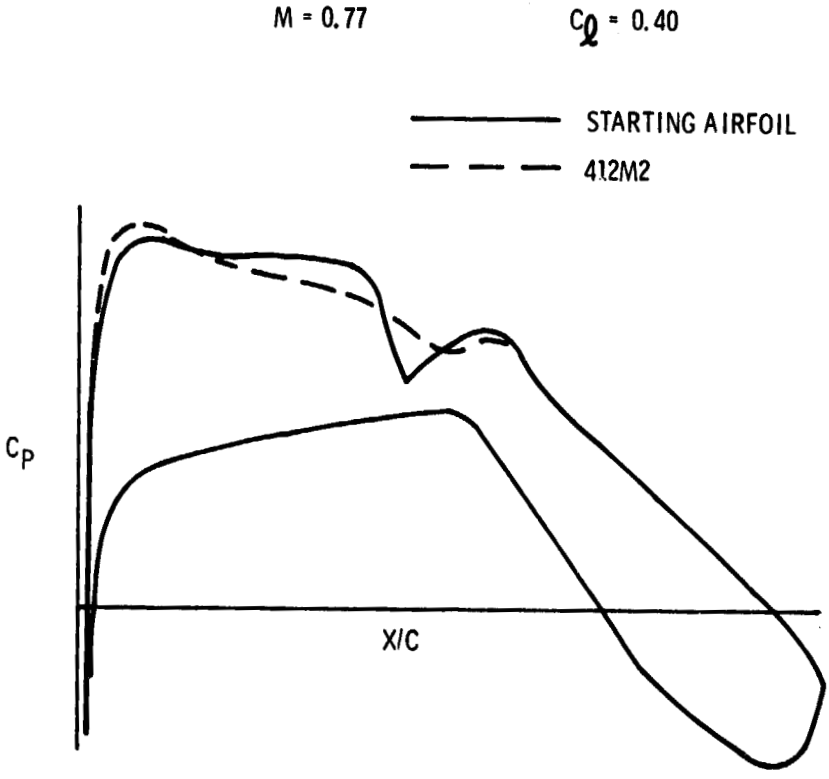

Figure 4.- Airfoil section pressure distributions.

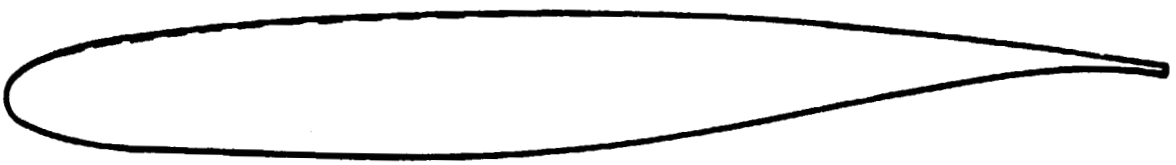

Figure 5.- Airfoil geometry comparison.

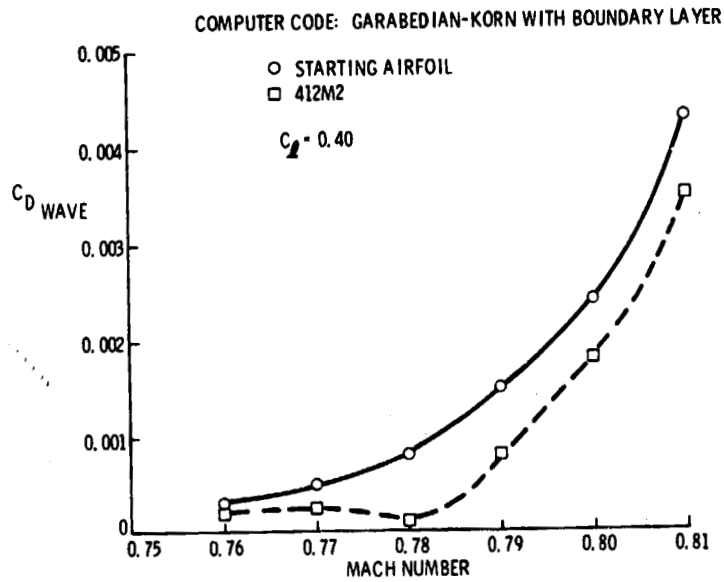

Figure 6.- Comparison of wave drag characteristics for the starting airfoil and optimized airfoil 412M2.

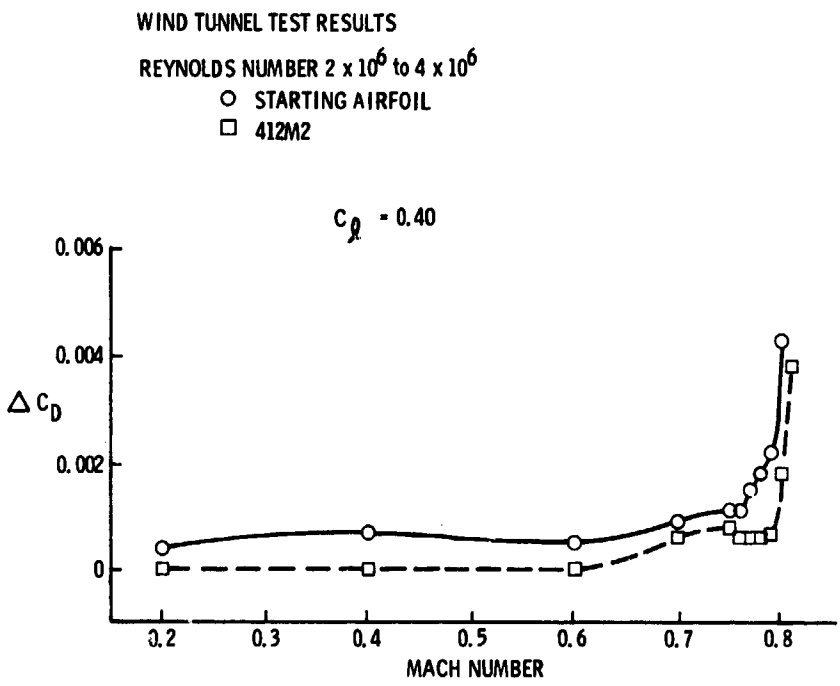

Figure 7.- Experimental drag characteristics for the starting airfoil and optimized airfoil 412M2 at C_ℓ = 0.40.

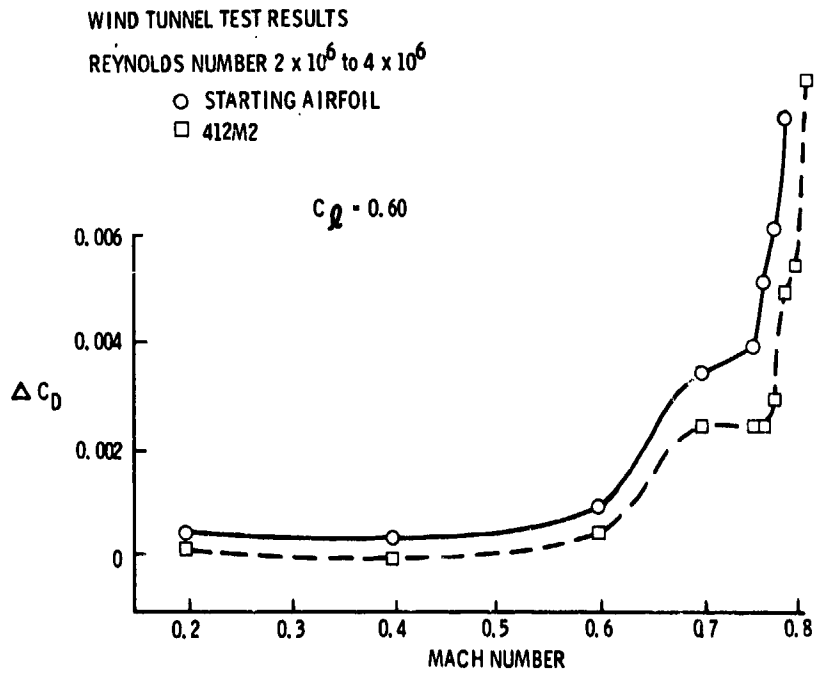

Figure 8.- Experimental drag characteristics for the starting airfoil and optimized airfoil 412M2 at C_ℓ = 0.60.

IMPROVED PREDICTION OF LAMINAR LEADING EDGE SEPARATION

R. N. Herring and W. L. Ely
McDonnell Aircraft Company
McDonnell Douglas Corporation

SUMMARY

This research was conducted in order to provide a definite criterion for the prediction of the bubble burst on airfoils typical of those used for fighter wings. The approach taken was to correlate existing airfoil bubble burst data using various parameters at the laminar separation point. The method due to Weber was modified to provide a continuous analytic solution for the velocity distribution around the airfoil leading edge. This proved to be as accurate as any available. Coupling the modified Weber method with the Stratford laminar separation prediction method leads to a universal chart giving the conditions at separation as a function of stagnation location and leading edge radius. Application of the combined method to available two-dimensional airfoil data resulted in an empirical criterion presenting the limiting local velocity gradient at separation as a function of the boundary layer momentum thickness at separation for bubble burst. The correlation leads as well to the qualitative explanation of two types of laminar stall: thin airfoil and leading edge. The validity of the correlation is demonstrated by predicting the lift coefficient and angle of attack for stall on airfoils with leading edge or trailing edge flaps.

INTRODUCTION

Airfoil laminar bubble burst is the cause of excessive drag due to lift on very thin airfoils and of maximum lift stalling on moderately thin airfoils. It has been the subject of considerable experimental and theoretical research. However, efforts to apply previous research to the subject of maneuvering drag due to lift on swept thin wings typical of transonic fighter aircraft proved unrewarding. The present research was undertaken to provide the basis of a technique to predict laminar bubble burst on such wings.

As pointed out by Goradia and Lyman (Reference 1) bubble burst is quite likely to be a function of conditions at the laminar separation point. The problem therefore consists of determining those conditions and correlating the experimental data.

NOMENCLATURE

A	Average value of A(x)
A(x)	Velocity ratio due to thickness at $\alpha = 0$
B	Average value of B(x)

$B(x)$	Velocity ratio due to thickness at angle of attack
C_L	Lift coefficient
g	One half the leading edge radius divided by chord
R_c	Freestream Reynolds number based on chord
R_θ	Local Reynolds number based on momentum thickness
s	Arc length along the airfoil surface, divided by chord
u	The ratio of local velocity to freestream velocity
u_p	Peak value of the velocity ratio
u_s	Separation value of the velocity ratio
V	Local velocity
V_∞	Freestream velocity
x	Distance from the nose along the chord divided by chord
x_s	Stagnation location
α	Angle of attack

LAMINAR SEPARATION

As discussed in Reference 2, the theory of Stratford, Reference 3, is very accurate. But, like most other methods it requires accurate, smooth longitudinal pressure gradients. Utilization of experimental pressures with attendant imprecision of measured pressures and pressure tap location proved impossible. Using the currently available powerful finite difference theories presented equal difficulties due to the inherent discontinuous pressure gradient.

A new method was derived based on that of Weber, Reference 4. While not mathematically rigorous, this method has proved to be of very high precision near the airfoil nose both in pressure level and in pressure gradient. It has been derived for the general airfoil shape, but is best illustrated for the uncambered airfoil. The local velocity is given by

$$\frac{V}{V_\infty} = u = \frac{A(x)\ \mathrm{Cos}\ \alpha \pm B(x)\ \mathrm{Sin}\ \alpha\sqrt{\frac{1-x}{x}}}{\frac{ds}{dx}}$$

The functions A(x) and B(x) are functions of the thickness distribution, but for most airfoils are nearly independent of x. Furthermore, the surface slope

function can be approximated by a parabola. Thus, the velocity and gradient are readily found by

$$u = \frac{A \cos \alpha \sqrt{x} + B \sin \alpha}{\sqrt{g + x}}$$

$$\frac{du}{ds} = \frac{1}{2}\left[\frac{A\, g \cos \alpha - (\pm B \sin \alpha)\sqrt{x}}{(x + g)^2} \right]$$

The stagnation (V = 0) location is therefore,

$$\frac{x_s}{g} = \left(\frac{B}{A}\right)^2 \frac{\tan^2 \alpha}{g}$$

It is convenient to give the local velocity in terms of the stagnation location, rather than angle of attack. It is apparent that the airfoil velocity distributions become universal functions of x/g and x_s/g as shown in Figure 1. It is also apparent that certain key events are also functions of these parameters as shown. In particular, the laminar separation point and conditions at that point are direct functions of x_s/g.

The Stratford method can be applied to the non-dimensional velocity distributions to derive a universal chart for the velocity, position, and gradient at separation. This is given in Figure 2. The figure can be used for any airfoil once the stagnation point is known. This formulation is particularly useful in that the correct non-dimensionalizing parameters become obvious.

BUBBLE BURST CORRELATION

The available two-dimensional airfoil data was analyzed using this method to determine boundary layer and velocity gradient parameters at the laminar separation point at or near the angle of attack for laminar bubble burst. The best correlation obtained is shown in Figure 3. The data scatter results from a $\pm$ 1/2 degree angle of attack precision in the bubble burst angle of attack data. It should be noted that velocity gradient parameter is a 1/7th power function of the Reynolds number parameter in keeping with the general postulation that bubble burst is a failure of the turbulence level to re-attach.

Figure 3 is a key element of airfoil analysis but is not the only factor. If the Reynolds number is high enough, transitions will occur prior to laminar separation, precluding bubble formation. There is no wind tunnel data available at high enough Reynolds number to demonstrate such a phenomenon. But, on the other hand, there is considerable data at very low Reynolds numbers to indicate what has been called long bubble stall. Presumably this occurs when the separated laminar boundary layer does not immediately transition to turbulent. It is therefore unable to re-attach and the so-called short bubble does not form. It is generally thought that this occurs for $R_\theta < 125$.

Post stall analyses are very difficult because of the total reliance on unreliable experimental pressure distributions. However, there is good evidence to lead to the conclusion that as the short laminar bubble bursts, the pressure distribution must adjust, with increasing angle of attack, so that conditions for laminar bubble burst are maintained. In other words, the bubble burst boundary applies not only for the burst angle of attack, but for post burst angles as well.

Figure 4 shows the sequence of events and the relation to two well known phenomena: leading edge stall, and thin airfoil stall. For instance, airfoil A is typical of moderately thin airfoils (i.e., 64A010). At very low angles of attack, laminar separation does not occur near the leading edge, but aft of maximum thickness (if at all). As angle of attack increases the separation moves to the airfoil nose and a short bubble forms. As angle of attack is increased up to the burst boundary, a typical short bubble is obtained with little impact on the overall forces and moments. Further increases in angle of attack cause a drastic reduction in lift as the laminar separation condition moves down the boundary.

In the case of airfoil B, typical of thinner airfoils (i.e., 64A006), the same sequence of events occurs. However as the bubble bursts, and as angle of attack is increased, conditions at laminar separation move below $R_\theta = 125$. The separated layer does not transist and the long bubble is formed. Lift continues to increase, but at a reduced rate.

MAXIMUM LIFT PREDICTION

While this research was aimed primarily at drag prediction at high angles of attack, it does form the basis for prediction of maximum lift for airfoils of the "leading edge stall" type. This is illustrated in Figure 5. The effects of a leading edge flap are shown on a 64A010 airfoil, and of a trailing edge flap on a NACA 0009 airfoil. In the former case, it was noted during the test that separation occurred at the hingeline for flap angles in excess of 15°. Up to this angle, the current method predicts both $C_{L_{max}}$ and angle of attack for $C_{L_{max}}$ very well.

In the case of the trailing edge flap, no attempt was made to adjust the predicted airfoil nose pressure distribution for viscous effects on the flap itself. Even so, the angle for $C_{L_{max}}$ is well predicted and the prediction for $C_{L_{max}}$ is consistent with the approximation.

CONCLUDING REMARKS

Rational approximation to airfoil theoretical pressure has yielded an accurate method for prediction of conditions at laminar separation and given insight into a universal correlation of the bubble burst phenomenon. This, in turn, has led to a basic understanding of thin airfoil and leading edge stall.

REFERENCES

1. Goradia, S. and Lyman, V., "Laminar Stall Prediction and Estimation of $C_{L_{max}}$," Journal of Aircraft, September 1974, Vol. II, No. 9.

2. Curle, N. and Davies, H.J. Modern Fluid Dynamics, Vol. I Incompressible Flow, The New University Mathematics Series 1968.

3. Stratford, B.S., "Flow in the Laminar Boundary Layer Near Separation," A.R.C. R&M 3002, 1957.

4. Weber, J., "The Calculation of the Pressure Distribution on the Surface of Thick Cambered Wings and The Design of Wings with a Given Pressure Distribution," A.R.C. R&M 3026, 1955.

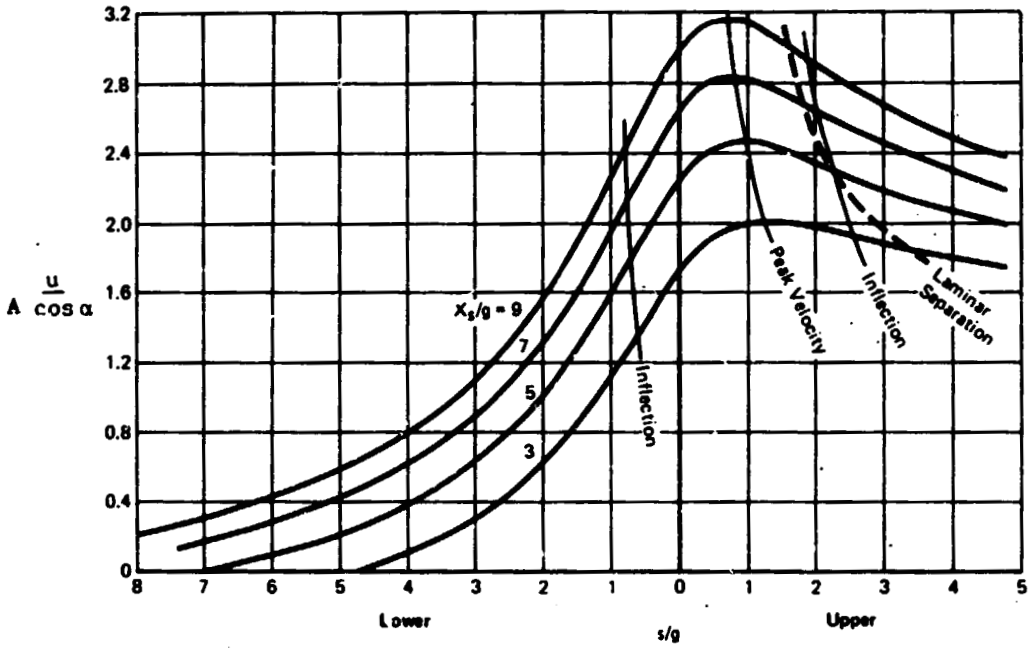

Figure 1.- Typical nondimensional velocity profiles.

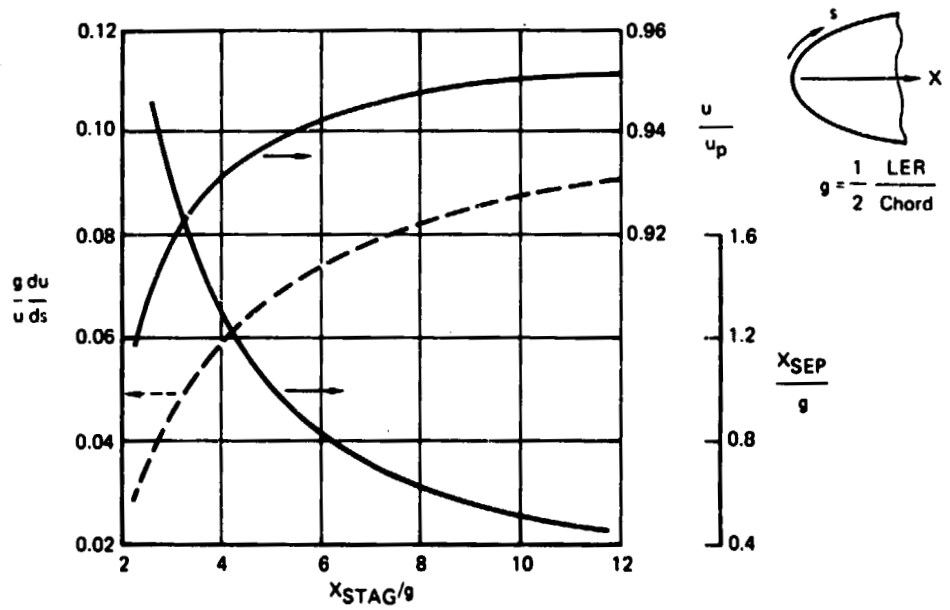

Figure 2.- Conditions at the laminar separation.

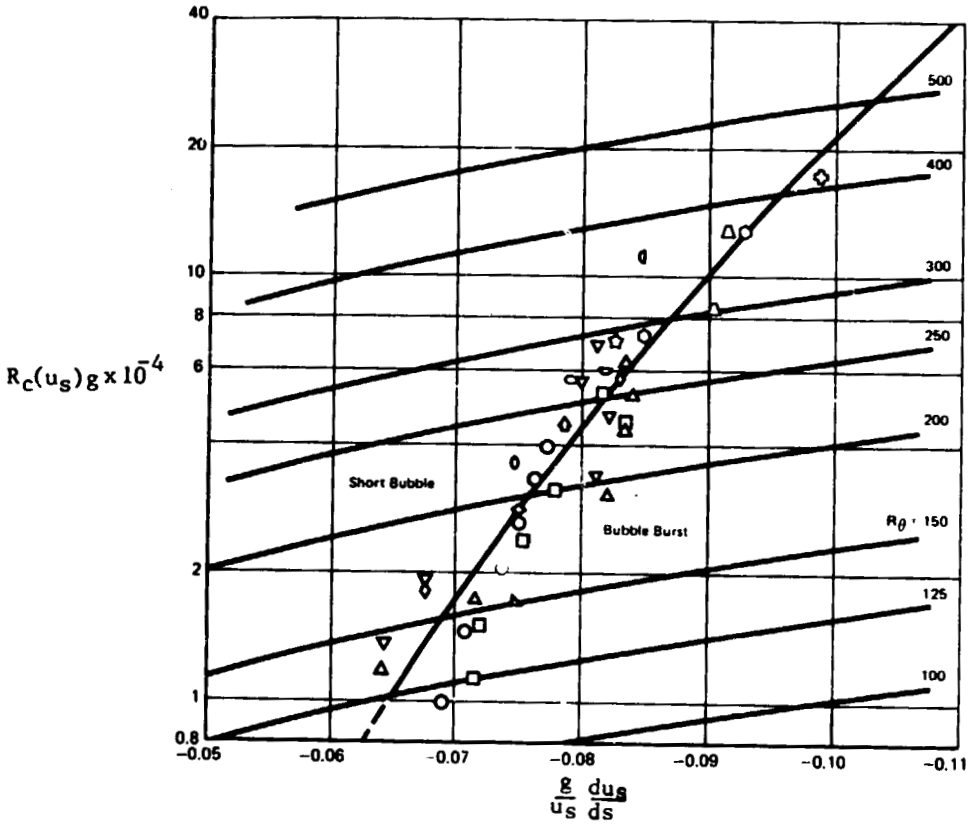

Figure 3.- Correlation of parameters affecting laminar bubble burst.

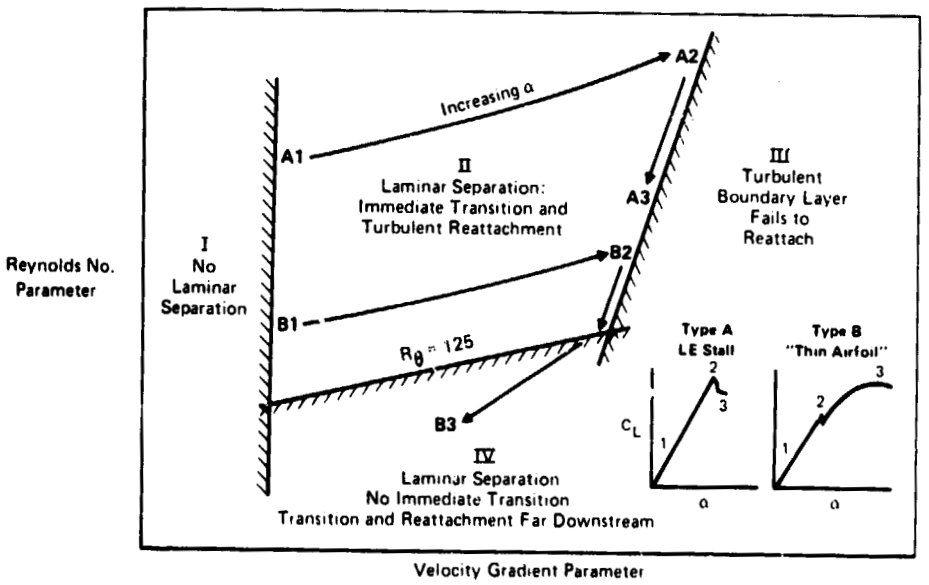

Figure 4.- Leading-edge stall development.

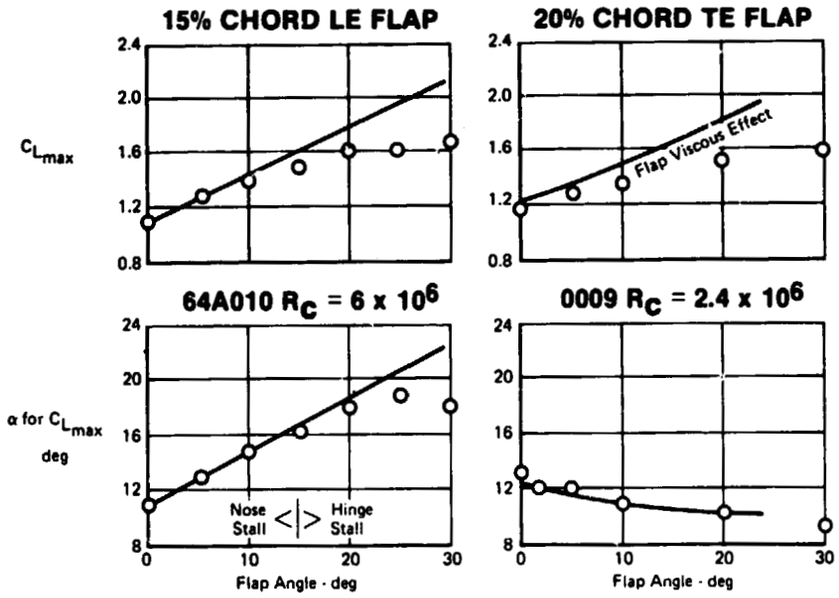

Figure 5.- Predicting leading-edge stall. Flapped airfoils.

D21

N79-20051

21

THE PREDICTION OF TWO-DIMENSIONAL AIRFOIL STALL PROGRESSION

Lloyd W. Gross
McDonnell Aircraft Company
McDonnell Douglas Corporation

SUMMARY

A generalized boundary condition potential flow calculation method has been combined with a momentum integral boundary layer method and a base flow theory of separation to predict airfoil viscous-inviscid interference up to and beyond stall. The resultant program considers laminar and turbulent separation and is, therefore, applicable to thin or thick airfoil stall. The calculated flow field includes the airfoil and the separation bubble recombination region behind the airfoil.

Calculated pressure distributions and equivalent airfoil shapes, including the displacement thickness of the viscous regions, are compared with flow field measurements for several airfoils. The measured displacement thicknesses and wake centerlines corroborate the calculated shape. The comparison also suggests the use of the analytical solution to evaluate the measurements.

INTRODUCTION

As part of a program for the prediction of the aerodynamic characteristics of aircraft at high angles of attack, the problem of determining the flow field around a stalled wing was addressed. A necessary preliminary step has been the development of a method of calculating the flow around a stalled two-dimensional airfoil. This capability is useful in itself, but it was developed primarily to verify the applicability of the theoretical components prior to their extension to a three dimensional calculation method.

Three types of boundary layer separation have been identified as contributing to airfoil stall. They can occur singly or in combination. The classical type of stall is due to trailing edge separation. The separating boundary layer can be either laminar or turbulent. Separation first occurs at the airfoil trailing edge and moves forward with increasing angle of attack. This type of separation leads to airfoil stall on relatively thick airfoils ($t/c > 15\% - 18\%$). Another form of separation is short bubble laminar separation where laminar separation is followed almost immediately by transition to turbulent flow and boundary layer reattachment. This bubble develops as the airfoil angle of attack is increased, or as Reynolds number is decreased, until reattachment no longer occurs. The bubble then is said to have "burst". On thick airfoils short bubble laminar separation causes a thicker downstream boundary layer, but on thinner airfoils, short bubble bursting can lead directly to airfoil stall.

When the short bubble bursts, a free shear layer is formed that recombines with the flow from the lower surface behind the airfoil trailing edge. However, under certain circumstances of airfoil thickness and Reynolds number, the flow reattaches to the airfoil surface and a new turbulent boundary layer is formed. This is referred to as a long laminar separation bubble. Increases of angle of attack cause the bubble length to increase until reattachment moves behind the airfoil trailing edge.

The present analytical description of airfoil stall progression is based upon a potential flow calculation method that allows either the airfoil shape or pressure distribution to be used as the boundary condition over any portion of the airfoil surface. This potential flow calculation method is combined with momentum integral boundary layer calculation methods and a component analysis description of separated base flow to form a unified viscous-inviscid interaction theory. The three types of separated flow mentioned above are included whether they occur singly or in combination.

NOMENCLATURE

c	airfoil chord
C_p	pressure coefficient
t	airfoil thickness
U	velocity on airfoil surface
U_∞	freestream velocity
x	horizontal distance
α	angle of attack

MATHEMATICAL MODEL

The viscous-inviscid interaction around an airfoil with separation is modeled by finding the equivalent displacement surface of the viscous flow around the airfoil and into the wake. Paneling is laid out on the chord line of the airfoil and is extended beyond the trailing edge to include the wake. An inviscid calculation is made as the initial step of an iterative procedure. A boundary layer calculation method is used to determine the displacement thickness of the attached viscous flow and the point of separation. The displacement thickness is added to the basic airfoil to form the equivalent airfoil shape. Downstream of separation, the displacement thickness is not known, so the pressure predicted by a base flow theory is used as the boundary condition. The output of this calculation is an updated pressure distribution and equivalent airfoil shape. The updated pressure distribution then is used as the

input for improved viscous flow calculations. This procedure is repeated until the pressure distribution of the equivalent airfoil is compatible with the pressure rises predicted by the viscous theories. The analytical methods that were used are described in detail in Reference 1. However, the potential flow calculation method and the method of modeling the separated flow region will be described because of their importance to the method.

Potential Flow Calculation

Bristow (Reference 2) recognized that when the boundary conditions of a chord-line singularity potential flow calculation method are linearized in the region of the body surface, the boundary condition for each singularity can be interchanged between the surface slope and the tangential flow velocity at the panel control point. The resulting Generalized Boundary Condition method allows the geometry to be specified for areas where the viscous flow is attached to the body and the velocity or pressure to be specified for areas with separated flow or in the wake. This approach is illustrated in Figure 1. It was recognized that a chord-line singularity method is less accurate than a surface singularity method. However, a generalized boundary condition surface singularity method is still in development (Reference 3) and it was felt to be desirable to develop the methodology of the viscous solution in the meantime.

Separation Bubble Model

The model for a separation bubble was taken from the component analysis base flow theory developed by Chapman, Korst and Chow (e.g., Reference 4). This theory assumes a turbulent shear layer between the outer potential flow and the inner recirculating flow (Figure 2). Then, with the argument that the momentum within the shear layer originates in the outer flow, a streamline is identified such that the momentum of the total shear layer is contained within the equivalent inviscid flow between this streamline and the outer edge of the shear layer. If this is the limiting streamline between the inner and outer flows, the momentum balance of the outer flow is assured. The velocity of the limiting streamline determines the pressure rise across the separation bubble since it approaches its stagnation pressure at the point of reattachment or recombination with the shear layer from the lower surface. Initially, the pressure within the bubble is constant. Then, at some point within the bubble (near the airfoil trailing edge for a trailing edge bubble), the pressure starts to increase toward the pressure at reattachment or recombination. It is from this recompression region that mass is pumped into the forward part of the bubble in order to set up the circulation within the bubble.

Application of the base flow theory to describe trailing edge separation is shown in Figure 2. In this case the shear layer from the upper surface combines with the shear layer from the lower surface and forms a wake. The same physical picture is assumed to occur in the leading edge separation bubbles except that the shear layer intersects the airfoil surface. At this point a new turbulent boundary layer is formed which continues downstream.

From this physical picture, it can be seen that the pressure within the separation bubble is limited by the static pressure at the closure of the bubble and not by the pressure at separation. A solution to the flow problem is reached when the presence of the separation bubble modifies the pressure distribution around the airfoil sufficiently that the pressure at separation agrees with the bubble pressure.

VERIFICATION OF THE METHOD

The Generalized Boundary Condition potential flow calculation method and the separation bubble model were combined with momentum integral boundary layer methods into a procedure for calculating the viscous-inviscid interactions for a wide range of airfoils. The resulting program is self-contained and includes all of the logic for distinguishing between the types or combinations of separated flow that are present. An iterative procedure is used to go from the initial inviscid solution to the viscous solution. In addition, iterative sub-loops are required to determine the proper bubble pressures for the long laminar separation bubble and the trailing edge bubble. The iteration procedure is described in Reference 1.

In order to test the ability of this analytical model to predict the flow field around an airfoil with various types of separated flow present, five airfoils of different thickness ratios were studied. The experimental data for these airfoils were taken from References 5 and 6. They were: (1) the 63$_3$-018 airfoil with stall development by progression of turbulent separation from the trailing edge forward, (2) the 63$_1$-012 airfoil which stalled by the sudden bursting of a short separation bubble, (3) the 63-009 airfoil that also stalled by short bubble bursting, (4) the 64A-006 airfoil with stall development by the progressive growth of a long separation bubble until its reattachment point moved past the airfoil trailing edge, and (5) the GA(W)-1 airfoil which stalled similarly to the 63$_3$-018 airfoil but represented more advanced airfoil design. The calculations were made for the specific angles of attack at which the surface pressures on the model had been measured.

Representative calculated pressure distributions and equivalent airfoil surfaces are shown in Figures 3 and 4. The inviscid pressure distribution is shown for comparison with the calculated pressure distribution and the measured pressures. The equivalent airfoil shape is the combination of the airfoil and the displacement surface of the viscous flow. The limiting streamline between the continuing viscous flow and the recirculating bubble flow also is shown.

Figure 3 shows a thin airfoil with a long laminar separation bubble. In order to simulate this flow, it was necessary to assume a bubble pressure and a point of reattachment. The pressure distribution was prescribed between separation and reattachment, and the airfoil shape was prescribed outside of this region. The subsequent equivalent airfoil shape was determined by the Generalized Boundary Condition program and the shape of the limiting streamline from the base flow theory. Reattachment was defined as the point where the limiting streamline intersected the airfoil surface. If the pressure rise between separation and reattachment corresponded to the predictions of the

base flow theory, then the solution was complete. Otherwise a higher bubble pressure was assumed, and the assumed reattachment point was updated by the results of the previous calculation.

The predicted bubble pressures shown in Figure 3 are somewhat lower than experiment and there is a kink in the pressure distribution at reattachment. The first effect is due to the inherent limitations of the chordline singularity potential flow calculation method. The second is due to the use of finite paneling. Also shown in Figure 3 are displacement thicknesses calculated from the measured boundary layer velocity profiles of Reference 5. These compare closely with the calculated equivalent airfoil surface, indicating that the shear layer growth across the separation bubble is calculated properly.

Figure 4 shows the calculated results for the NACA 63_1-012 airfoil at an angle of attack that is sufficiently high that short laminar separation bubble bursting has occurred. This figure is a good illustration of the fact that the equivalent airfoil contour terminates in an open wake. The method therefore has the potential for calculating the drag of the airfoil as well as the lift and pitching moment. This was not done since the present method is not considered to be sufficiently accurate for such a sensitive parameter. However, the method using a surface singularity potential flow method should be capable of this calculation.

The equivalent airfoil surfaces of the NASA GA(W)-1 airfoil were calculated at three angles of attack and are shown in Figures 5, 6, and 7 superimposed on the flow field measurements of Seetharam and Wentz (ref. 6). The measured boundary layer displacement thickness and wake centerlines also are shown. It was the object of this effort to try to develop some insight on just how the bubble matched the pressure isobars. This should be of importance for the development of a surface singularity method. It should have the further advantage of allowing an evaluation of the measured flow field; in particular, it should give an appreciation of the effect of the wind tunnel walls.

Figure 5 shows the wing at an angle of attack $\alpha = 10.3°$. A true separation bubble has not yet formed as evidenced by the pressure recovery all the way to the trailing edge. However, there is some recirculating flow just aft of the trailing edge. The measured displacement thickness agrees reasonably well with the equivalent airfoil surface as does the wake centerline. The calculated wake is much thicker than the measured wake indicating that the calculations did not allow sufficient pressure rise in the wake.

At an angle of attack $\alpha = 14.4°$, a full separation bubble has formed (Figure 6). In this case, the measured displacement thickness does not agree with the calculated equivalent airfoil surface, although the measured wake centerline does. It is noted that the measured displacement thicknesses do not agree with the measured separation point. This is stated to occur at the point of largest pressure gradient on the airfoil surface while a projection of the displacement thicknesses to the airfoil surface indicates later separation. Measured and calculated separation points agreed within 1% of the airfoil chord.

A fully developed trailing edge separation bubble at an angle of attack $\alpha = 18.4°$ is shown as Figure 7. Of particular note is the constant pressure region that brackets the equivalent airfoil contour. The measured displacement thickness also agrees with the calculated contour. However, there is a marked deviation of the measured wake centerline. This is probably due to the effects of the wind tunnel floor and ceiling which are known to have a pronounced effect on the airfoil downwash when separated flow is present.

These results suggest an approach to the determination of wind tunnel wall corrections for separated flows. Potential flow calculation methods have been developed to simulate the flow around airfoils between parallel walls. The addition of singularity panels simulating such parallel walls in the current program should lead to closer agreement with the measured flow shown in Figure 7. The difference between the two cases would yield both streamline curvature and blockage corrections.

CONCLUDING REMARKS

The McDonnell Aircraft Company Generalized Boundary Condition potential flow calculation method has been combined with momentum integral boundary layer methods and a component analysis base flow theory to develop a method for predicting viscous-inviscid interacting flows on airfoils beyond the appearance of boundary layer separation. The physical models of the several phases of such flows have been identified and combined into a functioning whole that accounts for the interaction of attached flow, short and long leading edge separation bubbles, and trailing edge bubbles. The resultant computer program has been used to calculate the pressure distribution and equivalent airfoil shape for airfoils exhibiting the different types of separated flow. It also has been used to evaluate flow field measurements around an airfoil with trailing edge separation.

REFERENCES

1. Cross, L. W., "The Prediction of Two-Dimensional Airfoil Stall Progression," AIAA Paper 78-155, January 1978.

2. Bristow, D. R., "Computer Program to Solve the Three-Dimensional Mixed Boundary Condition Problem for Subsonic or Supersonic Potential Flow," McDonnell Douglas Corporation Report A3190, December 1974.

3. Bristow, D. R., "Recent Improvements in Surface Singularity Methods for the Flow Field Analysis about Two-Dimensional Airfoils," AIAA Paper 77-541, June 1977.

4. Korst, H. H., "A Theory for Base Pressures in Transonic and Supersonic Flow," Journal of Applied Mechanics, Vol. 23, Transactions ASME, Vol. 78, 1956, pp. 593-600.

5. McCullough, G. B. and Gault, D. E., "Examples of Three Representative Types of Airfoil-Section Stall at Low Speed," NACA TN 2502, July 1951.

6. Seetharam, H. C. and Wentz, W. H. Jr., "Experimental Studies of Flow Separation and Stalling on a Two-Dimensional Airfoil at Low Speeds," NASA CR-2560, July 1975.

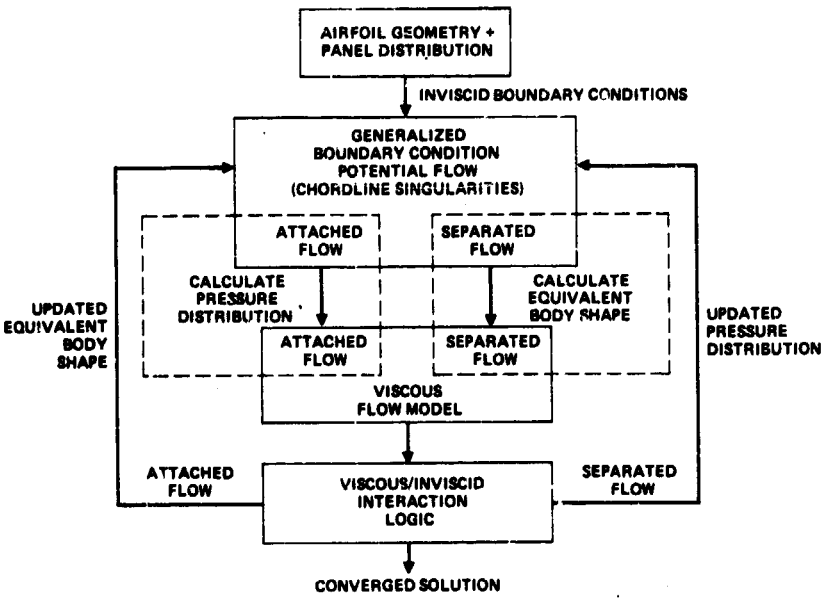

Figure 1.- Applications of generalized boundary conditions to separated flow modeling.

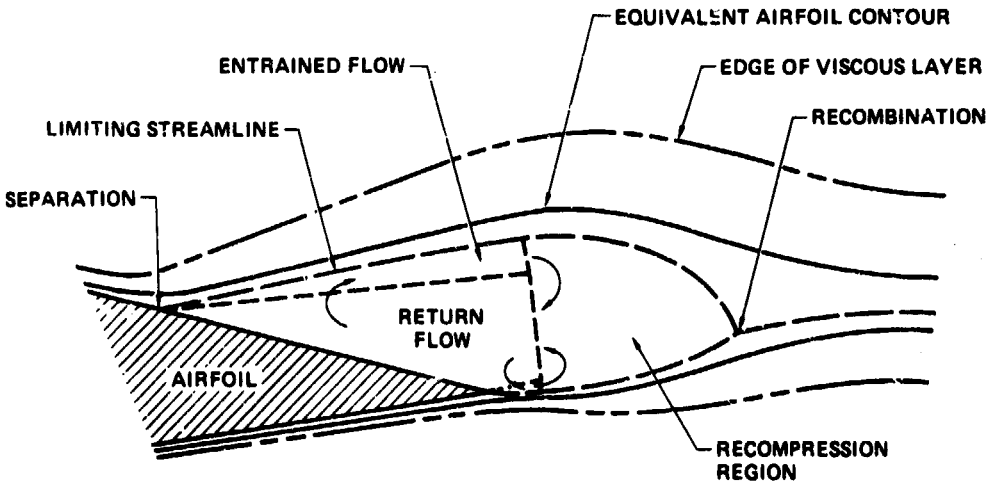

Figure 2.- Model of boundary-layer separation bubble developed from the component-analysis base-flow theory.

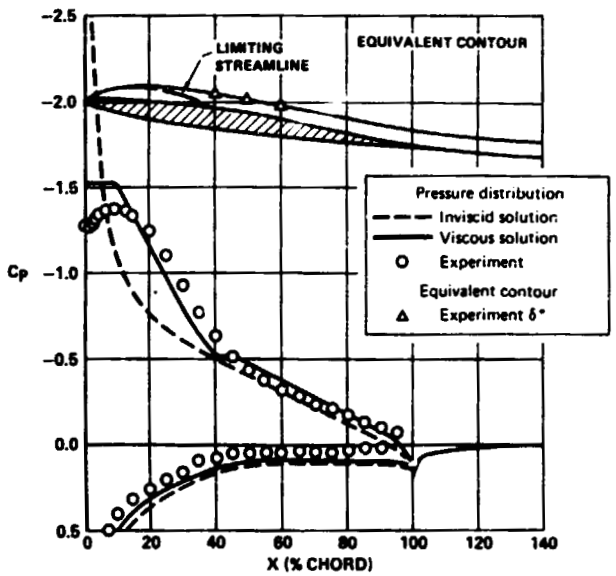

Figure 3.- Prediction of airfoil pressure distribution and equivalent contour 64A-006 airfoil. $\alpha = 7.31°$.

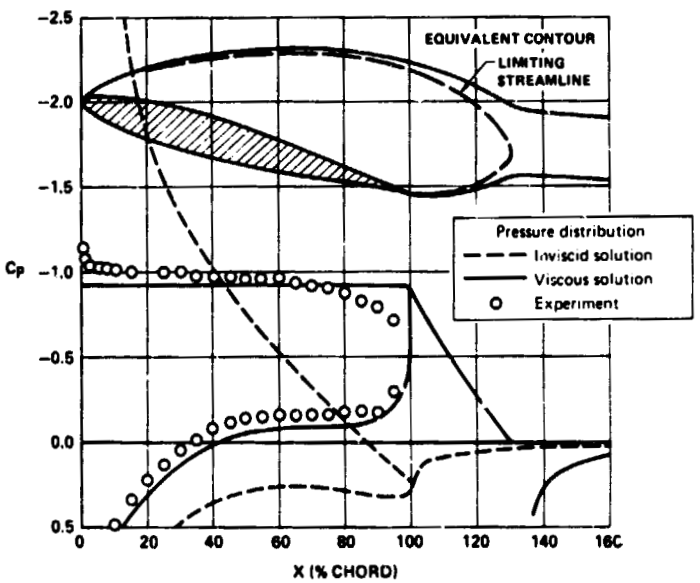

Figure 4.- Prediction of airfoil pressure distribution and equivalent contour 63_1-012 airfoil. $\alpha = 15.01°$.

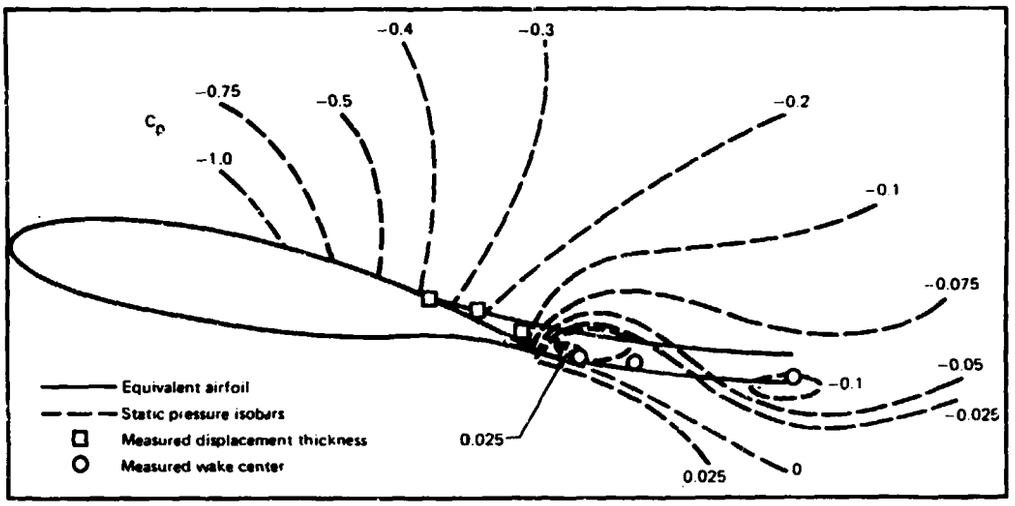

Figure 5.- Superposition of calculated equivalent airfoil shape on measured flow field of GA(W)-1 airfoil at $\alpha = 10.3^{o}$.

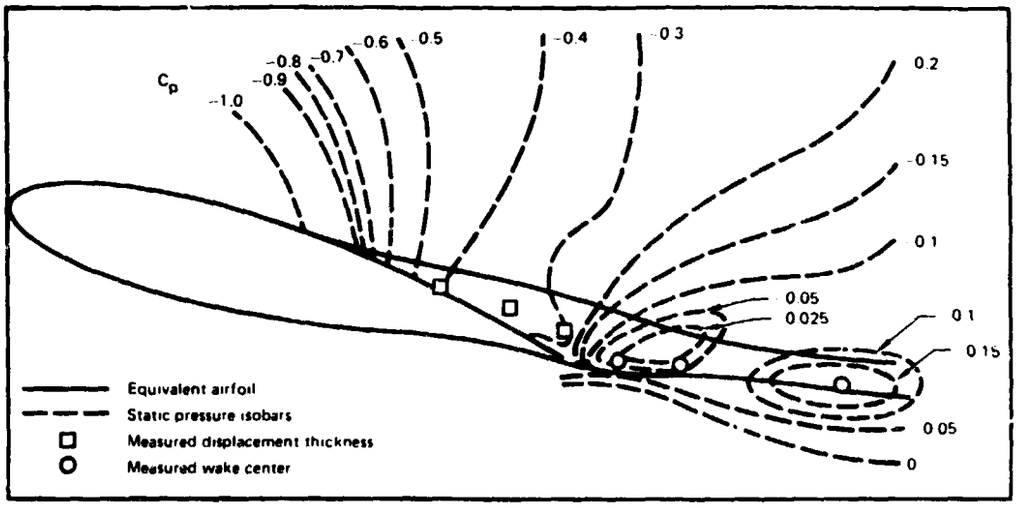

Figure 6.- Superposition of calculated equivalent airfoil shape on measured flow field of GA(W)-1 airfoil at $\alpha = 14.4°$.

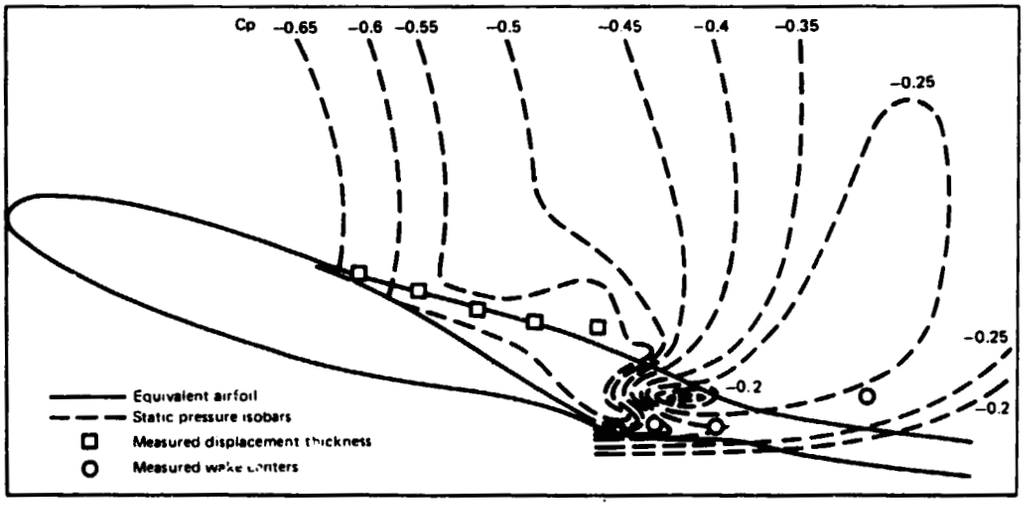

Figure 7.- Superposition of calculated equivalent airfoil shape on measured flow field of GA(W)-1 airfoil at $\alpha = 18.4°$.

D22

22

APPLICATION OF THE AMI $C_{\ell_{max}}$ PREDICTION METHOD TO A NUMBER OF AIRFOILS*

F.A. Dvorak and B. Maskew
Analytical Methods, Inc.

SUMMARY

A method for calculating the flow about airfoils up to and beyond the stall is described. It is an iterative procedure between potential flow and boundary layer solutions. The separated region is modeled in the potential flow analysis using free vortex sheets which require an inner iteration to establish their shapes. The free vortex sheet length is an important parameter in the potential flow calculation. Results so far indicate a possible correlation between wake length and airfoil thickness/chord ratio. Calculated and experimental results are compared for a series of airfoils.

INTRODUCTION

Boundary layer separation is one of the least understood but most important of fluid flow phenomena affecting aerodynamic forces and moments. Its accurate modeling is essential to the estimation of airborne vehicle performance. Currently, reliance is placed on wind tunnel tests to determine the consequences of separation, a procedure which is not entirely free of doubt because of Reynolds number effects. Successful theoretical modeling of separation is limited to a small number of special cases, one of which is two-dimensional turbulent boundary layer separation from airfoils or diffusers. The first successful model for trailing-edge separation was developed by Jacob (ref. 1). With Jacob's model, the separation region is simulated using source fluid, the distribution of which is chosen to give constant pressure everywhere in the separation region. In general, the method predicts the upstream pressure distribution in a satisfactory manner, although agreement with experiment for base pressure level is not consistent.

Recently a separation model has been developed by Analytical Methods, Inc. which replaces the source distribution in the separation zone by a vortex wake model. This model is described in

*Support was given by the U.S. Army Research Office, Research Triangle Park, N.C., for this work under Contract DAAG29-76-C-0019.

some detail in reference 2, but is discussed herein for reasons of completeness.

Symbols are defined in an appendix.

SEPARATION MODEL

Approximations for the Complete Flow Field

An approximate model of the flow about an airfoil with a region of separation is shown in figure 1. It is assumed that:

(i) The boundary layer and free shear layers do not have significant thickness and, hence, can be represented as slip surfaces; that is, streamlines across which there exists a jump in velocity.

(ii) The wake region does not have significant vorticity and has constant total pressure (lower than the free-stream total pressure). It is, therefore, taken to be a potential flow region.

The flow field in the potential flow is obtained using linearly varying vortex singularities distributed on planar panels. The wake is represented by sheets of vorticity shed at the separation points.

The mathematical problem is to find the vorticity sheet strength such that the appropriate boundary conditions are met. The position of the vorticity sheet representing the free shear layer is not known a priori.

Approximations For the Free Shear Layer

(i) Wake Shape

Initially, the streamlines are not known, and so the shapes of the free shear layers must be obtained iteratively starting from an initial assumption. Earlier calculations in which the vortex sheet shapes were obtained by iteration suggested an initial shape as follows. The upper and lower sheets are represented by parabolic curves passing from the separation points to a common point downstream. The slope at the upstream end is the mean between the free stream direction and the local surface slope. (Indications from further calculations are that this starting slope should be streamwise for calculations beyond the stall.) Once the wake calculation begins, the initial slope and downstream position of each wake is determined by iteration. The final wake position represents the separating streamline.

(ii) Wake Length

Early calculations indicated that the results were sensitive to the length of the free vortex sheets. Good correlation with experimental results was obtained only with relatively short wakes, i.e., wakes extending .1c to .2c beyond the trailing-edge. Such a model appears reasonable in the light of experimental evidence: the separated wake does, in fact, close quickly downstream of the trailing-edge, as a result of the strong entrainment process brought about by the rotation in the free shear layers (see reference 3). On the basis of several comparisons with experiment, a simple correlation was obtained for the wake length as a function of the airfoil thickness to chord ratio. This is discussed in detail in reference 2.

(iii) Wake Pressure

The approximation of zero static pressure drop across the free shear layer is used to obtain an expression for the total pressure in the wake in terms of the strength of the free vortex sheets. Considering the upper shear layer, if the average velocity in the layer is denoted by

$$\bar{V} = \tfrac{1}{2}\left(V_{outer} + V_{inner}\right)$$

then

$$V_{outer} = \bar{V} + \gamma_U/2, \text{ and}$$

$$V_{inner} = \bar{V} - \gamma_U/2,$$

since the vorticity, $\gamma_U = V_{outer} - V_{inner}$, on the upper sheet. (The vorticity in the lower shear layer is $\gamma_L = V_{inner} - V_{outer}$.) The jump in total pressure across the shear layer is then

$$\begin{aligned}\Delta H &= H_{inner} - H_{outer} \\ &= \left\{p_{inner} + \tfrac{1}{2}\rho\left(\bar{V} - \gamma_U/2\right)^2\right\} \\ &\quad - \left\{p_{outer} = \tfrac{1}{2}\rho\left(\bar{V} + \gamma_U/2\right)^2\right\} \\ &= -\rho\bar{V}\gamma_U = \rho\bar{V}\gamma_L\end{aligned}$$

given the boundary condition that the static pressure, p, has no jump in value across the shear layer.

Since the wake has constant total pressure (assumption (ii)), the jump in total pressure across the free shear layer is the same everywhere.

Once the vorticity strengths of the individual panels representing the airfoil and of the vorticity sheets representing the wake are determined, the velocity at any point in the flow field can be calculated.

The pressures are calculated from the velocities according to the Bernoulli equation which is expressed non-dimensionally as

$$C_p = 1 - \frac{V}{V_\infty}^2 + \frac{\Delta H}{q_\infty}$$

where $C_p = \frac{p - p_\infty}{q_\infty}$, $q_\infty = \frac{1}{2}\rho V_\infty^2$, and ΔH = increase in total pressure over that at infinity. Note that $\Delta H = 0$ everywhere except in the wake region for which it was previously shown that $\Delta H = \rho \bar{V} \gamma_L$.

CALCULATION PROCEDURE

Flow-Field Methods

The overall calculation procedure is shown in figure 2, and involves two separate iteration loops.

(i) Wake Shape Iteration

The iteration loop for wake shape is the inner loop and involves the potential flow analysis only. Within this loop the separation points are fixed. The separation points may be located anywhere on a surface panel; they are not restricted to panel edge points.

The wake shape is calculated as follows. Using the previous vorticity distribution, velocities are calculated at the panel mid-points on the free vortex sheets. The new wake shape is then determined by piecewise integration, starting at the separation points. The upper and lower sheet downstream end points, which were coincident in the initial wake, are allowed to move independently in subsequent iterations. At each iteration, the wake influence coefficients at the surface control points are recalculated, and a new potential flow solution is obtained.

The number of wake iterations is an input parameter in the current version of the program; convergence criteria have not been investigated yet.

(ii) Viscous/Potential Flow Iteration

This outer iteration loop takes the potential flow pressure distribution over to the boundary layer analysis and returns with the separation points and with the boundary layer source distribution. The source distribution is determined directly from the boundary layer solution as $\sigma = \frac{d}{ds}(U_e \delta^*)$ where U_e is the streamwise potential flow velocity at the edge of the boundary layer, and δ^* is the displacement thickness. The addition of this source distribution modifies the normal velocity, V_N, at each panel control point. The sources are set to zero in the separated region.

The program generates a new wake shape using the new separation points together with information from the previous iterated wake. A new potential flow solution is then obtained, and so on. The outer iteration is terminated when the change in C_ℓ is below 1%. A limit of eight iterations is currently imposed within the program.

Boundary Layer Methods

The boundary layer development on an arbitrarily-shaped two-dimensional lifting configuration with separated flow is very complex. A thorough and exact calculation of this development is properly the domain of the time-dependent solution to the general Navier Stokes equations. Unfortunately, the computer does not yet exist which is capable of handling such a problem in a reasonable time at a reasonable cost. Such a calculation is not, therefore, of practical interest to the aerodynamicist. Less difficult or costly are the finite-difference boundary layer programs now in existence. The amount of computer time required for each calculation still prohibits their use in an analysis procedure of the type reported herein. Having made the above evaluation, one must conclude that if the objective is a viscosity-dependent calculation procedure of practical use to the aerodynamicist for $C_{\ell_{max}}$ analysis, and, possibly for preliminary design, the method must be relatively simple to use and economic of computer time. This can only be achieved if integral boundary layer methods are used. In two dimensions, integral methods are typically about 100 times faster than finite-difference methods. They can, however, be expected to break down in the region of separation where none of the boundary layer methods (including three-dimensional) can be expected to be valid. It is anticipated, therefore, that integral methods will suffice for most applications of interest to the aerodynamicist for $C_{\ell_{max}}$ prediction.

In those cases of special interest to the aerodynamicist, such as the effect of area suction for boundary layer control or of roughness (rivets, etc.) on $C_{\ell_{max}}$, alternative boundary layer calculation modules are available. These methods are called as needed into the overall calculation procedure. A brief description of the boundary layer methods is given in the following paragraphs.

The laminar boundary layer development is calculated by Curle's method (ref. 4), an adaption of the well known method of Thwaites (ref. 5). The calculation proceeds either to laminar separation or to the end of the airfoil--whichever occurs first. The calculated boundary layer development is then interrogated to determine if transition, laminar separation or forced transition (boundary layer tripping) has taken place. If any of these phenomena have occurred, the downstream flow is assumed to be turbulent.

Methods for the calculation of turbulent boundary layers in two dimensions have been developed by many investigators. A review of these methods was made at a conference held in 1968 at Stanford University (ref. 6). One of the methods, an integral method by Nash and Hicks (ref. 7), compared very favorably with the more complex finite-difference methods. Now, several years later, the method remains an excellent approach for application to the current problem both in terms of accuracy and speed.

If surface roughness or area suction are of interest, an alternate turbulent boundary layer method developed by Dvorak (refs. 8 and 9) can be called. This method is capable of predicting the downstream development and the skin friction drag of a turbulent boundary layer over a rough surface, or a surface with area suction boundary layer control.

Turbulent boundary layer separation is predicted by either the Nash and Hicks or Dvorak methods when the calculated local skin friction coefficient reaches zero.

DISCUSSION OF RESULTS

The method was applied to a GA(W)-1 airfoil. This section shape represents a difficult test case and pressure distributions are available from experiments at NASA-Langley for a range of incidence.

The first set of results, figures 3 through 5, are for a Reynolds number of 6.3×10^6 with a boundary layer trip at .08c. Figure 3 shows a very good agreement between the calculated and

experimental pressure distribution at 20.05° incidence. The calculation took six viscous/potential flow iterations each with three wake shape iterations. For comparison, the attached potential flow solution at this incidence is also plotted, and indicates the large change in pressures due to the separated flow.

The wake shape history for a 21.14° incidence is shown in figure 4, and indicates very good convergence characteristics. Lift and pitching moment characteristics show excellent agreement with experiment, figure 5. The present calculations show considerable improvement over a previous Lockheed/Nasa-Langley calculation. The attached potential flow solution is included in figure 5 to put into perspective the magnitude of the change achieved by the new method.

Figure 6 shows the lift characteristics for the GA(W)-1 airfoil at a Reynolds number of 2.1×10^6. The calculations give good agreement with experiment up to $C_{\ell_{max}}$, but the turnover in the curve occurs 2 to 3 degrees later than in the experiment.

Additional comparisons were made with experiment for several airfoils. Shown on figures 7 and 8 are the results for the lift characteristics for the airfoils tested by McCullough and Gault (ref. 10). In the case of the NACA 63009 airfoil, the program predicts a trailing-edge stall while experimentally the airfoil stalls from the leading-edge. As shown in figure 7, a slight modification to the laminar separation reattachment criterion leads to a much improved correlation with experiment. This points out the need for a better understanding of the laminar separation bubble bursting phenomenon.

Comparisons between theory and experiment for the lift characteristics of the NACA 4412 at a series of Reynolds numbers are shown on figures 9, 10 and 11. A summary of the predicted and experimental $C_{\ell_{max}}$ variation with Reynolds number is shown in figure 12. The calculated values agree very closely with the experimental curve from reference 11. Calculations for lower Reynolds numbers were attempted, but problems with the laminar separation bubble bursting criterion produced inconsistent results.

A series of calculations were made to demonstrate the capability of the analysis method over a wide range of angles-of-attack. Figure 13 shows the calculated wake shape for a NACA 0012 airfoil at 90 degrees to the free stream. The corresponding pressure distribution is given in figure 14. The calculated lift and drag coefficients are $0.25^{(.15)}$ AND 2.1(2.08 - 2.3) respectively. These values compare well with measured lift and drag coefficients given in the enclosed brackets. Figure 15 shows a

comparison between measured and calculated lift coefficients for the NACA 0012 airfoil from 0 degrees through 90 degrees angle-of-attack. The agreement is surprisingly good.

CONCLUSIONS

The results of comparisons with experiment, including those presented in this paper, lead to the following conclusions

(i) the basic analysis method predicts both the lift curve and the maximum lift coefficient quite accurately for a wide variety of airfoils over a range of Reynolds numbers;

(ii) post-stall behavior is best predicted for the trailing-edge type of stall;

(iii) leading-edge and thin airfoil stall prediction could be considerably improved by a better laminar separation bubble bursting criterion.

(iv) the use of vortex sheets to represent the separated flow boundaries suggests that the model will be applicable to unsteady flows.

APPENDIX

Symbols

c	airfoil chord
C_d	drag coefficient
C_ℓ	lift coefficient
$C_{\ell_{max}}$	maximum lift coefficient
C_m	moment coefficient
C_p	pressure coefficient
H	total pressure
p	static pressure
q	free stream dynamic pressure
Re	Reynolds number, $V_\infty c/\nu$
V_N	normal velocity
$\overline{V}$	average shear layer velocity
V_∞	free-stream velocity
δ^*	displacement thickness
ρ	density
γ	vorticity
σ	boundary layer source strength $\equiv \frac{d}{ds}(V_e\delta^*)$
ν	kinematic viscosity
α	angle-of-attack
U	upper surface

L	lower surface
∞	value at free stream conditions
e	value at edge of boundary layer

REFERENCES

1. Jacob, K., "Computation of Separated, Incompressible Flow Around Airfoils and Determination of Maximum Lift", AVA Report 66, A, 62, 1967.

2. Maskew, B. and Dvorak, F.A., "The Prediction of $C_{\ell max}$ Using a Separated Flow Model", Proceedings 33rd Annual Forum of the American Helicopter Society, Washington, D.C., May 1977. (To be published in the AHS Journal.)

3. Seetharam, H.C. and Wentz, W.H., "Experimental Studies of Flow Separation and Stalling on a Two-Dimensional Airfoil at Low Speeds", NASA CR-2560, 1975.

4. Curle, H., "A Two-Parameter Method for Calculating the Two-Dimensional Incompressible Laminar Boundary Layer", J.R. Aero. Soc., Vol. 71, 1967.

5. Thwaites, B., "Approximate Calculation of the Laminar Boundary Layer", Aero. Quart., Vol. I, 1949.

6. Kline, S.J., Morkovin, M.V., Sovran, G. and Cockrell, D.J., "Computation of Turbulent Boundary Layers", Proceedings 1968 AFOSR-IFP Stanford Conference, Stanford University Press, Stanford, Calif., 1969.

7. Nash, J.F. and Hicks, J.G., "An Integral Method Including the Effect of Upstream History on the Turbulent Shear Stress", Proceedings Computation of Turbulent Boundary Layers--1968 AFOSR-IFP Stanford Conference, Vol. 1, Stanford University Dept. of Mech. Eng., Stanford, Calif.

8. Dvorak, F.A., "The Calculation of Turbulent Boundary Layers on Rough Surfaces in Pressure Gradient", AIAA J., Vol. 7, No. 9, September 1969.

9. Dvorak, F.A., "The Calculation of Compressible Turbulent Boundary Layers with Roughness and Heat Transfer", AIAA J., Vol. 10, No. 11, November 1972.

10. McCullough, G.B. and Gault, D.E., "Examples of Three Representative Types of Airfoil Section Stall at Low Speed", NACA Tech. Note 2502, 1951.

11. Pinkerton, R.N., "The Variation with Reynolds Number of Pressure Distribution over an Airfoil Section", NACA Report No. 613, 1938.

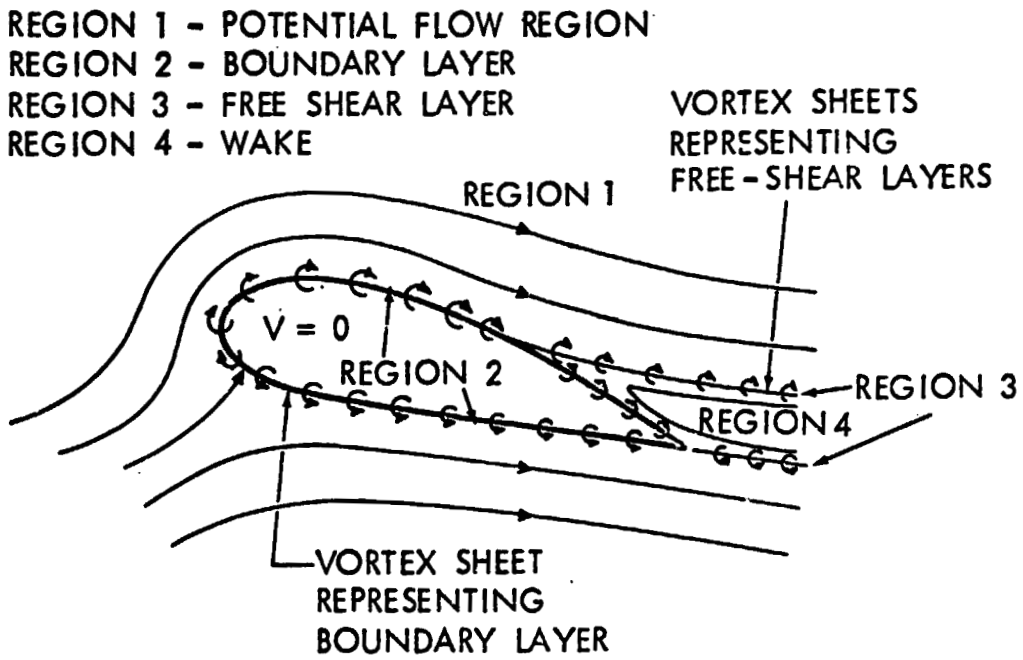

Figure 1.- Mathematical flow model.

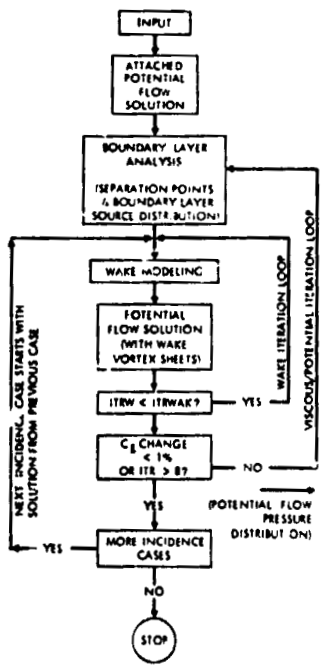

Figure 2.- Calculation procedure.

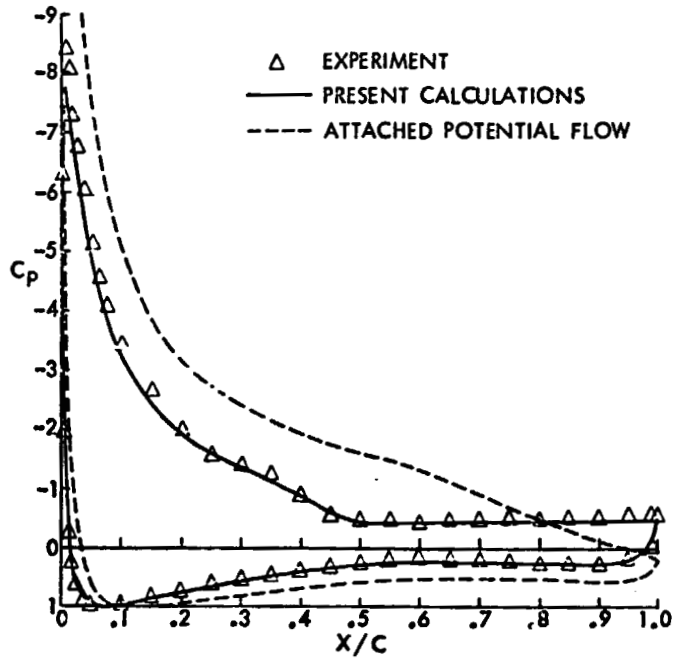

Figure 3.- Comparison of calculated and experimental pressure distributions on a GA(W)-1 airfoil post stall. Re = 6.3×10^6; $\alpha = 20.05°$.

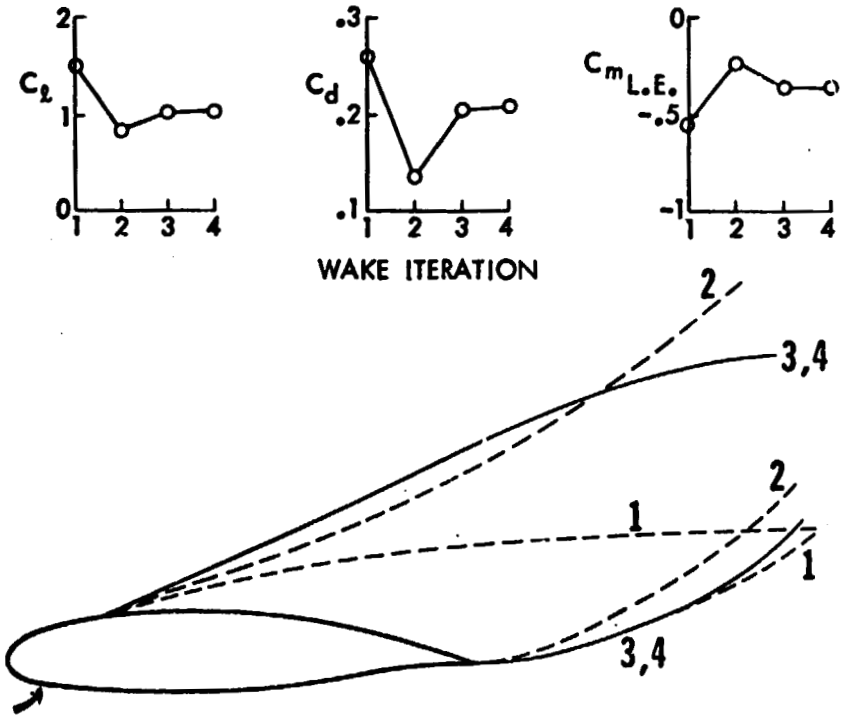

Figure 4.- Typical wake-shape iteration characteristics for an angle of attack beyond the stall.

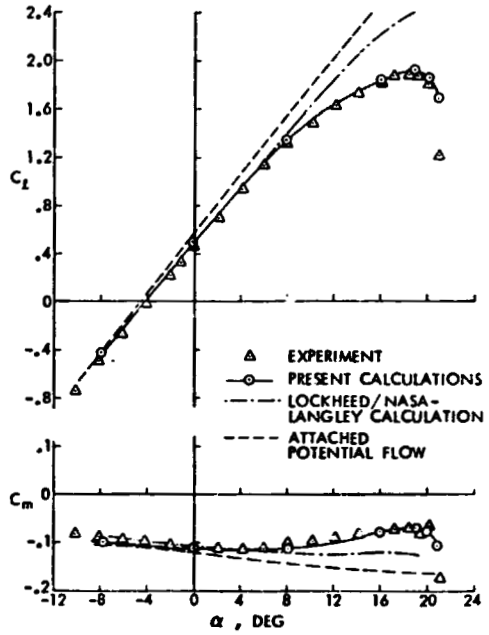

Figure 5.- Comparisons of calculated and experimental lift and pitching-moment characteristics for the GA(W)-1 airfoil. Re = 6.3×10^6.

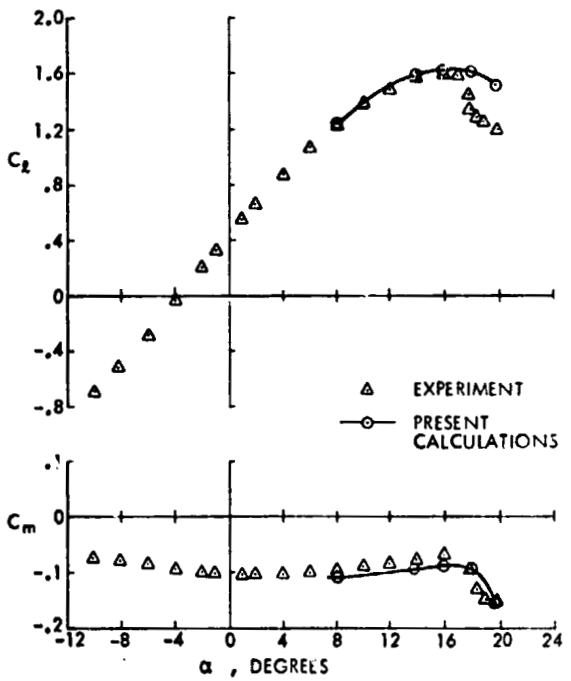

Figure 6.- Comparisons of calculated and experimental lift and pitching-moment characteristics for the GA(W)-1 airfoil. Re = 2.1×10^6.

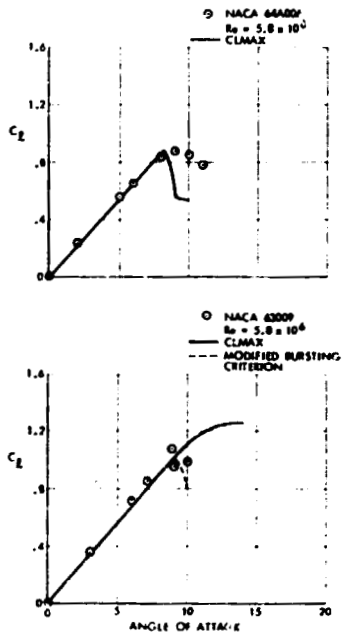

Figure 7.- Comparison of calculated and experimental lift characteristics for NACA 64A006 and 63009 airfoils.

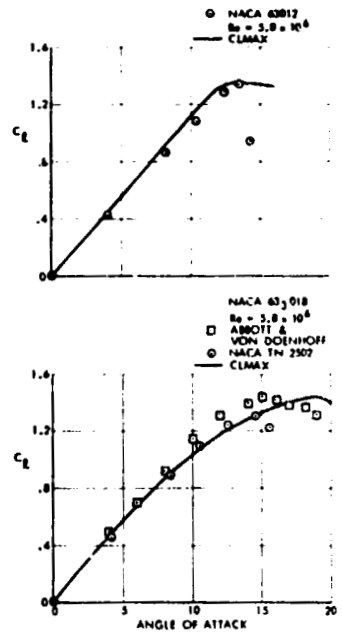

Figure 8.- Comparison of calculated and experimental lift characteristics for NACA 63012 and $63_3$018 airfoil sections.

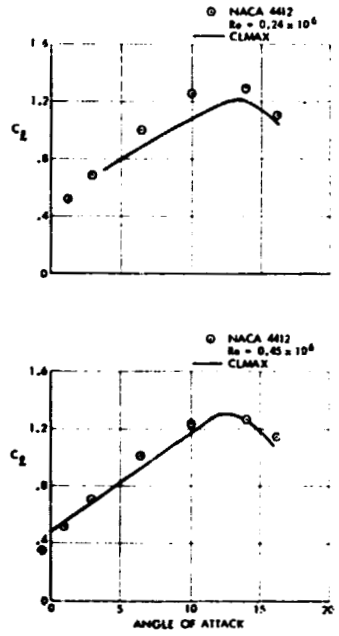

Figure 9.- Comparison of calculated and experimental lift characteristics for an NACA 4412 airfoil. Re = 0.24 × 10^6 and 0.45 × 10^6.

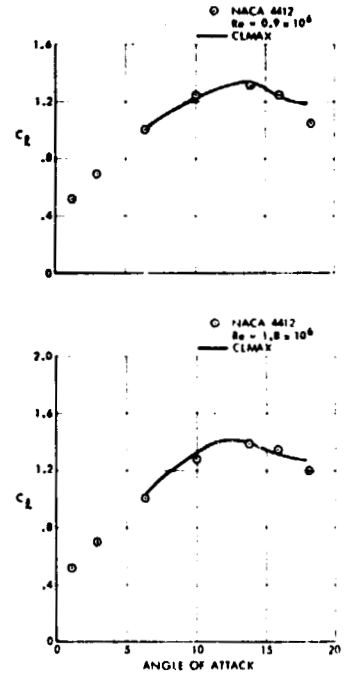

Figure 10.- Comparison of calculated and experimental lift characteristics for an NACA 4412 airfoil. Re = 0.9 × 10^6 and 1.8 × 10^6.

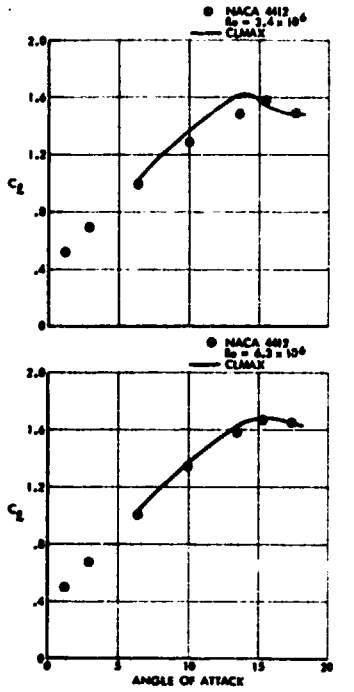

Figure 11.- Comparison of calculated and experimental lift characteristics for an NACA 4412 airfoil. Re = 3.4×10^6 and 6.3×10^6.

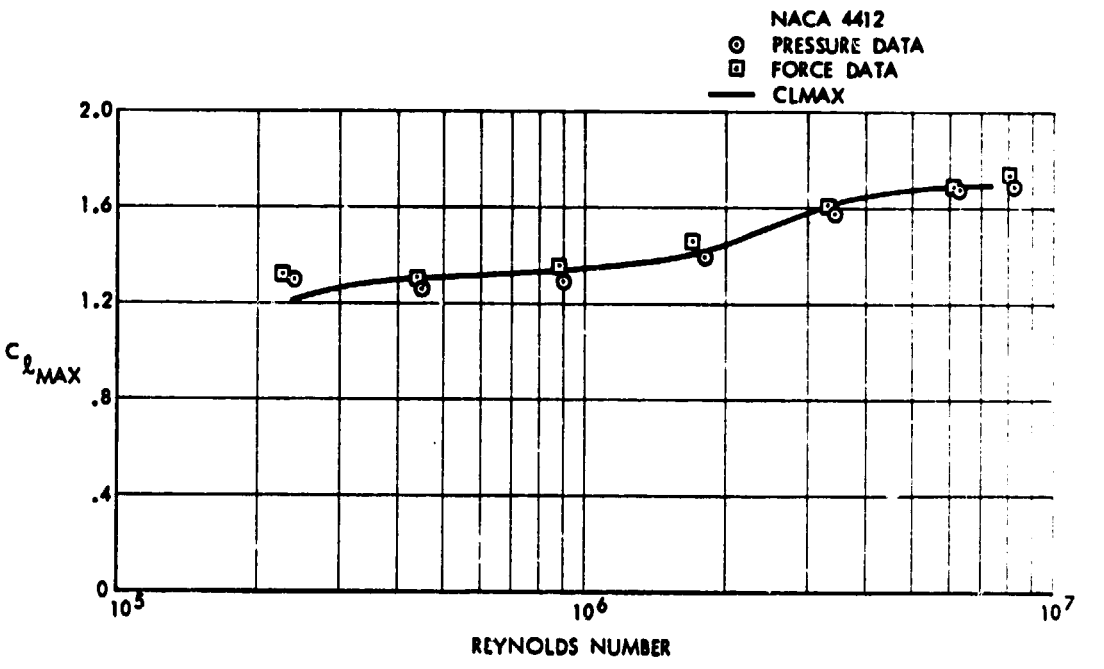

Figure 12.- Comparison of calculated and experimental $C_{\ell_{max}}$ variation with Reynolds number for the NACA 4412 airfoil.

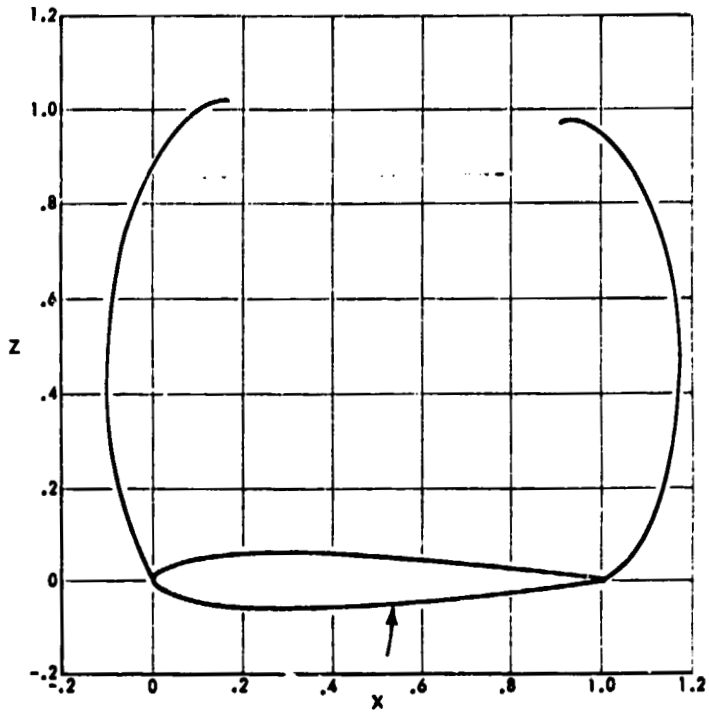

Figure 13.- Calculated wake shape for an NACA 0012 airfoil at 90° incidence after six viscous-potential flow iterations, each with three wake-shape iterations.

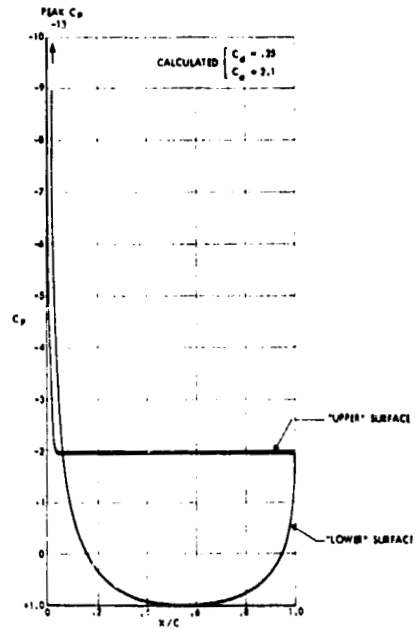

Figure 14.- Calculated pressure distribution on an NACA 0012 airfoil at 90° incidence. Re = 6.0×10^6; Mach number, 0.2.

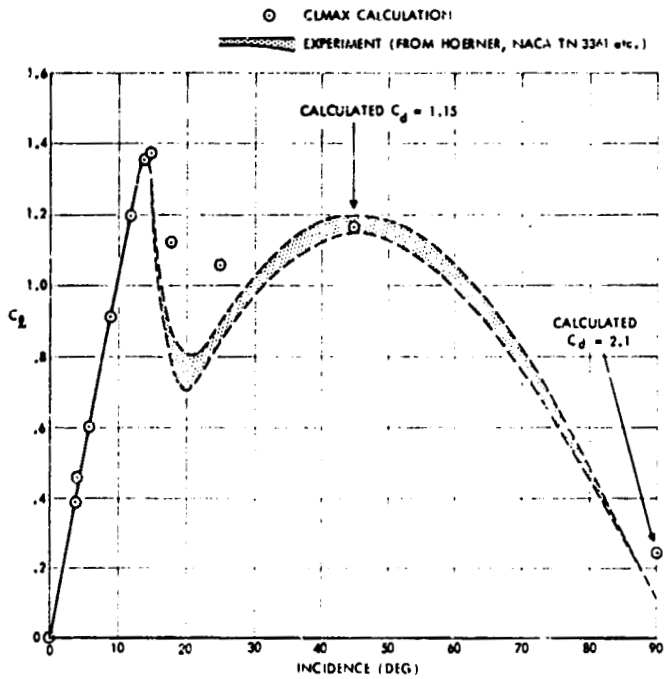

Figure 15.- Comparison of calculated and experimental lift characteristics for an NACA 0012 airfoil. Re = 6.0×10^6; Mach number, 0.2.

D23

23

A NEW FLOW MODEL FOR HIGHLY SEPARATED AIRFOIL FLOWS AT LOW SPEEDS*

Glen W. Zumwalt
Wichita State University

Sharad N. Naik
Beech Aircraft Corporation

SUMMARY

An analytical model for separated airfoil flows is presented which is based on experimentally observed physical phenomena. These include a free stagnation point aft of the airfoil and a standing vortex in the separated region. A computer program is described which iteratively matches the outer potential flow, the airfoil turbulent boundary layer, the separated jet entrainment, mass conservation in the separated bubble, and the rear stagnation pressure. Separation location and pressure are not specified a priori. Results are presented for surface pressure coefficient and compared with experiment for three angles of attack for a GA(W)-1, 17% thick airfoil.

INTRODUCTION

Separated flow on wings has drawn researchers' interest ever since it was found to be responsible for aircraft stall. Interest has recently intensified due to the ability of the new GA(W) series of airfoils to operate stably with flow separated up to half of the upper surface length. However, research was long restricted to experimental observation due to the complexity of the phenomenon. For very low Reynolds numbers, solution of the Navier-Stokes equations should provide an analysis of the flow, but even with modern computers, this is a costly task. For realistic airfoils, turbulent flows occur and require some sort of mathematical model. Several models have been proposed and solved by computers with various simplifying assumptions or empirical relations. Most of the previously proposed models consider the separated region to extend to infinity downstream or it is modeled as a bulbous region. The actual physical processes in the separated region have not been included in the models. Although some of these methods have produced reasonably good computational results, their ranges of applications are generally limited and empirical input is usually required.

A mathematical model was sought which included the principal physical features. The model was first formulated by logic, found to conform to the velocity and pressure data, and then tested by special wind tunnel and electric ana-

*This research was supported by NASA Grant NSG 1192 and is available in more complete form in NASA CR-145249 (ref. 1).

366

log experiments. Finally, a computational program was devised with the objective of minimizing the empirical information required for solution. This program was used to predict pressures on an airfoil for which detailed data were available for comparison and evaluation of the model.

Symbols are defined in an appendix.

ORIGIN OF THE FLOW MODEL

A sketch of the flow model is shown in figure 1. The flow has separated from the upper surface and leaves the lower surface at the trailing edge. The jet mixing sheets starting from the two airfoil separation points coalesce to form the separation bubble behind the airfoil. These two jets entrain air from the dead air region (near-wake). The entrained air has to be replaced by backflow of air which must be supplied from somewhere. If S and S' (fig. 1) are the two separation streamlines, it can be seen that the amount and width of flow entrained are growing in the downstream direction; consequently, the space available for backflow decreases and the demand for it increases. Since this cannot continue very far, a termination is required of the near wake recirculation region, and a stagnation point is formed. At this point the two streams rejoin defining the end of the separation bubble.

The entrained masses of the two jets are not the same, since their lengths and velocities are different. Generally, the upper one will entrain a larger mass. Therefore, the stagnating streamlines are not necessarily the separating streamlines, S and S'. Figure 1 shows two other streamlines R and R' stagnating at the rear point and providing passages for the flow to enter and leave the separation bubble. The mass flow rate through the corridor between R and S must be the same as that between R' and S'. Further, R and R' do not terminate at the stagnation point but must continue upstream and downstream. Mass conservation in the region requires the formation of two vortices and an S-shaped corridor of flow from bottom to top.

At this point experimental verification was sought for this seemingly logical model. No reference could be found to a stable free vortex above the trailing edge, nor was the existence of a free stagnation point documented. At Wichita State University, wind tunnel tests were in process for the GA(W)-1 airfoil under NASA contract. Detailed measurements of pressure and velocity were made downstream of the trailing edge at high angles of attack (ref. 2). Figures 2 and 3 are typical results of these tests and can be seen to verify (a) the locally high pressure region just aft of the trailing edge and (2) the recirculating flow region terminating at the rear high pressure point.

Based on experimental data, constant pressure is assumed in the whole separated region except in the neighborhood of the stagnation point, where a locally high pressure region will form along the RR' line, turning back the low velocity flows.

Viscous effects can be ignored in the neighborhood of the rear stagnation point and all velocity changes considered as being due to the pressure gradi-

ents. Thus, the region is divided into viscous dominated and pressure dominated regions. This follows the classical approach originated by Prandtl for boundary layers and more recently applied successfully to separated and reattaching flows in the Chapman-Korst mixing models.

The trailing edge plane is assumed to divide the constant pressure region of the separated flow and the region of pressure rise to the rear stagnation point. This plane is also the location for satisfying the mass continuity.

Since the vortex was not discernible, a simple flow test was devised to determine its existence. A 25.4 cm chord GA(W)-1 airfoil was placed in a low speed tunnel with a thin aluminum "splitter" plate mounted parallel to the flow at midspan. The plate extended downstream of the airfoil about one chord length. The plate was painted or spotted with a lampblack-and-oil mixture to provide visualization of streamlines, as shown in figures 4 and 5. (Flow is right to left.) The main observations are:

(1) The wake closes behind the airfoil to form a "bubble" with a free stagnation point quite close to the trailing edge.

(2) The recirculating flow in the near wake forms a large, unsymmetrical vortex above the rear portion of the airfoil.

(3) There is an upward flow from the lower wake of the airfoil flowing upstream in the separation bubble and then around the vortex to join the main stream. This S-shaped, lower-to-upper flow was clearly seen on the streaked plates.

With a view toward making a mathematical model, an electric analog of the separated airfoil flow was set up. The electric potential of the airfoil was adjusted to meet the Kutta condition at the lower trailing edge, and an additional voltage point was placed above and aft of the trailing edge. This created the S-shaped lower-to-upper flow, a topside separation, and a rear stagnation. The streamlines around the airfoil surface were found to be sensitive to the strength of the rear potential point, but quite insensitive to the exact location. This fact was used in formulating the mathematical model.

COMPUTATION OF THE MODEL

The mathematical model consists of a potential flow, a boundary layer on the airfoil surface, and a separated flow region. These are iteratively matched, together with mass conservation requirements, to reach a solution.

Assumptions Made

1. Steady, incompressible, plane flow of air.

2. The boundary layer is fully turbulent.

3. The rear stagnation point is located downstream of the trailing edge one-third the distance between the upper separation point and the trailing edge. This was empirically derived and the solution was found to be quite insensitive to this value, as the electrical analog study suggested.

4. There is a constant-velocity reverse flow region, a "core flow" for the recirculating air, having a velocity 20% that of the adjacent free stream. Experimental evidence for the constant-velocity profile was abundant but no logical model can be suggested to give a "core flow" from the reversal of a shear flow. Therefore, a purely empirical choice was accepted as necessary and the 20% value derived from the examination of several GA(W) wing flow measurements. Results were somewhat sensitive to this choice, and this is regarded as the one genuinely empirical value in the flow model computation.

5. The streamlines which stagnate behind the body do so without loss of total pressure. This is the commonly used Chapman-Korst jet-mixing flow model. The pressure variation from the trailing edge to the stagnation point is approximated by a parabolic variation to conform to experimental trends. Results were found to be insensitive to this choice.

Potential Flow

A potential flow solution method was required which would give velocities and pressures for specified geometries on the forward and lower airfoil surfaces, and also produce streamline geometry for a specified pressure distribution in the separated regions. The Mixed Boundary Condition potential flow program of McDonnell Aircraft Company, St. Louis, met this requirement and was made available. This program is a modification of the wing-body code developed by Woodward (ref. 3). The airfoil is divided into a number of panels on the chordline and the thickness, camber and angle of attack are represented by planar source and vortex singularities. Panel lengths chosen for computation were 1% of chord near the leading and trailing edges, and these increased 5% in the center of the airfoil. Near wake panels were also 1% long. The potential program treated the separated region as an extension of the airfoil, with the body terminating at the rear stagnation point.

Boundary Layer Analysis

Head's entrainment method (ref. 4) of calculating the turbulent boundary layer was chosen as being sufficiently accurate without undue complexity. The flow was assumed to be turbulent from the leading edge or, on the lower side, from the front stagnation point. After the potential flow solution was accomplished, the displacement thickness was computed and added to the airfoil surface. The augmented airfoil was again solved by the potential program and the process repeated to convergence. Since the potential program provided the separation streamline shape, the displacement thickness at the separation point was added to the ordinates of the separation streamline to obtain the effective displacement surface.

The criteria for separation of the boundary layer was the value of the shape factor, H, which is the ratio of the displacement thickness to the momentum thickness. Most integral methods assume H values of 1.8 to 2.4 as the separation indicator. The exact value appears to depend on surface curvature, backflow strength, and possibly the upstream boundary layer history. This value was varied in the program as a means of "ordering" the separation point to move. An initial value of 2.2 was used with separation at 95% chord.

Jet Mixing Analysis

A jet mixing computation was needed for the upper stream to permit calculation of the mass entrained. Since the model assumes, on the basis of experimental evidence, that the separated flow is at constant pressure (equal to the separation point pressure), a constant pressure mixing theory is needed. The Korst turbulent jet mixing method (ref. 5) was adapted to the incompressible case for the flow on the upper surface from separation to the rear stagnation point. The virtual origin method of Hill (ref. 6) was used to handle the effects of the initial boundary layer at separation on the jet mixing. This then produces a velocity profile at the plane of the trailing edge.

Determination of the Stagnating Streamlines

The two streamlines R and R' (see fig. 6) can be found from the two requirements (1) that their velocities are equal and (2) that the mass entering the separation bubble between R' and the lower surface must equal the mass leaving between streamlines S and R. The model assumes a constant static pressure separated region which applies to R' and R at the trailing edge plane. Their stagnation pressures are also equal, since they stagnate at the same point. Thus, their velocities must be equal. The equal mass flow requirement is performed at the trailing edge plane. A velocity value for R and R' is iterated until the mass requirement is met. A new rear stagnation point pressure results. If it differs from the value previously used, the potential flow and boundary layer must be recalculated and the new R and R' streamlines located.

Recirculating Mass Balance

The Korst error function velocity profile is used for variation from the local potential flow velocity to the reverse core flow velocity. The Goertler jet spreading parameter, σ, required for the mixing analysis, was used with the well-established incompressible value of 12. The airfoil upper surface is augmented by the displacement thickness at the lower trailing edge. This pictures the lower boundary layer as swirling almost unchanged around a small separation bubble at the trailing edge. The mass flow is integrated from the displaced upper surface of the airfoil to the S streamline in the transverse plane of the trailing edge. If the net mass flux is not zero, the value of the shape factor H for separation is changed and the entire computation process is repeated until mass conservation is reached.

2.5

COMPUTED RESULTS

Figure 7 illustrates the program logic. In this figure, P_R refers to the pressure at the rear stagnation point. This program was used to calculate the pressure distributions on the GA(W)-1 17% thick airfoil at three angles of attack (18.4°, 16.4°, and 14.4°) for which experimental data were available (ref. 7). The results are shown in figures 8, 9 and 10. It can be seen that agreement with experiment is good. The separation pressure is predicted quite accurately and the separation location is slightly aft of the experimental values. The rear stagnation pressures also agree well with experiments. Comparative values are given in Table 1.

The method does not prescribe any of the separation variables. Examination of the computational histories shows that the separation point and pressure vary freely as the iterations proceed. Accuracy is dependent upon the number of panels used. The computed pressures show deviations from experimental values at about 15% chord where panel size was increased suddenly. By choosing a larger number of panels the accuracy would be improved at the cost of increased computing time. Using 29 panels on the airfoil, computation times on an IBM 360/44 or 370/145 were 14 to 40 minutes, depending on angle of attack and iterative accuracy desired.

Some improvements are needed in the computational elements. The potential program used represented the airfoil by a singularity distribution on the chord line. This is adequate for thin airfoils, but for airfoils with large thickness or angle of attack, there can be significant errors. A potential program using surface singularities (but still of the mixed boundary layer condition type) would improve accuracy. Similarly, Head's boundary layer method is usable and simple, but is not the most accurate available. Computations should be made for other airfoils to evaluate the reverse flow velocity assumption.

However, even at this point of development, this model has been shown to include all of the significant physical features, to be capable of computation with reasonable computer times, and to give good surface pressure results.

APPENDIX

SYMBOLS

C	Chord Length
C_p	Pressure Coefficient
C_{P_R}	Pressure Coefficient at Rear Stagnation Point
H	Shape Factor of Boundary Layer
M	Mach Number
$\dot{M}$	Mass Flow Rate
P_R	Pressure at Rear Stagnation Point
R.N.	Reynolds Number Based on Airfoil Chord
R	Streamline which stagnates at rear
S	Streamline which separates from surface
X_{sep}	Length from separation point to airfoil trailing edge; fraction of chord length.
α	Angle of Attack
δ	Boundary Layer Thickness
δ^*	Boundary Layer Displacement Thickness
σ	Jet Spreading Parameter

Subscripts:

L	Lower side of airfoil
SEP	Separation point
U	Upper side of airfoil
∞	Free stream value

Superscript:

Prime indicates lower-side flow

REFERENCES

1. Zumwalt, Glen W.; and Naik, Sharad N.: An Analytical Model for Highly Separated Flow on Airfoils at Low Speeds. NASA CR-145249, 1977.

2. Seetharam, H.C.; and Wentz, W.H., Jr.: Experimental Studies of Flow Separation and Stalling on a Two-Dimensional Airfoil at Low Speeds. NASA NASA CR-2560, 1975.

3. Woodward, F.A.: Analysis and Design of Wing Body Combinations at Subsonic and Supersonic Speeds. Journal of Aircraft, Vol. 5, No. 6, Nov.-Dec., 1968.

4. Head, M.R.; and Patel, V.C.: Improved Entrainment Method for Calculating Turbulent Boundary Layer Development. British R&M 3643, March 1968.

5. Korst, H.H.: A Theory of Base Pressures in Transonic and Supersonic Flow. Journal of Applied Mechanics, Vol. 23, 1956, pp. 593-600.

6. Hill, W.G., Jr.; and Page, R.H.: Initial Development of Turbulent Compressible Free Shear Layer. ASME Paper No. 68 WA/FE-21, 1968.

7. Wentz, W.H., Jr.; and Seetharam, H.C.: The Development of a Fowler Flap System for a High Performance Subsonic Flow Analysis. NASA CR-2443, Dec. 1974.

TABLE 1.- RESULTS FROM PRESENT ANALYSIS AND EXPERIMENT (REFS. 2 AND 7)

			X_{sep}		$C_{p_{sep}}$		C_{p_R}		H_{sep}	
α	M_∞	R.N.	THEORY	EXPT.	THEORY	EIPT.	THEORY	EXPT.	THEORY	EXPT.
18.4°	0.16	2.5×10^6	52%	45%	-0.583	-0.60	-0.076	no data	1.9	no data
16.4°	0.21	2.9×10^6	57%	55%	-0.496	-0.50	+0.0595	no data	1.85	no data
14.4°	0.21	2.9×10^6	65%	70%	-0.285	-0.3	+0.1602	no data	1.8	no data
18.4	0.135	2.2×10^6	44%	45%	-0.640	-0.6	-0.135	≈-0.12	1.85	1.67
14.4	0.135	2.2×10^6	60%	65%	-0.33	-0.4	0.119	≈0.0	1.80	1.81

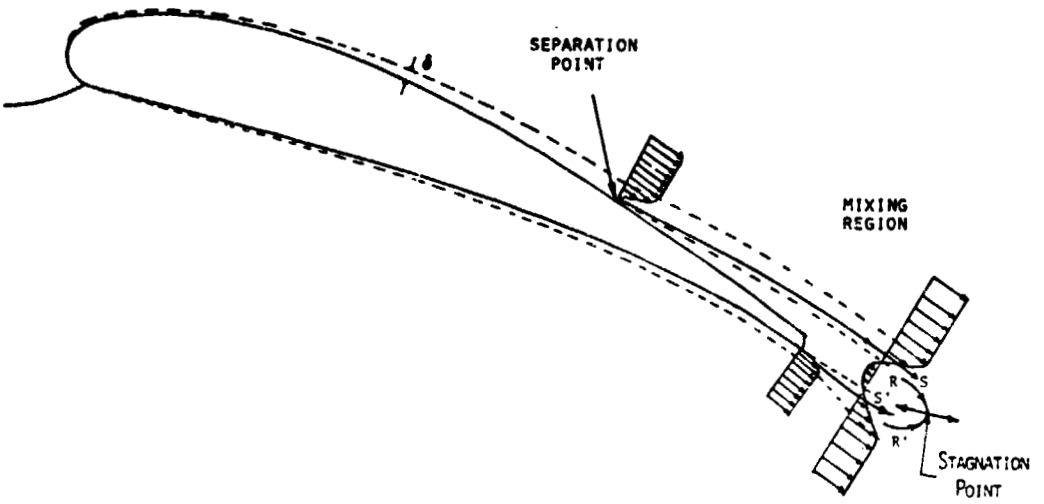

Figure 1.- Schematic diagram of separated flow model.

ALPHA =18•4 DEG•
RN = 0•222E 07
MACH NO• 0•130

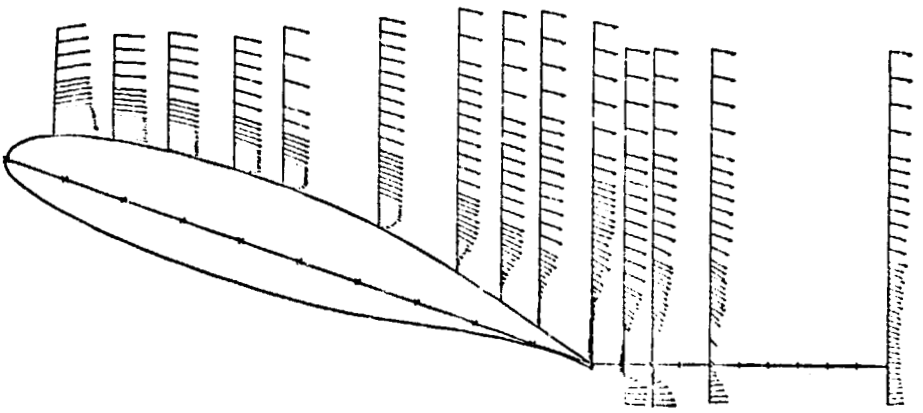

Figure 2.- Experimental velocity plot. GA(W)-1 airfoil.

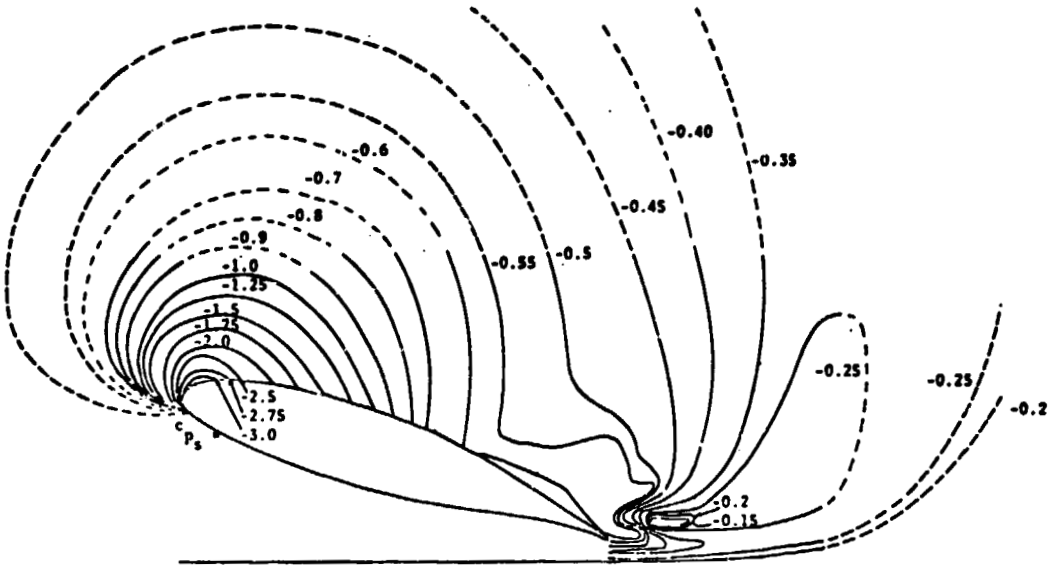

Figure 3.- Static-pressure field contours. GA(W)-1 airfoil. $\alpha = 18.4°$; R.N. = 2.2×10^6 (from ref. 2).

Figure 4.- Oil-streak flow visualization. $\alpha = 16°$; R.N. = 0.3×10^6.

Figure 5.- Oil-streak flow visualization.
$\alpha = 16°$; R.N. $= 0.3 \times 10^6$.

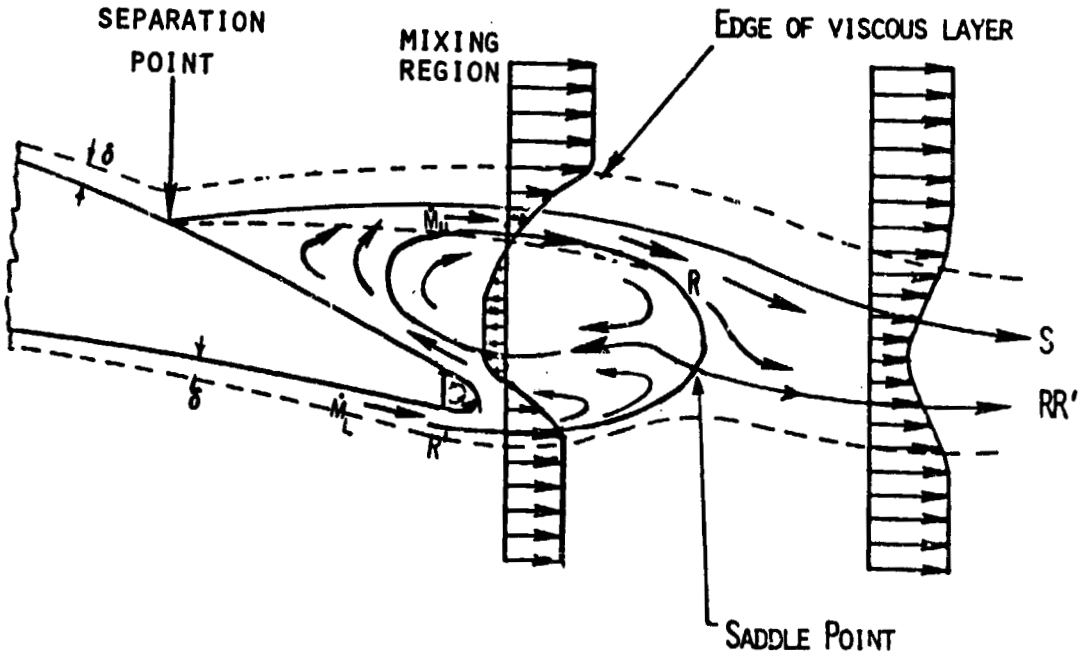

Figure 6.- Details of the separated region.

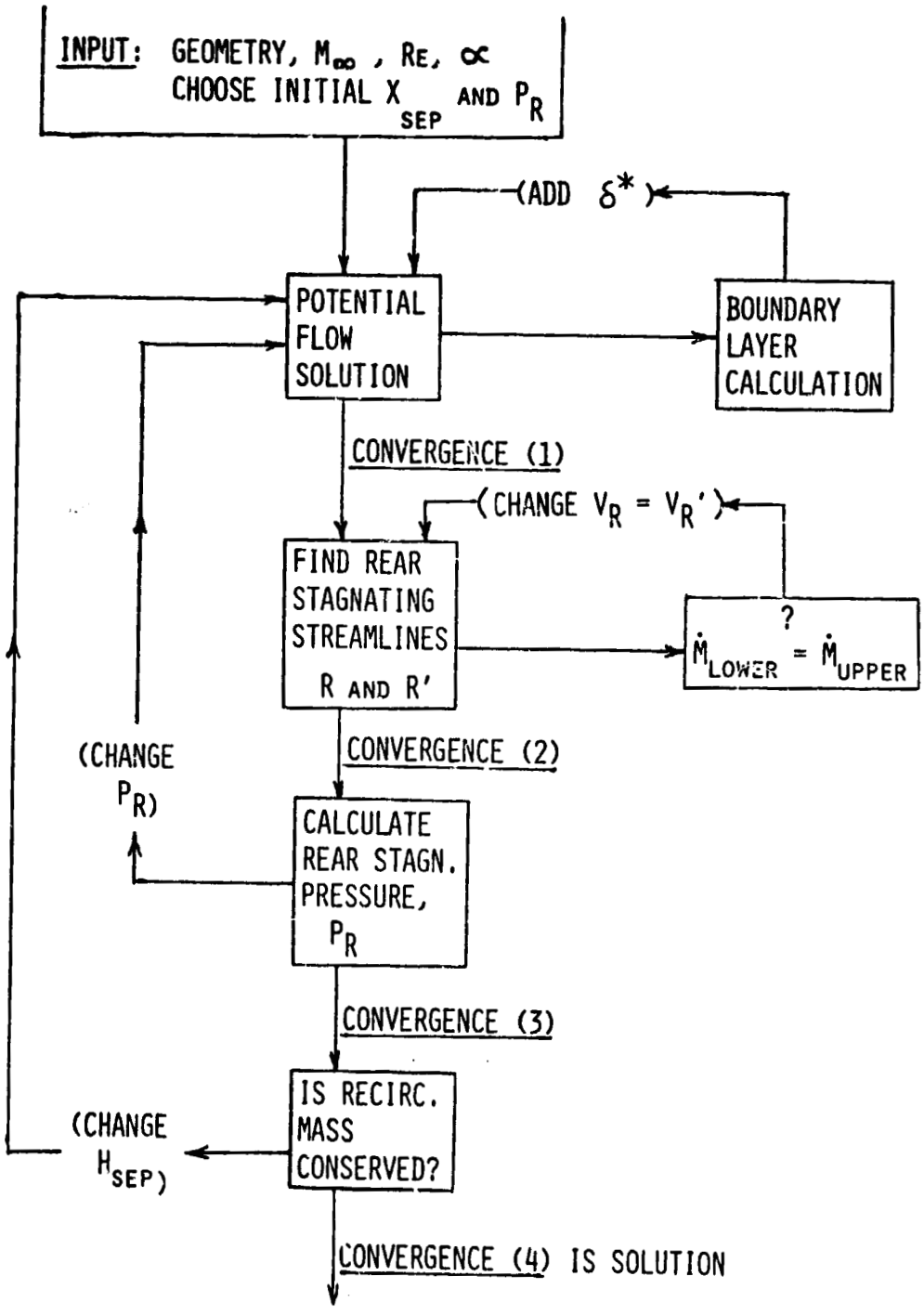

Figure 7.- Computer program logic.

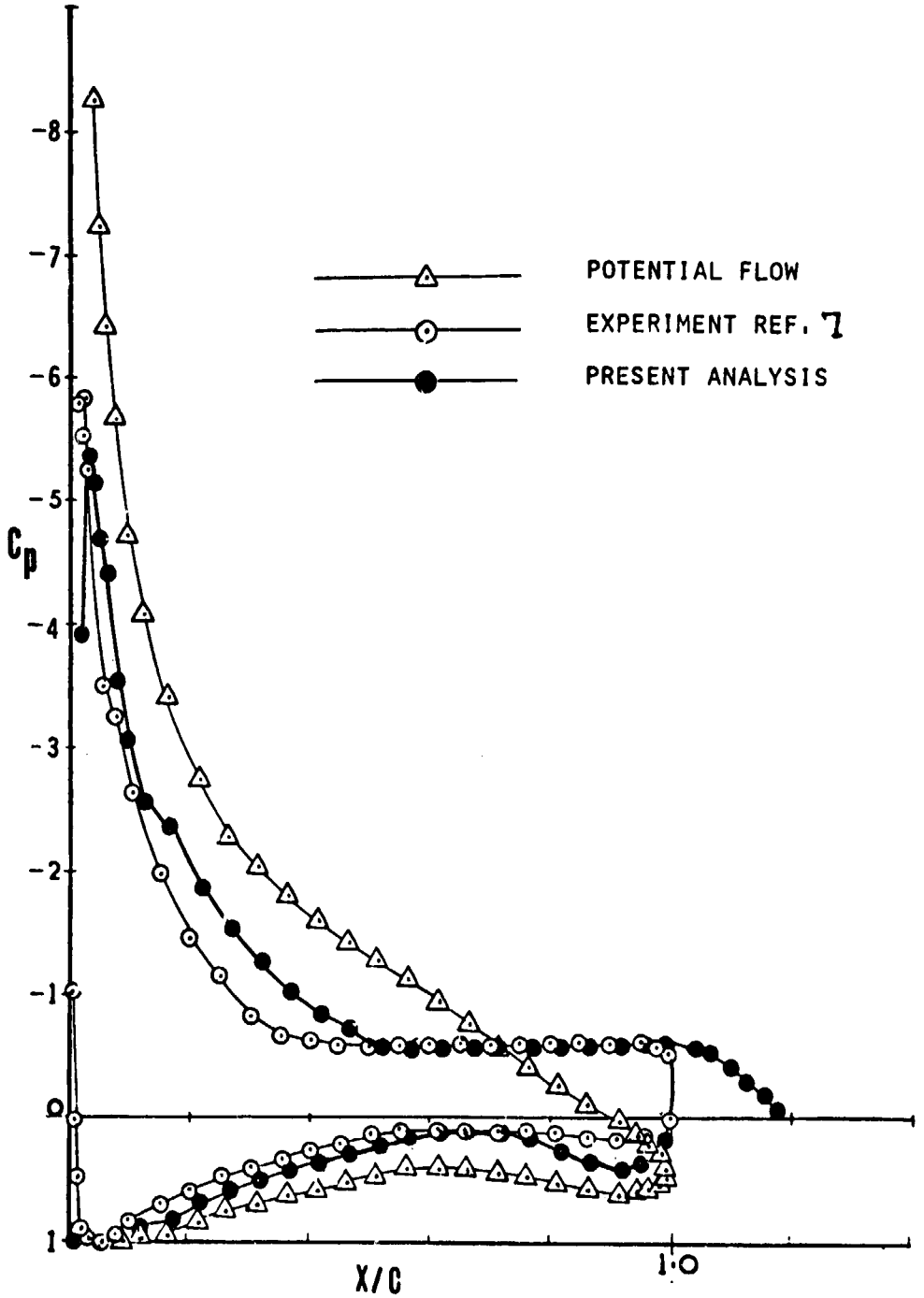

Figure 8.- Pressure distributions. GA(W)-1 airfoil. $\alpha = 18.4°$; R.N. = 2.5×10^6.

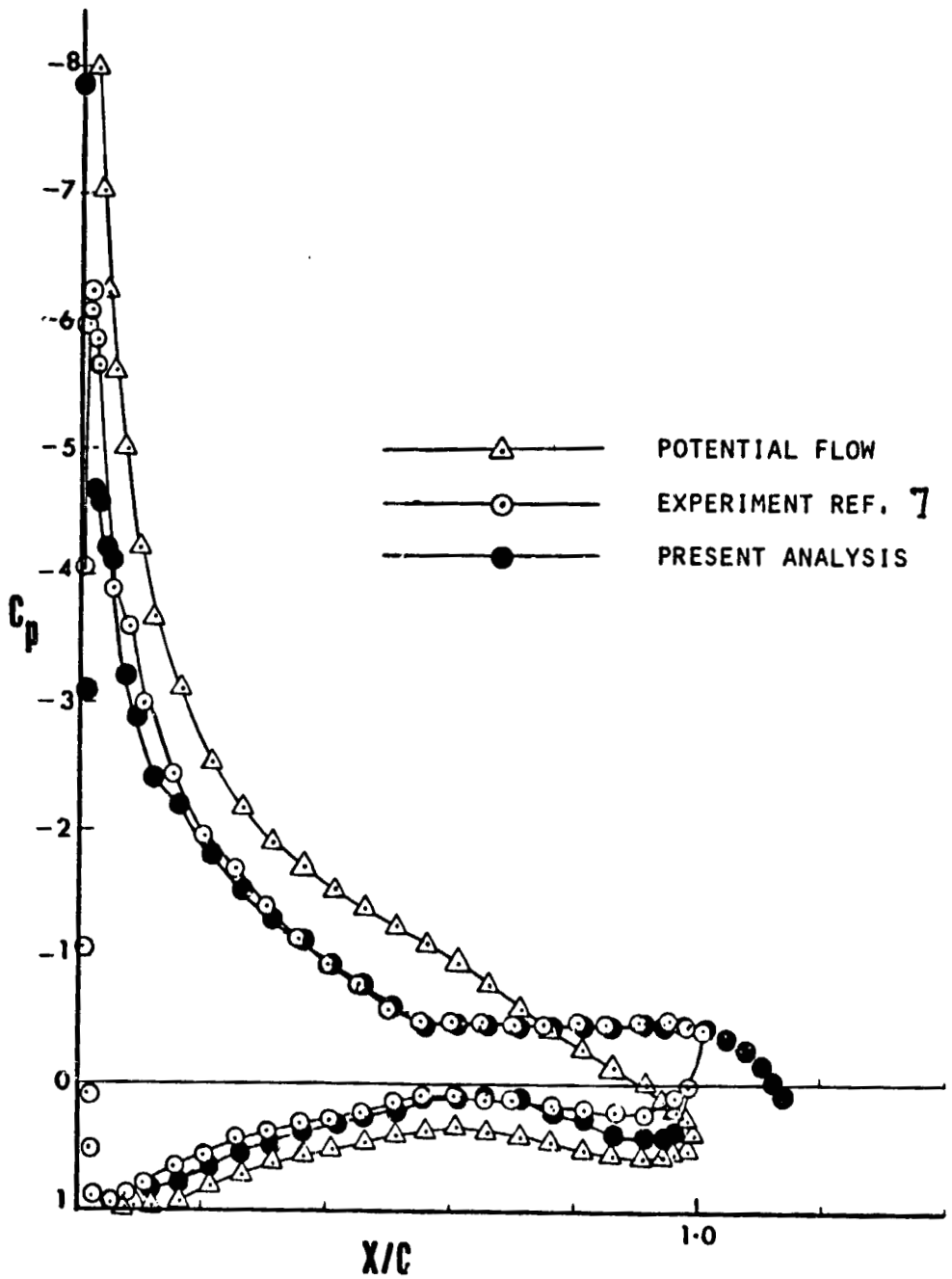

Figure 9.- Pressure distributions. GA(W)-1 airfoil.
$\alpha = 16.4°$; R.N. $= 2.9 \times 10^6$.

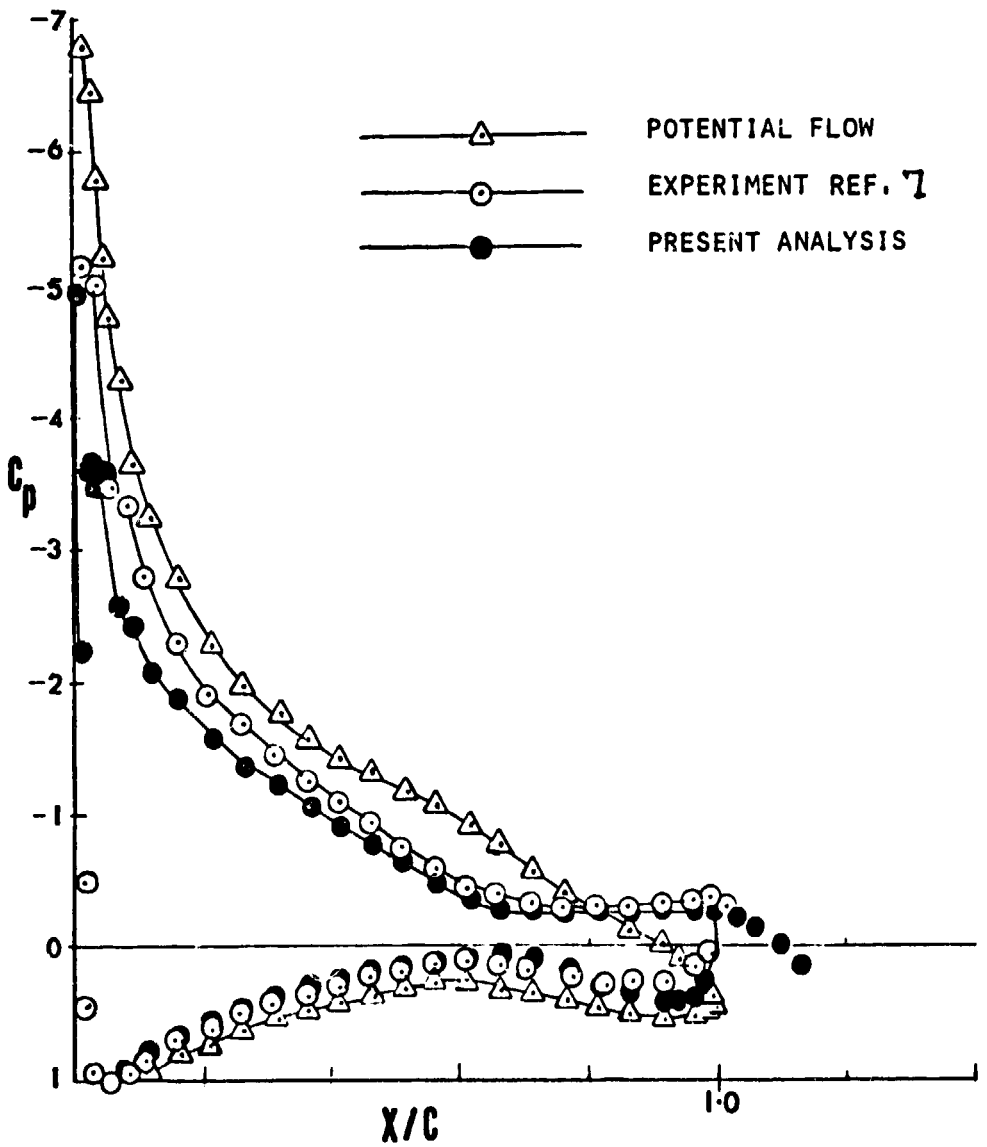

Figure 10.- Pressure distributions. GA(W)-1 airfoil. $\alpha = 14.4°$; R.N. = 2.9×10^6.

INVERSE BOUNDARY-LAYER TECHNIQUE FOR AIRFOIL DESIGN

M. L. Henderson
Boeing Commercial Airplane Company

SUMMARY

Presented is a description of a technique for the optimization of airfoil pressure distributions using an interactive inverse boundary-layer program. This program allows the user to determine quickly a near-optimum subsonic pressure distribution which meets his requirements for lift, drag, and pitching moment at the desired flow conditions. The method employs an inverse turbulent boundary-layer scheme for definition of the turbulent recovery portion of the pressure distribution. Two levels of pressure-distribution architecture are used - a simple roof top for preliminary studies and a more complex four-region architecture for a more refined design. A technique is employed to avoid the specification of pressure distributions which result in unrealistic airfoils, that is, those with negative thickness. The program allows rapid evaluation of a designed pressure distribution off-design in Reynolds number, transition location, and angle of attack, and will compute an airfoil contour for the designed pressure distribution using linear theory.

Comparison of pressure distributions and corresponding airfoil geometries resulting from different specifications of recovery-region boundary-layer form parameter will be presented.

INTRODUCTION

Airfoil design has traditionally been a trial-and-error process. Before large computers were available the airfoil designer had little option other than to make small changes to existing sections, guided by linear theory, in the hope that he would improve the section's performance in the area he wanted. Or, if he could afford the time and expense, the designer could undertake the testing of a large number of sections to try to find a good one for his application. Understandably, airfoil progress was a rather hit-or-miss proposition. Certainly, airfoil designers were guided by the physics of the flow around their sections but the mathematics required to describe the flow field adequately was too complex to solve in closed form and without computers, and it was too time consuming to solve numerically.

When relatively cheap computing equipment became available, methods for solving the inviscid flow field about an arbitrary airfoil evolved, and, soon after, methods for computing boundary-layer characteristics were developed and

are still evolving. These were powerful tools for the airfoil designer. He could now look at many more variations in his design variables and could be bolder in his departure from what had been previously tested. However, as good as these tools were, he was still using the cut-and-try method to design an airfoil to new requirements. Because of the highly nonlinear way the different variables in the airfoil-design problem interact there is no guarantee that cut-and-try will produce an overall improvement in performance; it is all too easy to design a section which is superior in one aspect of performance only to find it is totally unacceptable in another.

To get around the inherent problems of cut and try, the inverse of the airfoil-analysis problem needed to be solved more rigorously. Instead of computing the performance characteristics of a given section, one needed to specify the performance and compute the section. At present, this inverse airfoil problem is being attacked in two parts, as was airfoil analysis, that is, the inverse inviscid and the inverse boundary-layer problems.

The inverse inviscid problem, that is, specifying a pressure distribution and computing an airfoil contour, has been well developed recently as evidenced by several excellent papers on the subject given in this volume. However, while the techniques for performing the inverse inviscid computations are seemingly well in hand, the use of these techniques for airfoil design is not so well off. The reason is that although there is a real, unique inviscid pressure distribution for every airfoil at every angle of attack, the reverse is not true in a practical sense. One can easily specify a pressure distribution which results in an airfoil with negative thickness. Although such an airfoil is a perfectly valid solution to the inverse inviscid problem in a mathematical sense, one might have a little trouble building one. The fact is that most arbitrarily defined pressure distributions result in unrealistic airfoil contours if present inverse inviscid techniques are applied blindly. Future programs which allow specification of both pressure distribution and thickness by using weighting and advanced solution techniques (such as least-squares or Newton's method) to resolve the over-specified nature of the problem may aid the design. However, these programs have yet to appear in general use. So, one must be very careful in the choice of pressure distribution if the existing inverse invsicid programs are to be used to advantage.

How should the pressure distribution be defined? With a little thought one can see that at low Mach numbers the performance of an airfoil is either defined by or limited by the boundary layer and the requirement of a reasonable (or buildable) thickness form. In order to proceed with a rational design process one must have a boundary-layer technique that, given boundary-layer parameters, will compute a pressure distribution and, hopefully, is constrained to produce only pressure distributions that are realistic.

With such a computational tool in hand the designer might take advantage of the airfoil design process shown in figure 1. The most notable aspect of this process is that it proceeds from performance requirements to initial contour entirely in the inverse mode - first to compute a desirable pressure distribution and then to compute an initial airfoil contour. The last block, the detailed analysis and refinement stage, is the last remnant of trial and

error; and for the small changes involved in refinement this is probably desirable (or at least inevitable).

Assuming one has the capability for computing an airfoil from a pressure distribution (which is, after all, primarily a problem in mathematics, not aerodynamics) the primary task of the aerodynamicist is to define a desirable pressure distribution, hopefully the best pressure distribution, for the job at hand. In the remainder of this paper I will discuss a computer technique which I believe will greatly aid the designer in this task.

The symbols used herein are defined in an appendix.

TECHNIQUE

The Inverse Boundary-Layer Equations

An inverse boundary-layer technique is a solution to the boundary-layer equations where boundary-layer parameters are specified and a pressure distribution is computed. For the program I will discuss in this paper, I have used the boundary-layer momentum equation, Garner's equation for form parameter variation, and the Ludwig-Tillman equation for the wall shear stress (ref. 1). These equations have been arranged to solve for a velocity distribution given a variation in the form parameter $H = \delta^*/\theta$. The solution technique is shown as follows:

Solving Garner's equation for the velocity derivative gives

$$\frac{d(u/u_\infty)}{d(s/c)} = -\frac{dH/d(x/c)}{(u/u_\infty)e^{4(H-1.4)}} - \frac{0.0135(H-1.4)(u/u_\infty)}{(R_\theta)^{1/6}\,(\theta/c)} \qquad (1)$$

From the momentum equation solve for

$$\frac{d(\theta/c)}{d(s/c)} = \frac{\tau_o}{\rho u^2} - \frac{(H+2)(\theta/c)\;d(u/u_\infty)/d(s/c)}{u/u_\infty} \qquad (2)$$

The wall shear stress coefficient $\tau_o/\rho u^2$ is given by Ludwig-Tillman:

$$\frac{\tau_o}{\rho u^2} = 0.123(R_\theta)^{-0.268} \times 10^{-0.678H} \tag{3}$$

The momentum thickness ratio θ/c and velocity ratio are given by integrating equations (1) and (2) numerically with a known $H(x/c)$ (and thus a known $dH/d(x/c)$):

$$\theta/c = \frac{d(\theta/c)}{d(s/c)} \Delta s/c \tag{4}$$

$$u/u_\infty = \frac{d(u/u_\infty)}{d(s/c)} \Delta s/c \tag{5}$$

where $\Delta s/c$ is the integration step in arc length. Equations (1) to (5) should be relaxed at each step for average values of u/u_∞ and θ/c.

Pressure-Distribution Synthesis

With this inverse turbulent boundary-layer technique and an appropriate pressure-distribution architecture one may quickly design a pressure distribution on one surface of an airfoil. To explain the way the pressure distribution is synthesized consider the simpler of the two architectures available - the roof top (fig. 2). This architecture is characterized by an acceleration region starting at the leading edge and terminating at an input fair point. Constant pressure is assumed from the fair point to the input beginning of curbulent recovery (recovery point). The turbulent recovery spans the remainder of the foil and facilitates pressure recovery from the roof-top pressure to the desired trailing-edge pressure. The roof-top pressure is not input and is found by the inverse boundary-layer equations by employing an iterative procedure explained subsequently.

Iterative Procedure for Determining Minimum Cp

Given a fair point, a recovery point, a trailing-edge pressure, and a guess at roof-top pressure $C_{p_{min}}$, the pressure distribution is assembled up to the recovery point. This pressure distribution is then analyzed to provide the starting values of H and θ/c for the inverse turbulent boundary-layer module. Having these values, the recovery pressure distribution is computed from $C_{p_{min}}$ at the recovery point to the trailing edge by using the desired variation of form parameter in the recovery region. If the computed trailing-edge pressure is not that desired, $C_{p_{min}}$ is incremented, the pressure distribution up to the recovery point is reassembled, and the process is repeated to convergence.

The Lower Surface Pressure Distribution

Since the total pressure distribution must represent a realistic airfoil and the upper surface pressure distribution is defined by boundary-layer considerations alone, the lower surface pressure distribution must be defined by the thickness requirements specified by the designer. In the present program, a standard thickness form is used, the NACA OOXX, which is scaled to the designer's desired maximum thickness. So with a single input t/c_{max}, the designer gets a lower surface pressure distribution which will result in an airfoil which has the upper surface shape required to give him his designed upper surface pressure distribution and a lower surface contour which results from an NACA OOXX thickness form of the desired maximum t/c. Linear airfoil theory is used to accomplish this and I will not discuss it further in this paper.

The Four-Region Architecture

Although the roof-top architecture is effective and simple to use for the preliminary stages of pressure-distribution optimization, it allows very little flexibility for controlling the laminar and transitional portion of the boundary layer. As will be shown later, the transition-point position is often of first-order importance to the airfoil-design problem. To allow for more precise control of the laminar boundary layer, the four-region pressure distribution was devised.

This architecture is shown in figure 3 and is characterized by an acceleration region (1), a region of constant pressure gradient (II), a laminar stressing region (III), and finally the turbulent recovery region (IV). The fair point is input as before; and, in addition, the desired value of pressure gradient is given for region II, and a desired point of initiation of laminar stressing and a desired value of laminar form parameter are given for region III. A simple, inverse, laminar boundary routine is used to produce the pressure distribution required to produce the desired laminar form parameter. Region III may be used for either stressing the laminar boundary layer to achieve rapid transition without separation or may be used to avoid transition - depending, of course, on the value of H specified. The equations used in this region are

$$u/u_\infty = C(s/c)^{\left(\frac{1 - H/2.55}{0.94}\right)}$$

$$C = (u/u_\infty)_o \; / \; (s/c)_o^{\left(\frac{1 - H/2.55}{0.94}\right)}$$

where $(\;)_o$ refers to the values at the beginning of region III.

In the derivation of these equations some liberty was taken in dropping terms for simplicity; however, practice has shown this relationship is remarkably accurate. The symbol $C_{p_{min}}$ is defined as the pressure at the beginning of region III. Region IV, the turbulent recovery, is defined by the inverse turbulent boundary-layer technique as described earlier.

Optimization Using an Interactive Program

The pressure-distribution design technique I have described has been implemented in an interactive optimization program. That is, the program user is operating the computer program in a conversational mode where input is requested by typed messages and given to the program, real time, by responding with typed input at a terminal. Output is printed or plotted immediately at the terminal at the request of the user.

Why an interactive program? Pressure-distribution design is a highly overdefined optimization problem. Constraints and secondary requirements are tough to quantify and the weight given them often reflects the judgement of the designer alone. In deciding how to implement this technique I adopted the philosophy that it is desirable to leave the judgement in the hands of the user and that a computerized pressure-distribution design tool should eliminate the computation in the design process and amplify the user's judgement by quickly and clearly illuminating the important relationships between the variables and constraints of the design problem at hand.

An interactive program is a natural outcome of this philosophy as it allows an adaptive flexibility in the optimization process impossible using batch-type computing. Furthermore, and not a bit less important, we have found that being a part of the optimization process is very educational for the user, especially when he is designing in a flow regime where he has little experimental experience. Lastly, it is one heck of a lot more fun to compute this way - as anyone who has tried it will agree. While this may seem a trivial concern - the fact that the computation is now pleasant, rather than a chore, often means one will tend to stick out a really tough problem longer.

The options available in this optimization program are illustrated in figure 4. I will just summarize them here.

The design is initiated by giving the program the flow conditions and details of the architecture chosen. The type of form-parameter variation is then chosen - this program allows a constant form parameter or linear, quadratic, or exponential variation to be specified with very little input. An arbitrary H variation may be used if a file of the desired values of H vs. x/c has been previously generated. This complete, the program enters the design module and displays C_ℓ, C_d, C_m, and a plot of the designed pressure distribution. This whole process takes about 30 seconds. At this point the user may redefine the H variation, or any other of the design parameters, or if he is satisfied with the design-point pressure distribution he may analyse the pressure distribution at an off-design Reynolds number or trip location or he may analyse the pressure distribution off-design in lift (accomplished by adding an angle-of-attack velocity distribution to the design distribution using linear theory). The results of any of these off-design analyses are printed and plotted immediately at the terminal. In the event that a desirable pressure distribution is generated, a preliminary airfoil contour may be obtained simply by request. This is accomplished by a simple linear inverse program due to Trukenbrodt (ref. 2), and the airfoils produced should be considered as starting points for more accurate design methods. They are, however, excellent bench marks to check the resulting airfoil's fidelity to structural restraints (such as a restraint on maximum camber or compound surfaces).

To indicate the power of this approach, consider that to define a pressure distribution, it should be checked at several Reynolds numbers and off-design angles of attack, and to produce a preliminary airfoil takes about 7 minutes on a PDP 11-70 or about 8 minutes on a CDC Cyber 175. The reason the more powerful machine takes longer is that the data-transmission rate to our terminal is 300 band on the 175 and 9600 band on the 11-70. Most of the time is used during transmission and user head scratching in deciding what to do next.

Some Illustrative Results

Figure 5 displays a comparison of pressure distributions and their corresponding airfoil geometries resulting from different specifications of recovery-region boundary-layer form parameter (H). The 'C', 'L', and 'E' denote constant H, linearly varying and exponentially varying H, respectively. Each pressure distribution was designed to a lift coefficient of approximately 1.6. The impact of the variation of the form parameter on both airfoil performance and shape is striking. The L/D (ε^*) ranges from 172 for constant H (2.06) to 225 for the exponentially varying H (1.45 at x/c = 0.3 to 2.0 at x/c = 1.0). Pitching moment varies from 0.057 to -0.186 for the same two examples. The airfoil contours, I think, speak for themselves. Again, the values of H for each type of variation were picked so that the pressure distributions all produced a design-point lift coefficient of about 1.6.

In the designs of figure 5, natural transition occurred near the fair point (x/c = 0.1) due to very high design-point Reynolds number ($Rn = 30 \times 10^6$). In figures 6 and 7 I have tried to illustrate the powerful effect that transition has on the design of a pressure distribution. In figure 6 a design was again undertaken at a Reynolds number of 30×10^6 with a roof-top architecture and

natural transition. The result was a pressure distribution of modest performance with transition occurring very near the fair point.

Using the four-region architecture, an attempt was made to maintain laminar flow as far aft on both surfaces as possible. The result was a pressure distribution that produces significantly better performance. The L/D at the design point went from 215 for the roof top to 317 for the four-region pressure distribution. Design C_ℓ was increased from 1.42 to 1.68 for the same specification in form parameter, whereas the pitching-moment coefficient remained relatively unchanged. Although the final pressure distribution in this figure shows remarkable improvement and impressive performance, work still needs to be done to achieve acceptable off-design performance as one might expect considering the section's rather sharp leading edge.

Figure 7 displays the effect of tripping the laminar boundary layer on design lift and L/D at a Reynolds number of 4×10^6 for several recovery locations. Laminar flow is extensive when no trip is specified due to the lower Reynolds number, even though the roof-top architecture is used throughout, so one would expect tripping to have a significant impact. The curves show it does. The peak design C_ℓ is reduced from 2.25 to 1.3 by tripping and the L/D is reduced from 177 to 77. The explanation for this sharp reduction in performance is that early transition produces a much thicker boundary layer at the recovery point due to the more rapid growth of a turbulent boundary-layer relative to the laminar layer. This thicker boundary layer is able to withstand less adverse pressure gradient and so must recover from a lower velocity. Thus, there is a loss in lift and L/D.

Figure 8[1] summarizes the performance of some of the pressure distributions we have designed to date. With the exception of points 3 and 4 all were low C_ℓ designs with heavy restrictions placed on the maximum camber and all used the simple roof-top type architecture with tripping to produce a turbulent boundary layer at the recovery point where necessary. Because of this, one should not interpret the results as an attempt to plumb the limits of L/D at each Reynolds number but rather consider these results only as an example of the type of information obtainable from this program with a relatively modest amount of time and expense. Points 3 and 4 were attempts at optimizing L/D at their design Reynolds numbers, and although they do perform credibly, more effort is required to refine the designs and guarantee good off-design performance.

CONCLUSIONS

We need more experience with this program to say with any certainty whether it can be used to determine an optimum pressure distribution for the flow conditions where the theories are valid. However, the following aspects of this technique are already apparent:

---

[1]Dr. John McMasters assisted in preparing this paper and allowed me to use the data in figures 5 and 8 which he generated for a Boeing internal study of the L/D potential of moderately cambered airfoils.

1. The inverse boundary-layer technique is a powerful and efficient device for defining a pressure distribution.

2. The pressure-distribution architecture need not be excessively complex to control the laminar and transitional regions of the pressure distribution.

3. The simple inverse laminar equation is an effective tool for stressing the laminar boundary to transition without causing separation.

4. Allowing a scaled thickness form to define the lower surface pressure distribution does constrain the program to produce pressure distributions which result in realistic sections. However, more flexibility is needed in this area so that aerodynamic considerations may also play a part in definition of the lower surface distribution. This may take form as optional thickness forms or arbitrary thickness forms constrained only in maximum thickness and to positive thickness everywhere.

5. The interactive type of execution seems to have value beyond the obvious advantages of speed and immediate response in the display of intermediate results, that is, it is very educational and pleasant to use.

APPENDIX

SYMBOLS

H	boundary-layer form parameter, δ^*/θ
U	velocity at outer edge of boundary layer
U_∞	free-stream velocity
s/c	airfoil-surface arc length normalized with chord
x/c	distance along airfoil chord, normalized with chord
Rn	Reynolds number based on airfoil chord
R_θ	Reynolds number based on local value of momentum thickness θ and velocity U
θ/c	boundary-layer momentum thickness (normalized), $\frac{\theta}{c} = \int_0^\infty \frac{u}{u_\infty}\left(1 - \frac{u}{u_\infty}\right) dy/c$
δ^*/c	boundary-layer displacement thickness, $\frac{\delta^*}{c} = \int_0^\infty \left(1 - \frac{u}{u_\infty}\right) dy/c$
ρ	density
C_ℓ	section lift coefficient
C_d	section drag coefficient
C_m	section pitching-moment coefficient
C_p	pressure coefficient, $C_p = 1 - \left(\frac{u}{u_\infty}\right)^2$
t/c	airfoil thickness (normalized)
ε^*	design-point section L/D
ε	maximum section L/D

REFERENCES

1. Schlichting, H.: Boundary Layer Theory. McGraw-Hill Book Co. Inc. pp. 238-251, 391-406, 566-579.

2. Riegals, F. W.: Airfoil Sections. Butterworth and Co., Publishers Ltd., 1961, pp. 80-83.

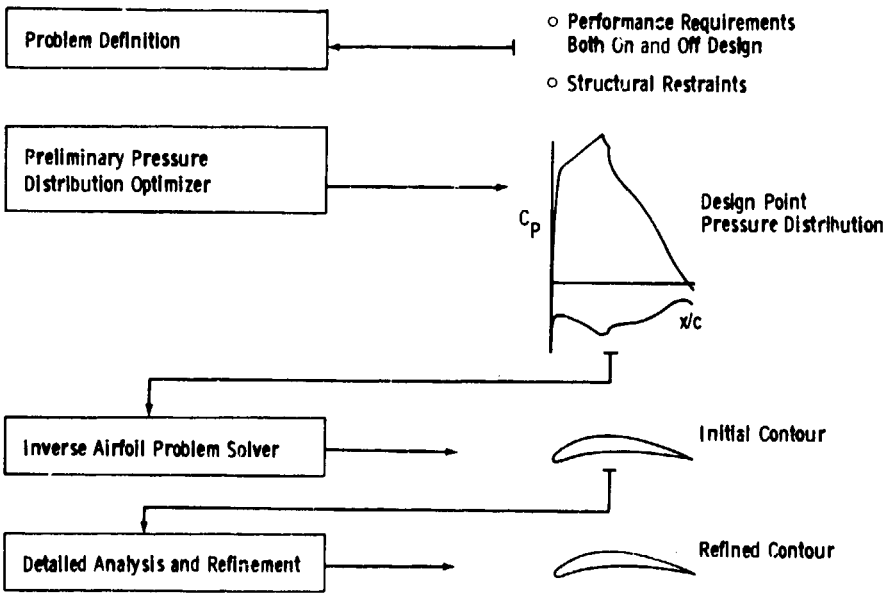

Figure 1.- Airfoil design process.

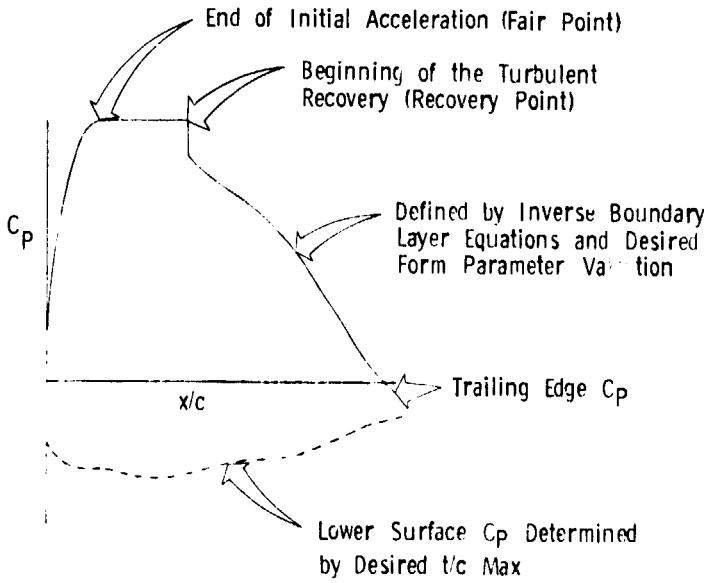

Figure 2.- The roof-top architecture.

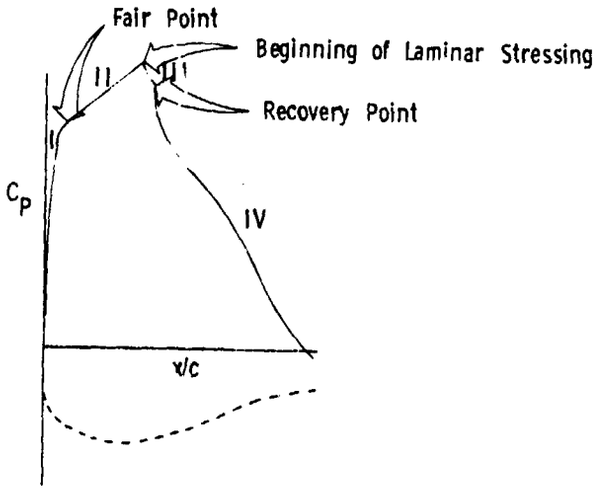

Figure 3.- Four-region architecture.

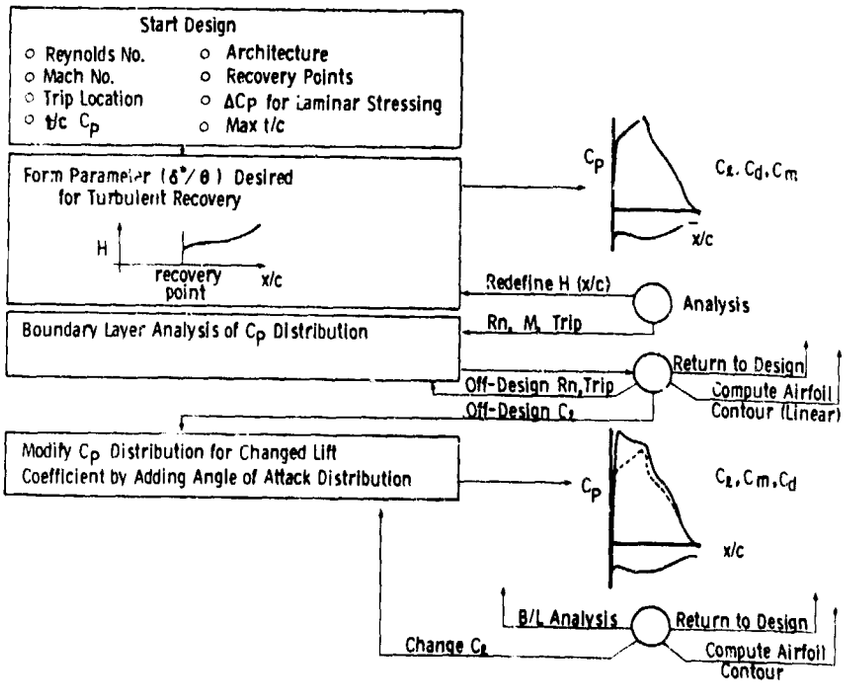

Figure 4.- Block diagram of interactive pressure-distribution optimizer.

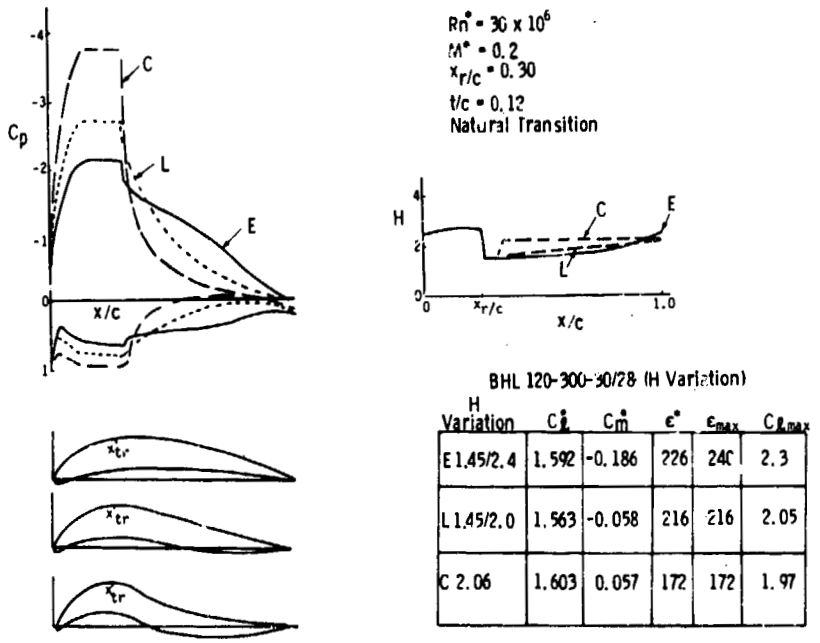

H Variation	C_{ℓ}^*	C_m^*	ϵ^*	ϵ_{max}	$C_{\ell_{max}}$
E 1.45/2.4	1.592	-0.186	226	240	2.3
L 1.45/2.0	1.563	-0.058	216	216	2.05
C 2.06	1.603	0.057	172	172	1.97

Figure 5.- Comparison of pressure distributions and corresponding airfoil geometries resulting from different specifications of recovery-region boundary-layer form parameter H.

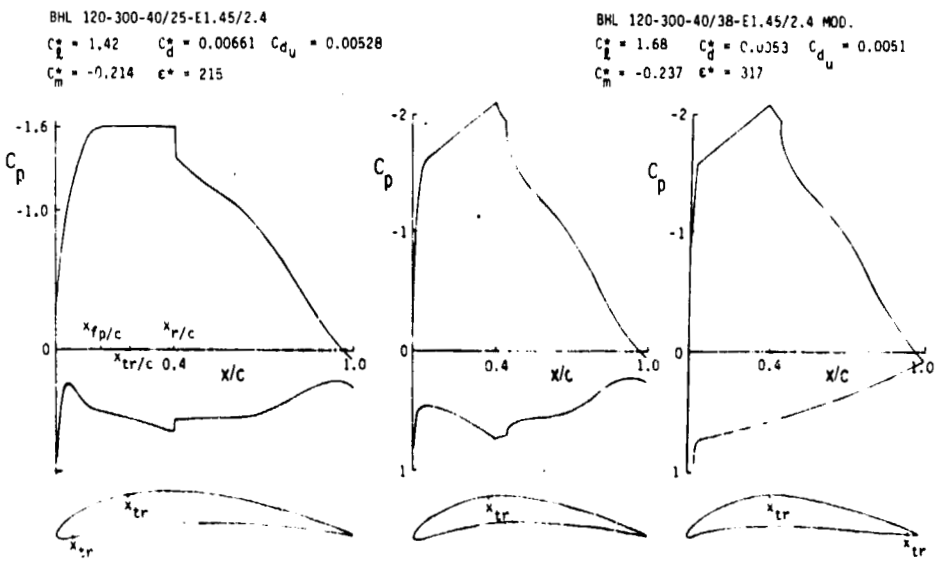

Figure 6.- Examples of basic pressure-distribution architecture.

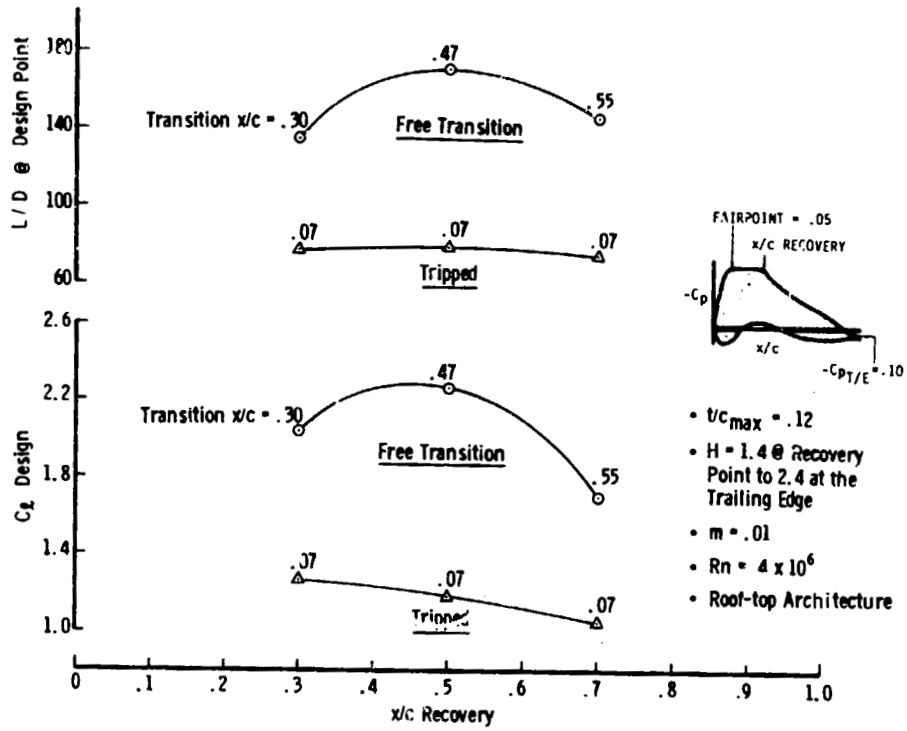

Figure 7.- Effect of transition location on design C_ℓ and L/D.

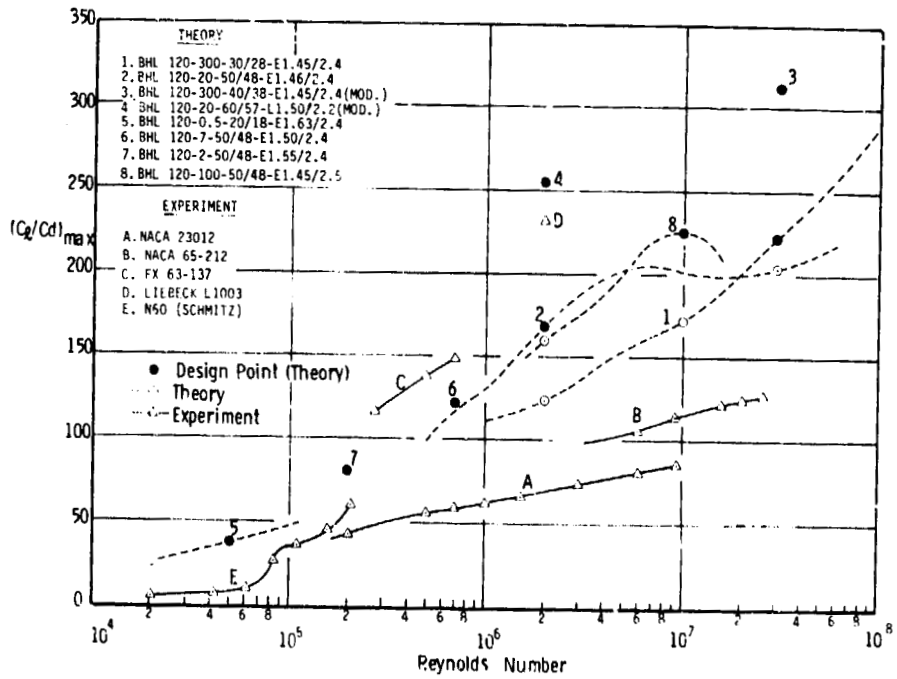

Figure 8.- Maximum L/D plotted against Reynolds number.

D25

25

LANGLEY'S TWO-DIMENSIONAL RESEARCH FACILITIES — CAPABILITIES AND PLANS

Edward J. Ray
NASA Langley Research Center

SUMMARY

In recent years there has been a renewed interest in the development of a wide variety of advanced airfoils and a systematic documentation of airfoil characteristics in the subsonic-transonic flight regime. In 1973, the National Aeronautics and Space Administration (NASA) responded to the resurgence of interest in systematic airfoil research by establishing a comprehensive airfoil program. This program included provisions for the rehabilitation of existing facilities, the exploration of new test techniques, and the development of new test facilities.

This paper describes the current capabilities and the forthcoming plans for Langley's two-dimensional research facilities. The characteristics of the Langley facilities are discussed in terms of Reynolds number, Mach number, and angle-of-attack capabilities. Comments are made with regard to the approaches which have been investigated to alleviate typical problem areas such as wall boundary effects. Because of the need for increased Reynolds number capability at high subsonic speeds, a considerable portion of the paper deals with a description of the 20- by 60-cm two-dimensional test section of the Langley 0.3-meter transonic cryogenic tunnel which is currently in the calibration and shakedown phase.

INTRODUCTION

As pointed out in reference 1, for many years Langley Research Center placed a strong emphasis on the combined application of aerodynamic theory and two-dimensional experimental facilities in the development of advanced airfoils. In the 1950's and 1960's, however, with the extensive emphasis on the three-dimensional aspects of swept wings, supersonic flight, and the minimization of component interference, airfoil research was virtually nonexistent.

Interest in airfoil research was rekindled when the development of supercritical and other advanced airfoils demonstrated that additional performance gains could be realized by the application of new airfoil design concepts. In response to this renewed interest, Langley began, in about 1968, to upgrade its airfoil test capability. The purpose of this paper is to present an overview of Langley's current two-dimensional test capability and to indicate the additional capabilities planned for the near future.

398

SYMBOLS

c	model chord
M	Mach number
P_t	stagnation pressure
q	dynamic pressure
R_c	Reynolds number based on model chord
T_t	stagnation temperature
t/c	thickness-to-chord ratio
α	angle of attack

DISCUSSION

Several facilities will be discussed in this paper. In the area of low-speed research, the continuous-flow Langley low-turbulence pressure tunnel provides essentially the same outstanding high Reynolds number capability that it provided during the 1940's. In the area of high-speed research, three facilities are described. The Langley 6- by 19-inch transonic tunnel was developed as a pilot airfoil facility and is currently dedicated to the study of wall effects and the development of test techniques. The Langley 6- by 28-inch tunnel provides a high-speed, moderate Reynolds number capability. The Langley 0.3-meter transonic cryogenic tunnel, Langley's newest two-dimensional facility, is currently under development and will provide a high Reynolds number capability with unique operating envelopes.

A detailed description of the characteristics of these facilities and an indication of Langley's current and projected two-dimensional programs follow.

Langley Low-Turbulence Pressure Tunnel

The Langley low-turbulence pressure tunnel (LTPT) is described in references 2 and 3, and the Reynolds number envelope is shown in figure 1. (The Reynolds number for this and all subsequent figures is based on a typical model chord for the particular facility.) A sketch of the LTPT is presented in figure 2. Even though the LTPT was constructed over 30 years ago, it still fulfills a very important requirement in that it adequately covers both the regions of interest for general aviation aircraft and the high-lift landing and take-off conditions for a wide variety of aircraft. With its 10-atm capability it provides a Reynolds number of about 30×10^6 at a Mach number of about 0.25. Another desirable characteristic of the LTPT is that its

large test section (0.08 by 0.19 m (3 by 7.5 ft)) provides a large model chord capability. The photograph shown in figure 3 illustrates the comparatively large two-dimensional test section with a 0.6-m (2-ft) chord model installed. There are obvious advantages of the large chord model when considering model accuracy and multielement airfoil testing. The LTPT is a continuous-flow facility that operates from very low velocities up to a Mach number of about 0.35 and is designed to provide the capability for exceptionally good flow quality.

The research programs conducted in the LTPT are varied. Under the current programs, there is a considerable amount of effort being placed on the development of new, general aviation airfoil concepts and the low-speed assessment of supercritical sections. The development of the general aviation airfoils is discussed in reference 4. Renewed attention is being placed on laminar flow research. A photograph of a passive laminar flow airfoil for the LTPT is shown in figure 4.

Insofar as projected program extensions, the LTPT with its large model chord and low-speed, high Reynolds number capability will continue to be Langley's prime facility for the development of high-lift, multielement systems. At present the improvements which are scheduled for this facility include the installation of a fast pressurization system and a computer-driven wake-survey apparatus. Modifications will be made to provide additional improvements to restore the flow to its original high quality and to provide stagnation temperature control.

In order to provide Langley with a valid and useful high-lift development capability, provisions are being made to incorporate a sidewall boundary-layer control system and a new high load balance system. The new boundary-layer control system will provide control by blowing through slots in the sidewalls. The data shown in figure 5 illustrate the typical effects of this type of sidewall control on the lift characteristics of a multielement airfoil. Section lift coefficients are plotted against angle of attack. The three different cases shown are the lift near the wall without blowing (lower curve), the lift at midspan without blowing (middle curve), and the lift at the midspan and near the wall with blowing (top curve). It is obvious from the two lower lift curves that, without blowing, the flow across the airfoil is not two dimensional. With blowing (top curve), the sidewall boundary layer is apparently energized, resulting in uniform flow across the airfoil.

An additional improvement scheduled for this facility is a suction system for application of active laminar-flow control to airfoils.

Langley 6- by 19-Inch Transonic Tunnel

The Langley 6- by 19-inch transonic tunnel (ref. 5) was placed in operation in 1970 and represented one of the first steps in reestablishing Langley's airfoil research facilities. Its Reynolds number envelope is shown in figure 6. The Langley 6- by 19-inch tunnel is a blowdown to atmosphere type with a Mach number range of 0.5 to 1.2. It is a low Reynolds number facility with no

independent control of Mach number and Reynolds number. The photograph shown in figure 7 presents exterior and interior views of the tunnel. The vertical test section as shown in the interior view lends itself to simple, inexpensive modifications. This facility is currently dedicated to the development of new two-dimensional testing methods and techniques. Two current programs of this type are the solid flexible wall studies and the parametric slotted wall interference studies. A sketch illustrating the parametric slotted wall study is shown in figure 8. Descriptions of the wall interference studies which have been conducted in this tunnel are presented in references 6 and 7. The Langley 6- by 19-inch tunnel will continue to be used for the development of refined transonic wall configurations.

Langley 6- by 28-Inch Transonic Tunnel

The Langley 6- by 28-inch transonic tunnel is described in reference 8. A plot of the Reynolds number - Mach number envelope is shown in figure 9, and a photograph of the tunnel is shown in figure 10. The tunnel, which is shown on the upper level in the photograph, was placed in operation in 1974. It is a blowdown type, operating over a Mach number range of 0.3 to 1.2 and a stagnation pressure range of 1.2 to 6 atm. The pressure capability provides a low to moderate Reynolds number capability with independent Mach number and Reynolds number control. The tunnel, with its transonic and 15 x 10^6 Reynolds number capability, is dedicated to a wide range of airfoil research. Current tunnel programs include the development of supercritical airfoils, supercritical propellers, and rotor aircraft airfoils. The rotorcraft airfoil studies are particularly extensive and figure 11 shows a photograph of some of the models which have already been tested. The rotorcraft program is discussed in more detail in reference 9.

Projected programs for the Langley 6- by 28-inch transonic tunnel include the development of high-speed general aviation airfoils and dynamic stall research. The facility will be updated in the near future with the addition of a sidewall boundary-layer suction system incorporated in the model turntables. The projected programs also include plans to provide an oscillating airfoil system. This system will enhance the dynamic stall research effort in addition to providing for oscillating airfoil studies.

Langley 0.3-meter Transonic Cryogenic Tunnel

Langley's newest two-dimensional research facility is the 20- by 60-cm test section of the Langley 0.3-meter transonic cryogenic tunnel (TCT). A more complete description of the basic 0.3-meter TCT is presented in reference 10. The Reynolds number - Mach number envelope for the two-dimensional test section is presented in figure 12, and a photograph of the facility in figure 13. As indicated on figure 13, the test section is located in the top leg and the flow is clockwise. The tunnel is a fan-driven, continuous-flow tunnel which utilizes the cryogenic pressure tunnel concept. The test medium is gaseous nitrogen which provides a temperature range varying from about 77 K (-320° F) to about 327 K (130° F). The photograph indicates

the nitrogen injection station and the exhaust stacks. The cryogenic temperature capability provides a multiple increase in Reynolds number of about six over that at ambient temperature. The reduced temperature capability, combined with the 5-atm capability, results in a very high Reynolds number at relatively low model loading. For example, to achieve this Reynolds number in a conventional pressure tunnel of the same size would require a stagnation pressure of about 30 atm. The operating envelope shown in figure 12 indicates that a Reynolds number of about 50×10^6 can be obtained at a Mach number of about 0.85. The tunnel with its unique pressure and temperature capability provides independent control and assessment of Mach number, Reynolds number, and aeroelastic effects: An example of this attractive capability is shown in figure 14. This figure represents a dynamic pressure - Reynolds number envelope for a 15-cm (6-in.) chord model at a Mach number of 0.80. The conditions which define the outer boundaries of this envelope are the horizontal pressure lines and the diagonal temperature cuts. Conventional pressure tunnels operate along the ambient temperature line, and increases in Reynolds number are accomplished by increasing the stagnation pressure. This obviously results in large increases in dynamic pressure q and model loading. The addition of the temperature parameter expands the envelope, and a large range of either pure Reynolds number studies (horizontal cuts) or pure aeroelastic studies (vertical cuts) can be accomplished with just one model. For example, at a stagnation pressure P_t of 5 atm, a pure Reynolds study could be made at Reynolds numbers from about 8 to 50×10^6. The ability to conduct pure aeroelastic studies or maintain a constant shape over a wide Reynolds number range may become extremely important in the assessment of airfoils having thin, highly cambered trailing edges. As shown in figure 15, the tunnel features removable model modules. In this photograph, the plenum lid and test-section ceiling have been removed and the module is in the raised position. The photograph in figure 16 is a top view looking down into the test section with the model module installed in the test position. This removable feature and the duplicate module assemblies will allow for the complete preparation of a model during the test of another model. The cryogenic tunnel incorporates computer-driven angle-of-attack and momentum-rake systems. The momentum rake (shown in the photograph in fig. 16) is programmed to traverse automatically through the wake, to determine the boundaries of the wake, and then to step through the wake at a prescribed rate and number of steps.

The Langley 0.3-meter transonic cryogenic tunnel is currently being utilized to extend cryogenic wind-tunnel technology and to develop a unique airfoil research capability. Studies are being conducted to develop cryogenic test techniques, define minimum operating temperatures, and support the development of the National Transonic Facility. Progress is being made toward the development of an airfoil research capability. Shakedown and calibrations are nearing completion, preliminary blockage tests have been conducted, and an NACA 0012 correlation model has been tested through the entire operating envelope. An assessment of the slotted walls and sidewall boundary-layer effects is in progress. In addition, work is being conducted to develop a preliminary sidewall boundary-layer control system.

Some of the plans which are projected for the new cryogenic facility are briefly described. The new classes of airfoils illustrated in figure 17, such

as the supercritical, peaky, and the new thick spanloader concepts will be assessed up to Reynolds numbers of 50 x 10^6. The unique test envelope will be used to evaluate highly cambered fighter airfoil concepts. Factors which affect Reynolds number sensitivity will be assessed and documented. The high Reynolds number experimental results will be used to evaluate and contribute to transonic viscous flow theories and to provide guidance in the utilization of conventional airfoil facilities. Plans are now being made to provide the tunnel with an advanced data-acquisition and tunnel-control system and a study is currently underway to update the current sidewall boundary-layer control system.

CONCLUDING REMARKS

It was mentioned previously that in order to provide an exact two-dimensional test capability, it was essential to control the unnatural tunnel-wall boundary effects and model-wall boundary-layer interactions as well as test at the correct Mach and Reynolds numbers. Throughout this paper it was indicated that the wall problems are being addressed in all of the Langley facilities. Progress is being made, but the alleviation of the various tunnel wall problems, particularly those at high Mach number and high lift coefficients, will require a considerable amount of research and tunnel refinements.

With regard to the Mach number and Reynolds number test capability, figure 18 summarizes Langley Research Center's current capabilities. This summary chart represents the flight Reynolds number design conditions for several classes of aircraft. In addition, it illustrates the test capabilities of the Langley facilities. The general aviation design envelope, shown in the low Mach number, low Reynolds number corner of the figure, has not changed drastically over the past several decades. The transport-cargo aircraft design trend, however, has changed dramatically, and the large transport-cargo types, such as the B-747 and C-5, tend to establish the upper requirement for two-dimensional design considerations. The attack helicopter design point represents a typical, higher Mach number design requirement. It will be noted from the figure that the Langley low-turbulence pressure tunnel still very adequately covers the general aviation requirements and that the Langley 6- by 28-inch tunnel fulfills the high Mach number helicopter requirement. The addition of the Langley 0.3-meter transonic cryogenic tunnel with its Reynolds number capability of 50 x 10^6 will eliminate the large gap which previously existed for the large transport-cargo class of aircraft. It is interesting to note that upper tunnel capabilities encompassed by the Langley low-turbulence pressure tunnel and Langley 0.3-meter transonic cryogenic tunnel envelopes are achieved in continuous-flow facilities. It can be seen from this figure that for Mach number and Reynolds number requirements, the Langley airfoil facilities provide the test capabilities required to adequately simulate the design flight condition for modern aircraft and rotorcraft.

REFERENCES

2. Von Doenhoff, Albert E.; and Abbott, Frank T., Jr.: The Langley Two-Dimensional Low-Turbulence Pressure Tunnel. NASA TN 1283, 1947.

3. Beasley, William D.; and McGhee, Robert J.: Experimental and Theoretical Low-Speed Aerodynamic Characteristics of The NACA 65_1-213, a = 0.50, Airfoil. NASA TM X-3160, 1975.

4. McGhee, Robert J.; Beasley, William D.; and Whitcomb, Richard T.: NASA Low- and Medium-Speed Airfoil Development. Advanced Technology Airfoil Research, Volume II, NASA CP-2046, 1979.

5. Ladson, Charles L.: Description and Calibration of the Langley 6- by 19-Inch Transonic Tunnel. NASA TN D-7182, 1973.

6. Everhart, Joel L.; and Barnwell, Richard W.: A Parametric Experimental Study of the Slotted-Wall Boundary Condition. Advanced Technology Airfoil Research, Volume I, NASA CP-2045, Pt. 2, 1979. (Paper 30 of this compilation.)

7. Newman, Perry A.; and Anderson, E. Clay: Analytical Design of a Contoured Wind-Tunnel Liner for Supercritical Testing. Advanced Technology Airfoil Research, Volume I, NASA CP-2045, Pt. 2, 1979. (Paper 33 of this compilation.)

8. Ladson, Charles L.: Description and Calibration of the Langley 6- by 28-Inch Transonic Tunnel. NASA TN D-8070, 1975.

9. Bingham, Gene J.; Noonan, Kevin W.; and Jones, Henry E.: Results of an Investigation of Several New Rotorcraft Airfoils as Related to Airfoil Requirements. Advanced Technology Airfoil Research, Volume II, NASA CP-2046, 1979.

10. Kilgore, Robert A.: Design Features and Operational Characteristics of the Langley 0.3-Meter Transonic Cryogenic Tunnel. NASA TN D-8304, 1976.

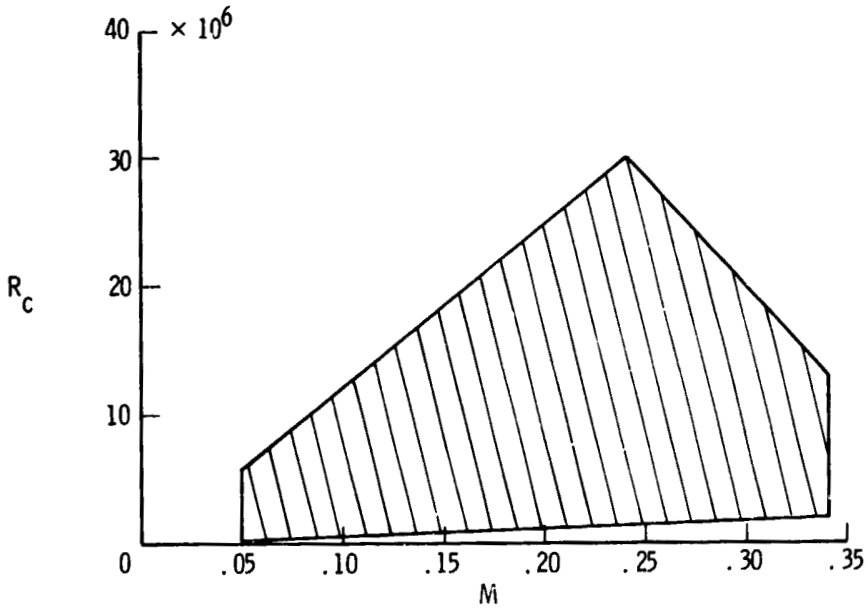

Figure 1.- Reynolds number envelope for Langley low-turbulence pressure tunnel.

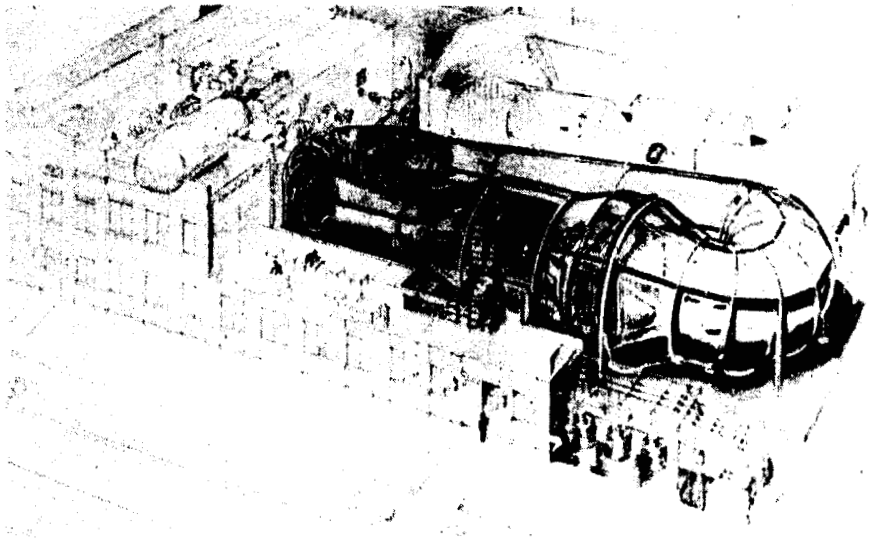

Figure 2.- Langley low-turbulence pressure tunnel.

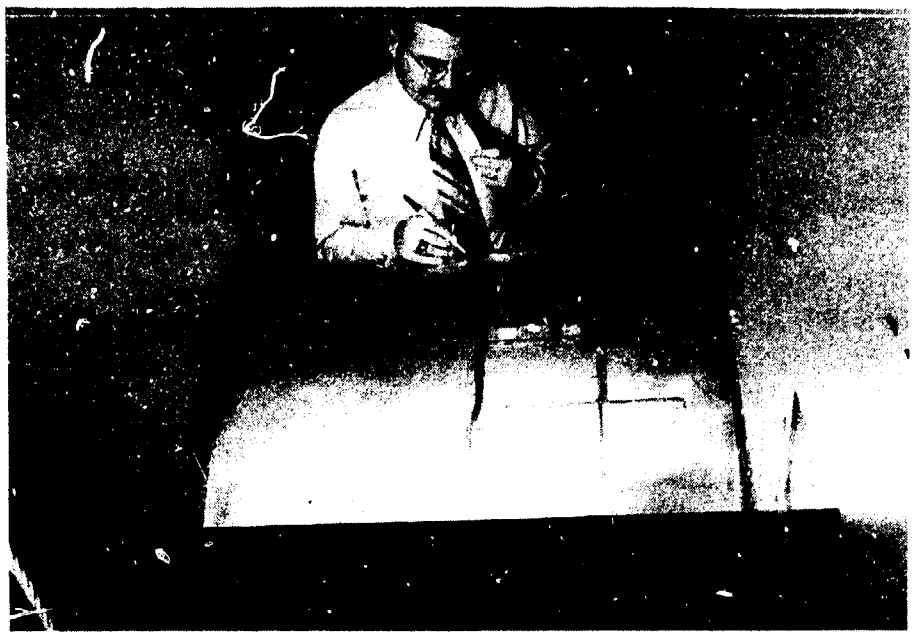

Figure 3.- The 60.96-cm (24-in.) model installed in Langley low-turbulence pressure tunnel test section.

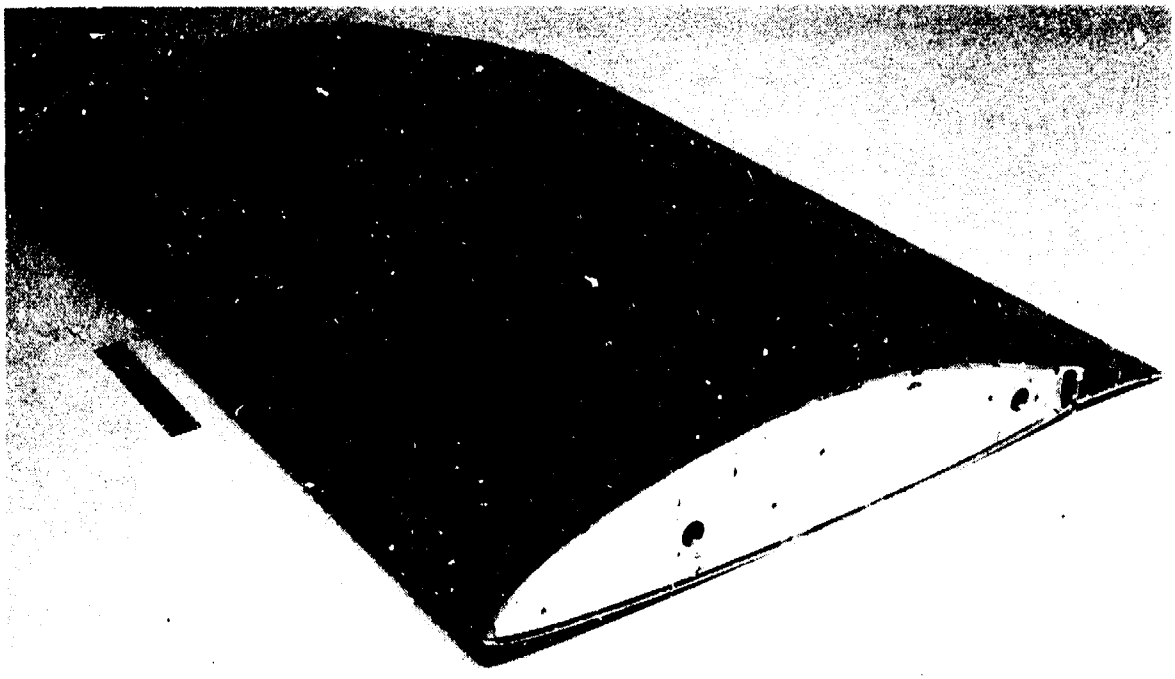

Figure 4.- Passive laminar flow airfoil for Langley low-turbulence pressure tunnel.

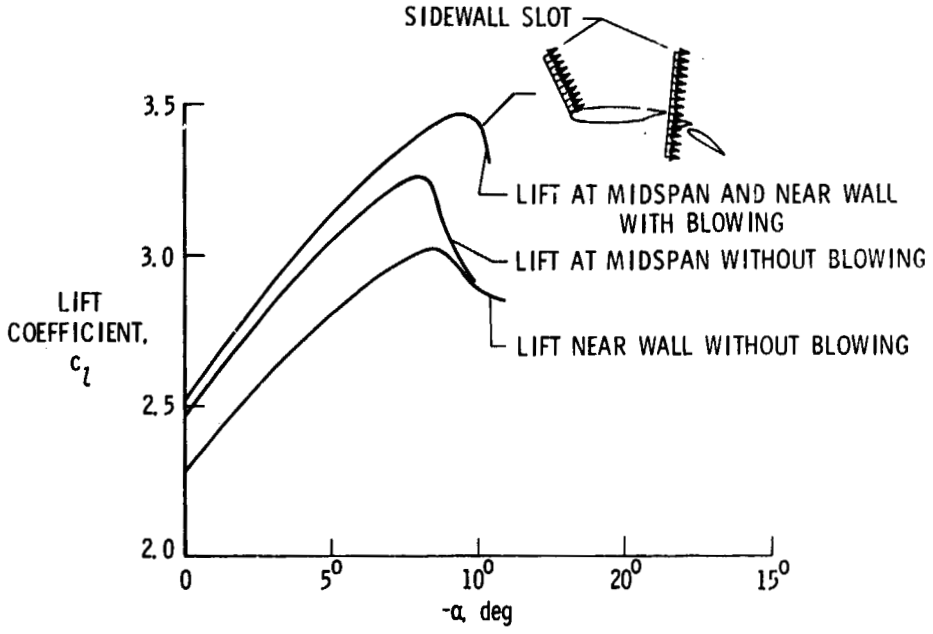

Figure 5.- Typical effects of boundary-layer control on lift characteristics.

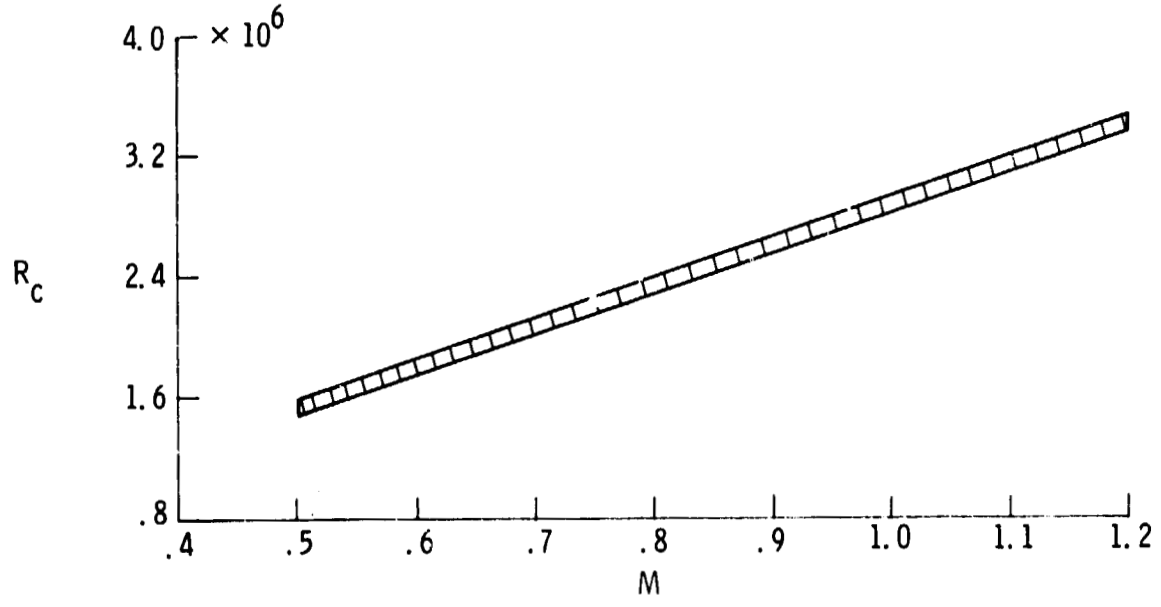

Figure 6.- Reynolds number envelope for Langley 6- by 19-inch transonic tunnel.

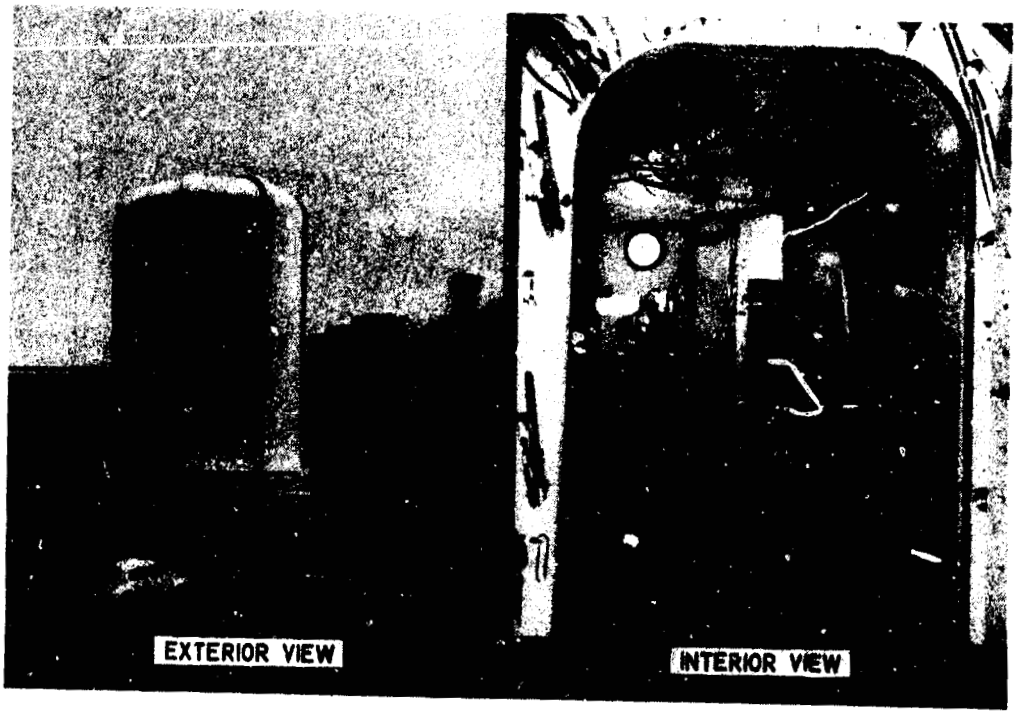

Figure 7.- Langley 6- by 19-inch transonic tunnel.

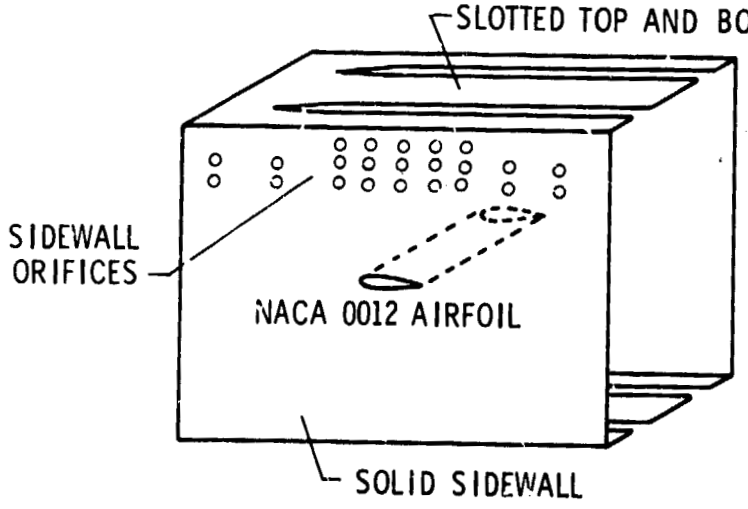

Figure 8.- Parametric slotted wall study for Langley 6- by 19-inch transonic tunnel.

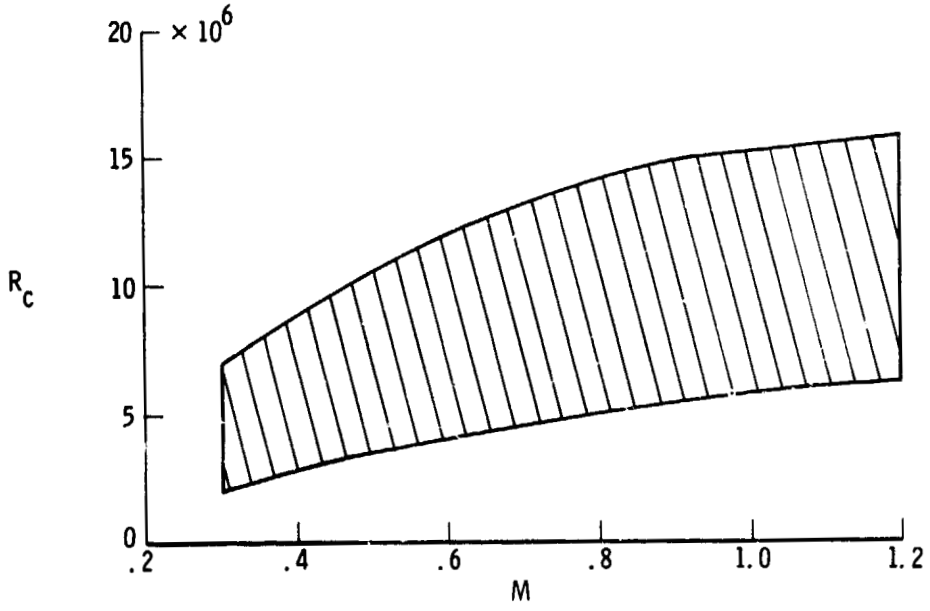

Figure 9.- Reynolds number envelope for Langley 6- by 28-inch transonic tunnel.

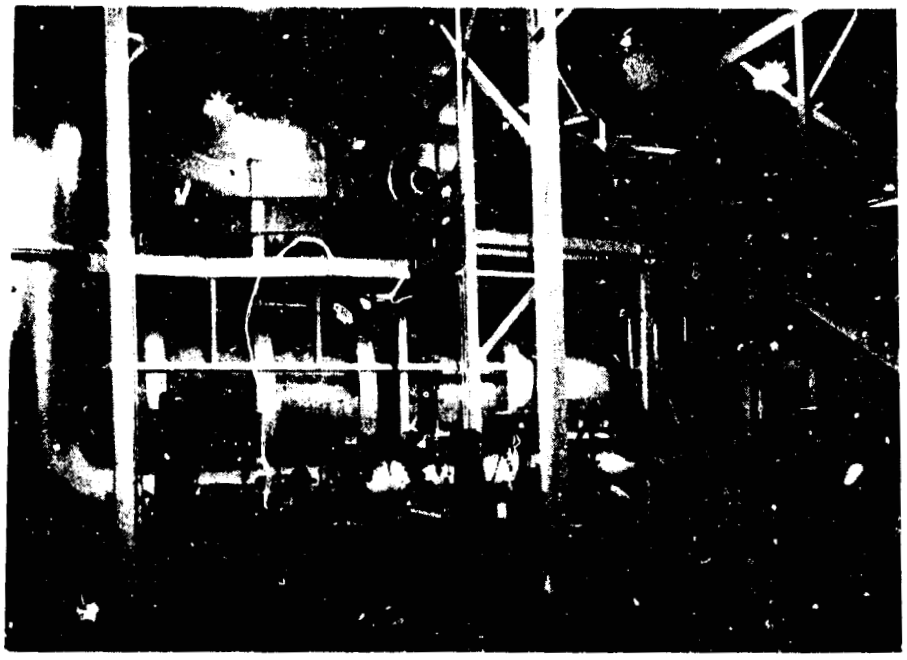

Figure 10.- Langley 6- by 28-inch transonic tunnel.

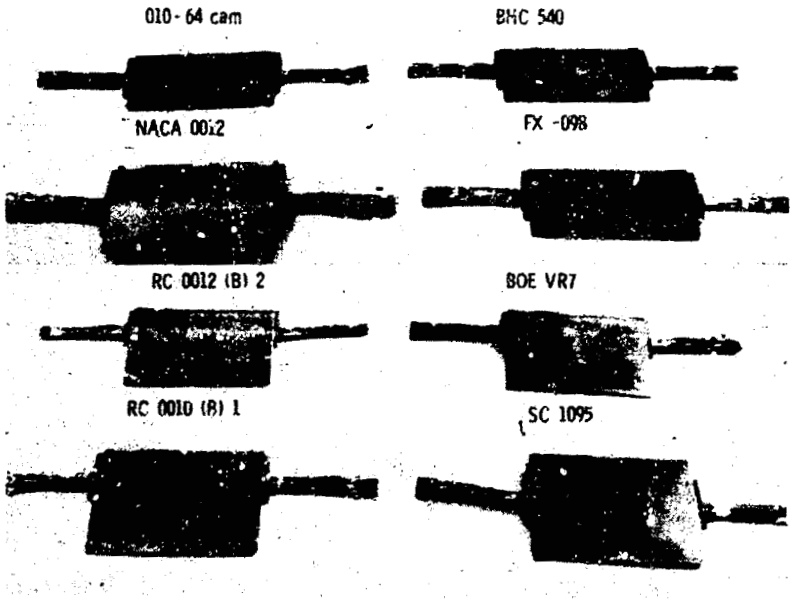

Figure 11.- Rotorcraft airfoil development models tested in Langley 6- by 28-inch transonic tunnel.

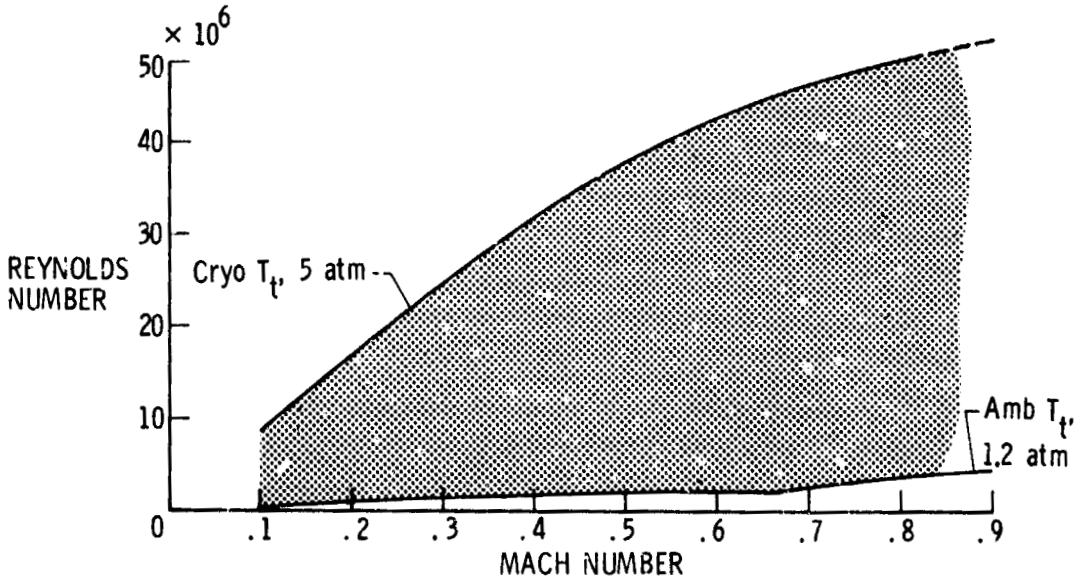

Figure 12.- Reynolds number envelope for two-dimensional test section in Langley 0.3-meter transonic cryogenic tunnel.

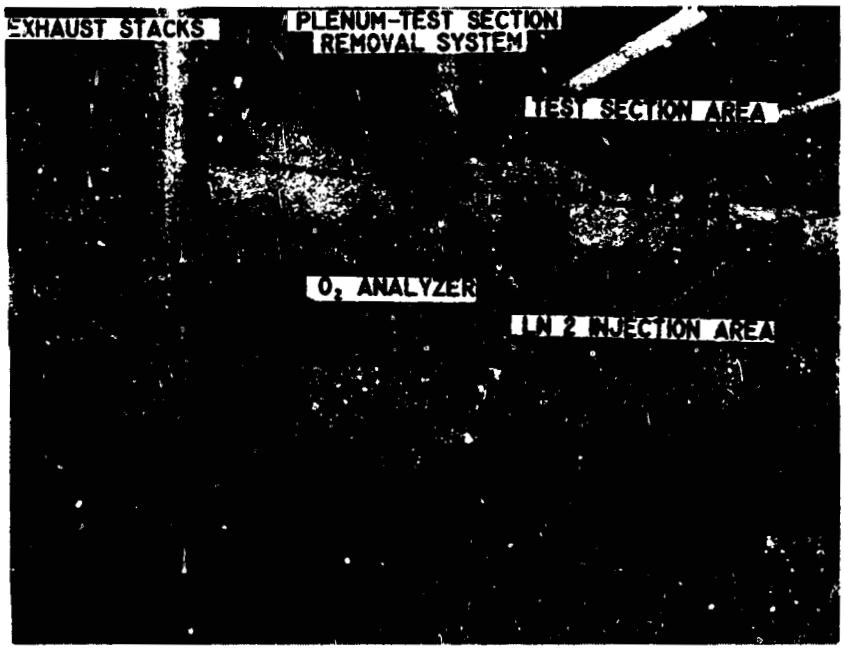

Figure 13.- Two-dimensional test section of Langley 0.3-meter transonic cryogenic tunnel.

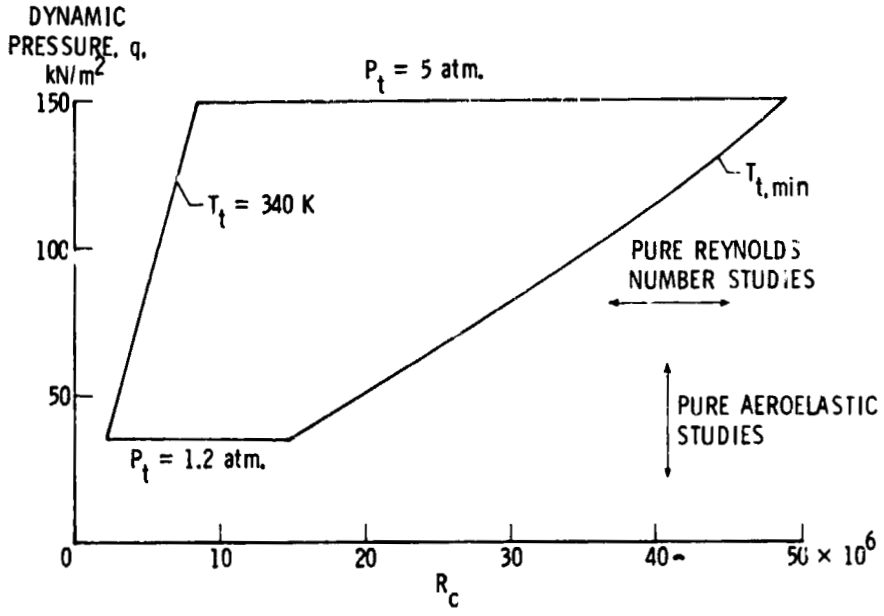

Figure 14.- Reynolds number - dynamic pressure envelope for two-dimensional test section in Langley 0.3-meter transonic cryogenic tunnel at M = 0.80 and c = 15 cm.

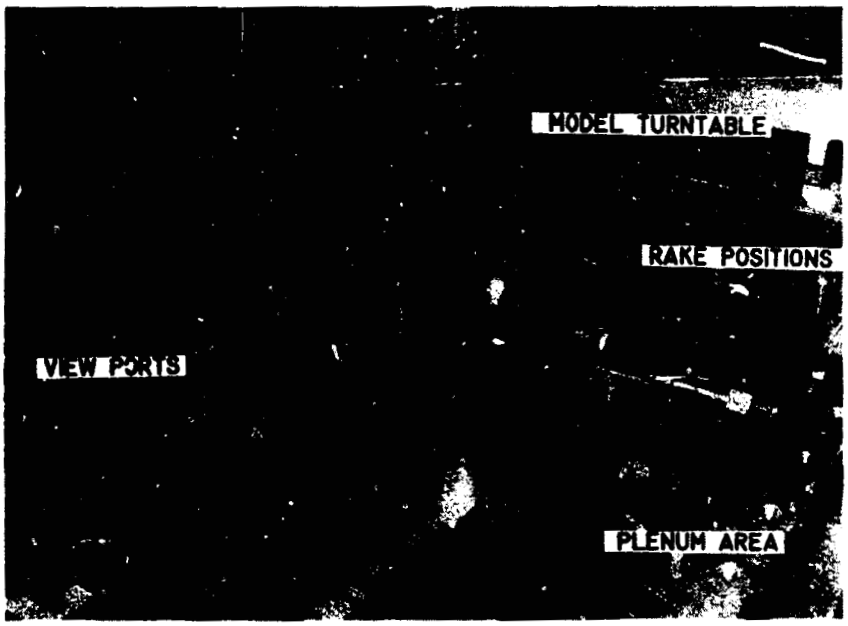

Figure 15.- Model modules in Langley 0.3-meter transonic cryogenic tunnel.

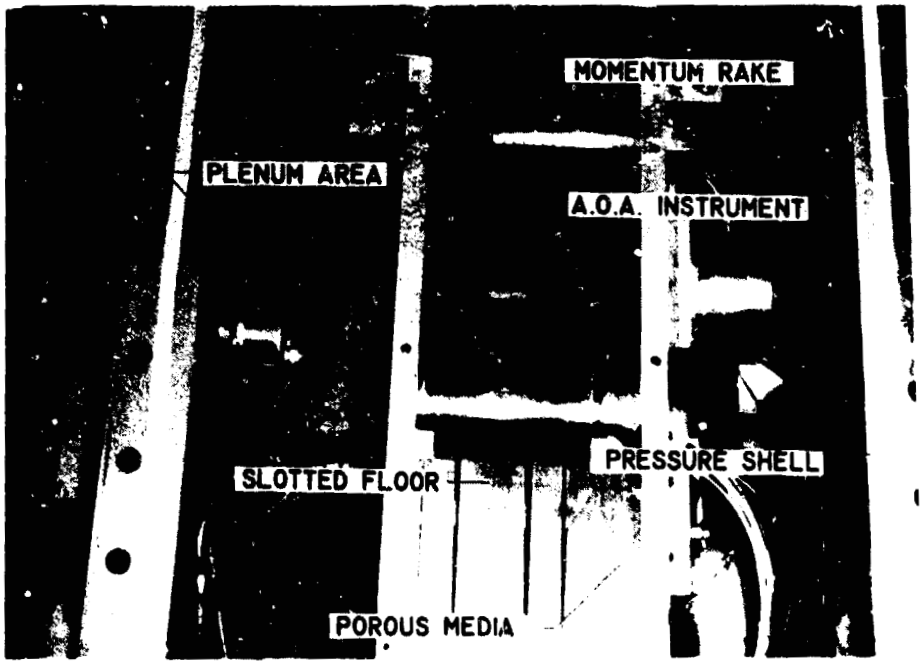

Figure 16.- Top view of two-dimensional test section in Langley 0.3-meter transonic cryogenic tunnel.

INVESTIGATION	AIRFOIL	t/c	c, in.
BLOCKAGE	0012-64	0.12	3
	0012-64	0.12	5
	0012-64	0.12	7
	0012-64	0.12	9
WALL	0012	0.12	6
BOUNDARY	65-213	0.13	6
CORRELATION	SCW	0.10, 0.14	6
	9510	0.11	6
FIGHTER		0.08	6
SPANLOADER		0.20	6
SURFACE FINISH		0.20	6

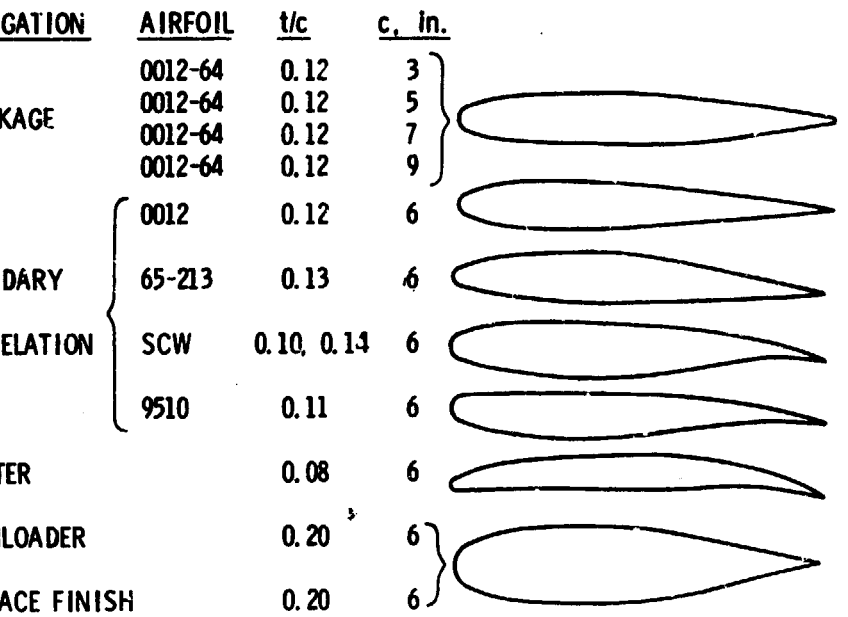

Figure 17.- Two-dimensional airfoil research program for Langley 0.3-meter transonic cryogenic tunnel.

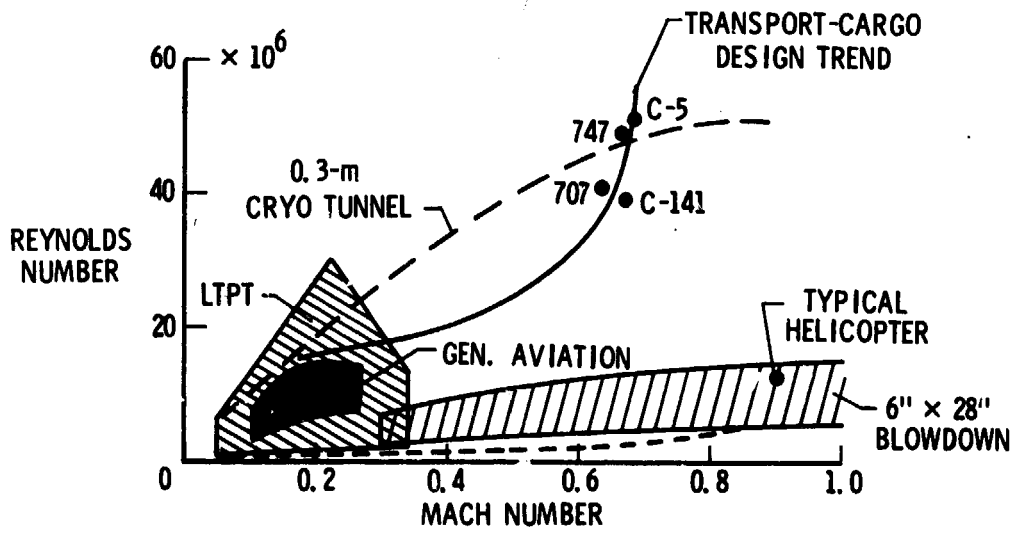

Figure 18.- Langley airfoil test capability.

D26

N79-20056

26

DEVELOPMENTS IN AIRFOIL TESTING TECHNIQUES AT UNIVERSITY OF SOUTHAMPTON*

Michael J. Goodyer

University of Southampton, Hampshire, England

SUMMARY

The evolution in Europe of the flexible walled test section, as applied to two dimensional testing at low and transonic speeds, is traced from its beginnings at NPL, London, in the early 1940's, and is shown to lead logically to the latest version now nearing completion at Southampton University. The principal changes that have taken place are improvements in the methods of choosing wall contours such that they rapidly follow appropriate streamlines, and reductions in the depth of test sections.

Most effort is directed to the simulation of an infinite two dimensional flowfield around a single isolated airfoil. Test data illustrates the large reductions of wall interference obtained as the wall contours are moved from the straight to streamlines in an infinitely deep flowfield.

The latest transonic test section presently under assembly at Southampton is described, the design drawing on the accumulated past experience. It has as its principal new feature the facility for the automation of wall streamlining with the aid of an on-line computer.

The versatility of the flexible walled test section is emphasised by reference to the simulation of alternative flows including cascade, steady pitching in an infinite flowfield, and ground effect. Finally, sources of error in streamlining are identified, with methods for their alleviation.

INTRODUCTION

The notion of providing a test section with walls curved in the streamwise direction is probably nearly as old as wind tunnel testing itself. The stimulus is the desire to reduce, ideally to eliminate, wall interference with the model such that it behaves as though in an infinite flowfield. For this purpose the walls are required to follow a streamtube encompassing the model. Obvious barriers to the implementation of the notion in three-dimensional testing include the difficulties of providing walls which will take double curvature, and the complication of the associated jacking system. Furthermore, as the flowfield and hence wall contours would be a function of model attitude, and the flow Mach and Reynolds numbers, changes of contour would be required with almost every change of test condition.

---

*Most of this work has been supported by NASA Grant NSG-7172.

The flowfield cannot be calculated with certainty; otherwise, presumably the model would not be under test. Therefore, the shape of a suitable encompassing streamtube is not known in advance.

The question would arise of the correctness of the wall contours which are imposing boundaries on the streamtube. The question can, in principle, be answered by flowfield calculations applied to the wall regions, calculations which can be made with reasonable confidence if the streamtube lies in potential flow. However, without the aid of a computer such calculations are a practical impossibility.

The situation is eased somewhat in two-dimensional flow. At least the mechanical design of walls and jacks is relatively simple. During World War Two the pressure to introduce a flexible walled test section increased with the discovery of severe wall interference effects at transonic speeds. NPL in London responded in 1941 by constructing a transonic two-dimensional test section, with two opposite flexible walls adjusted manually through jacks distributed along their lengths. The test section was conventional in terms of depth and length in relation to the airfoil chord, and is sketched to scale with other test sections on Figure 1. The walls were set to approximate streamline shapes by invoking some trends seen in two-dimensional potential flows calculated around simple bluff and lifting bodies: the infinite flowfield streamline and therefore wall contour lay roughly midway between the straight and the contour giving constant static pressure. The streamlining operation established an experimental procedure that is followed invariably today, namely that the contours are based on measurements made only at the wall. The measurements are of local wall position and static pressure.

The quality of the aerodynamic data taken from airfoil models in this tunnel was quite satisfactory, but eventually the emergence of the ventilated designs of test section superceded it because they did not require the slow, manual wall setting procedure. However, in moving to the ventilated design at least two features of testing were worsened: tunnel drive power rose, and flow unsteadiness increased.

There followed a lengthy lapse in interest in the use of flexible walls for reduced interference at low and transonic speeds, but then in the early 1970's at several different research establishments and perhaps responding to different stimuli, researchers re-examined test techniques and postulated new solutions. The following sections of this report summarise the features of the newer flexible walled tunnels in Europe, show typical test data obtained at Southampton, and underline the need and means for automation in the operation of such tunnels.

Reference citations are denoted herein by superscripts.

LOW SPEED TEST SECTIONS

The work at Southampton sprang from discussions held at Langley Research Center[1] in 1971, where attempts were made to identify reasons for the magnetic suspension and balance system failing to satisfy the needs of mainstream aero-

dynamic testing. Among the possible solutions to the problem were the cryogenic wind tunnel to raise Reynolds number without increase in tunnel size, and therefore without increase in the cost and power demands of the magnetic suspension system, and the use of a flexible walled test section to eliminate the need for ventilation with its bulky plenum chamber.

Because of the obvious cost, technical risk and complexity of such a three-dimensionally deformable test section, it was decided, in 1972, to proceed with a two-dimensional design. A computer would allow the rapid execution of the necessary wall-based calculations. A low speed wind tunnel was modified by the incorporation of flexible walls with 14 jacks on each wall. The tunnel began tests in May 1973. This design began a trend towards reduced depth which has since been followed, the depth:chord ratio being about 1.4 compared with about 3.4 in the NPL tunnel. The argument for reduced depth (or increased chord) is based on the achievement of low interference. In subsequent years the test section was progressively modified as it became clear that a greater length of streamlined wall was required, and so that symmetry[2] was desirable. The evolution is illustrated on Figure 1. The latest version of the low speed test section is 1.1 chords deep (the wing chord used is 13.72 cm), has eighteen jacks per wall, a total length of 9.4 chords, but a "streamlined" length of only about five chords centered about the quarter-chord point. The studies paralleling this work have shown the need for close jack spacing near to the model in order to adequately define wall shape. In fact, in the light of what we now know we would judge the old NPL tunnel to have had well chosen jack spacings. The sketches on Figure 1 show in most cases the point where the flexible walls are anchored to the contractions.

The wall measurements of contour and static pressure are particularly simple, and the subsequent computations should in principle be based[3] on the boundary layer displacement thickness contour. In practice, this requires estimates only of the small changes in thickness between model present and absent. The estimates can be based on boundary layer measurements, or on boundary layer theory using model-induced wall pressure gradients. The latter has been chosen. However, we find that the changes in thickness on the flexible walls are so small that whether or not they are taken into account has no measurable effect on the model in low speed testing. There seem to be much more serious effects from the sidewall boundary layers.

The setting of the walls to streamlines is necessarily iterative, with, in our early experience, several steps being required to take the walls from "straight" to "acceptable streamlines". One development in technique which has taken place in recent years, the importance of which must be emphasised, is Judds[2] predictive method for wall adjustment. The adoption of this method has reduced the average number of iterations from about eight[3] to about two[4] for each model attitude. There are proportional reductions in the time for streamlining, which of course is time not available for taking model data.

The reductions in wall interference by streamlining are illustrated on Figure 2 which shows the normal force coefficient C_N for an NACA 0012-64 airfoil tested in the latest (1976) version of the low speed test section and in Langley's LTPT as baseline data. It is seen that streamlining the walls

largely corrects the data except at the highest angle of attack investigated, 12 degrees. Some considerable effort has been expended in searching for reason(s) for this disparity, so far without positive conclusions. However, there is a strong indication that sidewall boundary layer effects might be responsible since the addition of small disk-shaped leading edge fences about 1 cm from the sidewalls went some way towards reducing the error in force coefficient. Despite the residual disparity at this angle of attack, with wing fences the streamlining of the walls had eliminated 82% of the "straight walls" interference.

It should be noted that data taken in any non-automated self streamlining test section is hard-won because of the slowness of the streamlining procedure. The data shown on Figure 2 is the most extensive so far published from any similar contemporary wind tunnel.

Besides the simulation of a single model in an infinite flowfield, the self streamlining wind tunnel can simulate a variety of other flowfields around a single model including[3] ground-effect and open-jet testing. More recently* the low speed tunnel has been used for simulating steady pitching of the same NACA airfoil, in the manner of the old Dynamic Stability tunnel at Langley. The photograph on Figure 3 shows the walls curved around an arc chosen to give negative rates of pitch. Note that in these tests the airfoil is mounted inverted. The curvature introduces a rate of pitch q of the airfoil which depends on the radius of curvature and airspeed v. There is as yet no rational method available for streamlining with a curved axis, therefore, in these tests the walls were deformed from arcs by the same amount that they had been deformed in streamlining from the straight in earlier non-pitching tests. The streamlining can therefore have been only approximate, but despite this the resultant data is encouraging. This is shown on Figure 4 as ΔC_N the change of normal force coefficient due to pitching, and ΔC_M the change of pitching moment about the leading edge due to pitching, each as functions of the ratio of rate pitch to airspeed q/v. The ΔC_N test data compares well with thin airfoil theory.

Finally, in connection with low speed testing mention should be made of the possibility of simulating cascade flows around one (or more) airfoils by imposing appropriate flow boundaries with flexible walls. A streamlining criterion has been laid down[3] and the test section built for a single airfoil is shown on Figure 1. Current effort is aimed at demonstrating the achievement of cascade flow, and at adapting the predictive method for rapid wall streamlining. This work will be reported separately by Wolf.

TRANSONIC TEST SECTIONS

In parallel with the low speed work at Southampton, Chevallier at ONERA constructed a transonic test section[5] of similar size, again with manually adjusted jacks. The proportions of the test section are conventional, but the number of jacks and their spacing we now believe to be rather inadequate for the satisfactory definition of wall shape in the presence of an airfoil model

* This work followed a suggestion by Mr. J. Pike of R.A.E. Farnborough

much larger than that shown and used. The test section has been used to demonstrate adequate streamlining of the wall at transonic speeds using the modern type of streamlining criteria.

Lastly on Figure 1 is sketched the transonic test section which has been manufactured for an existing induced flow atmospheric tunnel at Southampton. The test section has motorised jacks and provision for the rapid scanning of wall pressures and position transducers at each jack. The test section is intended for coupling to a PDP 11-34 computer for online streamlining[2], followed by the online acquisition of model data. The development program will include airfoil testing with comprehensive sidewall and wake instrumentation, followed by some testing of wing-body combinations with the aim of evolving streamlining methods which may alleviate wall interference in three dimensional flow. It is also planned to investigate the possibility of attenuating reflected shocks, to allow testing at high transonic speeds. The tunnel will begin running in mid 1978.

SOURCES OF ERROR

Length truncation

The test section can only reproduce a limited length of correctly contoured streamtube. The effects of truncation can be assessed as a correction to model data[2]. The correction is minimised by placing the model mid-way along the test section, and reduces with increase in the streamlined length of test section.

Boundary layers on flexible walls

The small effect of variation in displacement thickness has already been noted. At transonic speeds there could be a shock/boundary-layer interaction from the wing shock.

Sidewall boundary layers

The effects of unexpected or uncontrollable behaviour of these boundary layers can be profound. The problem is common to all two-dimensional testing and must be addressed if reliable data is to be obtained at all angles of attack.

Differences between the elastic structure and streamline

The flexible wall can only be constrained to pass through streamlines at discrete points coinciding with the jacks. Between jacks the wall departs from the streamline. The effect is minimised by closely spacing the jacks where the streamline curvature is strongest, that is adjacent to the model. A method for assessing the magnitude of the resultant wall errors has been developed by Wolf.[4]

Centreline Curvature

There seems to be the possibility of building into the test section some centreline curvature, when the tunnel is being set for "straight" walls with the test section empty, the curvature arising from the finite resolution of measuring instruments. The curvature will in turn induce flow errors at the position of the model. Assessments have been made of the required resolving power of the wall instrumentation.[2]

Wall pull-up

The unanchored end of the test section wall moves axially as curvature is built into the wall. Since wall geometry is known, simple corrections have been built into the data reduction software.

Imaginary flowfield calculations

This places on record the recognition of these computations as a possible source of error. The tunnel users are continually reviewing computational techniques to balance resolution with computing speed. An extensive series of computations has indicated that with one algorithm for the imaginary flowfields, reproduction of wall displacement in the algorithm accurate to about 0.03 mm is quite adequate.

CONCLUDING REMARKS

The combined European experience with wind tunnels with flexible walls leads to the conclusion that interference can be reduced and in many cases eliminated. Also, the tunnel appears to be usefully versatile in the flowfield types which can be produced. A predictive method for wall contouring has been successfully developed.

Once the newest transonic test section is commissioned in its automated form, we can expect to see not only further developments in streamlining techniques, but also the results of attempts to extend upwards the useful Mach number range of this type of test section, and attempts to alleviate interferences in three dimensional testing.

One final point which should be re-emphasised is the probable susceptibility of model behaviour to sidewall boundary layer effects when the sidewalls are not provided with appropriate treatment.

REFERENCES

1. Goodyer, M. J. A low speed self streamlining wind tunnel. AGARD - CP - 174, 1975.

2. Judd, M., Goodyer, M.J., Wolf, S.W.D. Application of the computer for on-site definition and control of wind tunnel shape for minimum interference. AGARD CP - 210, 1976.

3. Goodyer, M.J. The self streamlining wind tunnel. NASA TM X-72699, August 1975.

4. Wolf, S.W.D., Goodyer, M.J. Self streamlining tunnel - low speed testing and transonic test section design. NASA CR 145257, 1978.

5. Chevallier, J.P. Souffleric Transsonique a parois auto-adaptables. AGARD - CP - 174, 1975.

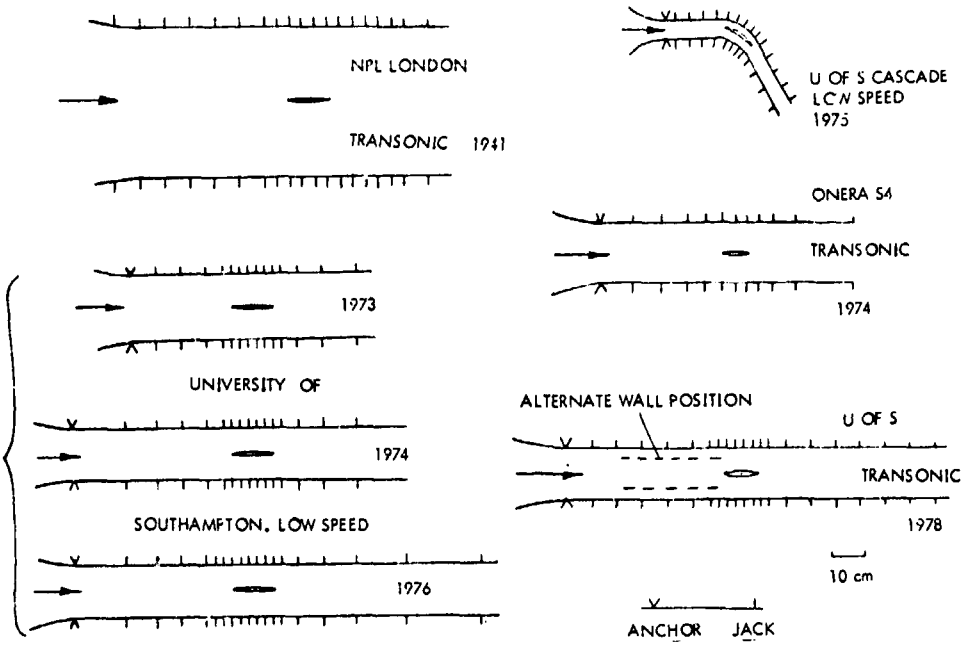

Figure 1.- European low-speed and transonic flexible-walled wind tunnels.

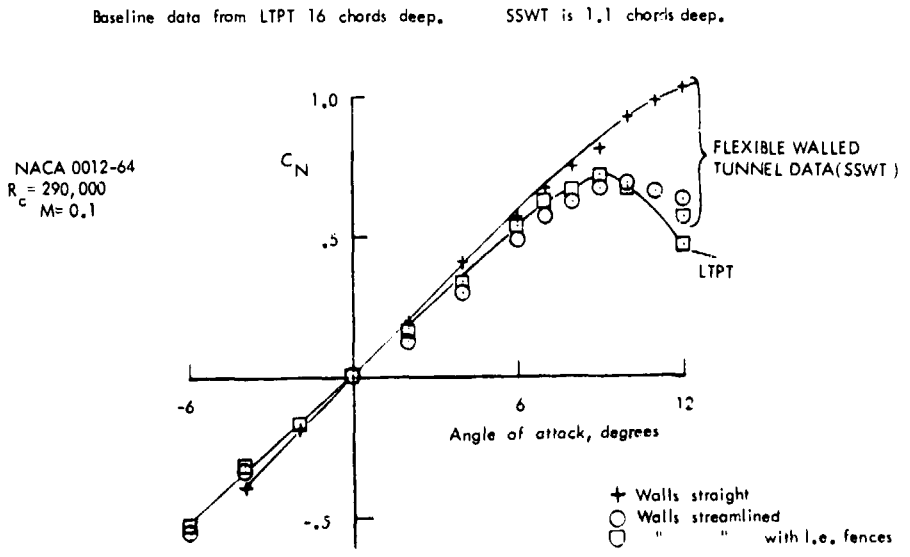

Figure 2.- Normal-force coefficient from integrated airfoil pressures where M denotes the Mach number and R_c denotes the chord Reynolds number.

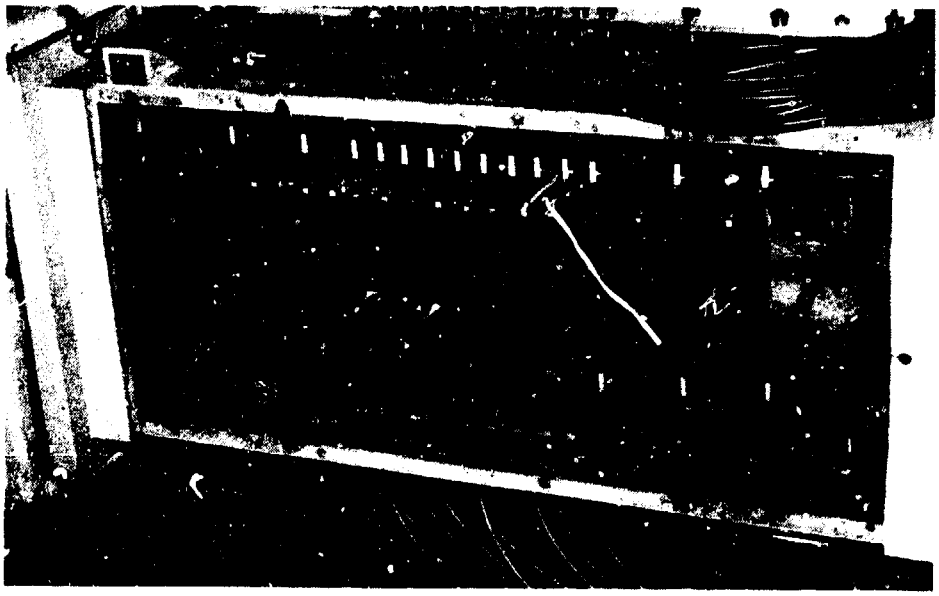

Figure 3.- View of low-speed test section. Axis curved for pitch-derivative measurement.

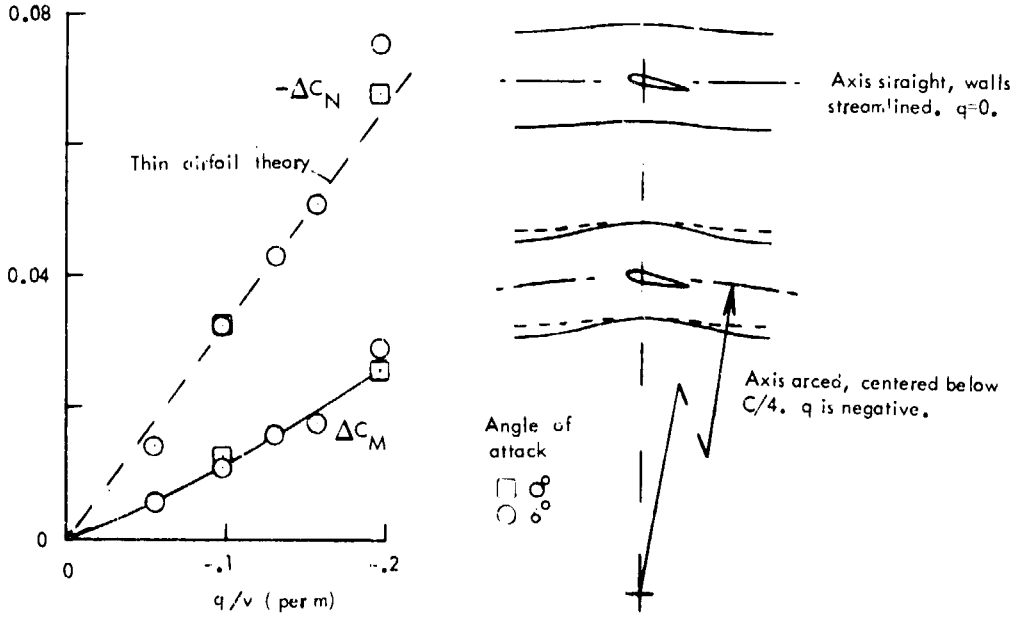

Figure 4.- Rate-of-pitch derivative data where c denotes the chord. Axis curved.

A NEW AIRFOIL RESEARCH CAPABILITY

Charles L. Ladson
NASA Langley Research Center

SUMMARY

The design and construction of a self streamlining wall test section for the Langley 0.3-meter transonic cryogenic tunnel has been included in the fiscal year 1978 construction of facilities budget for Langley Research Center. The design is based on the research being carried out by M. J. Goodyer at the University of Southampton, Southampton, England, and is supported by Langley Research Center. This paper presents a brief description of the project. Included are some of the design considerations, anticipated operational envelope, and sketches showing the detail design concepts. Some details of the proposed operational mode, safety aspects, and preliminary schedule are presented.

INTRODUCTION

In late 1974, a decision was made at Langley Research Center to support adaptive wall wind-tunnel research. This was accomplished by grants to the University of Southampton to support the work of M. J. Goodyer on the self streamlining wall concept (refs. 1 to 5), a grant to support the work of A. Ferri, and a request for funds for constructing a self streamlining test section for the Langley 0.3-meter transonic cryogenic tunnel to be based upon the design technology developed during the University of Southampton research program.

SYMBOLS

c model chord

h tunnel height

R_c Reynolds number based on model chord

x longitudinal distance

y vertical distance

DISCUSSION

The purpose of the new test section, in addition to providing airfoil test capability essentially free from floor and ceiling interference effects, is to increase the Reynolds number capability in the facility. This paper deals only with the design features and capabilities for the new test section and the reader is referred to references 1 to 5 for details of the concept. The proposed test section shown in figure 1 would have a 33-cm square test section and would be interchangeable with the two existing test sections for this facility. The new test section would make use of as much of the existing equipment as possible but would include a new minicomputer for the wall shape control.

Because the new test section must be compatible with the existing tunnel, its flow area must be about the same but the height and width could be different. As shown in figure 2, if the model chord is held equal to its span so that sidewall effects would be similar for all cases, an increase in chord Reynolds number can be achieved by reducing the tunnel height-width ratio. By making the tunnel height-width ratio equal to one as compared with the conventional two-dimensional tunnel ratio of four, an increase in Reynolds number by a factor of two can be achieved due to the increased chord allowed while maintaining the chord-span ratio. Although the blockage for this case is greater, the streamlined walls can still correct for it, as evidenced by the University of Southampton experience. The capability of the facility in terms of Mach number and Reynolds number is shown in figure 3 for the assumed chord-to-height ratio of 1.0.

The lower portion of this figure, which shows the existing Langley facilities and the current requirements of various types of aircraft, has been presented in reference 6. The currently envisioned region for advanced large cargo aircraft has been added. The point to be noted here is that the trend in requirements for transport aircraft is extended into the chord Reynolds number range of about 80×10^6 for advanced large cargo aircraft such as the spanloader concept. The envelope for the 33- by 33-cm test section of the Langley 0.3-meter transonic cryogenic tunnel is seen to adequately cover this requirement from the Mach number and Reynolds number viewpoints.

To illustrate the wall contouring capability, a typical streamlined wall shape is plotted in figure 4 for an NACA 0012-64 airfoil at a Mach number of 0.3 and angle of attack of 12°, or a lift coefficient of about 1.5. This is a potential flow solution and does not include any viscous effects. The case is for model chord c equal to tunnel height h and the two streamlines begin at $\pm\, y/h = 0.5$. The flexible walls are fixed at $x/h = 0$ and ends at $x/h = 4.5$. The quarter-chord of the model is located at the midpoint of the flex wall. Twenty-one jacks are mounted on each wall, with the downstream three being used for a fairing into the fixed diffuser. The close spacing of the jack in the region of the model is evident and is necessary to provide as close an approximation as possible to the streamline shape. For the case shown, the wall deflection from straight is about two-thirds the maximum design value. It should be pointed out that there will be limitations to this test section

with respect to the maximum lift coefficient which can be tested as well as a Mach number limitation due to shock reflections and sonic velocities reaching the wall boundary. Sidewall boundary layer will be removed by the same mechanism as will be used for the existing 20- by 60-cm two-dimensional test section.

A generalized operational schematic is shown in figure 5. A typical section of the flex wall to which a position transducer, pressure tap, and jack are attached is shown on the lower portion of the figure along with the main computer on the upper portion. The main computer, through appropriate software programs, uses the measured pressures to compute the internal flow velocities, the position transducer to compute the external flow velocities, and sends drive pulses to the motor driven jacks to change wall shape if necessary. A scanivalve system will initially be used to scan the wall pressure although the system can be expanded to accommodate an individual transducer for each wall orifice. A microprocessor based safety system is used as a backup to the main computer to prevent the flexible walls from being overstressed, thus protecting them from permanent damage.

Two view drawings of the proposed test section are presented in figures 6 and 7. From the end view (fig. 6) the tunnel flex walls and side walls are seen to be enclosed inside a plenum chamber which is the pressure vessel. The vertical sidewalls are solid and of one piece construction. The flexible top and bottom walls are attached through a thin, flexible membrane to two push rods which are connected to a crosshead. The crosshead is actuated by a motor-driven lead screw. The motors are staggered in vertical and lateral position in order to achieve the close spacing of the push rods which was desired. Both top and bottom wall actuating systems are the same. The angle of attack and traversing wake-survey-probe drive mechanisms are also located on the top of the test section. The model turntable is rotated by means of two push rods passing through the pressure vessel while the cantilevered survey probe is driven by a single push rod. All of the drive mechanisms and instrumentation are located outside of the tunnel pressure shell so as to be in an ambient temperature environment. The side view (fig. 7) shows the larger center door for model access as well as ports for instrumentation leads and boundary-layer removal flow ducts.

PROPOSED MILESTONE SCHEDULE

At present, the procurement package is being readied for advertisment. If acceptable bids are received, the contract could be awarded by late 1978 with about a 1-yr delivery time. The system is to be bench mounted for initial checkout of operation, which would extend to the end of 1979. The test section could then be mated with an existing low-speed compressor, bellmouth, and diffuser to provide some low-speed ambient temperature and pressure operational experience before committing it to installation in the Langley 0.3-meter transonic cryogenic tunnel circuit.

REFERENCES

1. Judd, M.; Wolf, S. W. D.; and Goodyer, M. J.: Analytical Work in Support of the Design and Operation of Two Dimensional Self Streamlining Test Sections. NASA CR-145019, 1976.

2. Goodyer, Michael J.: The Self Streamlining Wind Tunnel. NASA TM X-72699, 1975.

3. Goodyer, M. J.: A Low Speed Self Streamlining Wind Tunnel. Wind Tunnel Design and Testing Techniques, AGARD-CP-174, Mar. 1976, pp. 13-1 - 13-8.

4. Judd, M.; Goodyer, M. J.; and Wolf, S. W. D.: Application of the Computer for On-Site Definition and Control of Wind Tunnel Shape for Minimum Boundary Interference. Numerical Methods and Windtunnel Testing. AGARD-CP-210, Oct. 1976, pp. 6-1 - 6-14.

5. Wolf, S. W. D.; and Goodyer, M. J.: Self Streamlining Wind Tunnel-Low Speed Testing and Transonic Test Section Design. NASA CR-145257, 1977.

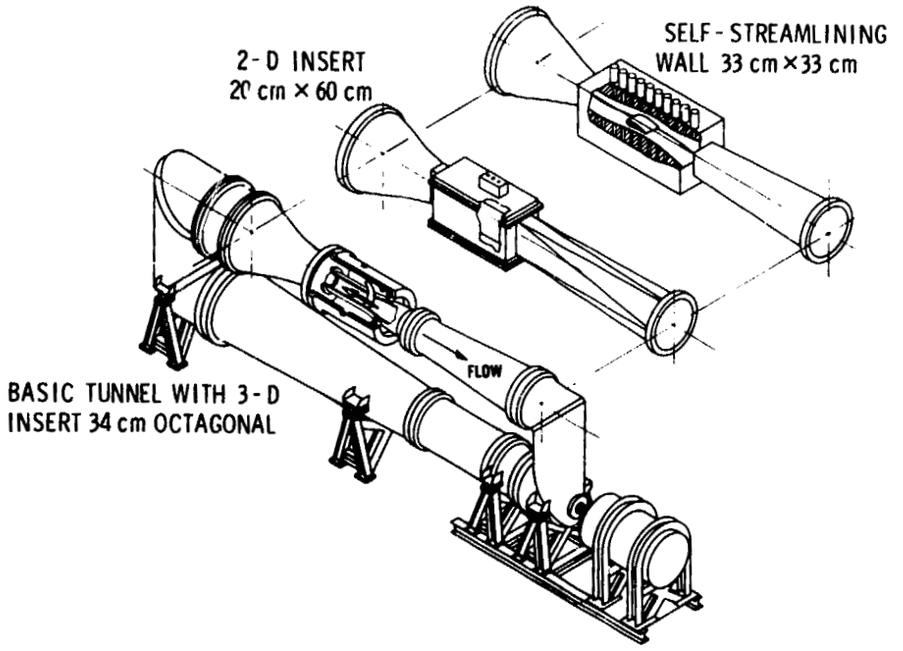

Figure 1.- Interchangeable test-section capability in the Langley 0.3-meter transonic cryogenic tunnel.

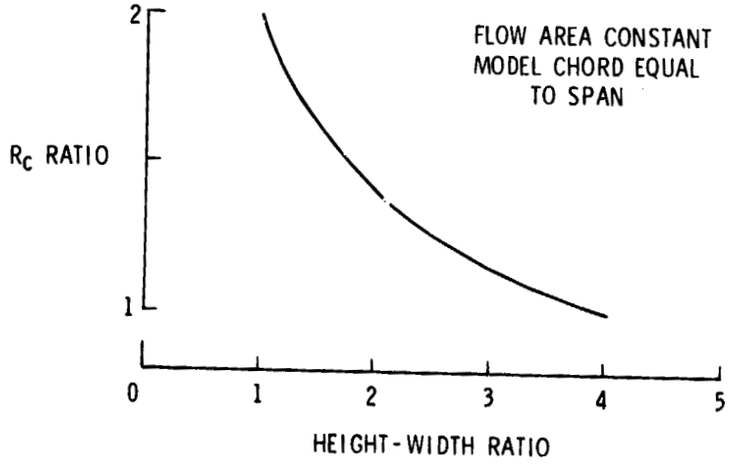

Figure 2.- Reynolds number variation with height-width ratio.

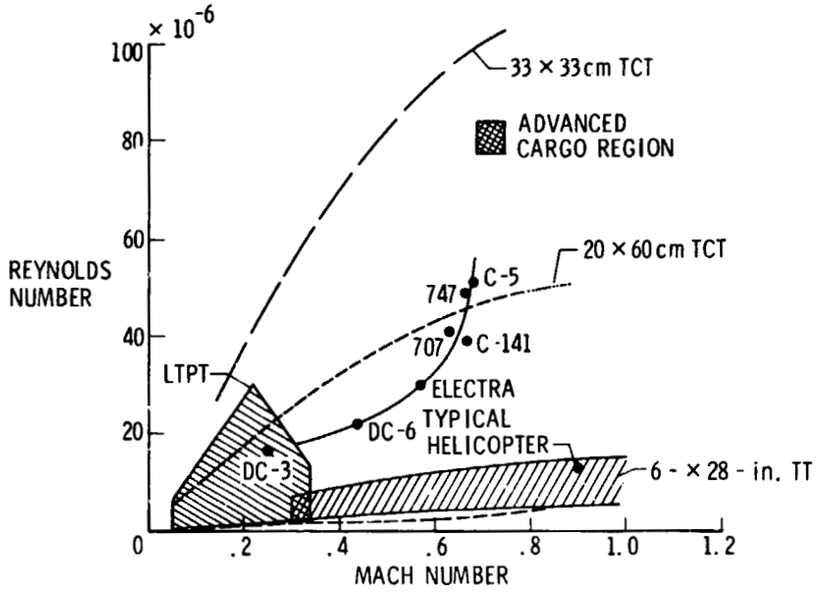

Figure 3.- Langley airfoil test capability.

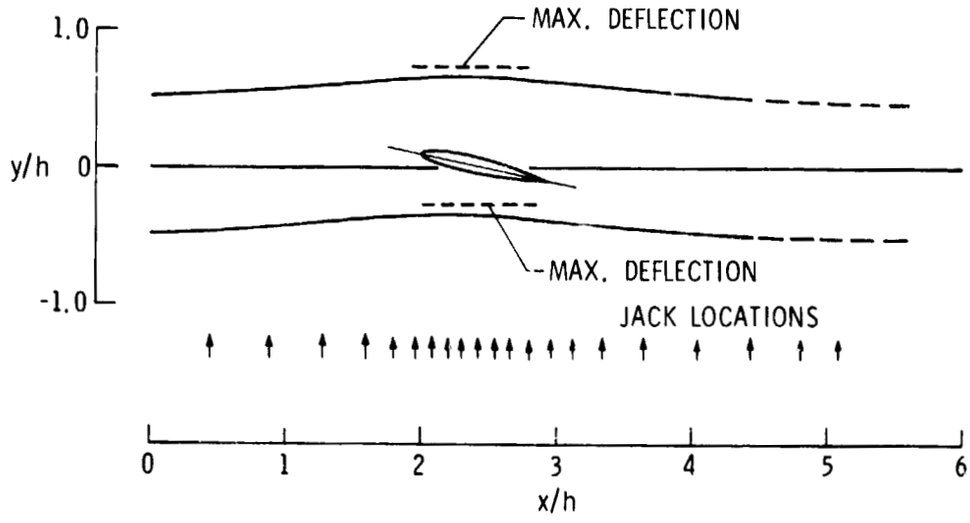

Figure 4.- Typical streamlined wall shape for an NACA 0012-64 airfoil at M = 0.3, α = 12°, and c = h.

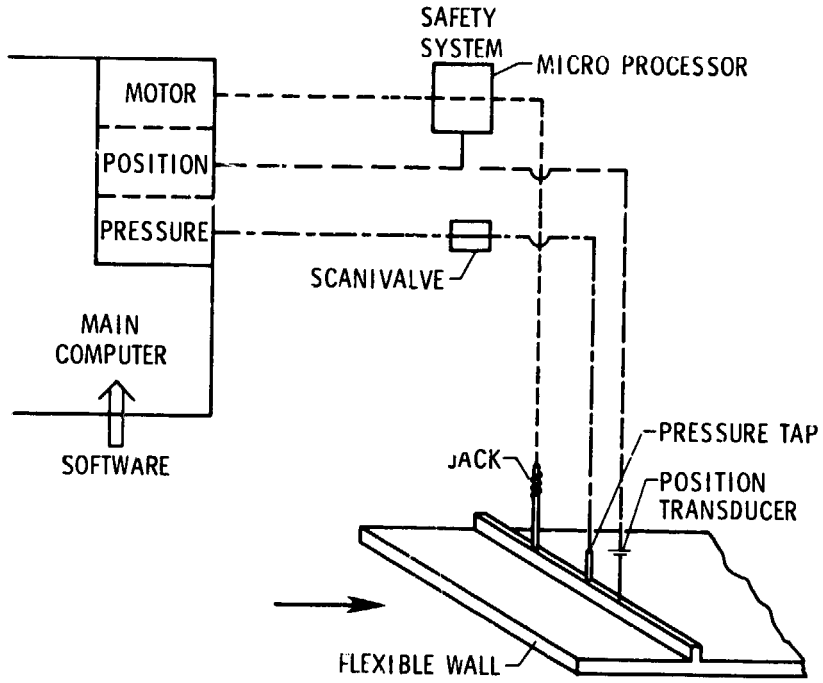

Figure 5.- Operation schematic.

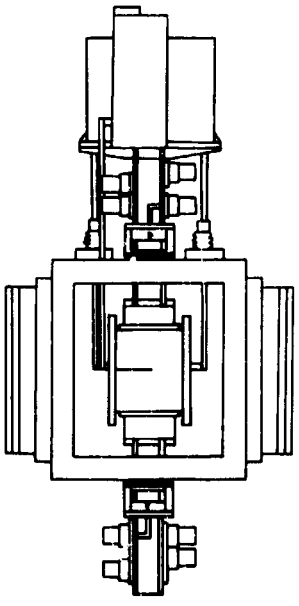

Figure 6.- End view of test section.

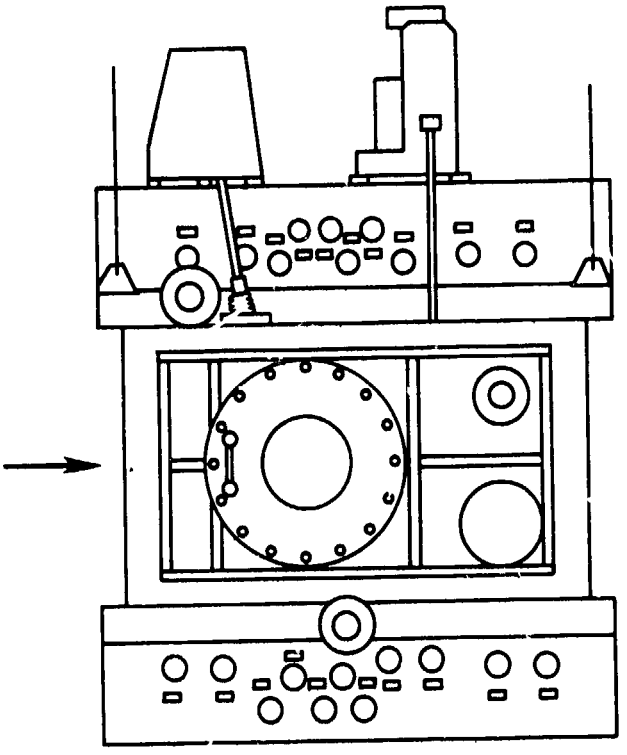

Figure 7.- Side view of test section.

D23

N79-20058

28

DESIGN AND CALIBRATION OF SLOTTED WALLS FOR TRANSONIC AIRFOIL WIND TUNNELS

Richard W. Barnwell, William G. Sewall, and Joel L. Everhart*

NASA Langley Research Center

SUMMARY

The traditional procedure for estimating the performance of slotted walls for airfoil wind tunnels is reviewed, and a modification which improves the accuracy of this procedure is described. Unlike the traditional procedure, the modified procedure indicates that the design of airfoil wind-tunnel walls which induce minimal blockage and streamline-curvature effects is feasible. The design and testing of such a slotted wall is described. It is shown experimentally that the presence of a model can affect the plenum pressure and thus make the use of the plenum pressure as a calibration reference questionable. Finally, an ONERA experiment which shows the effect of the sidewall boundary layer on the measured model normal force is discussed.

INTRODUCTION

Slotted walls have been used to reduce blockage in transonic wind tunnels for three decades. Traditionally, the performance of these walls has been estimated with a theoretical procedure based on the results of Davis and Moore (ref. 1); Baldwin, Turner, and Knecthel (ref. 2); and Wright (ref. 3). It is generally known that this traditional procedure does not work.

The analysis of the effects of slotted walls involves three general steps. First, a model of the flow in the vicinity of the wall must be developed. It will be shown that this flow model is a function of one parameter which depends on the wall geometry. Next, the interference for various values of the flow-model parameter must be determined. Finally, the flow-model parameter must be evaluated for a given wall geometry. In the past, it has been assumed generally that the last step was performed correctly with the theoretical method of Davis and Moore (ref. 1), and that the failure of the traditional procedure was due to one or both of the other steps. Recent work by Barnwell (ref. 4) indicates instead that the failure of the traditional procedure is due largely to the manner in which the third step has been performed. An alternate method for performing the third step, which is based on experimental data rather than theory, is presented in this paper.

---

*Former Graduate Research Scholar Assistant with Joint Institute for Advancement of Flight Sciences, George Washington University.

It is standard practice to use the plenum pressure as a reference for the calibration of transonic wind tunnels. The validity of this approach has been demonstrated for three-dimensional testing where the maximum model cross-sectional area is constrained to be a fraction of 1 percent of the tunnel cross-sectional area. However, this constraint is not met, in general, in two-dimensional tunnels where, instead, maximum model cross-sectional areas are typically from 2 to 4 percent of the tunnel cross-sectional area. It should not be too surprising that the presence of such a model would influence the plenum pressure and thereby make its use as a reference pressure unreliable. Experimental results for a sample case in which this phenomenon occurred are presented.

Results obtained in the ONERA RICh wind tunnel (ref. 5) which show that the sidewall boundary layer can have a substantial effect on the normal force measured on the model are discussed. A possible explanation for this effect is presented.

SYMBOLS

a	slot spacing
c_n	normal-force coefficient
h	tunnel semiheight
K	slotted-wall coefficient
k	flow-model parameter
M	Mach number
M_∞	free-stream Mach number
M_{PLENUM}	Mach number based on plenum pressure
x	coordinate in free-stream direction
y	coordinate perpendicular to free-stream direction
α	angle of attack
β	$= \sqrt{1 - M_\infty^2}$
δ	slot width
δ^*	displacement thickness
θ	flow angle with respect to free-stream direction

Subscript:

max maximum value

ANALYSIS OF SLOTTED WALLS

Flow Model at Wall

The first step of the analysis procedure is to develop a model of the flow near a slotted wall. The simplest form of this model, which was developed independently by Davis and Moore (ref. 1) and Baldwin, Turner, and Knecthel (ref. 2), among others, is the form used in this paper. A more complete form is given in references 4 and 6.

The flow in a slotted-wall tunnel is depicted in figure 1. The tunnel has a height of 2h. The coordinates in the free-stream and vertical directions are x and y, respectively. The angle which a streamline makes with respect to the free-stream direction is θ. Longitudinally slotted walls are located between the tunnel and the plenum. A cross section of these walls is shown on the right-hand side of figure 1. The slot width is δ and the slot spacing is a.

The flow model for slotted walls is obtained from the ideal slot condition, which states that the static pressure at the slot is equal to the plenum pressure. The boundary condition which results is

$$C_{p,w} = 2k \frac{\partial \theta_w}{\partial x/h} \tag{1}$$

where $C_{p,w}$ and θ_w are the pressure coefficient and flow angle in the tunnel near the wall, and k is the flow-model parameter. This parameter is a function of tunnel geometry.

Interference Effects

The next step of the analysis procedure is to determine the interference effects for various values of the flow-model parameter k. Baldwin, Turner, and Knecthel (ref. 2) and Wright (ref. 3) determined these effects for two-dimensional flow theoretically using the boundary condition given in equation (1). A comprehensive treatment of wall interference effects is given by Pindzola and Lo (ref. 7).

The downwash and blockage interference along the center line of two-dimensional slotted-wall wind tunnels is presented in figure 2. It should be noted that the downwash interference is the effect of the wall on the velocity component perpendicular to the free-stream direction, and the

blockage interference is the effect of the wall on the velocity component in the free-stream direction. The distance x has been made nondimensional with the quantity βh. The model depicted in figure 2 is scaled for a tunnel-height—model-chord ratio of 4, which is a typical value for two-dimensional transonic testing, and a free-stream Mach number of 0.85.

Consider the downwash effect first. It can be seen that this effect decreases from front to rear on a model in a closed tunnel ($k = \infty$) and increases from front to rear on a model in an open tunnel ($k = 0$). In both cases, the variation of downwash along the model is substantial for the case depicted in the figure. It can also be seen that, if the flow-model parameter k has a value of about 1.5, the downwash effect is almost constant along the model and for some distance ahead of and behind it. If this value of the flow-model parameter could be obtained, the streamline-curvature effect would be negligible, and a constant-downwash correction would suffice.

Now consider the blockage effect. Note that this effect is symmetric about the model location for slotted walls. (This is not the case for porous walls.) It can be seen that the blockage effect near the model is positive for a closed tunnel ($k = \infty$) and negative for an open tunnel ($k = 0$). This observation indicates that this effect causes the flow to speed up as it passes a model in a closed tunnel and slow down as it passes a model in an open tunnel. It can also be seen that, if the flow-model parameter k has a value of about 1.2, the blockage effect at the origin is zero. In addition, it can be observed that the average blockage effect along the model will be zero if the value of k is slightly larger than 1.2. It is concluded that both streamline-curvature and blockage effects can be minimized effectively if the flow-model parameter has a value of about 1.5.

Flow-Model Parameter

The last step of the analysis procedure is to evaluate the flow-model parameter k for a particular wall geometry. This parameter is usually written in the form

$$k = \frac{c}{h} K \tag{2}$$

where K is the slotted-wall coefficient. A theoretical solution for the coefficient K was obtained independently by Davis and Moore (ref. 1); Baldwin, Turner, and Knecthel (ref. 2); and others. This solution, which is depicted in figure 3, is for flat walls with sharp-edged slots. A different theoretical solution was developed by Chen and Mears (ref. 8). Barnwell (ref. 9) corrected an error in the solution of Chen and Mears and showed that the corrected solution, which is shown in figure 3, differs from that of Davis and Moore because the wall associated with the corrected solution of Chen and Mears is curved and has rounded slot edges. It should be noted that both of the solutions depicted in figure 3 are functions of the

tunnel-wall openness ratio δ/a and are independent of the slot-spacing—tunnel-semiheight ratio a/h.

Only three experimentally determined values for the slotted-wall coefficient K (refs. 8, 10, and 11) are known to have been published prior to this conference. These values are depicted with solid symbols in figure 3. A fourth experimental value can be inferred from the unpublished results of J. Osborne[1]. All four of these experiments were performed with symmetrical, nonlifting models. However, the Mach numbers and Reynolds numbers differ considerably.

It can be observed from figure 3 that the experimental data are self-consistent, and that neither of the theories agrees with the data. In fact, the values obtained from the most widely used theory, that of Davis and Moore, are consistently about one-fourth as large as the corresponding experimental values. In this paper, values for the slotted-wall coefficient K are obtained from the experimental data rather than from theory.

It should be noted that Everhart and Barnwell (ref. 6) have conducted a parametric study which has substantially increased the experimental data for the coefficient K. These data have the same type of dependence on the openness ratio δ/a shown in figure 3. However, the new data also indicate a dependence on the slot-spacing—tunnel-semiheight ratio a/h.

LOW-INTERFERENCE DESIGN

The procedure described in the previous section has been used to design a low-interference wall for the Langley 6- by 28-inch transonic wind tunnel. The data for the coefficient K shown in figure 3 rather than those presented in reference 6 were used in the design because the experiment described in reference 6 had not been performed then.

In the discussion of figure 2, it was concluded that the flow-model parameter k for a minimum-interference tunnel has a value of about 1.5. The designer must choose the number of slots the wall will have. Once this choice is made, the value of the slotted-wall coefficient K can be obtained from equation (2), and the value of the wall openness ratio δ/a can be obtained then from figure 3. Results for one, two, and four slots are given in the table below. On the basis of these results, the design involving one

Number of slots	K	Openness ratio
1	3.5	0.05
2	7	0.02
4	14	Very small

[1]Aerodynamics Department, Royal Aircraft Establishment.

slot was chosen. This choice was based on a desire to keep the crossflow in the slot from becoming sonic and choking as a result. Since the crossflow in the slot varies inversely with the openness ratio (see ref. 4), it is desirable to keep the openness ratio relatively large.

It should be noted that a minimum-interference tunnel would not be feasible if the theory of Davis and Moore were correct because that theory indicates that the slot openness ratio would have to be much less than 0.01 even for a one-slot configuration. This small an openness ratio would definitely exhibit the choked-crossflow behavior discussed above.

In figure 4, the results of theory and experiment for the wall-induced downwash in the Langley 6- by 28-inch transonic tunnel are compared. The results for the new wall and the previous wall (ref. 12) are depicted with a square and a circle, respectively. The experimental values were determined from comparisons of lift curves obtained in the 6- by 28-inch transonic tunnel and the Langley low-turbulence pressure tunnel. The latter tunnel is closed and hence should have no lift interference due to the top and bottom walls except that caused by streamline curvature. The closed-tunnel data were corrected for streamline-curvature effects with the method of Allen and Vincenti (ref. 13).

WIND-TUNNEL CALIBRATION

In general, either the plenum pressure or an upstream pressure is used as a reference for the calibration of transonic wind tunnels. Results are presented in figure 5 which show that the presence of a model can influence the plenum pressure and thus make its use as a reference pressure unreliable. The data presented in the figure were obtained by Everhart and Barnwell during the course of the experiment described in reference 6. The data shown are the Mach number based on plenum pressure M_{PLENUM} and the Mach number distribution along an orifice row on the tunnel sidewall near the top wall. This orifice row is one of those depicted schematically in figure 2 of reference 6.

Results are presented for two Mach numbers based on plenum pressure both with and without the model in the tunnel. It can be seen that for $M_{PLENUM} \approx 0.9$, the presence of the model causes M_{PLENUM} to increase relative to the upstream Mach number in the tunnel by approximately 0.03. For $M_{PLENUM} \approx 0.7$, the incremental increase in M_{PLENUM} due to model presence is reduced to about 0.01. Apparently, the plenum pressure is influenced by the flow through the slot, and this flow is influenced by the presence of the model. At transonic speeds the influence of the model is stronger at the wall and the effect on the plenum pressure is greater. It is concluded that, for this tunnel configuration at least, the pressure at an upstream orifice should be used as a calibration reference pressure.

SIDEWALL BOUNDARY-LAYER EFFECT

There are very few experiments which show quantitatively the effect of the sidewall boundary layer on the flow in the tunnel. One such experiment has been performed in the ONERA RICh wind tunnel (ref. 5), which is shown schematically in figure 6. Although this tunnel has porous top and bottom walls and a transonic capability, the experiment described here was performed with $M_\infty \approx 0.3$ and solid top and bottom walls. The tunnel is equipped with porous sidewalls and sidewall plena to which suction can be applied.

The experiment consisted of the measurement of the normal force on a model at a fixed angle of attack for different sidewall boundary-layer thicknesses. First, the sidewall boundary layer was measured near the model station in an empty tunnel for various values of the sidewall suction rate. Then the model was inserted and the chordwise pressure distribution was measured for the same values of the suction rate. The normal-force coefficients obtained from these pressure distributions are plotted in terms of the nondimensional tunnel-empty displacement thickness on the right-hand side of the figure. As pointed out in reference 5, the dependence of the normal-force coefficient on the displacement thickness is linear. It can be seen that, for this experiment, the apparent normal-force coefficient for zero sidewall displacement is about 10 percent greater than the normal-force coefficient for no suction.

This lift reduction may be due to the manner in which lift influences the growth of the boundary layer on the sidewall of the tunnel near the model. The effect of lift is to increase the flow speed above the model and reduce it beneath. Above the model the increased flow speed causes the sidewall boundary layer to thin somewhat so that the effective cross-sectional area above the wing is increased slightly. Consequently, the airspeed above the model is somewhat less than that for true two-dimensional flow so that the pressure on the suction side is slightly too high. Beneath the model, the opposite effects occur so that the pressure on the compression side is a little too low. The effect of reducing both the suction above the model and the compression beneath the model is to reduce the lift.

CONCLUDING REMARKS

A procedure for designing slotted walls for transonic wind tunnels has been developed. The measured downwash in a two-dimensional tunnel equipped with slotted walls designed with this procedure is in good agreement with the predicted value. Experimental results are presented which show that the plenum pressure is influenced by the presence of a model in the tunnel. It is concluded that the plenum pressure is not always a reliable calibration reference pressure. An ONERA experiment which shows the effect of the sidewall boundary layer on the measured model normal force is discussed, and a possible explanation for the observed effect is presented.

REFERENCES

1. Davis, Don D., Jr.; and Moore, Dewey: Analytical Studies of Blockage- and Lift-Interference Corrections for Slotted Tunnels Obtained by the Substitution of an Equivalent Homogeneous Boundary for the Discrete Slots. NACA RM L53E07b, 1953.

2. Baldwin, Barrett S.; Turner, John B.; and Knecthel, Earl D.: Wall Interference in Wind Tunnels With Slotted and Porous Boundaries at Subsonic Speeds. NACA TN 3176, 1954.

3. Wright, R. H.: The Effectiveness of the Transonic Tunnel as a Device for Minimizing Tunnel-Boundary Interference for Model Tests at Transonic Speeds. AGARD Report 294, 1959.

4. Barnwell, Richard W.: Design and Performance Evaluation of Slotted Walls for Two-Dimensional Wind Tunnels. NASA TM 78648, 1978.

5. Bernard-Guelle, R.: Influence of Wind Tunnel Wall Boundary Layers on Two-Dimensional Transonic Tests. Paper presented at 12th Applied Aerodynamics Colloquium, ENSMA/CEAT-Poitiers, Nov. 5-7, 1975, ONERA, 1976, pp. 1-22. (Available as NASA TT F-17,255.)

6. Everhart, Joel L.; and Barnwell, Richard W.: A Parametric Experimental Study of the Slotted-Wall Boundary Condition. Advanced Technology Airfoil Research, Volume I, NASA CP-2045, Pt. 2, 1979. (Paper 30 of this compilation.)

7. Pindzola, M.; and Lo, C. F.: Boundary Interference at Subsonic Speeds in Wind Tunnels With Ventilated Walls. AEDC TR-69-47, U.S. Air Force, May 1969.

8. Chen, C. F.; and Mears, J. W.: Experimental and Theoretical Study of Mean Boundary Conditions at Perforated and Longitudinally Slotted Wind Tunnel Walls. AEDC TR-57-20, U.S. Air Force, Dec. 1957.

9. Barnwell, Richard W.: Improvements in the Slotted-Wall Boundary Condition. Proc. of AIAA Ninth Aerodynamic Testing Conf., June 1976, pp. 21-30.

10. Baronti, P.; Ferri, A.; and Weeks, T.: Analysis of Wall Modification in a Transonic Wind Tunnel. Advanced Technology Laboratories TR-181, Feb. 1973.

11. Berndt S. B.; and Sörensén, H.: Flow Properties of Slotted Walls for Transonic Test Sections. AGARD Conf. Proc., no. 174, paper no. 17, 1975.

12. Ladson, Charles L.: Description and Calibration of the Langley 6- by 28-Inch Transonic Tunnel. NASA TN D-8070, 1975.

13. Allen, H. Julian; and Vincenti, Walter G.: Wall Interference in a Two-Dimensional-Flow Wind Tunnel, With Consideration of the Effect of Compressibility. NACA TR 782, 1944.

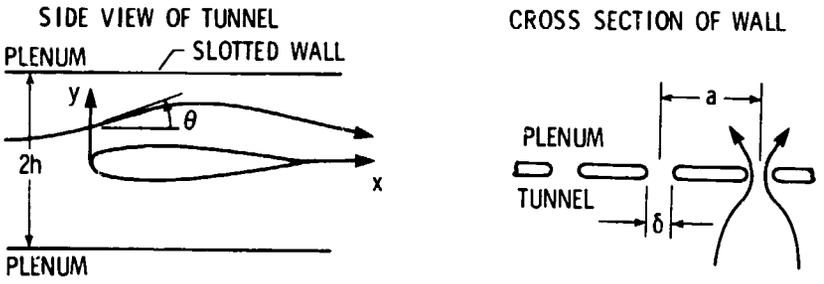

Figure 1.- Flow in slotted-wall tunnel.

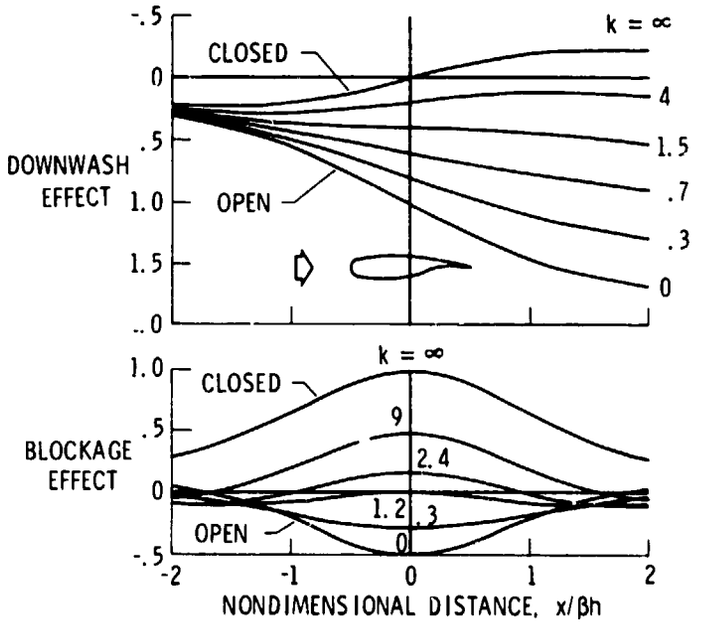

Figure 2.- Two-dimensional slotted-wall interference along tunnel center line.

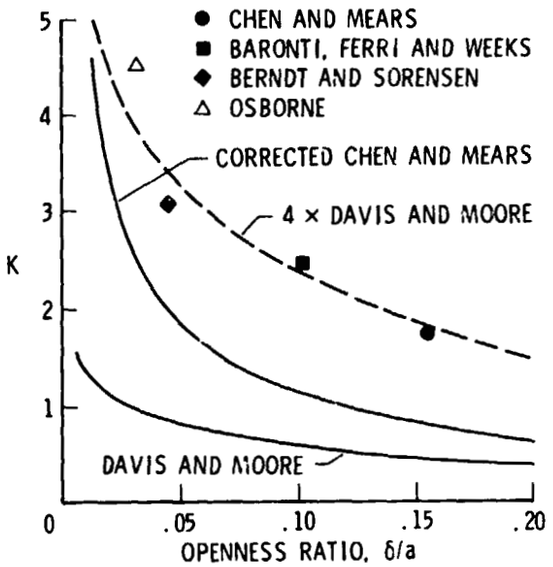

Figure 3.- Slotted-wall coefficient.

WALL-INDUCED DOWNWASH: THEORY AND EXPERIMENT

LANGLEY 6- BY 28-INCH TRANSONIC TUNNEL

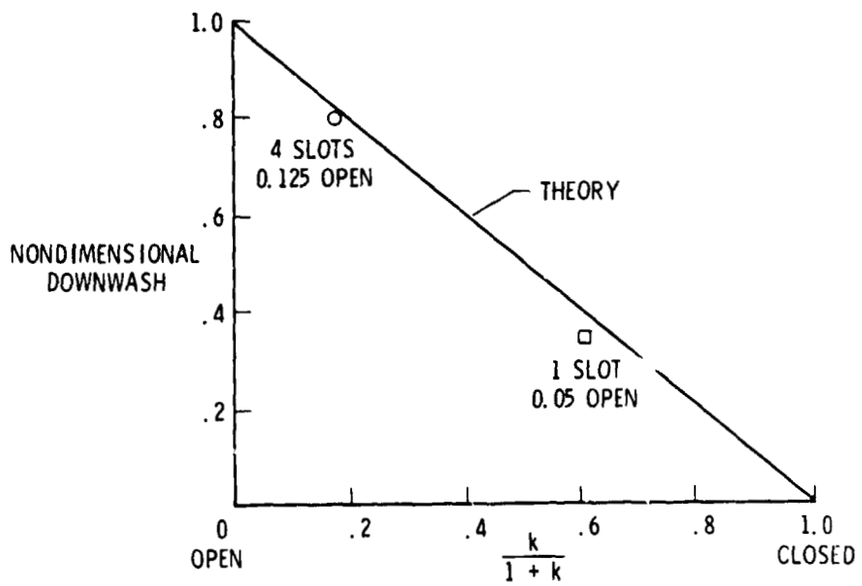

Figure 4.- Comparison of theory and experiment for wall-induced downwash in the Langley 6- by 28-inch transonic tunnel.

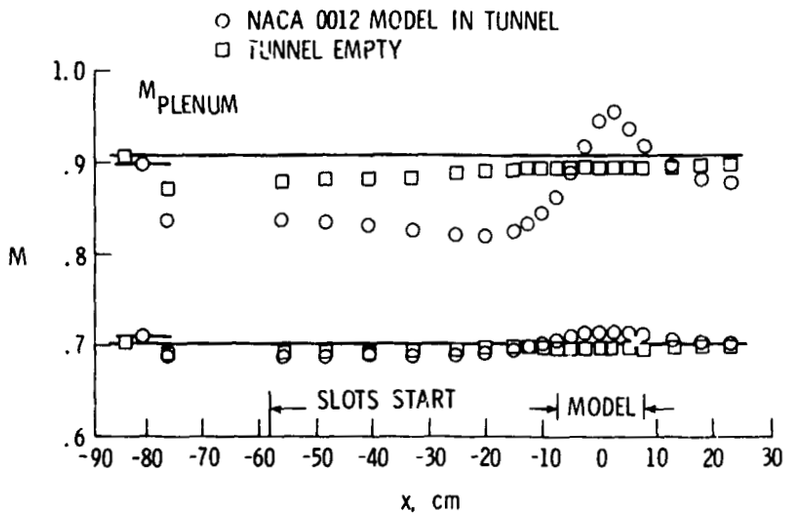

Figure 5.- Mach-number distribution on sidewall and Mach number based on plenum pressure for experimental configuration of Langley 6- by 19-inch transonic tunnel. Two slots; wall openness ratio, 0.05.

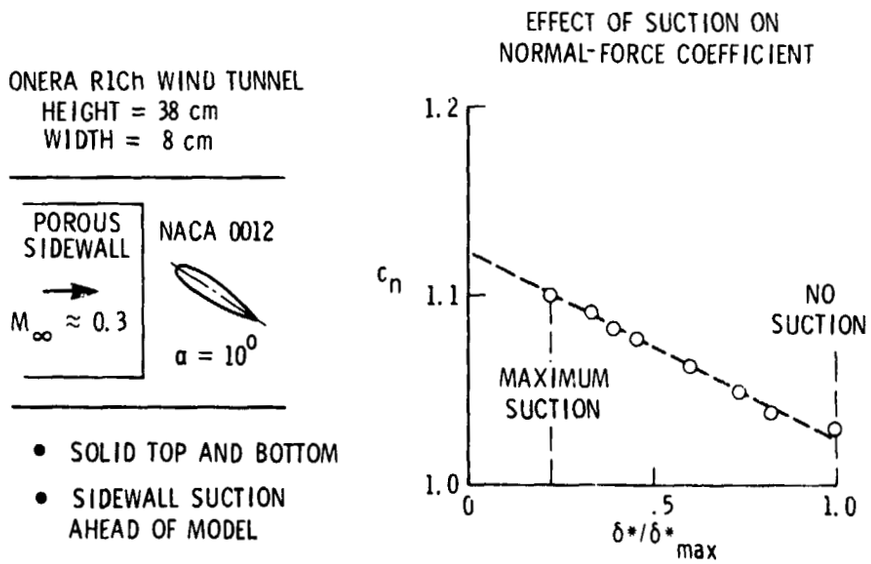

Figure 6.- Effect of sidewall boundary layer on model normal-force coefficient.

PROGRESS REPORT: SOME STEADY AND OSCILLATING AIRFOIL TEST RESULTS, INCLUDING THE EFFECTS OF SWEEP, FROM THE TUNNEL SPANNING WING

Franklin O. Carta and Arthur O. St. Hilaire
United Technologies Research Center

James B. Rorke and W. Donald Jepson
Sikorsky Aircraft Division
United Technologies Corporation

SUMMARY

A large scale tunnel spanning wing has been built and tested. The model can be operated as either a swept or unswept wing and can be tested in steady state or oscillated sinusoidally in pitch about its quarter chord. Data is taken at mid-span with an internal 6-component balance and is also obtained from miniature pressure transducers distributed near the center span region.

This paper presents a description of the system and a brief discussion of some of the steady and unsteady results obtained to date. These are the steady load behavior to Mach numbers of approximately 1.1 and unsteady loads, including drag, at a reduced frequency of approximately 0.1.

INTRODUCTION

It has long been recognized that conventional two-dimensional aerodynamic testing is not adequate for helicopter rotor blade applications. A typical section of the blade is simultaneously subjected to wide variations in Mach number, skew angle, and incidence angle, and all of these variations are both spatial and temporal. It is obvious that a traditional two-dimensional steady state test program can only satisfy a few of the quasi-steady needs of the designer, and even a sophisticated two-dimensional unsteady test is severely limited to incidence angle variations of the typical section. In recognition of this need for a test facility specifically geared to helicopter applications, United Technologies Corporation, through the combined efforts of its Sikorsky Aircraft Division and its Research Center (UTRC), has developed a minimum wall interference approach to obtaining airfoil aerodynamic data in the wind tunnel. Data are being obtained for both steady and unsteady pitching motions, both in oblique and conventional flow, over a wide range of Mach numbers and at representative full scale Reynolds numbers, using the same airfoil model and its associated measurement systems. The purpose of this paper is to present a brief description of the facility and its mode of operation and to discuss some of the results obtained to date.

SYMBOLS

Values are given in both SI and U.S. Customary Units. The measurements and calculations were made in U.S. Customary Units.

b	semichord, m
C_L, C_D, C_M	lift, drag, and pitching moment coefficient
C_N, C_c	normal and chord force coefficient
f	frequency, cycles/sec
k	reduced frequency
M	Mach number
r/R	span ratio
R_N	Reynolds number
V	velocity, m/sec
α	instantaneous incidence angle
α_M	mean incidence angle
$\Delta\alpha$	amplitude of motion
Λ	wing sweep angle
μ	rotor advance ratio
ψ	rotor azimuth angle
ω	frequency, rad/sec
$( )_N$	value taken normal to span
$( )_\infty$	free stream value

FACILITY DESCRIPTION

The wide range of parameter variations encountered in rotor craft is indicated by the plots in figs. 1 and 2. In fig. 1 a typical spanwise variation of lift coefficient as a function of Mach number for several blade attitudes (including hover) is superimposed on two operating conditions of concern to the designer, the drag divergence region and the potentially dangerous condition involving severe stall. (Note that the C_L peak near the blade tip in hover is caused by a trailing vortex encounter). Similarly, typical contours of constant skew angle (solid lines) and constant Mach number (dashed lines) are superimposed on a rotor disk in fig. 2. It is seen that the high load conditions are generally encountered at moderate Mach numbers on the retreating side of the disk, but that a need exists for high Mach number data as well. Furthermore, the effective blade sweep angle is zero only at azimuth angles of $\psi = 90^\circ$ and 270° and is 15° or greater over 60 percent of the rotor disk (as shown by the shaded region in fig. 2).

The first step in responding to these clearly defined needs was to build a versatile steady-state facility. The resulting Tunnel Spanning Wing system (TSW) was constructed by Sikorsky Aircraft in 1971. It consists of a basic tunnel spanning rectangular steel spar approximately 2.44 m (8 ft) in length, plus additional end pieces to complete the spar for installation at several available sweep angles or for installation in different wind tunnels with a test section that has one dimension at least 1.83 m (6 ft). Interchangeable airfoil-shaped shells with 40.64 cm (16 in) chord are mounted in sections onto the spar to provide the test configuration. A schematic view of this system is shown in fig. 3. It is seen that the model shell consists of two sets of pieces: the upper portions which surround the spar fore and aft, and the lower cover plates which complete the airfoil profile. Also shown in fig. 3 is the center span metric section, 20.32 cm (8 in) in width, which mounts to a pair of completely enclosed strain gage balances. This allows the airloads to be measured far from the tunnel side walls and ceiling. With this system it is possible to test several airfoil profiles in a single installation by replacing one set of model shells with another. The nominal chord length of 40.64 cm (16 in) allows data to be obtained at representative full scale Reynolds numbers and at a favorable tunnel height to chord ratio of 5.25 or greater for the tests conducted to date.

In addition to the internal balance in the metric section, two surface pressure tap systems are incorporated, arrayed principally in a chordwise direction. One system was originally installed along the centerline of the metric section to measure only steady state pressures for comparison with balance results. A second system was later installed in the model shell immediately adjacent to the metric section to measure both steady and oscillatory loads. As part of this system, some additional spanwise taps were included to measure spanwise loading and are so arrayed to relate the effects

of chordwise and streamwise surface pressure distributions when testing in oblique flow. Thus, the TSW incorporates dual airloads measurement systems which are redundant over a wide range of the test envelope and, together, are used as a data self-checking system. Hot film skin friction gages have also been included to assess the surface flow conditions in steady and oscillatory situations. A description of models and results of steady tests are presented in reference 1; the unsteady tests, not yet published, were performed by F. O. Carta at United Technologies Research Center (UTRC) under NASA Contract NAS 1-14873.

The TSW has been tested by the Navy and Sikorsky Aircraft in the NSRDC 2.13 m x 3.05 m (7ft x 10ft), 12 percent permeable transonic wind tunnel at zero sweep angle up to a maximum Mach number of M = 1.1 (ref. 1). The 3.06 m (10ft) span model installation is pictured in fig. 4. In this figure are shown a pair of part span supports from the tunnel floor to the model pressure surface. Tests with and without the struts installed showed conclusively that these supports had a negligible effect on the measured data. (The round object in the lower right corner of the tunnel was a part of the NSRDC sting mount system located several meters behind the TSW, and had no effect on the results). The Mach number/incidence angle and Mach number/Reynolds number envelopes achieved in these tests are shown in fig. 5. For comparison, a typical rotor envelope for a dive/pull-up maneuver is compared with the NSRDC M/α test envelope in the left panel, and the test range (dashed region) is compared with typical M/R_N variations for three helicopters in the right panel. It is believed that the test envelope represents some of the widest combinations of M and α achieved to date in a wind tunnel with a model having a full scale chord, and at conditions well above critical Reynolds number range.

A cooperative effort by UTRC and Sikorsky Aircraft has yielded the oscillatory system shown schematically in its unswept position in fig. 6. This system consists of a drive motor and transmission mounted beneath the UTRC 2.44 m (8ft) octagonal wind tunnel, which actuates a pair of push rods and oscillatory cranks to provide a sinusoidal motion of the model about its quarter chord (ref. 2). A swept, oscillating installation in the UTRC tunnel at $\Lambda = 30^\circ$ is pictured in fig. 7, looking upstream. In this test, one-third span supports were employed from both ceiling and floor of the tunnel to pivots located in the model spar. These were installed to overcome oscillatory bending deflections resulting from a small chordwise noncoincidence of model c.g. and pivot axis. (Note that the model was originally designed for steady testing only.) Steady-state oil flow studies have demonstrated that only a small portion of the airfoil surface area aft of the quarter chord was affected in the immediate vicinity of the supports, and that the effect on the center span flow was negligible. Oscillatory tests at $\Lambda = 30^\circ$ have been conducted at freestream Mach numbers as high as $M_\infty = 0.58$, and at reduced frequencies up to $k_N = b\omega/V\cos\Lambda = 0.1$ over a wide range of incidence angles and at amplitudes of $\pm$ 8 and $\pm$ 10 deg.

Testing was also conducted at $\Lambda = 45^{o}$ in steady state by Sikorsky Aircraft in the UTRC tunnel. This installation is pictured in fig. 8 as viewed from above. In this sequence of steady-state tests the model was subjected to a free stream Mach number as high as $M_{\infty} = 0.83$. or a normal to span Mach number of $M_N = M_{\infty}\cos\Lambda = 0.59$.

TEST RESULTS

A typical set of steady-state test results for the Sikorsky Aircraft SC-1095 airfoil are found in figs. 9, 10, and 11, obtained in the NSRDC tunnel (ref. 1). These figures contain the lift coefficient versus incidence angle, and the drag and pitching moment coefficients plotted as a function of lift coefficient for a wide range of Mach numbers from M = 0.3 to 1.075. The solid curves were obtained from balance measurements and the dashed curves are from integrated surface pressure and wake rake measurements. The flagged symbols represent repeat points. The internal balance measurement system was initially included for this type of testing to obtain drag data at high Mach numbers where compressibility effects preclude use of a wake rake. The several curves in each figure are plotted relative to a staggered set of origins, indicated by tic marks and zeroes along the left ordinate. The scale for the M = 0.3 curve is shown on the right ordinate. These figures show that all data exhibited excellent repeatability and data from both systems generally substantiated one another concerning the trends of he force coefficients with incidence angle and Mach number. The lift data from these separate measurement systems were in close agreement. The drag data from both systems were very similar, but at 0.9 Mach number the wake rake values were lower due to turbulent flow and/or compressibility effects. The pitching moment data from both systems were generally in agreement; however, at some conditions the balance coefficient data were more positive by + 0.015. After correcting for the differences in lift curve slope that occur between a ventilated and a solid wall wind tunnel, these data are in close agreement with the data obtained in UTRC 8 foot solid wall wind tunnel.

A few selected results from the unsteady UTRC tests are shown in figs. 12, 13, and 14 at $M_N = 0.3$ and 0.4 at $\Lambda = 0^{o}$ and 30^{o}. Recalling figs. 1 and 2, it can be seen that these conditions are of primary importance to the rotor designer because they are representative of the flow experienced on the retreating side of the rotor disk where unsteady stall conditions are encountered. In figs. 12 and 13 the results were obtained from integration of the unsteady pressure distributions at each instant of time and in fig. 14 the loads were calculated from the unsteady output of the internal balances.

The effect of varying frequency at constant incidence is shown in fig. 12 for the unswept SC-1095 airfoil. Here a mean incidence angle of $\alpha_M = 12^o$ and an amplitude of $\pm 8^o$ produces periodic penetration of the stall regime, and as expected (refs. 3, 4, and 5), an increase in frequency causes a progressively larger overshoot of both normal force and moment in the dynamic stall regime . In fig. 13 sweep and oscillatory effects are combined. The solid lines represent the unswept configuration and the dashed lines the swept, both for a mean incidence angle of $\alpha_M = 15^o$ and an amplitude of $\pm 8^o$ (measured in the plane normal to the wing leading edge). Although a single sample such as this is insufficient to establish a trend, it is seen that the effect of sweep is to reduce the magnitude of the unsteady excursion through the dynamic stall regime (i.e., sweep appears to "soften" the impact of dynamic stall). It is also interesting to note that for unsteady conditions there is <u>not</u> a further extension of the maximum lift coefficient in oblique flow as is experienced in steady oblique flow.

Finally, fig. 14 shows unsteady lift and drag coefficient variations for the unswept wing at two mean incidence angles as obtained from the balance system. The significant observation to be made here is that, for the moderate Mach numbers tested, the unsteady drag is generally greater for increasing incidence angle and follows a clockwise loop in the high incidence regime, similar to that of the unsteady normal force. This behavior is easily explained by noting that the drag is made up of a vector sum of the normal and chord forces, expressed in component form as

$$C_D = C_N \sin\alpha - C_c \cos\alpha$$

For incidence angles in the range 15^o to 20^o the cosine is approximately three times the sine, but the normal force is at least 10 to 20 times the chord force. Consequently, the $C_N \sin\alpha$ term dominates the equation in the dynamic stall regime and the unsteady drag behaves as shown.

CONCLUDING REMARKS

The TSW concept has been used to demonstrate that a consistent airfoil data bank can be obtained at representative full-scale Reynolds numbers using the same model system for a wide variety of test conditions approaching those that are encountered by rotary wing aircraft. This model system provides a means to minimize wall interference effects and to eliminate the complicating factors introduced by using different airfoil models and load measuring systems required to cover this extensive aerodynamic environment, both steady and unsteady. This paper illustrates the versatility of this system with the few examples presented herein.

REFERENCES

1. Jepson, W. D: Two Dimensional Test of Four Airfoil Configurations with an Aspect Ratio of 7.5 and a 16 Inch Chord up to a Mach Number of 1.1. Sikorsky Engineering Report SER-50977, April 5, 1977, performed under Contract No. N60921-73-C-0057.

2. Carta, F.O. and A. O. St. Hilaire: An Experimental Study of Sweep Effects on the Unsteady Aerodynamics of a Pitching Airfoil. United Technologies Research Center Report R76-411931, March 1976.

3. Carta, F. O. and C. F. Niebanck: Prediction of Rotor Instability at High Forward Speeds. Vol. III. Stall Flutter. USAAVLABS Technical Report 68-18C, February 1969.

4. Liiva, J., F. J. Davenport, L. Gray, and I. C. Walton: Two-Dimensional Tests of Airfoils Oscillating Near Stall. USAAVLABS Technical Report 68-13, 1968.

5. Carr, L. W., K. W. McAlister, and W. J. McCroskey: Analysis of the Development of Dynamic Stall Based on Oscillating Airfoil Experiments. NASA TN D-8382, January 1977.

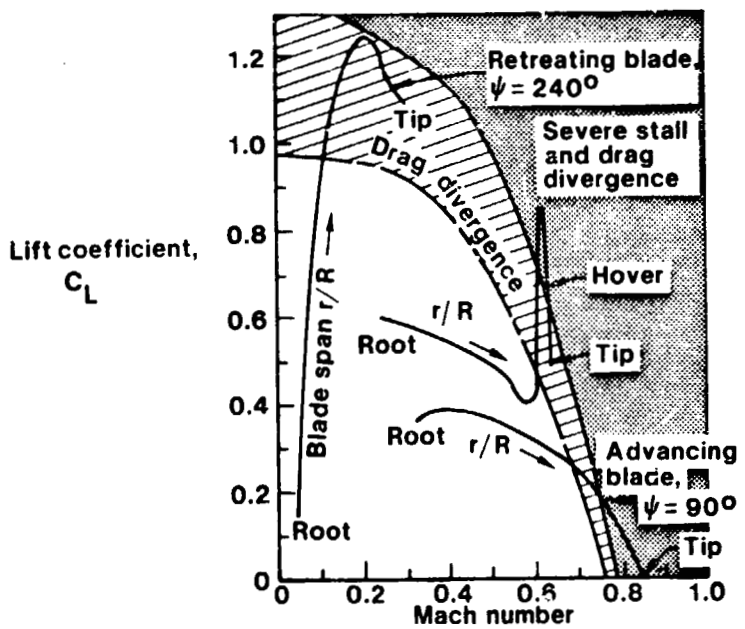

Figure 1.- Operating envelope.

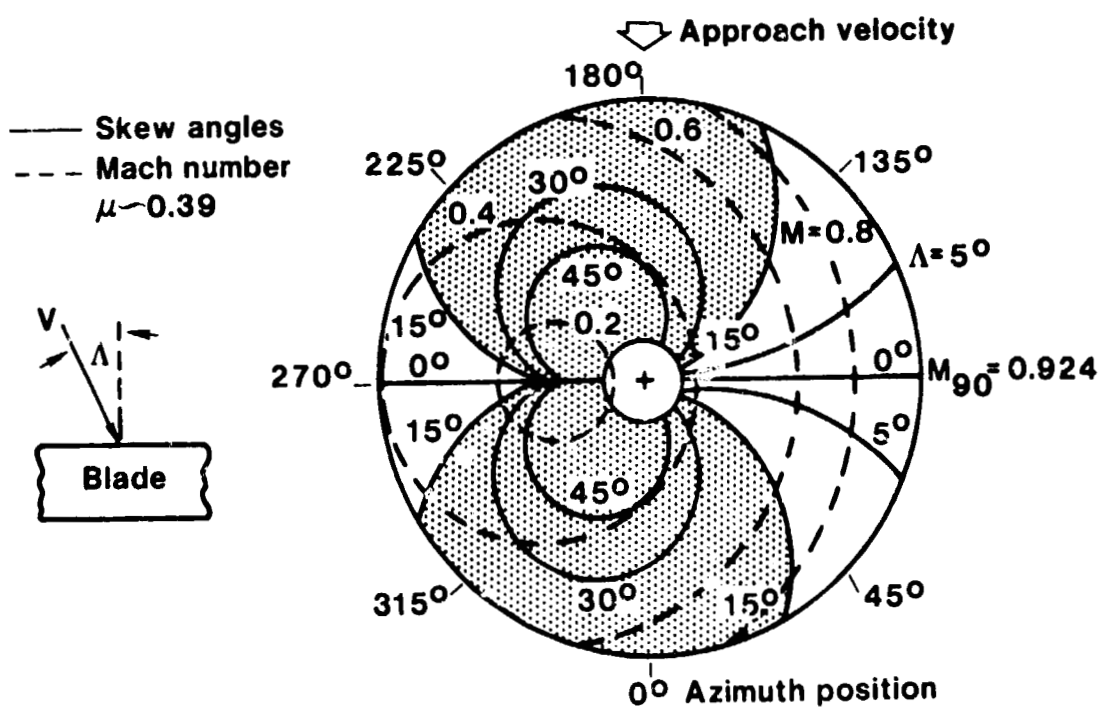

Figure 2.- Contours of skew angle and Mach number.

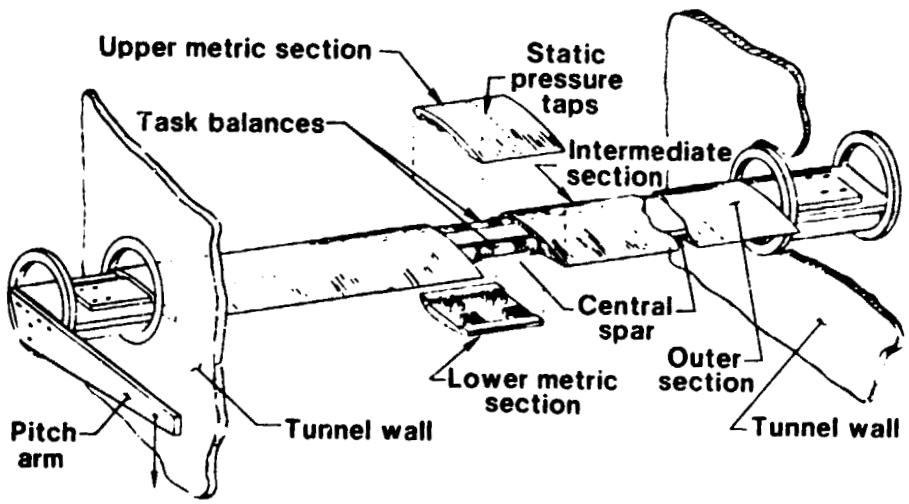

Figure 3.- Tunnel-spanning wing assembly.

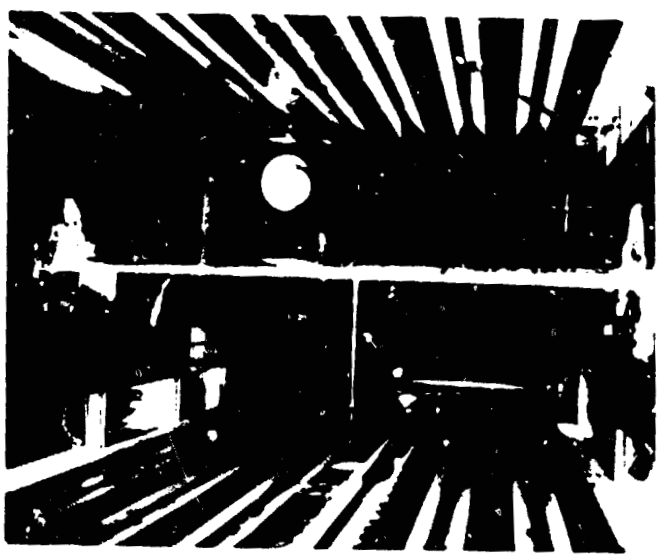

Figure 4.- NSRDC installation. $\Lambda = 0°$.

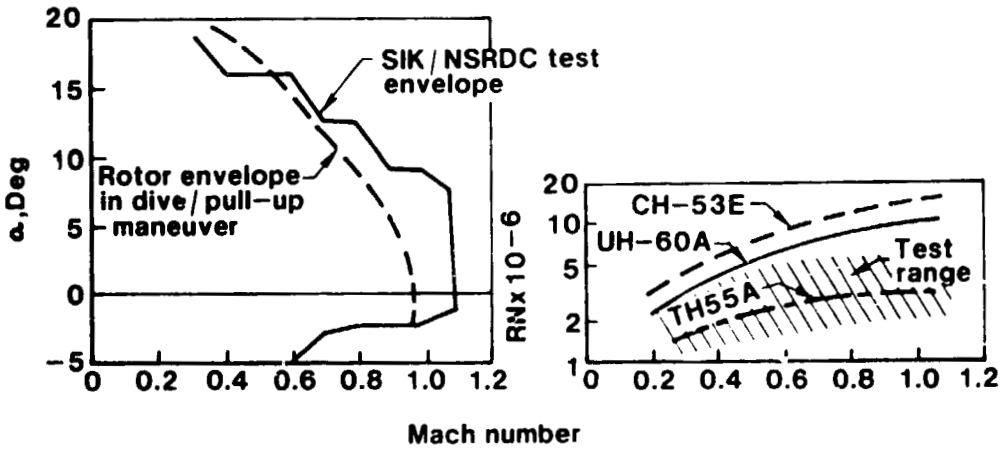

Figure 5.- Comparison of rotor and NSRDC test envelope. Steady state.

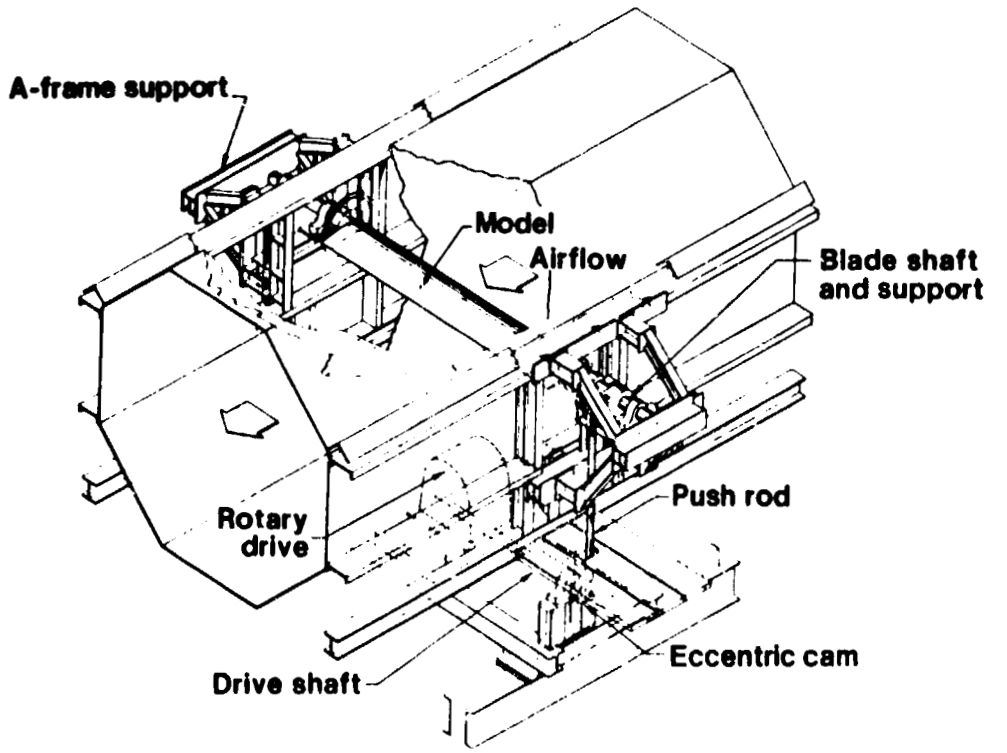

Figure 6.- UTRC main wind-tunnel oscillatory model system.

Figure 7.- UTRC installation. $\Lambda = 30°$.

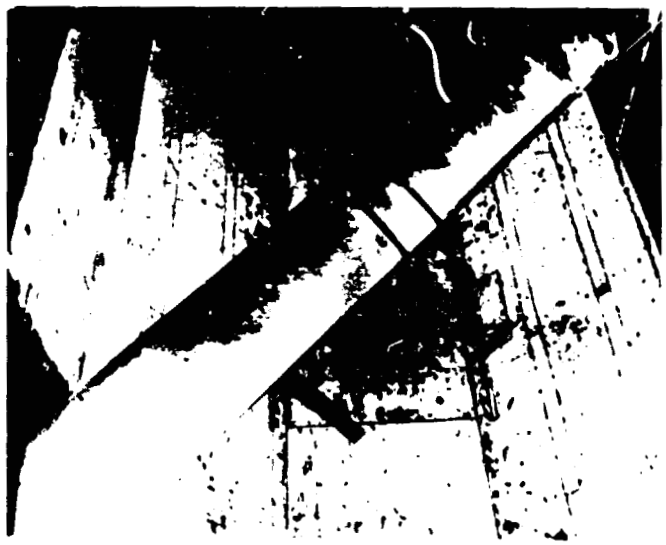

Figure 8.- UTRC installation. $\Lambda = 45°$.

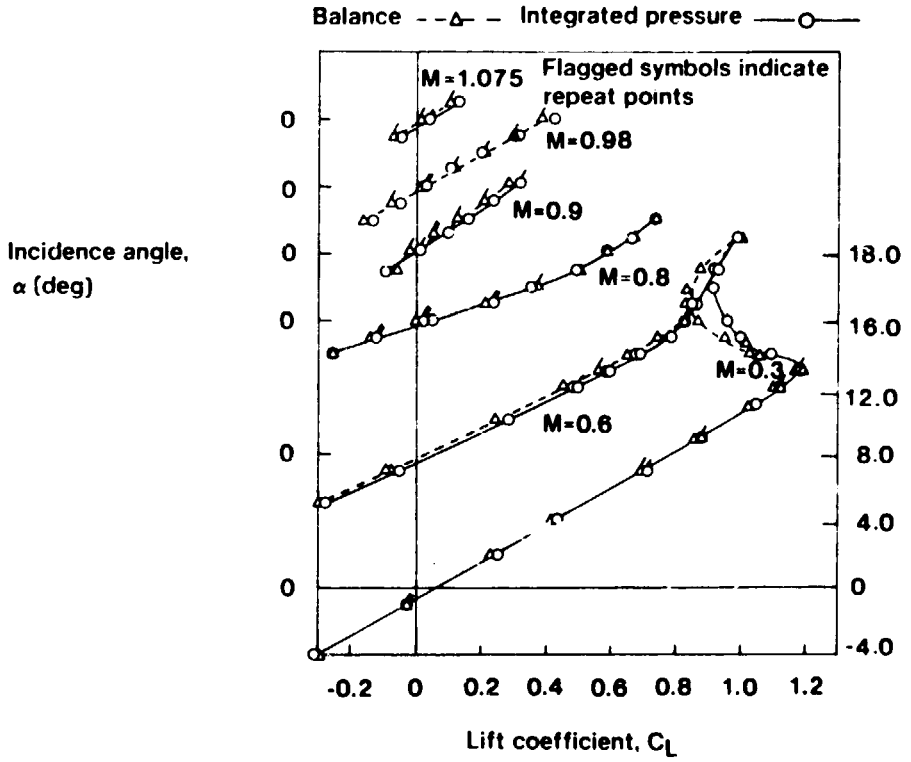

Figure 9.- Steady-state lift coefficient plotted against incidence angle.

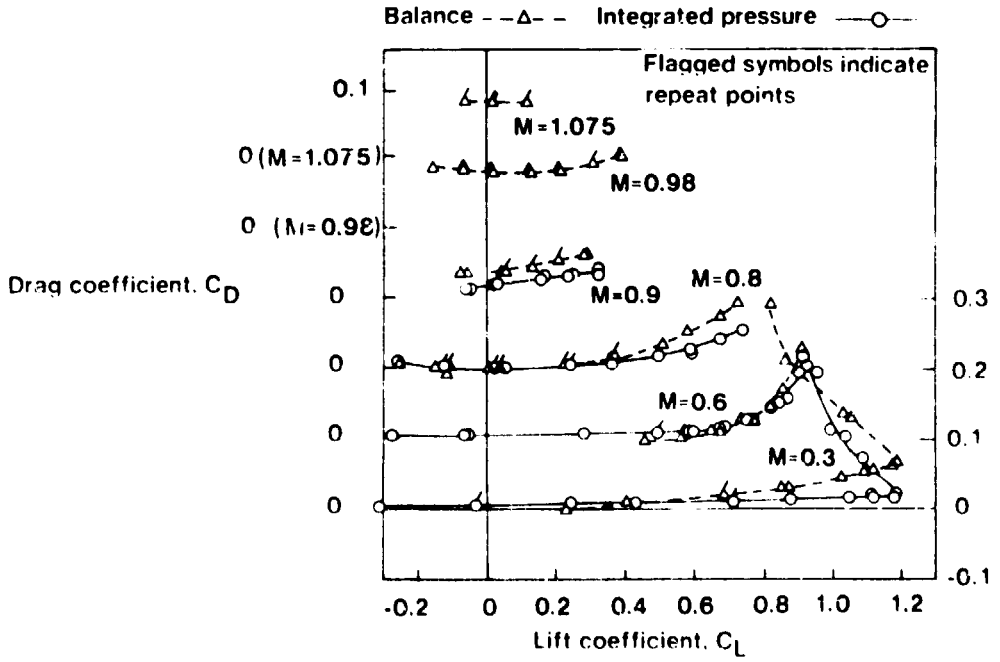

Figure 10.- Steady-state drag coefficient plotted against lift coefficient.

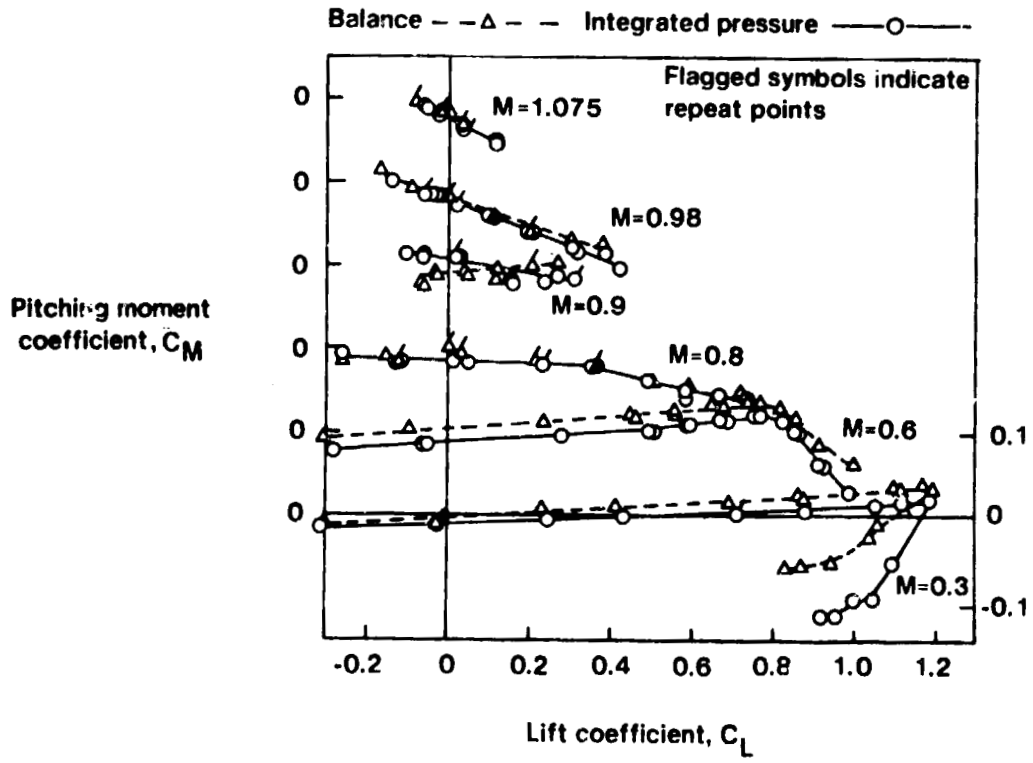

Figure 11.- Steady-state pitching-moment coefficient plotted against lift coefficient.

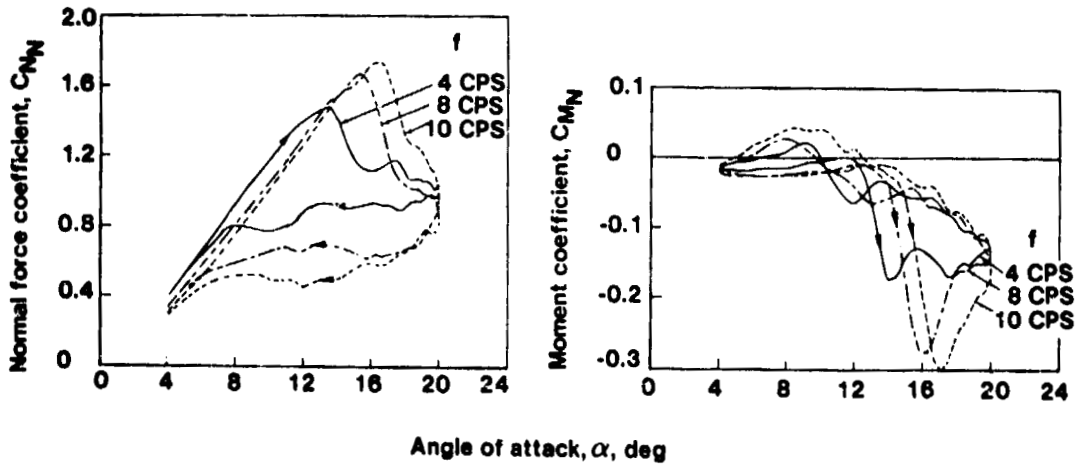

Figure 12.- Effect of frequency on oscillatory normal-force and moment coefficients from integrated pressures. SC-1095 airfoil; M = 0.4; $\Delta\alpha = \pm 8°$; $\alpha_M = 12°$

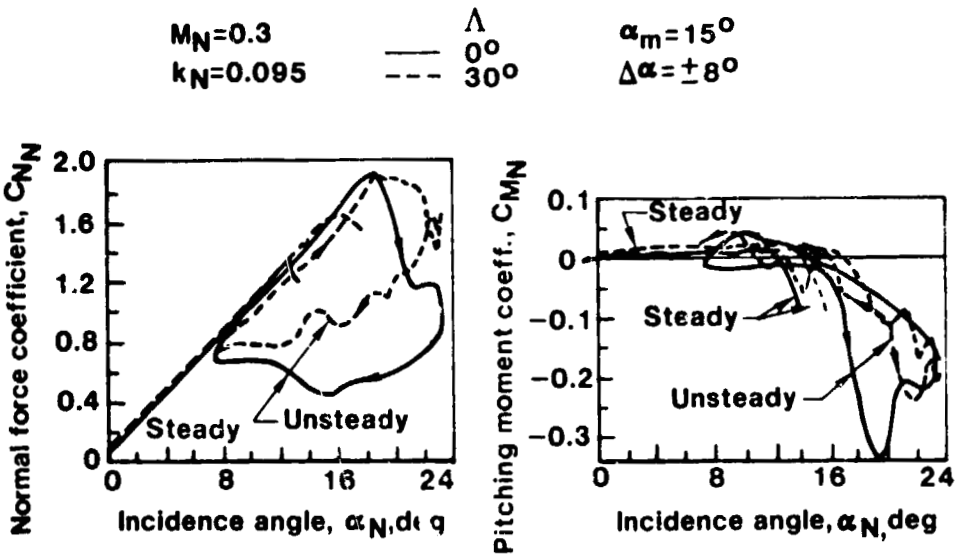

Figure 13.- Effect of sweep on oscillatory lift and moment coefficients from integrated pressures. SC-1095 airfoil.

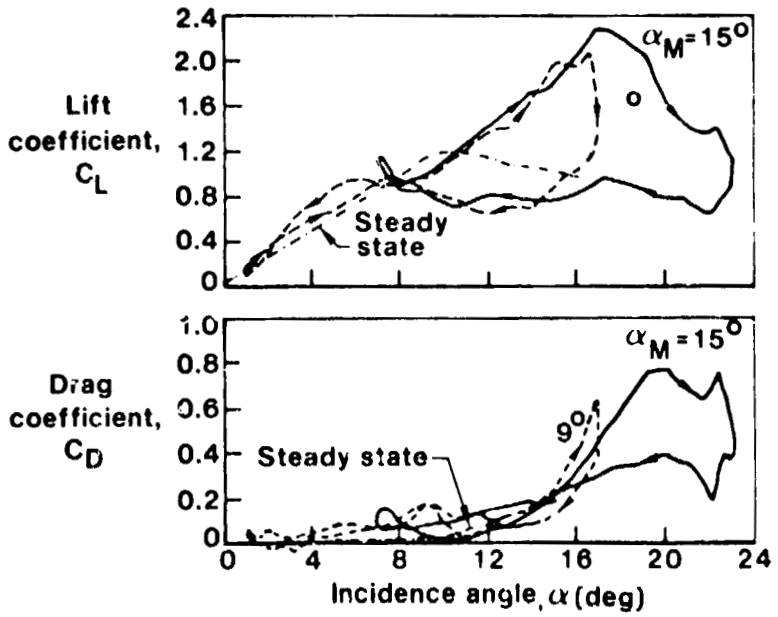

Figure 14.- Unsteady lift and drag coefficients from balance. SC-1095 airfoil; M = 0.3; Λ = 0°; Δα = ±8°; f = 3 cps; k = 0.096.